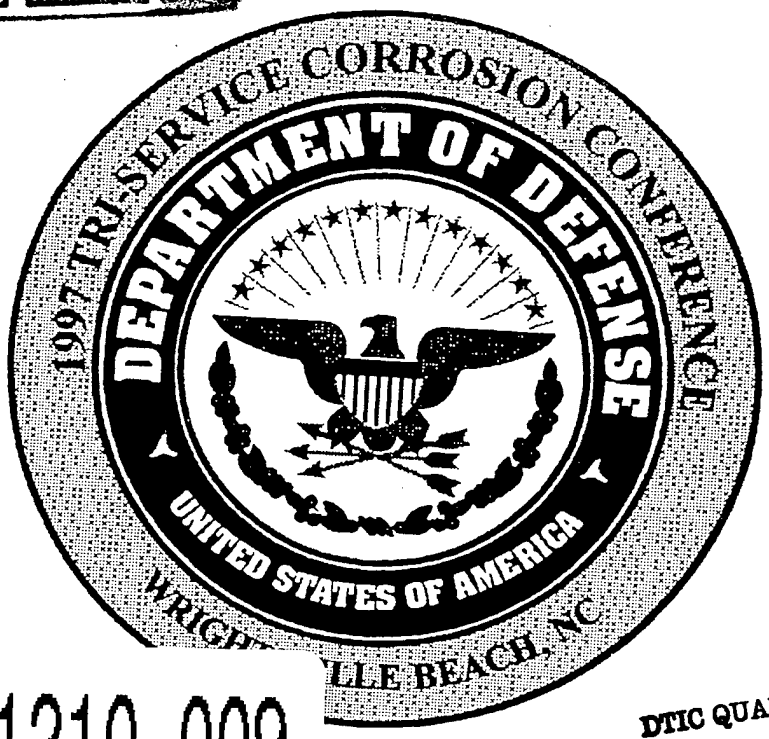
PROCEEDINGS
Vol. I

DISTRIBUTION STATEMENT A
Approved for public release;
Distribution Unlimited



19971210 009

DTIC QUALITY INSPECTED 2

1997 TRI-SERVICE CONFERENCE ON CORROSION

NOVEMBER 17-21, 1997

BLOCKADE RUNNER HOTEL
WRIGHTSVILLE BEACH, NC

Organized by
Naval Surface Warfare Center - Carderock Division

Sponsored by
Office of Naval Research

OFFICIAL PROGRAM



1997 TRI-SERVICE CONFERENCE ON CORROSION

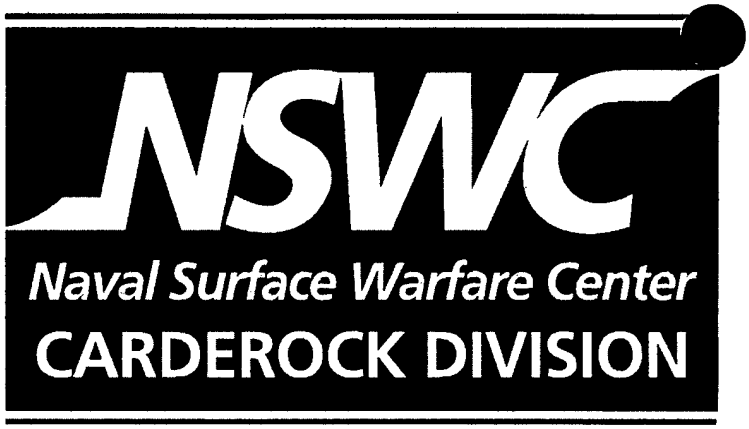
NOVEMBER 17-21, 1997

BLOCKADE RUNNER HOTEL
WRIGHTSVILLE BEACH, NC

Organized by
Naval Surface Warfare Center - Carderock Division

Sponsored by
Office of Naval Research





SPONSORED BY
OFFICE OF NAVAL RESEARCH

ORGANIZED BY
NAVAL SURFACE WARFARE CENTER
CARDEROCK DIVISION

DISCLAIMER

Contents of the papers presented in this proceedings is the sole responsibility of the author. The Survivability, Structure, and Materials Directorate of the Naval Surface Warfare Center - Carderock Division (Naval Sea Systems Command) and the United States Navy accept no responsibility for any consequences that might result from the use of the information presented in this proceedings.

Mention of any trade names or manufacturers in this proceedings shall not be construed as advertising nor as an official endorsement or approval of such products or companies by the United States Government.

The 1997 proceedings of the Tri-Service Conference on Corrosion was prepared under the auspices of the Tri-Service Committee on Corrosion, The Department of Defense. Neither the United States Government nor any person acting on the behalf of the United States Government assumes any liability resulting from the use or publication of the information contained in this document or warrants that such use or publication will be free from privately owned rights.

Approved for public release; distribution unlimited.

TECHNICAL SCHEDULE

	Time		Time	
Sun., 11/16		----	1700-1900	Registration
Mon., 11/17	0800-1200	Registration	1330-1700	Registration
			1315-1530	Service Overviews
NOTE: Presenting authors are required to check-in with their Session Moderator at breakfast (0700-0745) the morning of their respective session.				
Tues., 11/18	0800-1200	#1 - Corrosion Research I	1330-1700	#2 - Corrosion Research II
	0800-1200	#3 - Corrosion Monitoring & Testing I	1330-1630	#4 - Corrosion Monitoring & Testing II
Wed., 11/19	0800-1130	#5 - Understanding & Controlling Different Forms of Corrosion I	1330-1700	#6 - Understanding & Controlling Different Forms of Corrosion II
	0800-1000 1030-1200	#7A -Corrosion Control Methods-Coatings #7B - Preservation of Materials	1330-1630	#8 - Corrosion Control Methods - Surface Treatments/Conversion Coatings
Thurs., 11/20	0800-1130	#9 - Other Corrosion Control Methods	1330-1630	#10 - Materials in Corrosive Environments
	0800-1130	#11 - New Materials Development	1330-1630	#12 - Corrosion Control - Inhibitors
Fri., 11/21	0830-1100	#13 - Life Cycle Issues	1300-1600	NACE T-9 Committee (at LaQue Corrosion Services)

MONDAY, NOVEMBER 17, 1997 — 1315 - 1530 — Lee Room

1315 **Opening Remarks** — *Dr. William T. Messick - Manager, Materials Technology, Carderock Division, NSWC*

1325 **Remarks** — *Robert J. Ferrara - Chair of 1997 Tri-Service Organizing Committee*

1330 **U. S. Navy Overview** — *Dr. Alex I. Kaznoff - Engineering Directorate; Director, Code 03M- NAVSEA, Materials Engineering Group*

1400 **U. S. Army Overview** — *Richard Franke - Associate Director of Engineering Business Group, U.S. Army TACOM/TARDEC*

1430 **U. S. Air Force Overview** — *Major David D. Robertson - Manager, Air Force Corrosion Program Office, Robins AFB*

1500 **U. S. Marine Corps Overview** — *George N. Georgeadis, Head, Systems Engineering Branch, Marine Corps Systems Command*

RECEPTION — 1700 - 1900 — Nighthawk Room
Hors d'oeuvres and Cash Bar

WEDNESDAY, Nov. 19, 1997 0800 - 1130 Lee Room

Sessions 5 and 7 are Concurrent Sessions

Session 5: UNDERSTANDING AND CONTROLLING DIFFERENT FORMS OF CORROSION I

Moderator: ***Denise Aylor - Carderock Division, Naval Surface Warfare Center***

Introduction

0805 **Stress Corrosion Cracking of Naval Structural Alloys,** *R.A. Hays, Proteus Engineering; D.A. Davis, D.M. Aylor, CDNSWC*

0835 **The Effect of Heat Treatment on Hydrogen Trapping in AerMet 100 and Alloy K-500,** *B.G. Pound, SRI International*

0905 **Environment Assisted Fatigue Cracking of AerMet 100 Steel,** *E.U. Lee, K. George, W.E. Frazier, NAWC, Patuxent River, MD*

0935 **Ripple-Load Cracking Sensitivity in Engineering Alloys,** *P.S. Pao, S.J. Gill, R.A. Bayles, NRL; G.R. Yoder, ONR*

Break

1030 **The Fatigue and Corrosion Fatigue Properties of Alloy 625 and 70/30 Copper-Nickel Alloy Electroslag Surfacing,** *E.J. Czyryca, CDNSWC; R.B. Turpin, Oregon Graduate Institute of Science and Technology*

1100 **Role of Aqueous Environment on the Growth of Long Fatigue Cracks,** *A.K. Vasudevan, ONR; K. Sadananda, NRL*

Lunch

WEDNESDAY, Nov. 19, 1997 1330 - 1700 Lee Room

Sessions 6 and 8 are Concurrent Sessions

Session 6: UNDERSTANDING AND CONTROLLING DIFFERENT FORMS OF CORROSION II

Moderator: ***Dr. Harvey P. Hack - Northrup Grumman Corp., Annapolis, MD***

Introduction

1335 **High Strength Fasteners for Seawater Immersion Service,** *D.M. Aylor, C.A. Bowles, R.L. Tregoning, CDNSWC*

1405 **Kinetics of Pitting Corrosion and Effects on Fatigue Behavior of Aluminum Alloy 7075-T6,** *K.V. Jata, WPAFB; K.K. Sankaran, B. Johnson, R. Perez, The Boeing Company*

1435 **Galvanic Corrosion of Tungsten Coupled with Several Metals/Alloys,** *F.C. Chang, J.H. Beatty, M.J. Kane, J. Beck, ARL*

Break

1530 **Effect of Marine Biofilms on Galvanic Corrosion,** *J.P. LaFontaine, S.C. Dexter, University of Delaware*

1600 **New Techniques for Galvanic Corrosion Prevention in Piping Systems,** *D.A. Shifler, CDNSWC, D. Melton, LaQue Corrosion Services; H.P. Hack, Northrup Grumman*

1630 **Noble Metal Additions to Mitigate Hydrogen Embrittlement of Ultra High Strength Steels: Research in Progress** *P.F. Buckley, J.H. Beatty, ARL; P. Searson, Johns Hopkins University*

WEDNESDAY, Nov. 19, 1997 0800 - 1200 Nighthawk Room

Sessions 5 and 7 are Concurrent Sessions

Session 7A: CORROSION CONTROL METHODS - COATINGS

Moderator: ***Karen Poole - Carderock Division, Naval Surface Warfare Center***

Introduction

0805 **Thermal-Spray Coatings for Coastal Infrastructure,** *G.R. Holcomb, B.S. Covino, Jr., S.D. Cramer, S.J. Bullard, DOE; G.E. McGill, Oregon DOT*

0835 **Extending Use of Ion Vapor Deposited (IVD) Aluminum as a Replacement for Electroplated Cadmium,** *B.E. Placzankis, J.H. Beatty, ARL*

0905 **US Navy Coating Alternatives Utilizing Portable Systems,** *Mike Lincoln, COMNAVSURFPAC*

0935 **Functionalized Sol-Gel Conversion Coatings,** *W.E. Dorogy Jr., T. Tiano, M-L Pan, K. Jayaraj, Foster - Miller, Inc.*

Break

Session 7B: PRESERVATION OF MATERIALS

Moderator: ***Dr. Mike Donley - Wright-Patterson AFB***

1030 **Air Force Coatings Technology Integration Office: Operations and Objectives,** *Maj. W.K. Kuhn, WPAFB*

1100 **Utilities Engineered Management Systems: Maximizing the Impact of Limited Maintenance and Repair Resources,** *V. Van Blaricum, U.S. Army CERL*

1130 **Bonded Repairs for Corrosion Damage,** *A.P. Kerr, Advanced Repair Technology International*

Lunch

WEDNESDAY, Nov. 19, 1997 1330 - 1630 Nighthawk Room

Sessions 6 and 8 are Concurrent Sessions

Session 8: CORROSION CONTROL - SURFACE TREATMENTS/CONVERSION COATINGS

Moderator: ***Richard Kinzie - Robins AFB***

Introduction

1330 **Advanced Zinc Phosphate Conversion Coatings,** *I.C. Handsy, TACOM; T. Sugama, Brookhaven National Laboratory*

1400 **A Chromate-Free Chemical Conversion Coating for Aluminum and Steel Alloys,** *J.F. McIntyre, W.J. Claffey, R.J. Brent, Man-Gill Chemical; R. Conrad, CDNSWC*

1430 **Novel Chromium-Free Surface Pretreatment Process for Corrosion Inhibitors,** *T.M. Landy, TACOM; F.L. Keohan, H.J. Lizarralde, P. Phillips, A.C. Arvanites, Cape Cod Research, Inc.*

Break

1530 **Trivalent Chromium Conversion Coating for Aluminum - A Replacement for Hexavalent Chromium Pretreatment,** *F. Pearlstein, V.S. Agarwala, NAWC Aircraft Division*

1600 **Failure Analysis of ASTM F519 Specimens,** *J.T. Menke, US Army ARDEC*

THURSDAY, Nov. 20, 1997 | 0800 - 1130 | Lee Room

Sessions 9 and 11 are Concurrent Sessions

Session 9: OTHER CORROSION CONTROL METHODS

Moderator: ***Major David Robertson - Robins AFB***

Introduction

0805 **Development of an Alternative Material Selection System for Cadmium Electroplating**, *P. Decker, U.S. Army, TACOM; K. Cramer, Ocean City Research*

0835 **Demonstration of Ozone Treatment System for Cooling Towers at Thayer Hall, U.S. Military Academy at West Point, NY,** *V.F. Hock, R. Hess, U.S. Army CERL; D. Piskin, N. Labbe, Puckorius and Associates*

0905 **Post-Processing of Thermal Sprayed Coatings Using Hot Isostatic Pressing,** *D.A. Davis, R.L. McCaw, D.M. Aylor, CDNSWC; R.A. Hays, Proteus Engineering*

0935 **Demonstration of Electro-Osmotic Pulse Technology for Groundwater Intrusion Control in Concrete Structures,** *V. Hock, M.K. McInerney, E. Kirstrin, U.S. Army CERL*

Break

1030 **Integration of Wire Arc Spray Technology for Corrosion Protection of General Purpose Bombs at the Kadena AB Bomb Renovation,** *D.N. Neale, Science Applications International Corporation*

1100 **Design of Seawater Ballast Tank Impressed Current Cathodic Protection (ICCP) Systems,** *K.E. Lucas, M.F. Evans E.D. Thomas, P.F. Slebodnick, NRL; E.A. Hogan, Geo-Centers Inc.*

Lunch

THURSDAY, Nov. 20, 1997 | 1330 - 1630 | Lee Room

Sessions 10 and 12 are Concurrent Sessions

Session 10: MATERIALS IN CORROSIVE ENVIRONMENTS

Moderator: ***Randy Meeker - Wright-Patterson AFB***

Introduction

1335 **The Effect of Water Vapor on the Oxidation of Alloys that Develop Alumina Scales for Protection,** *R. Janakiraman, G.H. Meier, F.S. Pettit, University of Pittsburgh*

1405 **Corrosion Control for the AN/BQG-5A(V)1 Wide Aperture Array**, *H.P. Hack, D.G. Tipton, Northrop Grumman Corp.; J. Pinkham, NUWC*

1435 **Inhibition of Microbiologically Influenced Corrosion**, *P.M. Natishan, J. Jones- Meehan, B.J. Little, R. Ray, NRL; G.I. Loeb, N. Gray, American University; M. Beard, CDNSWC*

Break

1530 **Fungal Degradation of Military Assets**, *B. Little, P. Wagner, D. Lavoie, R. Ray, NRL*

1600 **Material Considerations for the Navy Shipboard Waste Destruction System,** *D.A. Shifler, C. Wong, CDNSWC*

THURSDAY, Nov. 20, 1997 — 0800 - 1130 — Nighthawk Room

Sessions 9 and 11 are Concurrent Sessions

Session 11: NEW MATERIALS DEVELOPMENT

Moderator: ***Dr. John Beatty - Army Research Laboratory***

Introduction

0805 **Localized Corrosion Behavior of Aluminum-Lithium Alloy 2097,** *J. Hunter, J.F. Dante, Univ. of Dayton Research Institute*

0835 **The Determination of the Corrosion Behavior of a Developmental Al-Mg-Li-Ag Alloy,** *T.A. Carmody, B.A. Shaw, Penn State University*

0905 **Preparation and Properties of Corrosion-Resistant Thin Ceramic Coatings on Metallic Substrates by Sol-Gel Processing,** *A. Nazeri, P. Slebodnick, NRL*

0935 **Oxidation and Embrittlement of Titanium Aluminides,** *J. Rakowski, R. Cerchiara, F.S. Pettit, G.H. Meier, University of Pittsburgh*

Break

1030 **Development of a Nano-Particle Composite Material with Corrosion Resistant EMI Shielding Properties,** *D.S. Dixon, NUWC; J. Masai, Western New England College*

1100 **Corrosion Behavior of Aluminum-Beryllium Alloys,** *T.J. Garosshen, V.C. Nardone, United Technologies*

Lunch

THURSDAY, Nov. 20, 1997 — 1330 - 1630 — Nighthawk Room

Sessions 10 and 12 are Concurrent Sessions

Session 12: CORROSION CONTROL - INHIBITORS

Moderator: ***I. Carl Handsy - Army TACOM***

Introduction

1335 **Combination Use of Dehumidification (DH) and VCI (Vapor Corrosion Inhibitor) for Corrosion Protection,** *C. Crotty, L. Gelner, Protec, Inc.*

1405 **A Recent Innovation in Corrosion Control for Electronics,** *B.L. Rudman, C. Chandler, Cortec, Inc; B. Westerfield, NAVSEADET PERA-CV*

1435 **A Post-Design Corrosion Inhibition Technique for Marine Corps Light Vehicles,** *P.P. Trzaskoma-Paulette, S.G. Lambrokos, H.N. Jones, NRL*

Break

1530 **Corrosion of Mk19 Grenade Launchers in Storage,** *M. Mortman, J.A. Senske, ARDEC, Picatinny Arsenal*

1600 **Design and Construction of Electronic Systems for Military Environments,** *E. Taylor, Northrop Grumman Corp.*

Session 13: LIFE CYCLE ISSUES

Moderator: *Norm Clayton - Carderock Division, Naval Surface Warfare Center*

Introduction

0835 **Corrosion Control Hardware Allowance Parts List (APLs): Logistics Support for Naval Surface Ship Corrosion Control Programs**, *W. Steiner, N. Clayton, CDNSWC*

0905 **Corrosion Control Systematic Approach and Trends**, *J.M. Sakai, B. Gilp, NAVAIRSYSCOM*

0935 **Approaches to Corrosion Control on the USMC Riverine Assault Craft (RAC)**, *W. Steiner, N. Clayton, CDNSWC*

1005 **AEGIS Corrosion Control Web Page**, *R. Hickman, K. Spiro, NAVSEA*

1035 **CLOSING REMARKS**

NACE TECHNICAL COMMITTEE T-9 MEETING **1300 - 1600**

LaQue Corrosion Services, Conference Building
702 Causeway Drive
Wrightsville Beach, NC

HISTORY AND PURPOSE OF THE TRI-SERVICE CORROSION CONFERENCE

The Tri-Service Conference on Corrosion has been an interservice coordination in the area of corrosion research and corrosion control. The first conference, arranged by the U.S. Air Force, was held in Denver in 1967. This was followed by an organized meeting by the U.S. Navy at Annapolis in 1969, and the U.S. Army at Houston in 1972. Since 1972, one of the services has taken the lead in organizing the Tri-Service Conference on an approximate biennial cycle.

The purpose of the Tri-Service Conference on Corrosion has been to identify important corrosion problems in military equipment and systems, increase the comprehension and visibility of DOD corrosion prevention and corrosion control initiatives, provide a forum for technical exchange on corrosion control, and promote interactions among the services. Corrosion control may involve changes of design, alternative material options, control of the environment, selection and application of coatings, the use of inhibitors, the application of cathodic protection, or some combination of corrosion control methods.

The Tri-Service Conferences on Corrosion have also promoted the interaction of the DOD community with other governmental agencies, industry, academia, and professional societies in order to improve integrated corrosion control that will lead to decreased life cycle costs. The conferences provide an opportunity for feedback, assessment, and recommendations for present and future corrosion control initiatives.

OBJECTIVES OF CONFERENCE

- To increase visibility and awareness of DOD corrosion prevention and control (CPC) activities and accomplishments
- To provide a forum for update and exchange of technical information, lessons learned and CPC technology transfer
- To promote CPC interactions among the services and other governmental agencies; to promote interactions of the DOD CPC community with industry, universities and professional society colleagues
- To encourage integrated CPC activities throughout system lifecycle; and to provide opportunity for feedback, assessment and recommendations on current and future DOD CPC directions.

1997 TRI-SERVICE CONFERENCE ON CORROSION

TABLE OF CONTENTS

OFFICIAL PROGRAM

OVERVIEWS -

- **U. S. Navy**
- **U. S. Army**
- **U. S. Air Force**
- **U. S. Marine Corps**

SESSION 1 - ***Corrosion Research I***

SESSION 2 - ***Corrosion Research II***

SESSION 3 - ***Corrosion Monitoring and Testing I***

SESSION 4 - ***Corrosion Monitoring and Testing II***

SESSION 5 - ***Understanding and Controlling Different Forms of Corrosion I***

SESSION 6 - ***Understanding and Controlling Different Forms of Corrosion II***

SESSION 7A - ***Corrosion Control Methods - Coatings***

SESSION 7B - ***Preservation of Materials***

SESSION 8 -*Corrosion Control - Surface Treatments/Conversion Coatings*

SESSION 9 - ***Other Corrosion Control Methods***

SESSION 10 - ***Materials in Corrosive Environments***

SESSION 11 - ***New Materials Development***

SESSION 12 - ***Corrosion Control - Inhibitors***

SESSIOn 13 - ***Life Cycle Issues***

ATTENDANCE LIST

INDEX - AUTHORS

ERRATA

OVERVIEWS

1330 **U.S. Navy Overview**

James Rudroff
Engineering Directorate
Environmental Engineer - Code 03M
Materials Engineering Group, NAVSEA
(replaces Dr. Alex Kaznoff)

1500 **U.S. Marine Corps Overview**

Julie Jacks
General Engineer
Marine Corps Systems Command
(replaces George N. Georgeadis)

SESSION 7A

0905 **Neural Networks for Electrochemical Impedance Spectroscopy,** *F.B. Mansfeld, Univ. of Southern California*
(presentation only; replaces "US Navy Coating Alternatives Utilizing Portable Systems" (paper included in Proceedings)

0935 **Corrosion Resistant Evaluation of High Performance Aircraft Coating Systems (HPACS),** *L.B. Reynolds, M. Khobaib, N.N. Voevodin, R.L. Twite, C.S. Jeffcoate, M.S. Donley, WPAFB*
(replaces "Functionalized Sol-Gel Conversion Coatings", canceled prior to conference; copy of technical paper included in Proceedings)

SESSION 9

1130 **Corrosion Prevention in Army Missile Systems,** *S.F. Carr, Redstone Arsenal*
(presentation only)

SESSION 11

1130 **Corrosion Resistant Sol-Gel Coating for Aircraft Aluminum Alloys,** *E.T. Knobbe, R..L. Parkhill, Oklahoma State Univ.; M. Khobaib, Univ. of Dayton; L.B. Reynolds, N. Grebasch, W.K. Kuhn, J.C. Liang, and M.S. Donley, WPAFB*
(presentation only)

TACOM Overview on System Life Cycle Corrosion Prevention and Control

Richard Franke
Engineering Business Group
U.S. Army TACOM/TARDEC
Warren, MI 48397-5000

The Army Materiel Command (AMC), responsible for combat and tactical systems life cycle management, has established a Corrosion Prevention and Control (CPC) Program co-chaired by the armaments Research, Development and Engineering Center at Picatinny Arsenal and the Tank-Automotive Research, Development and Engineering Center in Warren, MI. This formalized CPC Program and establishment of a Center for Technical Excellence in corrosion at the Tank-Automotive and Armaments Command (TACOM) are designed to address the high cost of corrosion (estimated at $2.5 billion annually) for the life cycles of Army materiel (combat/tactical vehicles and armaments) -- from design through sustainment -- and develop and implement new and existing technologies to extend systems' service lives and lower their sustainment costs.

As the Army combat and tactical system acquisition command, TACOM has focused our CPC approach on how to procure systems capable of meeting 20-25 year service lives in a hostile environment. With the continued drawdown in forces, increased OPTEMPO, and the incorporation of Acquisition Reform principles, which mandate the use of performance requirements wherever possible, TACOM and the rest of the Department of Defense (DOD) must learn to "buy smarter". To validate original equipment manufacturers' (OEMs') system designs, TACOM has developed the first full-sized system accelerated corrosion test (ACT) replicating the expected 20-25 year service environment. This ACT does not provide an absolute guarantee than an OEM design will meet our service life requirement; however, it does drive the OEM toward the use of quality materials and processes such as galvanizing.

The use of the ACT for the Family of Medium Tactical Vehicles contract is expected to save millions of dollars in operations and support costs. Based on the results of the first ACT on the original design, the OEM has incorporated over 50 materials changes to the 2-1/2 and 5-ton trucks still in production. TACOM is now looking to incorporate the Act contractual requirements into all Army system production contracts, including aviation. We are working with the Aberdeen Test Center to create an ACT track to provide a dedicated testing facility for DOD equipment.

As the Corrosion CTX and as stated earlier, TACOM realizes corrosion is a life cycle issue. As such, we are investing wifely in research and development programs to solve military-unique CPC issues. We are interacting with all of the AMC major subordinate commands' engineering centers to gather and prioritize project submittals for future funding. In an effort to combine CPC with pollution prevention, two seemingly different topics which are actually quite similar in nature, we are working with the ARDEC Green Bullet program to eliminate hazardous material usage while improving long-term performance.

To address the user community, those units who work with our systems everyday in the field, TACOM recently completed a three-year investigation into commercial-off-the-shelf (COTS) CPC technologies capable of improving the mean-time-between-repair due to corrosion by a minimum of 30%. All candidate materials/processes underwent accelerated laboratory testing, two-year static exposure testing on truck doors at Cape Canaveral, and 18-month dynamic exposure testing at the U.S. Army Pacific (USARPAC) headquarters. Working directly with the USARPAC Science Advisor's office, TACOM was able to identify five COTS technologies -- arc- and flame-sprayed zinc, high purity zinc-rich primer, epoxy battery box coating, rush inhibitor and lubricant -- from an original field of 30 potential products meeting our 30% service life extension requirement. TACOM is currently procuring and fielding these technologies at USARPAC sites and providing vendor training to ensure proper usage.

TACOM's approach to solving current Army CPC problems is based on the realization that corrosion is a life cycle issue. The establishment of the Corrosion CTX is the first step of many -- while we can now effectively present future CPC failures in the research and development and production phases, we cannot change the sins of the past. The efforts with USARPAC have only scratched the surface of the CPC issues of the user community; TACOM will continue to respond to their needs and requirements to maintain readiness despite the projected personnel decline.

Only with complete support of AMC Headquarters and the Secretary of the Army can we directly implement CPC measures into all of the systems' life cycle phases to effectively save dwindling procurement resources and restore trop confidence as to the quality of their equipment. Once we have convinced the entire Army acquisition community of the life cycle cost savings through effective CPC management, we can state that we have done our job as the Corrosion CTX. This is the task we have undertaken.

Overview and Strategy of the United States Air Force Corrosion Prevention and Control Program

Maj David D. Robertson
Air Force Corrosion Program Office
325 Second Street (Bldg 165)
Robins AFB, GA 31098-1639

ABSTRACT

The United States Air Force corrosion program is directed and guided by HQ USAF through an Air Force Instruction. This instruction outlines program responsibilities of the various agencies. It is centrally managed but implemented through coordination with System Program Directors (SPDs), Major Commands (MAJCOMs), Air Logistics Centers (ALCs), and field units. The program currently faces unique challenges due to aging systems, environmental constraints, lack of adherence to approved procedures, increased reliance on electronic and space assets, and decreased funding. A strategy to meet these challenges includes greater collaboration/communication among the various agencies and a shift in emphasis from an aircraft centered program to multi-system.

PROGRAM OVERVIEW

The Air Force corrosion program has a long history beginning around 1960 with the first publication of the Air Force Regulation governing the program. In 1980, the Air Force Logistics Command (AFLC) corrosion office at Warner-Robins Air Logistics Center (WR-ALC) was tasked by HQ USAF through AFLC/CC with managing the program and renamed the Air Force Corrosion Program Office (AFCPO). The following year Gen. Poe (AFLC/CC) gave the keynote address at the Tri-Service Corrosion Conference. A Joint Logisitics Commanders Panel (4 star level) on equipment deterioration was also convened. Within the Air Force a corrosion executive steering group was established at the 2 star level which met semi-annually to discuss the status of the program and resolve important issues unable to be dealt with at lower echelons of command. This steering group ceased meeting in the early 90's due to major reorganizations within the Air Force such as the merging of AFLC and Air Force Systems Command (AFSC) into the current Air Force Materiel Command (AFMC). Also at this time, environmental constraints and increased reliance on aging systems exerted extreme pressure on the corrosion program.

In an effort to reinvigorate the program, the AFCPO was organizationally realigned under Wright Laboratory in 1995. In conjunction with this, a Coatings Technology Screening Committee (CTSC) consisting of all the MAJCOM and ALC corrosion managers chaired by a single manager for coatings was created. In addition, a new office within Wright Laboratory, the

Coatings Technology Integration Office (CTIO), was created to identify and transition environmentally friendly coatings and coating removal processes for field and ALC use.

The AF corrosion program emphasizes corrosion preventative materials and processes (M & P) throughout the design life and facilitating a cross-flow of information by maintaining a close-knit corrosion community. Correct M & P is injected through Corrosion Prevention Advisory Boards (CPABs) for every major weapon system which meet annually from early in the design process throughout the life of the system. These CPABs are established and managed by the SPDs. Responsibilities of each MAJCOM includes appointing a command corrosion manager who establishes a command corrosion prevention and control plan and recommends appropriate training course content to Air Education and Training Command (AETC) for maintenance personnel. Another major element is monitoring the health of each MAJCOM's program through a corrosion prevention and control survey conducted approximately every four years. This non-attribution inspection allows the command corrosion manager to identify areas for improvement. The AFCPO is responsible for maintaining appropriate technical data and involved in all aspects of the program as a central focal point of technical expertise.

PROGRAM STRATEGY

The AF corrosion program currently faces problems due to aging systems where the projected service life for some aircraft now exceeds eighty years. In addition, environmental constraints have made many tried and true corrosion prevention practices difficult to accomplish or unlawful. Other problems include a lack of trained personnel and rapidly changing procedures (to meet environmental constraints), so the "best practices" are not always adhered to because of a lack of knowledge. Another major issue is a shift in emphasis throughout the Air Force from a reliance on air assets to an increased reliance on electronic and space assets. In the past, corrosion control of such systems have taken a back seat to aircraft and in many instances been ignored.

To meet these challenges the AF corrosion program must evolve to emphasize multi-systems and take full advantage of current resources by increased collaboration/communication among the many DoD and other government agencies as well as industry. To accomplish this, the key technical expertise in electronic and space systems must be acquired or trained if unavailable. Technical data for these systems must receive greater emphasis in corrosion prevention and control M & P. Also, consolidation of the technical data into general series technical orders will greatly improve the ability to inject better and new technologies across multiple systems. Improved communication and information dissemination among the corrosion control community is essential for incorporating new environmentally friendly technologies. In addition, the corrosion control community must continue to foster a partnership rather than an adversarial relationship with the environmental engineering and management community and remain a strong participant at all levels to ensure the environmentally compliant technologies are also corrosion preventative.

MARINE CORPS
CORROSION PREVENTION AND CONTROL
PROGRAM

The Marine Corps Corrosion Prevention and Control (CPAC) program was formally established by MCO 4790.18 dated 20 June 1994. The order provides policy for the management and execution of the Marine Corps CPAC program, placing management responsibilities at Marine Corps Systems Command (MARCORSYSCOM), Quantico, Virginia, with policy and oversight responsibilities residing at Headquarters, United States Marine Corps. The program has three major components:

- Acquisition: Incorporate appropriate corrosion control measures during the design and production phase.
- Fielded Equipment: Make recommendations that can be implemented via maintenance procedure or hardware modification.
- Technology: Evaluate commercial products for applicability to Marine Corps and develop/evaluate new technologies, as necessary.

MARCORSYSCOM has solicited the assistance of NSWC Carderock Division (Bethesda and Philadelphia offices) to resolve our corrosion challenges.

Corrosion Issues: The Marine Corps procures most tactical ground equipment through other Services, primarily the Army. For example, wheeled vehicles, tanks and engineering equipment (i.e., air conditioners, generators, water purification equipment, etc.) are procured by the Army, communication systems are procured by the Air Force, Army and Navy. Additionally, Marine Corps equipment is transported by ship, and operated in coastal areas, jungles and deserts. This contributes to a severe corrosion environment. As a result, incorporating Marine Corps corrosion requirements requires extensive coordination, in addition to identifying corrosion requirements.

Corrosion Initiatives:

The first effort pursued by the Marine Corps CPAC program was fielding a replacement for Chemical Agent Resistant Coating (CARC). CARC gives Marine Corps equipment its camouflage pattern but environmental restrictions in Southern California limit the amount that can be applied. Headquarters Marine Corps directed that an alternative be found. Extensive testing resulted in a coating that met all camouflage requirements but was not resistant to adsorption of chemical agents. This coating, now in use throughout the Marine Corps is referred as Waterborne Camouflage Coating (WBCC). It is the precursor of the Waterborne CARC being developed by the Tri-Service SERDP effort.

A major effort to incorporate corrosion requirements into acquisition documents has been initiated. Acquisition reform has mandated a fresh approach to procurement practices within DoD. No longer can MIL-Specs and Standards be used at will. Corrosion requirements must be translated into performance language. Basically, the Services must tell a prime contractor what is required, not how to meet the requirement. As a result, corrosion requirements must be identified

in terms of operational environment and required useful life. Tests to verify conformance may still be invoked. Generic wording for all acquisition documents required by DoD 5000 is being developed by a team composed of corrosion and acquisition personnel. Tailoring will be done for specific programs.

The Marine Corps is comparing accelerated test data from GM 9540P/B and ASTM G85 and B117 to marine atmospheric performance of metals and coatings. The objective is to identify the best method to verify conformance of a product to performance specifications.

The Marine Corps is currently evaluating corrosion improvements for many Marine Corps vehicles. Material substitutions for exhaust systems, fuel and brake lines and head lamp assemblies for HMMWVs and 5-ton trucks are being evaluated in marine atmosphere and field tests. Thermal spray aluminum is being evaluated for specific failure points on both vehicles, such as hard top latch, rear corner panels, door frames and posts and roof gutters on HMMWV and cab floor, hood cowl and tool boxes on 5-ton truck. Thermal spray plastic was applied to 5-ton battery boxes. Tests evaluating additives to washdown water and crevice coatings were also initiated.

Corrosion engineering support to Program Managers within MARCORSYSCOM is a major emphasis of the Marine Corps program. While life cycle cost data to support corrosion upgrades is difficult to obtain, the corrosion related maintenance burden is significant enough to justify the improvements. This effort includes design analysis, material and coating selection, evaluation of fleet condition, source selection criteria, and environmental and maintenance impacts. This work is done in coordination with other Services.

Environmental compliance issues plague most Marine Corps locations. Efforts to facilitate organizational maintenance prompted evaluations of surface preparation equipment and surface tolerant coatings. Other efforts to evaluate underbody coatings are underway. These efforts support fielded equipment and can be incorporated into new acquisition initiatives.

Controlled humidity preservation of equipment is being pursued for fielded equipment to isolate the equipment from it's environment.

A USMC Corrosion Control Web Site is being developed to encourage information exchange within DoD. Web site will provide information on the Marine Corps corrosion program and provide access to test data.

Vision for the Future:

As the Marine Corps prepares to enter the next century, many factors will impact the Marine Corps' ability to maintain a combat ready posture. One area that can benefit from technology and a joint service partnership is corrosion. The Marine Corps has developed a Plan of Action and Milestones as our strategy for the future. This strategy focuses on product and process improvement, training and education, partnerships with other Services and private industry and other futuristic initiatives. Our underlying intent is reduce or eliminate duplication of corrosion

prevention efforts within the Department of Defense. Through much interaction with acquisition agencies and groups such as NACE and Tri-Service Conference on Corrosion, the groundwork is laid. Our vision is for an integrated corrosion control working group at the highest level to address the problems of today and prevent the consequences of tomorrow.

Defining the Corrosion Chemistry of Supercritical Water Oxidation Systems

Digby D. Macdonald
Center for Advanced Materials
The Pennsylvania State University
University Park, PA 16802

A review is presented of recent work on developing sensors for probing the chemical properties of high subcritical and supercritical aqueous solutions. Thus, sensors have been developed for measuring pH, $[H_2]$, $[O_2]$, redox potential, and electrochemical emissions (in the coupling current between two identical metal specimens) at temperatures up to 600°C and at densities of up to ~0.12g/cm^3. These sensors are critically important for monitoring and controlling the chemical properties of the working fluids in Supercritical Water Oxidation (SCWO) systems and in Supercritical Thermal Power Plants (SCTPPs).

INTRODUCTION

Supercritical Water Oxidation (SCWO) is rapidly emerging as a key technology for the destruction of resilient organic waste (e.g., halogenated hydrocarbons) and for minimizing the volume of low level radioactive waste. Furthermore, in the quest for higher thermodynamic efficiency, many new fossil-fueled (coal, oil, natural gas) power plants operate at supercritical temperatures, with temperatures of the heat transfer fluid (water) ranging as high as 550°C. In both cases, but particularly in the case of SCWO, corrosion of structural reactor materials is a major concern. Furthermore, the deposition of salts that are produced in the oxidation process continues to complicate reactor design, and hence adds to the cost. However, both the corrosion problem and the deposition phenomenon result from chemical conditions that exist within the reaction medium at high subcritical (T=300°C-374°C) and supercritical (T>374°C) temperatures. Accordingly, monitoring and control of the conditions that exist within the reactor, in order to minimize the impact of corrosion and deposition, is critically important for cost effective, commercial operation.

In this paper, techniques that have been developed for monitoring chemical properties of high subcritical and supercritical aqueous systems are reviewed. Emphasis is placed on techniques for monitoring electrochemical (corrosion, redox) potential, pH, $[H_2]$, $[O_2]$, and spontaneous electrochemical emissions in the current from coupled metal specimens. The latter is proving to be most valuable for monitoring corrosion processes.

DEVELOPMENT OF pH SENSORS

Since the 1980s, high temperature pH measurements have been made using sensors based on yttria-stabilized zirconia (YSZ) membranes, hydrogen electrodes, and metal/metal oxide

electrodes. We discuss below a number of these sensors with emphasis on those that can be used (or potentially be used) for measuring pH at temperatures that extend into the supercritical region. Sensors for measuring pH in aqueous systems at lower temperatures (T<300°C) have been previously reviewed[1].

Metal/Metal Oxide pH Sensors

In this laboratory, we have undertaken a broad search for metal/metal oxide systems that are suitable for pH measurements in high temperature aqueous solutions. Several oxidized metals have been explored at temperatures up to 300°C, and some have been investigated in supercritical environments. These metals include: W, Mo, Ta, Nb, Zr, and V. All of these metal/metal oxide systems respond to changes in the pH of the solution, but only the tungsten/tungsten oxide electrode exhibited a Nernstian response and good stability[2]. The Zr/ZrO_2 system can be employed as well, but only in solutions with pH values that are far from neutral. The advantages of the metal/metal oxide pH sensing electrodes, compared to the YSZ membrane-based systems, are their simplicity and robustness, as well as their ability to operate over a broader temperature range and at much higher pressures.

pH Measurements in Subcritical Systems

A recently-developed electrode employs one YSZ membrane with two separate internal elements (Figure 1). One element is located at the tip of the YSZ tube, which is in contact with the test (monitored) solution, while the second internal element is located in the middle of the YSZ tube. This part of the membrane ("reference pH electrode") is exposed to the reference buffer or standard solution. The design is somewhat analogous to the metal/metal oxide combination pH bi-electrodes that we previously developed, and has the same advantages over electrodes employing an external pressure-balanced reference electrode (EPBRE).

pH Measurements at Supercritical Temperatures

Hydrogen Electrode - A hydrogen electrode can be used as a pH sensor if the hydrogen fugacity is known. In the present work, a hydrogen electrode, fabricated from platinized platinum, was evaluated at temperatures as high as 500°C in a buffer solution of 0.1 m H_3BO_3 + 0.01 m LiOH, saturated with 1 atm of hydrogen at 25°C (Figure 2). The reference electrode employed was a Ag/AgCl EPBRE with a salt bridge made from oxidized zirconium.

Tungsten/Tungsten Oxide pH Electrode - Tungsten/tungsten oxide combination pH electrodes have been tested at temperatures up to 600°C in solutions of sodium hydroxide, sulfuric acid, and ammonia (Figure 3). The reference electrode was a Ag/AgCl EPBRE with an alumina salt bridge.

Yttria-Stabilized Zirconia Membrane pH Sensor - We employed a YSZ membrane pH sensor with an internal element based on a low temperature melting alloy to explore pH measurements at temperatures as high as 600°C (Figure 4). The reference electrode was, again, a Ag/AgCl EPBRE with an alumina salt bridge.

The most striking feature of the cell potential (E) vs. temperature plots (Figs. 2-4) is the drastic change that occurs in E at near-critical temperatures, where the density of water decreases rapidly with increasing temperature. For the case of the hydrogen electrode, this potential drop could be explained, at least in part, by the significant decrease in the hydrogen fugacity at supercritical temperatures. However, from the similarity of Figs. 2 and 3, it is obvious that fugacity changes cannot account for this effect entirely, because the tungsten electrode exhibits the same behavior. Accordingly, the observed behavior most likely results from changes in the fundamental properties of the solution, primarily changes of the solution pH caused by changes in density, by changes in pK_w, and by ion pairing. An additional contribution may be due to the thermal liquid junction potential associated with the EPBRE, particularly at temperatures above 374°C.

Glass pH Sensor at Temperatures of 200°C-250°C

We have also developed a pH sensing electrode made from Pyrex glass that has operated effectively at temperatures as high as 200°C-250°C[3]. Due to the significant decrease in the electrical resistance of the glass with increasing temperature, it is possible to use a thick-wall Pyrex tube as a pH sensor in a form that can withstand high pressures and temperatures. In the present case, the electrode employed a Ag/Ag_2SO_4 sensor in concentrated sulfuric acid solution to form the half-cell Ag/Ag_2SO_4/Pyrex glass/soln(H^+). This electrode exhibited near-Nernstian response at sufficiently high temperatures in acid solutions (Figure 5). No glass dissolution was observed.

ELECTROCHEMICAL NOISE

Electrochemical noise monitoring is evolving as a useful tool in corrosion monitoring and control, including corrosion of metals and alloys in high temperature aqueous systems. Electrochemical noise provides useful "real-time" information on the corrosion activity in the system, which cannot be readily obtained by any other method. An electrochemical noise sensor, employing Type 304 stainless steel electrodes and a zero resistance ammeter to monitor the coupling current, was tested over a broad range of temperature in HCl solutions (Figure 6). These studies expand on our previous work on carbon steel in high subcritical and supercritical aqueous solutions[4]. Importantly, the highest noise amplitude is observed around the critical temperature of the solution, and is in good agreement with the corrosion patterns observed in SCWO systems, where corrosion damage is highly pronounced around the critical point of water.

HYDROGEN AND OXYGEN SENSORS

We have recently developed amperometric and potentiometric sensors for dissolved hydrogen in high temperature water. The amperometric sensor is based on a two-electrode cell employing platinum electrodes and a proton conducting solid electrolyte. The sensor employs a PTFE diffusion membrane, the permittivity of which increases with increasing temperature. This sensor shows a rapid response to changes in hydrogen concentration (Figure 7), and is capable of monitoring hydrogen in the low ppb range, which is adequate for most industrial process streams. A great advantage of this sensor over the Pd/Pt relative resistance sensor that we previously developed[5] is its great simplicity.

Potentiometric oxygen and hydrogen sensors based on solid electrolyte (YSZ) cells employing noble metal (H_2 sensor) or Ag (O_2 sensor) electrodes have been devised. These sensors, which are described elsewhere in this symposium, are capable of accurately measuring dissolved oxygen and hydrogen at temperatures up to 300°C. The upper limit is determined by the use of PTFE as a diffusion membrane, so that they must be employed in cooled side streams when being used to monitor supercritical systems. On the other hand, cells of the type $(Pt)H_2/H^+,H_2O/YSZ/HgO/Hg(Pt)$ have been employed by Ding and Seyfried[6] and by Eklund et al.[7] to measure hydrogen in supercritical systems. Electrodes of this type, which avoid the use of PTFE, represent a viable technology for the monitoring of hydrogen in supercritical aqueous systems, provided interfering redox species (e.g., O_2) are not present in the fluid.

Finally, we have extended the differential Pd/Pt sensor technology to measuring hydrogen in supercritical aqueous systems (Figure 8). The advantages of this system are its ruggedness and simplicity (two noble metal wires are exposed to the high temperature environment) and the fact that it can be used in the presence of species (e.g., O_2) that interfere with the potentiometric and amperometric sensors described above.

CONCLUSIONS

In this paper, recent advances in the development of several types of sensors for monitoring chemistry parameters in aqueous solutions at high temperatures, including super-critical aqueous systems, are described. Rugged sensors that are capable of measuring pH, $[H_2]$, $[O_2]$, redox potential, and electrochemical emissions at temperatures up to 600°C are also described. These sensors are expected to find significant application in supercritical water oxidation systems and in supercritical thermal power plants within the near future.

ACKNOWLEDGMENT

Financial support of this work was provided, in part, by EG&G Idaho National Engineering Laboratory under Contract C-88-101857, by the US Army Research Office under Grant DAAL 03-92-G-0397, by the Electric Power Research Institute under Contract RPC522-04, and by the US Department of Energy under Contract DE-FG07-96ER62303.

REFERENCES

1. Macdonald, D. D.; Hettiarachchi, S.; Song, H.; Makela, K.; Emerson, R.; and Haim, M. *J. Solut. Chem.*, **1992**, 21, 849.
2. Kriksunov, L. B.; Macdonald, D. D.; Millett, P. J. *J. Electrochem. Soc.*, **1994**, 141, 3002.
3. Kriksunov, L. B.; Macdonald, D. D. *Sensors and Actuators B (Chemical)*, **1996**, B32, 57.
4. Liu, C.; Macdonald, D. D.; Medina, E.; Villa, J.; Bueno, J. *Corrosion*, **1994**, 50, 687.
5. Macdonald, D. D.; McKubre, M. C. H.; Scott, A. C.; Wentrcek, P. R. *Ind. Eng. Chem. Fundam.*, **1981**, 20, 290.
6. Ding, K.; Seyfried, W. E. *Geochim. Cosmochim. Acta*, **1995**, 59, 4769.
7. Eklund, K.; Lvov, S.; Macdonald, D. D. *J. Electroanal. Chem.*, **1997**, submitted.

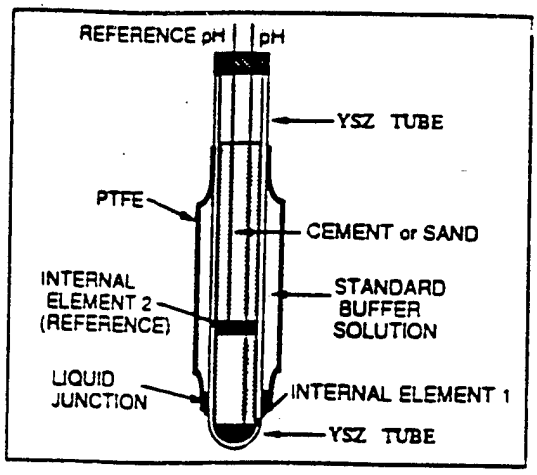


Figure 1. Combination pH electrode based on a YSZ membrane.

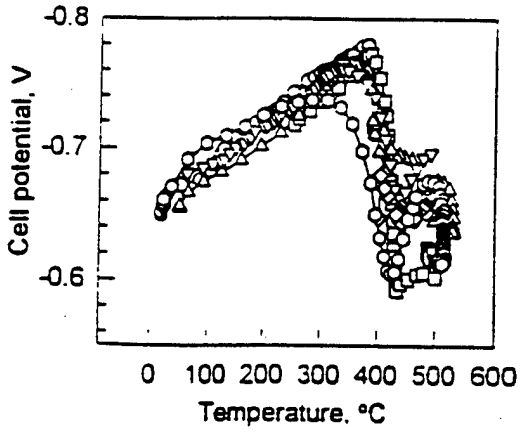


Figure 2. Potential of hydrogen electrode vs. EPBRE in boric buffer solution at 220-270 bars.

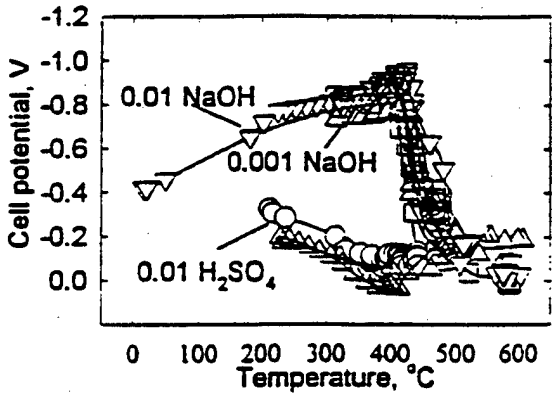


Figure 3. Potential of tungsten/tungsten oxide-Ag/AgCl combination electrode in several solutions at 320-380 bars.

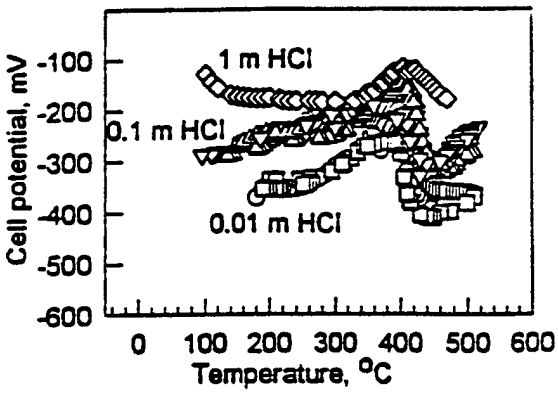


Figure 4. Potential of the YSZ membrane pH electrode vs. EPBRE at 315 bars.

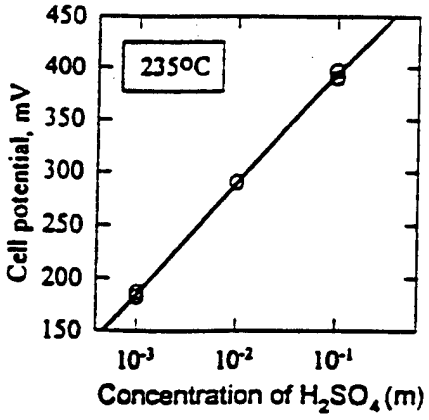


Figure 5. Potential of glass pH sensor vs. EPBRE.

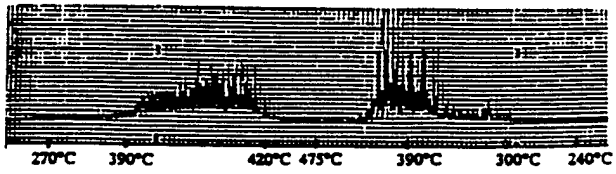


Figure 6. Electrochemical noise observed on Type 304 SS in a 0.1 m HCl solution.

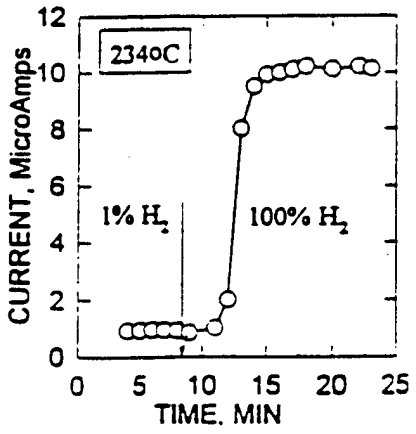


Figure 7. Hydrogen sensor current during change of sparging gas from containing 1% of H_2 to 100% H_2.

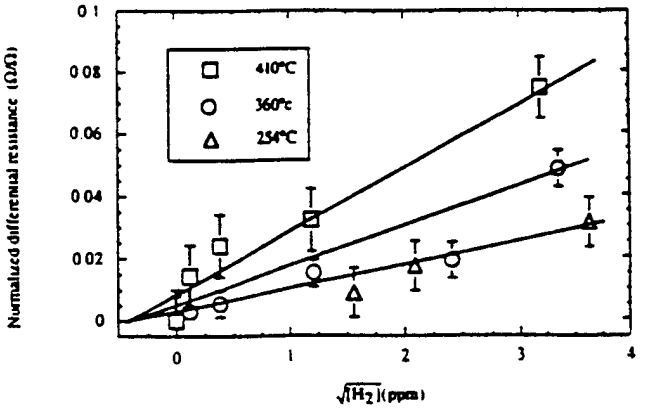


Figure 8. Simplified equivalent electrical connection schematic of the hydrogen sensor intaking into account of solution conductivity.

Corrosion Mechanisms in Supercritical Water Oxidation Systems for Hazardous Waste Disposal

R.M. Latanision, D.B. Mitton, S-H Zhang, J.A. Cline, M.S. Quintana and N. Caputy

H.H. Uhlig Corrosion Laboratory
Massachusetts Institute of Technology
Cambridge, MA, U.S.A. 02139

ABSTRACT

There is, currently, simultaneous public resistance to traditional waste handling procedures and a compelling need to destroy both military and civilian hazardous waste. While supercritical water oxidation (SCWO) offers an effectively methodology for destroying such wastes, systems need to withstand aggressive environments. To improve our understanding of degradation within these systems, analysis of failed components, exposure and instrumented tube experiments are being carried out. In addition dealloying and cracking were encountered for Hastelloy C-276 in chlorinated feed streams. The presence of a corrosion maximum at high subcritical temperatures previously suggested by analysis of failed Hastelloy C-276 components, was recently confirmed during instrumented tube tests.

INTRODUCTION

Although SCWO is technologically able to destroy hazardous wastes, the process must be carried out in a reactor which will withstand not only the high temperature and pressure conditions but also a very corrosive environment. Ultimately, corrosion may be the deciding factor in the successful fabrication and operation of a commercial supercritical water oxidation unit to be used for hazardous waste disposal [1-3]. Although nickel alloys are frequently employed for severe service applications[4], they are not sufficiently resistant to withstand certain conditions associated with SCWO [1,5-10]. These alloys tend to exhibit both significant weight loss and localized effects including stress corrosion cracking (SCC)[1] and dealloying[11,12].

For experiments conducted in an Inconel-625 SCWO reactor on the destruction of representative navy wastes,[13] there was little evidence for corrosion with non-chlorinated feed solutions and the effluent was somewhat enriched in Cr. Conversely, relatively high metal concentrations were observed in the effluent during runs employing chlorinated feeds and the effluent was enriched in Ni. These data suggest dealloying of chromium at some point within the reactor for non-chlorinated feeds and dealloying of nickel appears to be a problem. Certainly in alkaline environments depletion of Cr at grain boundaries is well known for Inconel 600[14].

Exposure studies were carried out in deionized water during commissioning of the corrosion test facility at MIT to provide a base-line assessment of the materials of construction. The results [2,5] of a preliminary short term exposure (24 - 96 hours) at 300, 400 and 500°C indicate varying degrees of film formation and localized corrosion for the three alloys tested (Inconel-625, Hastelloy C-276 and stainless steel type 316 L). The effect of exposure time (up to 10 days), in

deionized water at 500°C [9] suggest the potential for protective oxide formation for both Inconel-625 and Hastelloy C-276 and a non-protective film for the stainless steel.

One potential methodology for reducing corrosion damage during the destruction of aggressive feeds involves the use of a liner[15]. Although some progress has been made in circumventing corrosion problems in this way, this has not been extensively tested and tends to be expensive (titanium and platinum are currently the materials of choice). Some researchers have found that titanium provides outstanding performance at subcritical and performs at least as well as the Ni alloys at supercritical temperatures[16]. Similar results were found by Hazlebeck et al and this group asserts that titanium liners are the answer to chlorinated organic feeds[15]. Interestingly, however, other researchers have had problems with titanium and report through-wall pitting of liners during destruction efficiency testing of a chlorinated feed[17].

RESULTS

Failure Analysis

Figure 1 presents both a schematic representation of the experimental plug flow reactor (PFR) and a number of photomicrographs of the tube cross section at various locations within the PFR. Cross sections were cold mounted (EPON Resin 828 and Triethyenetetramine (TETA) in the approximate ratio 23:3) and polished (but not etched) prior to viewing. This system is employed to study the kinetics and reaction mechanisms of the destruction of organics in supercritical water. The organic preheaters (Figure 1(a)) were employed to heat an aqueous methylene chloride (CH_2Cl_2) feed solution (0.017 to 0.057 mol l^{-1} CH_2Cl_2) to the temperature of the reactor. Although isothermal conditions were maintained in the reactor (450°C - 600°C) during individual experiments, the preheater temperature varied from ambient at the entrance to supercritical at the exit. The Hastelloy C-276 tubes employed as organic preheaters were approximately 2500-3000 mm long and had an outside diameter (OD) of 1.6 mm. The total time of exposure to the Cl^- containing feed solution prior to failure was 104 hours for the first, 45 hours for the second and 56 hours for the third preheater. Ultimately, the units failed (Figure 1 (b)) by the development of an axial intergranular crack [7]; however, elemental depletion (Ni, Mo, Fe) of the corroded layer and elevated Ni concentrations in the effluent in conjunction with no observable change in the dimensions of the corroded and non-corroded regions of the same tube confirmed that dealloying was also occurring for this alloy at these conditions [12]. The time-to-failure for these three units represents an approximate crack propagation rate between 1.3×10^{-9} and 6.8×10^{-10}, which is within the normal range for stress corrosion cracking. It is significant that although different conditions (temperature, feed type and composition) were employed during the various experiments, failures were restricted to approximately the same 217 mm length of tube between 373 and 590 mm from the inlet end of the preheater. There was no appreciable corrosion either at the preheater inlet (Figure 1 (c)), which was at near ambient temperature or the exit (Figure 1(d)), which experienced significant HCl concentrations at supercritical conditions[7]. This observation in conjunction with the proximity of the failures suggested that failures were occurring within a subcritical temperature region of the tube. This hypothesis was corroborated by heat transfer calculations indicating that the failure site was at a high but subcritical temperature[12].

In the preheater, the corrosion rate, apparently, increases with temperature reaching a maximum within the high subcritical range. A further increase to supercritical temperature; however, results in a dramatic decrease in the rate of degradation. Thus, the exit to the preheater and inlet to the cool-down heat exchanger, which are at supercritical conditions, both reveal low rates of

corrosion. A short distance into the cool down heat exchanger the corrosion rate increases again at a point which is assumed to be at a high subcritical value. Finally, beyond this second maximum the corrosion rate decreases as a function of decreasing temperature.

Results from preheater units #2 and #3 are presented in Figure 2. These preheaters were cut into 30 mm sections, cold mounted, polished and viewed on a confocal laser scanning microscope. This figure presents, as a function of distance from the preheater inlet (ambient temperature), the calculated bulk fluid temperature and the extent of intergranular corrosion (% of tube wall penetrated). Each preheater was used for numerous experiments at various temperatures and flow rates and the calculated temperature shown is based on a "typical" value. The location of the crack observed for preheaters #1, #2 and #3 is indicated by arrows. All failures occurred within the region exhibiting high corrosion rates and these failures correspond to the subcritical temperature range indicated. In addition, the three corrosion maxima presented in this figure fall within the same temperature range. This figure confirms the original assessment suggesting a correlation between temperature and corrosion rate. In this figure, the maximum observed at a distance of 375 mm from the inlet for preheater #3 is on a straight section of tube; however, the maxima observed between about 500 - 550 mm correspond to a region where a 90° bend (radius ≈ 10 mm) is located, suggesting that stress is an additional contribution to the magnitude of corrosion[18].

Instrumented Tube Experiments

In order to provide a more controlled assessment of the correlation between temperature and corrosion rate, an experiment was designed in which a Hastelloy C-276 tube (1.6 mm OD) was instrumented with thermocouples (Figure 3). This experiment was designed to correlate as closely as possible to conditions associated with the failure of the organic preheaters previously discussed.

As one of the major products of the hydrolysis of CH_2Cl_2 occurring in the preheaters is hydrochloric acid, during the instrumented tube experiment, an aqueous HCl feed was introduced at a supercritical temperature and allowed to cool as it traveled the length of the tube. The ambient pH of the feed and the effluent were both approximately 2.

Figure 3 schematically presents (top) the measured temperature profile during the instrumented tube experiment, (center) a schematic representation of the experimental configuration and (bottom) photomicrographs of tube cross sections after the experiment. These are representative of the temperature measured by the corresponding thermocouple. The temperature measured for thermocouple No. 1 was supercritical (425°C). As revealed by the photomicrograph associated with this temperature, there is relatively little corrosion. Thermocouple No. 2 indicated a temperature of 368°C, which is in the general region of the supercritical/subcritical transition. While some corrosion is apparent, it has not developed the intergranular characteristics associated with thermocouples No. 3 and No. 4. At these two positions the temperature was close to 300°C and, as seen in the photomicrographs, both regions reveal severe intergranular penetration. Finally at a temperature of 277°C (thermocouple No. 5) the corrosion has decreased dramatically. This experiment establishes a clear correlation between temperature and corrosion rate for Hastelloy C-276 exposed to an acidic chlorinated feed.

Stability Diagrams

Recent work by Anderko et al [19] has shown the usefulness of "real solution stability diagrams". These are based on a thermodynamic model which combines both the Helgeson-Kirkham-Flowers

(HKF) equation of state for standard-state properties with a solution nonideality model based on the activity coefficient expressions developed by Bromley and Pitzer.

Diagrams for the major components of Hastelloy C-276 at 300°C are presented in Figures 4 (a-e) and a composite diagram is presented in Figure 4 (f). As reported[12] previously, analysis of the dealloyed layer revealed depletion of Ni, Fe and Mo, and enrichment of Cr and W. The data presented in Figure 4 confirm and elaborate on our previous work. Region (1) in Figure 4(f) delineates the conditions associated with the preheater failure analysis previously discussed. In this region, Ni and Fe are unstable while Cr, Mo and W all exhibit stability. Thermodynamic data were not available for W and no Mo oxide was indicated in our earlier work. The diagrams presented in Figure 4, however, indicate the presence of both Mo and W oxides. Elemental analysis of the dealloyed layer did indicate general enrichment of W; however, depletion of Mo was observed. Interestingly, however, recent analysis has revealed a stable Mo band at the interface between the alloy and the dealloyed layer, suggesting that the current diagram for Mo is, likely, correct.

Region 2 in Figure 4 (f) delineated that region within which Cr, Ni and Fe are all stable. This region has been restricted to potentials above the hydrogen line as oxidizing potentials are likely during SCWO. This should correspond to a region within which the corrosion rate would be reduced when compared to that observed for the preheaters assessed during this study. Attaining this region during destruction of a chlorinated waste could, potentially, reduce the corrosion damage associated with such wastes.

CONCLUSIONS

Further analysis of the failed Hastelloy C-276 preheater tubes from the PFR system at MIT confirms the original assessment. Thus, there is a strong indication of a correlation between temperature, corrosion rate and stress.

A more controlled assessment of the correlation between temperature and corrosion rate was achieved during an experiment employing a Hastelloy C-276 tube instrumented with thermocouples. The results of this experiment establish a clear correlation between temperature and corrosion rate for Hastelloy C-276 exposed to an acidic chlorinated feed.

Real solution stability diagrams presented within this paper for the main constituents of Hastelloy C-276 confirm and elaborate on our earlier work. They suggest a region within which reduced corrosion may be possible during the destruction of a chlorinated feed stream.

ACKNOWLEDGMENTS

We gratefully acknowledge the assistance of Dr. A. Anderko, OLI Systems Inc., for supplying the stability diagrams used in this paper. The financial support of the Army Research Office during this project is particularly appreciated.

REFERENCES

1 R.M. Latanision and R.W. Shaw, Co-Chairs, "Corrosion in Supercritical Water Oxidation Systems" -Summary of a Workshop held at MIT May 6-7, 1993 (Report No. MIT-EL 93-006, 1993).

2 D.B. Mitton, J.C. Orzalli, and R.M. Latanision, Proceedings of the Third International Symposium on Supercritical Fluids Nancy France October 17-19 Vol.3, p.43 (1994).

3 A.J. Thomas and E.F. Gloyna, "Corrosion Behavior of High Grade Alloys in the Supercritical Water Oxidation of Sludges," (Technical Report CRWR 229, University of Texas at Austin, 1991).

4 ASM Handbook, Vol 13: Corrosion, 9th ed., Materials Park, OH: ASM International, p. 641 (1987).

5 J.C. Orzalli: Master's Thesis, Department of Materials Science and Engineering, MIT (1994).

6 B. C. Norby, "Supercritical Water Oxidation Benchscale Testing Metallurgical Analysis Report," Idaho National Engineering Laboratory Report (EGG-WTD-10675 , February 1993).

7 R.M. Latanision, Corrosion, 51, 4, p. 270 (1995).

8 D.B. Mitton, J.C. Orzalli and R.M. Latanision: Science and Technology, ACS Symposium Series, 608, p. 327 ACS, Washington, DC (1995).

9 D.B. Mitton, J.C. Orzalli and R.M. Latanision: Physical Chemistry of Aqueous Systems-Meeting the Needs of Industry, 12th ICPWS, p.638, Begell House New York, NY (1995).

10 R.D. Kane and D. Cuellar, "Literature and Experience Survey on Supercritical Water Corrosion," CLI International Report, No L941079K, July 19, (1994).

11 T.T. Bramlette, B.E. Mills, K.R.Hencken, M.E. Brynildson, S.C. Johnston, J.M. Hruby, Feemster, H.C., Odegard, B.C. and M. Modell "Destruction of DOE/DP Surrogate Wastes with Supercritical Water Oxidation Technology,", Sandia National Laboratories Report, SAND90-8229 (November, 1990).

12 D.B. Mitton, P.A. Marrone and R.M. Latanision, J. Electrochem Soc.,Vol. 143 pp. L59 (1996).

13 S.F. Rice et al, "Destruction of Representative Navy Wastes Using Supercritical Water Oxidation" Sandia Report SAND 94-8203 UC-402 (0ct 1993).

14 D. A. Jones, Principles and Prevention of Corrosion (New York, NY: Macmillan Publishing Company, p. 305, (1992).

15 D.A. Hazlebeck, K.W. Downey, D.D. Jensen and M.H. Spritzer, in Physical Chemistry of Aqueous Systems-Meeting the Needs of Industry, Proc. 12th ICPWS, Begell House New York, NY, p.632 (1995).

16 G.T. Hong, D.W. Ordway and V.A. Ziberstein, First Int. Workshop on Supercritical Water Oxidation Jacksonville Florida (Feb 6-9 1995).

17 K.M. Garcia "Supercritical Water Oxidation Data Acquisition Testing" INEL report INEL-96/0267 (Aug 1996).

18 R.M. Latanision, D.B. Mitton, S-H Zhang, J.A. Cline, N. Caputy, T.A Arias and A. Rigos: Proceedings of the 4th International Symposium on Supercritical Fluids, Sendai, Japan May 11-14 Vol. C, pg 865 (1997).

19 A. Anderko, S.J. Sanders and R.D. Young, Corrosion, 53, 1, p. 43 (1997).

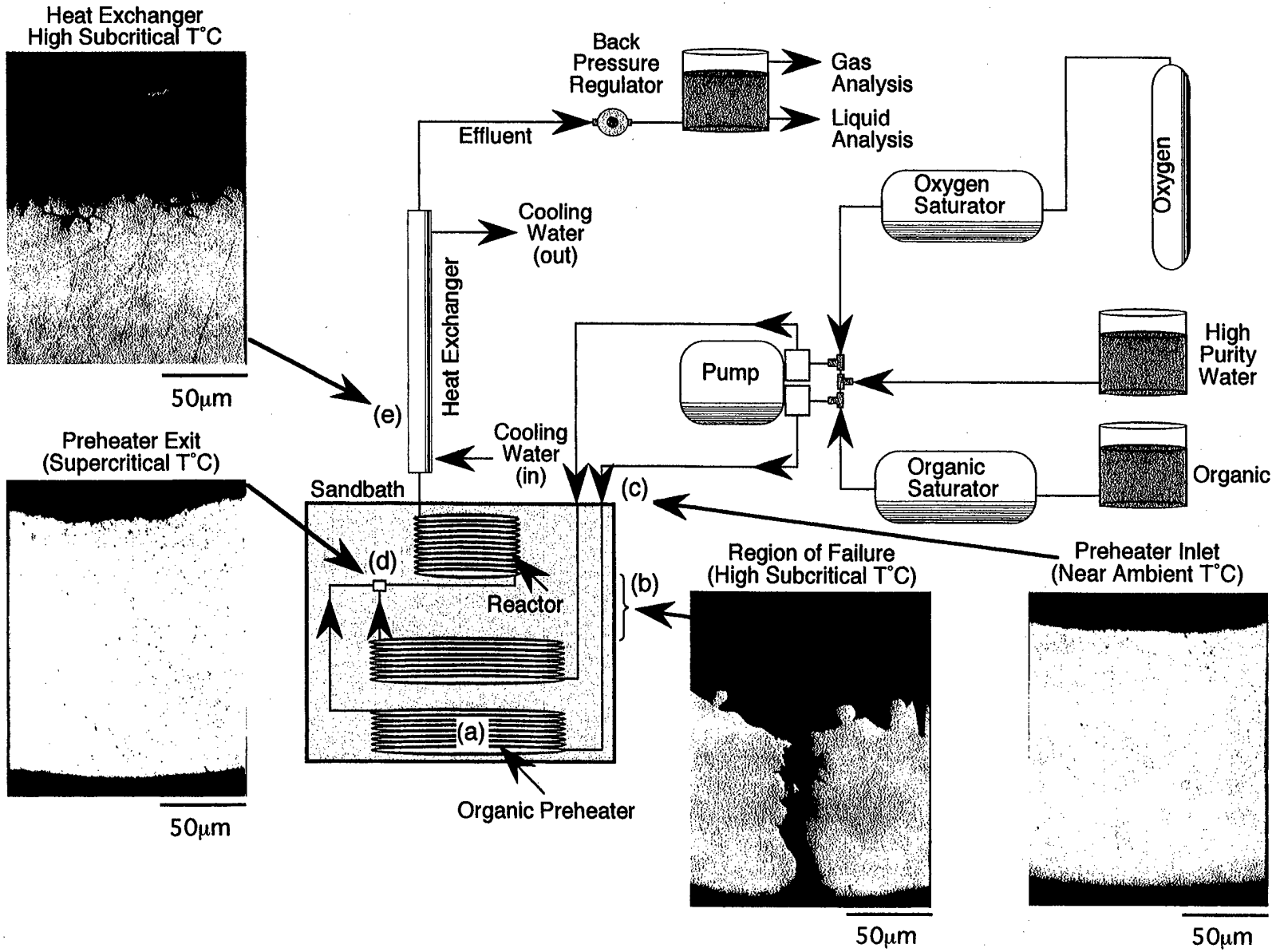


FIGURE 1. A schematic representation of the experimental plug flow reactor (PFR) employed to study the kinetics and reaction mechanisms of the destruction of organics in supercritical water at MIT and a number of photomicrographs of the tube cross section at various locations within the PFR.

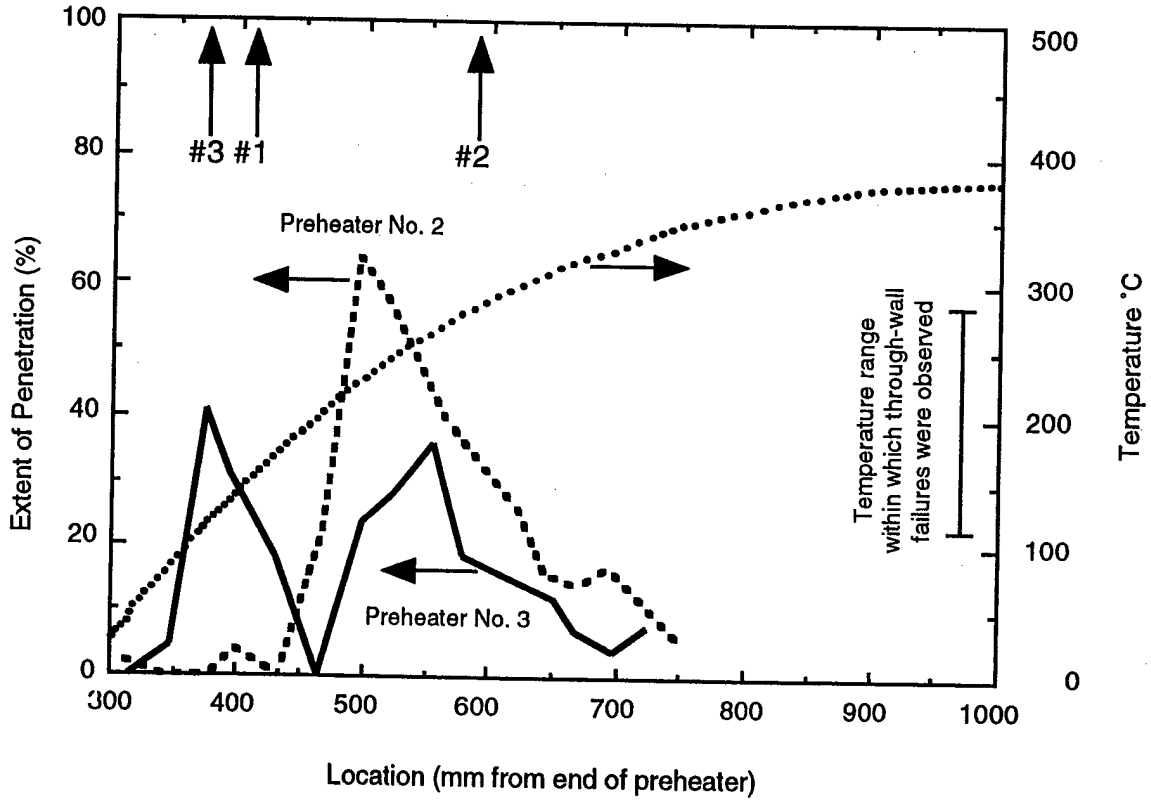


FIGURE 2. Presents, as a function of distance from the preheater inlet (ambient temperature), the "typical" calculated bulk fluid temperature and the extent of intergranular corrosion (% of tube wall penetrated) for preheater units #2 and #3. The location of the crack observed for preheaters #1, #2 and #3 is indicated by an arrow.

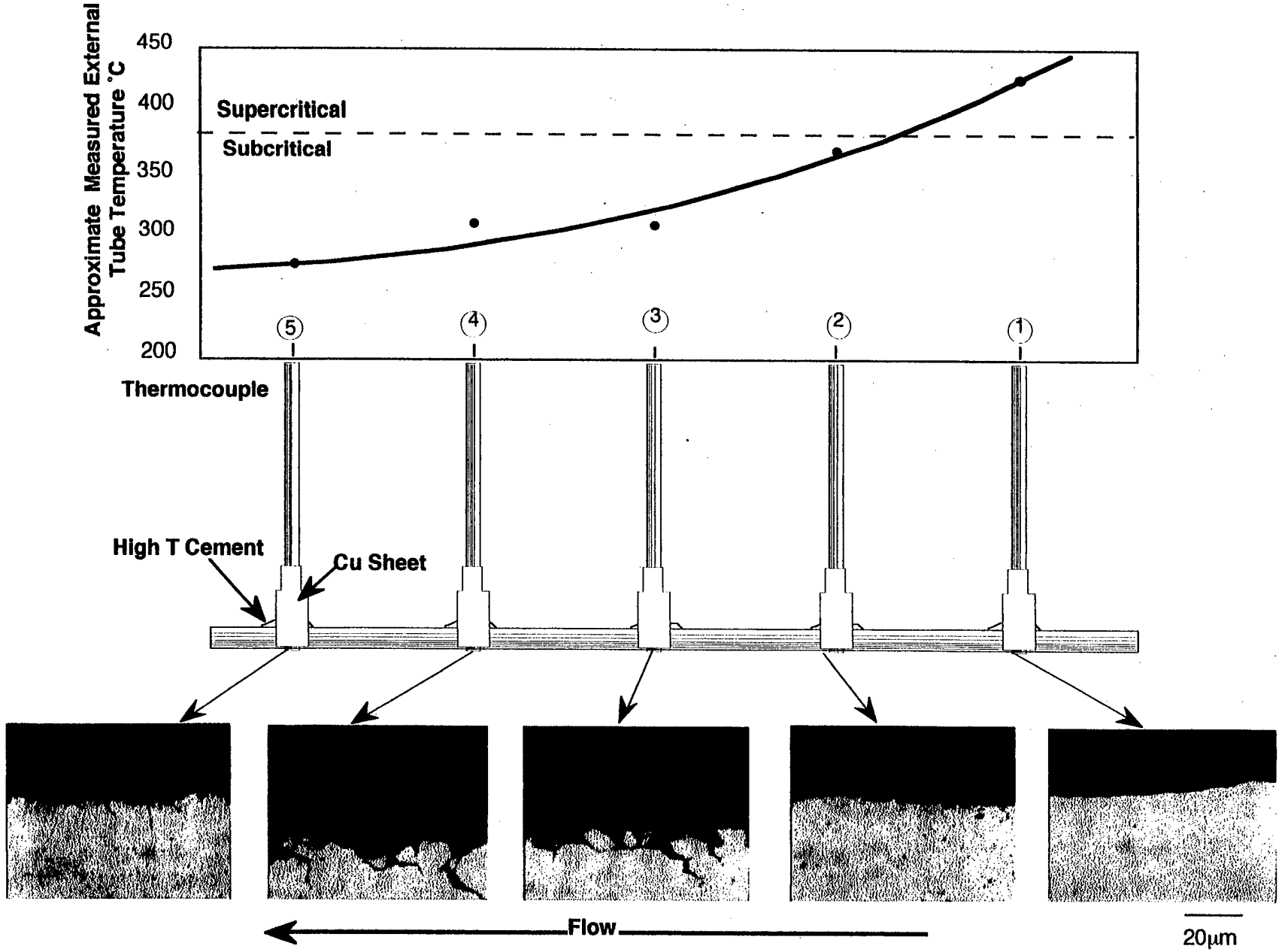
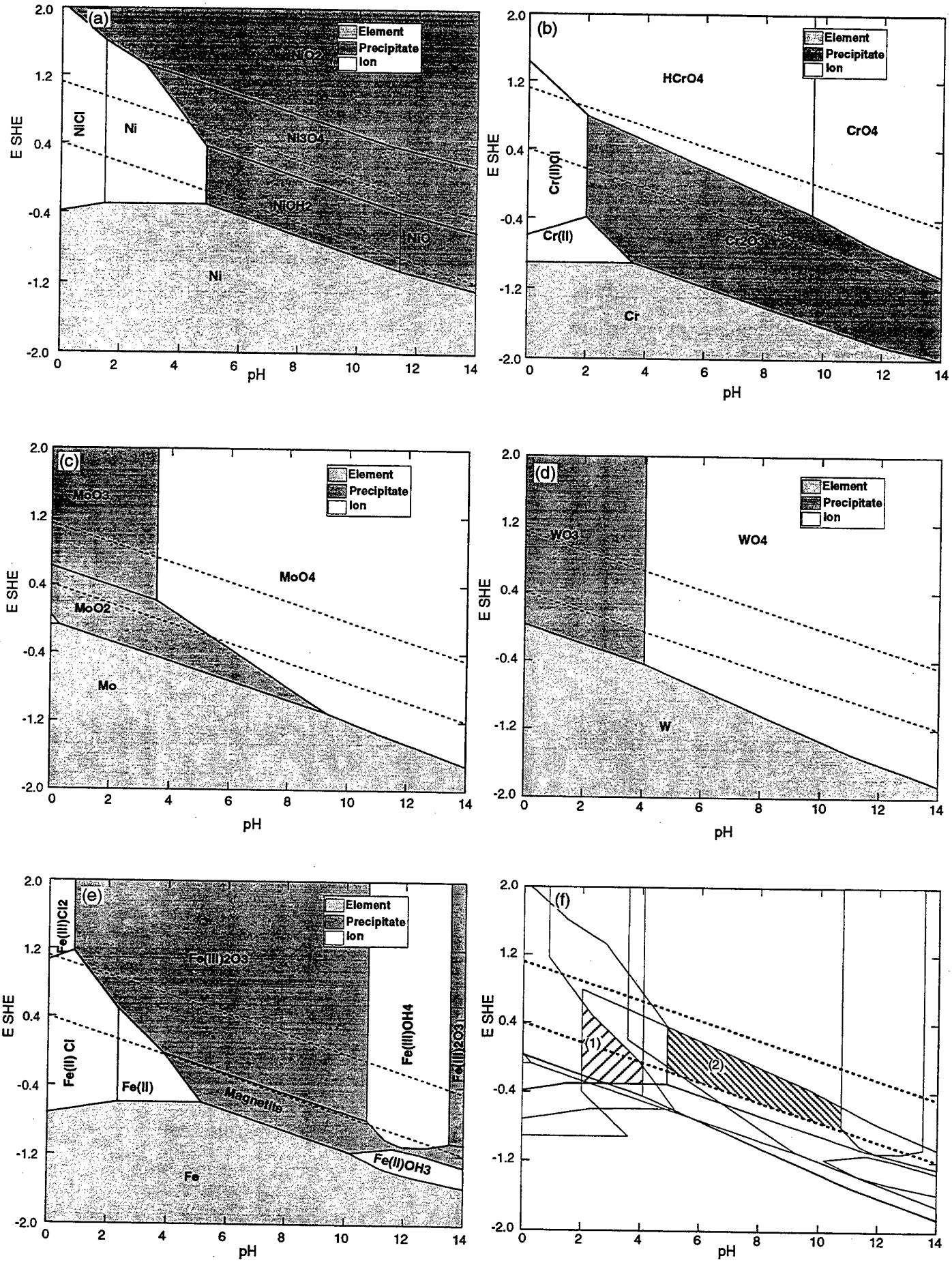


FIGURE 3. The measured temperature profile (top) during an experiment in which a Hastelloy C-276 tube was instrumented with thermocouples, (center) a schematic representation of the experimental configuration, and (bottom) photomicrographs of tube cross sections after experiment. These are representative of the temperature measured by the corresponding thermocouple. This experiment was designed to correlate as closely as possible to conditions associated with the failure of the organic preheaters.

FIGURE 4. Diagrams for the major components (a-e) and a composite diagram (f) of Hastelloy C-276 at 300°C.



Experimental Study of the Erosion-Corrosion of Copper and Copper-Nickel Alloys at the Corrosion Potential and at Anodic Potentials

Paul T. Wojcik,[1] Eric Charrière,[2] and Mark E. Orazem[1]

[1]Department of Chemical Engineering
University of Florida
Gainesville, FL 32611

[2]Swiss Federal Institute of Technology
Materials Department, Metallurgical Chemistry
MX-C Ecublens
Lausanne, Switzerland

ABSTRACT

The erosion-corrosion of copper and copper-nickel alloys in synthetic sea water was investigated using an impinging jet. Video microscopy, corrosion potential monitoring, and impedance spectroscopy were used to investigate the state of the system and the reactivity of the electrode surface. Shear-induced removal of salt films was observed and found to be associated with significant increases in surface reactivity. Direct shear-induced removal of oxide films, however, was not observed. Nevertheless, the protective oxide layer showed sensitivity in passively-aerated seawater to large fluid velocities and to small perturbations in potential. The films were stable under all conditions tested in continuously-aerated seawater.

INTRODUCTION

Copper and copper alloys are widely used in marine environments because they are resistant to corrosion in seawater. This resistance is associated with formation of protective layers on the metal surface. However, copper and its alloys are known to be susceptible to enhanced corrosion in seawater when there is sufficient relative motion between the metal and the fluid.[1-3] The flow-enhanced corrosion of copper alloys in seawater has been attributed to erosion-corrosion.[2]

In the absence of suspended particles, erosion-corrosion is associated with mechanical disruption or removal of protective layers by hydrodynamic shear.[2,4,5] Protective layers are assumed to be removed when the shear force is greater than the binding force between the film and the substrate. Direct observation of shear-induced removal of films has been reported for some systems. Giralt and Trass[6] showed that removal of solid naphthalene and trans-cinnamic acid by a submerged impinging jet of saturated solution is proportional to the wall shear stress above a critical or threshold value. Steele and Geankoplis[7] reported removal of material by an apparent shear erosion mechanism. Esteban *et al.*[8] used an impinging jet system to identify shear induced removal of poorly adhered filming inhibitors on steel in chloride solutions. The removal of the inhibitor was associated with enhanced corrosion in regions of large hydrodynamic shear.

Efird reported critical values of shear stress for the erosion-corrosion of copper and some copper-based alloys in sea water (see Table 1).[2] His test apparatus consisted of a series of

independent flow chambers with a rectangular cross section designed such that fresh sea water flowed parallel to the surface of the coupon. Flow establishment and disengagement regions were located up and downstream respectively to ensure a well-developed flow over the coupon. Coupons were removed and photographed after a thirty-day exposure. Accelerated corrosion was identified by the roughened appearance of corrosion products and of the metal surface after corrosion products were removed. A critical velocity for enhanced corrosion was identified which was correlated to shear stress. Onset of enhanced corrosion was consistently located at the leading edge of the coupon.

The experimental system used by Efird[2] was characterized by a uniform shear stress and a non-uniform mass transfer coefficient. The observation of a critical velocity for enhanced corrosion can therefore be attributed to either a shear-induced removal of protective films or to destabilization of the protective films by a differential mass transfer mechanism.

Using an impinging jet system for which mass transfer was uniform, Diem and Orazem[9] did not observe shear-induced corrosion on copper in alkaline chloride electrolytes for values of hydrodynamic shear which were as much as 10 times the critical shear stress reported by Efird.[2] In the alkaline chloride solutions used, passivation was observed in less than 100 seconds. The work of Diem and Orazem[9] cannot be compared directly to that of Efird[2] because the electrolyte was significantly different in composition from the seawater used in Efird's experiment. Steady-state films on copper alloys in seawater are reported to require 30 days or more to develop.[10-13]

The objective of this work was to determine whether shear-induced removal of protective films for copper and copper-nickel alloys could be observed in systems for which mass transfer is uniform. The exposure time for the coupons was up to 33 days, and ASTM standard synthetic seawater was used as the electrolyte.

EXPERIMENTAL PROCEDURE

The hydrodynamics and the experimental design for the submerged axisymmetric impinging jet used in this study are presented in this section.

Hydrodynamics of the Impinging Jet

The fluid mechanics within the region of the electrode is well-defined.[14-18] This geometry can be made to give uniform mass transfer rates across a disk electrode within the stagnation region. The stagnation region is defined to be the region surrounding the stagnation point in which the axial velocity, given by

$$v_z = -2\sqrt{a\upsilon}\phi(\eta) \tag{1}$$

is independent of radial position, and the radial velocity is given by

$$v_r = ar\frac{d\phi(\eta)}{d\eta} \tag{2}$$

where a is the hydrodynamic constant which is a function only of geometry and fluid velocity, r and z are the radial and axial positions, respectively, ν is the kinematic viscosity, andϕ is the stream function which is given in terms of dimensionless axial position $\eta = z\sqrt{a/\nu}$ as[18]

$$\phi(\eta) = 0.656\eta^2 - 0.16667\eta^3 + 3.6444 \times 10^{-3}\eta^6 - 3.9682 \times 10^{-4}\eta^7 \quad (3)$$

Esteban *et al.* used ring electrodes to find that the stagnation region extends to a radial distance roughly equal to the inside radius of the nozzle.[8]

Within the stagnation region, the surface shear stress τ_{rz} is given by

$$\tau_{rz} = -1.312r(\mu\rho)^{\frac{1}{2}}a^{\frac{3}{2}} \quad (4)$$

where μ and ρ are the viscosity and density of the fluid, respectively. The hydrodynamic constant can be determined experimentally using ring or disk electrodes at the mass-transfer-limited condition and is proportional to the jet velocity.[8,9] The shear stress on the electrode surface is given in Figure 1 as a function of jet velocity for the range of velocities used in this work. The critical shear stress values reported by Efird[2] for copper (9.4 N/m^2) and 70/30 copper nickel (47.9 N/m^2) are provided for reference in Figure 1.

Experimental Design

Because the mass transfer rate is uniform, differential mass transfer cells are not established for an electrode that lies entirely within the stagnation region. The impinging jet system can therefore be used in the absence of suspended particles to isolate the influence of the hydrodynamic shear stress. If the removal of protective layers by hydrodynamic shear is the primary cause of erosion-corrosion and the shear stress outside a certain critical radius is large enough to cause that removal, then the metal outside the critical radius will corrode at a significantly higher rate than the metal inside the critical radius. Since shear stress is a function of both radial position and jet velocity, the critical radius corresponding to the critical shear stress would be a function of jet velocity for fixed geometry.[8]

A schematic representation of the experimental setup is presented in Figure 2. The experimental impinging jet cell used for this work was a modification of the cell design used by Diem and Orazem.[9] The cell was enclosed completely to eliminate entrainment of air. The system was capable of continuous operation at a maximum mean jet velocity of 6.75 m/s which yielded a shear stress of 195 N/m^2 at 80% of the radius of a 0.635 cm (0.25 inch) diameter electrode. This value is 20 times larger than the critical shear stress of 9.8 N/m^2 reported by Efird for copper.[2]

The system was configured with the jet positioned facing down. The top sides of the impinging jet cell were angled at 45° and 60° from vertical and an access port was centered in each side to allow in-situ observation of the working electrode. The port which supported the video microscope contained a sapphire window sealed with an o-ring and held in place by an aluminum retaining ring. The other access port housed a thermometer to monitor cell temperature which was compared with reservoir temperature. At high flow rates, viscous dissipation caused the temperature in the cell to differ from that in the reservoir. The temperature in the cell was controlled at a desired value by adjusting the set-point temperature in the cooling bath.

Three *in-situ* experimental techniques were incorporated in this work. The corrosion potential with reference to a saturated calomel reference electrode was monitored continuously throughout the course of an experiment. Variable-amplitude galvanostatically-modulated (VAG)

impedance spectroscopy was used at specified intervals to investigate the reactivity of the electrode surface.[19,20] The VAG technique allowed collection of impedance data without altering the natural evolution of the corrosion potential with time. Video microscopy complimented the two electrochemical techniques by providing a visual record of the state of the electrode surface. Digital images of the surface were used to detect velocity-enhanced phenomena which were manifested as rings or halos on the surface of the disk electrode.

The surface reactivity was quantified through use of the measurement model approach.[21-26] This quantification followed three steps:

1. The frequency-dependent error structure was identified following the method presented by Agarwal *et al.*[23]
2. The portion of the spectrum that is consistent with the Kramers-Kronig relations was identified following the method presented by Agarwal *et al.*[24] The error structure found in step 1 above was used to weight the regression. High-frequency data were found to be corrupted by instrumental artifacts. The low-frequency data were typically found to be consistent with the Kramers-Kronig relations except for data collected early in the experiment where the system was changing rapidly.
3. The measurement model was regressed to the portion of the spectrum found in step 2 to be consistent with the Kramers-Kronig relations. The regressed parameter values were used to extrapolate to the zero frequency limit, and Monte Carlo simulations were performed using the standard deviations of the regressed parameters to estimate the confidence interval for the extrapolation. The polarization impedance was obtained by subtracting the regressed solution resistance from the extrapolated zero-frequency value.[26]

RESULTS

The experiments discussed here involved annealed electrodes made of 99.9% copper (CDA110) or a 70/30 copper/nickel alloy (CDA715). The electrolyte was ASTM-D-1141 synthetic sea water.

Copper in Passively-Aerated Electrolyte

In the experiments presented in this section, the electrolyte was aerated only by passive diffusion of air through the exposed air-electrolyte interface in the reservoir. The pH was measured to be 8.05, and the oxygen content of the electrolyte was 6 ppm. In the subsequent section, results are presented for continuously-aerated electrolytes, for which the air used for aerating the electrolyte was scrubbed to remove CO_2. Continuous aeration had no effect on the pH of the electrolyte, which remained at 8.2. The oxygen content of the continuously and passively-aerated electrolytes was 7 and 6 ppm, respectively.

Potentiostatic Experiments-The utility of the experimental setup for detecting shear-induced removal of films can be seen in the results of experiments conducted for 99.9% copper electrode in flowing (0.1 m/s) aerated synthetic sea water at anodic potentials. The current-time traces resulting from potentiostatic experiments are given in Figure 3 for values of 100, 200, and 400 mV (SCE). These potentials corresponded to regions of the polarization curve that were influenced by formation of salt films which, as seen in Figure 3, to decrease the current observed. The 200 mV (SCE) trace showed a decrease in the current followed by a sharp

increase that was evident at roughly 300 seconds. Successive video images were collected at a rate of 2/second for this experiment. The dashed lines in Figure 3 are the times corresponding to the video images given in Figure 4 of the coupon during the 200 mV(SCE) experiment. At short times (33 and 61 seconds), growth of salt films reduced the magnitude of the current. Following the current distribution on a disk electrode below the limiting current,[27] salt films formed first as a ring on the periphery of a copper disk electrode and then grew inward. During the early stage of dissolution (0 to 160 seconds), the video images showed three waves corresponding to formation of salt films. At 160 seconds, the beginning stage of the mechanical removal of a salt film layer was evident at the periphery of the electrode. (see Figure 4). This removal was coincident with a slight increase in current evident in Figure 3. At 341 seconds, more of the film has been removed, and, at still longer times, the film was removed completely and a new salt film was precipitated. The removal of the salt film caused a 30 percent increase in the observed current. The removal process initiated at the periphery of the electrode where the shear stress is the largest, and mechanical removal of chunks of the film was evident in the video. This work demonstrated that the reactivity of the copper is sensitive to removal of salt films and that the experimental technique can be used to observe shear-induced removal of films.

Galvanostatic Experiments at the Corrosion Potential.-The working electrode was 99.9% copper immersed in ASTM-D-1141 synthetic sea water. The corrosion potential is presented in Figure 5 as a function of time for a period of 33 days. The initial corrosion potential behavior of all the copper and copper/nickel alloys studied for this work was similar in the sense that the corrosion potential, immediately after submersion, increased rapidly during the first few hours.[28] As the corrosion potential became more positive, the rate of change slowed until a constant value was reached. The difference between the initial value and the constant value was as much as 70 mV. Electrohydrodynamic impedance measurements conducted under similar conditions showed that the electrochemical behavior of copper in synthetic seawater became insensitive to convective diffusion within 24 hours; thus, the electrochemical behavior of the copper was controlled by surface films after the first day of immersion.

The jet velocity for the first seven days was controlled at 1 m/s. A pseudo-steady-state value of -283 mV for the corrosion potential was reached after approximately 48 hours, and this value fluctuated by only 2 mV over the next five days. Impedance spectra collected during this same seven day period showed an initial decrease in the impedance followed by an increase to a pseudo-steady-state value. Following the seventh day, the solution was kept quiescent for 16 days after which a series of impedance scans was conducted to investigate corresponding changes in the electrode reactivity. Impedance scans taken before and after the 16 day quiescent period revealed an increase in the polarization impedance during period of time the solution was stagnant. Video images of the copper surface revealed the presence of a thick film.

After 556.6 hours, a large cathodic potential on the order of -1.3 V(SCE) was applied to the system for approximately 2 minutes resulting in the evolution of hydrogen from the electrode surface and removal of copper oxides. The impedance values after the potential excursion were reduced by a factor of 10 as compared to the impedance scans prior to the upset. A noticeable change in the appearance of the electrode surface was evident, and the presence of hydrogen bubbles on the surface was observed in the video images. The decrease in the impedance observed after the potential disturbance is consistent with removal of a protective film. This hypothesis is supported by the digital images which showed that portions of a surface film were removed, leaving bare copper visible around the periphery of the electrode.

Approximately 25 minutes after the potential disturbance, flow was resumed. Air that had accumulated in the lines was removed, after which the jet velocity was adjusted to 1 m/s. Data collection resumed 25 minutes after flow was started, and the resulting corrosion potentials are presented in Figure 6. The corrosion potential returned to the value before the potential disturbance after a period of 120 hours and remained constant for several days. A small adjustment of pH by addition of NaOH had no discernible effect on the corrosion potential. The corrosion potential changed abruptly, however, following an increase in jet velocities of 1.0 to 6.75 m/s. The values for the shear stress corresponding to these velocities at a radial position of $r/r_0 = 0.8$ are 14.5 and 195 N/m^2, respectively.

Impedance data collected during this leg of the experiment are presented in Figure 7. The impedance increased steadily after the potential disturbance, showing a decrease in reactivity as the protective films became reestablished. The value for the impedance approached a constant value after an additional 150 hours. The influence of pH modification from 8.05 to 8.24 on the impedance response was not discernible when plotted in impedance plane format, however, the influence of a change in jet velocity from 1.0 to 6.75 m/s on the impedance of the electrode is easily seen in Figure 7.

The polarization impedance corresponding to Figure 7 is shown in Figure 8 as a function of time. The polarization impedance and the associated confidence intervals given in Figure 8 were obtained by the measurement model concept developed in this group as part of the infrastructure for the erosion-corrosion experiments.[21-26] The polarization impedance increased with time. The impedance response was found to be sensitive to the small adjustment of pH 161 hours after the potential swing, and also showed a large increase in the reactivity of the surface following the increase in jet velocity.

The video micrographs shown in Figure 9 can give insight on the evolution of the electrode surface. The copper electrode at t=0, immediately after submersion in solution, showed polishing marks left by the 0.05 μm alumina powder used in the final stage of wet polishing. The presence of a uniform film at t=169 hours is consistent with electrohydrodynamic impedance spectroscopy measurements that showed that the electrochemical properties of the copper were governed by surface films after 24 hours of immersion. A similar uniform film was observed at t=671 hours after the system recovered from the potential excursion. After the increase in jet velocity, which resulted in a large reduction in the polarization impedance, a uniform film was still evident (t=814 hours). The apparently increased sharpness as compared to the image at t=671 hours is attributed to removal of a salt film, exposing the granular structure below. No ring-shaped features were evident in the micrographs.

Copper and 70/30 Copper/Nickel in Continuously-Aerated Electrolyte at the Corrosion Potential

The abrupt increase in reactivity with increased jet velocity shown in Figure 8 was reproducible for passively-aerated electrolytes, but was not observed for copper in continuously-aerated electrolyte. The corrosion potential transients shown in Figure 10 are typical of the results obtained in aerated ASTM-D-1141 synthetic sea water. Effects of velocity on corrosion potential were not seen. The extrapolated polarization impedance values given in Figure 11 showed that the surface reactivity stabilized after a period of 10 days and that increases in jet velocity from 1 m/s to 2 m/s, from 2 m/s to 4 m/s, and from 4 m/s to 6.2 m/s had no discernible

effect. Ex-situ analysis by XPS of the electrodes after immersion in continuously-aerated electrolyte revealed the presence of Mg and Fe salts that were not present on electrodes after immersion in passively-aerated electrolyte. These results, and observation of a small decrease in pH in the passively-aerated case, are consistent with the hypothesis that the nature of surface films formed had changed due to passive incorporation of CO_2 through the air-electrolyte interface in the reservoir.

The corrosion potential of the 70/30 copper nickel alloy in continuously aerated ASTM-D-1141 synthetic sea water reached a steady value within 5 days, though the measurement had considerably more scatter than observed for the copper system. The extrapolated polarization impedance values showed that surface reactivity stabilized after a period of 10 days, and that increases in jet velocity from 2 m/s to 6 m/s had no discernible effect.

CONCLUSIONS

Fully-developed oxide layers were observed in earlier work to be sensitive to small amplitude (50 mV) perturbations in potential.[19] Flow conditions resulting in a variation of potential across a copper surface can therefore disrupt protective oxide layers, not by direct mechanical removal, but by inducing electrochemical instability. Salt films resulting from an applied anodic potential were observed to be removed by shear forces, and removal of such films increased the reactivity of copper. This removal of salt films on parts of the electrode and not on others could contribute to a potential gradient that would destabilize oxide layers. Oxygenation cells are another source of potential gradients which could form when using a channel flow cell such as used by Efird.[2] The present work suggests that the enhanced corrosion seen by Efird may not be due to a shear-induced mechanical removal of an oxide film but may be due instead to destabilization of the film by a potential gradient across the electrode surface. The enhanced corrosion observed by Efird at the leading edge of the coupon is consistent with distribution of mass transfer expected for a channel flow cell, and the observation of a critical velocity is consistent with our observation of a critical potential for destabilization of the oxide layer.

The coupling of the VAG impedance algorithm and the extrapolation of impedance spectra developed for this work provides a powerful tool for assessing changes in the reactivity of an electrode. By setting the current to be equal to zero, galvanostatic modulation allowed the system to be held at the open-circuit condition, and the variable-amplitude technique ensured that the potential swing the system experienced was sufficiently small to ensure a linear response. The latter is particularly important because, in earlier work, a potential perturbation of 50 mV was sufficient to disrupt the passive films formed on copper in passively-aerated ASTM-D-1141 synthetic sea water.[19] The VAG impedance technique used in this work did not appear to affect the naturally occurring transients in the system associated with growth of surface films. The extrapolation technique developed here was intended to make maximum use of the available measurements by providing a convenient measure of reactivity. This was especially important in developing an assessment of the data presented in Figure 7 where the rapidly changing conditions made some low frequency data inconsistent with the Kramers-Kronig relations.

The films formed on copper in passively-aerated synthetic seawater appeared to be less stable than those formed in highly-aerated synthetic seawater. Such films were found here to be sensitive to changes in jet velocity. In earlier work, these films were found to be sensitive as well to changes in sinusoidal potential swings.[19] This result is consistent with the numerical

simulations of Moghissi which predicted that the oxide layers on copper would be sensitive to pH and, in the pH ranges typical of seawater, could be unstable to small perturbations of potential.[29]

ACKNOWLEDGMENTS

This research was supported by the Office of Naval Research under Grant Numbers N00014-93-I-0056 and N00014-93-I-1113 (Dr. A. J. Sedriks, program monitor).

REFERENCES

[1] F.L. LaQue, Marine Corrosion: Causes and Prevention, John Wiley and Sons, N.Y. (1975).

[2] K.D. Efird, *Corrosion,* **33** (1977), 3.

[3] R.J.K. Wood, S.P. Hutton, and D.J. Schiffrin, *Corrosion Science,* **30** (1990), 1177.

[4] H.R. Copson, *Corrosion,* **16** (1960), 86t.

[5] D. C. Silverman, *Corrosion,* **40** (1984), 220-226.

[6] F. Giralt, and O. Trass, *Canadian Journal of Chemical Engineering,* **53** (1975), 505.

[7] L. R. Steele, and C. J. Geankoplis, *AIChE Journal,* **5** (1959), 178.

[8] J. M. Esteban, G. Hickey, and M. E. Orazem, *Corrosion,* **46** (1990), 896.

[9] C. B. Diem and M. E. Orazem, *Corrosion,* **50** (1994), 290.

[10] H. P. Hack and J. P. Gudas, "Inhibition of Sulfide-Induced Corrosion by Clean Seawater Pre-exposure," Report DTNSRDC/SME-79-85, David Taylor Naval Ship Research and Development Center, 1979.

[11] J. R. Scully, H. P. Hack, and D. G. Tipton, *Corrosion,* **42** (1986), 462.

[12] H. P. Hack and J. R. Scully, *Corrosion,* **45** (1986), 79.

[13] H.P. Hack and H.W. Pickering, *Journal of the Electrochemical Society,* **138** (1991), 690.

[14] M. T. Scholtz, and O. Trass, *AIChE Journal,* **16** (1970), 82.

[15] M. T. Scholtz, and O. Trass, *AIChE Journal,* **16** (1970), 90.

[16] F. Giralt, C.-J. Chia, and O. Trass, *Industrial and Engineering Chemistry, Fundamentals,* **16** (1977), 21.

[17] C.-J. Chia, F. Giralt, and O. Trass, *Industrial and Engineering Chemistry, Fundamentals,* **16** (1977), 28.

[18] D.-T. Chin, and C.-H. Tsang, *Journal of the Electrochemical Society,* **125** (1978), 1461.

[19] P.T. Wojcik, P. Agarwal, and M. E. Orazem, *Electrochimica Acta,* **41** (1996), 977-983.

[20] P. T. Wojcik and M. E. Orazem, *Corrosion*, in press.

[21] P. Agarwal, M. E. Orazem, and L. H. García-Rubio, *Journal of the Electrochemical Society,* **139** (1992), 1917-1927.

[22] P. Agarwal, O. C. Moghissi, M. E. Orazem, and L. H. García-Rubio, *Corrosion,* **49** (1993), 278-289.

[23] P. Agarwal, O. D. Crisalle, M. E. Orazem, and L. H. García-Rubio, *Journal of the Electrochemical Society,* **142** (1995), 4149-4158.

[24] P. Agarwal, M. E. Orazem, and L. H. García-Rubio, *Journal of the Electrochemical Society,* **142** (1995), 4159-4168.

[25] M. E. Orazem, P. Agarwal, and L. H. García-Rubio, *Materials Science Forum,* **192-194** (1995), 563-572.

[26] M. E. Orazem, P. T. Wojcik, I. Frateur, and L. H. García-Rubio, "Application of Measurement Models for Interpretation of Impedance Spectra for Corrosion," to be presented at Electrochemical Methods for Corrosion Research, EMCR 97, Trento, Italy, August 25-29, 1997.

[27] M. E. Orazem and M. G. Miller, *Journal of the Electrochemical Society,* **134** (1987), 392-399.

[28] P. Agarwal, O. C. Moghissi, M. E. Orazem, and L. H. García-Rubio, *Corrosion,* **49** (1993), 278-289.

[29] O. C. Moghissi, *The Electrochemical Behavior of Copper in Chloride Solutions,* PhD dissertation, University of Florida, May, 1993.

Table 1. Critical velocity and shear stress for copper-based alloys in sea water as reported by Efird.[2]

Alloy / main components	Critical Velocity, m/s	Temperature, °C	Critical Shear, Stress N/m^2
CA 122 copper	1.3	17	9.6
CA 687 copper /zinc	2.2	12	19.2
CA 706 90/10 copper/nickel	4.5	27	43.1
CA 715 70/30 copper/nickel	4.1	12	47.9
CA 722 copper/nickel/chromium	12.0	27	296.9

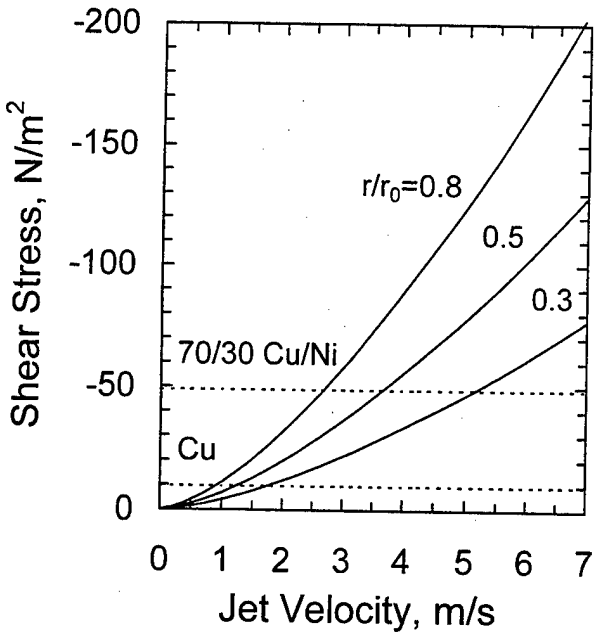


Figure 1. Shear stress as a function of jet velocity with dimensionless radial position on the electrode surface as a parameter for the impinging jet cell used in the present work. Critical shear stress values reported by Efird[2] are presented for reference.

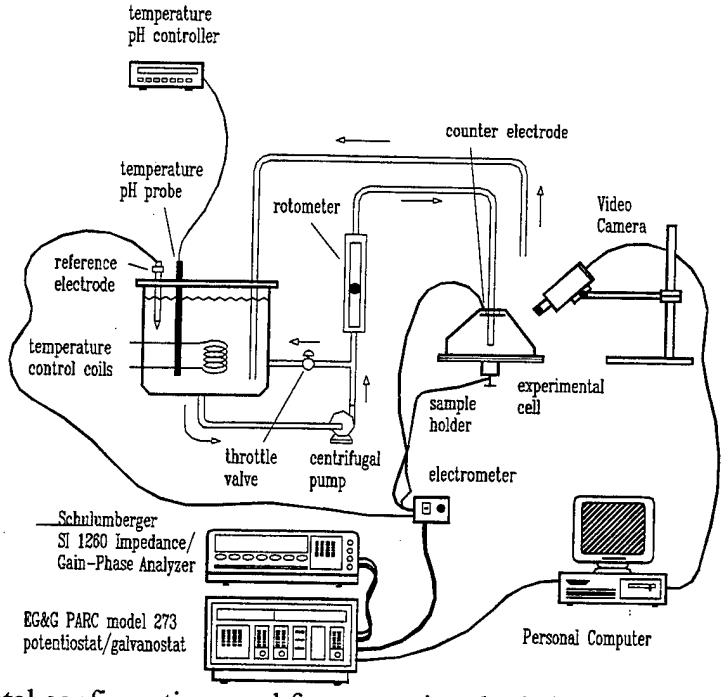


Figure 2. Experimental configuration used for measuring the influence of jet velocity on the corrosion of copper and copper alloys in synthetic sea water.

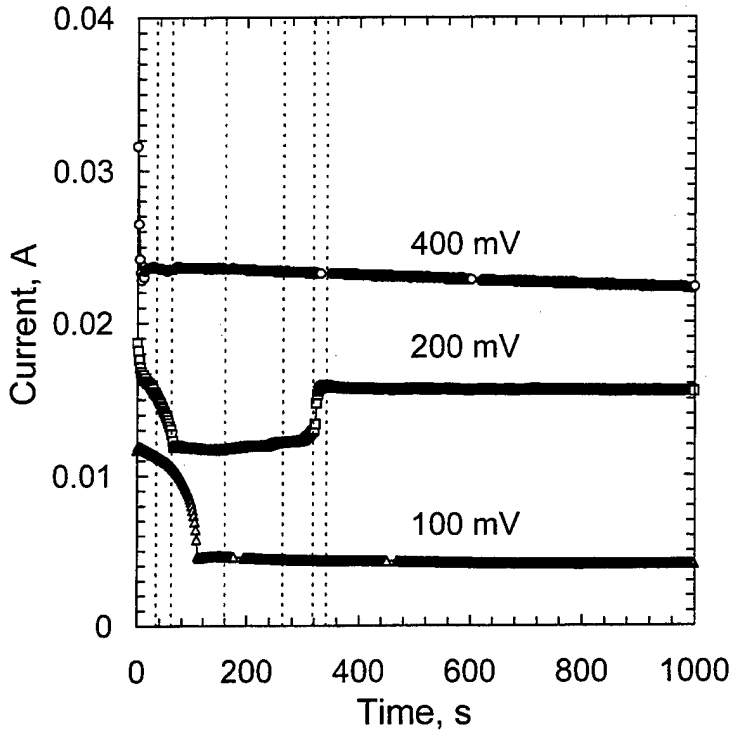


Figure 3. Current as a function of time for 99.9% copper in aerated synthetic sea water at a jet velocity of 0.1 m/s. The dashed lines correspond to the time at which images shown in Figure 4 were collected for the coupon held at 200 mV (SCE).

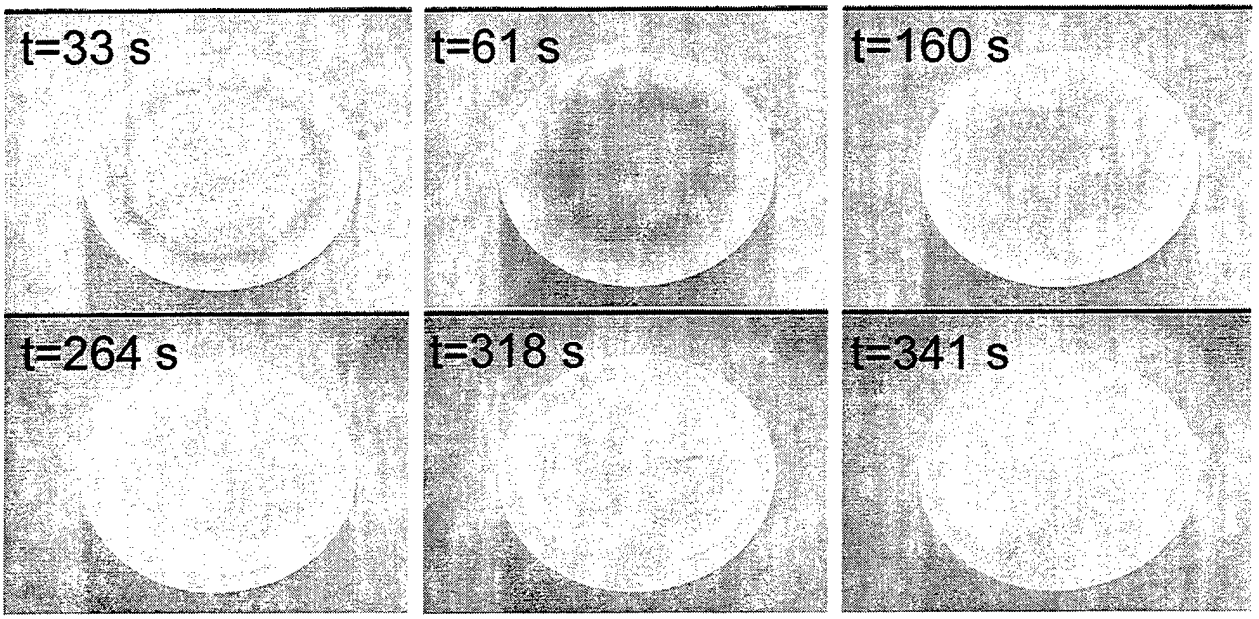


Figure 4. Video images collected for the coupon held at 200 mV(SCE) in Figure 3.

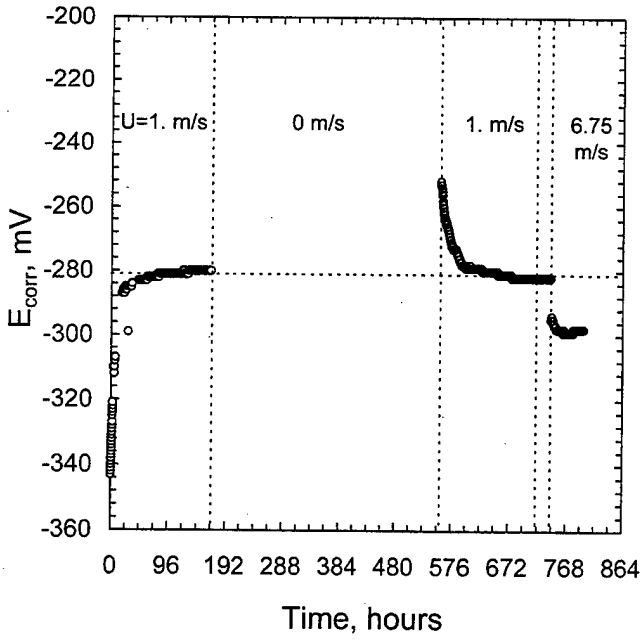


Figure 5. Corrosion potential as a function of time for 99.9% Cu in passively-aerated synthetic seawater. The time period for the experiment was 33 days. The electrode remained in stagnant fluid from t=190 to 550 hours, a cathodic potential was applied at t=556 hours, and flow was resumed at t=557 hours.

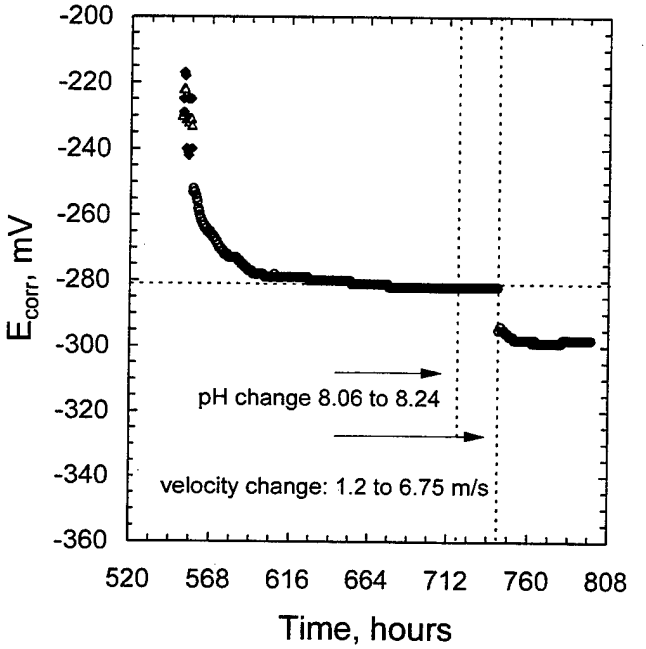


Figure 6. Corrosion potential as a function of time for the latter stage of the experiment presented in Figure 5.

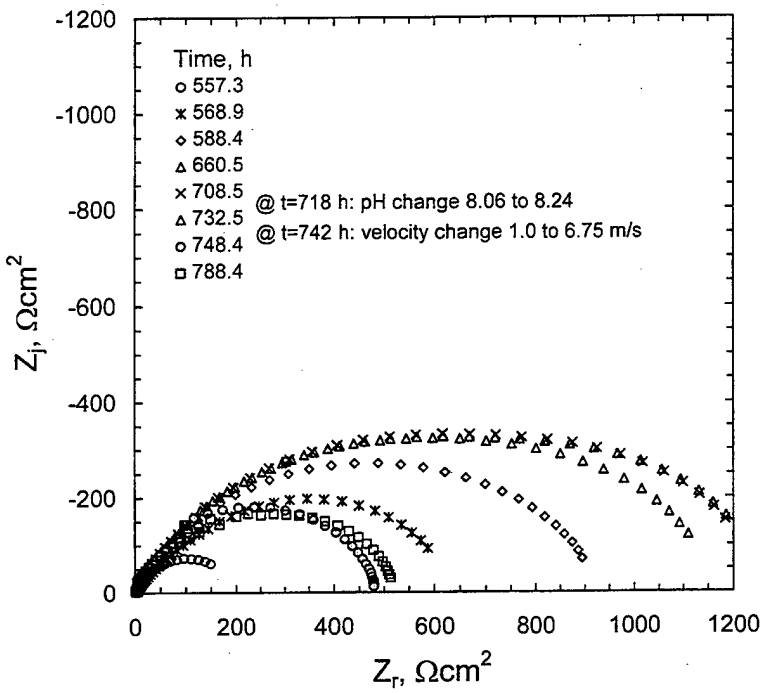


Figure 7. Impedance data collected for over the course of 231 hours corresponding to the corrosion potential data in Figure 6.

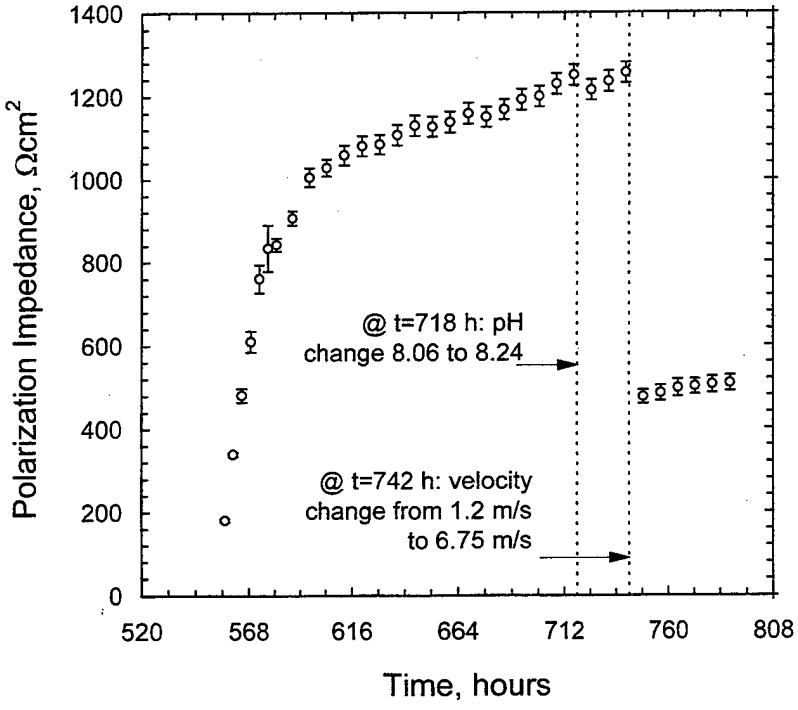


Figure 8. Polarization impedance for the impedance scans shown in Figure 7. Estimated values and associated standard deviation were obtained through the use of a measurement model.

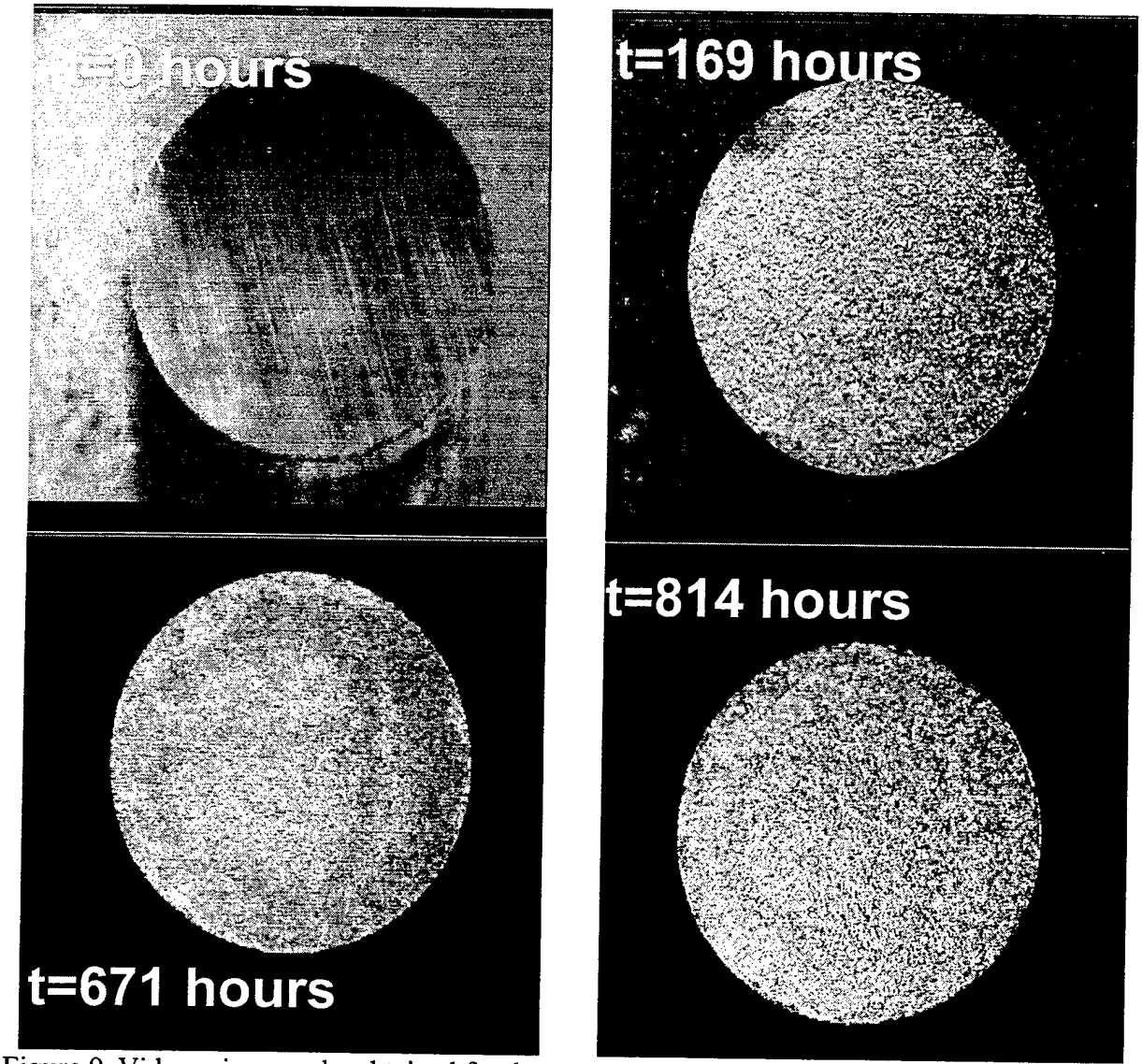


Figure 9. Video micrographs obtained for the experiment described in Table 1; t=0 hours: the initial condition immediately after submersion; t=169 hours: after steady flow at 1 m/s; t=671 hours: before increase in jet velocity; and t=814 hours: after increase in jet velocity.

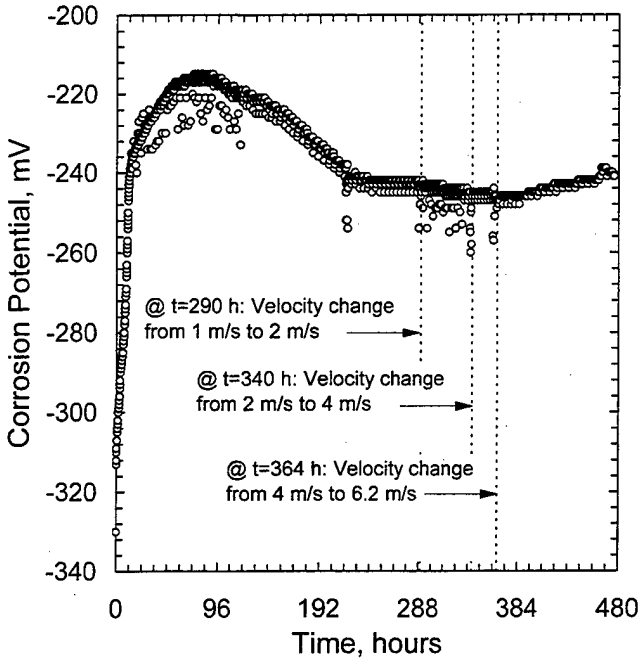


Figure 10. Corrosion potential as a function of time for 99.9% copper in continuously-aerated synthetic sea water electrolyte.

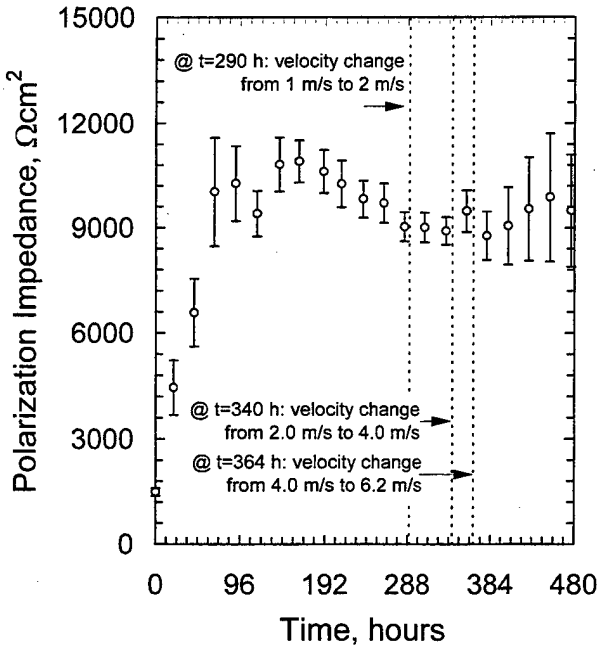


Figure 11. Polarization impedance for the impedance data collected during the experiment shown in Figure 10. Estimated values and associated standard deviation were obtained through the use of a measurement model.

The Effects of Dissolved Ozone on the Corrosion Behavior of Nickel, Stainless Steel and Aluminum-Based Alloys in Artificial Seawater

B. E. Brown, J. H. Stevens and D. J. Duquette
Materials Science and Engineering Department
Rensselaer Polytechnic Institute
Troy, NY 12180-3590

W. E. Wyllie II
3M Unitek
3M Dental Products Division
Monrovia, CA 91016

ABSTRACT

The effects of dissolved ozone on the corrosion behavior of nickel, stainless steel, and aluminum-based alloys in artificial seawater were studied and the results were compared with those obtained for aerated solutions. Corrosion rates and crevice corrosion information obtained from plate samples at intervals of 2, 4, 8, 16, 26, and 47 weeks were compared with eletrochemical measurements of corrosion potential, linear polarization resistance (LPR), and cyclic polarization curves from concurrently immersed wire samples. Overall, the general corrosion behavior of all of the alloys exposed to ozonated solutions did not appear to be very significant, although in the case of low molybdenum-containing stainless steels and nickel-based alloys, tight crevices should be avoided.

Keywords: ozone, bromide, hypobromous acid, chlorine, corrosion control, biofouling control, oxidizing biocide, seawater, stainless steel, aluminum, nickel, nickel-base alloys, molybdenum, transpassivity.

INTRODUCTION

In the early 1900s, ozone was first used to disinfect municipal drinking water in Nice, France.[1] Since then, water treatment by ozonation has been favored over chlorination in Europe because of improved taste, odor control and disinfection. Today, due to the environmental hazards of chlorination byproducts, ozone is currently being used in many fresh water treatment applications in the United States, where only chlorine has been used in the past. These applications include the sterilization of drinking water, treatment of sewage and waste water, algae control in swimming pools, and biofouling control in cooling tower waters.

Although most applications of ozone are in fresh waters, there is a growing number of applications for the use of ozone in seawater. Ozone has already been used successfully in several large aquaria for the treatment of biotoxins in recirculating seawater systems.[2] It is also being investigated for use in preventing biofouling in desalination processes as well as in heat exchangers which use marine waters for cooling.[3]

Ozone is one of the strongest oxidizers used in water treatment. An earlier paper by Wyllie, Brown, and Duquette covers the details of the chemical reactions that occur in ozonated seawater.[4,5] The reaction of ozone with the components of artificial seawater results in the formation of hypobromous acid and bromate ion (Figure 1). Table 1 shows the redox potentials calculated for different oxidizing conditions, indicating that ozone indeed has a very strong oxidizing effect.

This study focuses on the corrosion behavior of stainless steel, nickel-based and aluminum-based alloys in ozonated artificial seawater. The alloys that will be discussed in this paper include: stainless steel alloys 304 and AL6XN (UNS S30400 and NO8367); nickel alloys C-276 and 690 (UNS N10276 and N06690); and aluminum alloys AL1100 and AL5052 (UNS A91100 and A95052).(1)

EXPERIMENTAL PROCEDURE

Solutions

Three tanks of artificial seawater were ozonated with each tank containing a separate alloy group. Another three tanks were aerated as a control group.

Artificial seawater solutions were prepared by adding 1946 g of Forty Fathoms Bio-Crystals Marinemix(2) to 56L of distilled water in a 76-liter tank. This mix is a brand of artificial seawater that contains all of the components of natural seawater, in accordance with ASTM D 1141-90.[6]

Since the bromide ion is the main ion oxidized by ozone in artificial seawater, the initial bromide concentration of each tank was measured using a titration procedure[7] and adjusted by the addition of artificial seawater mix or distilled water, until the bromide concentration was in the range of 800-860 mM/L (63-69 mg/L).

Using a fritted glass bubbler, ozone was bubbled into each of the three tanks in combination with oxygen as a carrier gas, at a rate of 0.03 m^3/hr [1 SCFH (standard cubic feet per hour)], while another tank, used as a control, was aerated at the same rate.

The solution in each ozonated tank was measured for changes in pH, as well as concentrations of apparent residual ozone, bromide, hypohalite, and bromate, after 1

(1) UNS numbers are listed in *Metals and Alloys in the Unified Numbering System*, published by the Society of Automotive Engineers (SAE) and co-sponsored by ASTM.
(2) Registered Trademark of Marine Enterprises Intl. Inc.

day and 1 week of ozonation before samples were immersed. After sample immersion, these values were measured upon removal of test samples. The residual ozone was measured using the Indigo Trisulfonate Method.[8,9] Bromide, hypohalite, and bromate concentrations were measured using a titration procedure.[7,10] The control tanks were aerated for 4 days before immersion of samples; the free bromide concentration and pH of this solution were tested prior to sample immersion.

In order to compensate for evaporation and to prevent adverse build-up of byproducts, 6 liters of artificial seawater, in both the aerated and ozonated tanks, were extracted weekly and replaced with fresh solution, throughout the course of the experiments.

Ozone Generation and Delivery

Ozone was generated using a combination of an AirSep(3) AS-12 oxygen generator and American Ozone(4) GS2-14 ozone generator. The oxygen generator was set to operate at a pressure of 69 kPa (10 psig) and 55% of maximum output, delivering 90-95% oxygen (nitrogen balance) to the ozone generator at a flow rate of 0.28 m^3/hr (10 SCFH). With the ozone generator operating at a pressure of 21 kPa (3 psig) and at 85% power setting, this produced an ozone concentration of approximately 47 g O_3/m^3 (3.35 wt.% O_3 in 90-95% O_2).

The oxygen/ozone gas mixture was supplied to each tank via a stainless steel ball flow meter (0-2 SCFH range), set at 0.03 m^3/hr (1 SCFH), giving a rate of ozone input into each tank of 1.3 g O_3/hr with an oxygen input rate of 39 g O_2/hr. From the flow meters, ozone was delivered to each tank via PTFE(5) and Norprene(6) tubing. Only PTFE tubing was used inside the tanks.

Samples

The alloys tested in these experiments included: stainless steel alloys 304 (Fe-18Cr-8Ni) and AL6XN (Fe-21Cr-24Ni-6Mo); nickel alloys C-276 (Ni-16Cr-16Mo) and 690 (Ni-29Cr-10Fe); and aluminum alloys AL1100 (99Al) and AL5052 (Al-2.2Mg).

Three basic types of samples were used in these experiments:

1.) Weight Change (plate)
2.) Crevice (plate)
3.) Electrochemical Characterization (wires)*

*Wires of alloy AL5356 (UNS A95356) were used in place of alloy AL5052.

Three weight change and three crevice samples were cut from 0.158 cm (0.063 in) to 0.318 cm (0.125 in) thick plate into 2.5x5.1 cm (1.0x2.0 in) coupons, in which a 0.95 cm (0.38 in) hole was drilled. Eight samples of each of the wire alloys were prepared

(3) Registered Trademark of Airsep Corporation
(4) Registered Trademark of American Ozone Systems, Inc.
(5) polytetrafluroethylene
(6) Registered Trademark of Norton Performance Plastics Corp.

for testing. All samples were ground through 600 grit abrasive, rinsed with distilled water, ultrasonically cleaned in distilled water, and then rinsed again with distilled water.

Sample Fixturing

Three weight change samples of each alloy were suspended in the solution by inserting a glass rod through the holes, using PTFE tubing as spacers between the samples. Crevice samples were assembled between two PTFE crenelated washers, surrounding the hole. The sample and PTFE washers were clamped between Grade-2 titanium washers and secured with a Grade-2 titanium bolt and nut. For purposes of this discussion, the portion of the crenelated PTFE washer which was in contact with the surface of the sample to form the crevice is called the "plateau," while the region separating the plateaus is referred to as the "slot." A PTFE thread was tied to one of the PTFE washers used for each sample; the other end of the thread was tied to a PTFE O-ring for later fixturing. In order to prevent any contact between the sample and the bolt, the bolt was wrapped with PTFE tape prior to assembly. The crevice samples were assembled while submerged in aerated artificial seawater, in order to minimize air pockets and to initiate wetting under the PTFE crenelated washers. After crevice samples were tightened with one and a quarter turns from finger tight, the electrical resistance was checked between the sample and the bolt with a voltmeter. Each sample was re-checked after final removal from the tanks to verify that there had been no electrical contact between the sample and fixture.

Wire samples were bent so that only the cylindrical surfaces of the wires were immersed, in order to eliminate the effects arising from the cut ends of the wires.

Testing

Tests were performed at 1, 2, 4, 8, 16, 26, and 47 weeks following initial immersion. Before any samples were removed or tested in the tanks, the water chemistry was checked.

At each time interval, weight change samples were removed, rinsed in distilled water and allowed to air dry before weighing. After weighing, the samples were photographed, replaced on the glass rods and returned to the tank.

Crevice samples were removed at intervals after initial immersion of 4, 8, and 16 weeks. The assembly was then carefully taken apart, and the crenelated washer and fixture archived, if corrosion product was present. The samples were then rinsed in distilled water again and allowed to air dry. The samples were then weighed, photographed, and stored in a dessicator.

At each interval, one wire sample of each alloy was removed from each tank for electrochemical characterization, along with approximately one liter of solution. Care was taken to keep the wire submerged while moving both the wire and tank solution into a one liter cell. A bubbler was placed in the cell, bubbling either air or ozone at a rate of approximately 0.003 m^3/h (0.1 SCFH). Electrochemical measurements of steady state corrosion potential, linear polarization resistance (LPR) and cyclic

polarization were performed on the wires. Afterwards, the wires were removed from the cell and the submerged area of the wire surfaces measured.

One wire of each alloy was left in the tank over the course of the entire experiment. At each interval, the steady state corrosion potential and linear polarization resistance of these wires were measured while they remained in the tank.

Linear polarization resistance measurements were collected at a scan rate of 0.6 V/hr for all wire samples. Corrosion rates for all alloys were then calculated from the LPR data based on the assumption that $\beta_a=\beta_c=0.12$. Cyclic potentiodynamic polarization scans of nickel and aluminum wires were performed at a rate of 10 V/hr, while those of stainless steel wires were performed at a rate of 1V/hr.

RESULTS AND DISCUSSION

Solution Chemistry

After one week of ozonation, the solution chemistry of the artificial seawater reached stable values. The pH decreased slightly to a value of approximately 8.1-8.2. The residual ozone concentration stabilized at a value between 0.3-0.4 mg/L. Values for brominated species are given as percentages of total bromide, which was in the range of 820-880 μM (65-70 mg/L). Approximately 82-85% of the total bromide in solution was oxidized to bromate after 8 weeks of exposure. The amount of free Br^- was 8-16% of the total bromide in solution, while HOBr and OBr^- were between 0 and 3%.

After the samples were immersed, a reduction in the amount of residual ozone was observed, occurring over a period of 2 to 8 weeks. This decrease is believed to be due to an increase in ozone demand created by metallic corrosion of the samples, as well as to subsequent oxidation of metal ions by ozone. After the initial decrease, the residual ozone concentration in the tanks recovered to close to the initial value with time. In most tanks, these values were lower than the initial concentration prior to sample immersion, reflecting the ozone demand associated with ongoing metallic corrosion. The ozone is cathodically reduced on the surfaces of the metal samples in order to support the anodic dissolution of the alloys and to establish the passive films. With the onset of stable passivity the ozone demand was reduced. It is important to note that, in the absence of metal corrosion, the ozone concentration would be expected to rise above initial values, due to decreased chemical demand associated with a decreasing concentration of unreacted Br^- ion.

In ozonated seawater, voluminous amounts of black flocculent corrosion product precipitated in the nickel and stainless steel tanks within 24 hours of the immersion of the samples, plating onto the glass sides of the tanks. Fully immersed samples remained free of this reaction product. For partially immersed samples, the portions of the wire samples below the water line remained free of precipitate, while the sections above the waterline were covered with the precipitate. No black precipitate was observed in the ozonated tank containing aluminum samples.

The black precipitate was collected from the ozonated tanks, filtered and dried. Examination using energy dispersive spectroscopy (EDS) in the scanning electron microscope (SEM) revealed the presence of primarily calcium, oxygen, chloride, and nickel. Further analysis by x-ray diffraction indicated the presence of calcium oxide, sodium chloride, and hydrated nickel chlorate. The chlorate ion forms in these solutions by the oxidation of Cl^-->ClO^-->ClO_3^-. Utilizing the Pourbaix diagram and laboratory tests, the precipitate was reproduced within 48 hours of immersion of a pure nickel sample in a solution of ozonated distilled deionized water adjusted to pH 10 with NaOH. From these results, Pourbaix indicates that in oxidizing solutions of this pH range, nickel peroxide (NiO_2) initially forms.[11] Due to its instability, the nickel peroxide decomposes into nickelic and nickelo-nickelic oxides (Ni_2O_3, Ni_3O_4), of which Ni_2O_3 is indicated as being black in coloration. These oxides were not observed in the x-ray analysis, suggesting that they are amorphous or exist in quantities below the detection limit.

Steady State Corrosion Potentials

Electrochemical testing of stainless steel and nickel alloy wires in the tanks showed that the corrosion potential of wires exposed to ozonated artificial seawater is shifted to a stable value of 0.6-0.8 V noble to the corrosion potential of wires in aerated artificial seawater after 8 to 16 weeks of exposure. In contrast to this observation, the corrosion potential of aluminum alloys exposed to ozonated artificial seawater were initially active to the aerated corrosion potential by 0.5 V. After 47 weeks of exposure, the values of the corrosion potentials for aluminum wires in both the aerated and ozonated cases were similar. Table 2 shows the steady state corrosion potentials measured on wire samples after 47 weeks of exposure.

For ozonated solutions, the cathodic reaction is ozone reduction, with the half-cell potential (e) = 1.55 V_{SHE}, while in aerated seawater, the half-cell potential for oxygen reduction at pH 8.2 is 0.73 V_{SHE}. The potential shift observed on the passive alloys is approximately the same (+0.6 to +0.8 V) as the difference between the calculated reduction potentials for ozonated *vs.* aerated seawater, $\Delta e = 1.55 - 0.73 = +0.82$ V from Table 1. This correlation indicates that the corrosion potential of the alloys in ozonated seawater is influenced strongly by the presence of ozone rather than by the oxygen carrier gas. At the oxygen content in the feed gas (P_{O_2} = 0.90-0.95 atm), the calculated reduction potential for oxygenated seawater is 0.75 V_{SHE}, only 0.02 V noble to the aerated seawater value. Accordingly, higher oxygen concentrations in ozonated seawater, alone, are not the cause of the corrosion potential shifts.

Unlike metals which passivate and directly reflect the presence of a strong oxidant by a more noble corrosion potential, the corrosion potential of aluminum alloys in ozonated artificial seawater shifted in the active direction compared to the potential measured in aerated artificial seawater. Aluminum alloys can undergo cathodic corrosion in neutral solutions which negates the use of the normal superposition of independent anodic and cathodic reactions.[12] Normally, however, the case of cathodic corrosion exhibits an increase in corrosion rate with decreasing electrode potential.

With increasing exposure time, there was a convergence of the corrosion potential of the aluminum alloys measured in ozonated solutions with that measured in aerated artificial seawater. This result suggests that the corrosion potential is stable due to the oxide on the surface acting as a diffusion barrier; ozone is reduced on the oxide surface before dissociating. Oxygen, however, would be able to diffuse to the surface to be reduced, as it is a stable molecule.

Corrosion Rates

Despite the appearance of the voluminous black product, the calculated corrosion rates of all nickel and stainless steel alloys in ozonated seawater are still very low (<30 μm/y). Table 3 shows the instantaneous and averaged corrosion rates of samples after 16 weeks of exposure calculated using linear polarization resistance and weight change measurements. In most cases, the corrosion rates of metals exposed to ozone are higher than those in aerated solutions for the entire time period. The exception is the aluminum alloys, where the corrosion rates are higher in aerated solutions.

Nickel-Based Alloys - The corrosion rates calculated in aerated solutions were initially 16.5 μm/y for alloy C-276 and less than 1 μm/y for alloy 690. These values decrease to less than 1 μm/y after 47 weeks of exposure. Corrosion rates in ozonated artificial seawater were initially 7 μm/y for alloy C-276 and alloy 690, decreasing to 1.4 and 3 μm/y, respectively, after 47 weeks.

Nickel alloys exposed to ozonated *vs.* aerated seawater form an oxide layer. This is based on the observation that, in ozonated solutions, the only adherent corrosion product on nickel alloys is characterized by the presence of thin oxide films exhibiting interference type coloration. This oxide varies in apparent thickness from alloy to alloy and with time of exposure to ozonated solutions based on the changes in coloration. Additionally, dissolution is evident in ozonated artificial seawater, as indicated by the green coloration of the solution induced by dissolution of nickel as Ni^{++}.[11] The formation of an oxide is further substantiated by the temporal decrease of corrosion rates calculated from weight change and LPR measurements.

Stainless Steel Alloys - After 8 weeks the corrosion rates of alloy 304 and AL6XN in aerated artificial seawater were 5.3 and 1.5 μm/y, respectively. These values decrease to less than 0.2 μm/y after 47 weeks of exposure. Corrosion rates in ozonated artificial seawater were initially 13 μm/y for alloy 304 and 0.81 μm/y for alloy AL6XN, decreasing to 5.3 and 0.003 μm/y, respectively, after 47 weeks.

Aluminum-Based Alloys - The corrosion rates calculated for alloy AL1100 in aerated solutions range from 8 to 50 μm/y over the entire time period. The corrosion rates calculated from weight loss samples of alloy AL5052 show an increase in aerated corrosion rate with time of up to 44 μm/y, while LPR measurements of AL5356 indicate a corrosion rate of less than 5μm/y. Corrosion rates calculated in ozonated artificial seawater were initially 6 μm/y for alloy AL1100 and 1 μm/y for alloys AL5052

and AL5356, decreasing to less than 1 μm/y after 47 weeks. Based on these results, aluminum alloys appear to form a protective oxide layer in ozonated artificial seawater. Analysis of the films formed in both the aerated and ozonated environments showed that they were similar in composition.

Crevice Samples

For the nickel and stainless steel alloys, the creviced samples exposed to aerated artificial seawater exhibited a few small pits that initiated after approximately 4 weeks of exposure. Those initiated pits stabilized with no further growth. No other corrosion damage was observed on alloys exposed to aerated artificial seawater.

Nickel-Based Alloys - In ozonated artificial seawater, the exposed surfaces of alloy C-276 were covered by a thin oxide which refracted different colorations depending on the alloy and the time immersed. The coloration of alloy C-276 was a yellow-gold-bronze. The slot regions of alloy C-276 displayed a semi-adherent dark brown corrosion product, and bright metal regions where the corrosion product had spalled, leaving the base metal exposed. The plateaus of the alloy C-276, which were in contact with the crenelated washer to form crevices, were uncorroded. From examinations by SEM and EDS, the dark brown corrosion product in and around alloy C-276 slots was shown to exhibit significant amounts of iron, oxygen, and silicon. This behavior indicates that a differential oxidation cell develops between the high ozone activity at the bulk surfaces and the low ozone activity in the slot regions of the creviced washers.

In contrast to the behavior of the alloy 276, alloy 690 exhibited no colorful refractive oxide on its uncreviced surfaces when exposed to ozonated artificial seawater. The slot regions of the ozonated samples did exhibit a light blue oxide with some evidence of brown corrosion product which was found to be a semi-adherent film showing high iron and oxygen concentrations using EDS analysis. In ozonated solutions, a significant number of crevices exhibited extreme, deep pitting, similar to that experienced by alloy 304.

In both aerated and ozonated seawater, the nickel alloys containing molybdenum show resistance to classical crevice corrosion. Alloy 690, which does not contain molybdenum exhibits classical crevice corrosion; the initially passive surface actively corrodes under the tight crevice plateaus. The significance of molybdenum as an alloying element for reducing crevice corrosion susceptibility is clearly demonstrated by the results for alloy 690. In aerated seawater, crevice corrosion was also noted for alloy 690, although to much lower extent.[13] It may be noted that the Ni-Cr-Fe alloys which do not contain molybdenum, such as alloy 690, are usually selected for resistance to oxidizing conditions rather than for resistance to crevice corrosion in seawater.

Stainless Steel Alloys - In ozonated artificial seawater, alloy 304 experienced crevice corrosion attack beneath the plateaus of the crenelated washers. This attack produced large volumes of red corrosion product, identified as iron (III) oxide using EDS. The number of initiated crevice sites produced under ozonated conditions

decrease with time, reaching a penetration depth of 0.513 mm after 16 weeks of exposure.

In contrast to alloy 304, the corrosion attack of alloy AL6XN beneath the crenelated plateaus was minor in ozonated artificial seawater. Only the slot regions of this alloy were discolored by a black oxide with little evidence of pitting or crevice penetration.

Aluminum-Based Alloys - In ozonated artificial seawater, the exposed surfaces of alloys AL1100 and AL5052 exhibited a dark coherent oxide. Beneath the crenelated washer, there was little pitting or crevice corrosion of samples exposed to ozonated solutions. In contrast to this, samples in aerated artificial seawater were covered with regions of white corrosion product on the bulk and in the slot regions beneath the crevice. Many plateau areas underneath the crenelated washer were damaged by the growth of large pits. These results support the concept of enhanced film properties on aluminum alloys exposed to ozonated solutions.

Cyclic Potentiodynamic Polarization

Nickel-Based Alloys - Figure 2 shows that the aerated cyclic potentiodynamic polarization (CPP) curve of alloy C-276 after 47 weeks of exposure exhibits both primary and secondary passivity. At a potential of 0.32 V_{SCE} the aerated curve shifts to transpassive behavior, showing very little hysteresis on the return portion of the curve. After 47 weeks, the steady state corrosion potential of the ozonated alloy C-276 was 0.73 V_{SCE}, correlating with the transpassive transition in aerated solutions, indicating that the ozonated wires are in the transpassive region under steady state conditions. The curve for the ozonated condition also shows a very distinct hysteresis loop upon reversal, indicating susceptibility to pitting and crevice corrosion. The formation of a hysteresis loop for the ozonated condition was evident only after 2 weeks of exposure. The repassivation potential of alloy C-276 in ozonated artificial seawater after 47 weeks of exposure was $0.64V_{SCE}$, 0.25V noble to the zero current potential. Examination of the wires after polarization showed that significant amounts of pitting had occurred on the polarized portions of both aerated and ozonated wires below the waterline. Enhanced corrosion was observed at the polarization waterline of the ozonated sample. The appearance of this waterline corrosion was similar to the crevice corrosion observed on ozonated C-276 crevice samples, with the formation of a dark brown corrosion product which spalled away to reveal shiny metallic base metal.

Similar to alloy C-276, the aerated CPP curve of alloy 690 after 47 weeks of exposure exhibits both primary and secondary passivity. At a potential of 0.35 V_{SCE} the aerated curve shifts to transpassive behavior, showing very little hysteresis on the return portion of the curve. The repassivation potential was $0.18V_{SCE}$, 0.50V noble to the zero current potential. After 47 weeks, the steady state corrosion potential of the ozonated alloy C-276 was 0.79 V_{SCE}, correlating with the transpassive transition in aerated solutions, indicating that the ozonated wires are in the transpassive region under steady state conditions. Upon reversal of the potential, Alloy 690 does not form the usual hysteresis loop which is indicative of crevice corrosion, although this alloy displayed susceptibility t o crevice corrosion in plate tests.

Stainless Steel Alloys - Figure 3 shows that the aerated CPP curve of alloy 304 after 47 weeks of exposure exhibits both primary and secondary passivity. At a potential of 0.46 V_{SCE}, the aerated curve shifts to transpassive behavior, showing a large hysteresis loop on the return portion of the curve, indicating susceptibility to crevice corrosion. This result correlated to large, subsurface cavernous pits which developed on the wire surfaces as a result of testing. The repassivation potential 0.005 V_{SCE} of was found to be 0.01 V active to the zero current potential, indicating that existing pits would continue to grow when exposed to this environment. After 47 weeks, the steady state corrosion potential of the ozonated alloy 304 was 0.81 V_{SCE}, correlating to the transpassive transition in aerated solutions, indicating that the ozonated wires are in the transpassive region under steady state conditions.

As with alloy 304, alloy AL6XN exhibited both primary and secondary passivity regions. At a potential of 0.44 V_{SCE}, the aerated curve shifts to transpassive behavior. The steady state corrosion potential of the ozonated alloy AL6XN was 0.84 V_{SCE}, indicating that the ozonated wires are in the transpassive region under steady state conditions. Unlike alloy 304, alloy AL6XN did not exhibit a hysteresis loop in aerated solutions, but did in ozonated artificial seawater after 47 weeks of exposure. In ozonated solutions, the repassivation potential overlays the zero current potential, indicating susceptibility to localized corrosion. Examination of the wire surfaces after CPP testing showed that the ozonated wire had small hemispherical pits on the submerged surface, while the wire exposed to aerated conditions displayed no pitting.

Aluminum-Based Alloys - Alloy AL1100 and AL5356 exhibited very similar CPP curves in the two environments. Figure 4 shows that both the aerated and ozonated CPP curves of alloy 5356 exhibited a large hysteresis loop after 47 weeks of exposure. Correlating with the more aggressive attack on creviced plate samples in aerated solutions, the repassivation potential for the aerated condition is active to the zero current potential, indicating an increased crevice corrosion susceptibility. Unlike the aerated condition, the repassivation potential for the ozonated case is 0.2V noble to the zero current potential. Reflecting the lower corrosion rates measured in ozonated artificial seawater, the current densities reflected in the CPP curve are a magnitude of order less in ozonated compared to aerated solutions.

CONCLUSIONS

Ni-Cr-Mo Alloys

1. For nickel based alloys, ozonation polarizes the alloys into the transpassive region of the polarization curves, resulting in the production of a non-adherent, flocculent black reaction product.

2. For all the non-creviced alloys, the material loss that occurs in ozonated artificial seawater, while slightly greater than that observed in aerated seawater, is sufficiently low (< 10μm/y) such that general corrosion is not considered to be a problem.

3. Creviced nickel alloys containing molybdenum do not exhibit classical crevice corrosion behavior in ozonated solutions. Preferential corrosion occurs at the junction at the edge of the crevice former in contact with the base alloy plate, leaving the actual

crevice (plateau) protected due to differential oxidation. This preferential corrosion reaction, however, is not severe, and provides a degree of cathodic protection for the alloy inside the crevices Samples exposed to aerated solutions exhibited small pits in the crevices. However the pits, once initiated, were stable and showed no growth after long exposures.

Fe-Cr-Ni (Mo) Alloys

1. In general, ozone polarizes the stainless steel alloys into a region of secondary passivity. Under these conditions the pitting resistance of 304 is enhanced in ozonated solutions when compared with aerated solutions.

2. Alloy 304 exhibits classical crevice corrosion in tight crevices exposed to ozonated artificial seawater. Although crevice corrosion was noticed on several aerated samples, the extent of the corrosion was not as severe as under ozonated conditions.

3. More highly alloyed stainless steels showed excellent resistance to crevice corrosion in either ozonated or aerated seawater. However, in ozonated seawater, alloy AL6XN, which contains significant amounts of nickel, showed some evidence of superficial localized corrosion at the mouths of the crevices. In some cases this corrosion was identified as either shallow pitting or shallow intergranular attack. This behavior is similar, but not identical, to that observed for the nickel based alloys, and is believed to be due to transpassive dissolution of the nickel.

Al Alloys

1. The general corrosion and pitting corrosion behavior of aluminum alloys are improved when ozonated seawater exposure is compared to aerated seawater exposure.

2. The protective oxide film produced by exposure to ozonated seawater appears to be more dense than that produced in aerated seawater. Additionally exposure to aerated seawater produced a white, barely adherent corrosion product associated with pitting of the surface. No similar corrosion product was observed on aluminum samples exposed to ozonated seawater.

3 It appears that the improved corrosion resistance of aluminum alloys in ozonated seawater, when compared to aerated seawater, is due to the greater oxidizing potential of ozonated solutions. When localized corrosion processes occur, the corrosion product film produced in ozonated seawater increases the tendency for repair of the film.

ACKNOWLEDGMENTS

The authors are grateful for the support of the Office of Naval Research, and of Dr. A. J. Sedriks, under contract N00014-90-J-1439.

REFERENCES

1. P. C. Singer, Journal of American Water Works, 82, Oct. (1990) p. 77-88.
2. D. L. LaBonne, "Ozonation of Marine Mammal Pool Waters," 1990.
3. R. Sugam, J. H. Singletary, W. A. Sandvik and C. R. Guerra, Ozone Science and Engineering, 3, (1981) p. 95-107.
4. W. E. Wyllie II, B. E. Brown and D. J. Duquette, "Ozone in Seawater, Part 1: Chemistry, Part II: Corrosion of Metals," CORROSION/95, paper no. 269 (Houston, TX: NACE International, 1995).
5. W. E. Wyllie II, B. E. Brown and D. J. Duquette, "Interim Results on the Corrosion Behavior of Engineering Alloys in Ozonated Artificial Seawater," Office of Naval Research, 2, March, 1996.
6. ASTM D 1141-90, "Standard Specification for Substitute Ocean Water," (Philadelphia, PA: ASTM, 1990).
7. K. Grasshoff, Verlag Chemie, (1976) p. 324.
8. H. Bader and J. Hoigné, Water Research, 15 (1981) p. 449-456.
9. H. Bader and J. Hoigné, "Colorimetric Method for the Measurement of Aqueous Ozone based on the Decolorization of Indigo Derivitives," Ozonation Manual for Water and Wastewater Treatment, W. J. Masschelein (Chichester: John Wiley & Sons, 1982) 169-172.
10. W. R. Haag, Water Research, 15, (1981) p. 937-940.
11. M. Pourbaix, Atlas of Electrochemical Equilibria in Aqueous Solutions (Houston, TX: National Association of Corrosion Engineers, 1974).
12. H. Kaesche, Metallic Corrosion (Houston: National Association of Corrosion Engineers, 1985), p. 492.
13. H. H. Uhlig and R. W. Revie, Corrosion and Corrosion Control (New York: John Wiley & Sons, 1985).
14. W. R. Haag and J. Hoigné, J. Environ. Sci. Technol., 17, 5 (1983a) p. 261-267.

TABLE 1
REDUCTION POTENTIALS FOR VARIOUS OXIDIZING REACTIONS

Redox Couple	e^o (V_{SHE})	Nominal conditions in artificial seawater, pH 8.2	e (V_{SHE}) at nominal conditions
O_3/O_2	2.08	Ozonated, $p(O_3)$ = 0.024 atm	1.55
$HOCl/Cl^-$	1.48	Chlorinated, [HOCl] = 25 mg/l	1.15
$HOBr/Br^-$	1.33	Brominated, [HOBr] = 25 mg/l	1.08
O_2/OH^-	1.23	Oxygenated, $p(O_2)$ = 0.95 atm	0.75
O_2/OH^-	1.23	Aerated, $p(O_2)$ = 0.2 atm	0.73

TABLE 2
STEADY STATE CORROSION POTENTIALS OF WIRE SAMPLES
AFTER 47 WEEKS OF EXPOSURE

Alloy	Steady State Corrosion Potential (V_{SHE})	
	Aerated	Ozonated
304	0.066	0.812
AL6XN	0.115	0.842
C-276	0.014	0.731
690	0.190	0.795
AL 1100	-0.712	-0.830
AL 5356	-0.517	-0.428

TABLE 3
CORROSION RATES OF SAMPLES
AFTER 16 WEEKS OF EXPOSURE

Alloy	Aerated (μm/y)		Ozonated (μm/y)	
	Instantaneous Corrosion Rate (LPR)	Time Averaged Corrosion Rate (Weight Loss)	Instantaneous Corrosion Rate (LPR)	Time Averaged Corrosion Rate (Weight Loss)
304	0.001	0.26*	1.127	6.54
AL6XN	0.000	0.00*	0.358	0.20
C-276	0.099	0.94*	1.876	1.55
690	0.046	0.07*	1.103	2.84
AL 1100	6.262	27.6*	0.984	0.03*
AL 5356	0.211	10.6*	0.292	0.62*

*Samples gained weight in the formation of an oxide, therefore a mass balance of oxygen reacting to form the oxide was used to calculate the amount of metal in the oxide.

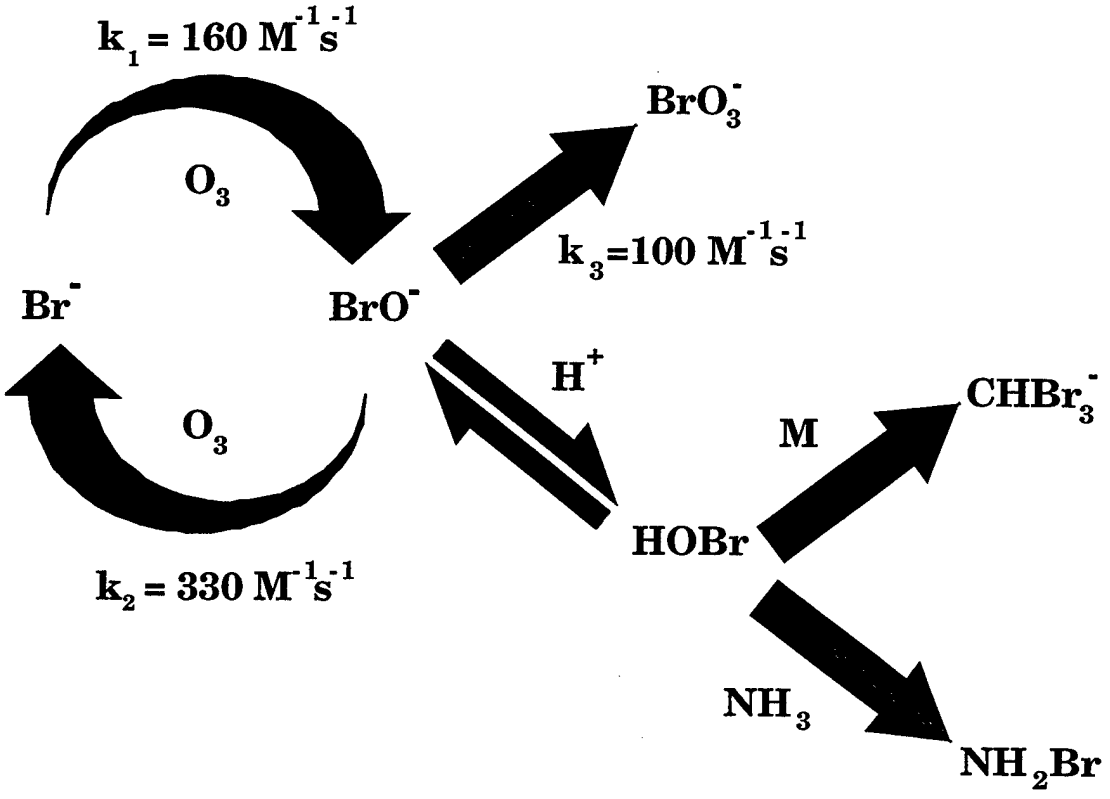


FIGURE 1. Reaction cycle caused by the ozonation of bromide in seawater.[14]

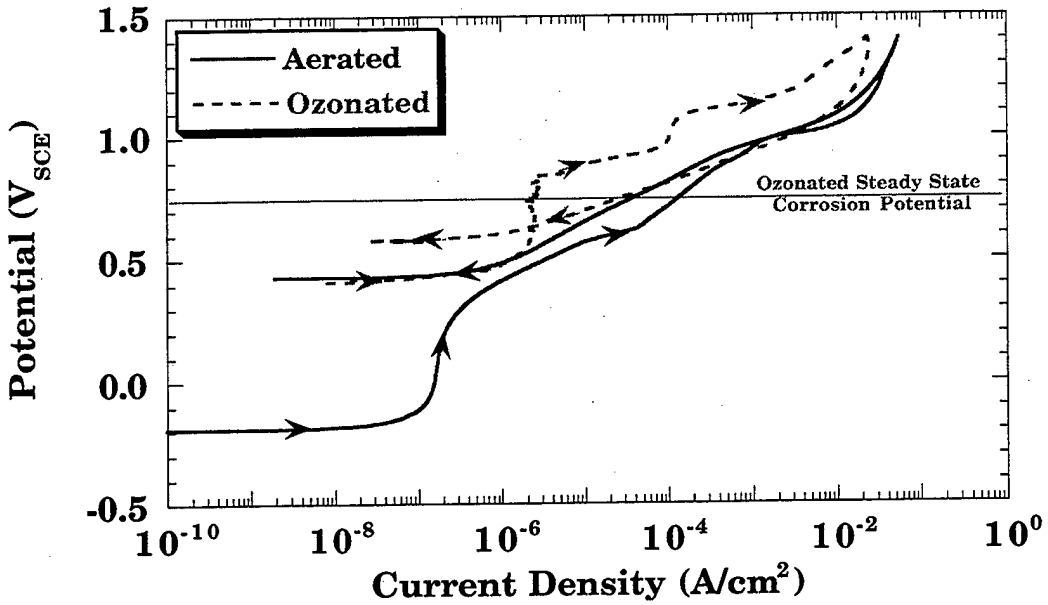


FIGURE 2. Cyclic polarization curves of alloy C-276 in aerated and ozonated artificial seawater.

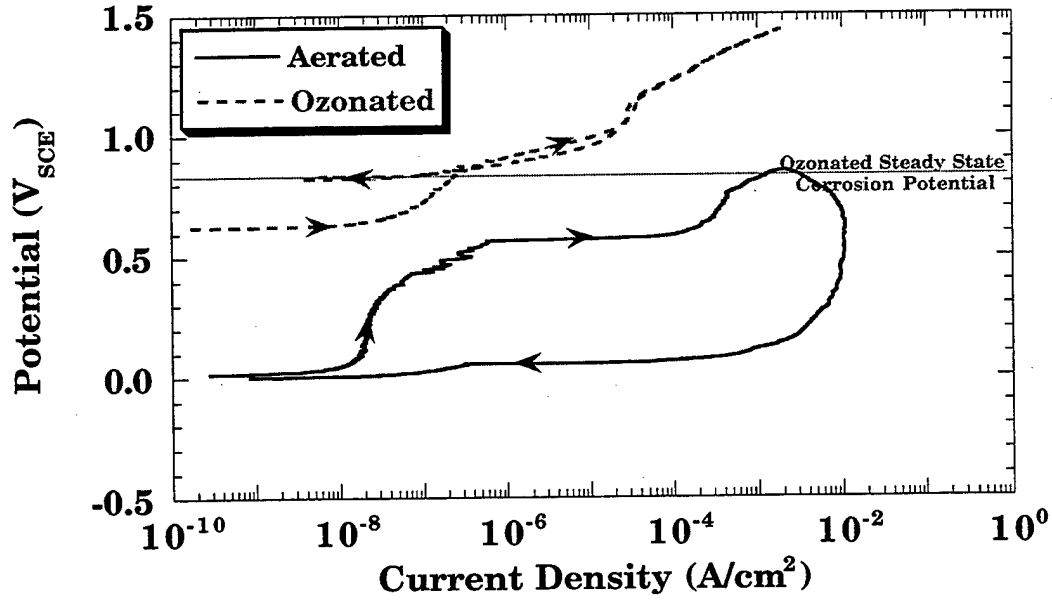


FIGURE 3. Cyclic polarization curves of alloy 304 in aerated and ozonated artificial seawater.

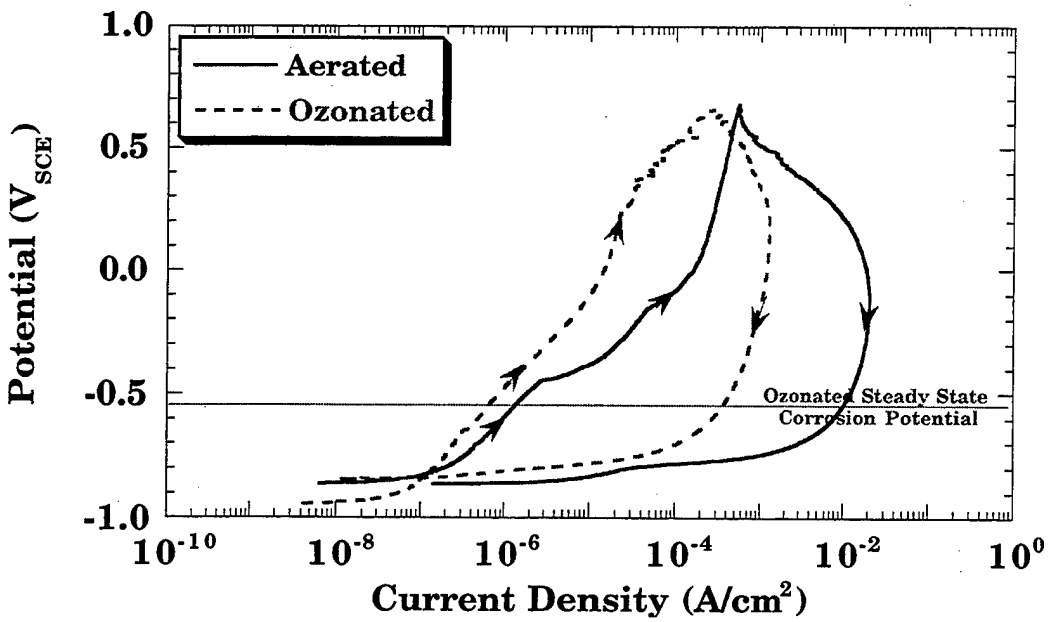


FIGURE 4. Cyclic polarization curves of alloy AL5356 in aerated and ozonated artificial seawater.

Corrosion Protection of Aluminum Alloys by Conductive Organic and Inorganic Polymers

R. Brown, S. Yang, R. Racicot and R.Clark
Corrosion Laboratory
The University of Rhode Island
Kingston RI 02881
J. Neely
Neely Industries
Butler PA

Abstract.

The corrosion resistance of two different coating systems on aluminum alloys was tested by potentiodynamic, electrochemcial impedance spectroscopy and salt spray testing. Both coatings were competitive with the comparison chromate coatings, but in different environmental ranges. The organic conductive polymer was more resistance as the pH decreased while the inorganic polymer showed better performance than the chromate under marine type conditions. While the exact mechanism of protection for the organic polymer is not known the inorganic polymer appears to protect by forming a protective layer on the aluminum. this provides good repair capabilities and damage tolerance

Introduction.

Aluminum alloys are employed in aircraft, both fixed and rotary, for their combination of strength with low weight. However, in service the alloys used in aircraft require protective schemes as alloying additions for increasing strength often decrease corrosion resistance. A good example would be copper addition to the 2000 series of alloys. It is well recognized that pitting results from the presence of copper rich particles in the alloy. The usual route for corrosion protection of aluminum alloys was a chromate conversion coating. These conversion treatments provided acceptable corrosion resistance when combined with a primer and topcoat system. However, due to detrimental health effects and legislative mandates, alternatives to chromates are being sought. The aim is to at least match the corrosion protection performance provided by the well tried and proven chromate coatings. Several studies have measured the corrosion protection afforded by alternate systems. In a large study (1), corrosion protection provided as well as economic and environmental factors were used as comparisons. However to date little has been shown to be competitive with the corrosion protection of chromates.

Although organic polymers have been around for some time it has been comparatively recently that these materials were produced in a conductive form. Since then an extensive effort has been made to determine the corrosion resistance they bring to metals. The main thrust of the research considered protection of steel by coating with conductive polymers. Both stainless and non stainless steels were investigated (2-5). For stainless steel a passive layer was thought to form on the surface. Other data indicated that the mechanism of protection was anodic protection a the open circuit voltage of the conductive polymer moved the open circuit potential of stainless steel into its passive region(2). Data from a conductive polymer coating on steel indicates a layer is formed during a two stage process(5). This layer is thought responsible for corrosion protection.

One of the major applications of conductive polymers on steel is by NASA for the space shuttle launch pads. The acidic environment resulting from launch as the fuels are burnt and cooling water is sprayed was producing considerable corrosion. Coating with conductive polymers has decreased the corrosion(6).

Although much research on steels is available, the applicability of these polymers to aluminum alloys for corrosion protection is not so clear. Aluminum alloys do not corrode in the same uniform manner that steels do, but rather by pitting corrosion.

At the University of Rhode Island, a polyaniline conductive polymer has been synthesized by a template guided polymerization reaction to produce a double strand polymer. The aim of developing this type of conductive polymer is to overcome some of the single strand polymer drawbacks, such as poor processability due to insolubility of the polyaniline, environmental degradation as leaching of dopants required to produce conductivity occurs and finally increasing high temperature stability. These conductive polymers have the same attributes as the single strand conductive polymers, they can be oxidized and reduced and can have several electrochemical states.

Some of the mechanisms for corrosion protection of steels by conductive polymers are thought to involve these different states (2). One mechanism involves the reduction of the conductive polymer followed by its re oxidation contributing to the protection process. Other suggested mechanisms include a traditional inhibitor mechanism, in that many of the conductive polymer contain inhibitors (7).

Another suggested mechanism could be similar to an electrostatic one suggested for chromates (8) with the negatively charged conductive polymer repulsing similar charged ions from the metal surface. This would keep the aggressive chloride ion away from the metal surface and stop pitting corrosion.

Another approach is to use an inorganic polymer as a coating for corrosion resistance. The hypothesis in this case was that the polymer would react in the environment to produce a protective layer on the aluminum surface. The inorganic polymer then must be capable of slow reaction. The corrosion protection in this case is diffusion controlled. The coating thickness is then critical along with the reaction rates of the components that form the protective layer. If the reactions are too rapid, then initially good protection will occur but it will not last. If the reactions are too slow, then insufficient protection will be available. Of course the reactive components have to form a protective layer as well as not contributing to any further health or environmental problems.

In this paper data from two different coatings are presented. One is a conductive organic polymer while the second is an inorganic conductive polymer. The objective was to determine if the coatings were protective and the protection mechanisms.

Experimental Procedures.

Substrate Materials.

The materials used in this study were aluminum alloys typical of those employed in the aircraft industry, AA 6061, 7075 and 2024. Prior to coating no treatments other than sand blasting for the inorganic coating or grinding to 600 grit finish for the organic conductive polymer were carried out. Samples were washed in acetone then distilled water and air dried before coating.

Coating Process.

Organic coatings were applied by dropping solution onto the sample surface and letting the solvent evaporate. Inorganic coatings were applied at Neely Industries by a spray process. Comparative coatings of chromates were either applied in the laboratory or conducted by a commercial coater to applicable military specifications. Two chromate types were used for comparison, comparable to Alodine 600 and Alodine 1200 processes.

Electrochemical Testing.

Potentiodynamic Tests - Cyclic potentiodynamic tests were conducted on $1cm^2$ exposed surface area of sample. A computer controlled potentiostat was used to collect the data. From a potential 50mV below the open circuit potential, a scan rate of $0.1mV.sec^{-1}$ was used with the sample as the working electrode, a saturated Calomel electrode as reference and a platinum counter electrode. Test environment was 0.5 N NaCl solution.

Electrochemical Impedance Tests - Electrochemical impedance spectroscopy (EIS) tests were conducted on the coating to determine their time dependent behavior and also for mechanistic studies. A $1cm^2$ area was clamped onto the end of a hollow glass tube with an "o" ring seal. A saturated Calomel electrode and a platinum counter electrode were employed. Perturbation voltage was 5mV over a frequency range of 10^5 to 0.003Hz. Uncoated samples were compared to the different coated ones. Test solutions in this case were 0.5 N NaCl and 0.5 N NaCl buffered with acid to a pH of 3.6. The aim of the acid treatment was determine the effect of pH on the coating performance.

Salt Spray Testing - Salt spray tests were conducted on samples 5cm by 5cm in area. A scratch was placed in an "X" style across the face of the samples. The edges were sealed with wax. Samples were visually inspected for corrosion products in the scratch and for undercutting of the paint.

Results.

Cyclic Potentiodynamic Scans.

Data from potentiodynamic scans for an uncoated and a conductive organic coated sample is shown in figure 1. A trend to a passive system is seen in the data. Upon reversal of the potential towards more anodic values, no hysteresis in the data was noted, indicating no trend to pitting. The uncoated alloy under the same conditions showed no passive behavior at all, fig 1. For Al 2024 the data indicated less protection. The breakdown potential in this case was -0.375 mV and a large hysteresis loop indicate that pitting would be active.

Figure 2 shows a similar test for the inorganic conductive polymer comparing it to two different chromate conversion coatings. The chromates show the usual data suggesting poor protection, while the inorganic polymer shows passive behavior over a wide potential range form around -0.350 V(SCE) to 3.5(SCE). On reversal of potential the reverse scan curve showed only slight hysteresis . Similar data was found for both Al 7075 and 6061 alloys.

Electrochemical Impedance Spectroscopy.

EIS data comparing the performance of a conductive organic polymer coating compared to both an Alodine 600 and bare Al7075 alloy is shown in figure 3. . The conductive polymer was at least equivalent to the chromate in EIS data. It should be noted that the chromate shows good protection in EIS that is absent in the potentiodynamic data. To determine the low pH corrosion protection of the conductive polymer, EIS tests were conducted at a pH of 3.6. Data from the test is shown in figure 4 for Al 7075. The chromates are non protective in this region as they are unstable at this pH. The EIS data confirms this behavior. However, for the conductive polymer, the data at this low pH indicates improved corrosion resistance than at higher pH regions.

For the inorganic polymer tested on Al 60621 and 7075, the data is shown in figure 5 and 6, as the charge transfer resistance of the alloy obtained from modeling EIS data. The charge transfer resistance of he inorganic coating is always higher than the chromates, indicating at the pH of 6.5

that the inorganic coating provides a stronger protection than chromates. when the inorganic coating is put on to simulate the pretreatment times and thicknesses associated with chromates, the protection decreases only slightly.

Salt Spray Testing.

For the conductive organic coating, less undercutting and a decrease in white product in the scratch region compared to chromate conversion coatings was noted after 200 hours of exposure. For the inorganic polymer, no white product or undercutting was found after 1000 hours of exposure.

Discussion.

The data for both the organic and inorganic conductive polymers indicates that the surface of the aluminum alloys were passivated reducing the corrosion rate. The mechanisms operating for each material case will be discussed.

Organic Conductive Polymer.

There is a limit to the conductive polymer protection which is pH dependent(9). A color change from green to blue occurs when the film is oxidized. Accompanying this green to blue change is a change in state from conductive (green) to non conductive (blue) for the organic polymer. At this time the polymer is no longer protective. The color change is both pH and potential dependent. At the potential for aluminum alloys the green color is dominant. However at the pH range of neutral or marine environments the organic polymer starts to change to the blue state. At this point protection ceases. However, if the pH of the environment is maintained low, as for the case of pH 3.6, then the green state will dominate. The conductive organic polymer then maintains its corrosion protection.

The polymer has been shown not to be a conventional barrier type coating, blocking the environment from reaching the metal surface(9).

No shift in open circuit potential a found for the inorganic polymer indicating that anodic or cathodic protection was probably not the mechanism of protection on this case. XPS studies were unable to identify any particular feature to indicate that a thin passive film was formed on the alloy surface. Clear evidence for this process was shown for similar conductive polymers when placed on steel(5). The oxide layer on steels was visible by scanning electron microscopy examination. However such clear evidence was not found in this case to date.

It should be noted that the data for this conductive polymer and its protection mechanism may be different between aluminum alloys and steels. When this same polymer was placed on steel substrate, a shift in open circuit potential in a positive direction was noted which was not found for aluminum alloy substrates. No passive type behavior was found but a decrease in corrosion rate typical of inhibitors (7).

One intriguing possibility is that of electrostatic repulsion similar to the mechanism for chromates on aluminum alloys (8). In this mechanism the negatively charged chromate ion repulses negatively charged chloride ions that initiate pitting corrosion. The reduced state of the polymer produced by slight oxidation of the aluminum below it will maintain a net negative charge to balance the net positive charge from the positive aluminum ions. This negative charge then repulses the negative chloride ion. Several pieces of data support this mechanism. Firstly as soon as the organic polymer ceases to be conductive then the corrosion protection ceases (9). This can be interpreted as the removal of charge no longer repulses the chloride ion. As these films are not the traditional barrier films the chloride can then rapidly reach the metal surface and attack it. The

conductive polymer does not behave as a barrier layer when not conductive. It is very permeable to water and oxygen. These components will allow a traditional oxide layer to form on the surface with a net positive charge on it.

Another intriguing possibility is that the conductive polymer can hold the chloride ion to maintain charge neutrality. One of the charge carriers in the conductive polymer is a hydrogen ion. This ion would have the capability to attract and hold the chloride ion in place. With the removal of conductivity this process would also be blocked. In this respect the conductive polymer acts as a selective ion membrane.

A third possibility is that it is a traditional inhibitor effect for these organic materials as they contain traditional inhibitor molecules such as the carboxylic group and quartenary ammonium groups (7). The positive groups of these ammonium ions will again electrostatically attract opposite charged species.

However until further research is conducted the definitive mechanisms or combinations of mechanism will not be know.

Inorganic Polymer Coating.

For the inorganic polymer coating, a shift to more noble potentials was found for the open circuit potentials. In addition a large passive region was found. XPS indicated a silicate rich region within the bare metal area of a scratch after salt spray testing. These results when combined together indicate that a corrosion resistant layer is formed from the inorganic polymer. The layer is a passive layer on the surface of the aluminum alloy. It is also formed in the scratched region of a sample indicating good damage tolerance and also repair capability.

Conclusions.

A double strand conductive polymer passivates the surface of aluminum alloys when in the conductive state.

When in the non conductive state, the conductive polymers lose protection.

Several mechanisms are possible for protection, including inhibitors, electrostatic repulsion.

An inorganic polymer protected aluminum alloys by forming a passive layer on the surface.

The inorganic polymer possessed good repair capabilities.

Acknowledgments

The organic conductive polymer study was funded by the Alcoa Foundation.

References.

1.P. Chalmers, "Chromate free conversion coatings", National Center for Manufacturing Science, Ann Arbor Michigan, 1995.
2. D.W. DeBerry, J. Electrochemical Soc, 132, 1021-1026, 1985
3. S. Ren and D. Barkey, J. Electrochemical Soc, 139, 1021-1026, 1992.
4. B. Wessling, Synthetic Metals, 907, 1991.
5. B. Wessling, Advanced Materials, 6,226-229, 1994.
6. New scientist, p24, Oct 1994.

7. S Sathiyanarayanan, K Balakrishnan, S.K. Dhawan and D.C. Trvedi, Electrochemica Acta, 39, 831-837,1994.
8. N Sato, Corrosion, 5,354-368, 1989.
9. R.Racicot, M.N. Alias, R. Brown, R.L. Clark, H.B. Liu and S. Yang, Proc, Mat Res Soc, 413, 529-534, 1996.

Figures.

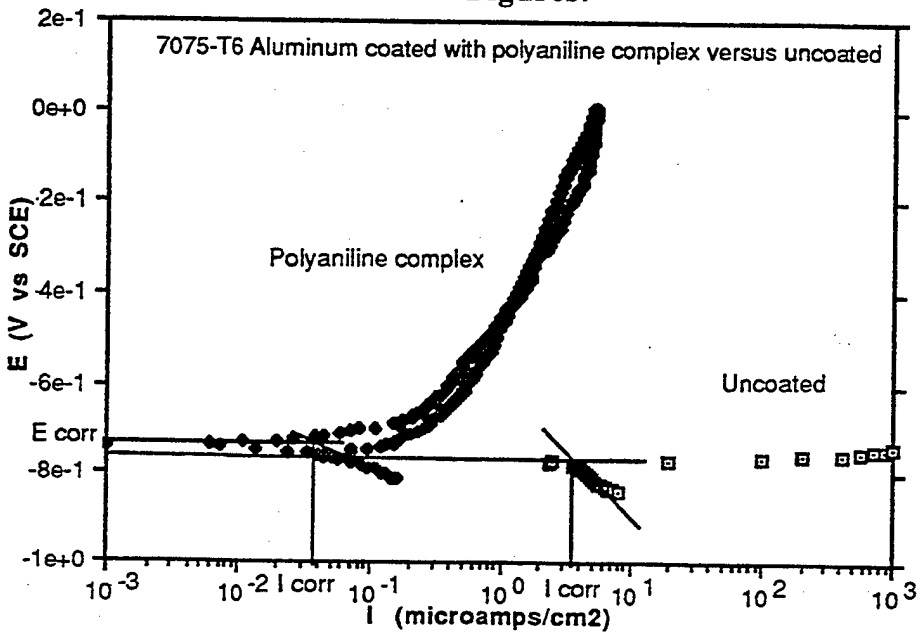


Figure 1. Potentiodynamic scan of Al 7075 - T6 aluminum alloy coated with a double strand conductive polymer compared to an uncoated sample in 0.5 n NaCl solution.

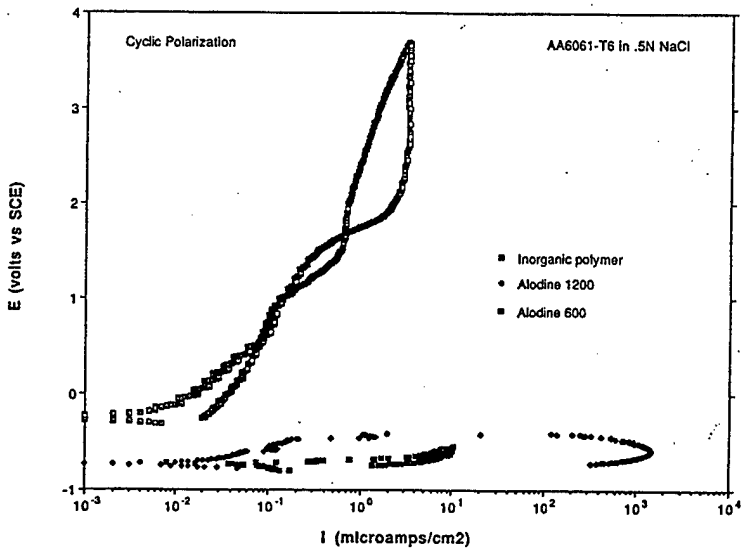


Figure 2. Potentiodynamic scan of Al 6061 - T6 aluminum alloy coated with an inorganic conductive polymer compared to an chromate coated sample in 0.5 n NaCl solution.

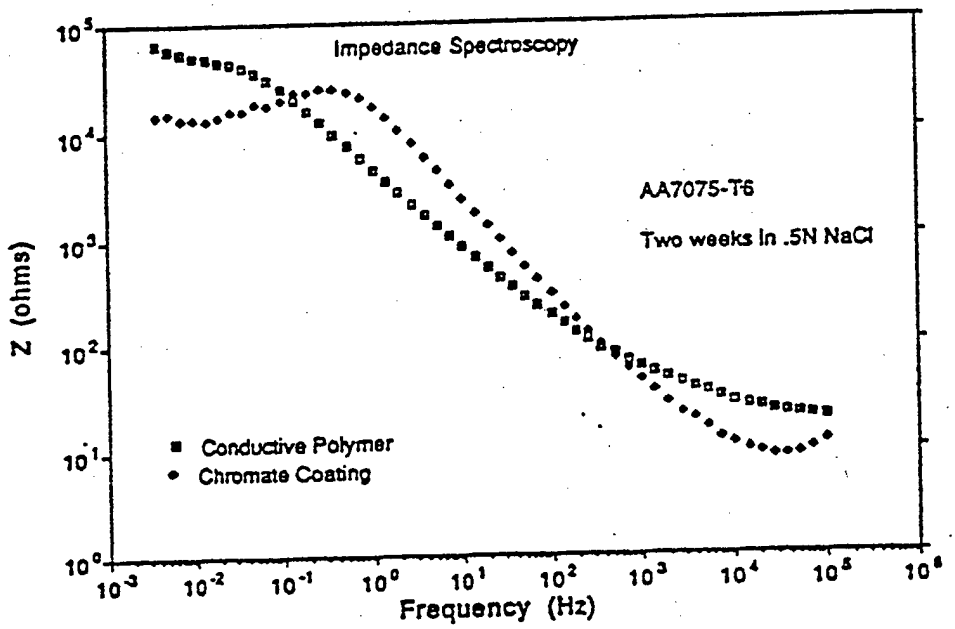


Figure 3. Electrochemical impedance spectroscopy data for a double strand conductive polymer compared to a chromate conversion coating.

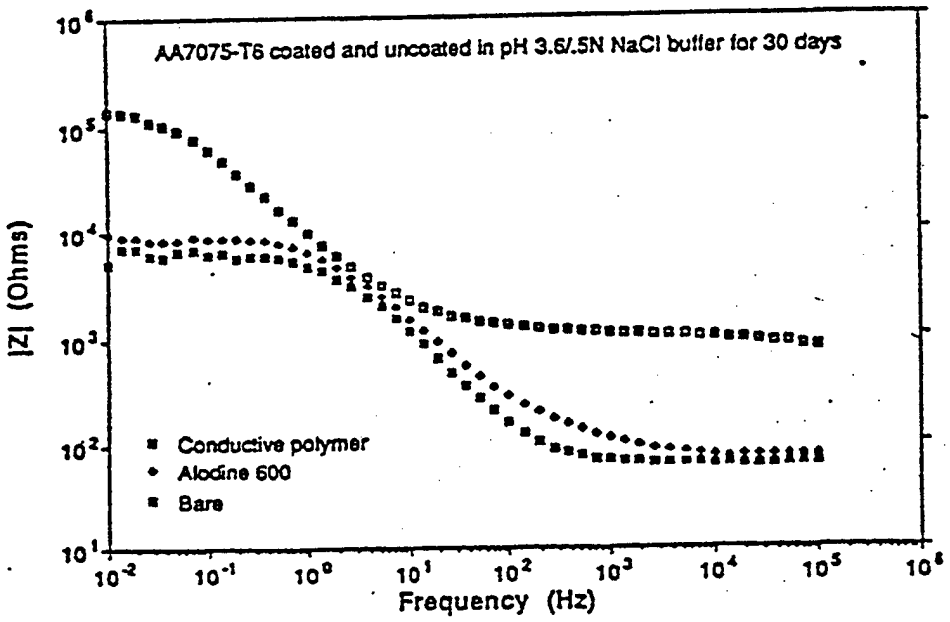


Figure 4. Electrochemical impedance spectroscopy data for a double strand conductive polymer compared to a chromate conversion coating in a 0.5 N NaCl solution at pH 3.6

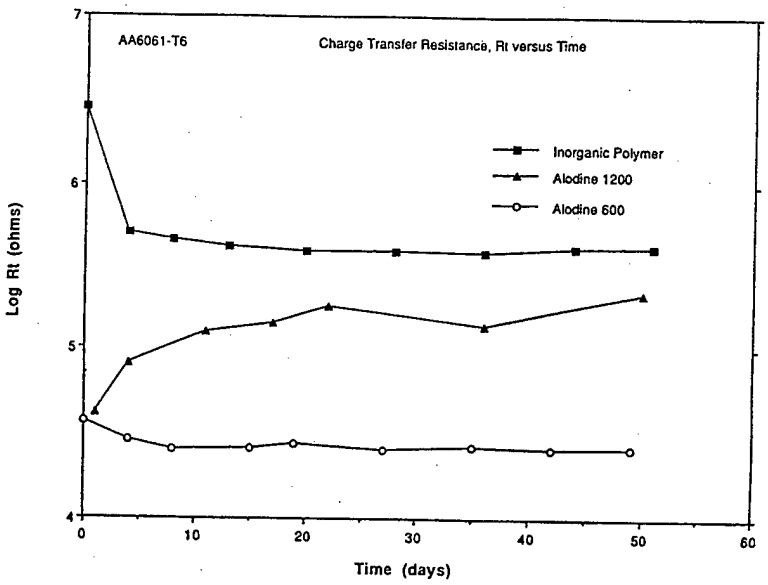


Figure 5. Data from modeling impedance spectroscopy data showing the charge transfer resistance against time for an inorganic polymer compared to two chromate conversion coatings on Al 6061-T6 in 0.5 n NaCl.

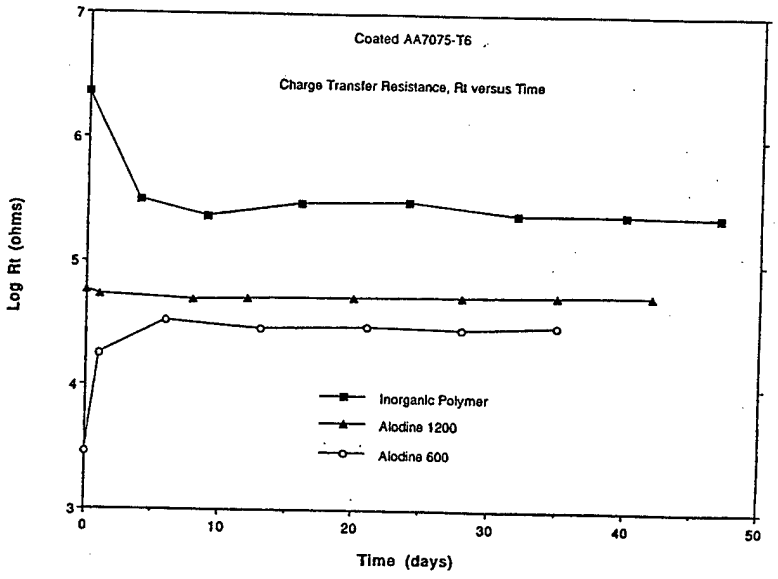


Figure 6. Data from modeling impedance spectroscopy data showing the charge transfer resistance against time for an inorganic polymer compared to two chromate conversion coatings on Al 7075-T6 in 0.5 n NaCl.

Effect of Minor Impurities on the Oxidation Resistance of Alumina-Forming Alloys

W.P. Allen* and N.S. Bornstein*
*United Technologies Research Center
East Hartford, CT

Abstract

The effect of minor impurity elements and alloy additions (e.g., carbon, boron, phosphorous, sulfur and yttrium) on the oxidation resistance of an alumina-forming NiCrAl alloy was investigated. Alloy samples were "desulfurized" to investigate the effect of these impurity elements on the environmental resistance of a low-sulfur alloy. Detailed characterization of bulk sample chemistry and surface segregation behavior suggests that the presence of increased boron contents can degrade the oxidation resistance of low-sulfur alloys. Although, the alloy exhibited excellent oxidation resistance with boron contents on the order of 15 wppm (for sulfur contents below the 1 wppm), performance of the low-sulfur material degrades as the boron concentration increases from 15 to 73 wppm. At the levels investigated, no measurable effect of carbon and phosphorous on the oxidation resistance of low-sulfur alloys was observed. Although boron has been shown to impact oxidation resistance, the effect of boron should be considered a secondary effect relative to sulfur.

Introduction

During thermal cycling in oxidizing and sulfidizing environments (as opposed to isothermal exposure), interfacial stresses develop as a result of differences in the thermal expansion coefficients of the aluminum-containing alloy and thermally grown Al_2O_3 scale. These interfacial stresses can result in localized spallation of the otherwise protective oxide scale exposing base metal to the environment and increasing the effective oxidation rate. Recent experimental work suggests that the interfacial adhesion between a metal and oxide is inherently strong in the absence of interfacial segregants (1). It has been shown that segregation of indigenous impurities (particularly sulfur [2-11]) to a metal/oxide interface can induce premature scale spallation (presumably through a reduction in the interfacial adhesive strength).

A large body of work exists supporting the suggestion that impurity sulfur (typically present at concentrations on the order of 10 wppm) can degrade the oxidation resistance of alumina-forming alloys and coatings (2-11). In fact, it has been shown that reducing the sulfur content to very low levels (< 1 wppm) can be used to achieve an oxidation performance comparable to that obtained through the addition of reactive elements such as yttrium (2,3). The observed benefits of reactive elements in promoting oxide scale adherence likely results from a reduction in the level of sulfur segregation/activity. Rare earth elements are known to form very stable sulfides and oxysulfides, and it is expected that the addition of these elements will getter free sulfur inhibiting its segregation to grain boundaries and metal/oxide interfaces (12).

Although the effectiveness of reactive element additions for promoting good oxidation resistance and the adverse effects of high sulfur contents in the absence of reactive elements are well-documented, relatively few studies have been conducted to analyze the effect of interfacial segregants other than sulfur on scale adherence. Considering previous work analyzing the effect of grain boundary segregants on the mechanical behavior of Ni (and Fe) based alloys, species other than sulfur likely to influence oxidation behavior include C, P, B and N (13-15). The principal objective of the present investigation was to determine whether these common impurity elements and/or minor element additions can affect the oxidation resistance of an alumina-forming alloy. Of particular interest was investigation of possible effects of other impurity elements on the oxidation resistance of alloys possessing a low sulfur concentration (<1 wppm).

Experimental Procedure

A single phase γ alloy composition, Ni-9.6 wt% Cr-6.0 wt% Al (Ni-10 at% Cr-12 at% Al), was selected for use in this investigation because of its ability to form an aluminum oxide scale and the fact that its aluminum and chromium concentrations are similar to those of current, single crystal, nickel-based superalloys. Controlled dopant additions of B, C, and P were made by initially preparing binary master alloys containing the intended dopant by arc melting and chill casting in a copper hearth. Master alloys of the following phase mixtures were prepared: $Ni+Ni_3B$, $Cr+Cr_{23}C_6$ (using Cr_3C_2 as the alloying addition) and $Ni+Ni_3P$ (using Ni_2P as the alloying addition), and these maser alloys were used as melt stock in preparing the doped NiCrAl alloys.

Alloy ingots (consisting of 20 cm long x 1.6 cm diameter bars) were prepared by induction melting in an aluminum oxide crucible and casting in a copper chill mold. In addition to the undoped baseline alloy, cast bars with dopant additions of boron, carbon, phosphorous and yttrium were prepared. Master alloy additions were made with the intent to yield boron, carbon, and phosphorous concentrations of 100, 220, and 75 wppm, respectively, and NiCrAlY alloys containing two different yttrium levels were prepared. After casting, samples of each alloy were homogenized at 1200°C for 24 hours in vacuum to remove the segregation resulting from solidification. Selected samples with a thickness of about 2 mm were subsequently desulfurized in a hydrogen atmosphere at 1300°C for 50 hours. Samples for oxidation testing were mechanically ground with 600 grit SiC paper.

Cyclic oxidation testing at 1200°C was used to assess the effect of alloy chemistry on oxide scale adherence. Each cycle consisted of a 60 minute exposure at the oxidation temperature followed by a 30 minute forced air cool, and specimens were weighed and examined periodically (usually daily) during testing. Glow Discharge Mass Spectrometry (GDMS) was used to measure impurity element concentrations. Sulfur, carbon, nitrogen and oxygen contents were also measured using the LECO™ combustion technique.

Hot-stage Auger Electron Spectroscopy (AES) was used to gauge sample-to-sample differences in the surface activity of various impurity species and to assess the likelihood that a

given species will segregate to oxide/metal interfaces. To simulate conditions that exist during oxidation testing, surface segregation studies were conducted at elevated temperatures (400-1000°C). A pin-shaped specimen, supported by a tantalum strip, was heated by passage of direct current through the strip. The sample was spot welded to the Ta heater to ensure good thermal contact, and an optical pyrometer and thermocouple were used to monitor sample temperature in-situ during AES characterization. After the chamber was evacuated to a pressure of 10^{-8} torr or less, the sample surface was sputter-cleaned for 20 minutes at room temperature. After cleaning, the sample was heated to the analysis temperature and sputter cleaned an additional 5-15 minutes. Reported time at temperature data are referenced with respect to completion of the latter sputter cleaning process.

Experimental Results

Cyclic Oxidation Testing

Homogenized Samples - The cyclic oxidation performance of homogenized alloy samples at 1200°C is shown in Figure 1. In terms of relative weight losses resulting from oxide scale spallation, two levels of performance were observed. The undoped, phosphorous-doped and yttrium-doped alloys all exhibited comparatively good oxidation resistance. Of these three specimens, the yttrium-doped alloy exhibited the best oxidation performance. In contrast, the boron- and carbon-doped alloy samples exhibited markedly worse oxidation resistance. As-cast alloys exhibited similar oxidation behavior, and the same trends were observed.

After completion of 255 cycles, edges and large areas of both flat surfaces of the undoped NiCrAl sample exhibited significant metal loss as a result of excessive oxidation/spallation. In regions where metal recession was relatively modest, characterization of the surface scale with Scanning Electron Microscopy (SEM) and Energy Dispersive Spectroscopy (EDS) indicates that it consists of an inner layer of pure aluminum oxide and an outer layer comprised of oxides of aluminum, nickel and chromium. Discreet patches of heavily oxidized regions (where the oxide was nickel-rich) were also distributed over the surface of the sample. In contrast to the undoped alloy, the homogenized, boron-doped NiCrAl after 1200°C cyclic oxidation exhibited much more severe metal recession (as much as 300 μm per side). Relative to the boron doped alloy, the carbon-doped alloy in the same heat treated condition exhibited a similar oxidation morphology and weight change behavior. The phosphorous-doped material exhibited an oxidation behavior comparable to that of the undoped alloy.

Desulfurized Samples - The oxidation behavior of "desulfurized" (DES) alloy specimens is compared to that of the yttrium-doped NiCrAl containing 945 wppm Y (about 0.1 wt%) in Figure 2. Testing was conducted for a duration of approximately 250 cycles, and in all cases, desulfurized samples exhibited a marked improvement in oxidation resistance relative to as-cast and homogenized specimens of the same alloy. Whereas the undoped, carbon-doped, and phosphorous-doped alloys exhibited comparable oxidation behavior in the DES condition, the desulfurized, boron-doped sample began to lose mass abruptly after completion of approximately

150 test cycles. In fact, weight loss exhibited by the DES boron-doped alloy after 250 cycles exceeded that of the undoped NiCrAl sample that did not receive a desulfurization heat treatment. The carbon-doped alloy, which exhibited rather poor oxidation resistance in the homogenized condition, showed the greatest improvement in performance as a result of desulfurization.

Figure 3a shows the cross section of desulfurized NiCrAl after completion of 250 oxidation cycles. Formation of an adherent and protective oxide scale is manifested by the lack of apparent metal recession and the presence of relatively few of the near-surface pores that have been attributed to the diffusional processes associated with excessive spallation/oxidation (16). Although the oxidized alloy exhibits what can be described as a convoluted morphology, the scale remains adherent to the substrate alloy. Relative to the DES NiCrAl sample, the DES NiCrAl+B specimen exhibits a highly convoluted scale/metal interface, a high concentration of pores adjacent to oxidized surfaces, a relatively thick oxide scale and pronounced metal recession at specimen edges (Figure 3b).

The NiCrAlY sample exhibited good oxide scale adherence, and no near surface porosity was discernible in the polished cross section. In contrast to the NiCrAl samples, the NiCrAlY specimen exhibited what is best described as an "undulating," rather than convoluted scale morphology, and oxide stringers extending well into the substrate alloy were also evident. These observations are consistent with previous investigations of MCrAlY oxidation behavior (17).

Chemical Analysis

GDMS analysis was performed on each of four doped alloys in both the homogenized and desulfurized conditions to measure the concentration of various impurities. Using GDMS, accurate measurement of the concentrations of C, N, O was not possible since these species represent common background impurities. For this reason, an alternative technique, LECO™ combustion analysis, was used to measure the carbon, nitrogen and oxygen contents. A compilation of GDMS and LECO™ results is shown in Table 1.

Chemical analysis of the heat treated and desulfurized samples is consistent with the observed oxidation behavior in that improved oxide scale adherence was achieved through a reduction in the bulk sulfur content. GDMS analysis shows that sulfur contents of the 2 mm thick specimens were reduced to levels below 1 wppm as a result of the hydrogen heat treatment. Although the NiCrAlY sample possessed a relatively high sulfur content, 12 wppm, the yttrium content, 945 wppm, was sufficient to promote excellent scale adherence. Examination of Table 1 indicates that the bulk concentrations of many impurity species were reduced as a result of the desulfurization process. The carbon content of desulfurized alloy samples ranged from 70 and 180 wppm, and in all cases the carbon content was reduced during desulfurization. Although the carbon content of the NiCrAl and NiCrAl+B specimens was reduced only slightly, the carbon content of the NiCrAl+C sample was reduced by a factor of 3X (from 391 to 132 wppm) during the desulfurization heat treatment. The alloy boron content was also typically reduced by a factor of about 3X. With exception of the P-doped alloy samples, the phosphorus content of all

specimens was below 1 wppm, and little or no change in the phosphorous content was detected following desulfurization.

Surface Segregation Behavior

Auger Electron Spectroscopy (AES) has been widely used in previous work to correlate interfacial chemistry and interfacial properties in nickel and iron based alloys, and in relatively recent work, it has been observed that AES characterization of free surfaces during in-situ heating can be used to identify likely interfacial segregants (12,18-21). Although the free energies associated with interfacial and surface segregation are expected to differ (22,23), a correlation is typically observed between species segregating at internal interfaces and free surfaces (18,23). In the present work, AES characterization was performed to guide the assessment of elemental effects on the oxidation resistance.

Homogenized NiCrAl+B - In initial work, surface segregation behavior of boron-doped NiCrAl in the homogenized condition was evaluated to define test conditions necessary to assess the surface segregation behavior of a variety of elements with increasing temperature. To define temperature requirements, AES characterization was performed at 400, 600, 800 and 1000°C for times up to 90 minutes at temperature. At each of the selected temperatures, Auger spectra were collected under two sets of conditions. In one case, the spectrum was collected while holding at temperature with power being supplied to the sample heater. In another series of experiments, the sample was allowed to cool after holding at temperature for varying lengths of time.

It was noted that significantly lower impurity levels were typically detected on the sample surface while holding at temperature than when cooling. Based upon a consideration of the variety of factors that can contribute to apparent differences in the segregation behavior under these two sets of conditions, it was concluded that detector interference resulting from the magnetic fields associated with resistive heating were the likely cause. The fact that magnetic field interference is expected to reduce the ability to detect electrons of low kinetic energy, and the absence of the nickel peak at 61 eV (while detecting nickel peaks corresponding to higher energy electrons with the heater on) is consistent magnetic interference effects. It should be noted that in other work electron beam heating has been used to minimize magnetic field effects otherwise resulting from resistive heating (24). Based upon a consideration these data, AES spectra were collected at 800 and 1000°C under isothermal as well as continuous cooling conditions. Collecting surveys during cooling after a given time at temperature would improve instrument sensitivity for detecting low energy electrons. Spectra were also be collected while the sample was held isothermally at temperature to verify consistency of data collected under the two conditions.

Desulfurized NiCrAl+B - Surface segregation behavior of the boron-doped NiCrAl sample was also performed following desulfurization in an attempt to correlate oxidation performance with segregation behavior. As mentioned previously, oxidation and surface segregation behavior of samples must be investigated following desulfurization to isolate possible effects of elements other than sulfur on oxidation resistance. Under conditions of isothermal holding at 800°C, only boron, carbon and nitrogen were detected, and nitrogen was present in the greatest abundance.

Whereas the measured nitrogen content increased continuously to approximately 8 at% during an 88 minute isothermal hold, the boron and carbon contents remained relatively constant at the 1-2 at% level. A final AES spectrum was collected from the same sample during cooling once the isothermal hold was complete. As observed with the homogenized sample, the measured concentration of impurity elements increased dramatically under these conditions. Most notable was the 13X increase in the measured boron content from 1.7 to 22.3 at%.

Changes in the surface concentrations of various impurity elements measured during cooling from 800°C are shown in Figure 4. In this case, AES spectra were collected with the heater off, and times indicated represent the total, accumulated time the specimen was held at 800°C. The most noteworthy observation is the relatively high surface concentrations of boron and nitrogen. As observed for homogenized NiCrAl+B, the measured increases in boron and nitrogen concentrations with increasing time appear to follow a parabolic rate law. A parabolic, least squares fit of concentration versus time yields R^2 values exceeding 0.98 in both cases, and measured increases in the sulfur concentration with time show similar behavior. These results would suggest that the measurements made during cooling actually reflect changes in surface chemistry occurring while the sample was at temperature. Consistent with data collected from the same sample while holding isothermally at 800°C, the three most abundant impurities were boron, nitrogen and carbon.

During isothermal exposure at 1000°C with the heater on, the desulfurized NiCrAl+B sample exhibited only a minor amount of sulfur (less than 0.5%) for times in excess of 30 minutes. Consistent with measured reductions in the bulk sulfur concentration, the amount of sulfur detected under these conditions was more than an order of magnitude lower than that measured from the same alloy prior to desulfurization. For identical test conditions, the homogenized alloy exhibited a measured surface sulfur concentration of approximately 10 at%. The spectrum collected during cooling after completing the isothermal experiment showed significantly higher levels of sulfur than that measured at temperature and relatively modest levels of boron, carbon and nitrogen (approximately 3 at% of each).

Data collected from the same sample during continuous cooling from 1000°C is summarized in Figure 5. Consistent with earlier observations, the segregant concentrations detected under these conditions were significantly different from those measured while at temperature. Although sulfur was the most abundant impurity element present in both cases, the sulfur surface concentration measured under conditions of continuous cooling achieved a level of about 13 at% after 60 minutes at temperature. Early stages of sulfur segregation (times up to 30 minutes) measured during continuous cooling were described well with a parabolic rate law (R^2 value of 0.995). For exposure times in excess of 40 minutes, boron was the second most abundant species with a measured concentration of about 3 at%. Carbon and nitrogen were both present at the 1-2 at% level.

Desulfurized NiCrAl+C - In comparing GDMS results for the various samples, it was noted that DES NiCrAl+B and DES NiCrAl+C possessed remarkably similar concentrations of sulfur, carbon, phosphorous and nitrogen. The only element exhibiting a significant difference in concentration was boron (see Table 1). Moreover, the sulfur content of both specimens was

reduced to the comparably low level of 0.25 wppm, and current experience indicates that such a reduction in the sulfur content should impart excellent oxidation resistance. Given the comparable impurity concentrations, the desulfurized NiCrAl+C sample was selected to serve as a low-sulfur, low-boron baseline. AES characterization of these alloy samples was performed to determine the effect of an increased boron concentration on the surface segregation behavior.

During isothermal holding at 800°C, only modest levels of nitrogen and sulfur were initially detected with AES. After approximately 40 minutes, the boron content increased from an undetectable level to about 4 at%, and a concomitant increase in the nitrogen content from 1.5 at% to 4 at% was also observed. Measurement of surface segregation on desulfurized NiCrAl+C during continuous cooling from 800°C is summarized in Figure 6. As noted previously, significantly higher impurity levels were detected relative to the corresponding isothermal data. As observed under isothermal conditions, however, boron and nitrogen were the most abundant segregants with measured concentrations of 6-8 at%.

Under isothermal conditions at 1000°C, the only segregating impurity element detected on the desulfurized carbon-doped sample was sulfur. The level of sulfur detected (approximately 1.5 at%) was slightly higher than that observed on the desulfurized NiCrAl+B specimen under the same conditions (approximately 0.4%). Segregation behavior measured during cooling (after holding at 1000°C for various times) is summarized in Figure 7. Consistent with the spectra collected under isothermal conditions, sulfur was the most abundant segregating impurity species. The sulfur concentration achieved a level of 14-15 at%, and the level of segregation was comparable the that of the desulfurized NiCrAl+B sample. It is interesting to note that the level of sulfur segregation on the two samples as well as the bulk sulfur concentrations were remarkably similar (Figure 6 and 7). As in the case of data collected at 800°C, the level of boron segregation was almost 2X greater on the boron-doped sample.

Discussion

The principal objective of this program was to identify elements limiting the environmental resistance of alumina-forming alloys possessing a low sulfur content/activity. Given the deleterious effect of sulfur on oxidation resistance observed in previous work, it is likely that the effects of other impurity elements (if any) will be masked by that of sulfur for elemental concentrations on the order of 1-100 parts-per-million. Therefore, the oxidation resistance of alloys doped with other elements (e.g., C, B, and P) was investigated following application of a desulfurization heat treatment. With such an approach, the effects of sulfur would be minimized, thereby revealing possible effects of other elements.

As shown in Figures 1 and 2, significant differences in oxidation performance exist between the various samples, and given the large number of impurities present at the 1-100 ppm level, a methodology must be defined to determine whether observed differences in behavior can be attributed to differences in the concentration/activity of a given element. Based upon prior investigations of oxidation and grain boundary embrittlement, establishing a correlation between oxidation resistance, bulk impurity content and surface concentration (measured with hot-stage AES) is an accepted approach for identifying possible effects of other elements. It should be

noted that impurity elements (or intentional dopants) can affect the oxidation resistance in any number of ways (e.g., scale adherence, plasticity and/or growth rate).

Effect of Sulfur and Yttrium on Oxidation Behavior

It is generally accepted that sulfur contents as low as only 5-10 wppm can degrade oxidation resistance of alumina-forming alloys and coatings (2-11), and a large body of data supports the contention that dramatic improvements in oxide scale adherence can be achieved by reducing the alloy sulfur activity. Historically, required activity reductions were unknowingly achieved through the addition of yttrium (or other rare earth elements) which react with impurity sulfur resulting in formation of stable sulfides or oxysulfides. Only after enhanced oxidation resistance was achieved through a reduction in the alloy sulfur concentration (without the addition of rare earth elements) was the actual influence of sulfur on oxidation resistance identified.

Even though correlations have been established between sulfur concentration and oxidation resistance of various materials, the precise mechanism through which sulfur acts to degrade oxidation resistance is unclear. The mechanism usually proposed or inferred involves segregation of sulfur to the oxide metal interface with a concomitant reduction in interfacial adhesive strength. Scale spallation then occurs during thermal cycling, and since a typical alumina-forming alloy or coating possesses a relatively modest aluminum content (typically 6 wt% [12 at%]), only a limited number of spallation events can be tolerated before the formation of a continuous aluminum oxide scale is precluded due to the reduced near surface aluminum activity and/or an insufficient aluminum mobility in the alloy. Once formation of a protective alumina scale is no longer possible, other less protective oxides begin to form, and oxidation/metal consumption proceeds at an accelerated rate.

A NiCrAlY alloy was used as a baseline for comparing the oxidation resistance of various desulfurized alloy samples. The sulfur contents of desulfurized samples was on the order of 0.5 wppm or less, and results of prior work (9-11) indicate that a reduction in the sulfur content to these levels should impart excellent oxidation resistance. Consistent with prior work, the oxidation test results demonstrate that a desulfurized alloy can exhibit a level of oxide oxidation resistance comparable to that achieved through the addition of yttrium (Figure 2). A discussion of morphological differences observed for oxidized NiCrAlY and DES NiCrAl is the subject of a separate publication.

Surface Segregation Behavior of Desulfurized NiCrAl

Chemical analysis with GDMS indicates that the sulfur contents achieved through application of the solid-state desulfurization heat treatment ranged between 0.25 and 0.6 wppm. It is interesting to note that although the alloys possessed very low sulfur concentrations, a significant level of sulfur was detected on the sample surface with AES during cooling from 1000°C (see Figures 5 and 7). Although these AES measurements were made under conditions of continuous cooling, kinetic analyses of the data suggests that the sulfur detected at the surface actually segregated while the sample was held at temperature.

Observed levels of sulfur surface segregation were higher than anticipated given the low bulk sulfur content and the excellent oxidation performance exhibited by the desulfurized NiCrAl+C specimen. Although calculation of the expected equilibrium surface segregation behavior and kinetics indicates that high concentrations of sulfur (5-10 at%) may be expected on the surface of desulfurized specimens with bulk concentrations below 1 appm (25), the observed behavior must be reconciled with accepted theory regarding the effect of sulfur on oxidation resistance. In the present work, surface sulfur concentrations were significantly lower on desulfurized alloys, and the reductions in surface and bulk sulfur concentrations were associated with a significant improvement in oxidation resistance. Furthermore, measurements made in this study reflect sulfur segregation to free surfaces rather than oxide/metal interfaces. Although hot stage AES represents a useful technique for assessing the level of free sulfur within a sample, the level of interfacial sulfur segregation is expected to be less than that observed at the free surface (22,26,27).

In addition to sulfur, other elements detected on the sample surface included boron, carbon, nitrogen, oxygen, and phosphorus. Of the observed surface impurity elements, phosphorus was present in the least abundance. On the homogenized NiCrAl+B sample, phosphorus was only detected during cooling from 800°C. Phosphorus was also observed on the desulfurized NiCrAl+C sample during cooling from 1000°C, but in both cases, the surface phosphorus concentrations were below 0.5 at% (approaching the delectability limit of AES). The low surface phosphorus activity is consistent with the fact that all of the samples characterized with hot-stage AES exhibited bulk phosphorus contents below 1 wppm.

In comparing the surface segregation behavior of samples under the various test conditions, it was apparent that surface boron and nitrogen concentrations of the boron-doped sample were significantly higher than those exhibited by the corresponding carbon-doped sample. In fact, although boron and nitrogen were the most abundant impurity elements on both samples during cooling from 800°C, the surface boron content of the boron-doped alloy was approximately 2X greater than that measured on DES NiCrAl+C. An analogous 2X difference in surface boron concentrations was also observed during cooling from 1000°C, and the observation of increased boron surface activity is consistent with the presence of a higher bulk boron concentration in the desulfurized NiCrAl+B sample. The increase in surface boron segregation exhibited by the DES NiCrAl+B sample was also associated with a corresponding increase in the level of nitrogen segregation. Although higher nitrogen segregation on the boron-doped alloy may be expected given its slightly higher nitrogen content (47 versus 33 wppm), increasing nitrogen segregation may also be excepted in the presence of a higher boron content due to the cosegregation expected for these elements (19). In contrast to observations regarding boron and nitrogen, no systematic differences in the segregation behavior of sulfur and carbon were observed for these two specimens.

Effect of Elements Other than Sulfur on Oxidation Resistance

In order to draw any conclusions regarding the effect of a specific impurity species on oxidation resistance, the effect of that species must be isolated from possible effects of other elements. Isolating the effect of a given element is complicated, however, by the fact that the

concentration of other impurities is also likely to vary from one sample to another. In order to make a conclusive statement as to the effect of a specific element, the bulk concentrations of other segregating impurities must either be comparable or be so low (e.g., less than 0.1 appm) that they can be assumed innocuous.

In comparing the GDMS results for the various samples, it was noted that two of the desulfurized specimens (DES NiCrAl+B and DES NiCrAl+C) possessed remarkably similar impurity concentrations (see Table 1). In this case, the concentrations of elements such as sulfur, carbon, phosphorus, and nitrogen were essentially identical in the two specimens, and the only nonmetallic impurity exhibiting a marked concentration difference between the two samples was boron. Measured differences were corroborated with a second GDMS measurement of the same sample. In contrast to the carbon-doped alloy, oxidation resistance of the high-boron sample degraded abruptly during cyclic testing (Figure 2). After initially forming a somewhat protective oxide scale, spallation became quite pronounced on the DES NiCrAl+B sample resulting in rapid weight loss. Prior to the onset of rapid weight loss, the boron-doped alloy exhibited more extensive scale spallation than the carbon-doped sample, and nickel oxide formation was much more prevalent (25).

Effect of Boron - The AES study focused on characterization of the desulfurized NiCrAl+B and NiCrAl+C specimens due their similar bulk impurity chemistries and dissimilar oxidation behavior. The observed difference in oxidation resistance cannot be attributed to variation in the sulfur or carbon concentrations, since no significant difference in bulk concentration existed and no systematic difference in surface segregation behavior could be discerned for either element. In fact, the level of surface sulfur segregation may have been reduced slightly on the boron-doped material due to the increased levels of boron and nitrogen segregation. Furthermore, a possible influence of segregated phosphorus can also be discounted given the low bulk and surface concentrations <1 wppm and <0.5 at%, respectively. The only elements exhibiting a systematic difference in surface segregation behavior on the two specimens was boron and nitrogen. Although the bulk nitrogen content of the two samples was similar, the boron content differed by a factor of 5X, and the difference in bulk boron content is consistent with a measured difference in boron segregation to the surface during cooling. Based upon these results, it is suggested that boron concentrations on the order of 75-100 wppm can degrade the oxidation resistance of alumina-forming alloys, and this debit in oxidation resistance can occur for alloys possessing a sulfur content well below the level otherwise expected to impart excellent oxidation resistance.

It should be noted that in prior work, the cyclic oxidation resistance of 304 stainless steel doped with boron and nitrogen (0.01 and 0.16 wt%, respectively) was investigated (28). In this case, the B+N-doped alloy exhibited a substantial improvement in oxidation resistance at 827°C, and the enhanced oxidation resistance was correlated with a reduction in the level of surface sulfur segregation at 727°C. The improved oxidation resistance was assumed to result from the improved oxide scale adherence achieved through reduced interfacial segregation of sulfur.

Although conclusions of the present investigation regarding the effect of boron appear inconsistent with that of prior work, it must be noted that Ikeda et al. (28) investigated the

behavior of undoped and boron-doped alloys with high sulfur contents (70-80 wppm). For these sulfur levels, site competition between boron and sulfur at the temperatures involved (827°C) may be expected to reduce the level of sulfur segregation and enhance the oxidation resistance. Prior results are not inconsistent with those of the current investigation in which it was observed that boron and nitrogen are the most abundant surface segregants at 800°C. Unlike the earlier work, however, the present study involved contrasting the oxidation resistance and segregation behavior of alloys with sulfur contents below 0.5 wppm. In this case, even though the level of sulfur segregation was reduced to comparatively low levels through application of a desulfurization heat treatment, a significant difference in the level of boron and nitrogen segregation on the two samples was observed. Based upon a consideration of current and prior data, therefore, it appears that although boron may enhance the oxidation resistance of high-sulfur alloys (at least at lower temperatures) by reducing the level of interfacial sulfur segregation, the presence of interfacial boron my debit the oxidation performance of low-sulfur alloys in which significant levels of interfacial sulfur segregation is already precluded by the low bulk concentration.

Effect of Carbon - Relative to the undoped alloy, NiCrAl+C (containing almost 400 wppm carbon) exhibited rather poor oxidation resistance in the heat-treated condition (see Figure 1). In fact, oxidation resistance of this sample was comparable to that of the boron-doped alloy. Although the carbon content of the undoped and carbon-doped samples differed by a factor of 2X (see Table 1), relatively poor oxidation performance of the latter sample can be attributed to the fact that the carbon-doped alloy possessed the highest sulfur content of all the alloys investigated (5.5 wppm).

The minimum carbon content observed in the various NiCrAl samples was 70 wppm, and as a result, investigating the oxidation resistance of low-carbon (less than 20 wppm) alloys was not possible. Moreover, the oxidation behavior of samples containing high (400 wppm) and intermediate (150-200 wppm) carbon levels could not be investigated due to the unintentional decarburization which occurred during the desulfurization heat treatment. Given the inability to produce high-carbon and low-carbon material with low sulfur contents, a systematic investigation of carbon effects analogous to that performed in the case of boron was not possible. However, based upon a consideration of the measured bulk concentrations, surface segregation behavior and oxidation performance, any effect of carbon on the oxidation resistance would appear to be minimal.

Effect of Phosphorous - In the present work, samples of the phosphorous-doped NiCrAl alloy, containing approximately 70 wppm phosphorous, exhibited cyclic oxidation behavior comparable to that of the corresponding undoped alloy containing less than 0.5 wppm phosphorous. In fact, the weight change behavior of the two materials during cyclic testing was remarkably similar, and in each condition, homogenized as well as desulfurized, the undoped and P-doped alloys exhibited comparable sulfur contents (Table 1). These results suggest that increasing the alloy phosphorous content to levels on the order of 50-80 wppm has no deleterious effect on the alloy oxidation resistance.

Results suggesting little or no effect of phosphorous on adhesion of a thermally grown alumina scale are consistent with those previously reported for adhesion of sputtered alumina films (29). In this case, 1 μm thick alumina films were applied using magnetron sputtering to a Ce-doped Fe-Cr-Ni alloy and to Ni-based superalloys containing yttria dispersions. Although segregation of sulfur to the free surface at 827°C (and presumably to the metal/oxide interface as well) was negligible in each case, very rapid surface segregation of P was detected on the cerium-doped alloys. Phosphorus segregation was relatively modest on surfaces of the alloy containing dispersed rare-earth oxide particles due to the availability of alternative sites for phosphorous segregation (i.e., internal oxide/metal interfaces). Even though significant differences in the level of phosphorous segregation were observed, all samples exhibited good coating and oxide scale adhesion (29).

Summary

Based upon results of this program, the effect of various impurity elements on the oxidation resistance of the Ni-10 wt%Cr-6 wt% Al alumina-forming alloy can be summarized as follows. Consistent with prior work, reduced alloy sulfur concentrations were observed to increase the alloy oxidation resistance by enhancing alumina scale adhesion. Oxidation resistance of the 2 mm thick coupons is compromised as the sulfur content increases from 0.7 to 2.1 wppm. In contrast to the very low levels of sulfur required to achieve superior oxidation resistance, the alloy is much more tolerant of impurity boron. In the latter case, the alloy can exhibit excellent oxidation resistance with boron contents on the order of 15 wppm provided the sulfur content is below the 1 wppm. However, even with a reduced sulfur content, environmental resistance of the alloy can be compromised for a high boron content, since performance degrades as the boron concentration of the low-sulfur alloy increases from 15 to 73 wppm. For the concentration levels investigated, no effect of carbon and phosphorous on oxidation resistance could be discerned.

Acknowledgements

The support of ONR Contract N00014-93-C-0232 (John Sedriks, Contracting Officer) is gratefully acknowledged.

7. References

1) E.W. King, Lawrence Livermore N.L., private communication,1991.
2) A.W. Funkenbusch, J.G. Smeggil and N.S. Bornstein, Final Report, N00014-82-C-0618, ONR (1983).
3) J.G. Smeggil and N.S. Bornstein, Final Report, N00014-85-C-0421, ONR (1987).
4) A.W. Funkenbusch, J.G. Smeggil and N.S. Bornstein, *Metall. Trans.*, 16A, 1164 (1985).
5) J.G. Smeggil, A.W. Funkenbusch and N.S. Bornstein, *Metall. Trans.*, 17A, 923 (1986).
6) J.L. Smialek, in High-Temperature Materials Chemistry-IV, edited by Z.A. Munir, D. Cubicciotti and H. Tagawa, Electrochem. Soc., Pennington, NJ (1988) p. 241.
7) N.S. Bornstein, M.A. DeCrescente and J.G. Smeggil, *Mater. Sci. Eng.*, A120, 175 (1989).

8) J.L. Smialek, in Corrosion and Particle Erosion at High Temperature, TMS-AIME, Warrendale, PA (1989).
9) B.K. Tubbs and J.L. Smialek, in Corrosion and Particle Erosion at High Temperature, TMS-AIME, Warrendale, PA (1989).
10) J.L. Smialek, D.T. Jayne, J.C. Schaeffer and W.H. Murphy, *Thin Solid Films*, 253, 285 (1994).
11) J.C. Schaeffer, W.H. Murphy and J.L. Smialek, *Oxid. Metals*, 43,1 (1995).
12) R.A. Mulford, *Metall. Trans.*, 14A, 865 (1983).
13) Erhart and Grabke, *Metal Sci.*, 15, 401 (1981).
14) R.G. Rowe, *Metall. Trans.*, 10A, 997 (1979).
15) C.L. Briant and R.A. Mulford, *Metall. Trans.*, 13A, 745 (1982).
16) W.P. Allen and N.S. Bornstein, United Technologies Research Center, unpub. work.
17) F.H. Stott and G.C. Wood, *Mat. Sci. Eng.*, 87, 267 (1987).
18) M.P. Seah and C. Lea, *Phil. Mag.*, 31, 627 (1975).
19) R.H. Stulen and R. Bastasz, *J. Vac. Sci. and Technol.*, 16, 940 (1979).
20) T. Miyahara, K. Stolt, D.A. Reed, and H.K. Birnbaum, *Scripta Metall.*, 19, 117 (1985).
21) C.L. Briant and K.L. Luthra, *Metall. Trans.*, 19A, 2099 (1988).
22) E.D. Hondros and M.P. Seah, in Physical Metallurgy, Edited by R.W. Cahn and P. Haasen, Elsevier Science Pub. (1983) pp. 855-931.
23) U. Otterbein, S. Hofmann ,and M. Ruehle, *Proc. Mat. Res. Soc. Symp.*, 288, 183 (1993).
24) J.J. Burton, C.R. Helms, and R.S. Polizzotti, *J. Vac. Sci.Tech.*, 13, 204 (1976).
25) W.P. Allen, Final Report, N00014-93-C-0232, ONR (1996).
26) C. Lea and M.P. Seah, *Scripta Metall.*, 9, 583 (1975).
27) U. Otterbein, S. Hofmann and M. Ruhle, *Proc. Mat. Res. Soc. Symp.*, 288, 183 (1993).
28) Y. Ikeda, K. Nii and K. Yoshihara, *Trans. Jpn. Inst. Metals, Suppl.*, 24, 207 (1983).
29) Y. Ikeda, M. Tosa,K. Yoshihara and K. Nii, *ISIJ Int.*, 29, 966 (1989).

Table 1: GDMS Analysis Results for NiCrAl Samples

Element	NiCrAl HT	NiCrAl DES	NiCrAl+B HT	NiCrAl+B DES	NiCrAl+C HT	NiCrAl+C DES	NiCrAl+P HT	NiCrAl+P DES	NiCrAl+Y HT
B	**42**	**14**	**140**	**73**	**50**	**15**	**0.58**	**2.1**	**<0.93**
C*	**222**	**179**	**143**	**137**	**391**	**132**	**121**	**70**	
N*	6.8	4	50.9	47	79.0	33	18	10	
O*	12.5	19	21.5	25	21.5	28	25	29	
F	<0.94	<0.070	<6.3	<0.095	<0.068	<9.2	<0.025	<0.038	<0.74
P	**0.38**	**0.40**	**0.30**	**0.47**	**0.23**	**0.78**	**52**	**80**	**0.090**
S	**2.1**	**0.61**	**3.4**	**0.29**	**5.5**	**0.23**	**3.1**	**0.70**	**12**
Cl	<1.5	<0.13	<3.6	<0.073	<0.29	<0.20	<0.035	<0.077	<0.69
As	0.35	0.42	0.35	0.18	0.14	<0.16	<0.25	<0.19	<0.069
Se	<0.066	<0.047	<0.11	<0.059	<0.10	<0.070	<0.025	<0.083	<0.16
Br	<0.059	<0.036	<0.050	<0.047	<0.031	<0.047	<0.063	<0.033	<0.083
Y	<0.90	<0.91	<0.59	<1.2	<1.5	<0.47	<1.2	<2.1	945

*Results of LECO™ Analysis

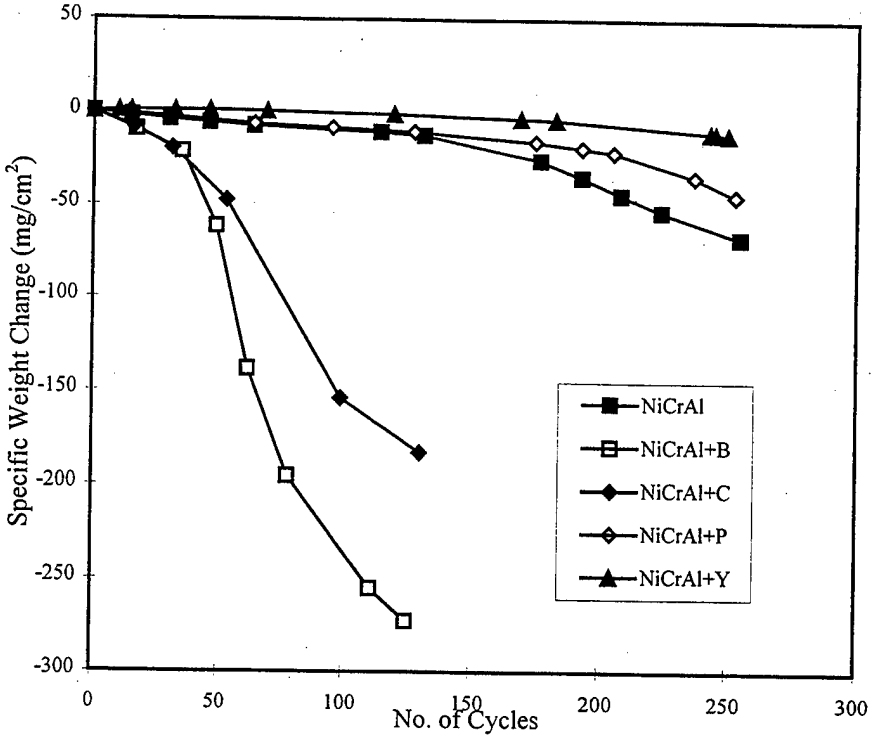


Figure 1: 1200°C cyclic oxidation testing of homogenized alloys.

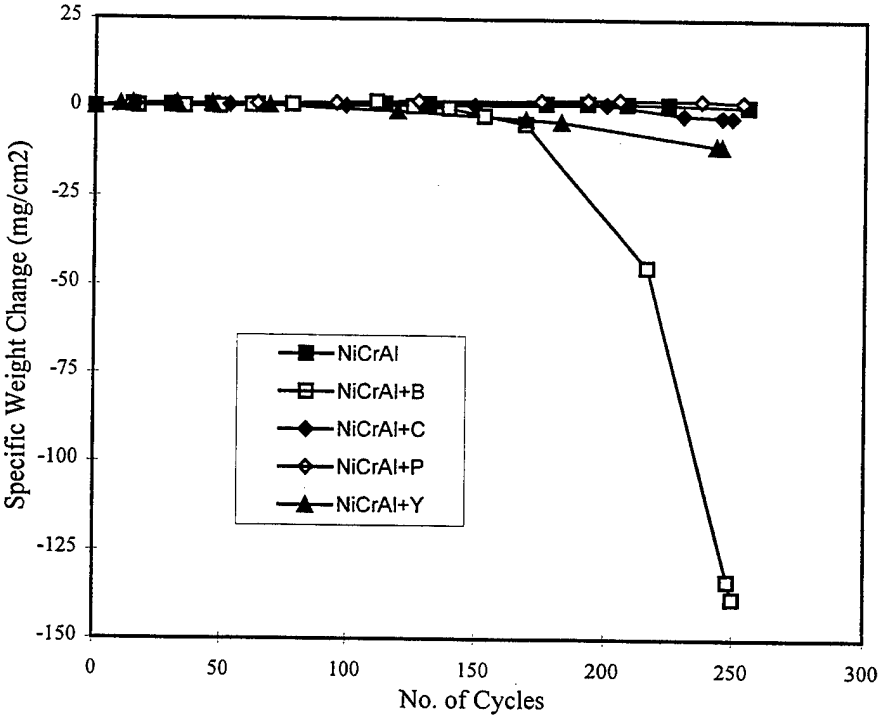


Figure 2: 1200°C cyclic oxidation testing of desulfurized alloys.

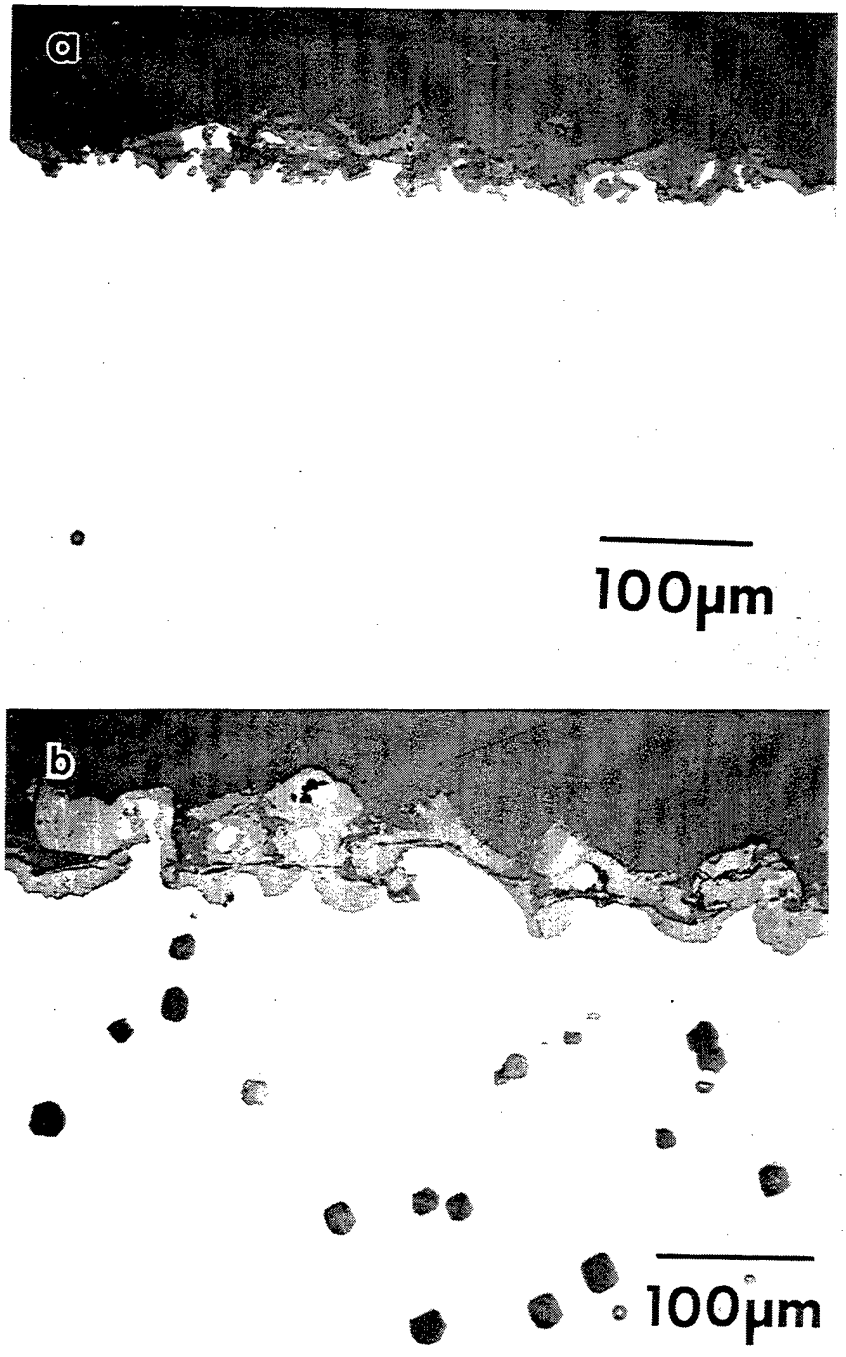


Figure 3: Oxidation morphology on desulfurized a) undoped NiCrAl and b) NiCrAl+B after 250 oxidation cycles at 1200°C.

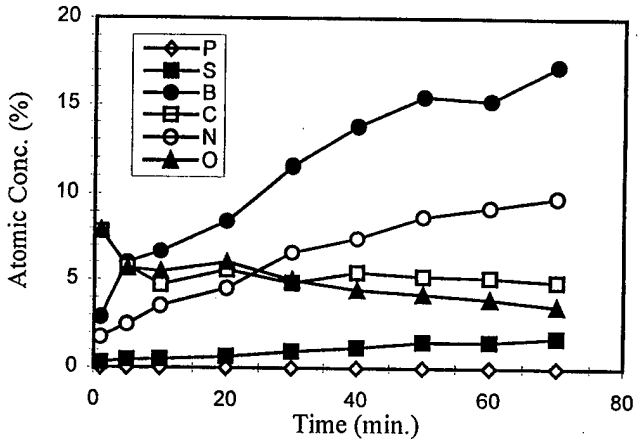


Figure 4: AES characterization of desulfurized NiCrAl+B during cooling from 800°C. Indicated time represents aggregate time at 800°C.

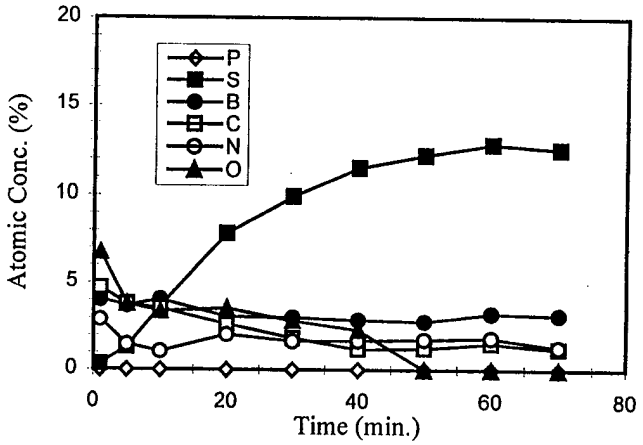


Figure 5: AES characterization of desulfurized NiCrAl+B during cooling from 1000°C. Indicated time represents aggregate time at 1000°C.

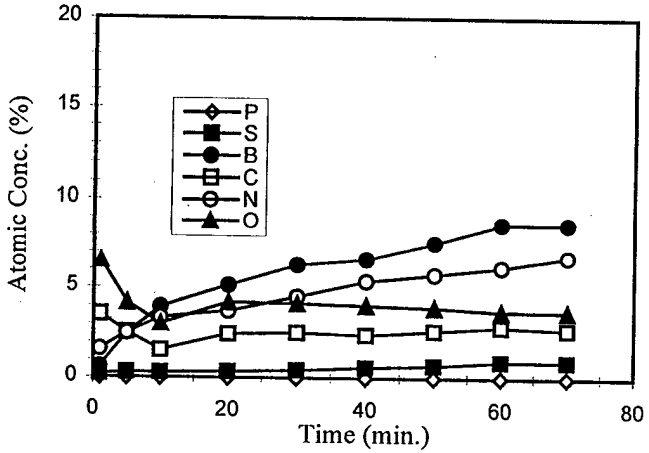


Figure 6: AES characterization of desulfurized NiCrAl+C during cooling from 800°C. Indicated time represents aggregate time at 800°C.

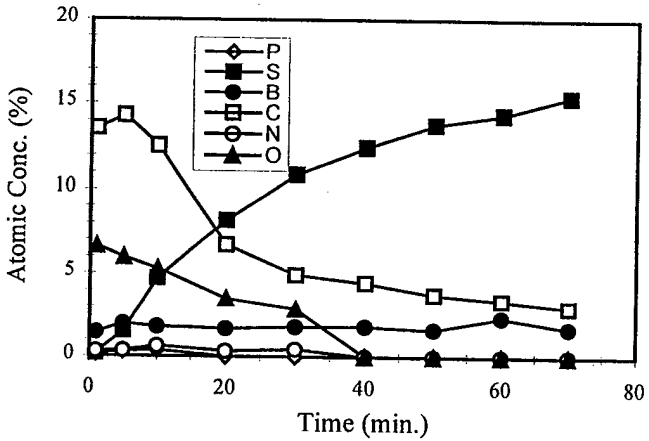


Figure 7: AES characterization of desulfurized NiCrAl+C during cooling from 1000°C. Indicated time represents aggregate time at 1000°C.

Environmental Cracking Limitations to the Application of High Strength Beta-Titanium Alloys in the Marine Environment

Brian P. Somerday and Richard P. Gangloff
Department of Materials Science and Engineering
School of Engineering and Applied Science
University of Virginia
Charlottesville, VA 22903

ABSTRACT

High strength β-titanium alloys are susceptible to severe intergranular environment-assisted cracking (EAC) in aqueous chloride solution, but only for specific electrode potential, crack tip strain rate, and microstructural conditions. Heat treatment for α-precipitation hardening of alloys such as Beta-C is a requisite for EAC; the threshold stress intensity for the onset of cracking (K_{TH}) is as low as 30% of K_{IC} for β/α microstructures, with K_{TH} and K_{IC} both decreasing with increasing aging time. Crack growth rates approach 100 μm/s. Single β-phase microstructures of Beta-C are immune to EAC at several levels of cold work, suggesting that yield strength increase is not the dominant cause of the deleterious aging effect. The fracture toughness of cold worked microstructures is low. Data from this research, and parallel studies on fracture toughness, are incorporated into an updated Ratio Analysis Diagram. Complex crack geometry and strain rate effects on K_{TH} may limit the use of this information in design and failure analysis.

INTRODUCTION

Two problems may limit the use of metastable β-titanium alloys in fracture-critical marine applications; low toughness at high strengths and susceptibility to intergranular environmental cracking in aqueous chloride solutions. The former problem is illustrated by the Ratio Analysis Diagram shown in Fig. 1. As suggested by Pellini, this plot of fracture toughness *vs* yield strength (σ_{YS}) represents the flaw-damage tolerance of a given class of alloys under plane strain, plane stress, or fully plastic loading and flaw size conditions.[1] CE is the *critical edge*, or boundary between plane strain and plane stress behavior for a 25 mm thick through-cracked component. The data and trend lines in Fig. 1 define the toughness behavior of modern α-precipitation hardened β-titanium alloys such as Beta-C, compared to that of state-of-the-art quenched and tempered martensitic ultra-high strength steels such as AerMet 100.[2-18] The majority of these materials exhibit plane strain fracture for the 25 mm section size. This diagram updates previous RAD results.[1,19]

For a given high yield strength in Fig. 1, the plane strain fracture toughnesses of the β-titanium alloys are well below those of high strength steels, even accounting for the elastic-modulus difference.[1] Such low toughnesses have precluded the realization of the high strength capability of

---

[1] Both energy and stress-based micromechanical models of fracture toughness suggest that $K_{IC} \propto \sqrt{E}$. The square root of $E_{STEEL}/E_{\beta\text{-titanium}}$ is 1.4.

these titanium alloys. The factors that limit the toughness of β-titanium alloys are not well understood compared to steels,[20] and this issue is not considered here.

Considering the second limitation, β-titanium alloys, age hardened to high strength by α precipitation, are susceptible to severe intergranular (IG) environment-assisted cracking (EAC) in aqueous halide solutions at 25°C.[21-27] Hydrogen environment embrittlement (HEE) is implicated as the cracking mechanism.[22,28] Lower strength, single phase β-titanium alloys are not prone to such brittle cracking[21,24]. The metallurgical properties of β-Ti alloys that promote IG EAC have not been determined; however; aging can affect a number of variables that may be important, including σ_{YS}, α precipitation, localized deformation, and grain boundary composition changes.

The yield strength effect can be isolated because σ_{YS} for the immune single-phase β alloy is increased readily by strain hardening. This procedure retains the β microstructure without precipitation of α, and does not vary composition. Increased σ_{YS} promotes EAC of steels and Ni alloys, particularly for cases of HEE and due to increased crack tip stress.[29] Results suggest a similar deleterious effect of increased σ_{YS} for EAC of aged β-Ti alloys,[25] but experiments are limited. The effect of cold work on the EAC resistance of single-phase β-Ti alloys has not been investigated previously. Apart from EAC-mechanistic considerations, this dependence is important for applications involving localized or extensive cold-worked microstructures.

Determination of metallurgical effects is complicated by the mechanical and electrochemical variables that influence IG EAC in aqueous halide solutions. Previous studies demonstrated important effects of electrode potential,[21,22,25] precracked *vs* smooth specimens,[25,30] and crack-tip strain rate[23,25-27,31] on EAC susceptibility of β/α and α/β Ti alloys. The windows of these extrinsic variables that promote EAC may depend on alloy σ_{YS} and microstructure. Interpretation of EAC experiments designed to probe metallurgical variables must recognize this complication.

The objective of this paper is to establish the effect of σ_{YS} on EAC of β-titanium alloys. A single-phase β alloy is cold worked to increase σ_{YS}, and alternately subjected to isothermal heat treatment for increasing times to produce σ_{YS} levels from α-precipitation hardening that are similar to the cold-worked case. Precracked specimens are tested in aqueous NaCl at fixed electrode potential under constant rising-displacement rate. Results are presented in the RAD-format to enable use in damage tolerant materials selection and component life prediction. The effects of α precipitation, localized deformation mode, and grain boundary composition changes during aging are considered elsewhere.[32]

EXPERIMENTAL PROCEDURE

Material

The alloy studied was Beta-C with a composition of Ti-3.4 Al-8.3 V-5.9 Cr-4.1 Mo-4.4 Zr (wt pct), as specified by the manufacturer, RMI Titanium Company. The product form was hot-rolled 41-mm-diameter round bar that was solution heat treated at 815°C for 1 h and air cooled to room temperature (ST condition). Since the β-transus for this alloy is near 750°C. The resulting microstructure consisted of single-phase β grains, equiaxed and 80 μm in size. The only additional phase present was a small amount of silicide particles.

The σ_{YS} of ST Beta-C was increased by two different means. First, ST Beta-C was cold worked to reductions between 20% and 65% (ST/CW condition). Parallel surfaces were machined along 75 mm to 150 mm lengths of the round bar to produce a cross section that was 15 mm thick by 41 mm wide at midplane. The thickness of these pieces was reduced by cold rolling parallel to the longitudinal direction of the bar and without intermediate annealing. The resulting microstructure consisted only of β grains, which were 40 μm by 90 μm in cross-section and 130 μm in length for ST/CW (65%) Beta-C. X-ray diffraction confirmed that no other phases were formed during cold rolling. Second, 40 mm to 75 mm lengths of the round bar of ST Beta-C were heat treated at 500°C for times between 1 h and 24 h to precipitate the α phase (ST/A condition), which formed as fine plate-like particles within β grains and as of order 0.1 μm thick layers on β-grain boundaries. These β/α microstructures are thoroughly characterized.[32] A third condition (ST/CW/A) was produced by aging ST/CW (20%) Beta-C for 24 h at 500°C to stimulate intragranular α precipitation.

Measured or estimated hardness, σ_{YS} and elastic modulus (E) for Beta-C are shown in Table 1. Rockwell C (R_C) hardness was measured for each condition of Beta-C and the average of 10 measurements reported in Table 1. Uniaxial tensile properties were measured for the ST and ST/A (24 h) conditions. Values of σ_{YS} for the remaining conditions were estimated from hardness, assuming a linear hardness *vs* σ_{YS} relationship given by the values for the ST and ST/A (24 h) conditions. These σ_{YS} estimates agree with a hardness *vs* σ_{YS} correlation reported for two other ST/A β-titanium alloys.[22] Elastic modulus was determined from tensile results, or estimated from the relationship between crack length and compact tension (CT) specimen compliance.[33]

EAC-Fracture Mechanics

Sidegrooved CT specimens were used for air fracture toughness as well as EAC measurements of crack propagation threshold and stable growth rates. For the ST and ST/A specimens, the crack plane was perpendicular to the longitudinal axis of the round bar with crack growth in the radial direction. The ST/CW and ST/CW/A specimens were in the TL orientation; *viz*, with the crack plane perpendicular to the rolling plane and with crack growth parallel to the cold rolling direction (the original longitudinal axis). Additional specimens of ST/CW (65%) Beta-C were in the LT orientation (crack growth perpendicular to the rolling direction). All specimens except ST/CW (65%) Beta-C had a gross thickness (B) of 6.3 mm, net thickness (B_n) of 5.1 mm and width (W) of 30 mm. The ST/CW (65%) specimens had reduced thickness, with B = 5.1 mm and B_n = 3.8 mm. The CT specimens were fatigue precracked in moist air, terminating with a K_{max} of 15 MPa$\sqrt{m}$ and a crack length-to-width ratio of approximately 0.53.

Each fracture mechanics experiment was conducted under monotonically rising crack mouth opening displacement (δ_m) at a fixed rate ($\dot{\delta}_m$) using a servohydraulic test system operated in δ_m-feedback control. A $\dot{\delta}_m$ equal to 30 nm/s was selected because this loading rate produced severe IG EAC in both ST/A Beta-C and ST/A Beta-21S.[21,22] The direct-current potential difference (DCPD) method was used to resolve crack tip damage initiation and measure subsequent crack extension. [34] The fracture mechanics were characterized using either an elastic stress intensity analysis, or the elastic-plastic J-integral when the "plastic" component of the total J was significant (ST/CW (20%) and ST cases).[33] All experiments satisfied an approximate criterion for plane strain constraint.[33,35] All fracture surfaces were flat macroscopically, without shear walls, and were normal to the crack opening direction without macroscopic branching or deflection.

The onset of crack extension was evaluated by three different criteria using both load (P) *vs* δ_m and DCPD *vs* δ_m data. For ST/A Beta-C aged 7 h to 24 h, as well as ST/CW/A Beta-C, loaded in aqueous NaCl, initial crack extension was indicated by an abrupt increase in potential above the initial baseline DCPD *vs* δ_m trend, which was linear with a zero or mildly positive slope. This point always coincided with the first increase in specimen compliance from the initial linear P *vs* δ_m behavior.[22,27] For all microstructures in air, as well as ST/A (1 h to 4 h) and ST/CW Beta-C in aqueous NaCl, the DCPD *vs* δ_m data did not exhibit an abrupt increase in potential at initial crack extension. Initiation for these experiments was defined at the first increase in slope of the baseline DCPD *vs* δ_m trend, and was coincident generally with the first compliance increase from the initial linear P *vs* δ_m data. The third procedure for ST Beta-C is described elsewhere.[21] The K level associated with initial crack extension in aqueous NaCl under rising δ_m is defined as a lower-bound threshold (K_{TH}). The K levels corresponding to initial crack extension in air (K_{ICi}) are lower bounds of the standardized values of fracture toughness, while K_{IC} or K_{JIC} are standard offset-blunting line definitions of toughness.[33,35]

Crack growth rates (da/dt) were generally calculated from DCPD-based crack length (a) *vs* time (t) data using a secant between successive a *vs* t data points. The applied K was evaluated at the mean crack length for each data pair.

Environment

Experiments were conducted at 25°C in either moist air or flowing neutral 0.6 M (3.5 wt pct) aqueous NaCl (pH = 5 to 6) at a fixed electrode potential of -150 mV (*vs* the saturated calomel electrode). This electrode potential produced severe IG EAC in both ST/A Beta-C and ST/A Beta-21S.[21,22] The environmental cell consisted of two matching plexiglass pieces that contacted the specimen on opposite sides. Threaded-rod fasteners secured the cell components tightly around the specimen, and unconstrained rotation of the specimen as well as δ_m-feedback control were allowed during loading. The solution flowed solely through the crack and starter notch, essentially parallel to the crack front in the CT specimen..

RESULTS

Initial Crack Extension

Aged Beta-C in Air---The hardness and σ_{YS} of Beta-C increase monotonically with increasing isothermal aging time; Table 1. The effect of aging time on two measures of the plane strain fracture toughnesses is shown in Fig. 2. Data for K_{ICi} and K_{JIC} are plotted as a function of σ_{YS}, and the aging time for each σ_{YS} value is indicated. Figure 2 shows that K_{ICi} and K_{JIC} decrease sharply after only 1 h of aging and a small strength increase, and are essentially constant thereafter for increasing aging time or σ_{YS}; K_{ICi} and K_{JIC} vary around mean values of 56 MPa$\sqrt{m}$ and 63 MPa$\sqrt{m}$, respectively, with some scatter. K_{JIC} is only modestly higher than K_{JICi} because fracture occurs under plane strain constraint and the resistance of Beta-C to stable crack growth is small.[35] The measured toughnesses and effect of aging shown for Beta-C in Fig. 2 are consistent with literature data.[36,37]

Figure 2 includes the K_{ICi} and K_{JIC} results for ST/CW/A Beta-C. This condition exhibits the highest σ_{YS}, but toughness values are below the K_{ICi} and K_{JIC} *vs* σ_{YS} trend lines for ST/A Beta-C extrapolated to this strength level.

Aged Beta-C in NaCl---Values of K_{TH} decrease upon aging ST Beta-C, however, the aging time or σ_{YS} dependence for K_{TH} differs from that for K_{ICi}. Figure 2 shows that while K_{TH} equals K_{ICi} for aging times less than 3 h (σ_{YS} less than 970 MPa), K_{TH} decreases below K_{ICi} for longer aging times or higher σ_{YS}. The extent of data variability (K_{TH} from 24 MPa$\sqrt{m}$ to 31 MPa$\sqrt{m}$) is shown for σ_{YS} equaling 1170 MPa (24 h age). The EAC threshold for ST/CW/A Beta-C included in Fig. 2 follows the K_{TH} *vs* σ_{YS} trend for the ST/A values, and is less than K_{ICi} for this high-strength microstructure. These data confirm that aged Beta-C is susceptible to EAC in chloride solution.

ST/CW and ST Beta-C in Air---Increasing cold reduction from 20% to 65% increases σ_{YS} and lowers K_{ICi} of ST Beta-C. Figure 3 shows K_{ICi} *vs* σ_{YS} for ST/CW Beta-C fractured in air and includes the trend lines for ST/A Beta-C from Fig. 2. Although K_{ICi} values for ST/CW Beta-C decrease with increasing σ_{YS}, data are insufficient to determine if the initial strong σ_{YS} dependence of K_{ICi} differs between the ST/CW and ST/A conditions. For σ_{YS} above 1000 MPa, K_{ICi} for ST/CW Beta-C is less than that of the ST/A microstructure. For ST/CW (65%) Beta-C, K_{ICi} depends only mildly on specimen orientation; crack growth normal to the rolling direction (LT) initiates at slightly higher K.

There are no reports of the effect of cold work on the fracture toughness of single-β-phase alloys. Tensile reduction-of-area for cold drawn Beta-C is independent of reductions up to 60%, decreases to a minimum at 75% reduction, then increases with additional cold work.[38]

ST/CW and ST Beta-C in NaCl---Figure 3 shows that K_{TH} for EAC of ST and ST/CW Beta-C in aqueous NaCl equals K_{ICi}. The K_{TH} of ST/CW Beta-C increases mildly in the LT orientation at 65% reduction, similar to K_{ICi}.

Crack Propagation

Aged Beta-C in Air---The crack growth behavior of β/α Beta-C under constant $\dot{\delta}_m$ loading and plane strain constraint is stable after initiation at K_{ICi}, typical of high strength alloys with low crack growth resistance.[39] For all cases, both stress intensity (K) and crack length (a) increased monotonically with increasing applied δ_m. The applied K often achieved a plateau, above K_{ICi}, and occasionally decreased mildly after several mm of crack growth.

Air-crack growth behavior depends on aging condition. For ST/A Beta-C aged for 1 h and 2 h, stable crack growth was interrupted by fracture instability, i.e., the crack advanced instantaneously through nearly the entire specimen ligament and da/dt could not be measured. The increment of stable crack growth was larger for ST/A (2 h) Beta-C (2.5 mm) compared to that for the ST/A (1 h) condition (0.5 mm).

Aged Beta-C in NaCl---The effect of aqueous NaCl on crack growth under constant $\dot{\delta}_m$ loading depends on aging condition. For ST/A Beta-C aged 1 h and 2 h, the crack growth behavior in air was not altered by aqueous NaCl exposure. In contrast environment-enhanced crack growth kinetics are observed for ST/A Beta-C aged 3 h and longer, as summarized in Figs. 4a and 4b. While the ratios of K_{TH} to K_{ICi} differ (Fig. 2), the a *vs* t and K *vs* t behaviors for ST/A Beta-C aged 3 h to 5.5 h are similar; data for the 4 h-age case are shown in Fig. 4a. Cracks in aqueous NaCl grow stably over the first 1 mm to 2.5 mm of extension in ST/A Beta-C aged 3 h to 5.5 h, similar to the behavior in air. After this slow da/dt sequence, the slope of the a *vs* t curve increases dramatically and K decreases (Fig. 4a). This rapid da/dt behavior differs from the fracture instability observed for ST/A Beta-C

aged 1 h and 2 h; *viz*, crack length increases regularly between successive data points and da/dt is finite. Rapid da/dt commence at K levels (72 MPa√m to 90 MPa√m) that exceed K_{ICi} and arrest after considerable crack extension (6 mm to 10 mm).

The a *vs* t and K *vs* t behaviors for ST/A Beta-C aged 7 h, 12 h and 24 h, as well as ST/CW/A Beta-C, in aqueous NaCl are similar, as represented by data for the 7 h case in Fig. 4b. Although slow da/dt follows initiation at K_{TH} similar to the 3 h and 4 h cases, the ensuing rapid da/dt sequence (with falling K) occurs after a smaller crack growth increment and the K levels (24 MPa√m to 46 MPa√m) are less than K_{ICi}. Several rapid da/dt sequences, with crack growth increments from 1 mm to 5 mm, are observed during each experiment, and are separated by periods of slower da/dt. This alternating slow-rapid da/dt was reported for α/β Ti-6V-4Al and ST/A (24 h) Beta-C under rising displacement in aqueous NaCl.[21,26,27] The alternating slow-rapid da/dt in Fig. 4b is unique to the chloride solution case and is not observed for moist air fracture. Crack length increases regularly between successive data points and da/dt is environment-enhanced in aqueous NaCl; *viz*, imposing a fixed δ_m during rapid da/dt immediately arrests crack advance in air, but not in aqueous NaCl.[27]

The environment-assisted da/dt *vs* K relationships, measured for segments of rapid crack growth in ST/A Beta-C (aged 3 h and longer), are presented in Fig. 5. These data represent the initial rapid-stable da/dt sequences for ST/A Beta-C aged 12 h and 24 h, the first two such events for ST/A (7 h) Beta-C and ST/CW/A Beta-C, and the final rapid-growth segments for the 3 h, 4 h, and 5.5 h cases. In each microstructure EAC occurs under decreasing K during constant $\dot{\delta}_m$ loading. The da/dt levels range from 10 μm/s to 100 μm/s, and do not vary systematically with aging time. Crack growth rates are high and could exceed one grain diameter per second.

Air crack growth rates measured for ST/A (7h) Beta-C are included in Fig. 5 for comparison to the aqueous NaCl data. (Each da/dt point represents a measurement from linear regression over Δa of 0.5 mm.) Air da/dt, which represents crack growth solely from a mechanical driving force, is less than the slowest EAC growth rates at similar $\dot{\delta}_m$, and is finite only for K levels above K_{ICi}.

ST/CW and ST Beta-C in Air---Crack growth behavior for ST/CW Beta-C in air depends on specimen orientation. For TL-oriented ST/CW Beta-C, cracks grew unstably immediately upon initial extension at K equaling K_{ICi}. Cracking in the LT orientation was similar to ST/A Beta-C aged 1 h and 2 h; *viz*, stable growth was interrupted by fracture instability after modest Δa. Cracks grew stably in ST Beta-C under steeply rising K during the entire experiment.[21]

ST/CW and ST Beta-C in NaCl---Aqueous NaCl does not alter the air-crack growth behavior for ST/CW Beta-C and ST Beta-C, at any K level or crack length.

Fractography

Aged Beta-C in Air---Microscopic plasticity dominates the air fracture surfaces for ST/A and ST/CW/A Beta-C, however, the morphologies are complex and vary with microstructure. Figures 6a through 6d show the air fracture surfaces for ST/A Beta-C aged from 1 h to 24 h, as well as for ST/CW/A Beta-C. The fatigue precrack is evident at the bottom of each scanning electron fractograph. Each fractograph represents the fracture mode for all crack lengths.

For ST/A Beta-C aged 1 h and 2 h (Fig. 6a), facet-like features are prominent on the fracture

surfaces. The facets can be larger than the grain size, consist of only one face which may have steps, are steeply inclined with respect to the macro-crack plane, and are covered by fine dimples visible at high magnification. These characteristics suggest that such facets result from shear instability rather than cleavage or IG separation. Inhomogeneous deformation is likely for these short-time-aged microstructures, as large regions of β grains are free of α precipitates and strain localization may be promoted in these soft regions. The shear facets are surrounded by dimple-like features typical of transgranular (TG) microvoid nucleation, growth and coalescence (MVC). Dimple shapes and sizes vary widely, characteristic of void nucleation at the interface of plate-like α of varying orientation.[40]

Fractographs for ST/A Beta-C aged for 3 h and 24 h in Figs. 6b and 6c show that as aging time increases above 2 h, the facet-like features in Fig. 6a appear less frequently while the TG dimple-like features dominate the air fracture surfaces. Two additional features evolve as aging time increases (Fig. 6c). First, distinct regions of the fracture surface consist only of finer dimples. Second, a small area fraction of facets is present, typical of IG separation, as reported for higher-strength β/α alloys in air.[40] The fracture mode in Fig. 6c is consistent with that reported for fracture toughness specimens of Beta-C aged at 500°C for 8 h.[36]

The air fracture surface of ST/CW/A Beta-C in Fig. 6d shows evidence of ductile rupture, but the crack is extremely planar and most features are finer than those observed for ST/A Beta-C (Figs. 6a through 6c). Regions of these ductile features do not resemble dimples. This unique fracture behavior of ST/CW/A Beta-C is likely due to extreme shear localization caused by very fine α from high-nucleation rate intragranular precipitation at dislocations introduced by cold work.[40,41]

Aged Beta-C in NaCl---Aqueous NaCl produces a pronounced transition from the air fracture mode for ST/A Beta-C aged 3 h and longer as well as ST/CW/A Beta-C, but not for ST/A Beta-C aged for 1 h or 2 h. Figure 7a represents aqueous NaCl fracture for the 1 h and 2 h cases, and shows that the surface morphology is nearly identical to that produced in air (Fig. 6a); *viz*, shear facets and regions of dimpled rupture are observed. (The fractograph in Fig. 7a shows an area 0.5 mm from the fatigue precrack.) Limited cracking transverse to the macroscopic fracture surface was observed for ST/A (2 h) Beta-C, but not for the 1 hour case.

For ST/A Beta-C aged 7 h, 12 h and 24 h, as well as ST/CW/A Beta-C, aqueous NaCl crack extension from the fatigue precrack is solely by IG separation. Figures 7b (12 h-age) and 7c (ST/CW/A) show that IG facets cover the entire fracture surface. The facets in Fig. 7c are elongated compared to those in Fig. 7b because of cold work. These fractographs are typical for all crack lengths and positions along the crack front. Figures 7b and 7c show no evidence of a transition region between the fatigue precrack and EAC fracture mode, as IG facets abut the air-precrack at the bottom of each fractograph. The extent and homogeneity of IG cracking in aqueous NaCl is striking.

For ST/A Beta-C aged between 3 h and 5.5 h, the fracture mode in aqueous NaCl changes during crack extension for a single experiment, as shown by the fractographs in Figs. 8a through 8c for the 3 h case. The fracture surface morphology near the precrack (Fig. 8a) resembles that produced in air (Fig. 6b), but after some crack extension IG separation occurs, as shown in Fig. 8b for Δa equaling 3.5 mm. The transition fracture morphology in Fig. 8b is not, however, a simple mixture of air fracture (Fig. 6b) and IG fracture (Fig. 7b). Rather, the IG component of the evolving fracture mode involves ductile fracture, as the IG facets exhibit significant plasticity. Evidence for IG

cracking was noted after less crack extension for ST/A Beta-C aged 4 h and 5.5 h compared to the 3 hour case. For all three aging times, the fracture mode changed ultimately to IG cracking, consisting almost solely of smooth facets, as shown by the fractograph in Fig. 8c taken from near the end of crack extension ($\Delta a = 12$ mm). These facets resemble those in Fig. 7b for ST/A Beta-C aged 7 h and longer. The onset of rapid da/dt for ST/A Beta-C aged between 3 h and 5.5 h (Fig. 4a) occurred while the fracture mode was in the transition region (Fig. 8b).

ST/CW and ST Beta-C in Air---Crack propagation in ST/CW and ST Beta-C is by MVC; the fracture surfaces produced in air are covered completely by dimples (Figs. 9a and 9b), but the morphologies differ. The dimples on fracture surfaces of ST/CW Beta-C (Fig. 9a; ST/CW (58%) Beta-C) are larger and more well-formed compared to those for the ST condition (Fig. 9b). The only void-nucleating particles for the ST and ST/CW conditions are Ti-Zr silicides,[42,43] which form during solution heat treating in the β phase field and are not associated with recrystallized β grain boundaries. Although these particles may have aligned during cold rolling, they do not account for the frequency and regularity of the dimples in Fig. 9a. Shear facets typical for fracture of Beta-C aged 1 h and 2 h were not observed for the ST and ST/CW cases.

ST/CW and ST Beta-C in NaCl---In contrast to the aged microstructures of Beta-C, aqueous NaCl does not produce a transition in fracture mode for ST/CW and ST Beta-C. The fracture surfaces produced in aqueous NaCl exactly resemble those typical of air cracking (Figs. 9a and 9b).

DISCUSSION

Effect of Aging Heat Treatment on EAC of β-titanium Alloys

Results show that the IG EAC resistance of Beta-C in aqueous NaCl is degraded strongly by aging heat treatment. The challenge is to elucidate the roles of σ_{YS}, α-precipitates, and associated factors such as deformation mode and elemental segregation in promoting EAC. This discussion only considers σ_{YS} effects on EAC.

Results are interpreted based on an EAC scenario proposed for β-Ti alloys in aqueous NaCl.[22,28] Environment-assisted crack extension is by hydrogen environment embrittlement (HEE) where atomic hydrogen (H) is produced by cathodic electrochemical reaction on the crack surface. Crack tip strain, which ruptures the thermodynamically stable passive film, exacerbates EAC since H production rates and surface adsorption, as well as subsequent diffusion into the crack tip process zone, are enhanced on the base alloy. Process zone H may be trapped at microstructural sites. The location of cracking (i.e., near-surface *vs* process zone), exact trap sites, and the mechanism by which H lowers the IG fracture resistance of β-Ti have not been identified.

The EAC susceptibility is a function of the concentration of H at the damage site, the level of crack tip stress, and the intrinsic "strength" of the grain boundary region.[44] The concentration of H is governed by electrochemical activity and surface adsorption, as well as the density and strength of trap sites for process zone EAC. Crack surface H concentration may be enhanced by increased crack tip strain rate.[27] Traps could be either preexisting microstructural features such as α/β interfaces, or plastic strain-generated during crack tip deformation. The maximum in the crack tip stress distribution is affected by σ_{YS} and work hardening, while the extent of the high-stress region

ahead of the crack tip is a function of K.[45] Grain boundary strength was likely controlled by local alloy chemistry, the presence of a thin layer of α, and/or by slip-grain boundary interactions.

EAC of ST/CW Beta-C: Role of σ_{YS}---Previous experiments demonstrated a dramatic difference in the IG EAC immunity of ST single-phase β Beta-C compared to the susceptibility of high-strength ST/A two-phase β/α Beta-C.[21] The present results show that ST Beta-C, cold worked to reductions between 20% and 65%, is similarly immune to IG EAC in aqueous NaCl under rising δ_m. This immunity is evidenced by equal K_{ICi} and K_{TH} (Fig. 3), MVC fracture modes in both air and aqueous NaCl (Fig. 9a), and the lack of enhanced da/dt even at K levels above K_{ICi}. Such results are of practical importance to fastener applications of ST/CW β-Ti alloys in marine environments. For example, localized regions of cold work at thread or cap regions should not be susceptible to IG EAC in aqueous NaCl. The fact that cold work dramatically reduced K_{ICi} must, however, be considered in applications of this single β-phase alloy.[2]

The behavior of ST/CW Beta-C indicates that increased σ_{YS} accompanying aging does not solely render the ST/A condition susceptible to EAC. Cold-work reductions between 36% and 65% do not alter the single-phase β microstructure or composition of ST Beta-C, but increase σ_{YS} to levels (975 MPa to 1100 MPa in Fig. 3) comparable to those of EAC-susceptible Beta-C aged 3 h and longer (975 MPa to 1275 MPa in Fig. 2). For constant β microstructure and composition, as well as loading rate and environment, this increased σ_{YS} does not promote EAC of Beta-C.

The fracture mode for ST/CW Beta-C in aqueous NaCl was fully TG MVC (Fig. 9a). Some IG separation should occur if the grain boundaries are inherently susceptible to HE. Previous experiments show that ST Beta-C is immune to EAC in aqueous NaCl solutions containing sulfide ions to promote H uptake.[21] Based on these results, it is reasonable to speculate that single-phase β ST and ST/CW microstructures of Beta-C are immune intrinsically to EAC.

Caution is required before eliminating an important role of alloy σ_{YS} in promoting EAC of ST/A Beta-C compared to the ST condition. First, the elongated grain shape of ST/CW Beta-C differs from the equiaxed grains in ST and ST/A Beta-C. This difference is addressed; the ST/CW (65%) Beta-C results in Fig. 3 include both the TL and LT orientations (Fig. 3). For these two cases, different amounts of grain boundary area are exposed to the propagating crack, but an environmental effect is not observed for either case. In fact, the TL orientation used for experiments on ST/CW Beta-C provides the most likely opportunity for IG EAC, but none occurs.

Second, K_{ICi} for ST/CW Beta-C in air is unexpectedly low compared to values for ST/A Beta-C (Fig. 3). For σ_{YS} above 1000 MPa, IG EAC is produced at K_{TH} levels for ST/A Beta-C that are nearly equal to K_{ICi} for ST/CW Beta-C at similar σ_{YS}. These K_{ICi} values for ST/CW Beta-C represent the maximum K levels sustained since crack growth was unstable. The ST/CW microstructures may

---

[2] Since the morphology of ST/CW Beta-C fracture surfaces is microvoid-based (Fig. 9a), it is possible that low K_{ICi} is traced to reduced work hardening with increasing cold work. Reduced hardening may accelerate the growth and coalescence stages of microvoid fracture and thus reduce K_{ICi}.[46] In addition cold work can increase the dislocation density around features which promote strain incompatibility and thus enhance void nucleation.

be susceptible to EAC at higher applied K.

Finally, the immunity of ST/CW Beta-C to EAC is only demonstrated for a single loading rate, and rapid unstable crack growth rate. The $\dot{\epsilon}_{CT}$ dependence of K_{TH} may be affected by cold work;[27] reduced K_{TH} could occur at values of $\dot{\delta}_m$ and da/dt that were not probed by the current experiments. For example, the grain boundary H concentration may be reduced in ST/CW Beta-C compared to the ST condition due to increased trapping at intragranular dislocations. Accordingly, EAC of ST/CW Beta-C may occur at slower loading rates that allow for more H accumulation at grain boundaries. The $\dot{\epsilon}_{CT}$ effect must be addressed to further assess the importance of σ_{YS} in IG EAC of single-phase β-Ti alloys; such experiments are presented elsewhere.[47]

EAC of Aged Beta-C: Role of σ_{YS}---The ST/A Beta-C aged for 7 h to 24 h, as well as ST/CW/A Beta-C, are susceptible similarly to EAC in aqueous NaCl under rising δ_m. This conclusion is based on results showing reduced K_{TH} below K_{ICi} (Fig. 2), a transition in fracture mode from ductile rupture in air (Figs. 6c and 6d) to fully IG cracking in aqueous NaCl at all K levels above K_{TH} (Figs. 7b and 7c), and high crack growth rates during rapid da/dt (Fig. 5). These results further demonstrate the susceptibility of high-strength aged β-Ti alloys to IG EAC, where K_{TH} can be less than 50% of K_{ICi} and subcritical da/dt can approach 100 μm/s (greater than one grain diameter per second). Similar observations are reported for ST/A Beta III and ST/A Beta-21S under rising displacement in aqueous halide solutions.[22,23,27]

The ST/A Beta-C, aged for short times between 3 h and 5.5 h, exhibits NaCl-EAC behavior that represents a transition between the immune ST case and the susceptible ST/A microstructure. The K_{TH} values equal K_{ICi} (Fig. 2) and initial crack extension from the fatigue precrack involves TG MVC for both air (Fig. 6b) and aqueous NaCl exposures (Fig. 8a). Aqueous NaCl EAC occurs, however, for the 3 h, 4 h, and 5.5 h cases as the crack extends and K increases above K_{TH}. The EAC is indicated by evolving IG fracture (Figs. 8b and 8c), and accelerating da/dt to rapid rates (Fig. 5), albeit for higher K. These microstructures of ST/A Beta-C are susceptible inherently to EAC in aqueous NaCl. This transition from EAC-resistant to susceptible is explained based on the idea that crack tip strain rate increases due to da/dt during stable mechanical tearing at K levels above K_{JICi}. Experiments at alternate loading rates, designed to produce faster $\dot{\epsilon}_{CT}$, prove this hypothesis.[47]

Aqueous NaCl has a modest effect on ST/A (2 h) Beta-C, but not for the 1 h-age case. Faceted features and TG dimples dominate the fracture surface for each environment (Fig. 6a compared to Fig. 7a), but aqueous NaCl exposure promotes some cracking transverse to the macroscopic crack (Fig. 7a) for ST/A (2 h) Beta-C. This mild alteration in the fracture mode is not manifest by either reduced K_{TH} below K_{ICi} (Fig. 2), or a change in the crack growth behavior. It is possible that both short-term-aged microstructures are inherently susceptible to EAC, and that higher K levels or alternate $\dot{\delta}_m$ will promote IG cracking similar to ST/A Beta-C aged between 3 h and 6 h. Experimental results support his view.[47]

The EAC results for ST/A and ST/CW/A Beta-C (Fig. 2) show that K_{TH} declines modestly with increasing aging time above 5.5 h, where crack extension at fixed $\dot{\delta}_m$ is fully intergranular for all crack lengths (Figs. 7b and 7c). While increasing σ_{YS} is not solely responsible for the EAC susceptibility of ST/A Beta-C compared to the ST case, strength may contribute to this dependence of K_{TH} on aging time. The HE models identify crack tip tensile stress, proportional to σ_{YS} and work

hardening, as the local driving force for crack extension.[44] Perhaps as a critical aspect of the aged microstructure rendered the alloy susceptible to EAC, and conjointly, the threshold for IG crack growth is reduced by increased σ_{YS} and crack tip tensile stress.

The experiments with ST/CW Beta-C establish the secondary role of yield strength, but do not identify the metallurgical change during the aging heat treatment that causes EAC. Parallel research is has examined the contributions of α-microstructure, plastic deformation mode, and elemental segregation to grain boundaries to EAC.[32] Once the causal factor is identified, it may be possible to develop high strength β-titanium alloys that resist EAC in marine environments.

RAD Representation of the Fracture Behavior of β-titanium in Marine Environments

The fracture toughness and EAC data obtained during this study are presented in the RAD of Fig. 10, containing the trend lines and literature results for β-titanium alloys from Fig. 1. K_{JIC} for both ST/A β/α-phase Beta-C (o) and cold worked β-phase Beta C (solid line without numbers) are replotted from Figs. 2 and 3, respectively. K_{TH} values from these figures are plotted for the ST/CW (▲) and ST/A (●) conditions of Beta-C. K_{TH} data for Beta-21S[22], Ti-15-3[22,26] and Beta-III[23,25] are replotted from the literature. This plot updates existing RADs describing the environmental cracking behavior of high strength β-titanium alloys.[1,19]

The comparison in Fig. 10 summarizes the findings of the current research. The measured values of fracture toughness and effect of isothermal aging for α-strengthened Beta-C are consistent with literature data.[3,36,37] A similar mild effect of isothermal aging time beyond 1 hour on fracture toughness is found for both Beta-C aged at 500°C[36] and Beta III aged at 620°C.[23] The toughnesses of the short-time ages are below the literature trends, probably because of the heterogeneous distribution of α-precipitates formed in the early stage of aging. The toughness (K_{JIC} = 63MPa√m) for the 24 h-aged microstructure (σ_{YS} = 1170 MPa) compares favorably with standardized values (57 MPa√m) reported for Beta-C with similar heat treatments and σ_{YS} (1220 MPa).[37] The low fracture toughness of the cold worked single-phase β microstructure is apparent.

The K_{TH} results in Fig. 10 demonstrate the reduction in fracture resistance of high strength β-titanium alloys caused by active straining in an aqueous chloride solution. The ST/A microstructures of Beta-C and Beta-III[23] exhibit substantial reductions in K_{TH} relative to K_{JIC}. While Beta-21S[22] is susceptible to intergranular cracking in chloride solutions, absolute values of K_{TH} are above those of Beta-C and Beta-III. (The fracture toughness of Beta-21S appears to be atypically high, Fig. 10.) Among the alloys studied in detail to date, only ST/A Ti-15-3 appears to be immune to EAC in chloride;[22,26] the similarity between K_{TH} and K_{JIC} is apparent in Fig. 10. As discussed with regard to Figs. 3 and 9, K_{TH} and K_{JIC} are equal for cold worked single β-phase Beta-C.

The EAC results presented in the RAD of Fig. 10 must be applied with caution. The use of standard fracture mechanics methods to predict component fracture resistance from laboratory data and stress-intensity similitude[1] is more complex for environmental cracking compared to brittle fracture. Several factors must be considered, including component constraint, alloy product form and size, electrochemical variables, crack size, and loading rate/crack tip strain rate.

For the yield strength and stress intensity levels depicted in Fig. 10, issues of constraint and net-section plastic deformation[1] are not important, at least for through-cracked component section

sizes on the order of 10 mm or larger. As alloy product-form size increases, changes in microstructure with position may affect K_{TH}. In this context, the effects of primary and secondary α size, distribution and morphology on K_{TH} have not been examined. Electrochemical variables, particularly electrode potential, have a strong influence on EAC in ST/A β-titanium alloys.[22,23,28] The K_{TH} results in Fig. 10 were generally obtained at potentials within $\pm$ 400 mV of the free corrosion level, and generally represent lower-bound values. Significant cathodic polarization mitigates EAC in β-titanium alloys due to reduced crack tip hydrogen production, however, embrittlement may be produced if extreme cathodic polarization and long exposure times favor hydrogen uptake from boldly exposed surfaces in contact with the bulk chloride solution, particularly is a means exists to destabilize the surface oxide film.

Two complicating factors may be particularly important to the application of RAD-K_{TH} data. First, K_{TH} for high strength steels in aqueous NaCl decreases with decreasing crack size, particularly below 1 mm.[48] In this case use of threshold data from laboratory fracture mechanics specimens with 10 to 40 mm long cracks will not accurately describe the behavior of small cracks in a component in the marine environment. The effect of crack size and shape on K_{TH} has not been examined for high strength β-titanium alloys. Second, experiments with Beta-C in NaCl show that K_{TH} and da/dt are strongly affected by crack tip strain rate.[27] As an example, a CT specimen with a transgranular fatigue precrack was loaded to a fixed K level of 48 MPa$\sqrt{m}$, and held in moist air for either 4 minutes or 24 hours, then exposed to NaCl. EAC occurred in the former but not the latter case. When the same experiment was conducted with a precrack that was intergranular, produced by prior EAC exposure, environmental crack growth did not occur for either hold-time. Presumably, these effects are traceable to prior creep and crack morphology effects on the crack tip strain rates that operate during solution exposure. It is tempting to hypothesize that this strain rate must be sufficiently active to destabilize the crack tip passive film to enable hydrogen production and uptake. The K_{TH} results in Fig. 10 were obtained with a superimposed active loading rate to maximize EAC. Crack tip strain rate issues have not been investigated sufficiently to support quantitative applications of RAD-type information for the EAC case.

CONCLUSIONS

1. Application of high strength metastable β-titanium alloys in marine environments may be hindered by low fracture toughness and susceptibility to intergranular environment-assisted cracking.

2. Aging renders immune single β-phase Beta-C susceptible to severe EAC in aqueous NaCl for conditions involving a fatigue precrack, intermediate loading rate, and fixed electrode potential near free corrosion. The threshold for EAC is 40% of K_{ICi}, subcritical crack growth rates equal 100 μm/s, and the crack path is intergranular in α-precipitate hardened microstructures.

3. The σ_{YS} increase due to α precipitation does not govern the EAC susceptibility of ST/A Beta-C. Solution treated and cold worked Beta-C is immune to EAC for high σ_{YS} comparable to that developed by aging. For several levels of cold work, fracture of ST as well as ST/CW Beta-C is by TG microvoid processes, with K_{TH} equaling K_{ICi}.

4. Cold work reduces the air fracture toughness of ST Beta-C below levels for ST/A microstructures at similar σ_{YS}, limiting the criticality of the EAC experiments.

5. An updated Ratio Analysis Diagram defines the EAC resistance of high strength β-titanium alloys, particularly Beta-C. Uncertainties are associated with electrochemical, crack size, and crack tip strain rate effects on the threshold stress intensity for environmental cracking.

ACKNOWLEDGMENT

This research was supported by the Office of Naval Research (Grant N00014-91-J-4164), with Dr. A. J. Sedriks as Scientific Monitor. Material was donated by the RMI Titanium Company and mechanical processing was provided by the General Electric Corporate Research and Development Center. Informative discussions were conducted with J.R. Scully and J.R. Hughes. These contributions are gratefully acknowledged.

REFERENCES

1. W.S. Pellini: *Criteria for Fracture Control Plans*, Naval Research Laboratory Report 7406, Washington, DC, 1972.
2. R.K. Bird, T.A. Wallace and W.D. Brewer: "Effects of Heat Treatment on Microstructure, Strength and Toughness of TIMETAL-21S", Unpublished research, NASA-Langley Research Center, Hampton, VA, 1994.
3. J.R. Wood, J.G. Ferrero, P.A. Russo and R.W. Schutz: in *Beta Titanium Alloys in the 1990's*, D. Eylon, et al., eds., TMS-AIME, Warrendale, PA, 1993, p. 463.
4. P.K. Poulose and M.A. Imam: in *Titanium '95: Science and Technology*, P.A. Blenkinsop, et al., eds., Institute of Materials, London, UK, 1996, p. 988.
5. G. Terlinde, H.-J. Rathjen and K.-H Schwalbe: *Metall. Trans. A*, Vol. 19A, 1988, p. 1037.
6. R. Chait and P.T. Lum: in *Toughness and Fracture Behavior of Titanium, ASTM STP 651*, ASTM, Philadelphia, PA, 1978, p. 180.
7. W.M. Garrison, Jr.: *Journal of Metals*, May, 1990, p. 20.
8. James Dahl: in *Advanced Materials Technology International*, Sterling Publications, London, UK, 1991, p. 40.
9. P. M. Novotny and J.M. Dahl: in *Mechanical Working and Steel Processing Proceedings*, Vol. XXVIII, Iron and Steel Society, Inc., Warrendale, PA, 1991, p. 275.
10. C.S. Carter: *Engineering Fracture Mechanics*, Vol. 3, 1971, p. 1.
11. A.J. McEvily, Jr.: *Atlas of Stress Corrosion and Corrosion Fatigue Curves*, ASM International, Metals Park, OH, 1990.
12. M.G.H. Wells: *Key Engineering Materials*, Vol. 77-78, 1993, p. 71.
13. T.V. Philip and T.J. McCaffrey: in *Metals Handbook: Properties and Selection: Irons, Steels, and High-Performance Alloys*, 10th Edition, Vol. 1, ASM International, Metals Park, OH, 1990, p. 430.
14. D.S. McDarmaid: *Br. Corros. J.*, Vol. 15, 1980, p. 172.
15. E.U. Lee and J. Waldman: *Naval Engineers Journal*, Vol. 106, 1994, p. 77.
16. Raghavan Ayer and P.M. Machmeier: in *Microstructures and Mechanical Properties of Aging Materials*, P.K. Liaw et al., eds., TMS-AIME, Warrendale, PA, 1993, p. 251.
17. *Aerospace Structural Metals Handbook*, Vol. 1, W.F. Brown, Jr., H. Mindlin and C.Y. Ho, eds., CINDAS/USAF CRDA Handbooks Operation, Purdue University, West Lafayette, IN, 1996, p. 1.

18. R.P. Gangloff and E.A. Starke, Jr.: *NASA-UVa Light Aerospace Alloy and Structures Technology Program*, Report No. UVA/528266/MSE97/122, University of Virginia, Charlottesville, VA, 1997.
19. R.J. Goode and R.W. Judy, Jr.: *Welding Research Supplement*, March, 1974, p. 135-s.
20. G.B. Olson: *Advanced Materials & Processes*, July, 1997, p. 72.
21. B.P. Somerday, J.A. Grandle and R.P. Gangloff: in *Proceedings of the Tri-Service Conference on Corrosion*, T. Naguy, ed., Materials Laboratory, Wright-Patterson Air Force Base, OH, 1994, p. 375.
22. L.M. Young, G.A. Young, J.R. Scully and R.P. Gangloff: *Metall. Mater. Trans. A*, 1995, Vol. 26A, p. 1257.
23. J.A. Feeney and M.J. Blackburn: *Metall. Trans.*, 1970, Vol. 1, p. 3309.
24. D.M. Aylor: *An Environmental Cracking Evaluation of Fastener materials for Seawater Applications*, CORROSION '94, Paper No. 484, NACE, Houston, TX, 1994.
25. M.J. Blackburn, J.A. Feeney and T.R. Beck: in *Advances in Corrosion Science and Technology*, Vol. 3, M.G. Fontana and R.W. Staehle, eds., Plenum Publishing, New York, NY, 1972, p. 67.
26. D.A. Meyn and P.S. Pao: in *Slow Strain Rate Testing for the Evaluation of Environmentally Induced Cracking: Research and Engineering Applications, ASTM STP 1210*, R.D. Kane, ed., ASTM, Philadelphia, PA, 1993, p. 158.
27. B.P. Somerday, L.M. Young and R.P. Gangloff: "Crack-Tip Strain Rate Effects in EAC of β-Titanium Alloys", 1997, in preparation.
28. D.G. Kolman: PhD Thesis, University of Virginia, Charlottesville, VA, 1995.
29. R.P. Gangloff: in *Corrosion Prevention and Control*, M. Levy and S. Isserow, eds., US Army Laboratory Command, Watertown, MA, 1986, p. 64.
30. D.G. Kolman and J.R. Scully: in *Effects of the Environment on the Initiation of Crack Growth, ASTM STP 1298*, W.A. Van der Sluys, R.S. Piascik, and R. Zawierucha, eds., ASTM, Philadelphia, PA, 1997, in press.
31. J.A. Moskovitz and R.M. Pelloux: *Corrosion*, 1979, Vol. 35, p. 509.
32. B.P. Somerday and R.P. Gangloff: "The Effect of Metallurgical Variables in EAC of Aged Beta-C", 1997, in preparation.
33. *Annual Book of ASTM Standards*, Designation E1737-96, ASTM, Philadelphia, PA, 1997, Vol. 3.01, p. 968.
34. J.K. Donald and J. Ruschau: in *Fatigue Crack Measurement: Techniques and Applications*, K.J. Marsh, R.A. Smith and R.O. Ritchie, eds., EMAS, West Midlands, UK, 1991, p. 11.
35. M.J. Haynes and R.P. Gangloff: *Journal of Testing and Evaluation*, 1997, Vol. 25, p. 82.
36. H.J. Rack: in *Titanium '80 Science and Technology*, H. Kimura and O. Izumi, eds., TMS-AIME, Warrendale, PA, 1980, p. 1627.
37. L. Wagner and J.K. Gregory: in *Beta Titanium Alloys in the 1990's*, D. Eylon, R.R. Boyer, and D.A. Koss, eds., TMS-AIME, Warrendale, PA, 1993, p. 199.
38. D.H. Wilson and C.M. Esler: in *Beta Titanium Alloys in the 80's*, R.R. Boyer and H.W. Rosenberg, eds., TMS-AIME, Warrendale, PA, 1984, p. 457.
39. K.S. Chan: *Acta Metall.*, 1989, Vol. 37, p. 1217.
40. G.T. Terlinde, T.W. Duerig and J.C. Williams: *Metall. Trans. A*, 1983, Vol. 14A, p. 2101.
41. G. Terlinde, H.-J. Rathjen and K.-H. Schwalbe: *Metall. Trans. A*, 1988, Vol. 19A, pp. 1037.
42. T.J. Headley and H.J. Rack: *Metall. Trans. A*, 1979, Vol. 10A, p. 909.
43. S. Ankem, D. Banerjee, D.J. McNeish, J.C. Williams and S.R. Seagle: *Metall. Trans. A*, 1987, Vol. 18A, p. 2015.
44. K.N. Akhurst and T.J. Baker: *Metall. Trans. A*, 1980, Vol. 11A, p. 1059.
45. R.M. McMeeking: *J. Mech. Phys. Solids*, 1977, Vol. 25, p. 357.
46. P.F. Thomason: *Ductile Fracture of Metals*, Pergamon Press, New York, NY, 1990.
47. B.P. Somerday and R.P. Gangloff: "The Effect of Crack Tip Strain Rate on EAC of Underaged and Cold-Worked Beta-C", 1997, in preparation.
48. R.P. Gangloff and A. Turnbull: in *Modeling Environmental Effects on Crack Initiation and Propagation*, R.H. Jones and W.W. Gerberich, eds., TMS-AIME, Warrendale, PA., 1986, p. 55.

Table 1 *Hardness, yield strength, and elastic modulus for Beta-C*

Condition	R_C Hardness	σ_{ys} (MPa)	E (GPa)
ST	27.6	875	87.5
ST/CW (20%)	30.0	900*	-
ST/CW (36%)	32.4	985*	-
ST/CW (51%)	35.1	1045*	-
ST/CW (58%)	36.1	1070*	-
ST/CW (65%)	37.4	1095*	-
ST/A (1 h)	30.0	900*	97*
ST/A (2 h)	31.1	950*	97*
ST/A (3 h)	31.7	970*	97*
ST/A (4 h)	32.3	985*	97*
ST/A (5.5 h)	34.1	1025*	97*
ST/A (7 h)	35.9	1065*	105*
ST/A (12 h)	37.9	1110*	105*
ST/A (24 h)	40.6	1170	105
ST/CW/A	45.6	1280*	105*

*Estimated

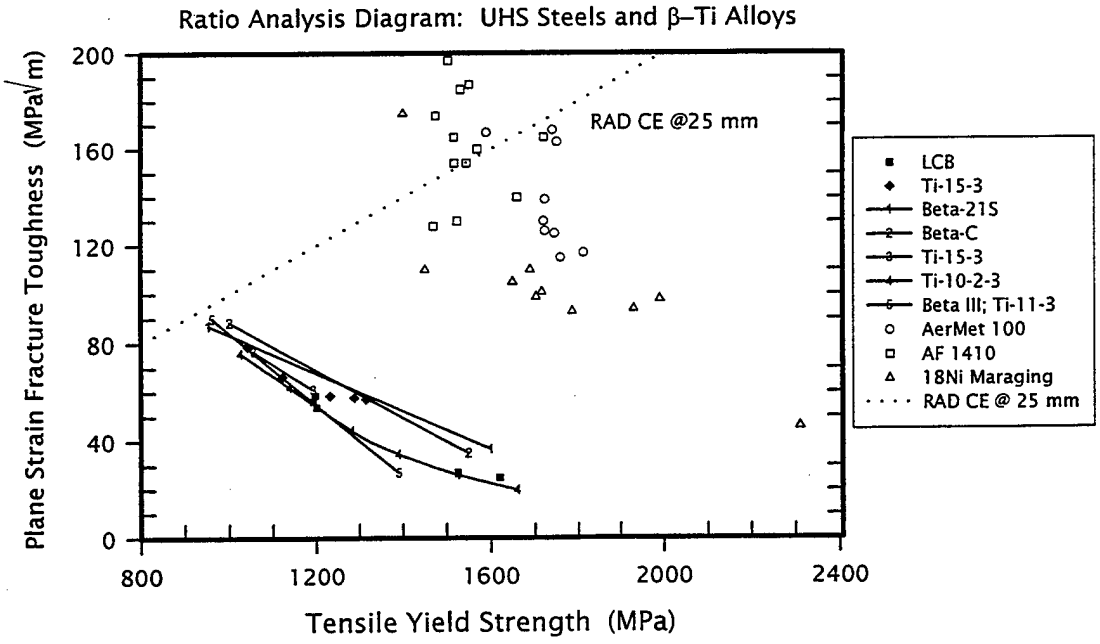


Fig. 1 Ratio Analysis Diagram showing plane strain fracture toughness for modern ultra-high strength steels and β-titanium alloys. Sources of data are cited in the text.

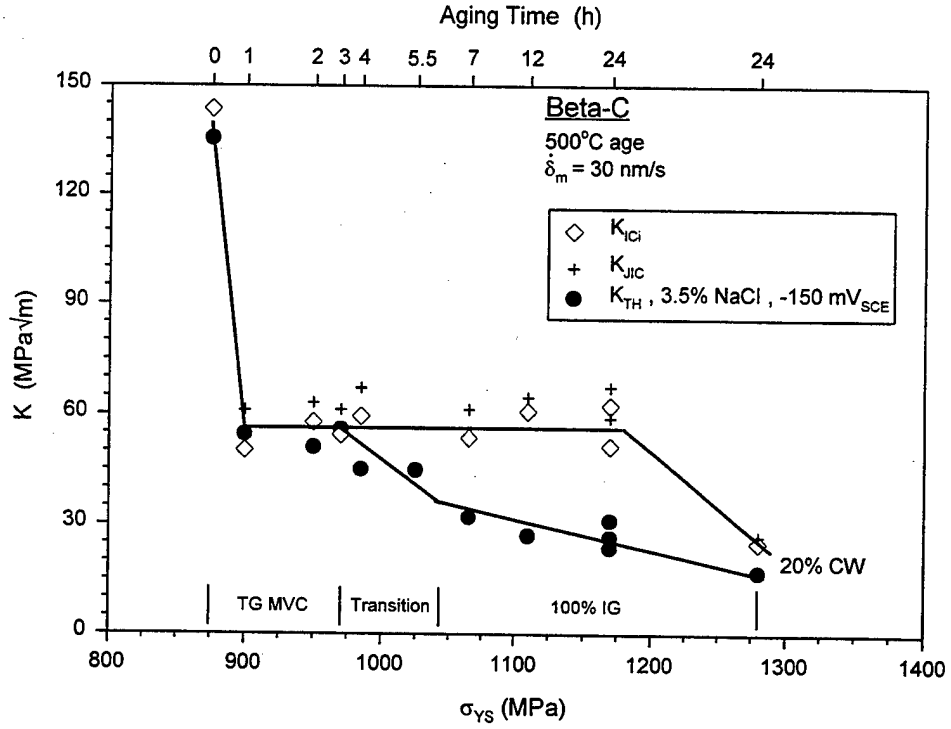


Fig. 2 Lower-bound and standardized fracture toughnesses, as well as EAC threshold stress intensity factors, for ST/A Beta-C as a function of σ_{YS} or aging time. The aqueous NaCl fracture modes for each range of σ_{YS} or aging time are indicated.

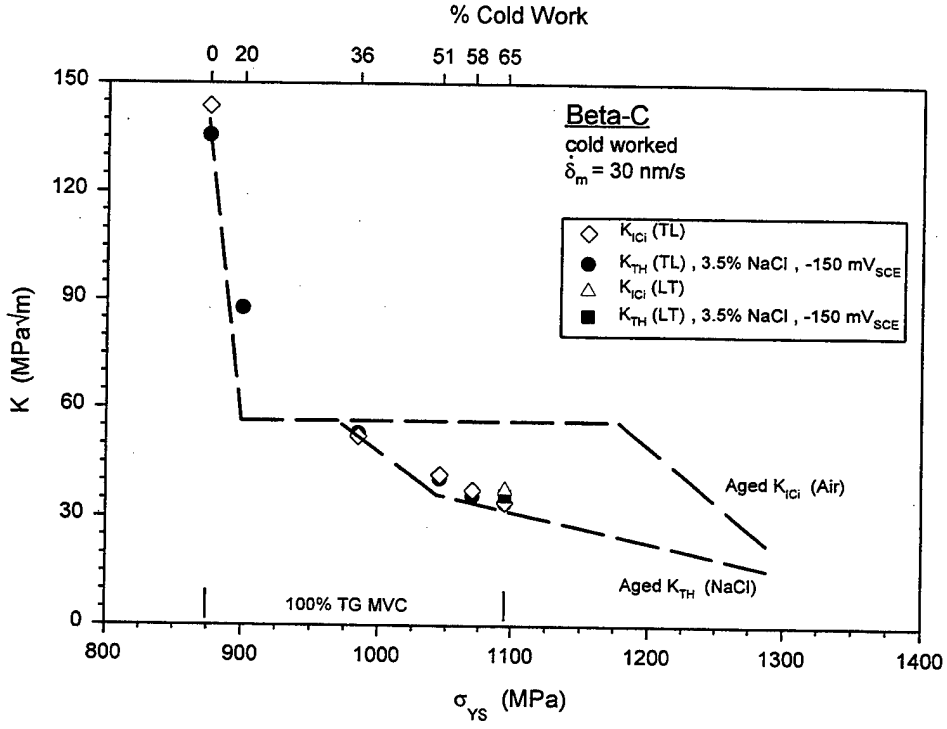


Fig. 3 Air fracture toughness and EAC threshold stress-intensity factor for ST/CW Beta-C as a function of yield strength and cold-work reduction. The fracture mode for both air and aqueous NaCl exposures is indicated. Dashed trend lines for the ST/A data in Fig. 2 are shown.

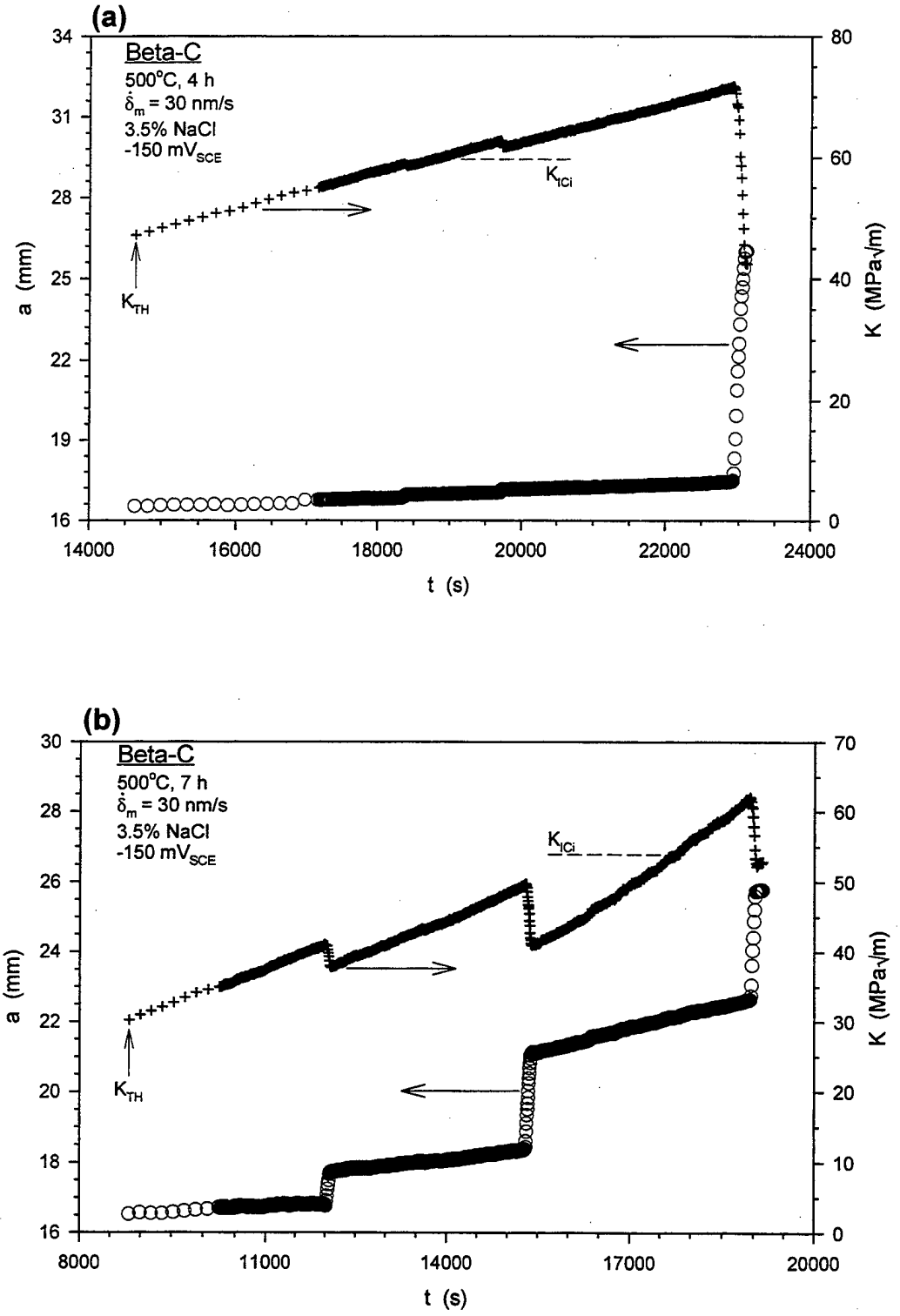


Fig. 4 Crack length and applied stress-intensity factor *vs* time data for: a) ST/A (4 h) Beta-C, and b) ST/A (7 h) Beta-C in aqueous NaCl.

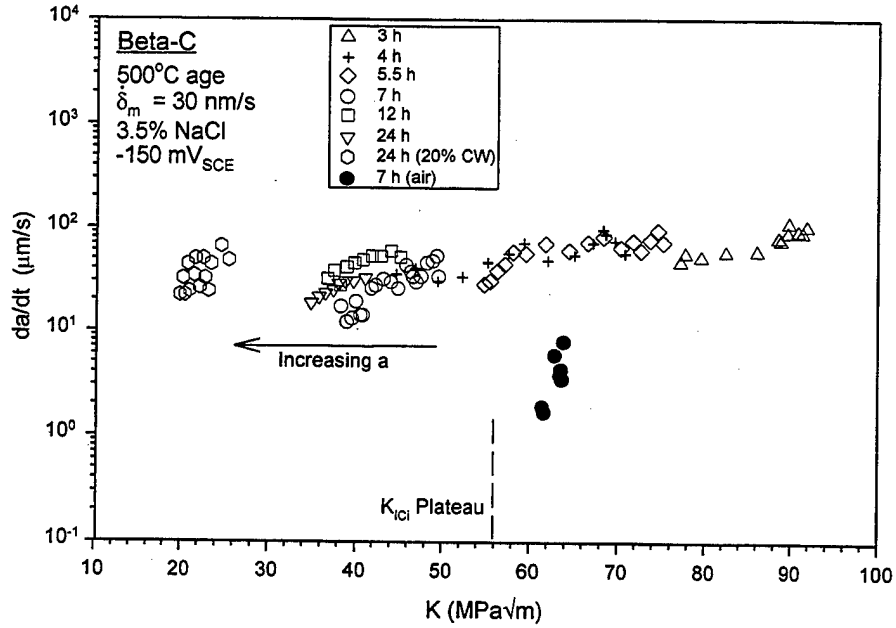


Fig. 5 Rapid crack growth rate *vs* applied stress-intensity factor data for ST/A and ST/CW/A Beta-C in aqueous NaCl.

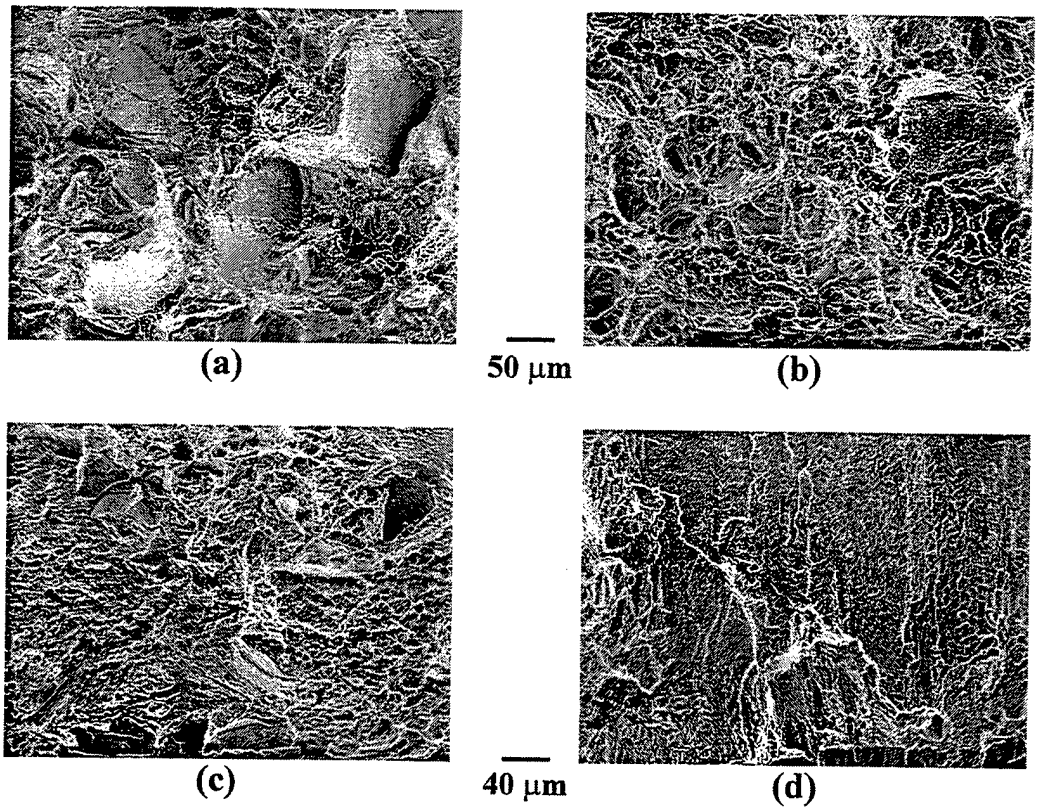


Fig. 6 Low-magnification SEM fractographs for air fracture of: a) ST/A (1 h) Beta-C, b) ST/A (3 h) Beta-C, c) ST/A (24 h) Beta-C, and d) ST/CW/A Beta-C.

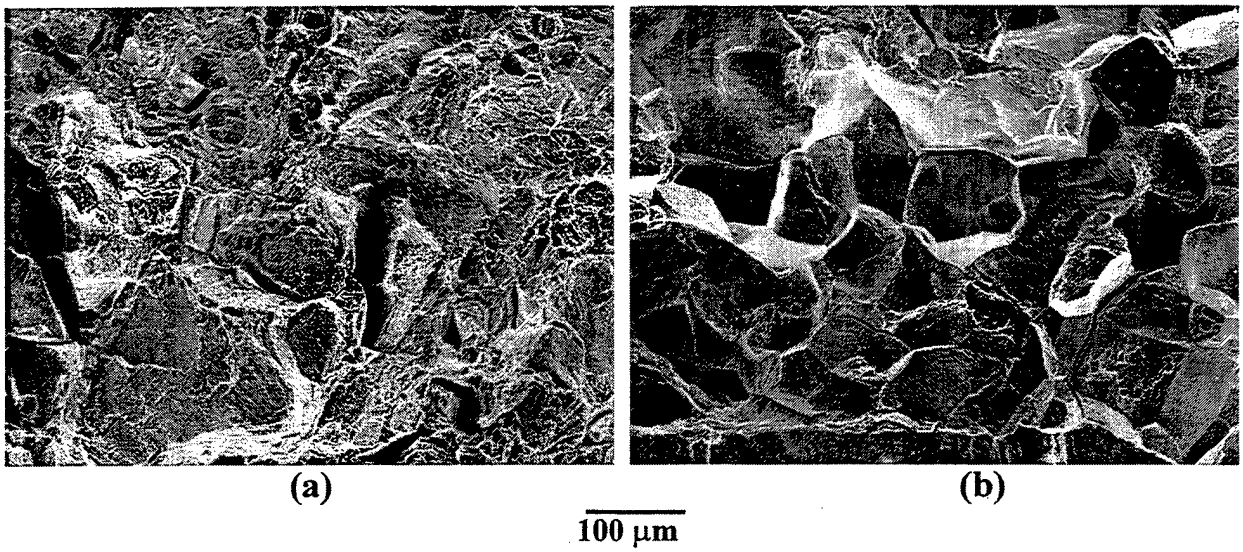


Fig. 7 Low-magnification SEM fractographs for aqueous NaCl EAC of: a) ST/A (2h) Beta-C, b) ST/A (12 h) Beta-C, and c) ST/CW/A Beta-C.

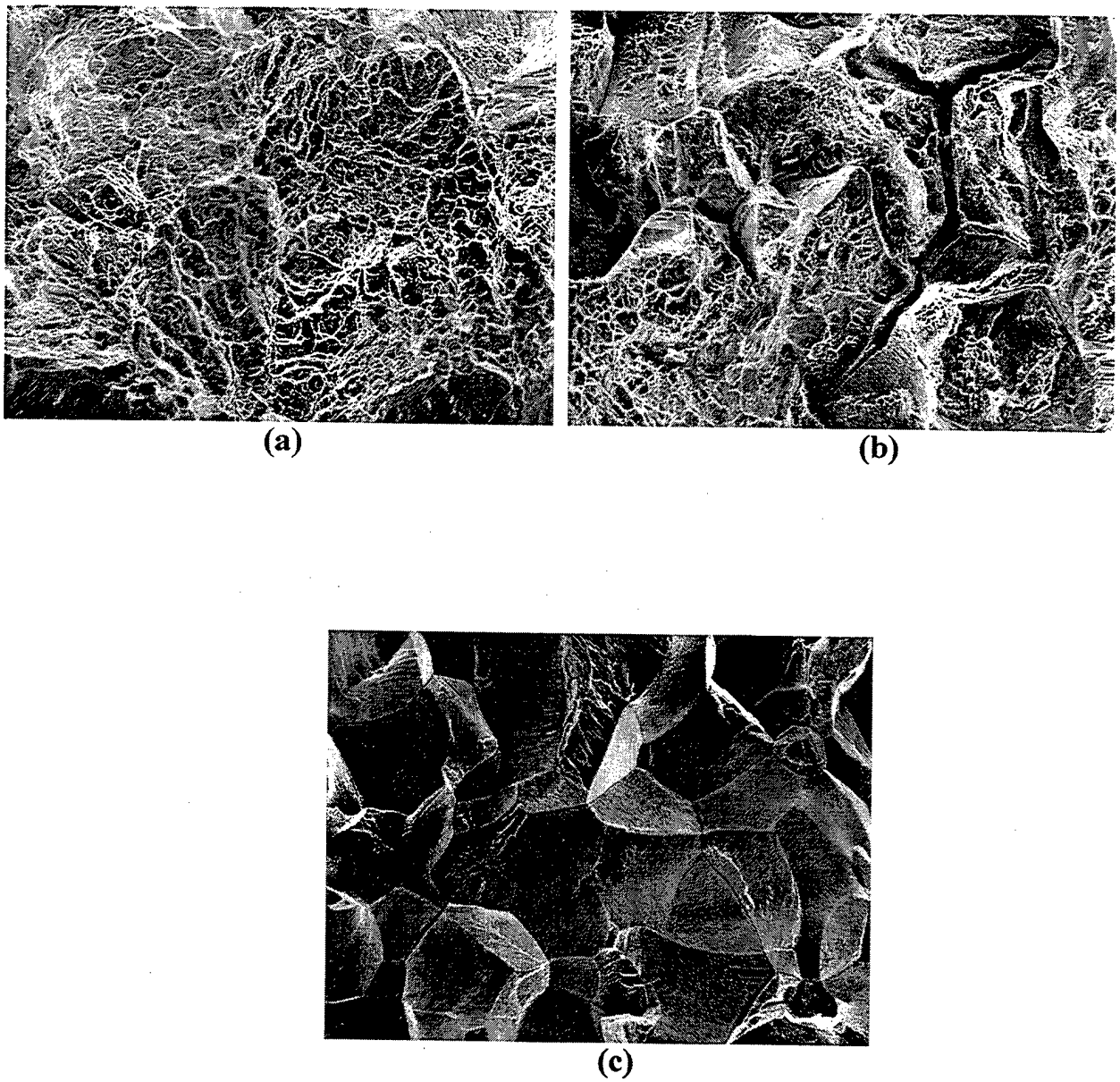


Fig. 8 Low-magnification SEM fractographs for cracking of ST/A (3 h) Beta-C in aqueous NaCl: a) near fatigue precrack, b) at $\Delta a = 3.5$ mm, and c) at $\Delta a = 12$mm.

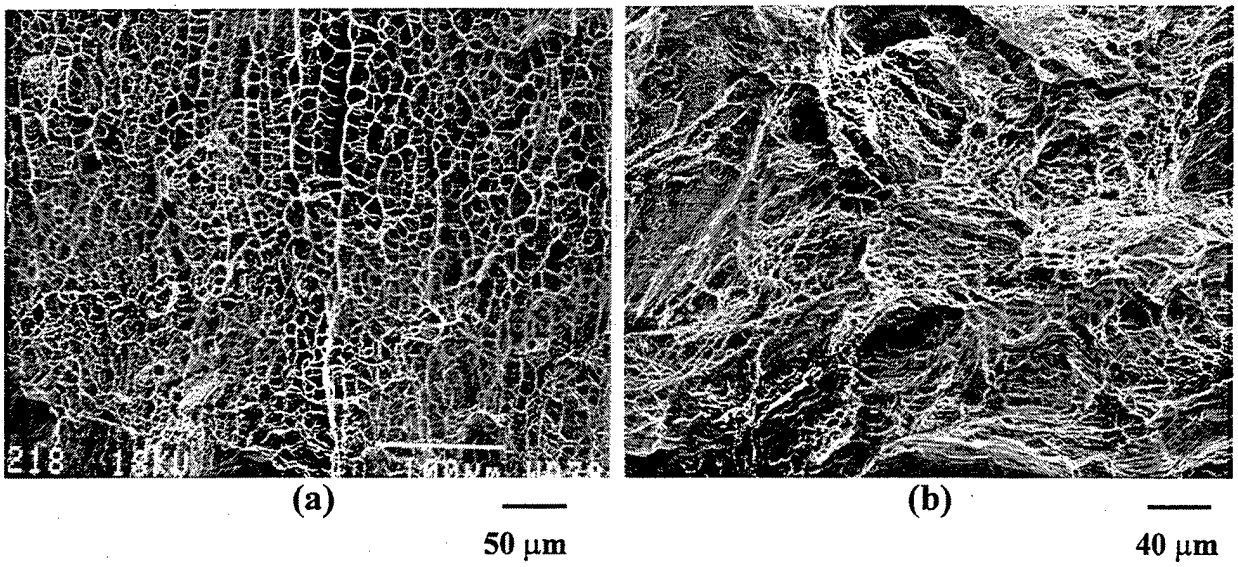


Fig. 9 Low-magnification SEM fractographs for both air and aqueous NaCl cracking of: a) ST/CW (58%) Beta-C, and b) ST Beta-C.

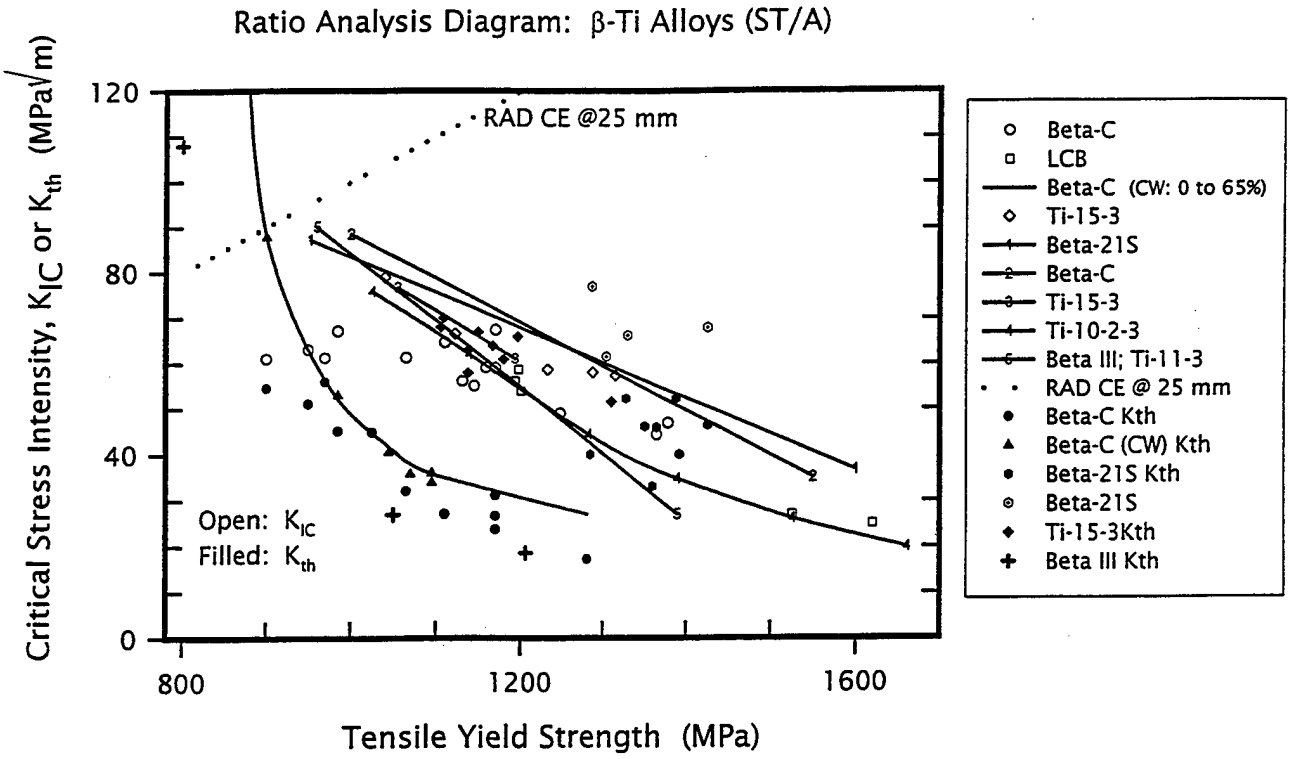


Fig. 10 Ratio Analysis Diagram showing plane strain fracture toughness and threshold stress intensity for EAC of high strength metastable β-titanium alloys. Sources of data are cited in the text.

Paint as a Corrosion Sensor; A Comparison of the Sensitivity of Different Coating Systems

J. Zhang and G. S. Frankel
Fontana Corrosion Center
The Ohio State University
Columbus, OH 43210

ABSTRACT

Paint systems containing color-change or fluorescing compounds have been found to be sensitive to underlying corrosion processes by reacting to the pH increase associated with the cathodic reaction that accompanies corrosion. The sensitivity of these coating systems for detection of cathodic reactions associated with corrosion was determined by applying constant cathodic current and measuring the charge at which color change or fluorescence is detected. Visual observation of coated samples with the unaided eye can detect changes resulting from a charge corresponding to a hemispherical pit with depth on the order of 3-15 microns. Electrochemical Impedance Spectroscopy was also performed to test the influence of the indicating compound addition on the coating corrosion protectiveness, and to correlate impedance change with color change.

INTRODUCTION

The early detection of corrosion in aging aircraft has both economic and safety implications. In airplanes, corrosion may occur in relatively inaccessible locations, such as deep within the lap joints of the skin of an airplane[1] as is shown schematically in Figure 1. As a result, detection of localized corrosion in a large, complex structure such as an airplane is extremely difficult. Many different sensors and techniques are being developed to detect corrosion.[2-4] However, these sensors are only effective if they are either physically located at the place where the corrosion is happening, or sensitive to corrosion occurring remotely.

The basic idea of this study is to modify paint in order to make it a sensor for corrosion since paint covers, and thus has access to, the whole surface of a plane. The goal is to sense the cathodic reaction that accompanies the oxidative corrosion reaction. The main cathodic reaction for any form of atmospheric corrosion is oxygen reduction:

$$O_2 + 2H_2O + 4e^- \rightarrow 4OH^- \quad (1)$$

For localized corrosion such as pitting, crevice and exfoliation corrosion, this cathodic reaction will tend to occur at more-accessible locations than the anodic reaction, i.e. nearer to the source of oxygen in the air, Figure 1. This reaction will cause an increase in the local pH at the location where it occurs, so a paint that is sensitive to pH increases generated by the cathodic reaction will indirectly be sensing corrosion occurring nearby.

Others have pursued similar approaches. Color-change pH indicators have been incorporated into organic coatings as a tool for determining the pH gradients associated with filiform corrosion beads[5]. Fluorescent dyes were applied to microelectronic test vehicles to detect pH changes associated with corrosion of Al or Au metallization under an applied bias in a humid environment[6]. Fluorescing and color-change dyes have also been applied to Al after corrosion in order to identify the locations of the hydrous aluminum oxide corrosion product[7]. More recently, Johnson and Agarwala incorporated into paint different chemicals that fluoresce upon oxidation or upon complexation with metal cations formed by the corrosion process[8, 9].

This work focuses on various coating systems with different organic matrices and indicating compounds that can be used to sense the pH change associated with the corrosion process. The sensitivity of these coating systems for detection of cathodic reactions associated with corrosion was determined by applying constant cathodic current densities and measuring the charge at which color change or fluorescence was detected. Electrochemical Impedance Spectroscopy was also performed after different immersion times in 1 M NaCl solution to test the influence of the indicating compound addition on the coating corrosion protectiveness, and to correlate impedance change with color change.

EXPERIMENTAL

pH Sensing Coating Systems

Clear acrylic paint (ECS-8 paint from Tru-Test Mfg Co, Cary, IL) was mixed with two pH indicators: phenolphthalein or bromothymol blue. Color change can be easily observed through the transparent acrylic matrix. These two indicators were chosen as additives because the pH ranges for which they change color are in the alkaline region, 8.2-10 for phenolphthalein and 6-7.6 for bromothymol blue. The indicators were added at 2.4 wt%, which is the saturation concentration for phenolphthalein in acrylic. Also used as an organic matrix was a commercial blue-tinted Al primer (#1200 from Tru-Test Mfg Co, Cary, IL), which contains acrylic resin, mineral spirits, glycol ethers and ethyl acetate. Phenolphthalein was added to the 1200 primer at four different concentrations (2.4, 1.0, 0.5 and 0.05 wt%). The 1200 primer was also mixed with the fluorescing compounds 7-hydroxycoumarin and coumarin at 0.1 wt% and 0.1 and 1.0 wt%, respectively. Both 7-hydroxycoumarin and coumarin are fluorescent acid-base indicators whose pH ranges for fluorescing are 6.5-8.0 and 9.5-10.5, respectively[10].

The indicating layers were coated on the surface of Al alloy samples that were previously mounted in epoxy and polished to #400 grit emery paper. These samples were then top-coated with a uniformly-sprayed clear acrylic (containing no indicating compounds), Figure 2. The combined thickness of the two layers was about 10-20μm. Color change was monitored with the unaided eye. Incident UV radiation was used for the systems containing fluorescent compounds.

Electrochemical Impedance Spectroscopy (EIS)

EIS has been used widely to evaluate the resistance of coated metals to corrosion[11-13]. Samples coated by 1200 primer/phenolphthalein (at 0.05, 0.1, 1.0 and 2.4 wt%) were examined by EIS after different immersion periods in 1 M NaCl solution using the Gamry Instruments EIS 900 system. The frequency range was from 10 mHz to 10^5 Hz, and the signal amplitude was 10 mV about the open circuit potential. Immersion cells were covered completely to ensure no concentration change during the immersion period, and the EIS measurements were made in fresh solutions.

RESULTS AND DISCUSSION

Characteristics of the Sensor Coatings

The first task in this study was to determine if the approach of using paint to sense corrosion is reasonable, and several preliminary experiments were performed. Samples of Al alloy 5454 were coated with different coating systems and immersed in 1 M NaCl. After a certain immersion time, colored spots were seen to appear, Figure 3. The spots were red and blue for acrylic-based coatings containing phenolphthalein and bromothymol blue, respectively. The black and white photos in Figure 3 unfortunately do not capture the clarity of the spots, but the relative size is shown. The time for the spots to be visible increased with decreasing chloride concentration. This suggested that the spots of color change were, in fact, the sites of increased pH associated with the cathodic reaction of the local attack of the coated Al alloy in the chloride solution.

In order to check the assumption that a remote cathodic reaction associated with crevice corrosion could be detected, an artificial crevice cell was assembled as shown in Figure 4. Two pieces of alloy 2024 were mounted in epoxy, one concentric to but isolated from the other. After polishing, and coating with a acrylic/phenolphthalein (2.4%wt) sensing system, the sample was clamped between two Plexiglas sheets so that the entire inner electrode and part of the outer electrode was covered. The assembly was immersed in 1 M NaCl and a potential of 500 mV was applied between the two electrodes such that the current flowing to the inner electrode was positive. The crevice corrosion process was simulated in this fashion by having a buried local anodic site surrounded by cathodic area that was partially buried. After 4 hr, a clear uniform red color developed on the portion of the outer cathodic electrode that was not covered by Plexiglas. The ohmic potential drop associated with current flow to buried regions of the

outer electrode resulted in most of the current flowing to the uncovered part of that electrode. After 4 hr the red color is not obvious in a black and white photo, but it can be clearly seen after 24 hr, upper right corner beyond the dashed line in Figure 5. After this extended immersion time, several pits formed on the outer part of this electrode despite the applied cathodic current. These pits may have been regions of cathodic corrosion, to which Al alloys are susceptible[14]. Nonetheless, the fact that the cathodic current flowed to the exposed cathodic area validates the approach of using a sensing coating system to detect buried crevice corrosion.

The critical pH values for color change or fluorescence of various compounds is well known. However, the values may change when these compounds are mixed with an organic matrix and applied to a surface. In order to determine the critical pH values of the coatings, titration tests were performed on samples consisting of glass slides coated with the matrix+compound layer, but no top coat. These samples were immersed in deionized water and NaOH was slowly added while monitoring the solution pH until a color change on the sample was observed. The results are given in Table 1. It was found that the acrylic/phenolphthalein coating and acrylic/bromothymol coating (both with 2.4 wt% indicator content) had almost the same critical pH value for color change of about 10. Note that this value is well above the range of pH for color change for bromothymol blue. The 1200 primer/phenolphthalein coatings had a critical pH value of 11. The 1200 primer/7-hydroxycoumarin coating had a critical pH value for fluorescence of 7.4, which is the lowest pH value of all of the coating systems studied. It is clear that the pH values for color change or fluorescence of these compounds are not necessarily the same after they are mixed with organic paint matrices.

Sensitivity Determination

In order to determine the sensitivity of the various coating systems to cathodic reactions, constant cathodic current densities from 0.01 – 50 $\mu A/cm^2$ were applied to samples of the type shown in Figure 2 (not in the artificial crevice cell) immersed in 1M NaCl solution, using a Pt counter electrode . The samples were immersed in the solution for 10 minutes before each test. The time of the initial color change or fluorescence determined by the unaided eye was measured for each value of applied current density.

Since current density, i, is defined as q/t, where q is charge density and t is time, the following relationship should exist between the elapsed time until detection, t_{DET}, the charge density passed at detection, q_{DET}, and the applied current density, i_{APP}:

$$\log t_{DET} = \log q_{DET} - \log i_{APP} \qquad (2)$$

Therefore, a plot of log t_{DET} vs. log i_{APP} should have a slope of -1, and an intercept that provides a value of detectable charge density, which is a measure of the sensitivity. The

data for the acrylic/phenolphthalein (2.4%wt) indicator coating as well as a fit to eqn. 2 are shown in Figure 6. The detectable charge density is found to be 5.26×10^{-4} C/cm^2. Assuming that this amount of charge was generated from a single hemispherical pit, the radius (or depth) of the pit, r, can be calculated from Faraday's law:

$$r(cm)=\left(\frac{3}{2\pi}\frac{q_{DET}A_{CATH}}{0.8}\frac{M}{\rho nF}\right)^{1/3} = 2.74\times10^{-2}\,(q_{DET}A_{CATH})^{1/3} = 2.2\times10^{-3}A_{CATH}^{1/3} \quad (3)$$

where A_{CATH} is the area over which the cathodic reaction is occurring in cm^2, M is the effective atomic weight of the alloy (close to 27 gm/mole for Al alloys), ρ is the alloy density (close to 2.7 g/cm^3 for Al alloys), n is the charge on the dissolved metallic ion (3 for Al), and F is Faraday's constant. It is also assumed in eqn. 3 that 20% of the anodic charge in the pit would be consumed locally by hydrogen evolution in the pit[15].

It is obvious from eqn. 3 that the size of a detectable "effective" pit should be related to the size of the cathodic area. In other words, if the anodic charge associated a pit is spread over a larger cathodic area, more charge (more time, or a larger "effective" pit) would be required to cause a color change. However, according to eqn. 2, the detection time should be independent of sample area for a constant value of applied cathodic current density. Figure 7 shows the effect of sample area on the sensitivity measurement for the acrylic/phenolphthalein system with an applied cathodic current density of 5μA/cm^2. It is clear that the detection time decreases with increasing sample area. Another way to approach this is to measure the detection time for different sample areas using a fixed applied current instead of a fixed current density. For a fixed current, I_{APP}, the time for detection in the sensitivity experiments should vary with the sample area according to:

$$t_{DET} = (q_{DET}/I_{APP})A_{CATH} \quad (4)$$

Figure 8 showed the effect of sample area on the detection time with a constant applied cathodic current of 5μA, as well as the relationship expected from eqn. 4 using the previously-determined value of q_{DET}. The experimental data matched the expected values well when the area was less than 1.2 cm^2. For larger sample areas, the measured detection times were smaller than the expected values. Another interesting observation was that the initial color change that occurred in these experiments happened at small spots rather than uniformly over the whole area. These spots of color change appeared at essentially the same time. This localized effect also occurred during corrosion at open circuit, as shown in Figure 3. These observations indicated that the approach taken here is valid only as a first approximation, and can be improved as described presently.

The applied current will not flow uniformly to the electrode surface, but will instead tend to flow to the defective areas in the coating. This is also the case in a real coated crevice. Since a larger sample area will statistically be more likely to have severe defects, the time for detection will actually decrease rather than increase with increasing sample area. Consider that the current flowing to a given coated sample is distributed among N defective points. The charge passed at the point of detection is then a total charge, Q_{TOT}, which is equal to ($N \times Q_{DET}$), where Q_{DET} is the critical charge required for detection of each single spot. The previous analysis can thus be modified:

$$I_{APP} = Q_{TOT} / t_{DET} = (Q_{DET}\, N) / t_{DET} \qquad (5)$$

$$\log (t_{DET} / N) = \log Q_{DET} - \log I_{APP} \qquad (6)$$

According to this analysis, a plot of log (t_{DET}/N) vs. log I_{APP} should have a slope of -1, and an intercept that provides a value of detectable charge. Figure 9 shows the data replotted in this fashion, along with a fitted line with slope -1. N was taken to be the number of the first color change spots to appear. Q_{DET} can be determined to be 1.22×10^{-4} C. The form of Faraday's law shown in eqn. 3 needs to be altered to consider the detection charge instead of charge density:

$$r(cm) = \left(\frac{3}{2\pi}\frac{Q_{DET}}{0.8}\frac{M}{\rho n F}\right)^{1/3} = 2.74 \times 10^{-2}\,(Q_{DET})^{1/3} \qquad (7)$$

This "effective" pit size is independent of the cathodic area, but dependent on the number of defects, N, since the intercept in plots like Figure 9 will be dependent on N. Using the value for Q_{DET} of 1.22×10^{-4} C, the size of an effective detectable pit with the acrylic/phenolphthalein system was then 13.6 μm. The critical pit depth determined in this fashion was used in this study as a measure of the sensitivity of the indicative coating systems. A small critical pit depth is thus associated with a highly sensitive coating.

Sensitivity of Various Indicator Coatings

Following the method discussed above, the sensitivities of different sensor coating systems were determined, Table 2. It should be noted that different ranges of applied constant cathodic current were used for the different coating systems due to the differences in color change or fluorescence response. The results in Table 2 are well correlated with the critical pH values determined for the different systems, Table 1. The sensitivity of the acrylic-based systems with phenolphthalein and bromothymol blue were

similar (and probably within the error of the analysis), which corresponds to the fact that the critical pH determined from titration for these two systems was identical. The 1200 primer/phenolphthalein system has a similar sensitivity to that of acrylic/phenolphthalein. The sensitivity of this system was found to improve as the content of phenolphthalein increased.

The 1200 primer with a very little amount of 7-hydroxycoumarin (0.1 wt%) was the most sensitive system studied. Interestingly, the fluorescence associated with this system was extremely long-lived. The fluorescent spots could be easily seen for long periods of time (several hr to several days, depending upon the charging conditions) after the application of a cathodic current, and removal from solution. In contrast, the systems with phenolphthalein reverted back to colorless after less than 1 hr following the cathodic treatment and removal from solution. This fading took somewhat longer, about 12 hr, following long term immersion in chloride solution at open circuit. The 1200 primer/coumarin system, which had a high critical pH value of about 13, did not fluoresce under an applied constant current of up to 100 μA for 10 min. It is therefore clear that the critical pH values of the organic/indicator mixtures have a strong effect in determining the sensitivity of the coating system for corrosion detection.

This approach to determination of the sensitivity of these coating systems to underlying corrosion suggests that a very small amount of corrosion can be detected. Standard NDE methods for corrosion detection are much less sensitive.

EIS Experiments

EIS measurements made periodically during immersion of Al 2024-T3 coated with 1200 primer/phenolphthalein indicated that the impedance decreased with increasing immersion, as presented by a typical Bode plot in Figure 10. The initial modulus, M_0, at the low frequency of 10 mHz can be determined by extrapolation to t=0 hr of several modulus values at different immersion times, Figure 11. M_0 tends to decrease as the phenolphthalein concentration increases. This indicates that the phenolphthalein addition, while adding the ability to sense corrosion, is somewhat deleterious to the protectiveness of the coating.

The surface of each sample was monitored during the immersion for the first signs of color change, at which point an EIS measurement was initiated. The 10 mHz modulus at the time of the first visible color change is considered to be a critical modulus, M_C, that indicates the extent of degradation of the coating required for the system to sense the corrosion. This is a measure of the sensitivity of the system determined by taking a different approach than that used above. Instead of impressing a fixed cathodic current density, the system is allowed to corrode at open circuit. M_C also has little dependence on phenolphthalein concentration, Figure 12. This is in contrast to the sensitivity determined by impressed cathodic current, which increases with phenolphthalein concentration as seen in Table 2.

Limitations of Approach

The approach to corrosion detection taken in this paper has several limits that must be considered. First of all, for visual observation, the organic matrix must be clear or transparent in the visible range. It may be possible to use another part of the spectrum with an appropriate detector. Given the other demands on a coating system, it is unlikely that a clear coat is viable for the exterior of an airplane. On the other hand, corrosion frequently initiates at various locations in airplane interiors. Still, both color change and fluorescence detection require visual access to the corroding area, which may be difficult at certain locations in the interior of a plane. Finally, only active corrosion is detected, although the time over which the color change or fluorescence is maintained following the cessation of corrosion needs further study.

CONCLUSIONS

The viability of using modified paint systems to detect buried crevice corrosion in the underlying metal was studied in this work. The approach was to add pH sensing compound to detect the pH increase associated with the cathodic reaction that accompanies the anodic corrosion reaction. Different combinations of organic matrix and indicating compounds were studied. The following conclusions can be made:

1. Color change or fluorescence associated with the pH increases caused by the cathodic reaction in the corrosion process was easily seen with the unaided eye.
2. The critical pH for color change or fluorescence changed when an indicating compound was mixed with an organic matrix.
3. The sensitivity of these coating systems was determined by passing cathodic current and determining the charge at which a color change or fluorescence was detected. This was related to the depth of an effective pit. Pit sizes on the order of 10 μm were found to be detectable with the coating systems studied.
4. Electrochemical impedance spectroscopy was used to monitor the degradation of the coatings with time during immersion in chloride solution.

ACKNOWLEDGMENTS

This work is supported by the Wright Patterson Air Force Base Materials Directorate through The Air Force Office of Scientific Research under Grant No. F49620-96-1-0042. Helpful conversations with R.L. Crane are greatly appreciated.

REFERENCES

1. D. Groner, in *38th AIAA/ASME/ASCE/AHS/ASC. Structures, Structural Dynamics, and Materials Conference and Exhibit, Apr. 7-10,* Kissimmee, Fl (1997).
2. A. Pourbaix, *AGARD Conference Proc.*, Paper No. 12, **CP 0549-7191**, 565 (1995).
3. V. S. Agarwala and A. Fabiszewski, Corrosion 94 Paper No. 342, NACE International, Houston, TX (1994).
4. W. Podney, *Rev. Prog. Quant. Nondestructive Eval.,* D. O. Thompson and D. E. Chimenti, Eds, **13**, New York, Plenum Press, p1947 (1994).
5. G. M. Hoch, *Localized Corrosion, NACE-3*. R. W. Staehle, B. F. Brown, J. Kruger, A. Agrawal, Eds., NACE International, Houston (1974).
6. L. White, *J. Electrochem. Soc.*, **128**, 953 (1981).
7. N.Cippolini, *J.Electrochem.Soc.*, **129**, 1517 (1982).
8. R. E. Johnson and V. S. Agarwala, Corrosion 97, Paper No. 304, NACE International, Houston, TX (1997).
9. R. E. Johnson and V. S. Agarwala, *Mat. Perf.*, **33**, 25-29 (1994).
10. *Encyclopedia of Analytical Science*, A. Townshend, Ed., Academic Press, London (1995).
11. P. Carbonini, T. Monetta, L. Nicodemo, P. Mastronardi, B. Scatteia and F. Bellucci, *Mat. Sci. For.*, **192-194**, 291 (1995).
12. J. V. Standish and H. Leidheiser, Jr., *Corrosion*, **36**, 390 (1980).
13. M. Kendig and J. Scully, *Corrosion*, **46**, 22 (1990).
14. G. S. Frankel, in "Corrosion Mechanisms in Theory and Practice," P. Marcus and J. Oudar, eds, Marcel Dekkar Inc., NY (1995).
15. G. S. Frankel, *Corrosion Science*, **30**, 1203 (1990)

Table 1. pH value for color change or fluorescence for pure compounds (from ref. [10]) and for compounds mixed into organic coatings.

	pH indicators		Fluorescing compounds	
	Pheno	Bromo	7-hydroxy	Coumarin
pure compound	8.2-10	6-7.6	6.5-8.0	9.5-10.5
clear acrylic	10	10		
1200 primer	9-12.5		7.4	13.1

Table 2. Sensitivities of different coating systems in 1M NaCl solution as determined by the size of an effective detectable pit.

Organic matrices:	Acrylic	Acrylic	1200	1200	1200	1200	1200
Indicator	pheno	bromo	pheno	pheno	pheno	7-hydroxy	coumarin
Content (%wt)	2.4	2.4	2.4	0.5	0.05	0.1	0.1
Effective pit radius (μm)	13.6	12.7	9.6	10.5	22.1	3.1	>100

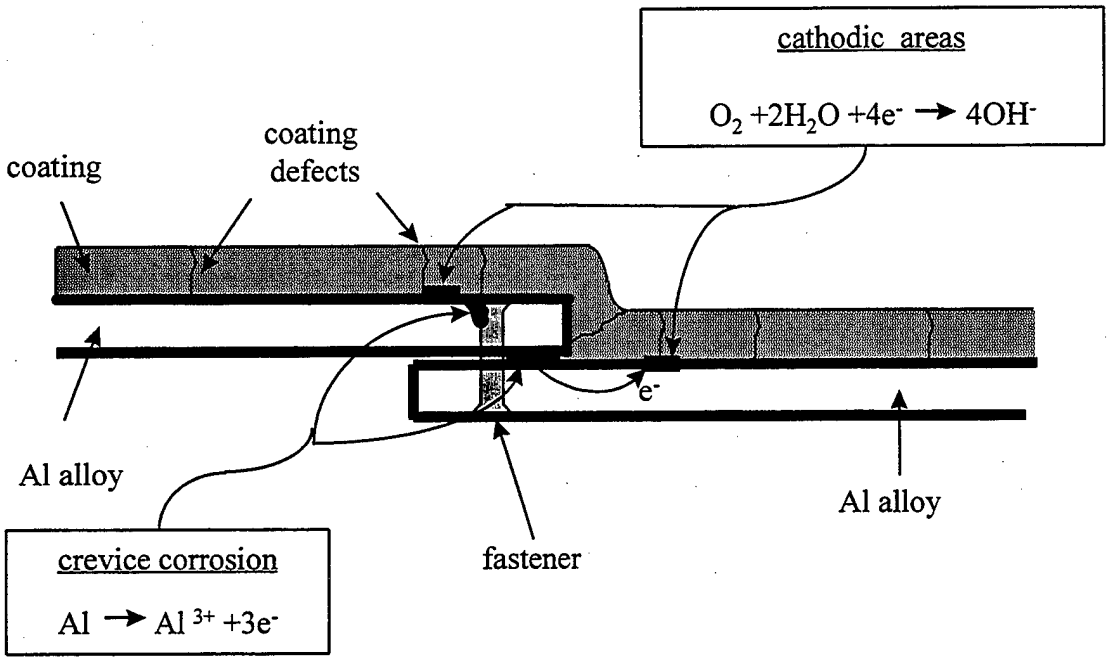


Figure 1. Schematic drawing of crevice corrosion in a painted lap joint.

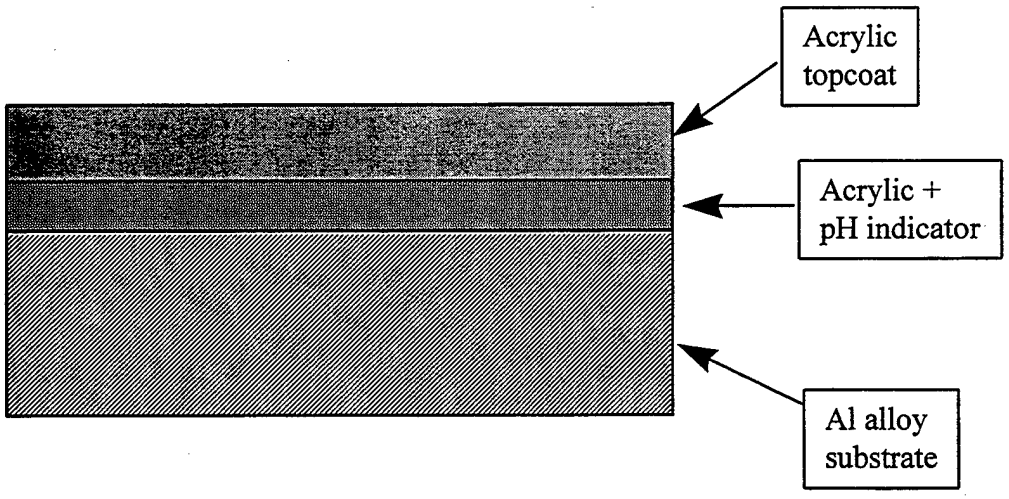
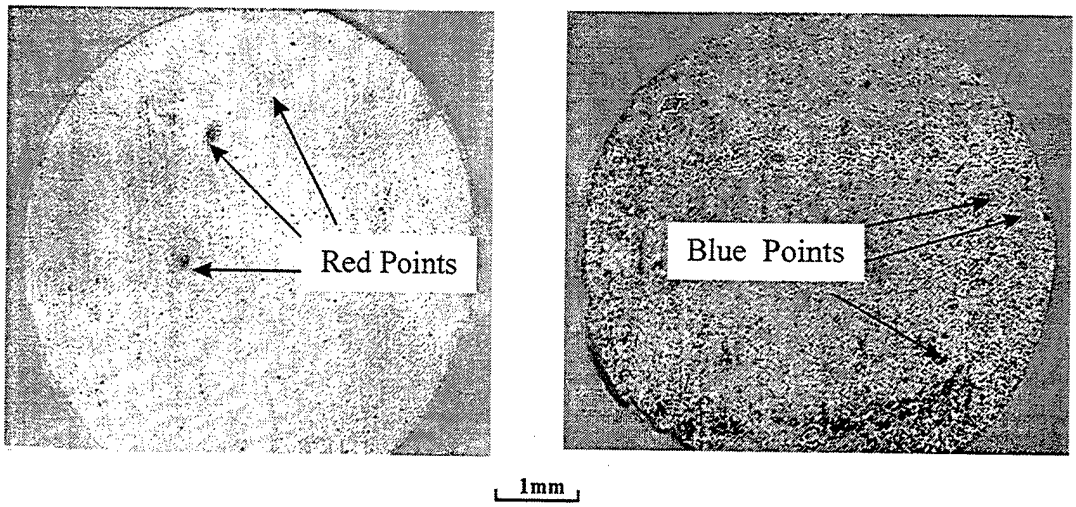


Figure 2. Schematic drawing of coating systems used in this study.



(a)Phenolphthalein paint after 8 days (b)Bromothymol paint after 13 days

Figure 3. Photographs of color change of two pH sensing coatings on Al 5454 substrate following immersion in 1.0 M NaCl solution.

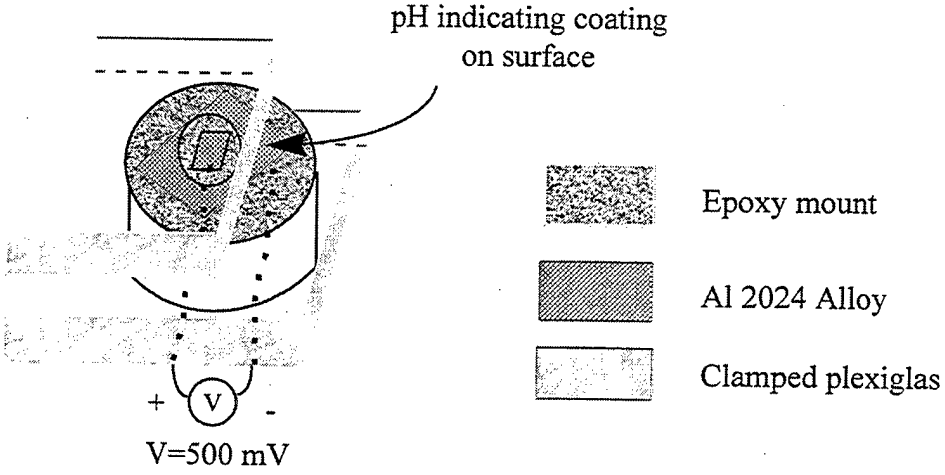


Figure 4. Schematic drawing of artificial crevice assembly

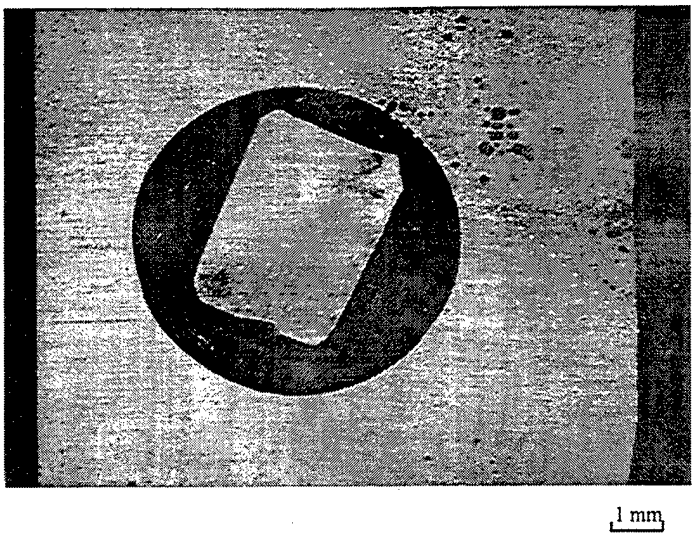


Figure 5. Photograph of artificial crevice sample with acrylic/phenolphthalein (2.4 wt%) coating after applying constant potential of 500 mV for 26 hrs in 1 M NaCl solution. Above dotted line was not under the crevice covering.

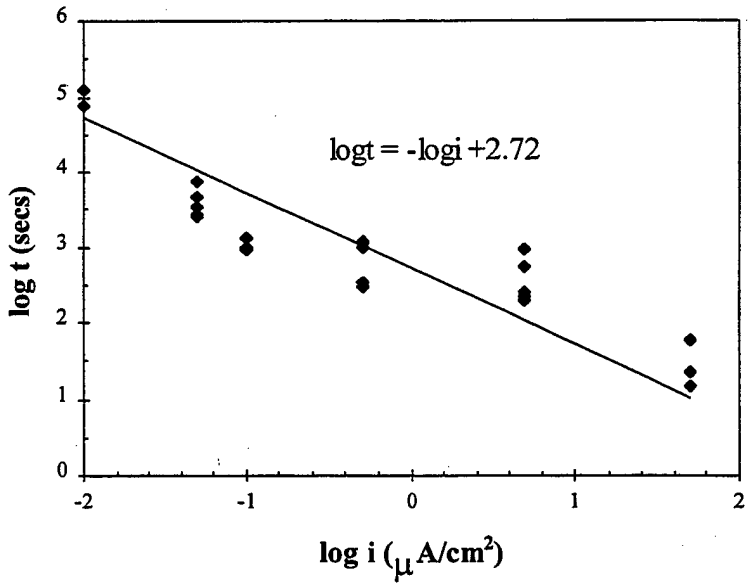


Figure 6. Detection time for color change vs. applied cathodic current density for Al 2024 alloy coated with acrylic/phenolphthalein coating in 1 M NaCl solution.

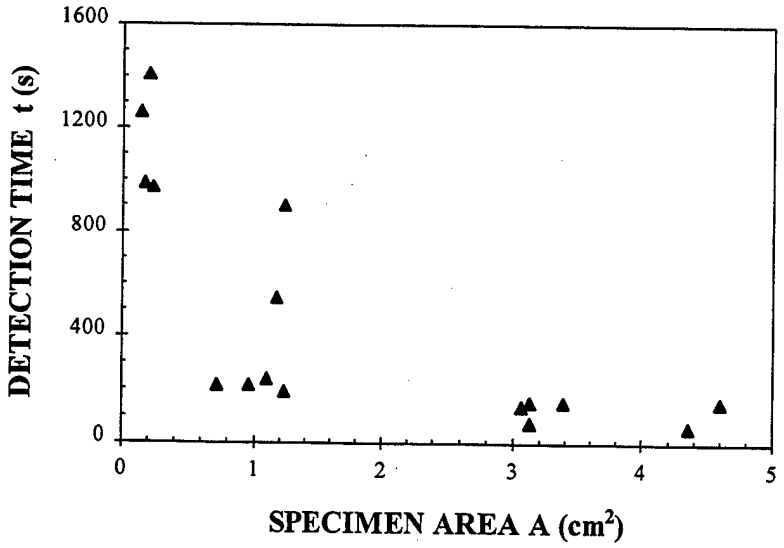


Figure 7. Effect of specimen area on the detection time for Al 2024 alloy coated with acrylic/phenolphthalein (2.4%wt) coating under constant current density of 5 $\mu A/cm^2$ in 1.0 M NaCl solution.

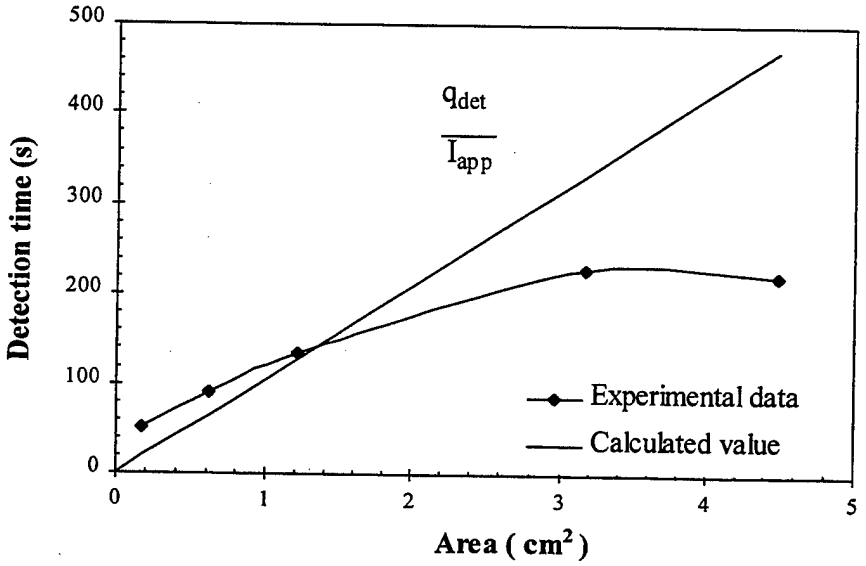


Figure 8. Comparison between experimental and expected relationships of detection time and sample area for Al 2024 alloy coated with acrylic/phenolphthalein (2.4%wt) coating with applied cathodic constant current of 5μA.

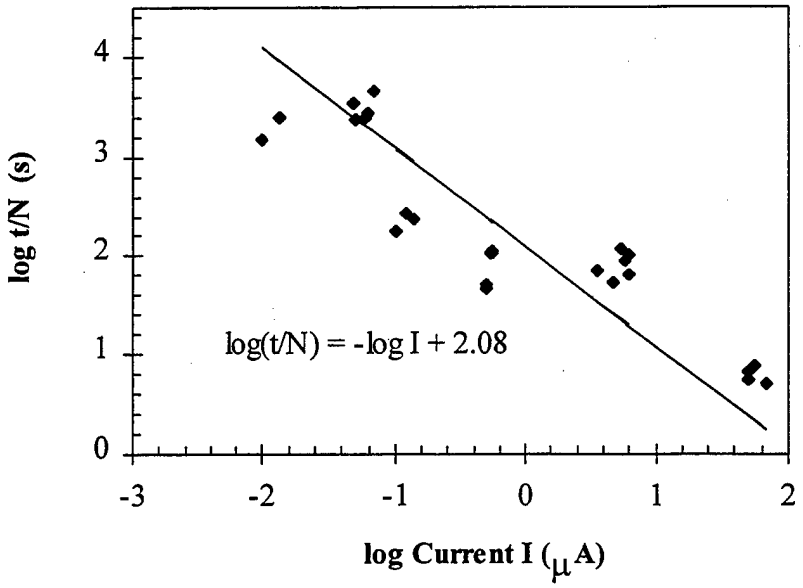


Figure 9. Sensitivity test results for acrylic/phenolphthalein (2.4%wt) indicator coating system in 1 M NaCl solution.

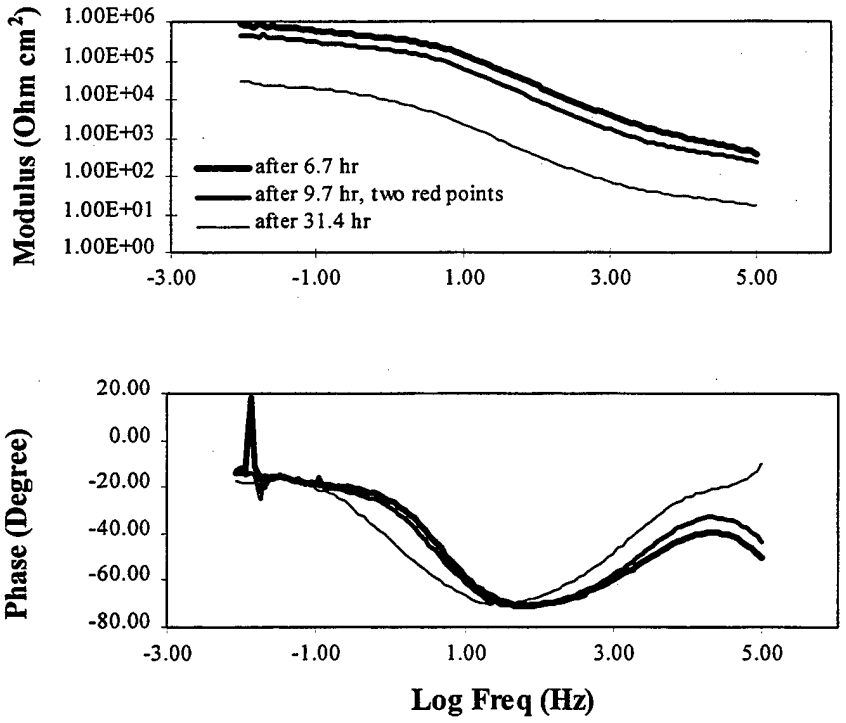


Figure 10. Electrochemical impedance spectroscopy of 2024 Al alloy coated with 1200/phenolphthalein (1.0%wt) coating following different immersion times in 1.0 M NaCl solution.

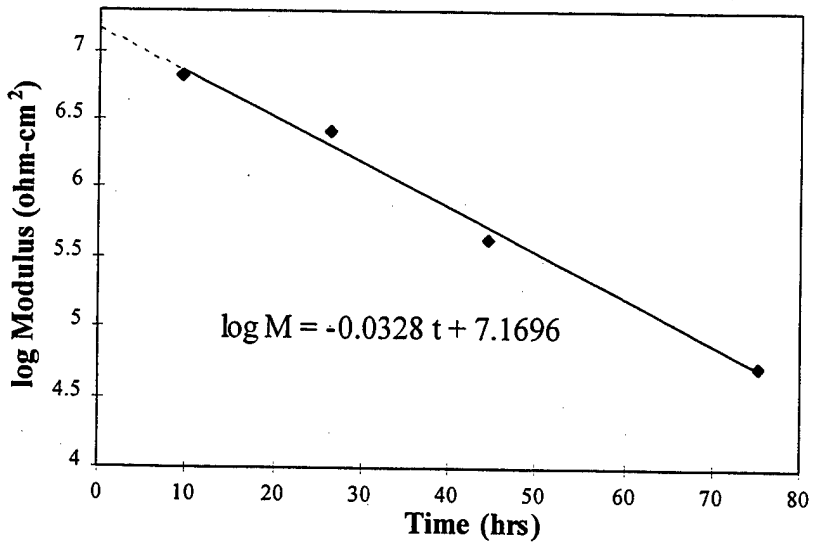


Figure 11. The modulus measured at 10 mHz at different immersion time in 1.0 M NaCl solution for 1200 primer/phenolphthalein (0.05%wt).

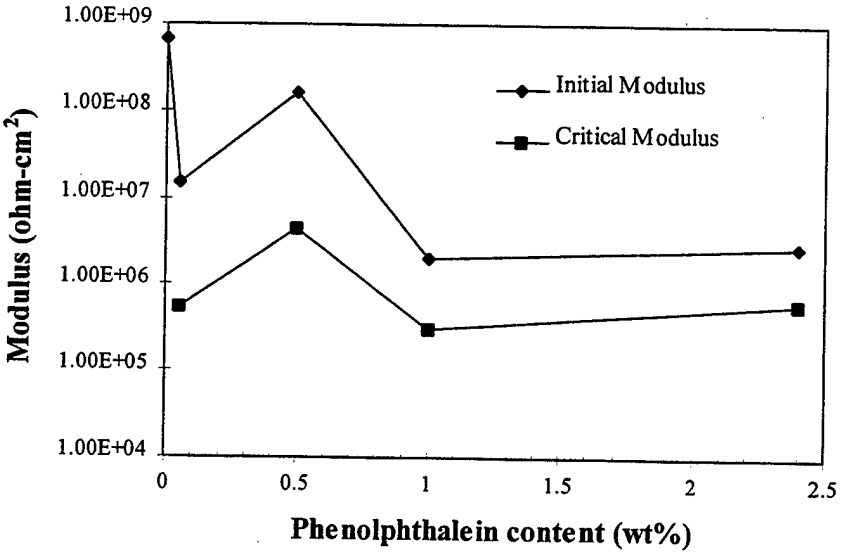


Figure 12. Dependence of initial modulus(M_0) and critical modulus(M_c) on phenolphthalein content in 1 M NaCl solution for 1200 primer/phenolphthalein coatings on Al 2024-T3.

Oxidized Dextrine Coatings for Preventing Corrosion of Aluminum

Toshifumi Sugama and Maria Gerena

Energy Efficiency and Conservation Division
Department of Applied Science
Brookhaven National Laboratory
Upton, New York 11973

ABSTRACT

To evaluate the usefulness of chemically and thermally oxidized dextrines (DEX) as primer coating films, emphasis was focused on investigating the role of oxygen-based functional derivatives formed in oxidized DEX in providing corrosion protection of the aluminum (Al) substrates, in enhancing chemical affinity for the 3-aminopropylpolysiloxane (APPS) topcoat, and in conferring resistance to fungal growth on DEX films. Oxidation at 200°C led to the formation of carboxyl derivatives caused by the cleavage of glycol C-C bonds in the glycosidic rings. At 250°C, Cerium (Ce)-complexed carboxylate salts were formed by the reaction between carboxyl and Ce from cerium (IV) ammonium nitrate that was used as a chemical oxidizing agent. These derivatives not only inhibited the growth of microorganisms on the films, but also reduced the rate of penetration of corrosive electrolytes through the films. Furthermore, the interactions between the derivatives and the amino groups in the APPS topcoat created amide bonds which linked DEX to the APPS layers, thereby greatly enhancing the protection of Al against corrosion.

INTRODUCTION

Our ongoing research program aims at developing an uniform, continuous, hydrophobic film of natural polymer that adequately protects Al against corrosion [1,2]. In this study, we employed dextrins (DEX) which are water-soluble polysaccharides ($C_6H_{10}O_5$) derived from corn starch by dextrination processes involving thermal acid hydrolysis, molecular rearrangement, and repolymerization. In the United States [3], the main source of starch comes from corn in which its demand is about ten times higher than all the other sources, such as topicoca, sago, wheat, potato, or rice. U.S. corn impacts prices worldwide because this country produces more than one-third of the world's corn and exports as much as 30 % of its production; this amount represents 80 % of all exports from other countries. Hence, it is economically worthwhile to use the DEX from corn as starch hydrolysates because of its relatively low cost.

One important concern about using starch- and its hydrolysate-based coating materials is the rapid growth of fungus on their surfaces due to the attack of microorganisms [4-6]. Once the films have suffered biological damage, they may lose the ability to protect metals from corrosion. Thus, it is very important to know whether or not the dextrine-derived coating films are susceptible to microbiological invasion and colonization.

Based upon the information described above, emphasis of our current study was directed toward investigating the characteristics of oxidized DEX as primer coating films deposited on Al surfaces. The factors to be investigated included alterations in molecular configuration, surface chemistry, morphology, and resistance to fungi for different films made by changing the extent of their oxidation. Moreover, an amine-containing siloxane polymer was superimposed as the topcoating system over the DEX-based primers. Thus, studies were also made of the chemical reactions at interfaces between the primers and topcoat, and their mechanisms. Finally, all the data were integrated and correlated directly with the ability of these coating films to inhibit the corrosion of Al.

EXPERIMENTAL PROCEDURE

Dextrin (DEX), supplied by ICN Biomedical, Inc., is a white powder derived from corn-starch. Cerium (IV) ammonium nitrate (CAN), obtained from Alfa, was used as the oxidizing agent. A colloidal solution of DEX was prepared by agitating a mixture of 1 g DEX and 99 g deionized water for 3 hrs at 70°C, and leaving it for 24 hrs at room temperature. Then, CAN of a 0.15 wt% by weight of the total DEX solution was incorporated into the solution. The pH of this primer solution was 2.27. The lightweight metal substrate was a 6061-T6 aluminum (Al) sheet containing the following constituents: 96.3 wt% Al, 0.6 wt% Si, 0.7 wt% Fe, 0.3 wt% Cu, 0.2 wt% Mn, 1.0 wt% Mg, 0.2 wt% Cr, 0.3 wt% Zn, 0.2 wt% Ti, and 0.2 wt% other elements. As a polymer topcoating, 3-aminopropyltrimethoxysilane (APS) monomer, was supplied by Petrarch Systems Ltd.. The film-forming APS precursor solution consisted of a 3.0 g APS, 1.2 g methylalcohol and 95.8 g deionized water, and it had a pH of 10.42. According to ASTM G 21-90, all the test fungi used for determining the resistance of the coatings were supplied by the American Type Culture Collection.

The Al surfaces were coated by CAN-modified DEX films in the following sequence. First, to remove surface contaminants, the Al substrates were immersed for 20 min at 80°C in an alkaline solution consisting of 0.4 wt% NaOH, 2.8 wt% tetrasodium pyrophosphate, 2.8 wt% sodium bicarbonate, and 94.0 wt% water. The alkali-cleaned Al surfaces were washed with deionized water at 25°C for 5 min, and dried for 15 min at 100°C. Then, the substrates were dipped into a soaking bath of DEX solution at room temperature, and withdrawn slowly. The wetted substrates were then heated in an oven for 120 min at 150, 200, or 250°C, to yield thin solid films; this heating process also promoted the rate of thermal oxidation of the films. Next, the topcoat was applied by immersing DEX-primed substrates into the APS solution at 25°C. After withdrawing them slowly, the APS-wetted substrates were left for 180 min in an oven at 150°C to complete conversion of the APS monomer into the 3-aminopropylpolysiloxane (APPS) polymer by thermal-catalyzed polycondensation reactions.

Specular-reflectance Fourier-transform infrared (SRFT-IR) spectroscopy was used to assess the changes in molecular configuration of CAN-modified DEX coatings over the Al as a function of temperature. An SRFT-IR study was also carried out to identify the interfacial bond structure yielded by the chemical reaction between oxidized DEX and APPS. The chemical states formed at the outermost surface sites of coating films were investigated using x-ray photoelectron spectroscopy (XPS). Investigating the morphological features and

elemental composition of the film surfaces by scanning electron microscopy (SEM) and energy dispersive x-ray spectroscopy (EDX) gave us information for evaluating the film-forming performance of the DEX coatings over the Al. The contact angle was measured by dropping APS solution onto the oxidized DEX films to determine the extent of wettability and spreadability of their surfaces as a function of oxidizing temperature. AC electrochemical impedance spectroscopy (EIS) was used to evaluate the ability of the coating films to protect Al from corrosion. Salt-spray tests of the DEX- and APPS/DEX-coated Al panels (75 mm x 75 mm, size) were performed in accordance with ASTM B 117, using a 5 % NaCl solution at 35°C. Biodegradation of the coating films was determined by ASTM test method G 21-90 describing the assessment of the resistance of polymeric materials to fungi. The DEX- and APPS/DEX-coated Al panels (75 mm x 75 mm) were placed in sterile petri dishes containing solidified nutrient salt agar. The fungal growth on panels left for up to 28 days in an incubator at 30°C was inspected using SEM. Also, EIS tests were made on all the panels incubated for 28 days to estimate the degree of damage to the films caused by fungal growths.

RESULTS AND DISCUSSION

APPS/DEX Films

In SRFT-IR studies, the spectral features of the 150°C-treated film reveal the glucosidic rings in the polysaccharide: namely, the absorption bands at 3420 cm^{-1}, belonging to the O-H stretching vibration of OH groups; at 2930 cm^{-1}, and 1460 and 1370 cm^{-1} which can be ascribed to the C-H stretching and bending modes of the methylene, respectively; at 1640 cm^{-1}, originating from the bending vibration of H-O-H in the absorbed H_2O; and also at 1150, 1090, and 1020 cm^{-1}, reflecting the stretching mode of C-O-C linkages. Increasing the temperature to 200°C resulted in the appearance of a new absorption peak at 1720 cm^{-1}, corresponding to the C=O band in the carboxyl groups, while the intensity of O-H stretching band at 3420 cm^{-1} slightly decreased. Hence, the oxidation of CAN-modified DEX films at 200°C introduces a carboxylic C=O derivative into its molecular structure. As described in our previous work aimed at oxidizing potato starch [2], C=O was formed by the cleavage of the glycol C-C bond caused by incorporating oxygens into the glycosidic rings, leading to the opening of the rings. By comparison, a strikingly different feature of the spectrum can be seen in the films treated at 250°C. The differences were (1) a considerable decrease in the intensity of the methylene-related bands at 2930, 1460, and 1370 cm^{-1}, and also of the C-O-C linkage-associated bands in the range 1120 to 1000 cm^{-1}, and (2) the emergence of strong new bands at 1600 and 1400 cm^{-1}, while the peak intensity of the O-H band becomes weaker. Since these new bands are due to the asymmetric and symmetric stretching of carboxylate, COO^-, it is possible to assume that the incorporation of more oxygens into the DEX transforms the carboxyl into carboxylate groups. From the difference (1), the increase in the rate of its oxidation also causes breakage of the C-O-C linkages, reflecting the decomposition of chain structures, and correspondingly, the removal of methylene and hydroxyl groups from DEX.

To support this information, investigation of the chemical states present in the outermost surface layers of the same films as those used in the IR analysis, was carried out by XPS. In XPS core-level spectra, the scale of the

binding energy (BE) was calibrated with C_{1s} of the principal hydrocarbon-type carbon peak fixed at 285.0 eV as an internal reference standard. A curve deconvolution technique, using a DuPont curve resolver, was employed to substantiate information on the carbon-related chemical states from the spectrum of the carbon atom. As is seen in Fig. 1, the C_{1s} region of the 150°C DEX films had two resolvable Gaussian components at the BE positions of 285.0 and 286.5 eV. The major peak at 285.0 eV reveals the C in the CH_2 and CH groups as the principal components; meanwhile, the secondary intensive one at 286.5 eV was associated with the C in $-CH_2O-$ (e.g. alcohol and ether). When the films were oxidized at 200°C, two additional peaks at 288.3 and 289.5 eV emerged in the C_{1s} region. The possible contributor to the former peak is the C in C=O, and the latter one corresponds to carboxylic carbon. This information agreed with the results from the FT-IR data; namely, the carboxyl groups were incorporated in the DEX structure during its oxidation at 200°C. Marked differences in the shape of the spectrum were observed in the 250°C-oxidized films: these were (1) a striking decay of the signal intensity at 286.5 eV, (2) the appearance of a new peak at 287.3 eV, and (3) a conspicuous growth of peak intensities at 288.3 and 289.5 eV. According to the literature [7,8], the contributor to this new peak emerged in a BE position between $-CH_2O-$ and C=O groups might be due to the C in the metal-complexed carboxylate compounds. In this case, the only source of metal species comes from the CAN; it is Ce. Thus, increasing the oxidizing temperature to 250°C seems to promote the transformation of carboxyl into the Ce-complexed carboxylate salts; correspondingly, the carboxylate groups identified in the FT-IR study earlier might originate from the formation of this complex salt. In addition, the $Ce_{3d5/2}$ region of 250°C films (not shown) included two signals at 884.6 and 882.4 eV; a possible assignment of the latter signal is the Ce in the CeO_2 [8]. Although no information was found in the literature on surface science, the former signal may be associated with the Ce in the carboxylate salt complexes. Such salt complexes may form through the following oxidation pathways: First, the vulnerable glycol groups in the glucosidic rings suffer oxidizing damage when the CAN oxidizing agent is attached to the DEX in the presence of atmospheric oxygen. This oxidation leads to the cleavage of glycol C-C bonds followed by ring opening, thereby introducing carboxyl derivatives into the DEX structure. Second, the incorporation of more oxygen into the DEX by the breakage of C-O-C linkages in the open rings and polysaccharide chains, leading to the production of a large number of carboxyl derivatives. Concurrently, the carboxyls favorably reacted with Ce in the CAN to form Ce-complexed carboxylate salts.

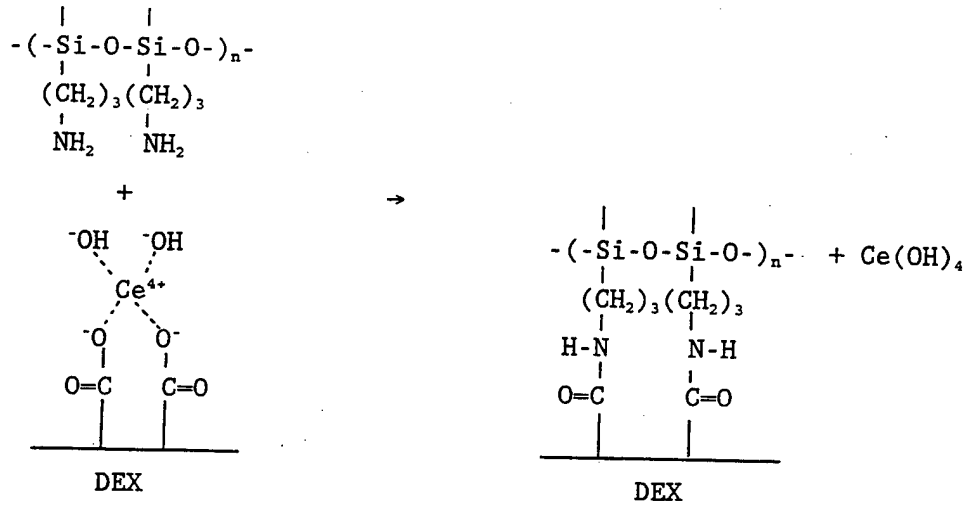
Investigating the SEM images coupled with the EDX spectra for the DEX film surfaces offered important insight into the film-forming performance of CAN-modified DEX solutions on Al surfaces. The thickness of these films determined by a surface profile measuring system was 0.4 and 0.2 μm for the 200 and 250°C films, respectively. No specific features, excepting the rough underlying Al surfaces, can be seen on the SEM images of these thin transparent films; the rough Al surfaces were completely covered with a smooth, continuous, uniform film. There was no evidence of aggregations and coalescent structures in the films. The EDX spectrum accompanying the SEM micrographs for the 200°C film had a principal line of Al together with moderate line intensities of the C and O elements. Since EDX is useful in detecting the elemental composition which exists on a subsurface layer up to $\approx$ 1.5 μm in depth, all the Al element virtually belongs to the underlying substrate, while the C and O elements are assignable to the DEX films. However, some O may originate from the oxidized Al compounds

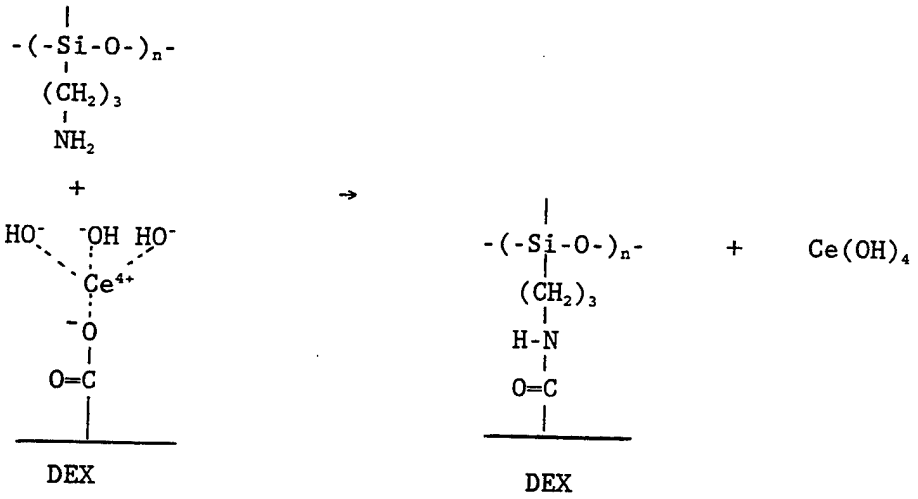
formed at the outermost surface site of Al. By comparison with this spectrum, the SEM micrograph of the 250°C film was characterized by a marked reduction in the line intensities of both C and O elements. Relating this finding to the IR data, the reason for such a reduction might be due to the elimination of carbonaceous and hydroxyl groups from the DEX films by oxidation damage at 250°C, and correspondingly, these films become substantially thinner. The 150°C film with a 0.4 μm thickness showed the morphological and spectral features similar to those of the 200°C polymer film (not shown).

In applying an APPS polymer topcoating onto the DEX-primed Al substrate surfaces, one of the particular concerns was forming a continuous, uniform film. Therefore, we focused on investigating the effectiveness of oxidation-induced functional derivatives in enhancing the magnitude of spreadability of the monomeric APS solutions over the primed Al substrate. Accordingly, we examined the contact angle of a water-based APS droplet on the 150, 200, and 250°C-treated DEX coating surfaces. For instance, if the contact angle was low, we judged that the APS solution had a good-spreading behavior, corresponding to the formation of APS film covering completely the DEX surfaces. A plot of the averaged contact angle of APS solution against the changes in treatment temperature of DEX primers (Fig. 2) showed that the magnitude of its spreadability depends upon the treatment temperature of DEX; the increase in temperature contributed to a lowering of contact angle, suggesting that DEX films treated with a high temperature are more susceptible to wetness of the APS solution. Relating this data to the surface chemistry, the incorporation of functional derivatives such as carboxyl and carboxylate groups onto the DEX film surfaces by oxidation appears to play an essential role in enhancing the magnitude of its spreadability.

Once the monomeric APS solution was converted into the APPS solid film on the DEX films, our attention was paid to the interactions at interfaces between the APPS and oxidized EDX films and their mechanisms. The analytical approach to obtaining this information was carried out by SRFT-IR, using the APPS film deposited to the DEX-primed Al substrates. Fig. 3 compares the SRFT-IR spectral features of the single APPS coating as reference sample, and the APPS-covered 150, 200, and 250°C DEX coatings, over the frequency range 1800-1000 cm^{-1}. The spectrum of the APPS reference film had absorption bands at 1650 and 1600 cm^{-1}, belonging to the CH_2 groups; at 1200 and 1140 cm^{-1}, corresponding to Si-methoxide compounds [9]; and at 1030 cm^{-1} which can be ascribed to the siloxane groups, Si-O-Si [10,11]. The formation of Si-O-Si linkages confirmed that the transformation of monomeric APS into the polymeric APPS occurred during the thermal treatment of films at 150°C. By comparison with the reference sample, the spectrum of the 150°C DEX film coated with the APPS included the additional bands at 1150 and 1020 cm^{-1}, due to the C-O-C linkages in the DEX. When the APPS film was deposited on the 200°C DEX, three major changes occurred: (1) the disappearance of the peak at 1720 cm^{-1}, that associates with carboxyl groups formed by the oxidation reaction of DEX at 200°C, (2) the emergence of a new band at 1550 cm^{-1}, and (3) the decrease in peak intensity of the NH_2 band at 1600 cm^{-1}. Regarding the aspect (2), the new band is likely to be associated with the formation of amide groups, -CONH-, [12,13]. The results strongly demonstrated that when APPS was attached to oxidized DEX, the NH_2 groups in APPS favorably reacted with carboxyl in DEX to form amide bonds. Conceivably, the formation of interfacial amide bonds

strongly link DEX to the APPS films. A further growth of amide band at 1550 cm^{-1} can be seen in the spectrum from APPS-coated 250°C DEX samples. Since the band at 1600 cm^{-1} in conjunction with that at 1400 cm^{-1} is also related to the COO^- groups in the carboxylate derivatives of the 250°C-oxidized DEX films, a declining intensity and disappearance of these bands seems to verify that the COO^- groups have a strong chemical affinity for the NH_2 groups in APPS, forming the amide bonds at APPS/DEX interfaces. The hypothetical interaction mechanisms for each of the Ce salt-bridge and half-salt formulations are illustrated below:





Electrochemical Impedance Measurement

All the data obtained were correlated directly with the ability of the single DEX and combined APPS/DEX films to protect Al substrates from the corrosion. As mentioned earlier, the thickness of single DEX films was a 0.4, 0.4 and 0.2 μm at 150, 200, and 250°C, respectively, the APPS-coated 150, 200, and 250°C DEX films were 0.9, 0.9, and 0.7 μm thick, respectively, while the single APPS films were 0.6 μm. AC electrochemical impedance spectroscopy (EIS) was used

to evaluate the effectiveness of these coating films in reducing the rate of corrosion of the Al substrate. The coated Al panels were exposed to a 0.5N NaCl solution at 25°C. Fig. 4 compares the Bolde-plot features [the absolute value of impedance $|Z|$ ($\Omega \cdot cm^2$) vs. frequency (Hz)] of the 150, 200, and 250°C DEX-coated Al panels. Particular attention in the overall impedance curve was given to the impedance value of the element $|Z|$, which can be determined from the plateau in the Bode plot occurring at sufficiently low frequencies. The impedance of the uncoated Al panels was $\approx 4.0 \times 10^3$ $\Omega \cdot cm^2$ at a frequency of 0.5 Hz. Once the Al surfaces were coated with the DEX, the polarization resistance, R_p, value of the coatings increased by one or two orders of magnitude over that of the Al. The R_p values reflect the magnitude of ionic conductivity generated by the electrolyte passing through the coating layers; namely, a high value of R_p can be interpreted as means of a low permeability of electrolytes into the coating films. The data demonstrated that the magnitude of the conductivity depends on the oxidizing temperate of DEX films, the highest R_p value was obtained from the 250°C DEX films. The values of 150 and 200°C DEX films were nearly one order of magnitude lower than that of 250°C one, allowing the electrolytes to permeate the films more easily than in the 250°C films. Thus, the 250°C-oxidized DEXs were the most effective films in ensuring a low rate of permeation of electrolytes. This interesting result suggested that although EXD films became thinner due to oxidation damage at 250°C, the Ce-complexed carboxylate salt derivatives formed in the DEX films seem to confer the protection of Al from corrosion. When these DEX films were covered with the APPS film, all the test panels showed R_p values in the range 1.5 to 4.5 x 10^6 $\Omega \cdot cm^2$ at 5 x 10^{-2} Hz, corresponding to an increase in $\approx$ one order of the magnitude over that of the single APPS-coated panels. It should be noted that the R_p value of this single APPS coating was almost the same as that of the 250°C DEX coating, suggesting that there were no significant differences between 250°C DEX and APPS coatings in reducing the permeability of electrolytes. Further, the effect of oxidizing temperatures on DEX films attached to the APPS coatings on conferring resistance to the permeation of electrolytes was in the following order: 250°C > 200°C > 150°C. Relating this finding to the FT-IR data, the formation of interfacial amide bonds which linked between APPS and DEX films appears to play an important role in reducing the rate of permeation of electrolytes, offering a good protection of Al against corrosion.

Salt Spray Testing

This information was supported by salt-spray resistance tests (ASTM B 177) for all the coated panels. We next prepared two additional coatings as reference samples to substantiate our finding that the most promising derivatives which afford adequate protection of Al from corrosion depend on the complexity of the Ce-linked carboxylate salts yielded from CAN-modified DEX at 250°C, but are not independent of the oxide compounds derived from the individual CAN and DEX materials. One sample was made from 0.15 wt% CAN in deionized water; the other was from a 1.0 wt% DEX solution without the CAN oxidizer. The deposition of these coatings onto the Al substrates was carried out by a simple dip-withdrawing method followed by heating for 120 min at 250°C. XPS and SRFT-IR analyses of the coated substrates provided the information on identifying the oxide compounds formed in these coating films. The principal oxide compounds for the CAN- and DEX-derived coatings were CeO_2 and uncomplexed carboxylate, respectively. The results form these panels are shown in Table 1. The entire surface of the four

coating systems, 150 and 200°C CAN-modified DEXs, and the reference samples, 250°C CAN and unmodified DEX, was corroded after exposure to salt fog for up to 68 hours. In contrast, although some rust stains were observed surrounding the drilled hole made for hanging the test panels, the 250°C CAN-modified films contributed remarkably to protecting them from salt-induced corrosion for 240 hours. Hence, it is clear that the formation of such Ce-linked carboxylate salt complexes in the CAN-modified DEX films acts to reduce significantly the rate of corrosion of the Al. With a single APPS coating, its ability to prevent the corrosion failed during exposure for 264 hours, corresponding to be a only 24 hours longer than that of the 250°C CAN-modified DEX coatings. Therefore, there were no marked differences in the protective efficacies of 250°C CAN-modified and single APPS films. In APPS/DEX coating systems, the localized peeling and blistering phenomena on the APPS topcoat were observed from the APPS/150°C DEX coatings after exposure in the salt spray chamber for 192 hours. These phenomena are likely to be associated with the susceptibility of this DEX primer layer to hydrolytic reactions caused by the attack of NaCl solution passing through the APPS layers; namely, the primer layers beneath the topcoat suffered from undermining damage, thereby resulting in a poor protection. A dramatic improvement in resistance to salt spray was seen in the APPS/250°C CAN-modified DEX coating system; this coating protected Al against corrosion for 820 hours.

Fungal Growth

The extent of fungus growth for the 150, 200, and 250°C DEX-coated Al panels and such panels covered with APPS was investigated using SEM. With the DEX coating films, the SEM image showed that the 150°C-treated DEX films (Fig. 5) had been degraded by the fungal consortium in one and two weeks of incubation after inoculation, reflecting their susceptibility to the growth of microorganisms. Contrary, SEM micrographs (not shown) for the 200 and 250°C DEX film surfaces did not show any evidence of fungal growth, even after 28 days. Thus, the 150°C films appear to have a suitable nutrient for sustaining fungal growth. Such microbial invasion and colonization probably is due to the presence of polysaccharide chains in the 150°C films which act as a nutrient source. However, once the changes in molecular configuration took place at higher temperature, reflecting the opening of glycosidic rings and the scission of polysaccharide chains caused by the thermal oxidation of DEX, the resulting carboxyl and carboxylate derivatives seems to confer resistance to fungal attack. Using APPS topcoat, no growth of fungi was observed on single APPS-coated panel surfaces after 28 days incubation; correspondingly, all APPS-covered DEX coating panels were unsusceptible to fungal invasion. Again, EIS was used to estimate the degree of biodegradation of the coating films caused by fungal growth. As expected, the R_p value for the inoculated 150°C DEX coatings declined almost one order during 28 days incubation, from $\approx 7.0 \times 10^{-4}\ \Omega \cdot cm^2$ before inoculation to $\approx 8.5 \times 10^{-3}\ \Omega \cdot cm^2$ at 5×10^{-2} Hz, implying that biodegradation of the coating films facilitates the penetration of electrolytes. In contrast, no marked changes in R_p value were recorded for all other inoculated coating systems which did not show any fungal growth in the same period.

CONCLUSIONS

When dextrine (DEX) films prepared by chemical and thermal oxidation reactions were applied as primer coatings ranging from 0.4 to 0.2 μm thick to aluminum (Al) substrate surfaces, changes in their molecular configuration played an important role in protecting Al from corrosion, in enhancing chemical affinity of the 3-aminopropylpolysiloxane (APPS) topcoat, and in conferring resistance to the growth of microorganisms on the DEX. Oxidation of DEX at 200°C in the presence of atmospheric oxygen led to the formation of carboxyl derivatives caused by the cleavage of glycol C-C bonds in the glycosidic rings, following the opening of rings. The incorporation of more oxygen into DEX by increasing the temperate to 250°C resulted in the scission of C-O-C linkages in the polysaccharide chains and open rings. Such a highly oxidized DEX not only introduced additional carboxyl derivatives in its structures, but also promoted the reaction between carboxyl and Ce from cerium (IV) ammonium nitrate (CAN) as chemical oxidizing agent to form Ce-complexed carboxylate salts. The carboxylate salt-containing coating film was very effective in conferring resistance to the permeation of electrolytes, indicating a better performance corrosion-preventing barrier. In fact, its ability to prevent corrosion of the Al was almost the same as that of the single APPS film. Furthermore, the oxidized films with these derivatives were unsusceptible to fungal invasion in contrast to unoxidized films which readily suffered biological attack.

In addition, these derivatives reacted with the amino groups in the APPS topcoat to form amide bonds at interfaces between oxidized DEX and APPS films. This interfacial amide bond linking DEX to APPS significantly contributed to protecting Al from corrosion. As a result, the APPS/250°C DEX coating system displayed a resistance to salt-spray of > 800 hours.

Acknowledgment

The authors are grateful to Dr. Robert R. Reeber, U.S. Army Research Offices (ARO), for his guidance and financial support.

References

1. T. Sugama, Mater. Letter., 25 (1995) 291.
2. T. Sugama and J.E. DuVall, Thin Solid Films, 289 (1996) 39.
3. F.W. Schenck and R.E. Hebeda (Eds.), Starch Hydrolysis Products: Worldwide Technology, Production, and Application, VCH Publishers (UK) Ltd, 1992, pp. 441-447.
4. R.D. Gilbert, V.T. Stanneth, C.G. Pitt, and A. Schindler, in N. Grassie (Ed.), Developments in Polymer Degradation, Appl. Sci. Publishers, London, 1982, pp. 259-293.
5. J.C. Huang, A.S. Shetty, and M.S. Wang, Adv. Polym. Technol., 10 (1990) 23.
6. U.R. Vaidya and M. Bhattacharya, J. Appl. Polym. Sci., 52 (1994) 617.
7. J.W. Bartha, P.O. Hahn, F. LeGoues, and P.S. Ho, J. Vac. Sci. Technol., 3 (1985) 1390.
8. J.F. Moulder, W.F. Stickle, P.E. Sobol, and K.D. Bomben, Handbook of X-ray

Photoelectron Spectroscopy, Perkin-Elmer Corporation, U.S.A., 1992, p. 218.
9. A.L. Smith, Spectrochim. Acta, 16 (1960) 87.
10. G.J. Su, N.F. Borelli, and A.R. Miller, Phys. Chem. Glasses, 3 (1962) 167.
11. R. Hama, J. Am. Ceram. Soc., 48 (1965) 595.
12. I. Mizushima, T. Shimanouchi, I. Ichishima, T. Miyazawa, I. Nakagawa, and T. Araki, J. Amer. Chem. Soc., 78 (1957) 2038.
13. M.St.C. Flett, Spectrochim Acta, 18 (1962) 1537.

Table 1.
Salt spray resistance of Al substrates coated with DEX and APPS/DEX systems

Coating system	Salt spray resistance, hrs
150°C CAN-modified DEX	< 24
200°C CAN-modified DEX	48
250°C CAN-modified DEX	240
250°C Unmodified DEX	48
250°C CAN	68
APPS	264
APPS/150°C CAN-modified DEX	192
APPS/200°C CAN-modified DEX	288
APPS/250°C CAN-modified DEX	820

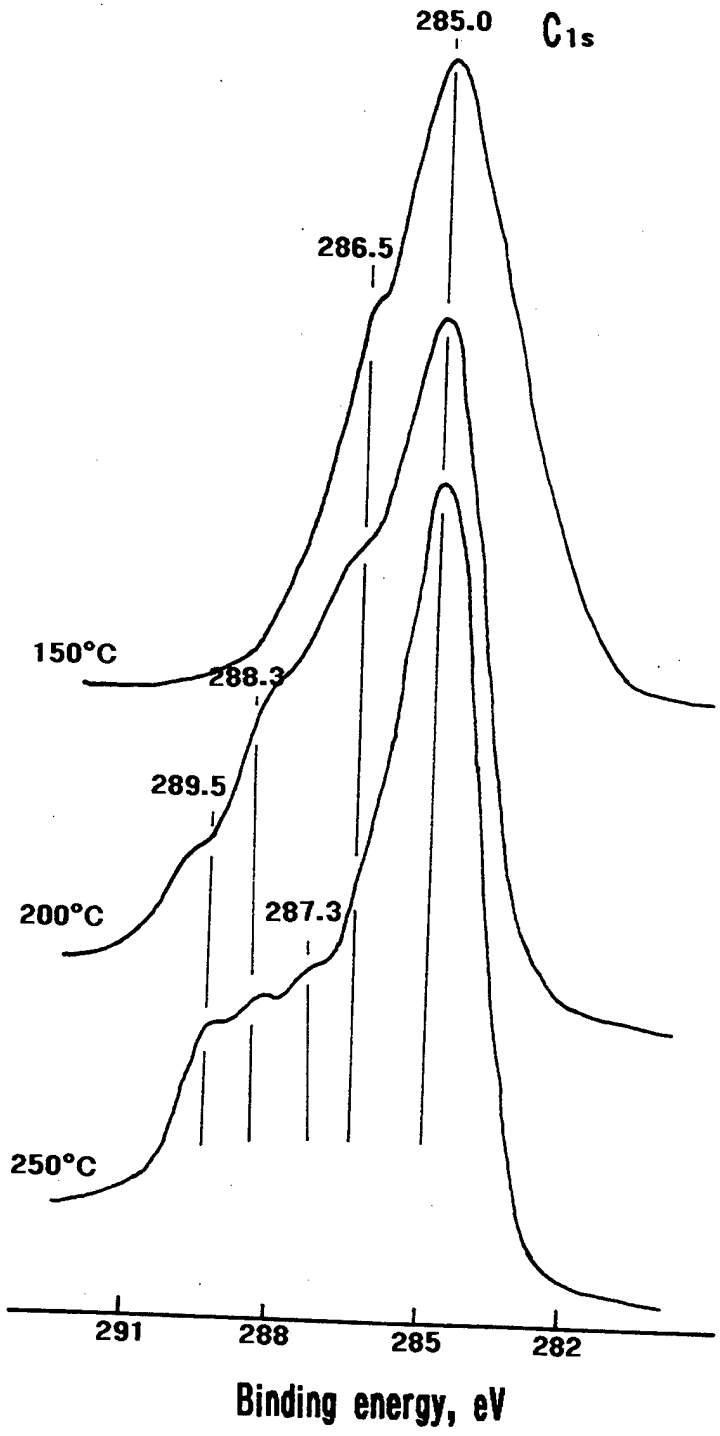


Fig. 1 C_{1s} core-level spectra for 150, 200, and 250°C-oxidized DEX film surfaces.

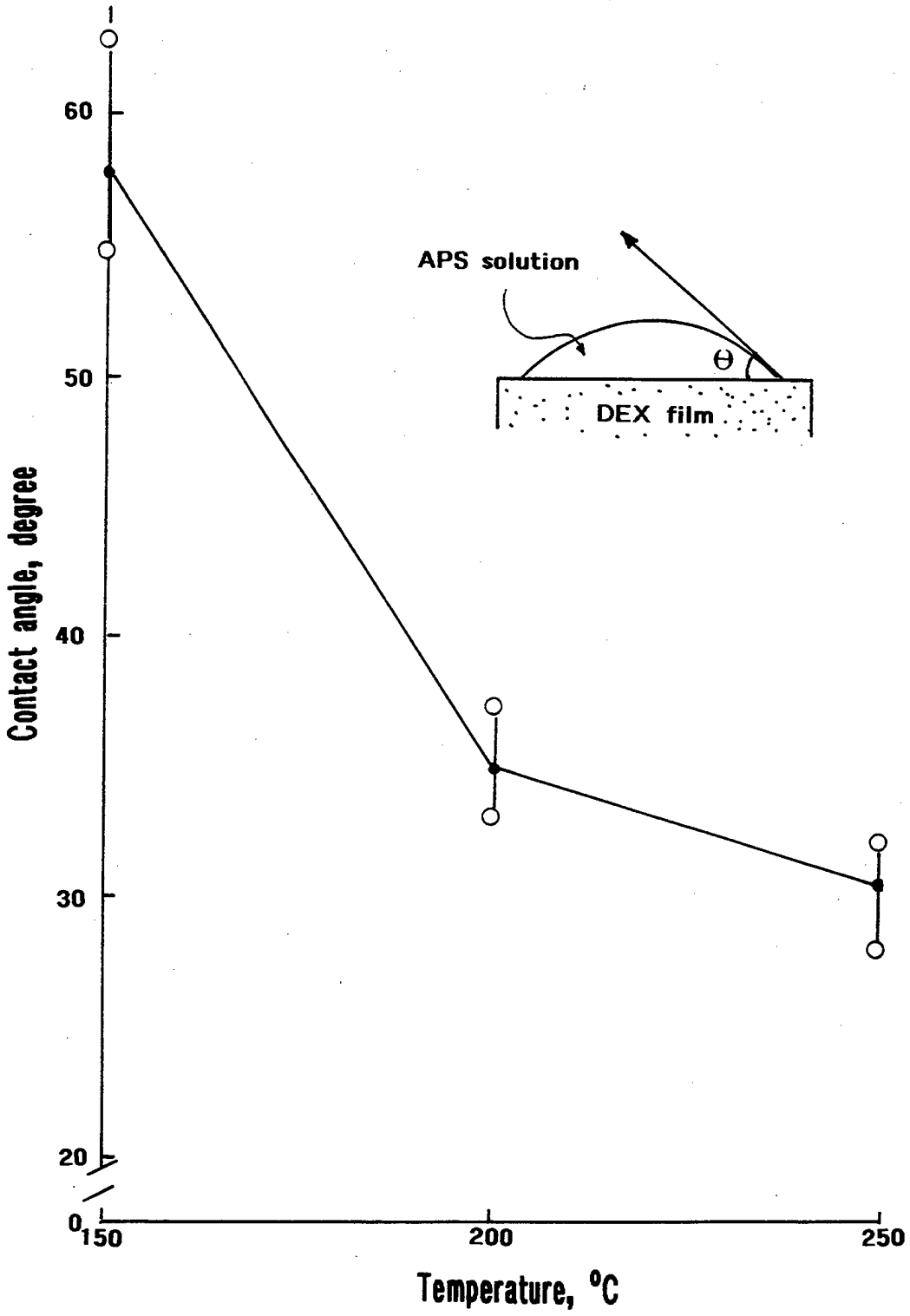


Fig. 2 Changes in contact angle of APS solution over DEX film surfaces as a function of thermal-oxidation temperatures.

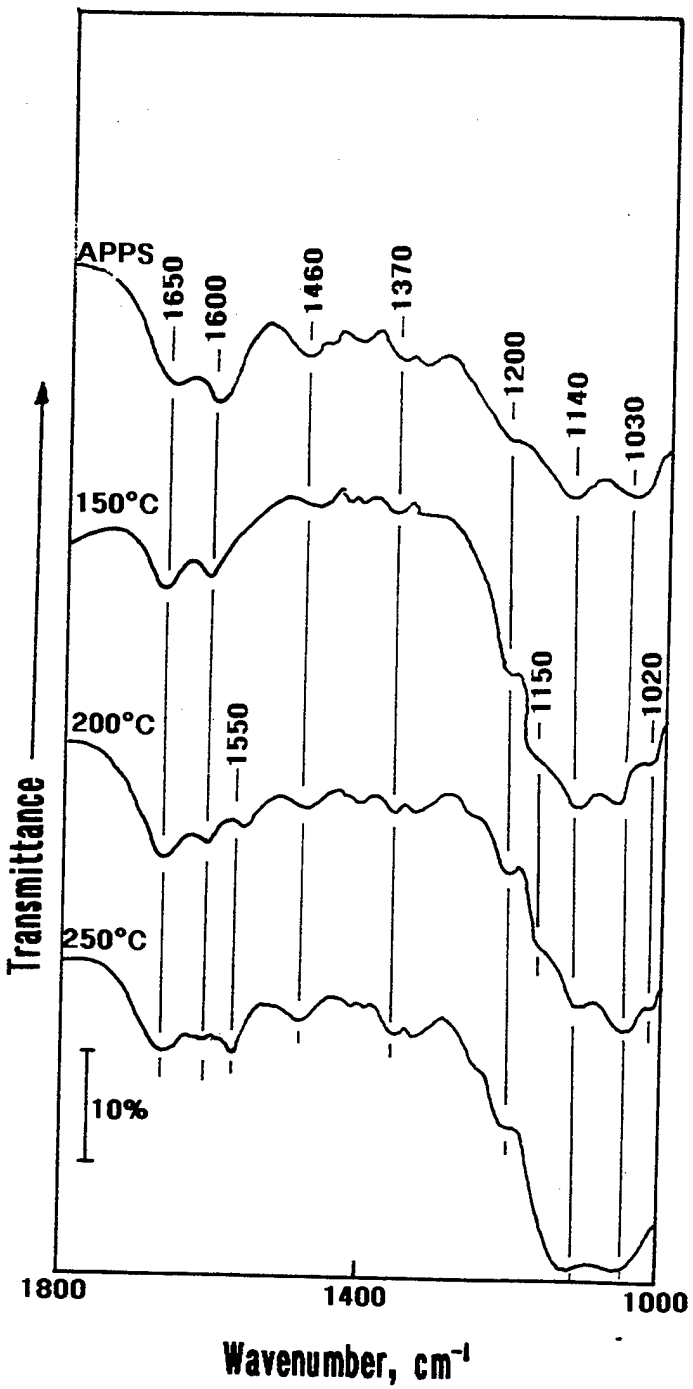


Fig. 3 Comparison between IR spectral features of APPS reference coating, and APPS-overlaid 150, 200, and 250°C DEX coatings.

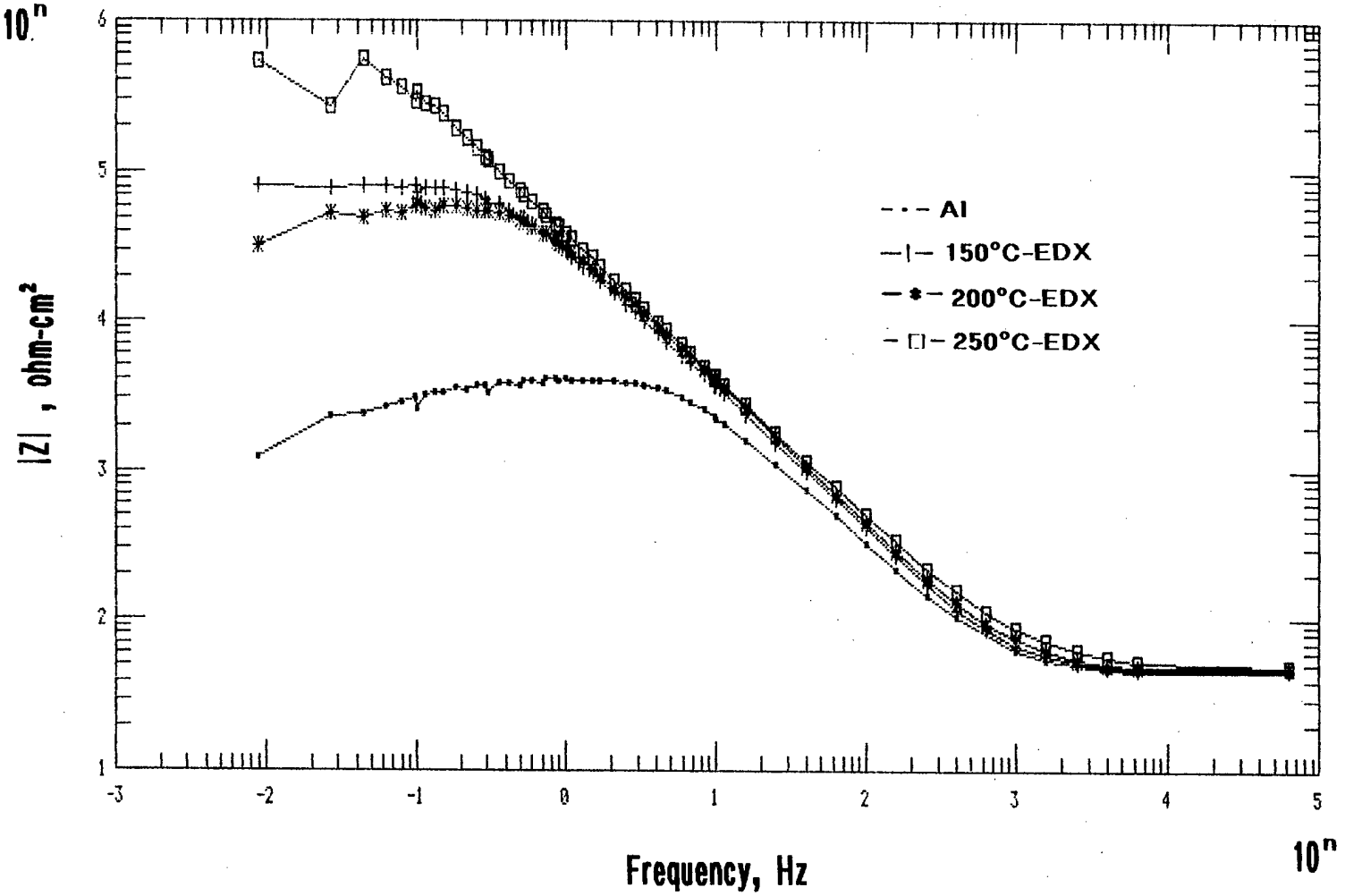
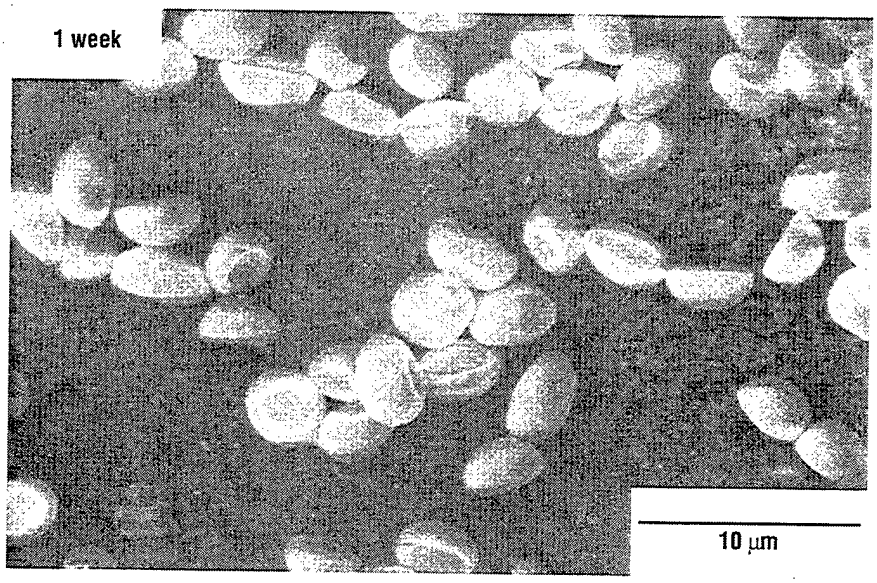
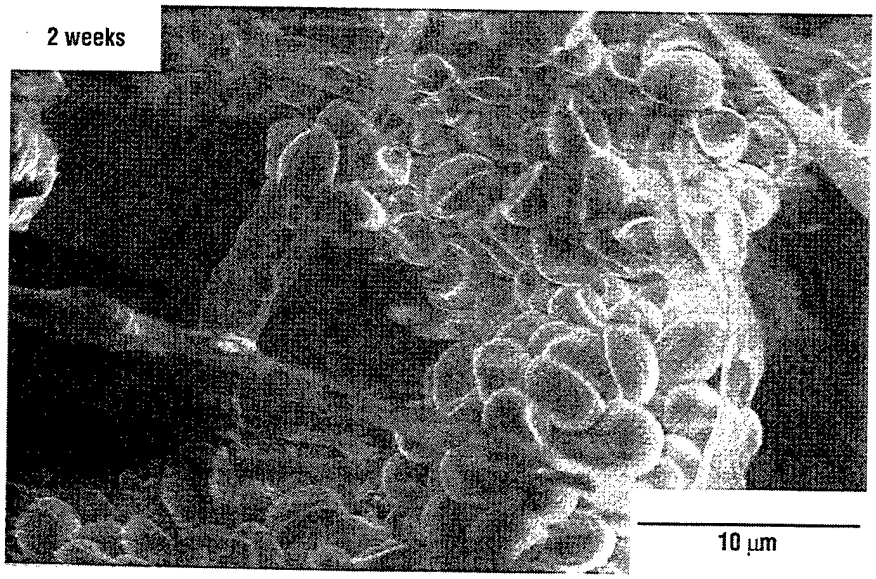


Fig. 4 Comparison of Bode-plot features (impedance, |Z|, vs. frequency) for 150, 200, and 250°C DEX-coated Al substrates.





SEM micrographs of 1- and 2-week-aged 150°C DEX film surfac
inoculating them with fungal consortium.

Detection and Monitoring of Crevice Corrosion Inside Pipe Flanges

Maria E. Inman, E. Jennings Taylor, Debbra L. Myers
Faraday Technology, Inc., 315 Huls Drive, Clayton, OH 45315

Patrick J. Moran
U.S. Naval Academy, Dept. of Mechanical Engineering, Annapolis, MD 21402-5042

Robert M. Kain
LaQue Corrosion Services, 702 Causeway Drive, Wrightsville Beach, NC 28480

ABSTRACT

The development of a novel approach for detection and monitoring of crevice corrosion in pipe flanges is discussed. The o-ring sensor places the electrodes for an electrochemical impedance measurement inside the o-ring within the flange, thus allowing direct ionic contact with the crevice site. Results from piping loop studies have demonstrated the feasibility of this method for remote sensing of crevice corrosion in seawater piping networks fabricated from Alloy 625 and Type 316 stainless steel. The o-ring sensor appears to be compatible with engineering considerations for the piping networks.

INTRODUCTION

N06625 has been reported to be resistant to attack at crevices formed by barnacles and specimen mounting insulators in both shallow water and deep ocean tests in natural seawater.[1,2,3] N06625 has exhibited resistance to crevice attack in numerous multiple crevice assembly (MCA) tests.[2, 4-7] Lennox[8] reported no localized corrosion for N06625 after 1.6 years ambient temperature seawater tests with polyethylene crevice formers, which produced attack on other nickel based alloys. Neiderberger et al[1] reported resistance for N06625 in 2-year natural seawater tests for metal to metal crevices formed by the same alloy material as that in the test, and affixed with a nylon fastener.

Although N06625 is resistant to crevice corrosion initiation over a broader range of geometric conditions than less alloyed stainless steels, several cases of relatively mild crevice attack of N06625 have been reported for long term seawater tests. In one test, crevice corrosion to a 11.02 mils (0.28 mm) maximum depth was detected beneath a polytetrafluoroethylene (PTFE) washer after 5.9 years in quiescent seawater.[9] Two other sites initiated within 10 years but neither exceeded 2 mils (0.05 mm) penetration. Anderson[10] reported a number of individual sites

initiated on N06625 panels with the MCA crevice former exposed for one year to low velocity, ambient temperature seawater. Penetration was limited to 1.2 mils (0.03 mm). In another study, Kain[2] reported crevice corrosion susceptibility for N06625 in 45 day natural seawater tests with perspex crevice assemblies. A maximum penetration of 9.45 mils (0.24 mm) was reported. Mathematical modeling studies[6] have shown N06625 to be indeed quite resistant, but have predicted crevice corrosion initiation for a number of crevice gaps (degree of tightness) and depths (distance from the mouth) considered. Increasing the degree of crevice tightness for a given crevice depth increases the chances for corrosion initiation. Inman et al reported crevice corrosion under vinyl sleeve crevice formers on N06625 pipe segments exposed to ambient temperature seawater for 60 days. [11] Propagation was within the range previously reported by Klein et al.[12]

The particularly troubling aspect of crevice corrosion of N06625 is the fact that it occurs in the tightest part of the crevice, such as in sealing surfaces or on critical mating surfaces. Consequently, crevice corrosion cannot be detected by visual observation of the interior of the piping system. Degradation of this type may cause a leak or loss of critical tolerances which may adversely affect the performance of a component. In addition, this type of corrosion is difficult to detect visually or with conventional non-destructive evaluation techniques because of the complex geometries which may be involved. Therefore, there is a need for a sensing device that can be used to detect crevice corrosion in-situ. Past work on vinyl sleeve piping loop tests showed that polarization resistance measurements could be used to detect the onset of naturally occurring, seawater induced crevice corrosion of N06625 and S31603.[13] The mass loss due to crevice corrosion correlated well with the measured polarization resistance. Additional work on N06625 flanges in the laboratory showed that localized corrosion in a N06625 flange, exposed to 3.5 wt% NaCl, could be detected using electrochemical impedance measurements.[14] These results supported the utilization of in-situ polarization resistance measurements for the detection and characterization of crevice corrosion, leading to the development of a sensor for in-situ detection of crevice corrosion inside flange joints.[16] The sensor incorporates the counter and reference electrodes for an electrochemical measurement inside the o-ring which sits inside the flange. The electrodes are in direct ionic contact with the crevice site through slits cut into the o-ring.

The main objective of this program is to demonstrate that impedance measurements in conjunction with the o-ring sensor can detect naturally occurring, seawater induced crevice corrosion, and correlate with some aspect of crevice corrosion attack, in actual flanges. The main purpose of this test was to show that the o-ring sensor concept works in a flange/crevice geometry. Additional objectives were to show that the impedance measurement does not initiate crevice corrosion and that this type of measurement is compatible with grease.

EXPERIMENTAL PROCEDURE

Materials and Specimens – Two 24 inch long spools of INCONEL® alloy 625 (UNS-N06625) and 24 spools of Type 316 stainless steel (UNS-S31603) were obtained for testing. Each spool comprised a grooved and a flat face geometry. The composition of these materials are given in Table 1.

Pre-cleaning and Weighing – Prior to testing, spools were degreased with acetone and weld heat tint removed with a commercial acid paste. Both flange surfaces, along with the pipe inner surface, were bristle brush scrubbed with a detergent-pumice-water mixture, rinsed with water, and given a final degreasing in fresh acetone prior to air drying.

Flanges and Assembly –The 26 spools were configured to produce a total of 28 flange joints; 25 S31603 flange joints and 3 N06625 flange joints. Table 2 lists each o-ring sensor number, the flange material, and the type of o-ring in each flange. Three S31603 flanges contained regular o-rings, to demonstrate that the wires embedded in the o-ring sensor do not initiate crevice corrosion. Further, 4 control o-ring sensors were not subjected to the impedance measurements, to demonstrate that application of this electrochemical technique does not initiate crevice corrosion. Four S31603 flanges, #'s 20-21 and 25-26, were pre-coated with Termalene® grease. The grease was intended to protect against crevice corrosion and permit these specimens to serve as crevice corrosion-free experimental controls for the duration of testing, as well as test the ability of the o-ring sensor to operate in the presence of grease. Specimens treated with the grease were positioned downstream of all flanges except #22, #23, #27, and #28.

The S31603 and N06625 spools were connected by PVC pipe fittings. The two sections of the piping loop were electrically connected via a length of wire fixed to the spools with hose clamps. The piping loop was assembled and the flange bolts torqued to 21 ft.lbs. The completed assembly, comprising 28 flange joints and PVC plumbing, with "U-bends" to accommodate the piping loop construction, is shown schematically in Figure 1.

O-ring Sensor Type – The o-ring sensor design, shown schematically in Figure 2, incorporates 2 platinum wires in a series of small slits around the circumference of the o-ring. Each electrode wire is inserted into a slit and manually threaded through the uncut rubber to the next slit using a needle. The length of each slit is approximately 5 mm, with a 5 mm spacing between each slit. The slits in the o-ring are in contact with the grooved or flat face of the flange, which acts as the working electrode. These embedded wires are used as the counter electrode (CE) and the reference electrode (RE) in conventional three-electrode impedance measurements. The reference electrode is embedded in one half of the o-ring, and the counter electrode in the other half. The electrodes are electrically isolated from one another by a 5 mm uncut length of the o-ring material. To enable outside connection to the electrodes, the wires are threaded through the outer sidewall of the o-ring at one point. Each Pt electrode wire is covered with a sheath of PTFE heat shrink from the exit point to the end of the wire, preventing electrical contact between the wire

and the flange. The wires are bound together after they emerge from the o-ring by a further layer of PTFE heat shrink, adding mechanical stability. Copper foil is crimped onto the end of each wire, to facilitate good electrical contact between the wire and the potentiostat connectors. Three types of o-ring sensor were tested, to determine the geometry best suited for detection of crevice corrosion in flanges. In the standard o-ring, used in most of the flanges, the slits faced down into the groove. In the second o-ring sensor, the slits faced the flat face of the flange. The third type of sensor incorporated slits facing both grooved and flat faces, to try and detect crevice corrosion on both sides of the flange. These three types of o-ring sensor were installed in flanges #8-#19.

Apparatus/Environment - The o-ring sensor was tested by setting up a seawater piping loop, made from S31603 and N06625 2-inch pipe flanges. Seawater was delivered to the inlet end of the above test "loop" via appropriate valving and a non-metallic pump, from Banks Channel, which is adjacent to the LaQue Corrosion Services test facilities at Wrightsville Beach, NC. Flow control was provided by a calibrated "rotameter" located at the down stream end of the once through system. Testing commenced on December 9th, 1996. Flow through the test specimens was maintained at 64 gpm (227 L/min). Based on the ID of the S31603 and NO6625 pipe, this equates to a nominal seawater velocity of 6 ft/s (1.8 m/s). The system operated continuously for 183 days.

Crevice Solution pH Measurements – Crevice solution leaked out of some flanges during the test. The pH of this solution was measured using universal pH paper.

Polarization Resistance/Impedance Measurements – The polarization resistance was determined from electrochemical impedance measurements which were obtained using a PAR Model 273A Potentiostat/Galvanostat and a PAR Model 5210 Lock-in Amplifier. A 10 mV rms AC signal was applied to each flange relative to the platinum reference and counter electrodes positioned inside the o-ring within the flange. The impedance data were obtained using a 10 mV rms AC signal obtained over the frequency range of 100 kHz to 10 Hz. The impedance response over this frequency range was used to estimate the polarization resistance assuming a Randles circuit model. The impedance measurements were conducted for each tube segment at days 3-5, 37, 38, 105-107, 133-135, 182, and 183.

Corrosion Potential Measurements – Measurements of the corrosion potentials inside each flange crevice site could not be made, as a true reference electrode could not be inserted into the o-ring sensor. The corrosion potential of the boldly exposed surfaces of the pipeline was measured periodically over the course of testing using a high impedance voltmeter with one lead connected to the pipeline, and the other to a Ag/AgCl seawater reference electrode positioned in a reservoir located upstream of the piping loop. The composite loop mixed corrosion potentials measured ranged from –0.06 V to + 0.05 V (Ag/AgCl). These values are not expected to give an indication of the corrosion potentials inside the flange crevices.

Post-test Cleaning and Evaluation - At the completion of the test, the piping loop was dismantled. The flat and grooved surfaces of each flange joint were bristle brushed to remove any loosely adherent corrosion products. Each flange face was then immersed in 30% HNO_3 for 15 minutes (at room temperature), water rinsed, and rescrubbed using detergent. After water rinsing and acetone rinsing, the flanges were air dried, and photographs of each flange face were taken. The amount of crevice corroded area for each crevice site on each flange face was determined by counting the number of mm^2 divisions showing attack in a transparent grid covering each affected site. The depth of crevice corrosion penetration at each affected site was determined with a needle point dial gage indicator. Twelve representative pit depth measurements were taken and averaged. These post-test characterization results are beyond the scope of this paper and will be the subject of a future publication. However, visual examination of each flange surface was completed after the flanges had been cleaned, and an estimate of the % affected area under each o-ring site was made. The % affected area was estimated to be the percentage of attack around the circumference of each o-ring site. Attack on the sidewalls of each groove, and on the inner raised face beside each groove was also noted. The flat and grooved surfaces of each flange joint were examined separately.

RESULTS AND DISCUSSION

Detection of Crevice Corrosion Inside N06625 Flanges

Electrochemical Results - Figure 3 shows the polarization resistance of the N06625 flanges as a function of time. In general, the measured R_p values were greater than 10 kΩ, suggesting passivity, with occasional excursions to R_p's below 1 kΩ. These short term excursions suggested possible localized attack, which repassivated almost immediately. The thick o-ring sensor (#23) showed consistently high R_p values, although a downward trend near the end of the test suggests that breakdown of passivity may have occurred.

Visual Characterization of Corrosion – Table 3 shows that no significant areas of crevice corrosion were visually observed on the flange faces after the completion of the test. The flanges pertaining to o-ring sensor #27 had a few suspect pits in the groove, and the groove for sensor #28 had 4-5 areas of minimal attack, corresponding to the slits cut into the o-ring (Figure 4). The flat face of the flange adjacent to the thick o-ring sensor showed no evidence of crevice attack.

Correlation Between Electrochemical Results and Visual Observations – The data presented in the previous two sections show good correlation between the electrochemical impedance measurements, obtained using the o-ring sensor, and the occurrence of localized corrosion within the N06625 flanges. Infrequent low R_p values were correlated with occasional slight attack; high R_p values correlated with no observed attack.

Detection of Crevice Corrosion Inside S31603 Flanges

Electrochemical Results – Figure 5 gives the polarization resistance results for all of the non-greased S31603 flanges as a function of time. This graph shows that although most of the R_p values were initially high, all of the flanges except one (#9) dropped rapidly to much lower values, and remained at those low values for the remainder of the test. This suggests that crevice corrosion initiated in most of the flanges at some point during the test. Only high R_p values were measured using o-ring sensor #9, suggesting no localized attack occurred, although this data may be misleading as impedance measurements were not made during the final three months.

Figure 6 shows the R_p values measured in the greased flanges throughout the test. The data was fairly scattered, and did not exhibit any obvious trends. The fairly high R_p values suggested that no crevice corrosion occurred in any of the greased flanges at any time during the test. The values of R_p measured for each flange were all of a similar magnitude.

Visual Characterization of Corrosion - Table 3 provides a summary of the extent of crevice corrosion on each flange face, by visual approximation of the % affected area. The table divides the attack into that observed in the region under the o-ring, on both flat and grooved flange faces, and the attack observed on other sections of the flange, i.e. not in direct contact with the slits in the o-ring. It is likely that only the attack under the o-ring could be detected using the o-ring sensor, as this is the only region in direct ionic contact with the electrodes. The long path between the embedded electrodes and corroding sites on other regions of the flange is prohibitive to detection of corrosion activity. However, this may be acceptable, as it is only crevice corrosion at the o-ring site which will affect the sealing ability of the flange. Pits on the outer surfaces of the flange, resulting from leakage of the corrosive crevice solution from the flange during the test, were observed, but are not noted in the table. The measured pH of the solution leaking from the flanges during the test ranged from 2 to 7.

Figures 7 and 8 show the crevice corrosion typically observed on the grooved and flat faces of the S31603 flanges, respectively. In general, there was a greater % attacked area on the flat flange face as compared to the groove. This observation applies equally to the three types of o-ring sensor tested *i.e.,* with the slits facing the groove, the flat face, or both groove and flat face. On average, the flanges containing regular o-rings had 50% attacked area in the groove and 85% on the flat face. The flanges which contained control o-rings (which had embedded wires, but which were not subjected to impedance measurements) had 31% and 70% attacked area in the groove and flat face, respectively. The non-greased flanges containing o-ring sensors, which were subjected to impedance measurements, had 34% and 61% attacked area in the groove and flat face, respectively. These results do not necessarily imply that the presence of the embedded wires inhibits crevice corrosion, but that there is no obvious acceleration of crevice corrosion initiation and propagation due to either the presence of wires embedded in the o-ring, or the use

of electrochemical impedance measurements on a regular basis. The attack on the flat flange faces under the thick o-rings was more extensive than that under the normal size o-rings. Visual observations suggested that the depth of penetration was considerably greater under the thick o-rings. Post-test measurements revealed that the deepest attack (2.93 mm) occurred under the thick o-ring sensor #24.

The greased flanges did exhibit minor crevice corrosion in the flange groove and on the corresponding location on the flat face; on average 11% of the groove bottom and 25% of the flat face were moderately attacked. However, far more extensive corrosion was observed on the inner raised face between the groove and inside wall of the spool(Figure 9), and on the flat face corresponding to that site. Additionally, the inner side wall of the groove was often heavily attacked. This can be contrasted with the comparatively light attack on the inner raised face and inner sidewall of the groove in the non-greased flanges. To our knowledge, this increase in crevice corrosion activity on the non-critical mating surfaces of greased flanges, as compared to non-greased flanges, has not been previously reported.

A number of the o-ring sensors electrically shorted to the flanges during the test. Examination of the data in Table 3 shows no significant distinction in % attacked area between the non-shorted and the shorted o-rings. The % attacked area was, on average, slightly higher for the non-shorted case. This suggests that the electrical shorting between the embedded wires and the flange does not cause accelerated crevice corrosion of the flange joint.

Correlation Between Electrochemical Results and Visual Observations – Table 3 compares the electrochemical data with the extent of crevice corrosion. The R_p measurements for each flange have been consolidated into an index, giving the number of R_p values above 10 kΩ as a percentage of the total number of measurements for each flange. The numbers are stated as a % for easier interpretation, as the total number of measurements was not the same for each flange. Higher numbers suggest less crevice corrosion activity during the test. By comparing the % R_p > 10 kΩ with the % attacked area, it can be seen that those flanges which had predominantly low R_p values (#11, 13, 14, 17, 19) had the highest % attacked area. This initial comparison should provide a good indication of the relationship between the electrochemical data and the more accurate pit depth and area of attack results to come. However, these initial data suggest that the electrochemical impedance measurement can be used to characterize the crevice corrosion activity inside a flange under normal conditions.

The flanges containing grease showed different behavior, when compared to the non-greased flanges. Crevice corrosion occurred predominantly on the inner raised faces of the greased flanges, and extended down the side wall of the groove, into the bottom of the groove. The polarization resistance measurements of the greased flanges did not detect any increase in the

corrosion activity in the flange. This lack of detection could possibly be due to interference of the grease with the impedance measurement.

CONCLUSIONS

This paper describes a crevice corrosion test program involving exposure of N06625 and S31603 flanges containing o-ring sensors to flowing seawater. These tests are intended to support the development of a diagnostic tool for in-situ detection of crevice corrosion.

- An o-ring sensor was successfully used to monitor the crevice corrosion activity inside S31603 and N06625 flange joints, in a seawater piping loop.
- The measured polarization resistance correlated with the occurrence of crevice corrosion inside S31603 flange joints.
- 92% of the S31603 flanges were attacked at the o-ring site.
- The N06625 flanges did not undergo significant attack; only a few small pits were detected in the grooved areas of the flanges.
- There was more attack on the flat faces of the flanges, as opposed to the groove.
- There did not appear to be any acceleration of crevice corrosion by the presence of embedded wires in the o-ring, or by the impedance measurements applied using the o-ring sensor.
- Crevice corrosion in the greased flanges occurred predominantly on the inner raised faces of the flanges, extending down the side wall of the groove, into the bottom of the groove. The polarization resistance measurements in the greased flanges did not detect the occurrence of crevice corrosion, possibly due to interference of the grease with the measurement.
- Occasional electrical shorting between the electrodes in the sensor and the flange, did not appear to accelerate the crevice corrosion.

ACKNOWLEDGEMENTS

This research was supported by a SBIR Phase II grant from the Office of Naval Research (Contract Number: N00014-94-C-0136; Program Manager: Dr. A. John Sedriks). The technical assistance of Mr Rich Hays and Mr Dan Davis during this program is very much appreciated.

REFERENCES

1. Neiderberger, R.E., R.J. Ferrara, and F.W. Plummer, Corrosion of Nickel Alloys in Quiet and Low Seawater, *Materials Performance*, **9**, 1970, p 18.
2. Kain, R.M., Effect of Alloy Content on the Localized Corrosion Resistance of Several Nickel Base Alloys in Seawater, Paper No. 229, *Corrosion '86*, Houston, TX, NACE International, March 1986.
3. Fink, F.W., and W.K Boyd, *Corrosion of Metals in Marine Environments*, Defense Metals Information Center Report 245, Batelle Memorial Institute, Columbus OH, 1970.
4. Hack, H.P., *Materials Performance*, **22**, 6, 1983, p 24.
5. Kain, R.M., Localized Corrosion Behavior in Natural Seawater: A Comparison of Electrochemical and Crevice Testing of Stainless Steel, Paper No. 74, *Corrosion '80*, Chicago, Il, NACE International, 1980.
6. Lee, T.S. and R.M. Kain, Factors Influencing the Crevice Corrosion Behavior of Stainless Steels in Seawater, Paper No. 69, *Corrosion '83*, Anaheim, CA, NACE International, 1983.
7. Unpublished Data from ASTM G1.09.02 Round Robin MCA Tests, American Soc. for Testing and Materials, Philadelphia, PA, Request No. RRG1-1011.
8. Lennox, T.J., M.H. Peterson, and C.W. Bellow, *Materials Performance*, **22**, 6, 1983, p 49.
9. *Huntington Alloys Resistance to Corrosion*, Bulletin S-37, Huntington, WVA, 1970.
10. Anderson, D.B., Statistical Aspects of Crevice Corrosion in Seawater, ASTM-STP 576 Galvanic and Pitting Corrosion, American Soc. for Testing and Materials, Philadelphia, PA, 1976, p 231.
11. Inman, M.E., A.K. Rawat, E.J. Taylor and P.J. Moran, Detection of Crevice Corrosion under an O-ring by Polarization Resistance Measurements using Electrodes Embedded in the O-ring, Paper No. 312, *Corrosion/'97*, NACE International, New Orleans, Louisiana, March 1997.
12. Klein P.A., Paper No. 112, *Corrosion/'89*, NACE International, March 1989.
13. Unpublished results, 1996.
14. Inman, M.E., E.J. Taylor, A.K. Rawat, M. Sunkara, R.M. Kain, P.J. Moran and R. Hays, Detection of Crevice Corrosion in Natural Seawater using Polarization Resistance Measurements, Paper No. 296, *Corrosion/'97*, NACE International, New Orleans, Louisiana, March 1997.

Table 1 Chemical composition (wt%) of N06625 and S31603 flanges used to construct piping loop at LaQue Corrosion Services.

Alloy	Ni	Cr	Mo	Fe	S	Si	C	Mn	Al	Ti	P
S31603	13.35	17.30	2.61	nr	0.001	0.48	0.01	1.53	nr	nr	0.024
N06625	62.25	22.06	8.95	2.72	0.001	0.07	0.01	0.05	0.29	0.12	0.005

nr = not reported

Table 2 Description of o-ring sensors installed in each flange in the seawater piping loop at LaQue Corrosion Services

O-ring No.	Material	O-ring Type	Electrode slit Facing	Impedance Measurements
1 (R)	S31603	Regular	-	-
2 (R)	S31603	Regular	-	-
3 (R)	S31603	Regular	-	-
4 (C)	S31603	Control Sensor	Groove	No
5 (C)	S31603	Control Sensor	Groove	No
6 (C)	S31603	Control Sensor	Groove	No
7 (C)	S31603	Control Sensor	Groove	No
8	S31603	Sensor	Groove	Yes
9	S31603	Sensor	Groove	Yes
10	S31603	Sensor	Groove	Yes
11	S31603	Sensor	Groove	Yes
12	S31603	Sensor	Groove	Yes
13	S31603	Sensor	Groove	Yes
14	S31603	Sensor	Flat	Yes
15	S31603	Sensor	Flat	Yes
16	S31603	Sensor	Flat	Yes
17	S31603	Sensor	Flat/Groove	Yes
18	S31603	Sensor	Flat/Groove	Yes
19	S31603	Sensor	Flat/Groove	Yes
20 (G)	S31603	Sensor	Groove	Yes
21 (G)	S31603	Sensor	Groove	Yes
22 (T)	S31603	Sensor	Flat	Yes
23 (T)	N06625	Sensor	Flat	Yes
24 (T)	S31603	Sensor	Flat	Yes
25 (G)	S31603	Sensor	Groove	Yes
26 (G)	S31603	Sensor	Groove	Yes
27	N06625	Sensor	Groove	Yes
28	N06625	Sensor	Groove	Yes

Note: (R) regular o-ring; (c) control o-ring sensor (no impedance measurements); (G) grease; (T) thick o-ring

Table 3 Visual Evaluation of Corroded Flange Surfaces on N06625 and S31603 Flanges.

O-ring No.	Electrodes Facing	% Affected Area Groove	% Affected Area Flat face	Other affected sites on flange faces†	% R_p > 10 kΩ
N06625 Flanges					
23 (T)	Flat	0	0	-	100
27	Groove	0	0	Few small pits in groove	83
28	Groove	0	0	Slit attack in groove	89
S31603 Flanges					
1 (R)	-	0	80	5% OSW	-
2 (R)	-	100	95	20% IRF; 20% IRFF	-
3 (R)	-	50	80	25% IRF; 10% OSW; 20% IRFF	-
4 (C)	Groove	50	85	-	-
5 (C)*	Groove	50	80	-	-
6 (C)*	Groove	0	40	25% IRF; 25% IRFF	-
7 (C)	Groove	25	75	90% IRF; 90%IRFF	-
8*	Groove	0	0	5% IRFF	-
9	Groove	0	25	5% IRF; 10% IRFF	100
10*	Groove	40	80	-	-
11	Groove	75	75	25% IRF; 20% IRFF	0
12*	Groove	10	40	-	-
13	Groove	0	90	60% ISW; 60% OSW; 20% IRFF	9
14*	Flat	60	95	-	10
15*	Flat	20	75	5% IRF	-
16*	Flat	0	60	40% ISW	-
17	Flat/Groove	90	80	30% ISW; 10% IRF; 10% IRFF	0
18*	Flat/Groove	40	60	-	-
19	Flat/Groove	80	80	20% ISW	0
20 (G)	Groove	20	30	95% IRF; 75% ISW; 95% IRFF	100
21 (G)	Groove	15	20	30% ISW; 30% IRF; 40% IRFF	100
22 (T)*	Flat	-	75	-	73
24 (T)*	Flat	-	30	-	-
25 (G)	Groove	0	0	30% IRF; 30% IRFF	100
26 (G)*	Groove	10	50	100% IRF; 40% ISW; 15% OSW; 100% IRFF	-

Note: (R) regular o-ring; (c) control o-ring sensor (no impedance measurements); (G) grease; (T) thick o-ring

* indicates that o-ring sensor electrically shorted to the flange at some time during the test.

† IRF - inner raised face; IRFF – site on flat face corresponding to inner raised face; ISW – inner side wall of groove; OSW – outer side wall of groove.

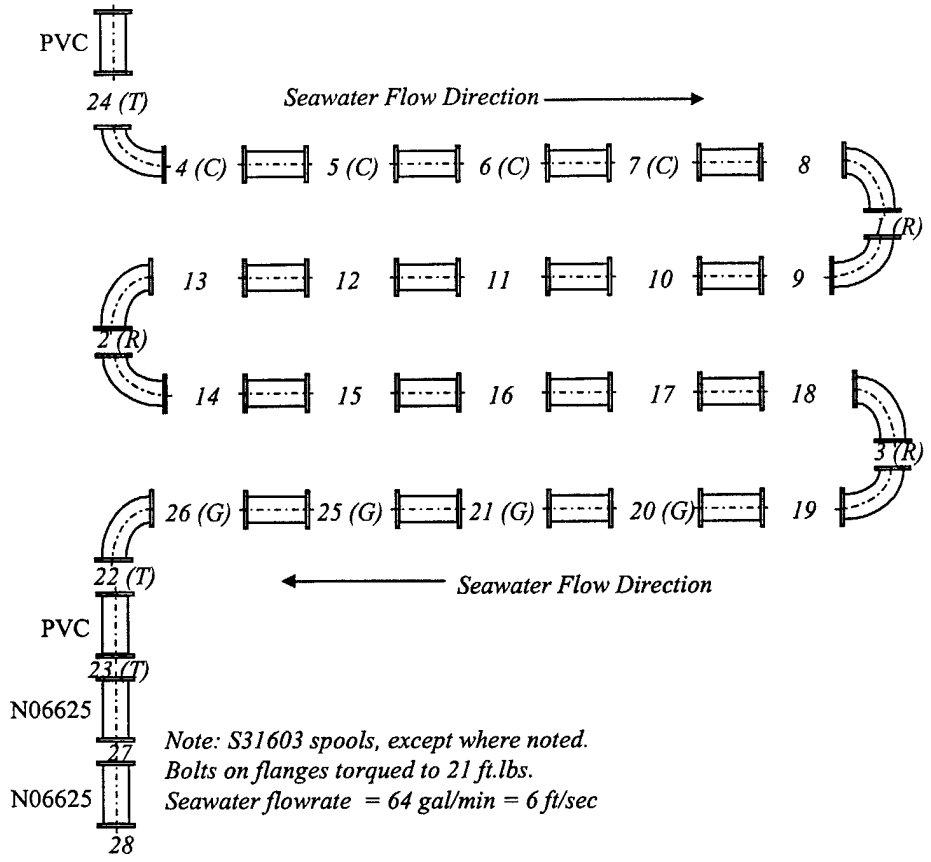


Figure 1 Layout of S31603 and N06625 spools in seawater piping loop at LaQue Corrosion Services.

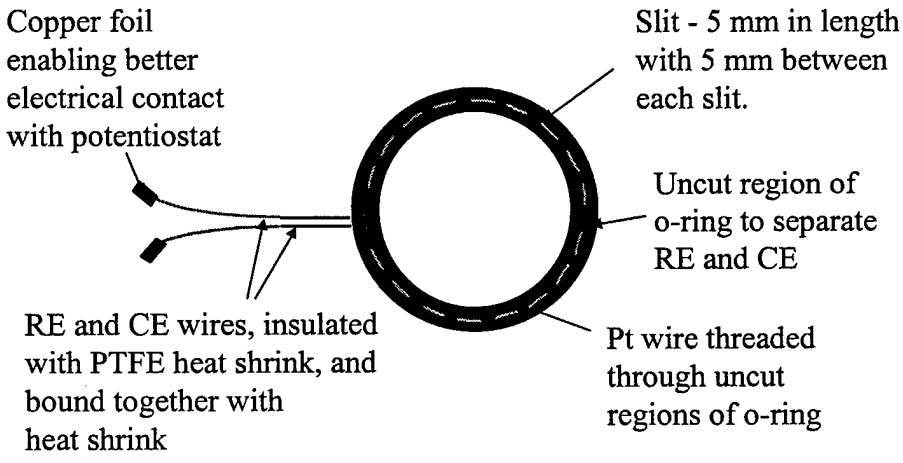


Figure 2 Schematic diagram of o-ring sensor, incorporating a discontinuous slit. Slits are 5 mm length, and separated by 5 mm of uncut o-ring.

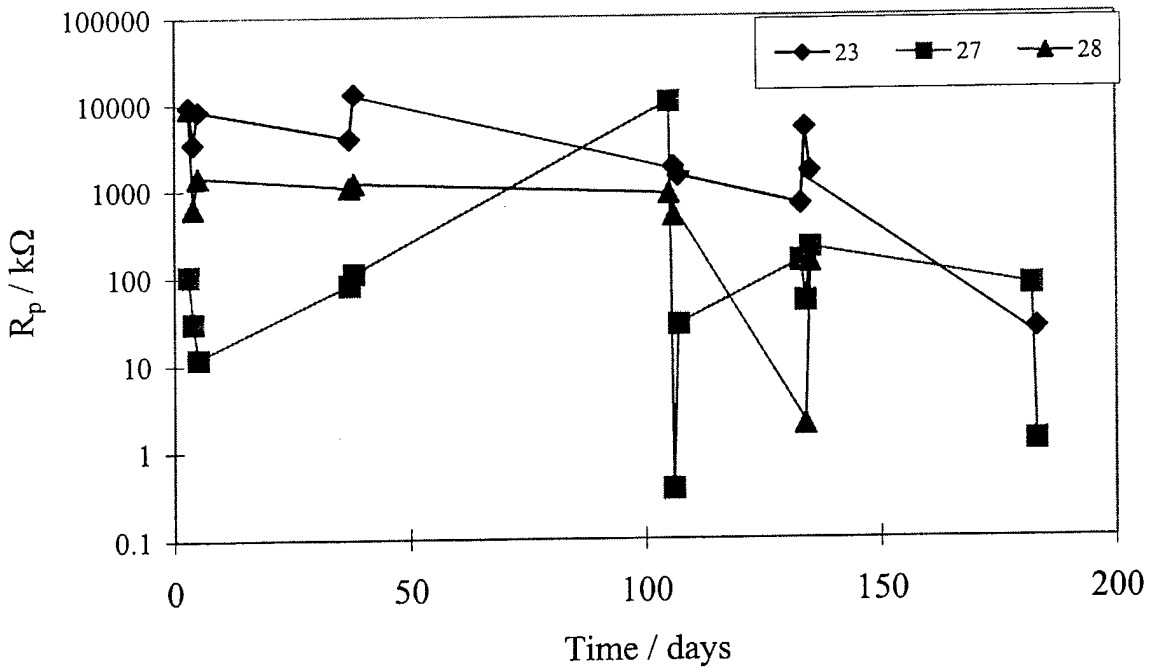


Figure 3 R_p as a function of time for N06625 flanges in seawater piping loop.

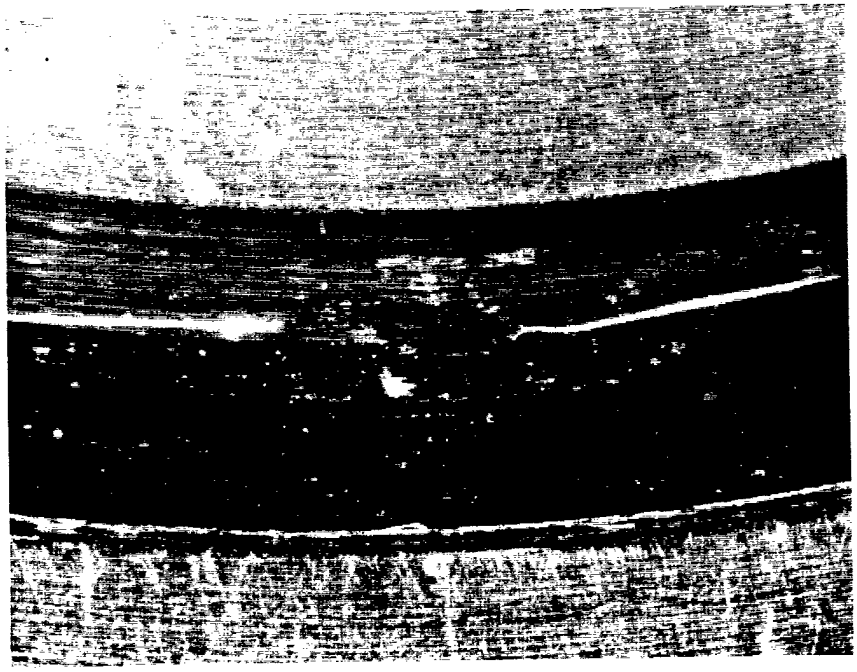


Figure 4 Macrograph of crevice corrosion in N06625 flange groove, exposed to flowing seawater for 6 months in piping loop. O-ring sensor #28.

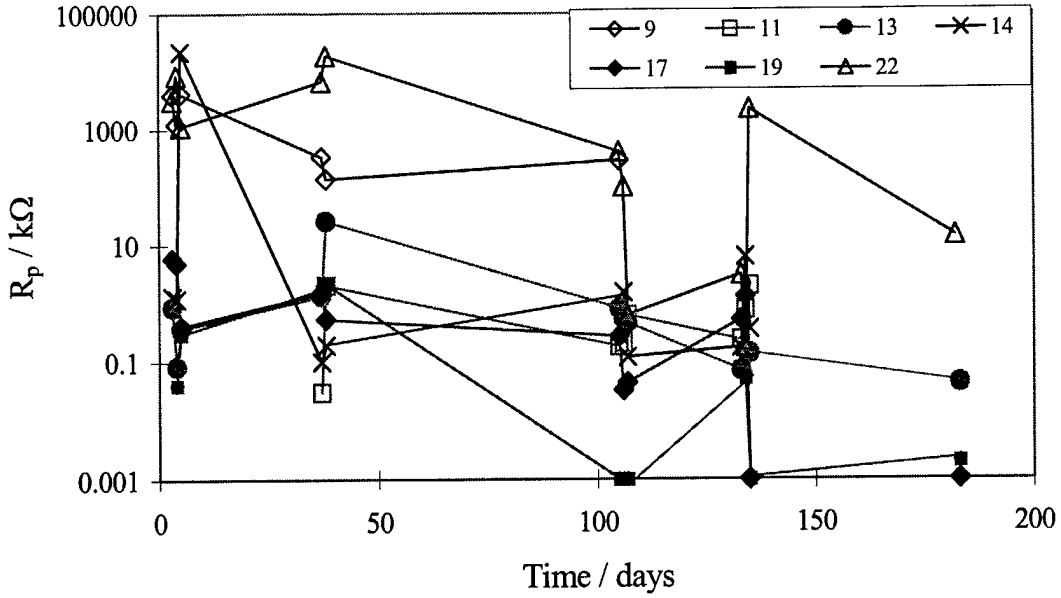


Figure 5 R_p as a function of time for non-greased S31603 flanges in seawater piping loop.

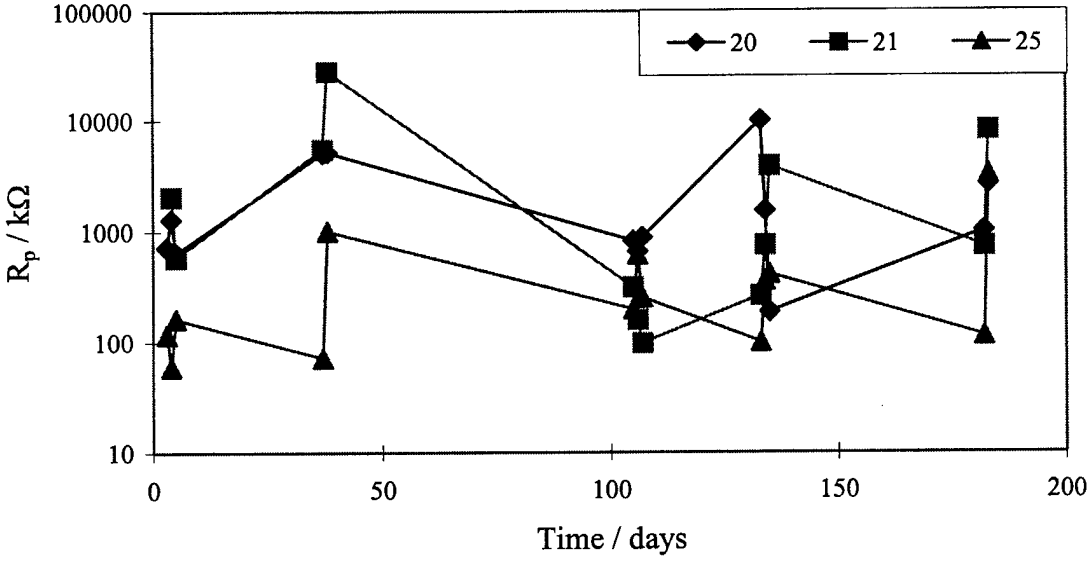


Figure 6 R_p as a function of time for greased S31603 flanges in seawater piping loop.

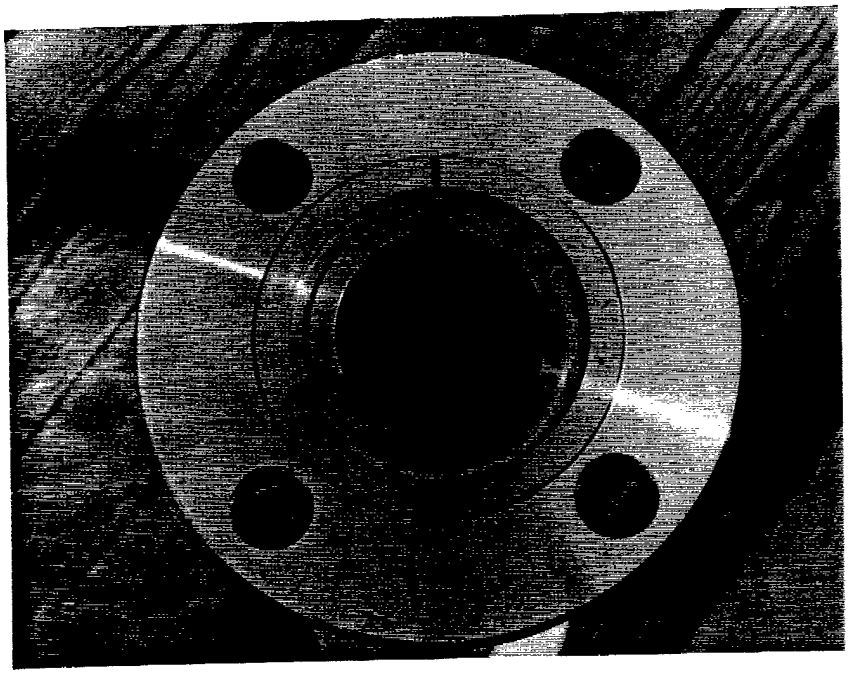


Figure 7 Photograph showing crevice corrosion in S31603 flange groove, exposed to flowing seawater for 6 months in piping loop. O-ring sensor #10.

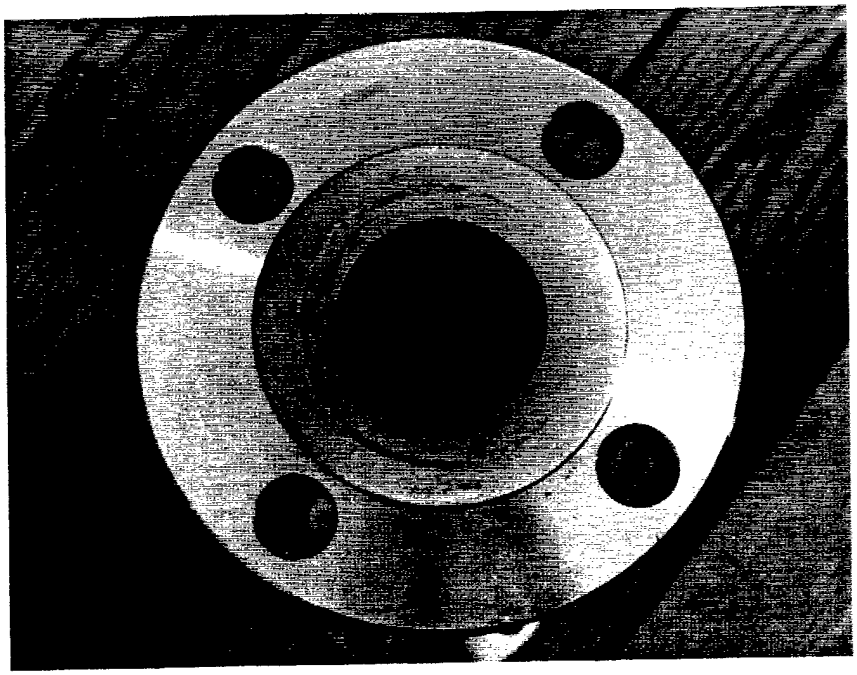


Figure 8 Photograph showing crevice corrosion on flat face of S31603 flange groove, exposed to flowing seawater for 6 months in piping loop. O-ring sensor #10.

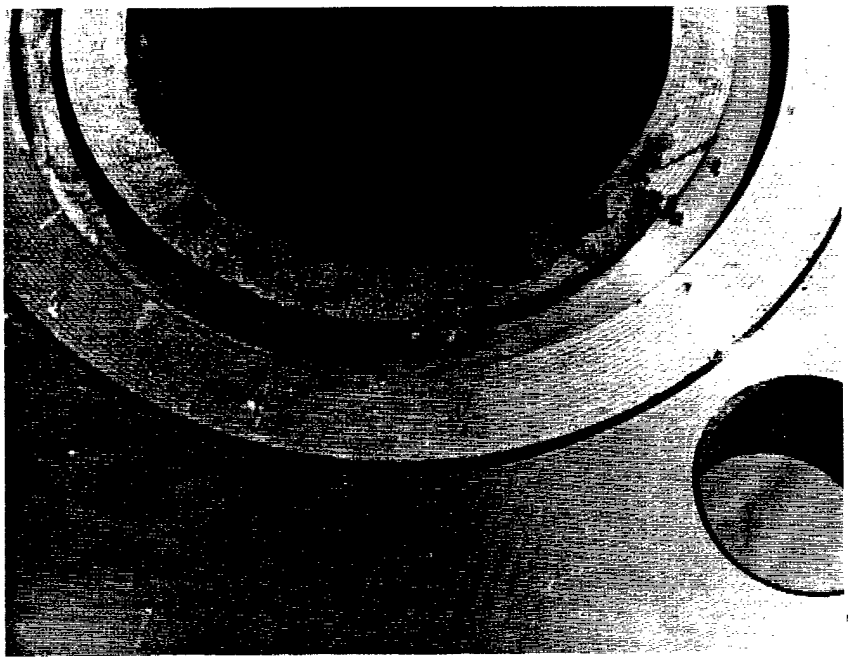


Figure 9 Photograph showing crevice corrosion on inner raised face of greased S31603 flange, exposed to flowing seawater for 6 months in piping loop. O-ring sensor #20.

Demonstration of Cathodic Protection Remote Monitoring Systems

Vicki Van Blaricum
U. S. Army Construction Engineering Research Laboratories (USACERL)
ATTN: CECER-FL-M
P. O. Box 9005
Champaign, IL 61826-9005

ABSTRACT

Cathodic protection (CP) is required by regulation and/or by Army policy on many underground and submerged structures to prevent corrosion. Declining resources have made it difficult for installations to perform the periodic CP system evaluations that are required to ensure continuous corrosion protection. Several companies have begun manufacturing CP remote monitoring units (RMUs), which reduce the time required for CP evaluation by allowing personnel to conduct measurements on multiple CP systems from a single master computer. The objective of this study was to evaluate the field performance of several commercially available impressed current CP RMU systems. RMUs were installed at two field test sites and their accuracy was evaluated by comparing their measurements with readings that were collected using traditional manual field testing procedures. RMU installation procedures, instruction manuals, software, and hardware reliability were also evaluated.

INTRODUCTION

Metallic structures that are buried in soil or submerged in water tend to corrode. Corrosion of storage tanks and piping systems can result in premature failures, losses of the substance being conveyed or stored, leakage of hazardous materials into the environment, and high life cycle costs. The Environmental Protection Agency (EPA) mandates the use of cathodic protection (CP) to prevent corrosion of metallic underground fuel storage tanks (USTs) and associated piping (40 CFR 280-281). The Department of Transportation (DOT) requires cathodic protection on metallic natural gas distribution piping (49 CFR192). In addition, Army guidance (ETL 1110-3-474) requires CP on a number of structures, including all steel water storage tank interiors, and underground heat distribution and chilled water piping in ferrous metallic conduit in soils with resistivity of 30,000 ohm-cm or less.

CP systems must be periodically evaluated to ensure that they are providing adequate, continuous corrosion protection. Testing frequency requirements have been set forth in the EPA, DOT, and Army documents mentioned previously. The evaluation is typically done by field engineers or technicians who travel to each CP rectifier and test station and conduct a series of measurements with handheld meters. Lack of manpower and money has made it difficult for Army Directorates of Public Works (DPWs) to perform this testing, so the Army has begun investigating the use of automation in helping meet the requirements.

Several companies manufacture remote monitoring units (RMUs) that are tailored specifically for evaluating impressed current CP systems. CP RMUs can be used to monitor rectifier inputs and outputs, as well as structure-to-electrolyte potentials. Remote monitoring equipment allows personnel to collect CP performance data from distant locations using a single modem-equipped IBM-compatible personal computer. This eliminates the need for personnel to travel to field sites to take measurements, dramatically increases the number of sites that can be evaluated during a given time period, and frees personnel for other duties. It is possible for the central computer to be located thousands of miles away from the rectifiers and test sites. Use of a modem-equipped laptop computer enables the CP system to be monitored from almost anywhere at almost any time.

Typically, each RMU is installed near a CP rectifier. A permanent copper-copper sulfate reference electrode is buried near the pipe at each monitoring location and the wire is routed to the RMU. The terminals of the RMU are connected to the CP equipment such that the rectifier output voltage and current, rectifier input voltage, and pipe-to-soil potential vs. the permanent reference electrode can be measured (RMU configuration may vary depending on the equipment manufacturer and the specific system being monitored).

Each RMU transmits its data to the central computer via standard telephone lines, cellular telephone, radio, or satellite. (Note: The RMUs in this study communicate via standard telephone lines only.) Structure-to-soil potentials may then be evaluated against NACE International cathodic protection criteria (NACE International Standard Recommended Practice RP0169-96) to determine whether or not the structure is protected from corrosion. Rectifier inputs and outputs may be monitored for significant fluctuations from normal values.

EXPERIMENTAL PROCEDURE

Market Survey

The first step in this investigation was to conduct a market survey to identify commercially available CP RMUs that best met Army requirements, which were (1) units must currently be ready for production and testing, (2) units must be manufactured in the United States, (3) units must be able to monitor a typical CP system without extensive rewiring, configuring, or programming by the user, and (4) units must be competitively priced.

The three RMUs that best met the requirements were selected for testing. It is important to note that this study should not be considered all-inclusive. It includes only the CP RMUs that best met the requirements at the time of the manufacturer survey in early 1995. The hardware that was tested was procured between July and October of 1995. Some of the manufacturers may have improved their hardware since that time, but these updates were not included in this study.

Procurement of RMUs

The ordering specifications for the RMUs included in the study were determined on the basis of what an Army installation would require. Some of the requirements were specific to the test sites used in the study as noted below. The initial requirements were:

1. RMUs shall be able to read both on-potentials and instant-off potentials (IOPs) from 0-4 Volts with a resolution of 10 mV using an existing reference electrode permanently installed at each test site.
2. The manufacturer shall supply external relay control or other means necessary for RMUs to measure IOPs by interrupting the rectifier current. If possible, units shall be equipped to interrupt all of the same make units on site simultaneously.
3. RMUs shall be able to read rectifier voltages of 0-60 Volts DC (site-specific requirement) with a resolution of 100 mV.
4. RMUs shall be able to read rectifier DC amperage from 0-12 Amperes (site specific requirement) with a resolution of 100 mA.
5. RMUs shall be able to read rectifier AC voltage with a resolution of 1 Volt at a test point located after the rectifier circuit breaker. Units shall be supplied to operate from the specified AC voltage. (AC voltages of 120, 240, and 480 were tested.)
6. RMUs shall have a battery backup that will be used in the event of power failure.
7. RMUs shall notify the master PC when an "out of Limits" condition is measured and shall identify the location and nature of the problem ("alarm feature").
8. The manufacturer shall supply all software required to operate and monitor the RMU.

Table 1 lists the specific features of each RMU.

Evaluation of Equipment Accuracy at USACERL Test Site

One RMU from each of the three selected manufacturers was installed at the U. S. Army Construction Engineering Research Laboratories (USACERL) in Champaign, IL on an outdoor CP test facility. All tests were performed on a buried, uncoated steel pipe that was 3 inches in diameter and 40 feet in length. A permanent $Cu/CuSO_4$ reference cell was installed approximately 24 inches from the pipes at the pipeline depth. Two telephone lines were routed to the RMUs from a nearby building.

Measurements were gathered daily (Monday through Friday) to evaluate the accuracy of the equipment, both on site with independent meters as well as through the remote monitoring systems. The following readings were taken each day:

- Rectifier DC voltage (1) by each RMU and (2) by a digital multimeter (DMM).
- Rectifier DC current (1) by each RMU and (2) by the DMM.
- Rectifier AC voltage by each RMU.
- Pipe-to-soil "on" potential measurement (1) between each RMU and the permanent reference electrode, (2) between the DMM and permanent reference electrodes, and (3) between the

DMM and portable $Cu/CuSO_4$ reference electrode placed on the surface of the soil directly above the pipe.

- Pipe-to-soil IOP measurement (1) between each RMU and the permanent reference electrode, (2) between DMM and permanent reference electrodes, and (3) between DMM and portable $Cu/CuSO_4$ reference electrode placed on the surface of the soil directly above the pipe. For the measurements with the DMM, the rectifier current was interrupted by switching the rectifier off. The IOP reading was taken on the second meter update (typically less than 1 second) after the current was interrupted.

Rectifier settings (i.e., tap settings) were varied every few weeks throughout the test period to determine the effects on the various RMUs. During the final month of testing, on-potential and IOP measurements were taken with a waveform analyzer (WFA), a cathodic protection analyzer (CPA), and a portable oscilloscope, in addition to the RMUs and the DMM to provide an additional basis for comparison.

Evaluation of Equipment Accuracy at Army Installation Test Site

Two RMUs from each of the three manufacturers were installed on the CP system that protects the underground high temperature hot water distribution system at an Army installation in the northeastern United States. A permanent reference cell was buried 12 to 24 inches from the pipe at each location. To evaluate Unit A's full differential channel design, one of them was configured to monitor a dual-circuit rectifier which powered two separate CP systems on electrically isolated pipelines.

The accuracy of the remote monitoring equipment was checked immediately after it was installed by comparing the RMU readings with readings taken on-site with a graphical multimeter. RMU readings and on-site manual readings were taken within 5 minutes of each other so that the environmental conditions were approximately the same for both.

Measurements from this site were collected weekly by interrogating the RMUs remotely from USACERL. Four sets of readings were taken from each RMU during the interrogation, approximately 15 seconds apart. The four readings for each parameter were averaged and used as the weekly reading for that parameter. This technique was used consistently throughout the evaluation for RMU readings. Data was copied into a spreadsheet program for analysis and plotting. The following measurements were performed at each rectifier equipped with a remote monitoring system:

a. Rectifier DC voltage.
b. Rectifier DC current.
c. Rectifier AC voltage.
d. Pipe-to-soil on potential measurement.
e. Pipe-to-soil instant-off potential measurement.

A second site visit was performed in June 1996. Again, the accuracy of the remote monitoring equipment was checked by comparing the RMU readings with readings taken on-site with the graphical multimeter.

Evaluation of Software

Each manufacturer provided a Windows-based software package for use in configuring the RMUs and acquiring data. Software was evaluated based on the following factors:

- Ease of configuring the software and time required for installation
- Amount of technical support required
- Ease of operation (user friendliness)
- Software versatility: A good software package should be easily adaptable to a variety of situations and configurations. Evaluation of this capability involves questions such as: Can the software interrogate both single units and multiple units? Does the software allow remote configuration of the RMU? Does the software have an automatic alarm capability that will notify the operator if a problem has occurred with the CP system? Can the software to interrupt several rectifiers simultaneously (synchronized interruption)?
- Software appearance
- Help function: On-line help was evaluated for its usefulness and completeness.
- Data report format: This refers to the clarity, flexibility, and appearance of the standard data reports produced by the RMU software.
- Exportability: This refers to the ability of the software to organize and format data for use by other programs such as spreadsheets.
- Presence of an un-install feature

Evaluation of Hardware Features

Safety, surge protection, reliability of the relay which interrupts the CP current, and ability to program the RMU remotely from the master computer were several of the features considered.

Evaluation of Other Factors

Other factors were evaluated during the study. These included ease of hardware installation and quality of documentation..

Ranking of RMUs

A hardware matrix and a software matrix were developed to rank the RMUs according to the evaluated features. Each feature was assigned a weighting factor on a scale of 1 to 10 based on its importance, with the most important features receiving a factor of 10. Each RMU system received a grade for each feature on a scale of 1 to 5, where 5 was considered excellent, 4 was considered very good, 3 was considered average, 2 was considered acceptable, and 1 was considered unacceptable. To obtain the score for each feature, the weighting factor was multiplied by the grade. The scores for each RMU were then added to obtain a hardware score

and a software score. The hardware and software scores were added to obtain an overall score. Using this scoring system, the highest and lowest possible scores for hardware or software were 250 and 50 respectively. The highest and lowest possible overall scores were 500 and 100 respectively.

RESULTS

Evaluation of Equipment Accuracy

Figures 1 through 4 show the weekly average results of the testing at the USACERL test site. Measurements taken during the Army installation site visits are shown in Table 2.

Unit A- Unit A accurately tracked rectifier outputs, on potentials, and IOPs at the CERL test site. Any fluctuations were linear and were readily correctable with calibration. During the last month of the evaluation, where IOPs were taken with the CPA, portable oscilloscope and WFA, it was determined that the IOPs gathered with the DMM were slightly inaccurate (Figure 5). The IOPs taken with the DMM were regularly 100 to 200 mV less negative than the IOPs provided by the CPA, WFA, and oscilloscope. The measurement methodology was changed in Unit A by altering the unit sampling rate to 200 milliseconds for the remainder of the evaluation. Its readings then closely corresponded to those taken by the more accurate WFA and CPA.

At the Army installation test site, the readings that were taken on-site with the graphical multimeter in December and June 1996 matched almost exactly with the readings taken remotely on the same day with Unit A. Weekly on-site readings from the Army installation were not available for comparison with the readings taken remotely from USACERL, however, each Unit A gave readings every time it was contacted, and those readings were within the range of values that would be expected during normal CP system operation.

Unit B- Readings taken by Unit B typically fluctuated somewhat from the control voltages taken with the DMM. Rectifier voltage output measurements varied up to 2 Volts from the voltages taken with the DMM. In addition, IOPs were occasionally more negative than the "on" readings. Unit B manufacturers stated that the problem was due to faulty calibration, but the problem persisted throughout the evaluation despite unit recalibration. Troubleshooting solved some of the problems. However, there was never a time in the evaluation where every channel on Unit B consistently provided accurate readings. The units were out of service for several long periods of time and data is not presented for those intervals.

As stated previously, during the last month of the evaluation it was determined that the IOPs gathered with the DMM were slightly inaccurate. The measurement methodology was changed for Unit B by altering the unit sampling rate to 10 milliseconds for the remainder of the evaluation. The readings then corresponded to those taken by the more accurate WFA and CPA.

Unit C- Unit C did not provide any accurate readings during the evaluation period, therefore its accuracy was rated as unacceptable.

Evaluation of Software

Software Loading and Configuration- All software loaded in 1 to 5 minutes. Unit B's software was easy to configure without any assistance from the manufacturer. Unit A's software was relatively easy to configure with the telephone support provided by the manufacturer. Furthermore, Manufacturer A had a control unit at their offices that could be used to assist in configuring RMUs remotely. Unit C's software could not be completely configured because the RMUs did not operate.

Technical Support- Technical support was found to be an important consideration. Availability of toll-free support is also an advantage. The manufacturer with the best technical support had a toll-free number and knowledgeable engineers who returned calls quickly. The manufacturer with the lowest rating on technical support did not have a toll-free number and sometimes took several days to return calls.

Ease of Operation- All software was Windows-based. Unit A's software was relatively user friendly. Unit B's software was extremely user friendly; however, this may have been due to its somewhat limited capabilities. Both packages were attractive and organized in a manner that most users, novice and experienced, should find easy to operate. The Unit C software appeared to be user friendly, but it could not be fully evaluated because the RMUs did not function.

Software Versatility- Unit A software allowed the monitoring of either single or multiple units, and could configure the units remotely. According to the manufacturer, alarm reporting capabilities and synchronized interruption of multiple RMUs would appear in the next version of the software. Unit B's software was considered adequate for monitoring one RMU at a time, but was incapable of automatically interrogating multiple units. In addition, the Unit B software cannot configure an RMU remotely. The lack of flexibility in handling multiple units simultaneously would be awkward for monitoring CP systems with multiple rectifiers on a single piping network. Unit B's manufacturer claimed that it had alarm reporting capabilities, but this capability could not be made to function during this test. Unit B did not have synchronized interrupt capabilities, and the manufacturer did not plan to add it. Unit C's software versatility was never fully evaluated because none of the RMUs were operational. A review of the functions available in the software provided evidence that the software may be marginally adequate, although it did not have alarm reporting or synchronized interrupt capabilities.

Help Function- Unit A and Unit B software both had comprehensive on-line help. In some cases, the help function provided very detailed information that was much more complete than the actual software manual. Unit C's software had on-line help that was only slightly better than the rudimentary user manual.

Data Report Format- Unit A's data reports were extremely clear and easy to read. The output file was in comma delimited text format and could be imported into a variety of spreadsheet or word processing software. Data from each individual Unit A was stored on the master computer in a separate file, and the software allowed the user to create a file containing a

subset of data that was measured during a user-specified range of dates. The software also contained an automated graphing function which allowed data to be analyzed immediately without importing it into a spreadsheet program. Unit B's standard data reports were relatively simple. The data was automatically maintained by the software in a format that may not be clear and easy to understand if multiple units are being interrogated because it is stored sequentially in a common file by date of interrogation. Sorting or extracting subsets of data was not possible except by exporting the data to a spreadsheet program. The standard data reports provided by the Unit C software were not evaluated as none of the units were fully operational.

Un-install Feature- Only Unit A had a built-in un-install feature which quickly and automatically removed the program and its subdirectories, and made the necessary changes in the Windows configuration files. This could be a problem for novice computer users if the software ever needed to be removed from the computer.

Evaluation of Hardware Features

Unit A- Unit A experienced only one hardware problem during the test period, and it was caused by an oversight during installation. The installer did not connect the internal backup battery. A power outage occurred and Unit A reset itself automatically, so its time setting was different from the master computer's time setting. The problem was corrected by connecting the back-up battery and synchronizing the time settings between the master PC and Unit A.

Unit A was the only RMU with surge protection on all of its inputs and outputs. It remained fully functional through several power losses and surges during the evaluation period except for times when there were problems with site telecommunication. Unit A was the only RMU with full differential channels; the unit that was set up to monitor two isolated structures simultaneously performed successfully and reliably throughout the evaluation. Unit A's ferroelectric random access memory (FRAM) was found to provide an advantage in that the unit could be reprogrammed and problems could be diagnosed from a remote PC. Unit A was the only unit supplied with a magnetic relay. The relay operated correctly throughout the evaluation.

Unit B- As stated earlier, Unit B often made inaccurate readings. Recalibration did not solve the problem. Detailed troubleshooting revealed some hardware problems that were most likely the cause of the inaccurate readings. The most serious problem in Unit B was in the relay switch that interrupts the CP current during an IOP reading. The relay regularly stuck in the open position when an IOP reading was attempted at the Army installation test site, thereby leaving the structure without cathodic protection. This occurred even though Unit B's relay was rated at 20 A and the currents at the test site never exceeded 12 A. The problem was not experienced at the CERL site where the maximum current was on the order of 1.5 A. It is believed that the relay problem was partially responsible for the extreme variations in the IR-Free readings that were observed throughout the evaluation. Unit B had a spring loaded solenoid-type relay.

The cause of the problem with receiving acceptable IR-Free readings with Unit B at the CERL test site was discovered inadvertently while troubleshooting another problem. One of the

jumper switches in the unit was missing. After installation of the jumper, relatively accurate IR-Free readings were achieved at the CERL site. The units at the Army installation possessed the jumper switch, so this did not contribute to their problems with accurate readings.

Another problem with unit B was the lack of surge protection on RMU inputs and outputs. It is likely that the lack of surge protection caused two malfunctions at the CERL test site. In one case, a power surge apparently occurred along the phone lines at CERL during a lightning storm. The ground for Unit B's modem burned and curled up on the circuit board due to the power surge. As a result, the modem continually emitted a signal that interfered with the telephone communication to the other monitored units. The problem was fixed by replacing the circuit board. Another problem occurred at the same time as the modem problem. In the process of adjusting rectifier settings at the CERL test site, the pipe-to-soil potential momentarily surged higher than 4.0 V dc. The diodes which are used in processing the reference cell voltages malfunctioned as a result of the overload. The result of this problem was a complete failure in receiving a reliable reference cell voltage and large fluctuations in other readings. Replacement of the circuit board solved this problem.

Unit C- There were major hardware problems with Unit C. Only one Unit C responded one time to modem calls throughout the evaluation. The readings on this unit were on the order of 600 V for an actual rectifier voltage of 24 VDC. The other units were completely inoperative. The relays that were supplied for Unit C were in the "normally open" position. This means that if power to the unit was interrupted, the relay would open the CP circuit and leave the structure unprotected. The unit that answered modem calls had too large of a relay; the clicking caused by the activation of the relay could be heard over 200 ft. away. Unit C did not have a safety ground for lightning protection. The units also did not have breaker connections or safety disconnects.

Evaluation of Other Factors

Ease of Installation- Units A and B were relatively easy to install, however, there were minor problems with both. The configuration of the case enclosing Unit A and the relay did not provide adequate space for making the required connections. The unit had to be removed from the case. On one Unit B installed at the Army post, a component on the circuit board was partially out of its slot. The unit did not function properly until the component was reseated into the correct position. Unit C was difficult to install, primarily to the lack of an installation manual. The unit had to be opened and the various circuits had to be traced to determine how the unit was to be installed.

Documentation- Hardware manuals for Units A and B were complete and easy to follow, however, supplemental installation instructions were prepared to assist electricians who were unfamiliar with CP RMUs in making the proper connections. There was no hardware manual available for Unit C. Software manuals for Units A and B were complete and easy to follow, and included examples illustrating the use of commands. The software manual for Unit C was unclear and would be difficult for all but the most experienced computer and RMU users to

follow.

Ranking of RMUs

The hardware and software matrices used to rank the RMUs are shown in Tables 3 and 4. Unit A received the highest (best) rating with an overall score of 418. Unit C received the lowest rating with an overall score of 124.

CONCLUSIONS

Three different commercially available impressed current CP remote monitoring systems were evaluated. Unit A was the only evaluated RMU that was found to be fully operational, accurate, and reliable during the test period. Unit B was not fully functional and did not regularly provide accurate and reliable data during the test period. It sometimes provided inaccurate or fluctuating data, and several hardware problems impacted the unit's reliability. Unit B could provide an acceptable level of service for locations with a limited number of RMUs, but only after additional modifications are made by the manufacturer to fix the problems noted. Unit C was not yet operational at the conclusion of the tests. It is not expected that it will be available for use in the near future.

Several features were found to be particularly important in terms of overall RMU performance. These included:

- Type of relay used to interrupt protective current: In this study, units with magnetic relays performed better than units with spring-loaded solenoids.
- Surge protection: Units with surge protection on all inputs and outputs (including data channels, power, and telephone) performed most reliably.
- Channel type: Presence of full differential channels was found to be an advantage when monitoring isolated structures with the same RMU.

REFERENCES

Code of Federal Regulations (CFR), title 40, parts 280-281.

Code of Federal Regulations (CFR), title 49, part 192, subpart I.

Engineer Technical Letter (ETL) 1110-3-474, *Cathodic Protection* (Headquarters, Department of the Army, 14 July 1995).

Standard Recommended Practice RP0169-96, *Control of External Corrosion on Underground or Submerged Metallic Piping Systems* (NACE International, September 1996).

Table 1. Comparison of RMU Features.

Characteristic	Unit A	Unit B	Unit C
Circuitry	100% solid state	100% solid state	100% solid state
Component Grade	100% industrial	industrial	industrial
No. of Data Channels	3, 4, 6, or 8	8	4 or 8
Call Up Addressable	Yes	Yes	Yes
Data Channel Type	Full Differential	Common Ground	Differential
Standard DC Voltage Ranges	300V, 40V, 4V, 400mV	0-4 Volts	160V, 2.5V, 160mV, 40mV
Standard AC Voltage Ranges	240V, 40V, 4V, 400mV	250 Volts	Not Available
Optional DC Voltage Ranges	4 & 40 millivolt	None	Not Available
Input Impedance	10 megohms, standard ranges	10 megohms, standard ranges	100 megohms
Autoranging	Yes	No	No
Software Selectable Ranges	Yes	No	Yes
Hardware Selectable Ranges	Not Required	No	Yes
CP Equipment Independent	Yes	Yes	Yes
Country of Manufacture	USA	USA	USA
Power Supply	120 or 240 Volt AC	120 Volt AC	120 or 240 Volt AC
Battery Backup	1200 mA Hour 9 Volt Lithium	Yes	190mAH
Power Supply Lightning Protection	Yes	No	No
Phone Line Lightning Protection	Yes	No	No
Data Channel Lightning Protection	Yes	No	Yes
Cost Per Channel, Base Unit	$100 to $300	$100 to $200	$125 to $250
Data Memory	8 Kbytes Non Volatile FRAM	16 Kbytes	128 Kbytes
Stored Data Volatile	No	Yes	Yes
Program Storage	Flash Ram	EPROM	EPROM
Modem Included	Yes	Yes	Yes
Hayes Compatible	Yes	Yes	Yes
Modem Rate	2400 Baud Standard	2400	2400
Error Checking Protocol	Proprietary	Proprietary	16 CRC, Sequence Num.
Data Transmission	Full Duplex	Half Duplex	Half Duplex
Auto Call	Yes	Yes	Yes
Instant Off Potential	Yes	Yes	Yes
Case	Aluminum	All Metal	No, extra cost option
Software Base	Windows	Windows	Windows
Software Flexibility	Yes	Yes	Yes
OLE 2.0 Compliance	No	No	No
ODBE Compliance	No	No	No
Graphical Data Analysis	By Export to Excel, Lotus, etc.	By Export to Excel, Lotus, etc.	By Export to Excel, Lotus, etc.
Installation/Removal Requirements	Waterproof Quick Disconnect	Screw Type Terminal Strip	Screw Type Terminal Strip
Temperature Rating	Degrees C, -40 to +85	Degrees C, -30 to +80	Degrees C, -40 to +70
Humidity Rating	100% Hosedown	90%	To be Determined
UL Listing	Yes	No	No
Warranty	1 Year Parts and Labor	1 Year Parts and Labor	1 Year Parts and Labor
12 Month Lease Rate	$400 per unit/includes software	$400 per unit/includes software	$250 per unit/includes software

Table 2. Army installation field data.

	Unit A Bldg. 11050		Unit A Bldg. 10030 Circuit #1		Unit A Bldg. 10030 Circuit #2		Unit B Bldg. 4405		Unit B Bldg. 10612	
	RMU	IM	RMU	IM	RMU	IM	RMU	IM	RMU	IM
Rect. Output Voltage (V)										
14 Dec 1995	59.4	58.8	N/I	N/I	N/I	N/I	37.4	54.7	N\I	N/I
18 Jun 1996	58.4	58.3	56.5	56.8	57.4	57.8	N/O	N/O	N/O	N/O
07 Aug 1996	N/R	N/R	N/R	N/R	N/R	N/R	0.0	42.8	41.1	60.0
Rect. Output Current (A)										
14 Dec 1995	0.86	1.05	N/I	N/I	N/I	N/I	37.2	11.36	N/I	N/I
18 Jun 1996	0.69	0.66	6.63	6.60	2.64	2.64	N/O	N/O	N/O	N/O
07 Aug 1996	N/R	N/R	N/R	N/R	N/R	N/R	107.9	10.3	0.44	1.80
Pipe to Soil "On" Potential (-V)										
14 Dec 1995	1.16	1.20	N/I	N/I	N/I	N/I	0.80	1.16	N/I	N/I
18 Jun 1996	1.068	1.078	1.647	1.65	1.647	1.65	N/O	N/O	N/O	N/O
07 Aug 1996	N/R	N/R	N/R	N/R	N/R	N/R	1.857	1.798	0.916	1.047
Pipe to Soil IOP (-V)										
14 Dec 1995	1.10	1.10	N/I	N/I	N/I	N/I	0.87	0.98	N/I	N/I
18 Jun 1996	0.989	0.991	1.417	1.42	1.419	1.42	N/O	N/O	N/O	N/O
07 Aug 1996	N/R	N/R	N/R	N/R	N/R	N/R	1.588	1.499	0.654	0.760

IM = reading taken with independent meter (control)
N/I = unit not yet installed on this date
N/O = unit installed but not operable on this date
N/R = unit not read on this date

Table 3. Hardware matrix.

Feature	**Factor**	**Unit A**		**Unit B**		**Unit C**	
		Rating	**Score**	**Rating**	**Score**	**Rating**	**Score**
Hardware manual	2	4	8	3	6	1	2
Ease of installation	3	4	12	3	9	1	3
Safety (high voltage exposed)	5	1	5	1	5	1	5
Safety warning labels	3	1	3	1	3	1	3
Technical support (hardware)	5	5	25	2	10	1	5
Interrupter relay	5	5	25	1	5	1*	5
Data accuracy	10	5	50	1	10	1*	10
Reliability	10	4	40	2	20	1*	10
Surge/ lightning protection	5	5	25	2	10	1*	10
Remote programming	2	5	10	1	2	1*	2
Hardware Score			**203**		**80**		**50**

* = could not be rated due to inoperative status of unit C

Table 4. Software matrix

FEATURE	Factor	Unit A		Unit B		Unit C	
		Rating	Score	Rating	Score	Rating	Score
Software manual	1	3	3	5	5	3	3
Software manual (novices)	1	1	1	5	5	1	1
Software manual (experts)	1	3	3	5	5	3	3
Technical support (software)	5	5	25	3	15	1	5
Toll free number	1	5	5	5	5	1	1
Software operation	5	4	20	2	10	1[A]	5[A]
Software loading	1	5	5	5	5	3	3
Software configuration	2	5	10	2	4	1[A]	2[A]
Software versatility	5	5	25	2	10	1[A]	5[A]
Software appearance	2	5	10	2	4	5	10
Help function	2	5	10	5	10	1	2
Ease of operation (single unit)	2	4	8	5	10	1[A]	2[A]
Ease of operation (multiple units)	4	5	20	2	8	1[A]	4[A]
Data report format	3	5	15	2	6	1[A]	3[A]
Exportability to MS Excel	2	5	10	2	4	1[A]	2[A]
Spreadsheet formatting	2	5	10	2	4	1[A]	2[A]
Alarm capability	5	3[B]	15[B]	3[C]	15[C]	3[A]	15[A]
Synchronized interruption	5	3[D]	15[D]	1	5	1[A]	5[A]
Un-install feature	1	5	5	1	1	1	1
Software Score			**215**		**131**		**74**

A: Unable to evaluate due to non-operational condition of Unit C
B: Alarms available in latest Unit A software version, unable to verify during this evaluation.
C: Unable to verify due to malfunction in Unit B.
D: Next version of Unit A software to have this feature.

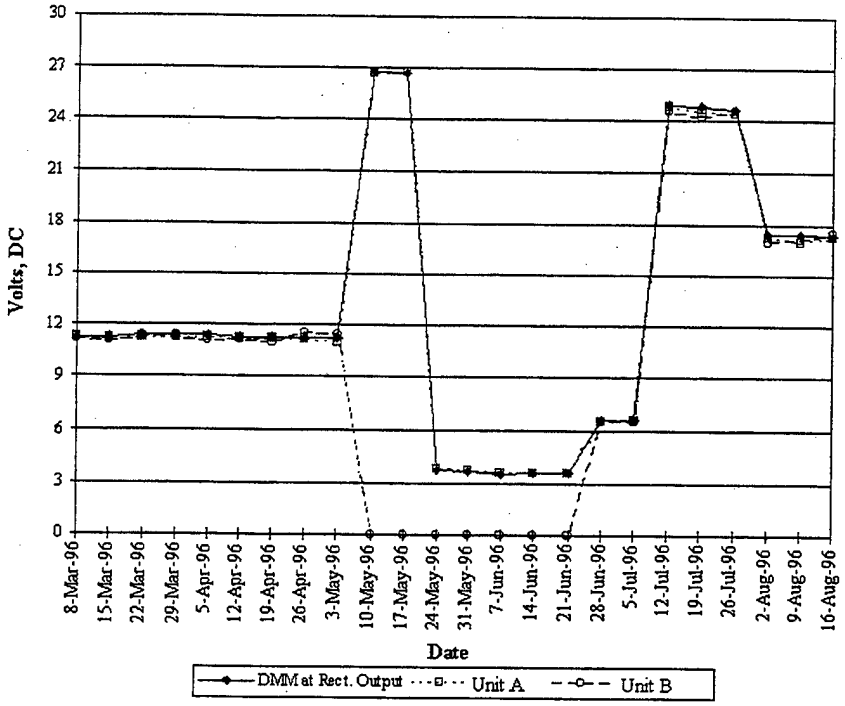


Figure 1: Weekly average rectifier output voltage at USACERL test site.

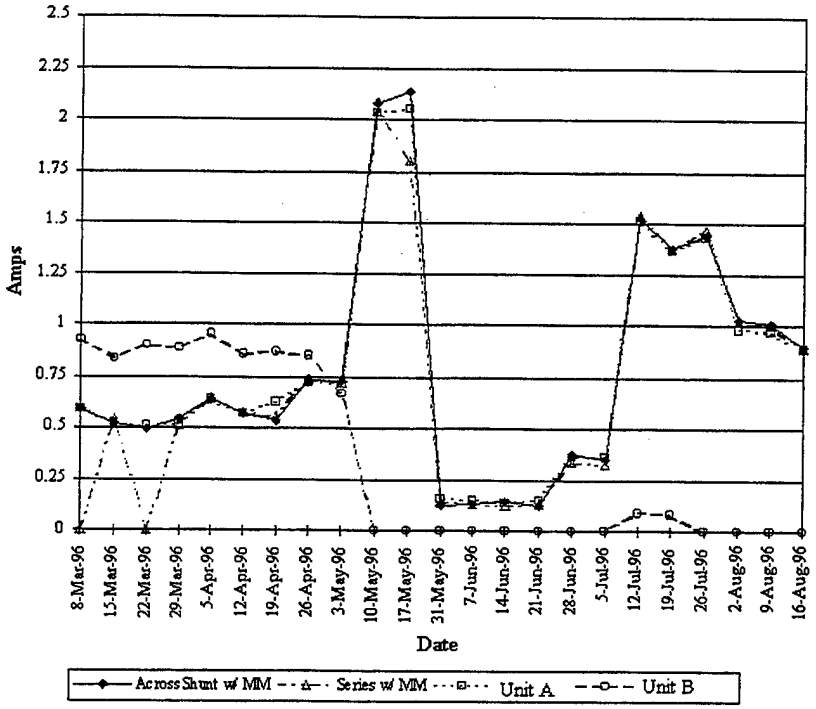


Figure 2: Weekly average rectifier current at USACERL test site.

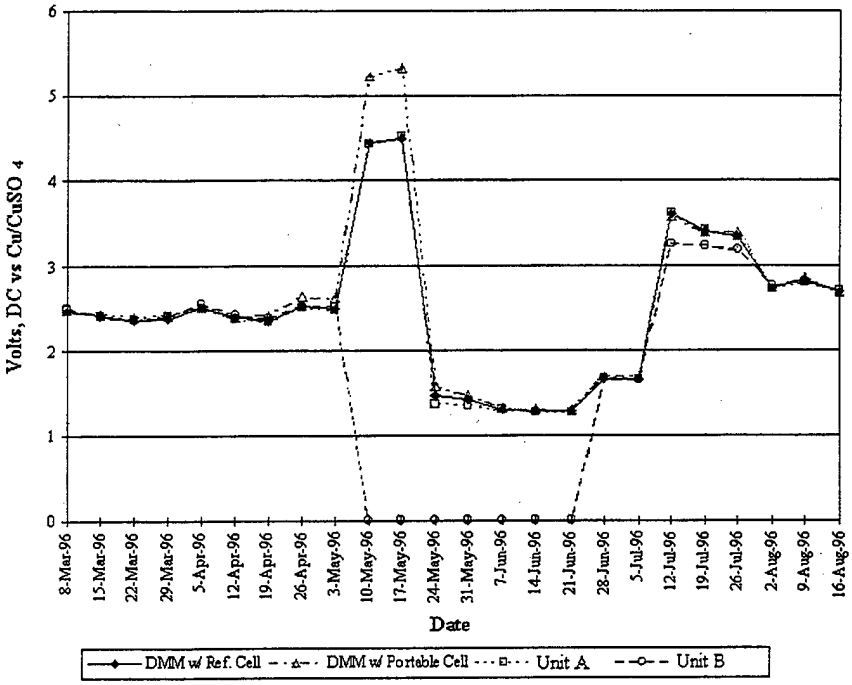


Figure 3. Structure-to-soil "on" potential at USACERL test site.

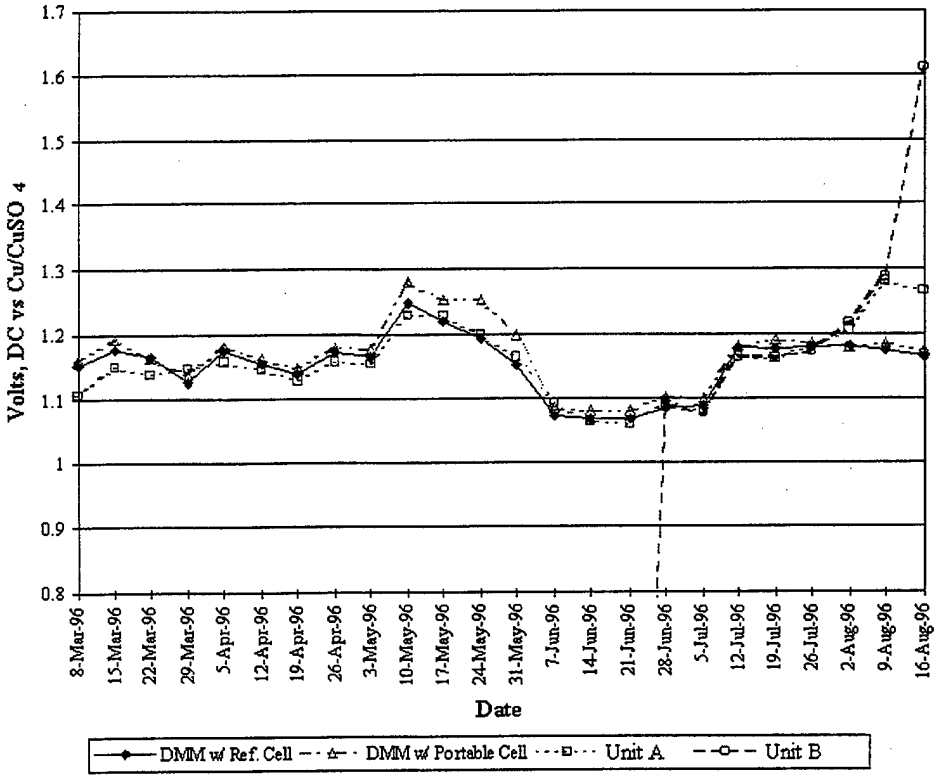


Figure 4. Structure-to-soil IOP at USACERL test site.

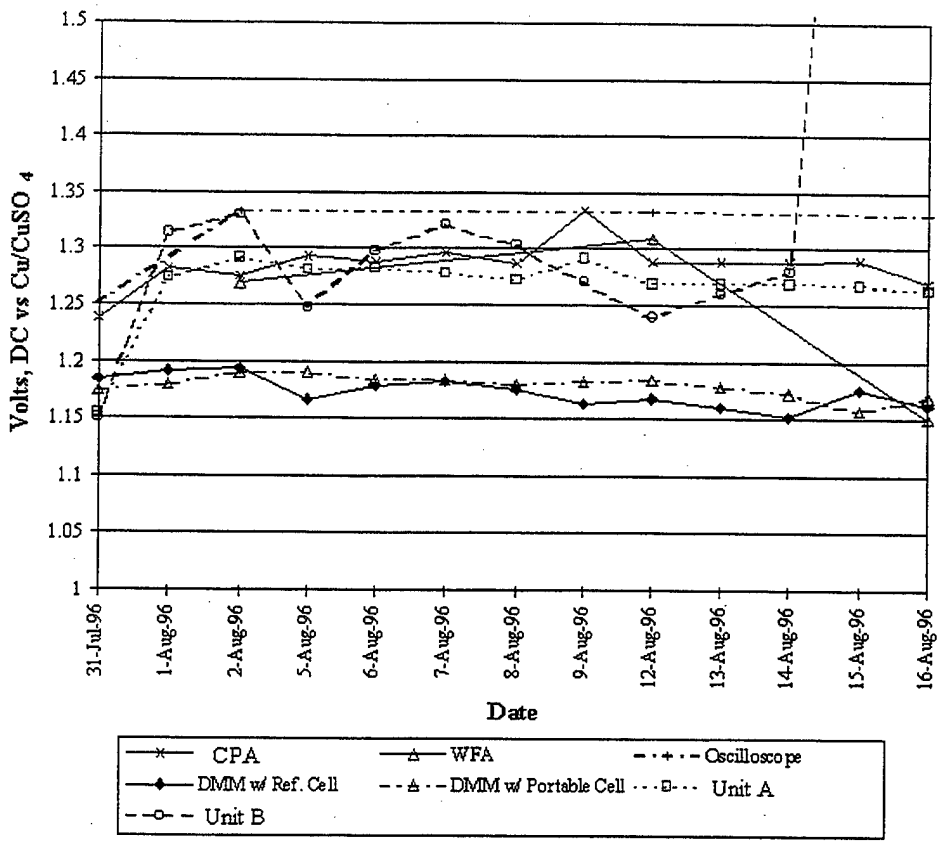


Figure 5: IOPs using various instruments at USACERL test site.

FLUORESCENCE-BASED CORROSION INDICATORS: EXPLORATION OF SCHIFF-BASE COMPOUNDS

Krishna S. Rajan and Fred Daniel
IIT Research Institute, Chicago, IL 60616

Richard E. Johnson
LeTourneau University, Longview, TX 75607

Vinod S. Agarwala
Naval Air Warfare Center, Aircraft Division
Patuxent River, MD, 20670

ABSTRACT

Studies have been undertaken with a view to explore a number of selected Schiff-base compounds as potential fluorescence-based indicators for metal surface corrosion. The underlying technical approach involves an examination of (i) their reversible oxidation/reduction and metal chelation due to co-occurring surface corrosion reactions; and (ii) the resultant production of strong fluorescence. Six different Schiff-base compounds derived from substituted aminoanthraquinones and salicylaldehyde (and terephalaldehyde) were prepared and characterized for their fluorescence spectral characteristics. Results of this research are presented and the potential of the underlying technical approach discussed.

BACKGROUND

A critical review of the work done so far of fluorescence-producing compounds (dyes and others) for surface corrosion detection indicates that even the most satisfactory ones among them appear to undergo chemical interactions with the surface-borne aluminum oxide film as well as the aluminum ion contamination in paints (primers and top coats), and yield fluorescence even under non-corrosion conditions. A search for compounds that would go from non-fluorescence under normal surface conditions to strong fluorescence under conditions of surface corrosion has been initiated through this research. The technical approach in this research involves the exploration of the Schiff-bases, as a special class of compounds, that could lend themselves to reversible oxidation/reduction due to co-occurring surface corrosion reactions and at the same time could lend themselves to yielding strong fluorescence from an initial non-fluorescence.

Alternately, the selected Schiff-base compounds could produce strong fluorescence as a result of chelation reactions with metal ions such as Al, Ti and Fe released due to surface reactions.

Since Schiff-bases are composed of (1) a primary amine component and (2) an aldehyde component each of which is attached to an aromatic backbone, they are open to a wide range of functional group substitutions. They, therefore, constitute an interesting group of compounds that could be explored for their redox and chelation interactions associated with fluorescence.

EXPERIMENTAL

In accordance with the technical approach outlined above, a number of Schiff-base compounds were designed and synthesized. Salicylaldehyde and terephthalaldehyde constituted the aldehydic compounds. The primary amines used for reacting with the two aldehydes were the following: (1) 1,2-diaminoanthraquinone (**1,2-DAAQ**); (2) 2,6-diaminoanthraquinone (**2,6-DAAQ**); (3) 1,4-diaminoanthraquinone (**1,4-DAAQ**); (4) 1,5-diaminoanthraquinone (**1,5-DAAQ**); (5) 1,5-diamino-4,8-dihydroxyanthraquinone (**1,5-DADHAQ**); (6) 2-aminobenzophenone (**2-ABPh**); and (7) 3,4-diaminobenzophenone (**3,4-DABPh**). All the amines and aldehydes listed above were procured from domestic commercial sources.

Synthesis of Schiff-Bases

All the Schiff-based compounds designed for this research were prepared by the condensation of each of the aldehyde components with the selected amine components under anhydrous conditions. The procedure described below is generally applicable to each one of the Schiff-base compounds.

A three-necked flask of suitable capacity is fitted with a condenser and a pressure-equalizing separatory funnel. The third neck is fitted with a calcium chloride guard tube. A known quantity of the aldehyde compound is taken in the flask to which required amounts of dimethylformamide (DMF), or any other selected solvent, is added and stirred. Calculated quantity of the diamine (2 moles of the aldehyde per mole of diamine or 1 mole of the aldehyde per mole of monoamine) is dissolved in DMF (or other solvents) separately and is added dropwise to the agitated (using magnetic stirrer) aldehyde in the reaction flask at room temperature. At the end of the addition, the reaction mixture is then warmed to 60-70°C and

maintained at this temperature overnight. The reaction mixture is allowed to come to room temperature and the solid compound (Schiff-base) separating in the reaction flask is then filtered into a Buchner funnel. The solid product is washed with small amounts of ether and dried under vacuum. The molecular structures of a few of the Schiff-bases thus synthesized are shown in Figure 1.

Fluorescence Measurements

Fluorescence emission of the Schiff-base compounds were generated by exposure to visible photo flood lamp and ultraviolet light and photographed with automatic exposure on a camera. Fluorescence screening was done by using each of the solid Schiff-bases alone and under an epoxy primer coating.

Cyclic Voltametry (CV)

This consisted of a potentiostat interphased with a 486 PC computer and related software. (The system is CMS 100 from Gamry Instruments, Willow Grove, PA.) The electrochemical cell (shown in Figure 2) consists of a platinum working electrode, a graphite counter electrode and a standard calomel electrode as the reference electrode.

RESULTS AND DISCUSSION

Fluorescence of Schiff-Bases

Test coupons of 7075 chrome conversion coated alloy plates were cleaned with isopropanol and prepared for epoxy primer coating. A small amount of Schiff-base was spread on the alloy surface and standard Navy epoxy primer paint was mixed and dropped onto the surface. The clear paint (in methylethylketone solvent) spread on the surface satisfactorily. The samples were then observed under white and UV radiation. A summary of the observations is given in Table 1 (illustrated in Figures 3a and 3b) for pure solid Schiff-bases and for the solid samples under epoxy primer coating. The two Schiff-base compounds that fluoresced were, 2-aminoanthraquinone with salicylaldehyde (**2-AAQS**) and 2,6 diaminoanthraquinone with salicylaldehyde (**2,6-DAAQS**).

Table 1. Fluorescence Characteristics of Schiff-Base Compounds

Schiff-Base Compounds	Solid Alone		Solid Under Epoxy Paint	
	Visible Light	UV Light	Visible Light	UV Light
1,2DAAQS*	Purple	None	Purple	Red
2AAQS	Green	Red	Brown	Yellow
2,6DAAQS	Tan	Orange	Brown	Orange
2,6DAAQT*	Tan	None	Brown	Yellow
1,5DAAQS	Maroon	None	Orange	Orange
1,5DAAQT	Red	None	Orange	Orange

* S = Salicylaldehyde; T = terephthalaldehyde

Both these compounds were reduced by two alternate methods, i.e., (1) interacting an isopropanolic solution of the Schiff-base in the presence of palladium on carbon and (ii) reacting an alkaline (aqueous) solution of the compounds with sodium borohydride. In the latter case the reduced form of the Schiff-bases are soluble in water as the sodium salt. Fluorescence emission spectra of the two compounds are shown in Figures 4 and 5. The normal oxidized form of **2,6-DAAQS** (Figure 4) with an emission peak at 580 nm, shifts to a peak emission at about 480 nm. with a shoulder peak at 550 nm on reduction. On reoxidation, the 480 nm peak decreases and the 550 nm shoulder peak increases.

The fluorescence spectra of **2-AAQS** exhibits an emission peak at 550 nm with an emission peak at 480 nm and a shoulder at 570 nm for its reduced form.

Cyclic Voltammetry

Samples of the Schiff-bases, **2-AAQS** (0.150 g) and **2,6-DAAQS** (0.165 g) dissolved in 75 mL dioxane (and 75 mL 1.0 M KNO_3) were subjected to cyclic voltametric analysis using the scan range, 1 V to -0.6 V to 1 V to 1 V, 100 mV/s, 2 mV/pt. The cyclic voltametry of potassium ferri-cyanide (0.1 M in 1 M KNO_3) was carried out and used as a comparison. The results indicated only small changes in the cyclic voltametric profiles of **2-AAQS** and **2,6-DAAQS**.

Conclusion

Among the Schiff-bases (designed and synthesized) explored in this study, two compounds, viz, **2-AAQS** and **2,6-DAAQS** have exhibited a change in fluorescence when they were reduced and reoxidized. This was observed by color photography as well as spectro-fluormetric measurements. Further when they were incorporated into Navy's epoxy primer coating on 7075 alloy (chromium conversion coated) surface, they exhibited reversible oxidation-reduction reaction with the associated change in fluorescence emission. However, the effects were small. Likewise, their cyclic voltametric profiles indicated only small changes. More Schiff-base compounds are being designed and synthesized with the objective of enhancing the desired effects.

Acknowledgement

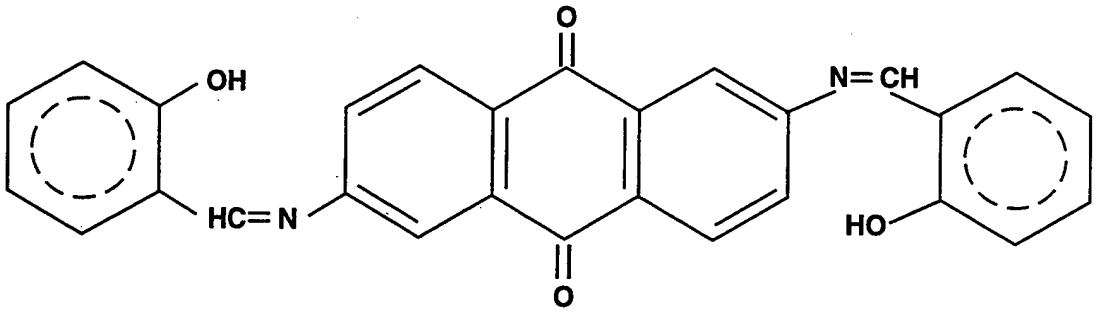
This research was sponsored by U. S. Naval Air Warfare Center, Aircraft Division, Patuxent River, Maryland under contract No. N00421-96-C-5055.

REFERENCES

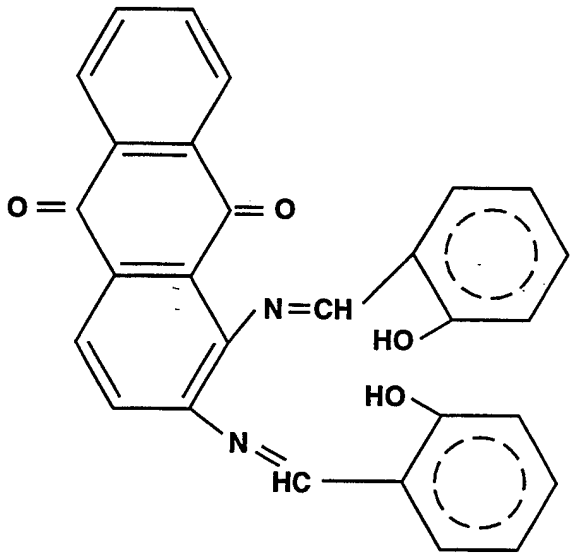
1. V. S. Agarwala, "Chemical Sensors for Integrity of Coatings" Proc. of Tri-Service Conference on Corrosion, Plymouth, MA, Editor: M. Levy (Watertown, MA, U.S. Army Materials Tech Lab, 1992), pp. 341-349.

2. R. E. Johnson and V. S. Agarwala, "The Use of Fluorescent Compounds and Complexes of Metals As Early Warning Detectors for Corrosion." Paper No. 332, CORROSION/94, Baltimore, MD, Materials Performance, 25-29, 1994.

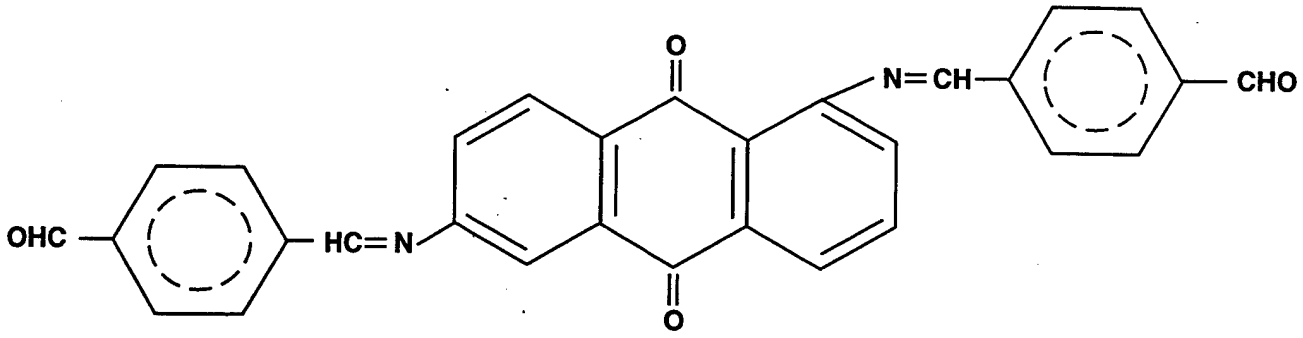
3. R. E. Johnson and V. S. Agarwala, "Development of Florescent Metal-Ligand Complexes As Smart Coating Sensors for Corrosion." Progress Report (1995) to U. S. Naval Air Warfare Center, Patuxent River, MD.



SCHIFF BASE OF 2,6-DIAMINOANTHRAQUINONE WITH SALISYLALDEHYDE (2,6-DAAQS)



SCHIFF BASE OF 1,2-DIAMINOANTHRAQUINONE WITH SALICYLALDEHYDE (1,2-DAAQS)



SCHIFF BASE OF 1,5-DIAMINOANTHRAQUINONE WITH TEREPHTHALALDEHYDE (1,5-DAAQT)

FIGURE 1. SCHIFF BASES OF AMINOANTHRAQUINONES

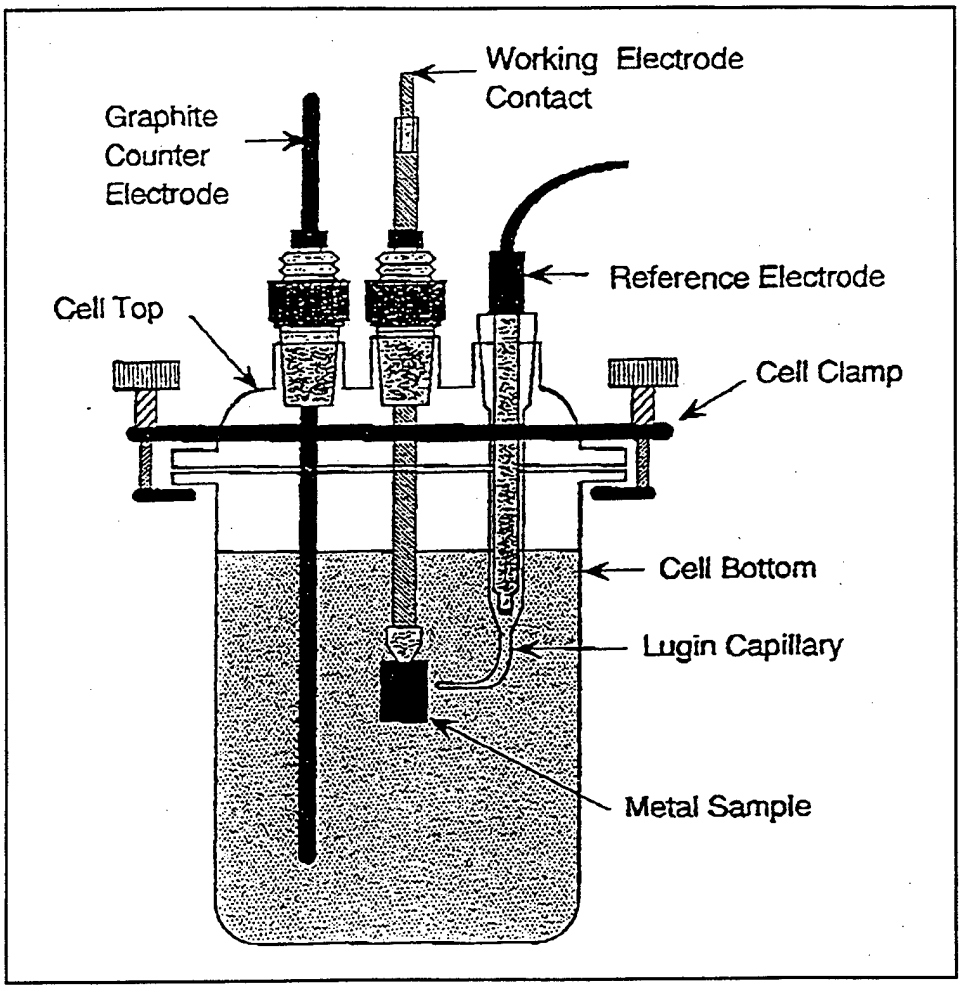


Figure 2 Electrochemical cell for cyclic voltametric analysis of Schiff bases

Figure 3b Fluorescence of Additional Schiff Bases in Epoxy Primer Coatings on 7075 Aluminum Alloy Plates.

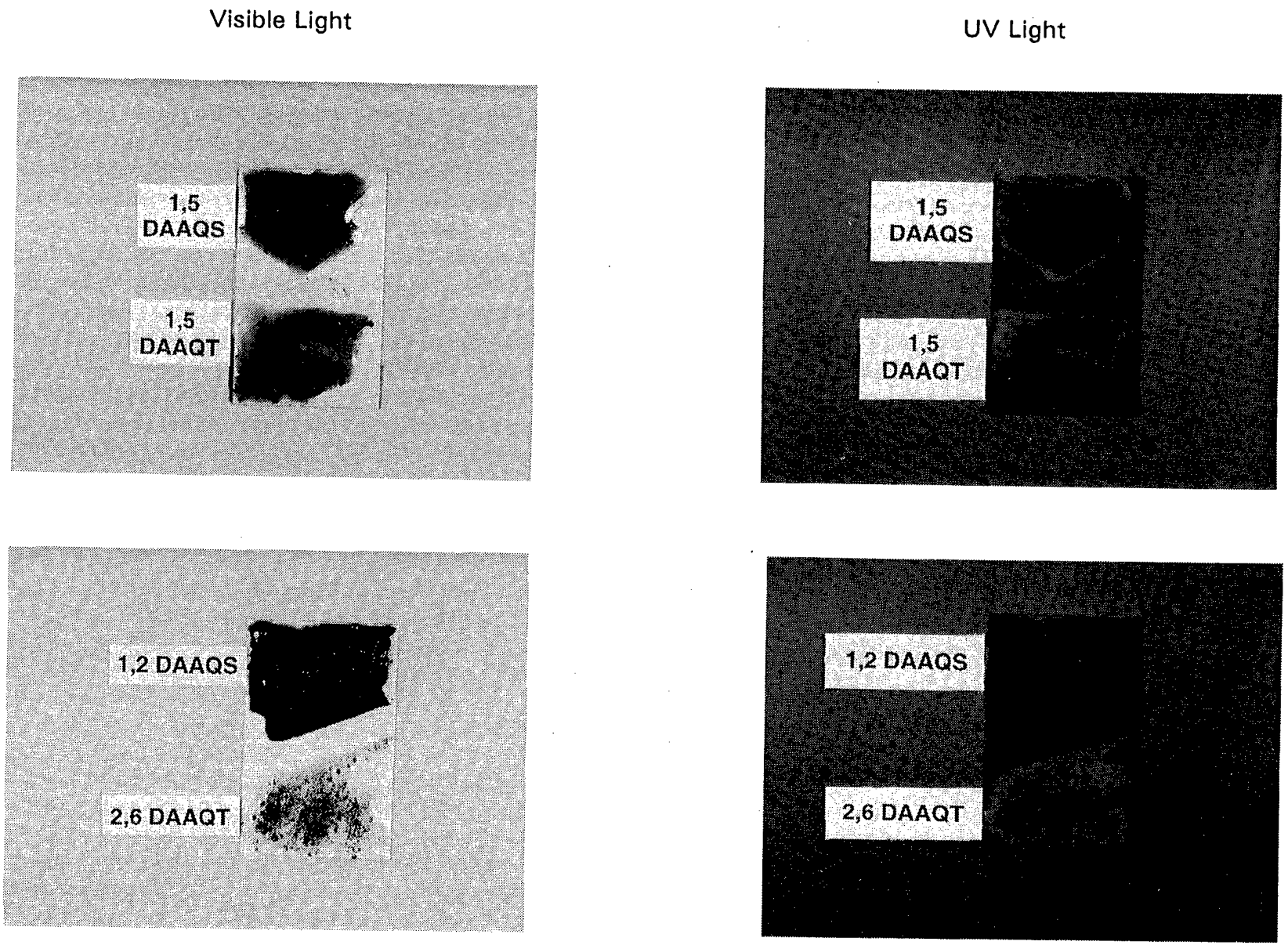
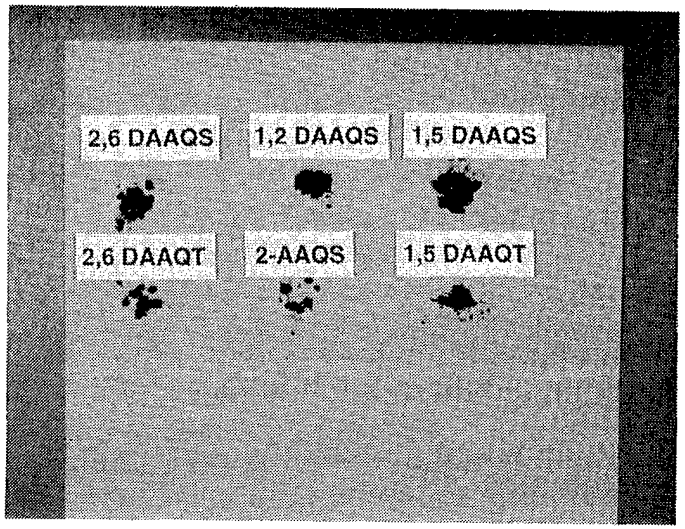
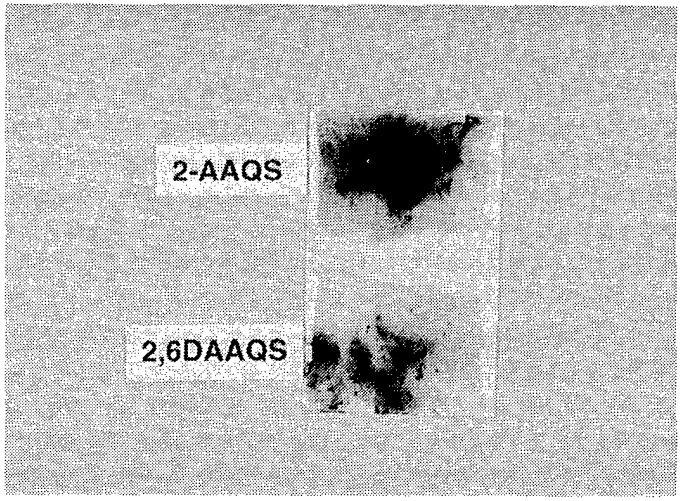


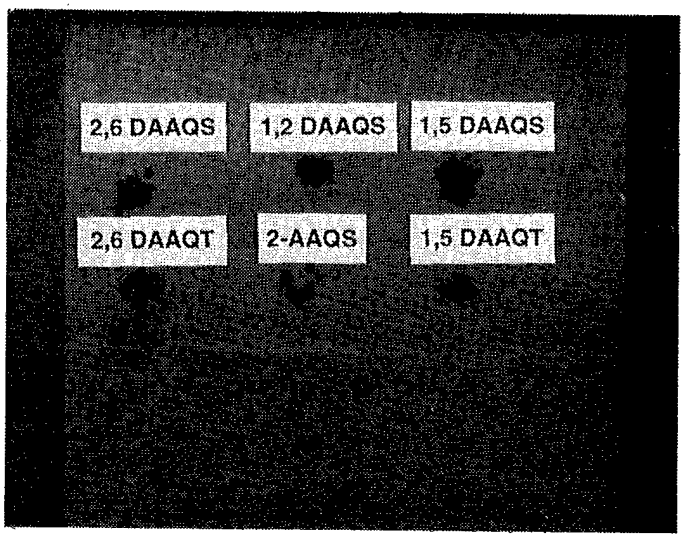
Figure 3a Fluorescence of Schiff Bases in Pure Form and Incorporated into Epoxy Primer Coatings on 7075 Aluminum Alloy Plates.

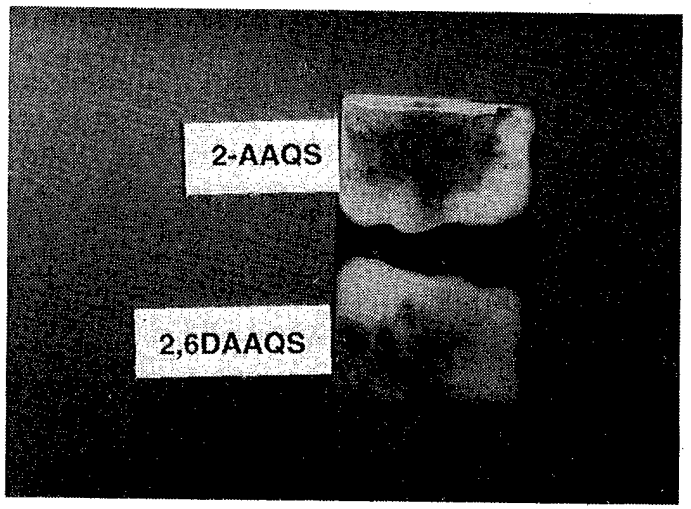
Visible Light





UV Light





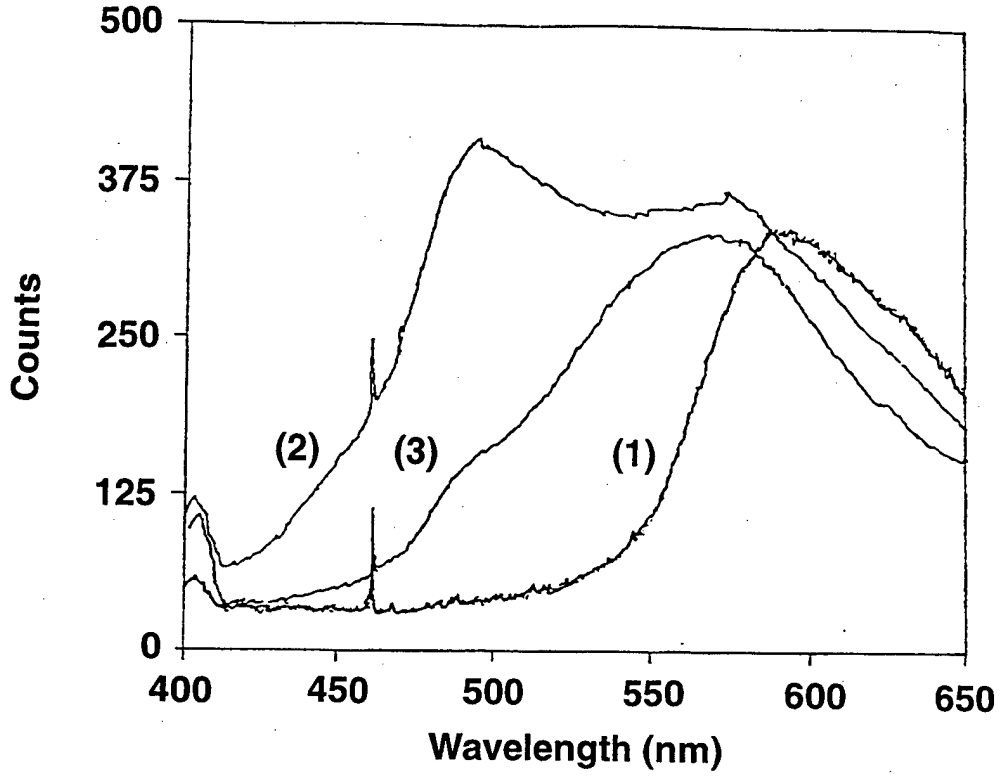


Figure 4 Fluorescence emission spectra of Schiff base 2,6DAAQS in oxidized and reduced forms under epoxy resin on 7075 plates. (1) oxidized 2,6DAAQS (2) reduced 2,6DAAQS (3) reduced after 9 days.

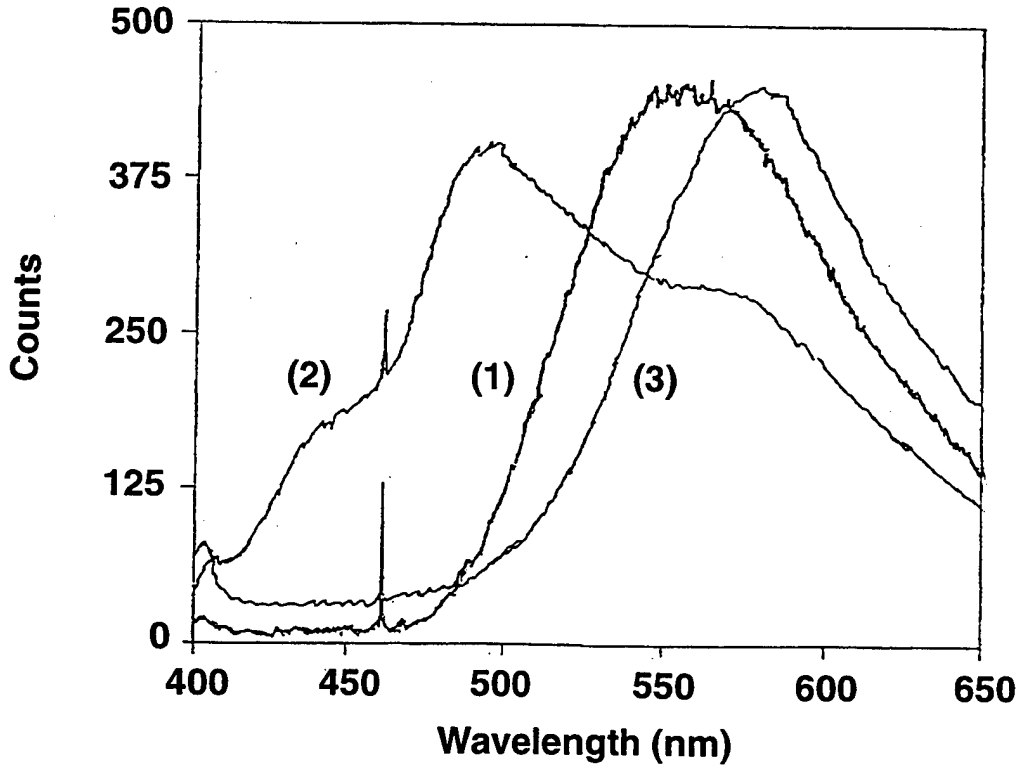


Figure 5 Fluorescence emission spectra of Schiff base 2AAQS in oxidized and reduced forms under epoxy resin on 7075 plates. (1) oxidized 2AAQS (2) reduced 2AAQS (3) reduced after 9 days.

Corrosivity Monitoring on Operational Aircraft Using Thin Film Galvanic Sensors

Dr. Vinod Agarwala
Naval Air Warfare Center Aircraft Division
Bldg. 2187, Unit 5, Suite 3356, 48110 Shaw Road
Patuxent River, MD 20670-1908

Kenneth Lerner and Irving Shaffer
Navmar Applied Sciences Corporation
65 West Street Road, Warminster, PA 18974

ABSTRACT

The Unites States Navy is investigating the use of a thin film based corrosion monitoring system on operational aircraft. Installation /operational parameters have been developed to effectively monitor environmental corrosivity without affecting flight operations. Data collection and analysis procedures have been successfully tested on an ongoing program involving United States Coast Guard HH-65 helicopters. Installation on United States Navy CH-53 and P-3 aircraft is expected to be completed shortly.

Introduction

The purpose of this work is to use in-situ corrosion measurements and analysis to provide information that will permit maintenance intervals for corrosion control to be tailored with respect to both the aircraft operational environment and the corrosion susceptibility of specific aircraft design types. The information obtained from the corrosion measurements will be used to provide a means of evaluating corrosion damage in aircraft locations that are not readily accessible. This provides maintenance personnel with early warning with respect to damage in critical areas and may permit the adjustment of maintenance and inspection scheduling based upon measured corrosion sensor output. Collation of the historical corrosion sensor data for specific aircraft, basing, and operational environments will permit maintenance intervals for corrosion control to be tailored with respect to both the aircraft operational environment and the corrosion susceptibility of specific aircraft design types.

This paper describes the installation of the Navy Corrosion Monitoring System (CMS) in a United States Coast Guard HH-65 Helicopter as part of a planned two year test program. Initial test results are presented. The HH-65 discussed in this paper is stationed at USCG Air Station, Corpus. The methodologies developed during this HH-65 installation, along with lessons learned, have contributed to the development of comprehensive procedures for the generic aircraft installation and operation of the CMS. The support and assistance provided by USCG personnel was instrumental in successfully completing this effort. Comprehensive documentation detailing hardware and sensor installation, system tutorial/step by step procedures, and maintenance/support procedures (CMS-HH-65 Users Guide) have been generated.

The Corrosion Monitoring System (CMS) has grown from research performed by Dr. Vinod Agarwala (NAWC-AD) to develop a corrosion sensor[1&2] **(Figure 1)**, which measures corrosivity and can easily be installed in a variety of military and commercial structures.

The CMS is used to monitor both the corrosivity of the enclosed volume of space where the sensor is located and corrosivity of any liquids present on the surface where the sensor is affixed. The CMS outputs a galvanic current, with respect to time, generated by a bimetallic thin film sensor, datalogger, and a datalogger input module. This galvanic current data is a measure of the corrosivity at, and in the region of the sensor. Placement of the corrosion sensor in enclosed areas will permit detection of the failure of sealants, gaskets, and other barrier materials. Sensors placed in locations which mirror the exterior ambient environment (i.e. an unsealed location), will record the effect of the operational environment on galvanic corrosion at the sensor location and the immediate vicinity of each sensor.

The galvanic current generated by a liquid or gas bridging the two metals plated on the sensor can be analyzed to provide a picture of the cumulative damage experienced at a sensor location. Integration of the Galvanic Current data yields Cumulative Coulombs. The Cumulative Coulombs Value describes the total output of the sensor over time. The correlation of Cumulative Coulombs to specific observed levels of corrosion will permit the generation of Maintenance Cues which can be utilized to evaluate inaccessible areas and to perform remedial maintenance before an overhaul is required to repair severe damage.

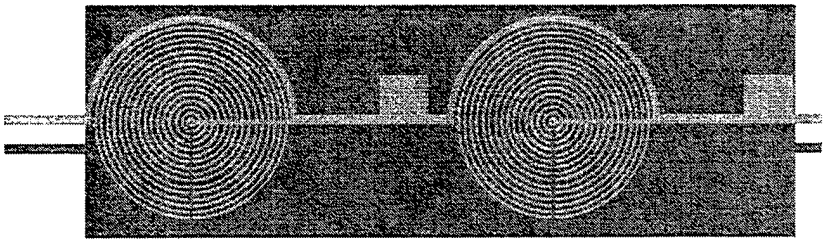


Fig 1. Bimetallic (Alternating Anodes &Cathodes), Thin Film Corrosion Sensor, Thickness = .002".

This sensor enables measurement of the corrosivity of various environments, and provides a tool for determining the onset of corrosion. The corrosion sensor is a thin film material plated with two different metals. These two metals interact with corrosive environments to yield an electrical (Galvanic) current. The magnitude of galvanic current, I_g, produced by the sensor depends on the thickness of condensed film, it's conductivity, corrosive nature, and the extent to which the electrodes are polarized. The current due to corrosion can be approximated by the modified Stern-Geary equation,

$$I_g = 2.3 \times I_{corr} \bullet \Delta\eta[1/\beta c) + (1/\beta a)]$$

where βc and βa are the Tafel slopes of the cathodic and anodic polarization, and η is the overvoltage or polarization of the galvanic couple. The detailed discussion of the principles involved are reported elsewhere.[3] The current measured between the two elements is directly proportional to the corrosivity of the active metal and is caused by the nature of electrolyte present. This Galvanic current is then measured and recorded by a custom data logging and current measuring input system (**Figure 2**). Additionally, Relative Humidity and Temperature are recorded by a small probe connected to the Datalogger (**Figure 3**).

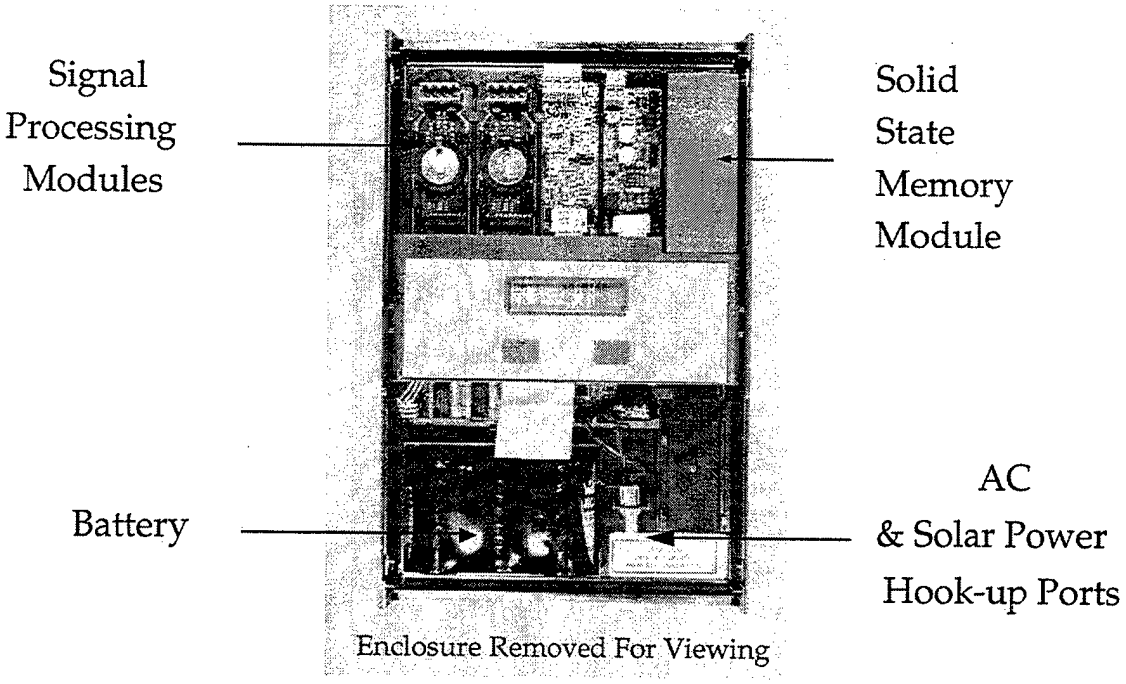


Figure 2 - CMS Datalogger (11.7"L x 7.6" W x 1.875" H, 1.13 Kg)

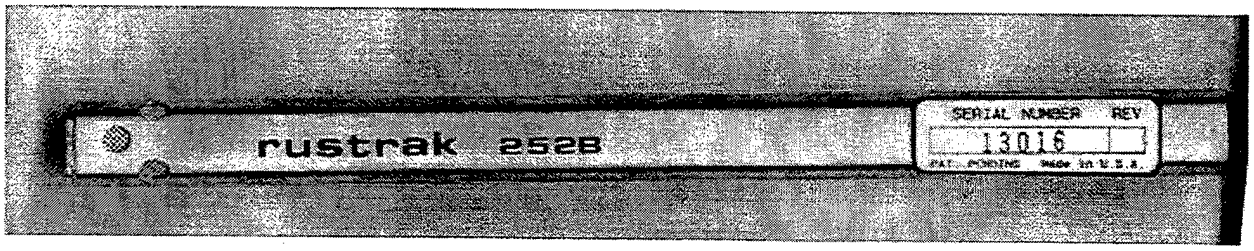


Figure 3 - Relative Humidity Temperature Probe (0.5"Diam. X 7.25" L)

Background

Determining the functional and structural integrity of an aircraft is vital for the readiness, reliability and safety of operational aircraft. Since most damage due to corrosion in aircraft systems is hidden, it can be devastating. Currently, corrosion damage is assessed only through periodic time-based inspections or when the system fails to perform. This is a very costly and inefficient use of resources and, in an extreme case, unsafe. Use of damage detection and monitoring sensors during service or storage will provide "system health" information to management and maintenance personnel.

In the work reported earlier[1,2,& 4], sensor evaluation was conducted via laboratory testing. For reference, these are summarized as follows:

1. Environment corrosivity characterization - study of various laboratory test environments such as salt-spray chambers, controlled humidity and cyclic environment cabinets, and dry boxes.

2. Coating performance - characterization of coating properties in terms of environmental permeability, corrosion protection and substrate bonding.

3. Properties of sealants and adhesives - determination of moisture barrier properties in metal/metal and metal/composite joints and early signs of crevice corrosion.

4. Hidden corrosion detection - monitor early signs of corrosion in lap splices and simulated structural cavities.

5. Composite degradation - tested as early warning sensors when embedded in bismalpolyimide (BMI)/graphite composite to detect presence of moisture and/or hydroxides due to galvanic effects.

These sensor studies were highly informative, and demonstrated a high transition potential in both the civilian and military applications.

Current CMS installations include: laboratory, aircraft in storage (preservation), outdoor testing of lap joints and coatings, military bases. Underway CMS installations of operational Navy aircraft includes Ch-53's, and P-3's. F-18 installation is planned for FY98.

Thin film galvanic corrosion sensors were highly successful in assessing environmental corrosivity during in-laboratory testing. The sensor output correlated well with the magnitude of corrosive elements present in the environment (cf. **Table 1**). (The magnitude of the corrosion

current was directly related to relative humidity in measurements made at NAWC-AD). Preliminary results show that the sensors hidden in lap joints showed very early activity, < three weeks. This corresponds well with the laboratory testing where extensive crevice corrosion in the lap joints occurred when corrosion currents increased by 2 to 3 orders of magnitude. It must be noted that these lap-joints did not have any sealant at the fastener locations or at the overlap edge. Without sealant protection, the environment has easy access through fastener holes and edges, thus, causing crevice corrosion.

	Cd-Au Sensor Output, μA (Cd Surface Area ~ 4 mm²)			
Test Environment	Value at Start, <1 Hours		Value After 120 Hours	
	Low	High	Low	High
60% RH	0.001	0.003	0.002	0.005
80% RH	0.01	0.05	0.08	0.12
100% RH	0.12	1	1	10
100% RH + Cl	1	12	10	20
100% RH + SO2	8	18	12	18
5% NaCl Spray	60	120	70	80
100% RH + HC1	10	30	120	150
5% NaCl + SO2	200	300	1200	1500

Table 1 - Response of Thin Film Cd-Au Sensors in Various Laboratory Environments [5].

The thin film galvanic sensors capability for in-situ corrosivity monitoring in military hardware environment have been successfully demonstrated on stored aircraft, test panels exposed on aircraft carriers, military bases and on ammunition stockpiles stored in silos. Their use as early warning devices to monitor hidden corrosion in structural joints was very successful. The results show a good correlation of the field and with laboratory data (collected in previous study). It was demonstrated that even in low humidity environments, the magnitude of corrosion currents very much depended on the corrosive elements present in the environment.

Purpose

The purpose of this work was to use in situ corrosion measurements and analysis to permit the evaluation of the corrosive environment experienced by HH-65 Helicopters. The information obtained from corrosion measurements will be used to provide a means for evaluating corrosion damage in aircraft locations that are not readily accessible. This evaluation will provide maintenance personnel with an early warning of damage in critical areas and may permit the adjustment of maintenance and inspection scheduling based upon measured corrosion sensor output.

An aircraft operational environment exhibiting low environmentally induced corrosion rates does not need the same rate of inspection and maintenance as an aircraft operating in an environment conducive to high corrosion rates. Interior aircraft locations which are not readily accessible can be monitored to determine when inspection or remedial action is required. The use of corrosion measurement data provides information that will enable the measurement of the corrosivity of the environment at various locations within an aircraft's airframe. This will enable a correlation to be made between the output of a standardized corrosion sensor and the actual corrosion exhibited within the region being monitored.

It is anticipated that the compilation of in situ aircraft corrosion measurements will permit the development of a refined operational methodology for scheduling aircraft maintenance, resulting in reduced maintenance expenditures and increased aircraft availability rates.

Corrosion Monitoring System Overview

The Corrosion Monitoring System (CMS) is an integrated galvanic corrosion measuring system. The operational aircraft battery powered configuration supports unattended operation for approximately 30 days. This system includes a corrosion sensor (yielding a microcurrent output signal), a Rustrak Ranger II Datalogger, a solid state memory Data Pack, a Valve Regulated Lead Acid Battery, and Input Modules which either record temperature, humidity, or microcurrent Zero Resistance Ammeter (ZRA) module. The CMS consists of onboard sensors, cabling and data logging equipment in combination with off-board Personal Computer interfaced hardware and software to permit Galvanic Corrosion data collection, reduction and analysis.

Corrosion Sensor

The corrosion sensor is a .002" thin piece of Kapton film plated with Gold and Cadmium in a pattern which enables generation of a galvanic current in the presence of a corrosive

medium. These two metals interact with corrosive environments to yield a small current. This current is measured and recorded by the Rustrak Ranger II (RR2) Datalogger and ZRA input module.

Relative Humidity/Temperature (RH/Temp.)Probe

An RH/Temp. Probe is installed at the Datalogger to provide localized temperature and humidity data. This information is used to provide a profile of the aircraft operational temperature and relative humidity environments.

Ranger II (RR2)

The Rustrak Ranger II is an eight channel datalogger used to record and store data from Input Modules. The time duration over which data can be stored is dependent upon the sampling rate, the presence of a data pack, and the availability of power to operate the device. Standard power supply types are AC, Batteries, and diode regulated Photovoltaic Cells (Solar Panels). The RR2 can be operated with up to 4 Input Modules. Each Input module can interface up to two data channels to the RR2; yielding an RR2 storage capacity of 8 data channels. The RR2 stores data in an internal memory. The data is transferred from the internal memory to a Data Pack automatically when a Data Pack is installed and when a recording session is completed. Normally the internal memory will need to be manually downloaded to the Data pack during servicing. When a Data Pack with available capacity is installed the RR2 will continue recording until the Data Pack is full. The Data Pack is removed from the RR2 and connected to a Data Pack Reader. The Data Pack Reader is used to transfer the data from the Data Pack to a computer.

Input Modules

Input Modules are either a temperature, humidity or microcurrent measuring device. They can send one or two channels of data to the Rustrak Ranger II.

Data Packs

Data Packs are used to store data after the end of a test or when the Rustrak Ranger II's internal memory is full. Recording will continue until the Data Pack is full. Periodically, an operator will download data from the internal memory to a Data Pack for analysis (normally at 30 day intervals). The Data Pack can then be placed in a Data Pack Reader which can transfer the data to a computer.

Data Pack Reader

The Data Pack Reader permits the transfer of the data to a computer for display, analysis, and output. A parallel port connection to a standard PC is all that is required to hook the Data Pack Reader to a computer. The Data Pack Reader interfaces with the computer via the PRONTO software package.

PRONTO Software

The PRONTO Software enables the display, analysis, and output of data recorded by the Rustrak Ranger II. PRONTO will be used to output test data to dedicated analysis and charting packages. PRONTO is also used to format and erase Data Packs.

Field Support

Approximately every 30 days, data is downloaded to a Data Pack. Also, at this time the battery is replaced with a fully charged replacement. The use of standard aircraft disconnects enables the replacement of the battery in a minute or two. Downloading data to the Data pack is accomplished via activation of a program embedded in the datalogger's firmware. The datapack is then shipped to NAWC-AD for analysis.

Installation Overview

The Corrosion Monitoring unit was installed in four HH-65 Coast Guard Helicopters (two at Elizabeth City ARSC, and one each at Corpus Christi and Detroit Air Stations) over the period 4/96 through 9/96. This paper presents data collected from HH-65 #6554 stationed at Corpus Christi Air Station. A methodology to perform the installation was developed with the input of NAWC-AD, Coast Guard, and contractor (Navmar Applied Sciences Corporation) personnel at Elizabeth City (E-City). This installation methodology included sensor, signal cable and datalogger location selection, datalogger mounting hardware design, and sensor adhesive selection. The installations at E-City and Corpus Christi were performed by USCG and NAWC-AD personnel. The Detroit installation was performed solely by USCG personnel.

Items installed include the following:

- •Rustrak Ranger Datalogger including:
  - (3) Zero Resistance Ammeter (ZRA) Input Modules.
  - (1) Temperature and Relative Humidity Input Module.
  - (1) 4.2AHr, 4 Volt YUASA valve regulated lead/Acid Battery.
  - (2) 8" pieces of 20 Gauge Wire and (2) Quick Splice connectors for the battery hookup RayChem# M 81717/11-200.

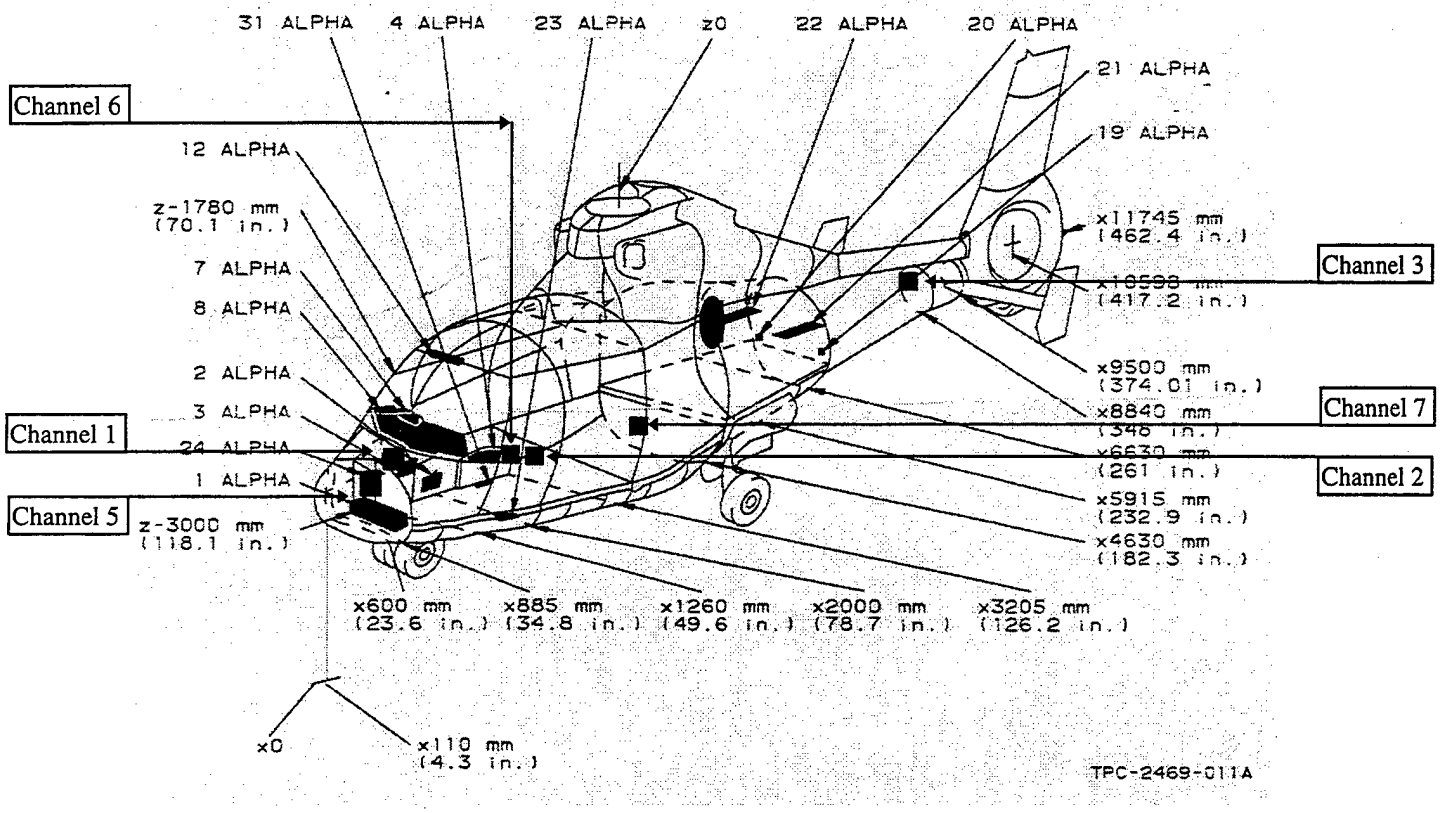
- •Rustrak Ranger Datalogger mounting hardware
- •Rustrak Ranger Temperature and Relative Humidity Probe.
- •6 Navy Corrosion Sensors fastened with Dow Corning 3145 RTV adhesive sealant (Mil-A-46146).
- •Sufficient cable for each sensor's cable run to the datalogger (RayChem cable vendor, Part # M27500-20SD2T23, CSR 2275, Double Shielded. Cable Marking: M27500-20SD2T3-06090).
- • Crimp Connectors and Environmental Splices for signal cabling. (RayChem# M81824-1-2, & ESN 5940-60-271-7741
- •Various sizes of Cable Ties and Standoffs.

Sensor Installation

The six sensor mounting locations for the HH-65 helicopter are described in **Figure 4**.

ALPHA PANEL LOCATIONS: HH-65A WIRING

MANUAL - USCG T.O. 1H-65A-2-2



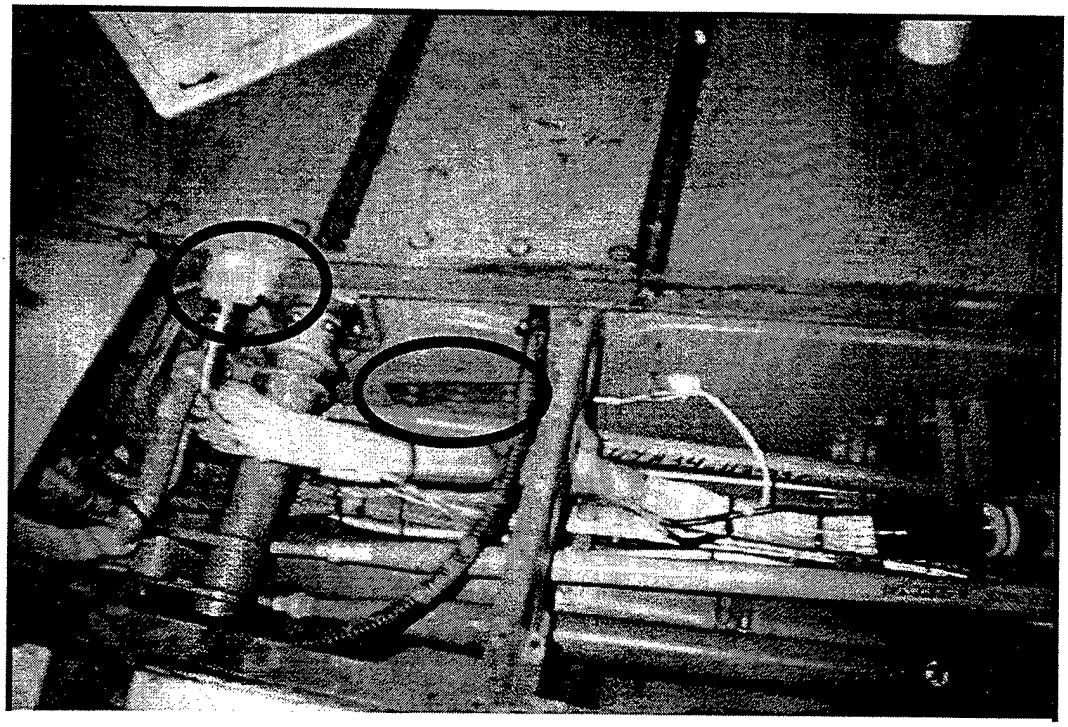
■ = Corrosion Sensor Locations

● = Data Logger & RH/Temp. Probe Locations

Figure 4 - Data Logger, Corrosion Sensor, and RH/Temperature Probe Locations, HH-65

All sensors were attached to the aircraft using Dow Corning 3145 RTV adhesive sealant (Mil-A-46146). The sensor placed beneath the floorboard (Channel 2) was covered with a .002" scrim cloth to prevent damage and electrical shorting when the floorboard was replaced after installation. **Figure 5** is a photograph of the sensors described as Channel 2 & Channel 6.

TOP



(Channel 2) Single Cell Sensor: Beneath Fishplate
(Channel 6) Three Cell Sensor: Splash
HH-65

Figure 5 - Photograph of Installed Corrosion Sensors (Channel 2 & Channel 6)

Datalogger Mounting and Installation

In summary, the Datalogger was attached to a plate; This plate was then attached to two brackets mounted forward of the door in the baggage compartment. See **Figure 6.**

Relative Humidity/Temperature Probe Installation

The RH/Temp. Probe is secured to one of the upper Datalogger mounting bolts using a rubber padded wire clamp. The clamp fits around the probe and has a tab containing a hole that permits fastening with one of the mounting fasteners. This fastener is 1/2" longer than the other mounting bolts to accommodate the probe clamp. See **Figure 6.**

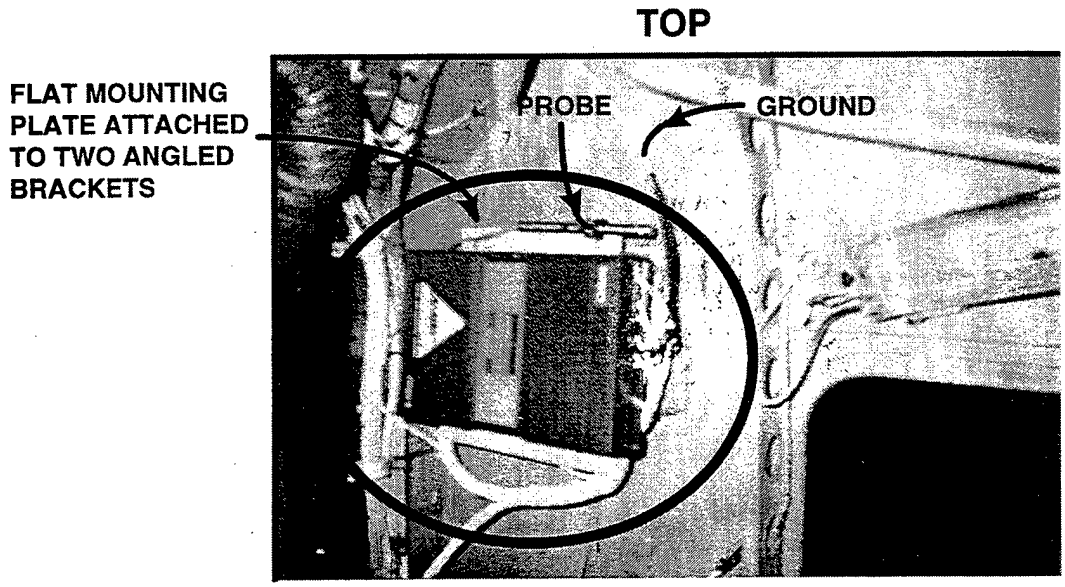


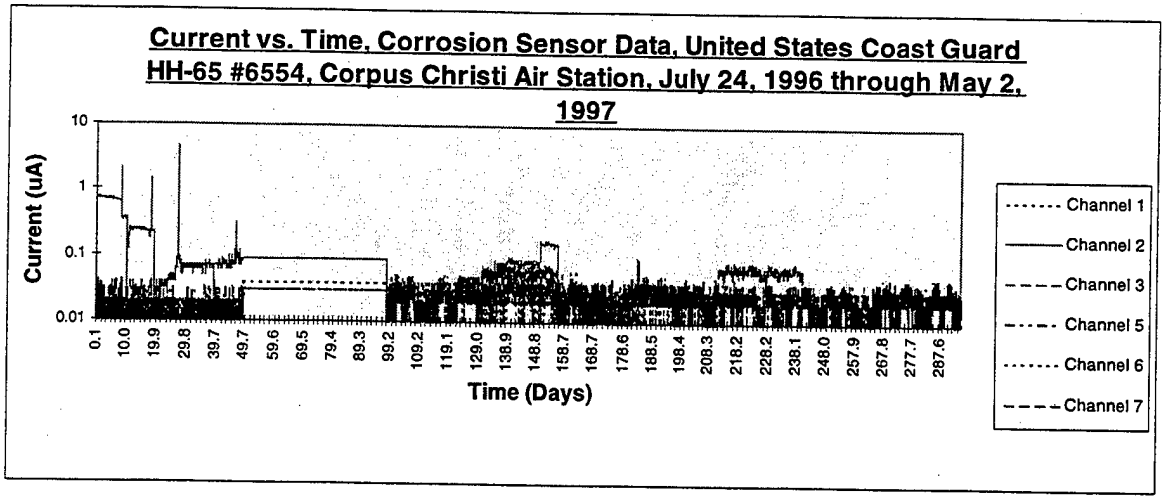
Figure 6 - Installed Data Logger & RH/Temperature Probe

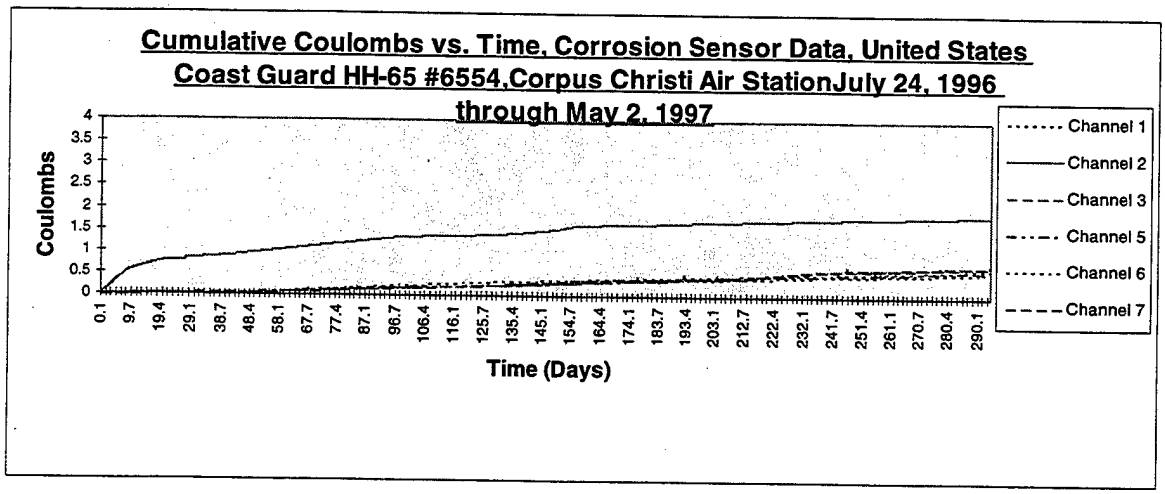
Ground Connection

All corrosion sensor signal cables were grounded to aircraft ground connection points.

Data Analysis/Results

Corrosion sensor data is being downloaded and analyzed approximately every 30 days. Data is plotted as Current, Cumulative Coulombs, Temperature, and Humidity verses Time. The results will be compared with operational and observational data provided by the USCG. Operational CMS data to date has confirmed that HH-65 avionics and external EMI/RF sources do not interfere with the operation of the installed CMS. Data to date for HH-65 #6554 is presented in Figure 5. There was no data collected between days 49 and 99 due to an inadvertent disconnection of the sensors from the datalogger.





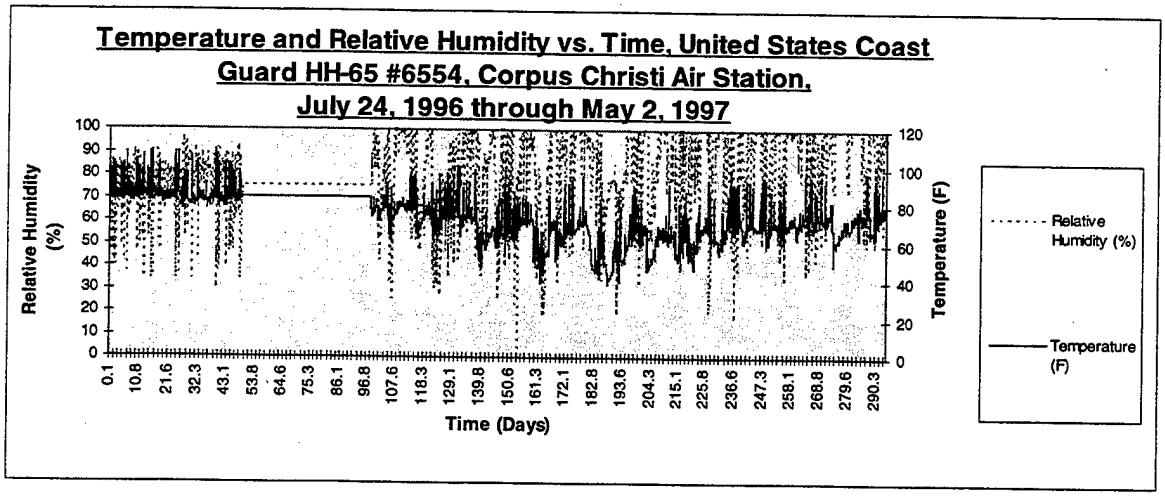


Figure 7 - CMS Data from HH-65 #6554

The corrosion sensor that is designated by the data channel 2 clearly shows activation more than one order of magnitude above the ambient signals generated by the other sensors. This data suggests that the sealant used to prevent moisture infiltration beneath the floorboards (fishplate) has been breached and corrosion is occurring in this area. This information provides maintenance personnel with a que that can be used as direction for the focus of inspection and remedial repair efforts. Examination of the cumulative coulomb analysis confirms that Channel two the sensor beneath the floorboard is experiencing a corrosive environment to a much greater extent than other monitored areas of the aircraft. Examination of the affected area should be conducted prior to the next regularly scheduled inspection interval. The Relative Humidity and Temperature data clearly shows condensate formation as a function of temperature fluctuations resulting from both night to day transitions and operational induced temperature swings. Excessive moisture condensation can be construed as a contributing factor to corrosion sensor activation and therefore an important factor in the corrosivity of the aircraft basing and operational environment.

Summary/Future Plans

The work performed to date provides the tools to measure and quantify the corrosivity of HH-65 aircraft using the Corrosion Monitoring System (CMS). Corrosion measurements have been made at aircraft locations exhibiting the most severe corrosion (recommended by USCG personnel). The number of Coulombs galvanically generated at each sensor was recorded at 30 minute intervals. This data still remains to be compared with actual observed corrosion damage. Input from USCG personnel will be used to explore methodologies to correlate measured galvanically generated coulombs with actual aircraft damage.

CMS data should be analyzed to determine to what extent measured corrosion data can be correlated with observed damage. Aircraft maintenance records need to be carefully compared to the temporal profile of the collected corrosion data. Investigation should examine in detail, measured corrosion activity in any sensor locations deemed to have experienced corrosion damage as noted by maintenance personnel. A Range of threshold CMS measurement should be identified with specific levels of corrosion damage. The degree of confidence to which the

domain of the range of CMS measurements can be reliably identified with specific levels of corrosion damage will determine the magnitude of the impact CMS data will have on the conditioned based maintenance process. The population of CMS data that will be generated for each aircraft type, platform, and deployment environment will provide a baseline for the given operational conditions. This baseline should be examined as the basis for maintenance procedures modification.

The generation of a database of aircraft site specific corrosion values will assist in the correlation of sensor generated corrosion values with the requirement for specific levels of maintenance and repair (i.e. for each sensor location an attempt should be made to determine what level of corrosion damage requires remedial action. This determination of the level of corrosion damage can then be used to schedule maintenance to the affected area).

It is anticipated that the collation of the historical corrosion sensor data for specific aircraft, basing, and operational environments will permit maintenance intervals for corrosion control to be tailored with respect to both the aircraft operational environment and the corrosion susceptibility of specific aircraft design

References

1. V.S. Agarwala, "Sensors for Corrosion Detection and Monitoring in Hidden Areas", proceedings of the Symposium on 'Chemical Sensors II', Eds. M. Butler, A Ricco, and N. Yamazoe, The Electrochemical Society, Pennington, NJ, Vol 93-7, 698-708, 1993.

2. V.S. Agarwala and A. Fabiszewski, "Thin Film Microsensors for Integrity of Coatings, Composites, and Hidden Structures", NACE CORROSION/94 Conference, Baltimore, MD, Paper No. 342, NACE International, Houston, TX.

3. V.S. Agarwala, "Corrosion Monitoring of the Shipboard Environment", STP-965, American Society for Testing and Materials, Philadelphia, pp 354-365, 1988.

4. V.S. Agarwala, "In-Situ Corrosivity Monitoring of Military Hardware Environments", NACE CORROSION/96 Conference, Baltimore, MD, Paper No. 632, NACE International, Houston, TX., P. 632/4.

5. V.S. Agarwala, "In-Situ Corrosivity Monitoring of Military Hardware Environments", NACE CORROSION/96 Conference, Baltimore, MD, Paper No. 632, NACE International, Houston, TX.

Lessons Learned: Leak Detection Sensors for Water, Fuel, and Energy Pipe Systems

Jeff Timmins, Robert A. Weber, and Vincent F. Hock
U.S. Army Corps of Engineers
Champaign, IL, 61826, USA
217-352-6511
217-373-6732

ABSTRACT

Leak detection and location in piping systems is a crucial technology needed by government and industry. A single leak repair can cost in the range of $2,000-15,000 per leak, due in large part to the multiple trenching required to locate the leak source. Moreover, a single gallon of gasoline can render a million gallons of water non-potable. In researching the available leak detection technologies, USACERL has performed 8 site surveys. The objective of this work is to publish a lessons learned document based on the evaluation of passive leak detection technology applicable to water, fuel and energy pipe systems.

INTRODUCTION

The U.S. Army Toxic and Hazardous Materials Agency (USATHAMA) estimates the average clean up cost of a petroleum leak to be $193,000, ranging higher where ground water is contaminated. The cost of effecting leak repairs is approximately proportional to the amount of trenching needed to access the leak, and some passive leak detection systems can provide leak location to within 6 inches of the leak location, saving critical time, and minimizing unproductive trenching for repairs.

There are five main technologies in use for the detection of liquid leaks, each associated with the physical phenomena which occurs either at a leak site or in the system due to the leak. Chemical concentration detection is referred to by the term "sniffing" and requires the leak to provide concentrations which are detectable above normal, naturally occurring concentration levels. Acoustic systems rely on noise produced by turbulent liquid flow to detect leaks in piping systems. Impedance methods involve laying a cable in probable leak sites and monitoring the change in the cable's impedance to determine when it comes in contact with a liquid. Infrared methods rely on the difference in temperature between the piping system and surrounding soil to provide a thermal signature which can be observed by special imaging equipment. Supervisory Control and Data Acquisition (SCADA) systems use process control sensors to detect discrepancies in the performance of a system which can indicate a leak, and require the use of a computer, sensor data acquisition, and an analysis algorithm to evaluate the sensor data and produce a leakage determination.. One subset of the SCADA system category which is often used as a stand-alone leak detection system is Level Monitoring which can be used only in closed systems which allow for an accounting system to detect losses. Another SCADA subsystem which is also used as a stand-alone system is Mass Flow measurement methods which rely on various

physical phenomena to obtain accurate measurements of the total mass flow between two points on a pipeline. Each technology mentioned has a detection sensitivity associated with the system it is used with. These five technologies are evaluated here in terms of the phenomena exploited, their system applicability, and their advantages and disadvantages when applied to the detection of leaks in a buried pipe system responsible for carrying liquids.

LEAK DETECTION TECHNOLOGY DESCRIPTIONS

For simple binary indicators, such as the conductive cable systems, detection of the leak is dependent on the triggering of the sensor, requiring no computational accuracy. A more complex systems, such as the cable impedance systems require not only the sensors be sensitive to the liquid to be detected, but also that computations have sufficient numerical precision to accurately locate the leak source. The type of phenomena the sensors are designed to detect directly affects the computational accuracy required for reliable leak detection and location.

Cable Systems

Impedance Mismatch cable systems usually utilize a coaxial cable with a permeable outer shield which is excited at a known frequency. Because the dry cable has a known impedance and length, when a leak changes the dielectric properties at a particular location within the cable, it creates an impedance which can be located along the length of the cable by signal attenuation and phase measurement. This technology is used to detect leaks of fuels, solvents, electrolytes, acids, bases, and aqueous leaks. The advantages of this system is that it can be sensitive to different types of liquids and can be easily installed. The disadvantages of this system is that after exposure to water or fuel, the cable may need to be replaced.

Conductivity cable systems utilize two conductors, generally stainless steel, which are woven into a specially treated cable or ribbon. When a conductive liquid forms a continuity path between the two wires, a leak condition is indicated and can signal an alarm. The system is generally installed in locations which are accessible during or after installation. The system is used for aqueous leak detection or (with special polymers) detection of petroleum leaks. The advantages of this method is that it can be used in piping systems as well as storage tanks. The disadvantage of this method is that leak location cannot be determined. System design allows for false indications depending on initial designed sensitivity.

Acoustic Methods

Acoustic leak detection methods rely on piezoelectric transducers to translate pressure waves generated by fluid escaping the piping system to an electrical signal. Current systems rely on an operator listening to the filtered output signal to determine whether a leak exists, without locating the leak. This relies on operator experience and can lead to false leak or no leak indications. Currently a Joint Department of Defense, Department of Energy, and Environmental Protection Agency Strategic Environmental Research and Development Program (SERDP) is developing an acoustic technology which has detected leaks of 0.1 gallons per hour. The passive acoustic leak

detection technology is also capable of locating leaks within inches of their source. The acoustic leak detection technology has the potential for providing the most cost effective, reliable, method of leak detection and location for petroleum and aqueous based piping systems.

Mass Flow Sensors

Magnetic inductive flowmeters rely on the conductive properties of the liquid. The flow passes through a magnetic field and this produces a voltage difference over the cross-section of the flow area. This voltage is proportional to the (average) flow velocity. By knowing the conductivity of the liquid, the strength of the magnetic field, and the cross-sectional area, the flow velocity can then be determined by measuring the potential. A key advantage is that he sensors are relatively inexpensive and are very accurate, but there are velocity restrictions which depend on the liquid being pumped.

Calorimetric flow sensors utilize the calorimetric principal to determine flow velocity at a certain point in the flow field. The flow is locally heated and then the temperature is sensed a short distance downstream. Based on the thermal permitivity (the temperature dependent rate at which thermal energy propagates through a given medium) of the material, the temperature differential indicates the flow velocity. Assumptions on flow field profile are then used to calculate the volumetric flow rate from which the mass flow rate can be determined for a liquid of known density. These sensors have a highly accurate flow detection. The main disadvantage is precisely controlling the temperature at the sensor. Fouling of the sensor can also be a problem depending on the liquid being transported in the piping.

Ultrasonic flowmeters utilize time-of-flight measurements of wavefront propagation or doppler shift of the ultrasonic signal, the flow velocity average can be determined using two piezo-electric transducers, one a "sender" and the other a "receiver". Ultrasonic flowmeters can be used for a wide range of materials from sewage to ammonia, nitrogen, natural gas, air, acids, heavy oils, or desalinated water. The Ultrasonic sensor systems have high measuring accuracy, no pressure loss or flow obstructions, low power consumption, and can be purchased in the intrinsically safe version for explosive environments. A disadvantage is the high initial cost of the signal processing equipment.

Gas Sniffing

Gas sniffing technology utilizes electro-chemical sensors that are calibrated to background concentration levels of the particular compound of interest. In some situations this compound can be an additive to the liquid to make detection feasible. Sensors are located or transported to a suspected leak location where readings are taken and compared with threshold values to determine either a "leak" or "no leak" condition. These sensors are commonly used with Volatile Organic Compounds (VOCs) which produce highly localized concentrations of vapor when a leak occurs. This system is good for some liquids, such as petroleum products, which produce vapor that can permeate through the soil covering the pipe system and produce an area of concentration sufficient for detection around the leak location. Leaks of liquids with varying ambient concentrations, such as water, can easily be masked by the background noise. It is also not

possible to chemically detect the presence of a water leak without adding potentially toxic marker compounds to the water.

Infrared Imaging

Infrared inspections are performed with a video camera capable of recording infrared radiation. The camera records the temperature differential and the images are processed to show the different temperatures in a color spectrum. Data can be videotaped for future review and processing. These systems are generally used for systems which can produce significant thermal signatures even through several feet of earth. This limits them to use with piping systems which can transport liquids which will tolerate temperatures significantly above the surrounding ambient air temperature, such as heating water or steam. When conditions permit, the system or suspect locations within the system are scanned for leak indications. The advantages of this system are that it can be used to scan large areas at a time and does not require any excavation. The infrared technique is especially useful for surveying heating and cooling distribution piping systems. The disadvantages of this process are that it cannot be used for any system that doesn't present a temperature differential.

Level Monitoring

Level monitoring uses high precision storage tank liquid level measurements to determine the volume of liquid contained in each tank of the system. In a closed system, the volume should be constant for a given pressure and temperature when there is no leak present in the system. Any variation in the level generates an alarm that something is out of specification ranges for the system. Sensors can be float switches, capacitance, or continuity. Any petroleum distribution system which goes to a static state for suitable length of time would be a candidate for liquid level monitoring for leak detection. The implementation of this system for leak detection is relatively inexpensive, directly related to the accuracy required for the particular system to detect leaks of a particular rate. Liquid level monitoring requires the system to be in a static state for a period of time which is dictated by the resolution of the sensors and the volume of the system. A large volume system would require extremely precise measurement sensors which would be subject to noise, or an excessively lengthy static state holding period to detect small leaks in the system.

SCADA Systems

Supervisory Control and Data Acquisition (SCADA) systems rely on process monitoring sensors to convert physical phenomena such as pressure, temperature, flow rates, and density into electronic signals which can be integrated by the control system. SCADA systems rely on the combination of sensor inputs to determine the state of the system which is then used to modify the control inputs to bring the system (heat distribution, petroleum delivery, etc.) to the desired state. Complete information about the liquid system is precisely determined at sensor locations. The sensor inputs at adjacent measurement locations can be used to determine leak locations as well as rates. The time frame required to detect and locate a leak in the system is only dependent on the frequency with which the system is sampled. The cost of sensors and data communication equipment necessary for implementing a SCADA system on a large piping system is prohibitive.

FIELD SURVEY RESULTS

Several sites were surveyed for leak detection systems installed on water, fuels, and energy pipe systems. The only systems found were for the detection of fuel leaks. Several technologies discussed above could be adapted for water and energy pipe systems, however the cost of the technology is not easily offset by the cost of possible losses, due to the lack of perceived environmental impact from a large scale loss.

Personnel were queried about the system's utility, system effectiveness, false alarm rates, maintenance requirements, and the overall abilities of their system. The following is a summary of these site visits.

Pensacola NAS, FL

The leak detection system is made by Arizona Instruments Inc. (AZI) and had the sensor tube buried between the pipes during construction of the pipe line, as shown in Figure 1. The line is monitored by 10 remote monitoring stations which cover the entire pipeline. Each monitoring station can be contacted via modem and controlled remotely as well as being controlled by operator input at the monitoring station by means of a touchpad. The monitoring stations are also capable of calling the host computer system and reporting alarms. The system operates by cycling clean, dry air from the monitoring station out the length of each segment (blowdown) and then drawing a soil gas sample across an electronic gas analyzer to detect hydrocarbons. The literature provided by AZI quotes a lower detection limit for commercial gasoline of 150 ppm, and for JP4 Jet Fuel of 60 ppm. The lower detection limit for either JP5 or JP8 is not specified.

Experience showed that the rising and falling water table levels would occasionally drown the system by not allowing it to pull a vapor sample. The sensor pipe was used as a riser to try to mitigate the ground water problem. The major length of the sensor tube was run horizontal and then turned upwards at the sensing location providing a vertical column which could be cleared during the blowdown phase of the test and then used to acquire a vapor sample. Despite the modification, the operator suggests not installing this particular leak detection system in areas of high ground water.

Anchorage Airport - Anchorage, AK

The leak detection and location system is controlled and tested by the Hansa Consult system. The system was installed in 1988. The leak detection is done by pressurizing the 8 mile pipe line to 16 bar and then holding pressure for about 20 min, as shown in Figure 2. The pressure is measured 75 times then is reduced to 6 bar and held for 20 min. The pressure is measured 75 times and then raised again to 16 bar and measured again 75 times. Testing takes place during the night hours because the system must be taken off-line. The system is reported to have worked very well. System operation can be verified by opening a bleed off valve during testing. However, all the computer programming code is written in German and any problems have to be resolved by staff personnel located in Germany.

Elmendorf AFB, AK

The leak detection system is a Permalert PAL-AT system with four cables, two for the diesel fuel and two for the mogas. One cable on each system detects water and the other detects fuel. The Permalert system relies on the conductivity and impedance of the cable loop to detect liquids. Leak location can realistically be determined to within one or two feet if the leak is immediately detected. The system had no problems until some additional construction was done and water apparently entered the jacket. The cables for detecting water, in both the mogas and diesel pipelines indicate water in the system.

North Island NAS, CA

The leak detection system is a constant pressure volumetric leak detection system from Vista Research. The system controls line pressure by adding the necessary volume of product to the line to compensate for thermal deviations in the product line, as shown in Figure 3. The system has been certified by third party blind testing to be capable of detecting leaks of 0.1 gal/hr with 95% confidence level (per EPA standards). A 'Tightness Test' consists of maintaining an equilibrium pressure for approximately one hour and then raising the pressure and maintaining the new equilibrium pressure for a similar length of time, with 25 minutes of stabilization time required prior to test initiation. The system verified pipe integrity with a leakage reading of 0.0001 gallons per hour which was considered measurement noise.

Travis AFB, CA

The leak detection and location system, shown in Figure 4, was manufactured by Argus Technologies and was installed by the contractor 1 ft. above the top of the main line with sand backfill added to cover the sensor tube while the remaining trench depth was filled with native soil. The leak detection system observed at this location consisted of a semi-permeable diffusion tube with air sampling. The system pumps clean, dry air through the system and uses a marker gas to signal the end of the test. In this way, a leak location can be interpolated from the time differential between the arrival of the contaminated air sample and the arrival of the marker gas. Approximate air velocity in the tube during a test is 3 ft./sec.

The system remains idle to allow a sufficient concentration of vapors to build up in the sensor tube. The system literature claims leak location resolution of 1 percent of line length. This can be reduced by interspersing the total line length with test points at which marker gas is injected to produce a segmented test flow for the system. Leak rate detection and resolution is a function of system installation and soil composition. The system was non-functional during the site visit and the Air Force indicated that the system has yet to perform to a satisfactory level.

Ft. McCoy ANG-POL Facility, WI

The leak detection system, shown in Figure 5, is the Raychem TraceTek. It is a two cable system which operates on the same principals as the Permalert system installed at Elmendorf AFB and as such, has the same resolution and capabilities. They have had no problems with the monitor.

About the beginning of August 1996 the leak detection system reported water in the conduit near the road. They are in the process of investigating the leak.

Whiteman AFB, MO

Tracer Research provides the intermittent testing of the pipeline integrity by inoculating the stored fuel with a proprietary marker gas (which is compatible with the JP8 fuel) at trace levels about 1 week prior to testing. Technicians then sample each of the approximately 1400 sensor wells spaced at 20 ft. intervals along the pipeline. The soil gas sample is then analyzed using a portable gas chromatograph to detect the trace levels of the marker gas which would result from a fuel leak.

The difficulties experienced with the Tracer Research system at this site are generally due to leaks from leaking connections in the fueling pits which release fuel into the pits. The fuel then migrates through either a crack in the pit wall or through the air and is detected in one of the nearby sample wells. There is also a non-functioning Argus Technologies vapor detection system at this site which the site personnel tested first by placing the sensor tube alongside a pan of JP8, then by covering both the pan and the sensor tube with a sheet of plastic, and then finally by immersing the sensor tube in the JP8 at which point the system finally registered hydrocarbon levels above normal background levels.

Ellsworth AFB, SD

Ellsworth uses an AZI leak detection system with wells spaced at 200 ft. intervals. The system takes a soil gas sample from each well and passes the sample across an electronic hydrocarbon detector to measure hydrocarbon concentration in ppm. Each well is connected to a perforated tube buried approximately 1 ft. above the fuel line. The sampling of each well takes an average of 10 minutes per well with the closer (to the monitoring station) wells taking slightly less time.

The system has three wells which are in contaminated soil which are still indicating leaks even after having a chip with higher concentration level capabilities installed. The line with the indicated leakage has been verified to not be leaking by tank level measurements.

Often the sensor well restrictor assemblies will become blocked by water after a heavy rainfall. The proprietary restrictor assemblies are not dryable and must be replaced if they become immersed in water.

The sensor tube can be prone to splitting, which results in a "port open" malfunction of the leak detection system if the line is exposed to ultraviolet light (bright sunlight) for any substantial length of time before burial.

DISCUSSION

Two leak detection systems manufactured by Argus Technologies were surveyed and neither was functional. The system at Whiteman was abandoned in favor of the Tracer Research system when the quoted repair price of the Argus system exceeded the installation cost of the new Tracer Research system. The system installed at Travis AFB was installed with the pipeline to specifications by the pipeline construction contractor, but has failed to perform satisfactorily. The system is based on sound scientific principals, however the system cannot be recommended due to two factors; 1) The time required for a given minimum leak to diffuse into the sensor requires the system to remain idle for so long that a leak of dangerous magnitude could remain undetected long enough to create a significant spill and 2) the system's apparent unreliable performance.

An AZI system in operation was surveyed at two sites, Pensacola NAS and Ellsworth AFB. These systems have proven themself in the field with the major drawback being the susceptibility of the system to water invasion and the resulting inability to monitor some sections of the piping system. In addition, experience has shown that the remote operation capabilities of the system can be a liability. Specifically, a lightning strike at the Pensacola NAS disabled several monitoring stations for several days. Another drawback to the AZI system is the location of the leak source. At the Pensacola installation, the sensor tubes cover 20 ft. of pipeline per sensor well. This means a leak indication can be located to within only 20 ft. of its source. The detection levels for a given leak rate are also dependent on the installation of the system, particularly the backfill surrounding the sensor tubing and pipeline. AZI recommends a minimum percolation value that is to be obtained by a given backfill in order for the system to perform to it's minimum concentration detection levels.

The Tracer Research system was used at Travis AFB before the installation of the Argus Technologies system. The system Tracer was considered too maintenance intensive after several of the probe wells were damaged by construction and grounds maintenance equipment. The same type of wells are used at Whiteman AFB and have not experienced the same rate of attrition. The 20 ft. well spacing of the Tracer system allows leak location to within 10 ft. of the source by comparison of relative concentration levels. The deficiency of the Tracer system is similar to that of the Argus Technologies system in that it is not a continuous monitoring system. Leaks of dangerous magnitude can exist undetected until the next scheduled testing date.

Two volumetric systems were surveyed. A pressure differential system by Hansa Consult and a constant pressure volumetric system from Vista Research. Both systems are capable of detecting extremely small leaks, but leak location remains a problem.

Two cable systems were also surveyed, one by Permalert and one by Raychem. Both cable systems were performing as advertised and one was indicating a water leak condition. The disadvantage of the cable systems is that they require replacement of any length of cabling which comes in contact with liquid and they must be installed in a conduit pipe, effectively negating their applicability for an existing system and increasing the installation cost of a new system. The cable systems are ranked lowest in performance and cost. Water intrusion is a major problem for cable

systems and since the cables must be protected, their use is limited to double-wall piping systems which increases the initial cost of system installation and prevents retro-fitting existing systems.

The acoustic leak detection technology was shown to be capable of detecting and locating small (0.1 gallons per hour) leaks in both the laboratory and small scale field testing. The SERDP project also proved the acoustic technology capable of locating a leak within a few inches of the source in a 200 foot long pipeline. It is estimated that the installation and operation of a finalized acoustic leak detection system will cost under $10.00 per foot of piping installed.

Cost Data

Questionnaires were sent to both installations and vendors to determine applicable current pricing on installation, materials, and maintenance costs for the system types surveyed. Table I. illustrates the relative breakdown of the cost data obtained. Vendors were supplied with a hypothetical piping system 1000 ft long, carrying JP-8 in a single wall pipe buried 4 ft. beneath grade.

CONCLUSIONS AND RECOMMENDATIONS

To achieve sufficient performance from a leak detection system, the piping system should first be verified for integrity, then have a continuous monitoring system installed and tested. The system must also be relatively maintenance free and inexpensive to operate. None of the systems surveyed or researched provide the optimal level of leak detection and location alone. Developing technologies, especially the current SERDP research into passive acoustic leak detection, show promise for an all encompassing solution to leak detection, quantification, and location.

Of the current COTS leak detection systems investigated, the most promising technology for reliable detection of fuel leaks in underground fuel piping systems appears to be the gas sniffing system. This system has proven it's ability to detect numerous hydrocarbons from natural gas, to hydraulic fluid, to JP8. However, the system is not applicable to water or energy pipe systems and susceptible to water invasion on some current systems. The AZI leak detection and location system provides sufficient sensitivity to detect smaller leaks and has the ability to continuously monitor the piping system, while giving leak location to within 10 feet.

The tracer gas systems are suitable for intermittent pipeline integrity tests and do not depend on prior knowledge of the pipeline condition. Cable systems are useful for both energy pipe systems and new potable water systems which incorporate double wall piping. There are also cables available for the detection of hydrocarbon liquids which makes this technology applicable to fuel, water, and energy pipe systems.

The gas sniffing systems are at present the best technology and commercial solution available for petroleum leak detection, followed by cables for overall leak detection (in double walled pipe), however, as advanced acoustic leak detection comes on line, its capabilities should meet or exceed those currently found in all of the previously researched systems.

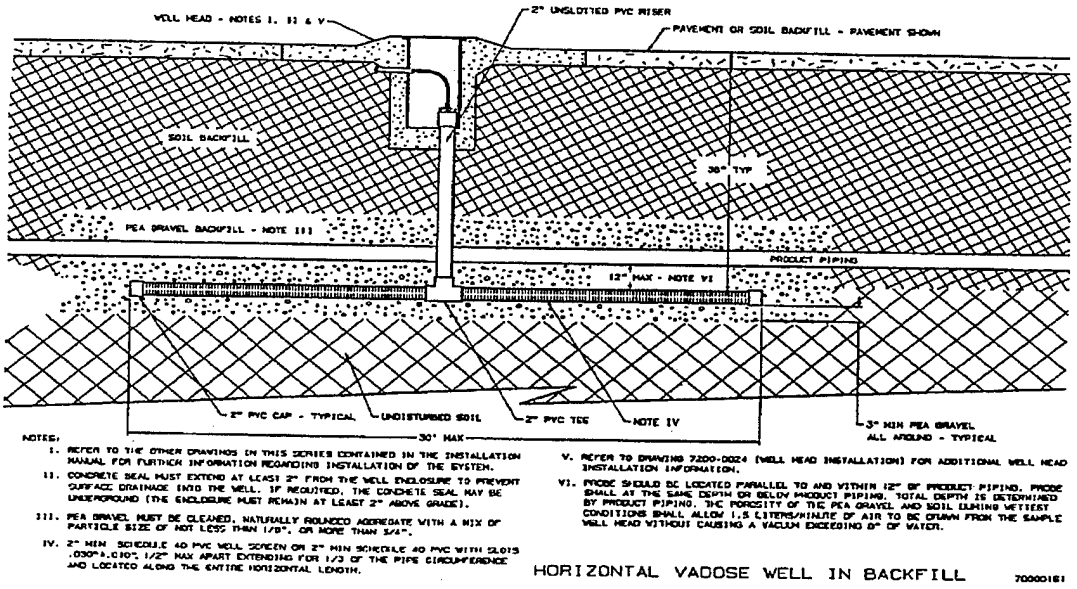


Figure 1. AZI Model Twelve-X installation schematic

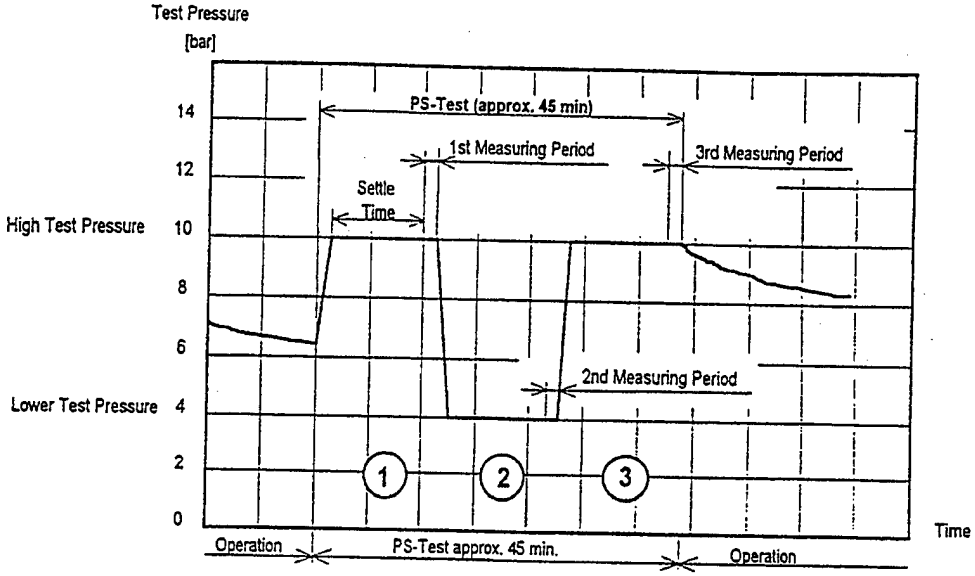
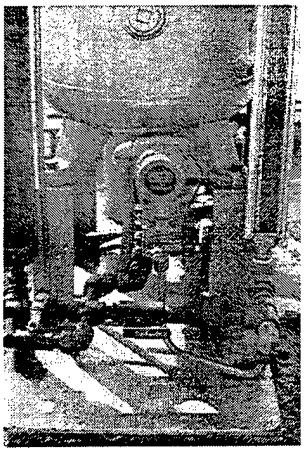


Figure 2. Hansa Consult Sample Pressure Step Test



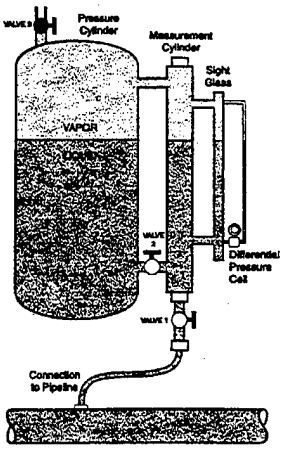
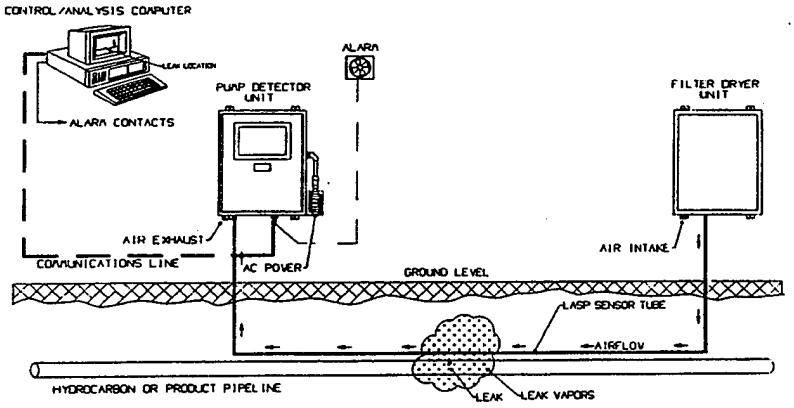


Figure 3. Schematic Diagram of the Vista Research LT100 system with a picture of the valving, graduated cylinder, and resevoir tank.



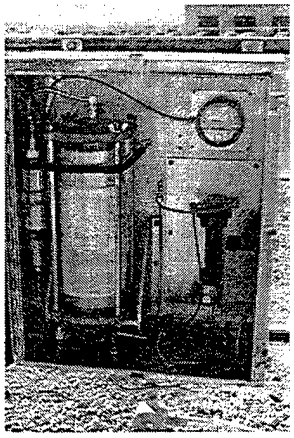
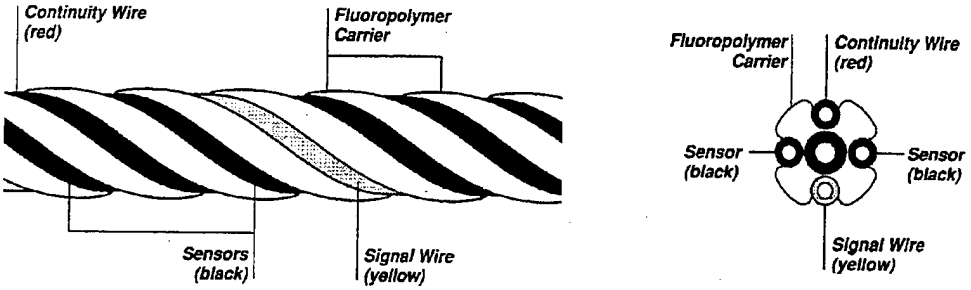


Figure 4. Argus Technologies LASP system functional diagram and Drying and Filtration Unit



Drawing not to scale

Cable diameter:	.240 inches nominal
Cable diameter with connector:	.510 inches nominal
Continuity and signal wires:	2 x 26 AWG with insulation of fluoropolymer
Sensor wires:	30 AWG with jacket of conductive fluoropolymer
Carrier:	fluoropolymer
Cable weight (50-ft length):	2 lbs

Figure 4. Raychem TraceTek cable diagram

TABLE I. SURVEYED COST DATA

Leak Detection System	Cost Data Source	Installation Cost	Equip. and Constr. Materials	Maintenance Cost (Annual)	Length of Pipline in feet	Total Cost in first Year	Total Cost Per Foot
Soil Sentry 12XP Pipeline and AST Environmental Monitoring System	Site Costs Pensacola NAS (Based on 26,400')	$274,000		$300	26,400	$274,300	$10.39
AZI Soil Sentry (Tracer Research Tracer Tightness used on storage Tanks - not included in cost data)	Site Costs Ellsworth AFB (Based on 7908')	$104,000	$40,000	$300	7,908	$144,300	$18.25
Soil Sentry 12XP Pipeline and AST Environmental Monitoring System	Manufacturer Estimate (Based on 1000')	$15,500	$10,750	$995	1,000	$27,245	$27.25
Tracer Research: ALD 2000	Manufacturer Estimate (Based on 5,000')	$134,941		$25,883	5,000	$160,824	$32.16
Raychem: Trace Tek (Quote by Tracer Research)	Manufacturer Estimate (Based on 5,000')	$113,000		$8,000	5,000	$121,000	$24.20
PermAlert: PAL-AT Leak Detection System	Manufacturer Estimate (Based on 5,000')	$49,246			5,000	$49,246	$9.85
Vista Research: Model LT100	Manufacturer Estimate (Based on 1,000')	$42,000			1,000	$42,000	$42.00
Hansaconsult: TCS Tightness Control System	Manufacturer Estimate (Based on 1,000') and Converted to US Dollars	$66,000			1,000	$66,000	$66.00
Argus Technologies	Manufacturer Estimate (Based on 5,280')	$209,457			5,280	$209,457	$39.67

Electrochemical Impedance and Noise Data for Polymer Coated Steel Exposed at Remote Marine Test Sites

F. Mansfeld, L. T. Han, C. C. Lee and G. Zhang
Corrosion and Environmental Effects Laboratory (CEEL)
Department of Materials Science and Engineering
University of Southern California
Los Angeles, CA 90089-0241, U. S. A.

ABSTRACT

The degradation of different polymer coating systems on steel exposed to natural (NS) and artificial (AS) seawater has been monitored using electrochemical impedance spectroscopy (EIS) and electrochemical noise analysis (ENA). The aim of this project is to determine the impact of microorganisms on degradation of the protective properties of polymer coatings on steel during exposure to NS. The marine test sites were Port Hueneme, California and Key West, Florida. A new approach has been developed to obtain electrochemical impedance spectra and noise data using equipment placed at the remote test sites via modem from the laboratory. Potential and current noise data were determined simultaneously. The experimental approach is described and representative data from exposure to NS and AS are presented for coating systems with different combinations of primers and topcoats. Electrochemical noise data have been analyzed in the time and frequency domains. Noise data presented as spectral noise plots have been compared to impedance spectra in Bode plots. The limitations of ENA due to the limited available bandwidth compared to EIS have been discussed. The noise resistance R_n was found to be independent of frequency and equal to the polarization resistance R_p only for frequency-independent spectral noise plots.

INTRODUCTION

In a project devoted to the evaluation of the effects of microorganisms on corrosion protection by polymer coatings twelve coating systems applied to steel have been exposed for more than one year to natural seawater (NS) at Port Hueneme, CA and Key West, FL and to artificial seawater (AS) in the laboratory as control electrolyte. Degradation of the protective properties of these coatings has been monitored using electrochemical impedance spectroscopy (EIS), electrochemical noise analysis (ENA) and visual observation. EIS has been found to be a very powerful tool for evaluation of coatings properties in many applications, while ENA seems to be promising as a monitoring tool due to the simplicity of data collection and low cost of instrumentation. A special monitoring approach has been developed for collection of EIS and ENA data from remote test sites. ENA has been performed for data obtained in the time and the frequency domains. Power spectral density (PSD) and spectral noise plots have been found useful for evaluation of the frequency dependence of electrochemical noise data. Of special interest was the relationship between electrochemical impedance and noise data which can be examined in the frequency domain. Examples of coating performance at the two marine test sites and in artificial seawater are given for polymer coatings with different types of primers or topcoats.

EXPERIMENTAL APPROACH

Materials and Methods

Materials -- In the CR series of coatings systems (Table I), the nature of the primer, midcoat or topcoat was varied in order to allow comparisons of the effects of coating type on corrosion protection in general and attack by microorganisms in particular. CR 1 and 2 had the same primer, but different mid- and topcoats. CR 5 and 6 had the same primer and midcoat, but

different topcoats, while for CR 6 and 7 the midcoat and topcoat were the same, but the primer was different. A comparison of the results for CR 6 and 7 is expected to allow determination of the effects of the primer, since the midcoat and topcoat were identical, while comparison of the results for CR 5 and 6 on the one hand and for CR 7 and 9 on the other hand will allow to assess the effects of the nature of the topcoat on corrosion protection. The total coating thickness ranged from about 125 μm for CR 2 to 275 μm for CR 5 (Table I)[1].

Methods -- Impedance spectra were collected once a week for more than one year at Port Hueneme, CA (PH) and Key West, FL (KW). The traditional approach using a frequency response analyzer (FRA) (Solartron model 1250) and a potentiostat (Solartron model 1286) was applied in laboratory studies. For collection of electrochemical impedance spectra at remote test sites, a different approach had to be applied in which the potentiostat was eliminated and a multiplexer was used to connect the recording system to the different coating systems (Fig. 1)[1,2]. A PC and the equipment shown in Fig. 1a were placed at the marine test site. Communication between the computer at USC and the computer at the test site was established as shown in Fig. 1b. Data obtained at the two remote test sites were transmitted by commercial telephone line to the computer at USC. Electrochemical potential and current fluctuations were collected simultaneously for two coated samples of the same type with the potentiostat acting as a ZRA (Fig. 1a)[1-4]. Electrochemical noise measurements (ECM) were carried out for 1024 sec. at a rate of 2 points/sec. Relative large samples (15.2 cm x 10.2 cm) were used in order to lower the impedance of the coating systems. The exposed area was about 250 cm^2 for each sample. Visual observation was performed once a month according to ASTM D 610 at PH and in the laboratory. Electrochemical impedance and noise data were analyzed using appropriate models and software developed in this laboratory[1-4].

EXPERIMENTAL RESULTS AND DISCUSSION

The type of information obtained with EIS and ENA during exposure to AS and NS will be discussed in the following for coating systems CR 5, 6 , 7 and 9, which have a zinc-rich primer (CR 5 and 6) or an epoxy polyamide primer (CR 7), an epoxy polyamide midcoat and a latex topcoat (CR 6 and 7) or a polyurethane topcoat (CR 5). CR 9 is an all-epoxy polyamide coating. Polyurethane has been reported to be degraded by microorganisms [5,6].

For CR 5 visual observation after one year indicated a total area of rust spots between 0.03 and 0.1 % of the exposed area (250 cm^2). Both samples of CR 6 and one sample of CR 7 were removed when the total rust area had reached 0.3% after 7 and 9 months exposure at PH, respectively. Removed samples were subjected to observation with an environmental scanning electron microscope (ESEM) in order to determine the spatial relationships between corrosion damage and location of bacteria[7]. For the remaining CR 7 sample less than 0.03% of rusted area was observed. All samples of CR 9 were exposed for almost three years and no loss of corrosion protection was indicated in impedance or noise data.

Fig. 2 shows impedance spectra obtained in NS (Port Hueneme, CA) (PH) for CR 5, 6, 7 and 9 after 1, 4 and 7 months. Spectra obtained in AS for the corresponding time periods had similar features[1]. It can be assumed that the continued decrease of the impedance indicated an increase of the delaminated area at which corrosion occurs. An increasing influence of mass transport phenomena at the lower frequencies was observed as pores developed in the coating and very small rust spots became apparent. The coating model[8,9], which has been used in many cases for analysis of EIS data for polymer coated metals, could not be used for analysis of the impedance spectra for CR 5, 6 and 7 shown in Fig. 2. A comparison of the time dependence of the pore resistance R_{po}, which was assumed to be proportional to the delaminated area[8,9], is given in Fig.

3a for the coating systems CR 5, 6 and 7 exposed at PH. R_{po} was estimated as the value of the impedance at which the phase angle showed a minimum. The lowest values of R_{po} were observed for CR 6, which performed the poorest according to visual observation. The increase of R_{po} for CR 5 after about 80 days seems to be due to plugging of pores in the coating by corrosion products and perhaps also bacteria. Preliminary data obtained by observation with ESEM indicated that bacteria were concentrated in pores of the coating.

The breakpoint frequency f_b increased continuously for CR 6, but leveled off at values below 100 Hz for CR 5 and CR 7 (Fig. 3b). For CR 9 f_b remained below 1 Hz at all times. The delaminated or corroding area A_d can be estimated from f_b which is defined as[8,9]:

$$f_b = (2\pi R_{po}C_c)^{-1} = A_d(2\pi R^o_{po}C_c)^{-1} = \Delta(2\pi R^o_{po}C^o_c)^{-1} \quad (1),$$

where R^o_{po} is the specific pore resistance in ohm.cm^2 and C^o_c is the specific coating capacitance in F/cm^2. The area fraction $\Delta = A_d/A$, where A is the total exposed area, can be estimated based on Eq. 1 provided R^o_{po} is known. $C^o_c = \varepsilon\varepsilon_o/d$ can be calculated using the dielectric constant ε of the polymer coating and its thickness d. Fig. 4 gives a comparison of Δ values calculated based on Eq. 1 and the results of visual observation for CR 6 exposed at PH and to AS. R^o_{po} was fixed by assuming that the Δ value obtained by visual observation after about 110 days and that calculated from f_b were the same. This approach resulted in R^o_{po} values of 1025 and 1250 ohm.cm^2 for PH and AS, respectively, which are close to the polarization resistance R_p values obtained for bare steel in AS by weight loss and impedance measurements. Apparently corrosion occurred mainly in pores filled with rust and therefore the parameter obtained by analysis of the impedance spectra was R_p instead of R_{po}. This result suggested that the commonly used model for analysis of impedance spectra for polymer coated metals[9] needs to be modified as will be discussed below. Excellent agreement between the Δ values obtained by the two methods was observed over a four months period (Fig. 4). During the entire test period Δ for CR 6 increased by about a factor of 30 in both media. A comparison of the results in Fig. 3 and 4 for CR 6 in PH shows that f_b = 1000 Hz corresponds to Δ = 0.1%.

The impedance spectra for CR 6 have been analyzed using the equivalent circuit in Fig. 5. The coating capacitance C_c, represented here by a generalized constant phase element (CPE), is shortened by R_p which is in series with an open boundary finite length diffusion (OFLD) element which models the diffusion impedance when the diffusion layer has finite dimensions (Fig. 5). Using Boukamp's notation[10] the mass transport impedance is given by[11,12]:

$$Z_{OFLD} = \{\tanh (B(j\omega)^{1/2})\}/Y_o(j\omega)^{1/2} \quad (2\ a),$$

where $B = l/(D)^{1/2}$ is the characteristic diffusion parameter, l is the diffusion length, D is the diffusion coefficient and $Y_o = (\sigma(2)^{1/2})^{-1}$. For infinite values of l this model becomes the Randles circuit, in which the Warburg impedance Z_w is in series with R_p and is given by:

$$Z_w = \sigma(1 - j)\omega^{-1/2} \quad (2\ b),$$

where σ is the Warburg coefficient.

Excellent agreement between the experimental spectra and the fit to the model in Fig. 5 was observed for CR 6. Fig. 6 shows the results for CR 6 exposed to AS for 162 days. The deviation between the two curves at the highest frequencies in the Bode-plot was due to instrumental artifacts. Fig. 7 shows the time dependence of the Warburg coefficient σ and the fit parameter B. As the corroding area A_d increased, σ decreased and a similar increase of Δ with time as that shown in Fig. 4 was determined qualitatively. Assuming $D = 10^{-5}$ cm^2/sec for oxygen in the aqueous solution assumed to fill the pores in the coating and using the average coating thickness of about 200 μm for the diffusion length l results in B = 6 (sec)$^{1/2}$ which is close to the average value observed during the first five months (Fig. 7). In the following time B increased to about 15 (sec)$^{1/2}$.

Fig. 8a shows the time dependence of the mean values of the potential of the coupled electrodes E_{coup} vs a Ag/AgCl reference electrode for CR 5, 6 and 7 during exposure at PH. E_{coup} increased slowly for CR 5 in the first three months from values typical of zinc to those of actively corroding steel. For CR 6 E_{coup} first increased and then decreased to values close to - 500 mV. For CR 7, which had an epoxy polyamide primer and midcoat, much more positive values of E_{coup} were observed (Fig. 8a). The mean coupling current I_{coup} was usually higher for CR 6 than for CR 5 and 7 (Fig. 8b). After about six months the sign of I_{coup} changed for CR 6 (Fig. 8b).

From the experimental electrochemical noise data collected in the time domain, the noise resistance R_n was obtained by statistical analysis as $R_n = \sigma\{V(t)\}/\sigma\{I(t)\}$, where $\sigma\{V(t)\}$ and $\sigma\{I(t)\}$ are the standard deviations of potential V and current I fluctuations, respectively. Spectral noise ($R_{sn}(f)$) plots were obtained by analysis in the frequency domain as the ratio of the Fast Fourier Transforms (FFT) of potential and current fluctuations at each frequency f. The spectral noise resistance R^o_{sn} was defined as the limit of a spectral noise plot for f --> 0[1-4, 13]. In Fig. 9 $\sigma\{V(t)\}$ and $\sigma\{I(t)\}$ are shown as a function of time. The time dependence of $\sigma\{V(t)\}$ was very similar for all three coatings with $\sigma\{V(t)\}$ fluctuating around 1 mV (Fig. 9a). After about two months $\sigma\{V(t)\}$ was the highest for CR 7 at most times. Very low values of $\sigma\{I(t)\}$ were observed for CR 5 (Fig. 9b). This result pointed to a limitation of the equipment used for these measurements indicating that the lowest value of $\sigma\{I(t)\}$ which could be detected was about 0.7 nA. Since $\sigma\{V(t)\}$ generally had values close to 1 mV, the maximum values of R_n which could be measured reliably were about 1 Mohm corresponding to about 10^8 ohm.cm^2. Fig. 10 shows the time dependence of R_n and R^o_{sn} for CR 5, 6 and 7 at (PH). The values and time dependence of these two parameters were similar to those of R_{po} shown in Fig. 3. It will be noted that R_n usually had smaller values than R^o_{sn} (Fig. 10).

Additional information can be obtained from power spectral density (PSD) plots since the slopes of these potential and current plots are considered to depend on the prevailing corrosion mechanism. PSD plots are shown in Fig. 11 and 12 for CR 6 at KW for two exposure times. These figures also present comparisons of impedance spectra and spectral noise plots which can be obtained as discussed above or from PSD plots as $R_{sn}(f) = |V_{PSD}/I_{PSD}|^{1/2}$, where V_{PSD} and I_{PSD} are the potential and current power levels, respectively. FFT and PSD plots provide a convenient check of noise data quality which is difficult to obtain in the time domain. In general, V_{PSD} decreased and I_{PSD} increased continuously with constant slope as polymer coatings degraded[1].

In the PSD plots for polymer coatings exposed to NS and AS no dc limit was observed which probably was due to the very low PSD values. In fact, as shown in Fig. 11a, I_{PSD} remained at or below the current power level of about 10^{-20} A^2/Hz arising from the potentiostat used as ZRA

until coating damage occurred. The slopes of the potential PSD plots remained close to - 2, while the slopes of the current PSD plots changed from initial values of 0 to - 2 once sufficient coating degradation had occurred and the instrumentation threshold level had been exceeded. For equal values of the slopes of both PSD plots the R_{sn} plots become independent of frequency.

Initially the R_{sn} plots were significantly lower than the impedance plots (Fig. 11) due to experimental I_{PSD} values which were too high and therefore produced R_{sn} values which were too low. As I_{PSD} exceeded the instrumentation limit, R_{sn} plots approached impedance plots (Fig. 12) suggesting that both types of measurements could provide the same data in the frequency domain. Fig. 11b and 12b also include R_n. After 33 days R_n was lower than R^o_{sn} and R_p due to the instrumentation threshold discussed above. As time increased, R_n approached R^o_{sn} and R_p, but always remained below these two values. This result was considered to be due to the manner in which these data were collected. R^o_{sn} was obtained as the dc limit of spectral noise plots (or the average of the last 10 lowest frequency points), while R_n was determined at the sampling frequency $f_s = 2$ Hz.

More recently, noise data have been obtained with instrumentation having better current resolution (AutoAC DSP, ACM Instruments, Cart-in-Carmel, UK). Experimental potential and current noise data are shown in Fig. 13a and b for CR 9 exposed to AS for 780 days. The corresponding PSD plots are shown in Fig. 13c and d. The current PSD data at higher frequencies are close to the instrument limit of about 10^{-25} A^2/Hz due to the very protective nature of the coating on CR 9 (Fig. 13 d). Despite this problem, excellent agreement between the spectral noise plot and the impedance spectrum collected on the same day was observed (Fig. 13e). This result demonstrates that the impedance of the system can be measured either by applying an external signal as in the traditional EIS technique or by analyzing the naturally occurring potential and current fluctuations. Fig. 13 also lists E_{coup} and I_{coup} as well as the standard deviations σV and σI used to calculate R_n.

Assuming that identical spectra can be obtained from noise and impedance measurements a relationship between the slopes S_V and S_I of potential and current PSD plots, respectively, and S_{rsn} of the spectral noise plot can be obtained. For PSD plots

$$\log V_{PSD} = a_V + S_V \log f \tag{3a}$$

$$\log I_{PSD} = a_I + S_I \log f \tag{3b},$$

while for the spectral noise plot

$$\log R_{sn} = a_{rsn} + S_{rsn} \log f \tag{3c}.$$

Since $R_{sn}(f) = |V_{PSD}/I_{PSD}|^{1/2}$, it follows that:

$$S_{rsn} = 1/2\ (S_V - S_I) = S_Z \tag{4},$$

where S_Z is the slope of the Bode plot. For an impedance spectrum with a dc limit for $f > f_s$, $S_V = S_I$ according to Eq. 4, while for a capacitive spectrum $S_V - S_I = -2$. It will be recognized that the relationship $R_n = R_p = R^o_{sn}$ will only be valid for equal slopes of the PSD plots[14,15]. For all other conditions R_n will depend on f as discussed elsewhere[14]. Mansfeld and Xiao[4,16] have observed satisfactory agreement between R_n, R^o_{sn} and R_p for iron exposed to NaCl solutions of different corrosivity.

The main question remaining in the analysis of electrochemical noise data was the frequency dependence of R_n[14,15]. In order for R_n being equal to R_p, R_n obviously has to be independent of frequency, since R_p is defined as:

$$R_p = \lim_{f \to 0} (|Z(f)|) - R_s \qquad (5)$$

for a simple R_p - C circuit with a solution resistance R_s. Based on Eq. 4 and 5 R_n will be equal to R_p only if $S_V = S_I$. This conclusion is based on the assumption that spectral noise plots and impedance spectra are identical. For the majority of the spectral noise plots obtained for polymer coated steel exposed to seawater $S_V = -2$ was observed. Therefore R_n equals R_p for $S_I = -2$. It will be noted that for polymer coated metals the physical meaning of R_p as defined in Eq. 5 depends on the equivalent circuit describing the observed impedance behavior.

For the coating system shown in Fig. 13 the impedance spectrum was capacitive in the frequency region in which noise data were obtained. For $S_{rsn} = -1$ and $S_V = -2$, Eq. 5 predicts that $S_I = 0$. In this case R_n will not be equal to R_p. The dependence of R_n on the bandwidth $f_{max} - f_{min}$ can be determined by integration of the potential and current PSD plots[17,18]. Since the variance $\sigma\{X(t)\}^2$ of a random signal X equals the integrated value of its PSD plot (PSD_X) between two frequencies f_{max} and f_{min}, it follows that:

$$R^2_n = \frac{\int_{f\,min}^{f\,max} PSD_V(f)df}{\int_{f\,min}^{f\,max} PSD_I(f)df} = \frac{\int_{f\,min}^{f\,max} PSD_I(f)df \cdot R^2_{sn}}{\int_{f\,min}^{f\,max} PSD_I(f)df} \qquad (6).$$

According to Eq. 6 R_n equals R^o_{sn} only if the spectral noise plot is independent of f in agreement with the previous conclusions based on Eq. 4. In this case it also follows that $R_n = R_p$.

Eq. 6 can be used to determine the dependence of R_n on bandwidth, i.e. f_{max} and f_{min}. The results for coating system CR 9 are shown in Fig. 14, where R_n has been calculated according to Eq. 6 for decreasing values of f_{max} at fixed f_{min}. Obviously R_n increased with decreasing bandwidth and can therefore not be related to any characteristic coating property in a simple manner. The different R_n values are plotted in Fig. 14 as a function of $f_{max} = 0.5\ f_s$. The spectral noise plot is presented for the original values of $f_{max} = 1$ Hz and $f_{min} = 0.98$ mHz. Bertocci et al[18] have obtained results similar to those in Fig. 14 for Al in 1 M KCl. They stressed the point that R_n varies with sampling frequency and tends to be lower than the zero frequency limit of |Z|. R_n was therefore lower than R_p for this system.

Fig. 15 is an example for a coating system which had degraded sufficiently for the impedance to reach a dc limit in the measured frequency range. Good agreement between spectral noise and Bode plots was observed again. In this case the spectral noise plot had a slope close to zero and R_n showed only a slight dependence on bandwidth.

Inspection of spectral noise plots and impedance spectra in Fig. 11 - 15 demonstrates the limited frequency range in which spectral noise plots can be obtained. The high-frequency limit could be extended by increasing the data collection rate beyond the presently used 2 points/sec., however instrumentation noise limits this possibility. The low-frequency limit could be decreased by increased time for data collection (1024 sec. at present), however this possibility is not very attractive. In fact, one of the reasons that ENA has become quite popular is the - perhaps

erroneous - assumption that electrochemical noise measurements can be performed in a very short time.

SUMMARY AND CONCLUSIONS

Since the performance of CR 6 was inferior to that of CR 5 and CR 7, one can conclude that the nature of both the primer (zinc-rich primer (CR 5 and CR 6) vs. epoxy polyamide (CR 7)) and the topcoat (polyurethane (CR 5) vs. latex (CR 6 and CR 7)) play an important role in corrosion protection. No coating degradation was observed for the all-epoxy polyamide system CR 9 (Table I) during exposure for more than two years at PH and in AS and for more than one year at KW. Based on the results obtained for all CR coatings with EIS, ENA and visual observation for exposure at Port Hueneme, CA and Key West, FL as well as in laboratory experiments it can be concluded that the effectiveness of corrosion protection decreased in the sequence CR 9 > CR 7 > CR 5 > CR 6 > CR 1 > CR 2. This conclusion is in general agreement with the results by Murray and Hack[19], who exposed CR 1, CR 5, CR 6 and CR 9 to AS, and by Tsai and Mansfeld[8], who exposed the same materials as well as CR 2 to 0.5 N NaCl. The relatively poor performance of the alkyd-based paints CR 1 and CR 2 and the excellent corrosion protection by the all-epoxy polyamide paint CR 9 were found in all cases. However, in the earlier studies[8,19] CR 6 performed better than CR 5. A detailed analysis of the effects of coating properties and microorganisms on corrosion protection of steel by polymer coatings will be performed when all samples have been removed from the test sites in California and Florida and the laboratory.

The relationship between spectral noise plots and impedance plots is subject to on-going investigations using the vast amount of data collected for the coating systems exposed at Port Hueneme, CA and in AS for three years and at Key West, FL for more than two years[14,15]. Potential and current data have to be obtained simultaneously and analyzed in the frequency domain to obtain FFT or PSD plots. Spectral noise plots can be determined from such plots and compared with impedance spectra. Provided that instrument limitations do not affect the validity of electrochemical potential and current measurements, very similar spectra can be obtained from noise and impedance measurements. The dependence of R_n on bandwidth can be obtained by integration of the PSD plots as a function of f_{max} or f_{min} (Eq. 6). The results in Fig. 13 - 15 obtained with improved instrumentation for current measurements have shown that spectral noise plots and impedance spectra are identical once valid current PSD plots can be obtained[14,15]. This means that the dc limit of an impedance spectrum in a Bode plot corresponds to a spectral noise plot with zero slope in the same frequency range. R_n, R^o_{sn} and R_p will have the same value only in this case. In the capacitive region of the spectrum the slopes of the potential and current PSD plots will differ by - 2 and R_n will depend on bandwidth. For very protective polymer coatings on steel with capacitive impedance spectra in the frequency region for which meaningful noise data can be obtained - usually 1 Hz to 1 mHz - R_n will have a strong dependence on bandwidth and therefore does not have a definite relationship to a particular coating property. For degraded coatings, for which the impedance has reached a dc limit for f > 1 Hz, the relationship $R_n = R^o_{sn} = R_p$ will be observed with the meaning of these parameters depending on the equivalent circuit appropriate for the particular coating/metal system. A frequency independent spectral noise plot will be obtained only if the slopes of the potential and current PSD plots have equal values. R_n is therefore only independent of bandwidth of the noise measurement when $S_V = S_I$. In all other cases R_n might provide a qualitative measure of coating degradation, but can not be related to a specific coating property.

ACKNOWLEDGMENT

This project is being funded by the Office of Naval Research (Dr. A. J. Sedriks) under Contract No. N00014-94-1-0026.

REFERENCES

1. H. Xiao, "Development of the Electrochemical Noise Analysis Technique and its Application in Monitoring of Localized Corrosion Phenomena", Ph. D. thesis, Univ. Southern California, Sept. 1995.

2. H. Xiao, L. T. Han, C. C. Lee and F. Mansfeld, "Collection of Electrochemical Impedance and Noise Data for Polymer Coated Steel from Remote Test Sites", Corrosion (in press)

3. F. Mansfeld, C. Chen, C. C. Lee, and H. Xiao, Corros. Sci. 38, 497 (1996).

4. H. Xiao and F. Mansfeld, J. Electrochem. Soc. 141, 2332 (1994).

5. R. G. Baker, G. H. Kitchen and R. R. Welch, Nat. Bur. Stand. (US) Spec. Publ. 452, 25 (1976).

6. K. J. Seal and R. A. Pathirana, Int. Biodet. Bull. 18, 81 (1982).

7. F. Mansfeld, H. Xiao, L. T. Han, C. C. Lee and C. Chen, Corrosion/96, paper No. 659, NACE (1996)

8. C. H. Tsai and F. Mansfeld, Corrosion 49, 726 (1993).

9. F. Mansfeld, J. Appl. Electrochem. 25, 187 (1995)

10. B. A. Boukamp, "Equivalent Circuit (Equivcrt.Pas)", Univ. Twente, May 1989

11. A. H. Windle, in "Polymer Permeability", Elsevier, 1986

12. F. M. Geenen, J. H. W. deWit and E. P. M. Van Westing, Prog. Org. Coat., 18, 299 (1990)

13. F. Mansfeld and H. Xiao, ASTM STP 1232, 42 (1994).

14. F. Mansfeld and C. C. Lee, "The Frequency Dependence of the Noise Resistance for Polymer Coated Metals", J. Electrochem. Soc. (in press)

15. F. Mansfeld, C. C. Lee and G. Zhang, "Comparison of Electrochemical Impedance and Noise Data in the Frequency Domain", Electrochim. Acta (in press)

16. F. Mansfeld and H. Xiao, ASTM STP 1277, 59 (1996)

17. U. Bertocci, C. Gabrielli, F. Huet and M. Keddam, J. Electrochem. Soc. 144, 31 (1997)

18. U. Bertocci, C. Gabrielli, F. Huet, M. Keddam and P. Rousseau, J. Electrochem. Soc. 144, 37 (1997)

19. J. N. Murray and H. P. Hack, Corrosion 48, 671 (1992)

Table I : Composition and Thickness of Coating Systems (CR series)

Sample Name	CR1	CR2	CR5	CR6	CR7	CR9
Substrate	Hot Rolled Steel	Hot Rolled Steel	Hot Rolled Steel	Hot Rolled Steel	Hot Rolled Steel	Hot Rolled Steel
Primer	Alkyd high solid[1]	Alkyd high solid[1]	Zn - rich Primer[4]	Zn - rich Primer[4]	Epoxy Polyamide[5]	Epoxy Polyamide[5]
Midcoat	Low VOC Alkyd[2]	Silicone Alkyd[3]	Epoxy Polyamide[5]	Epoxy Polyamide[5]	Epoxy Polyamide[8]	Epoxy Polyamide[8]
Topcoat	Low VOC Alkyd[2]	Silicone Alkyd[3]	Urethane[6]	Latex[7]	Latex[7]	Epoxy Polyamide[9]
Average thickness (μm)	164	125	275	254	196	192

Note :

1. TT-P-645B
2. TT-E-489H
3. TT-E-49
4. SSPC-20, type 2
5. MIL-P-24441, Formula 150
6. MIL-C-85285
7. MIL-P-28578
8. MIL-P-24441, Formula 151
9. MIL-P-24441, Formula 152

a)

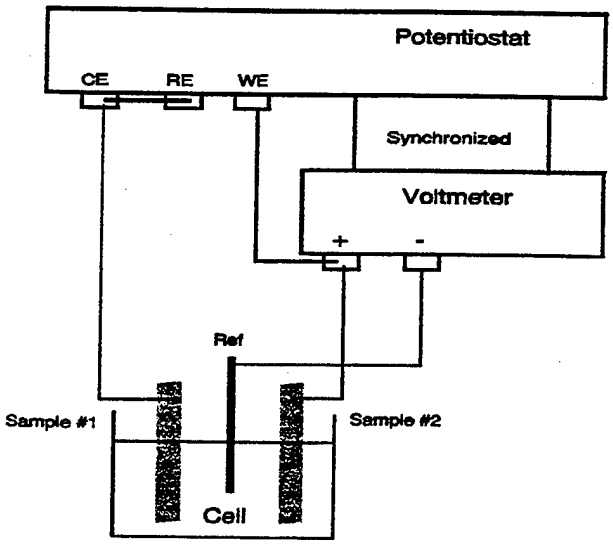


Fig. 1a

b)

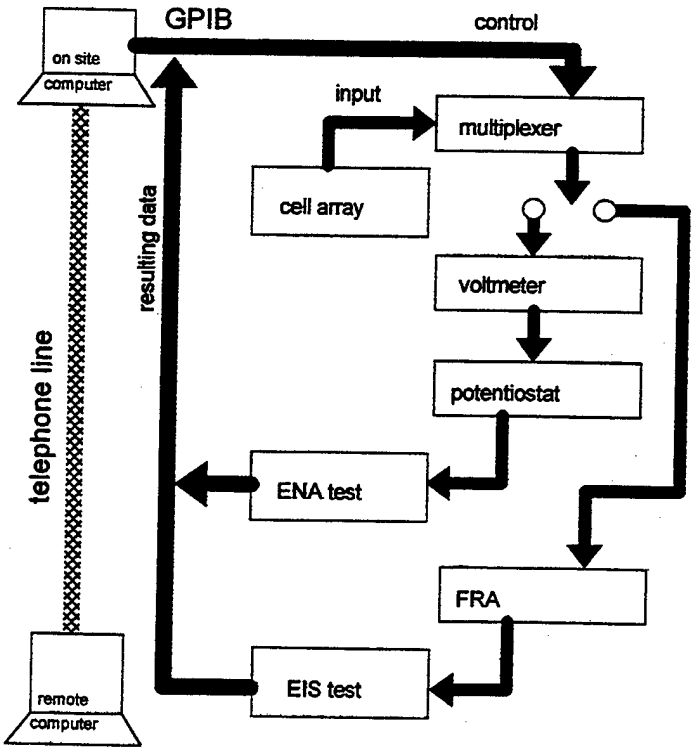


Figure 1. Experimental approach for collection of electrochemical impedance and noise data from a remote test site [1].

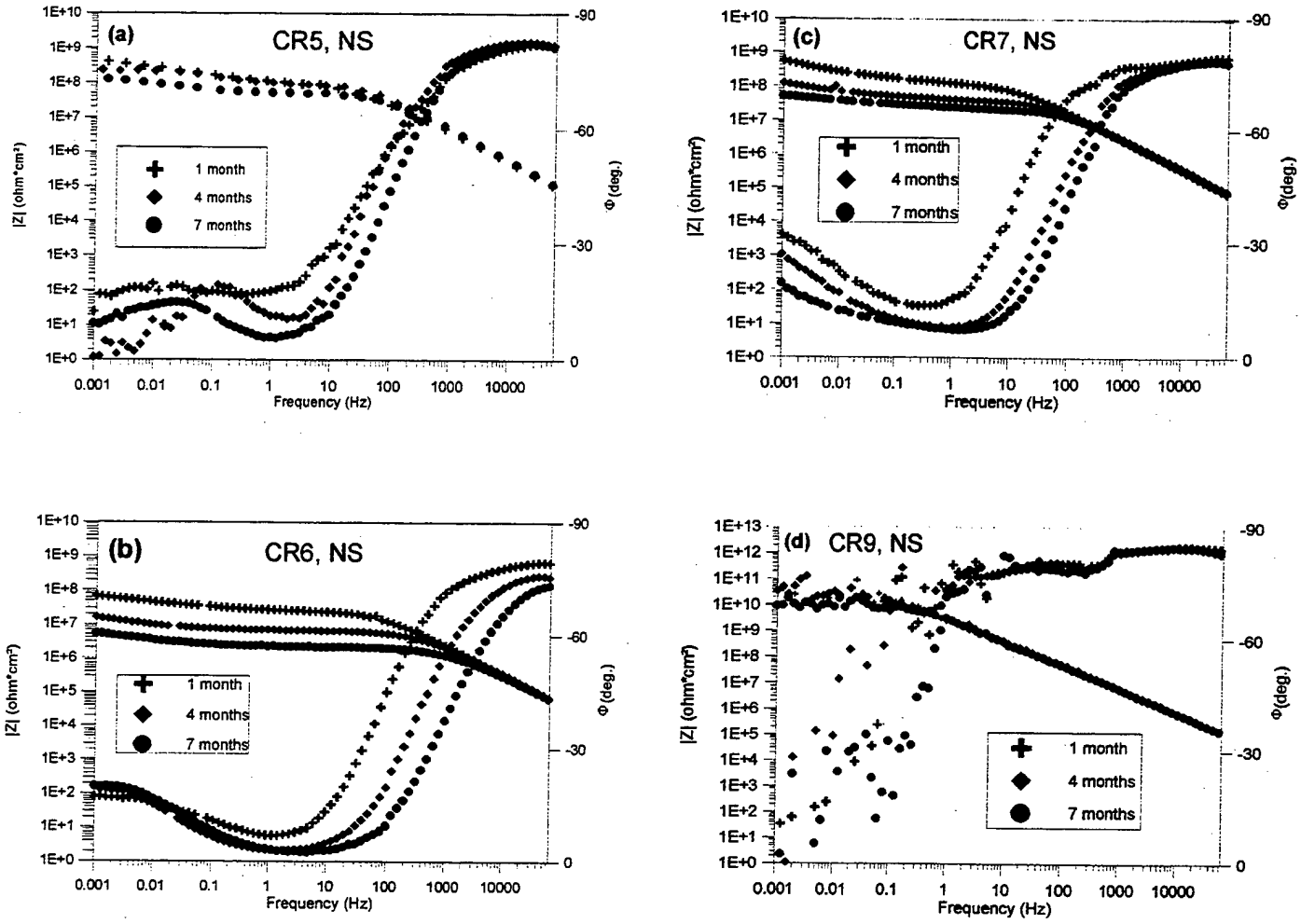


Figure 2. Impedance spectra for CR 5, CR 6, CR 7 and CR 9 exposed to natural seawater for 1, 4 and 7 months at Port Hueneme (PH), CA.

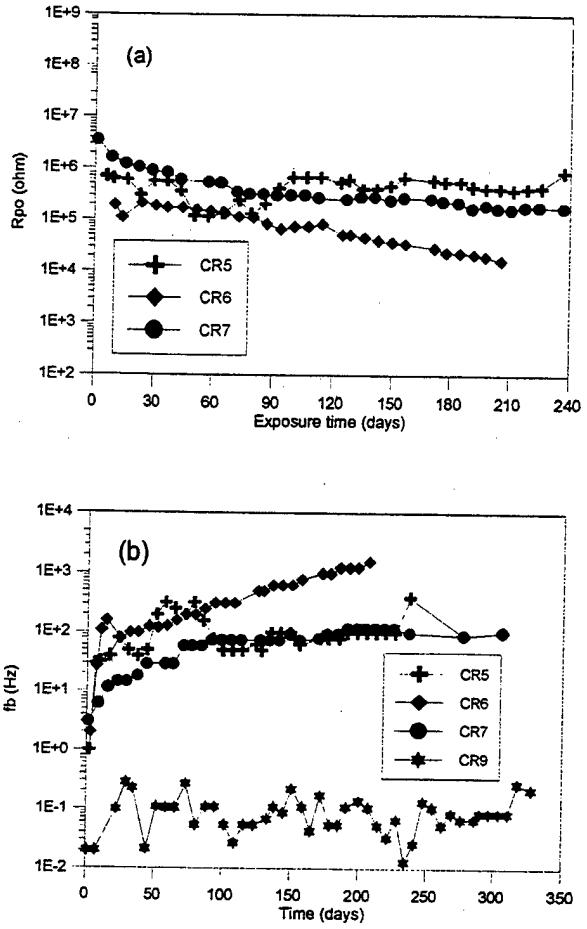


Figure 3. Time dependence of pore resistance R_{po} (Fig. 3a) and breakpoint frequency f_b (Fig. 3b) for CR 5, CR 6, CR 7 and CR 9 exposed at Port Hueneme, CA.

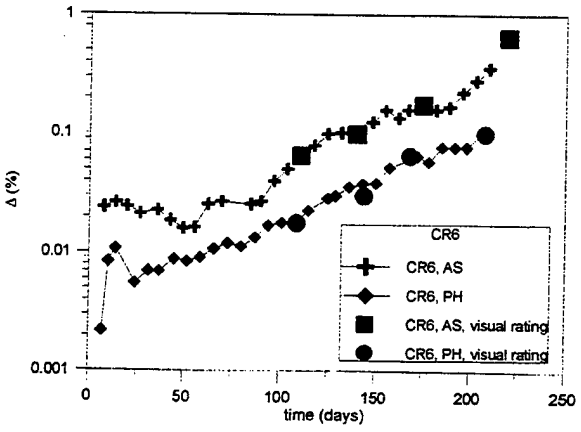


Figure 4. Time dependence of corroding area obtained from f_b and by visual observation according to ASTM D 610 for CR 6 exposed at Port Hueneme, CA.

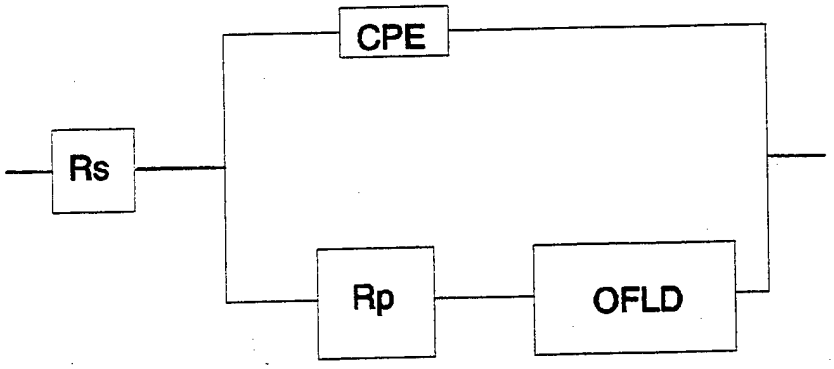
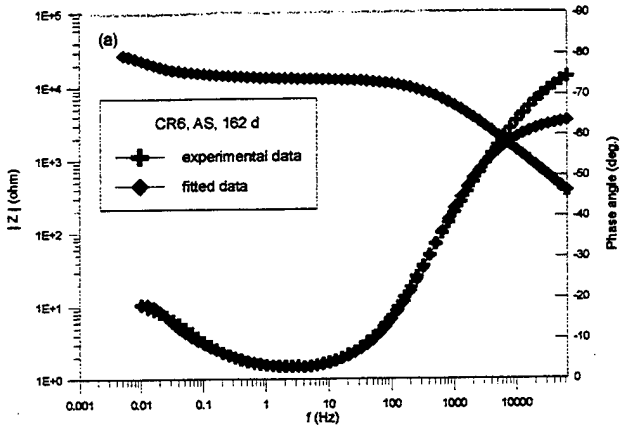


Figure 5. OFDL model for impedance spectra with charge transfer and mass transport contributions.



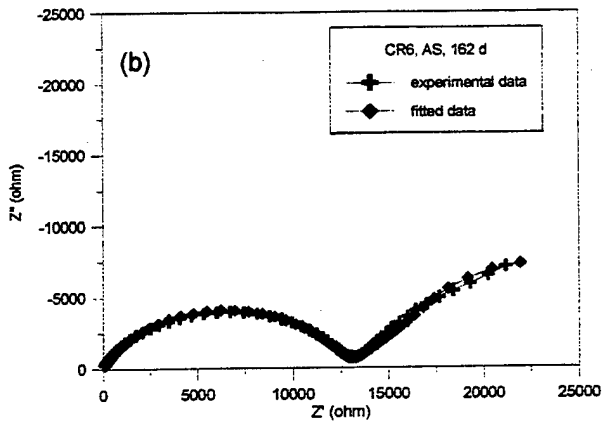


Figure 6. Comparison of experimental and fit data for CR 6 exposed to AS for 162 days. Fit parameters were CPE: $Y_o = 2.36\ 10^{-7}$ $(ohm)^{-1}$, n = 0.723; $R_p = 1.38.10^4$ ohm; OFLD: $Y_o = 3.84.10^{-4}$ $(ohm)^{-1}$, B = 6.64 $(sec)^{1/2}$.

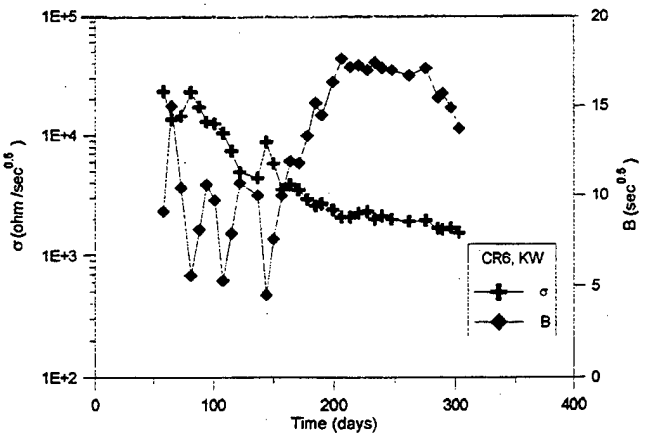


Figure 7. Time dependence of Warburg coefficient σ and and fit parameter B for CR 6 exposed to KW.

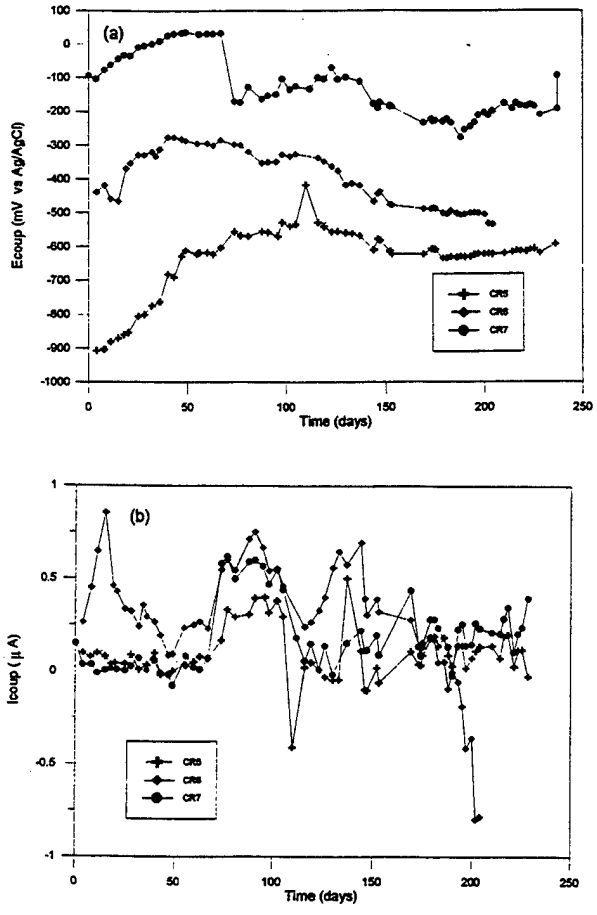


Figure 8. Time dependence of E_{coup} (Fig. 8 a) and I_{coup} (Fig. 8 b) for CR 5, CR 6 and CR 7 exposed at Port Hueneme, CA.

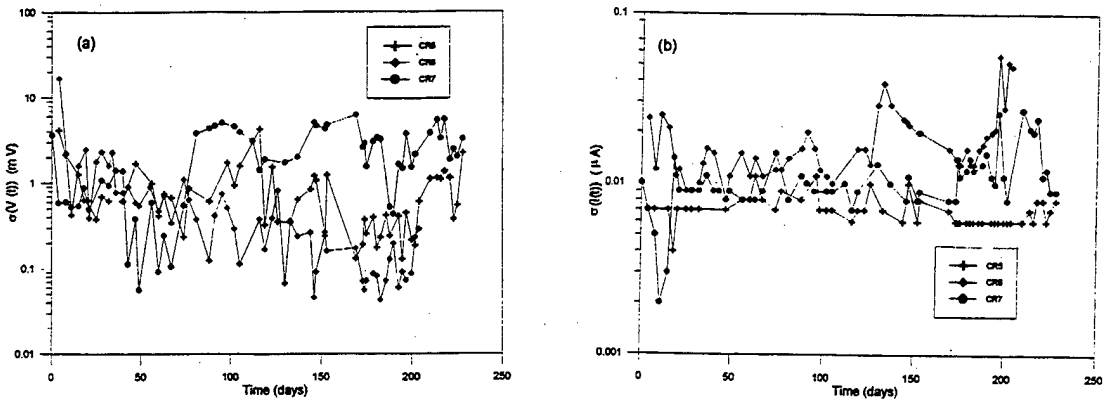


Figure 9. Time dependence of $\sigma\{V(t)\}$ (Fig. 9 a) and $\sigma\{I(t)\}$ (Fig. 9 b) for CR 5, CR 6 and 7 exposed at Port Hueneme, CA .

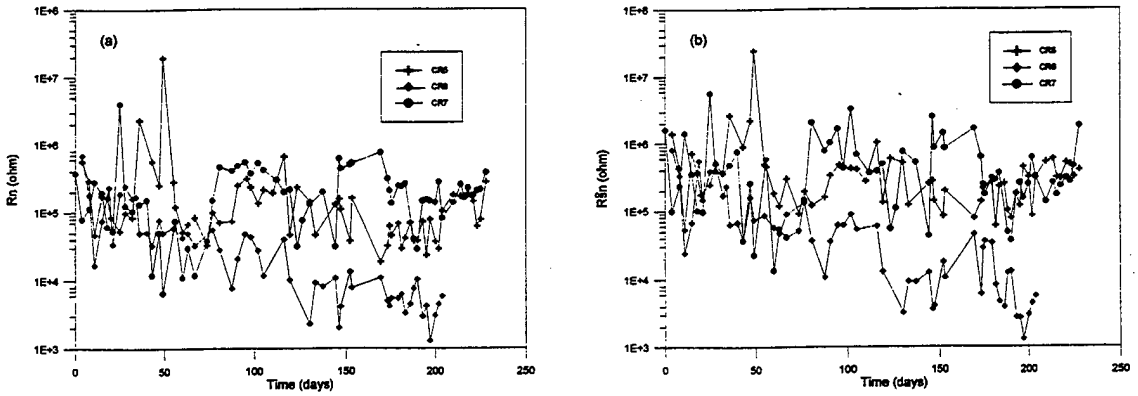


Figure 10. Time dependence of R_n (Fig. 10 a) and R^o_{sn} (Fig. 10 b) for CR 5, CR 6 and CR 7 exposed at Port Hueneme, CA.

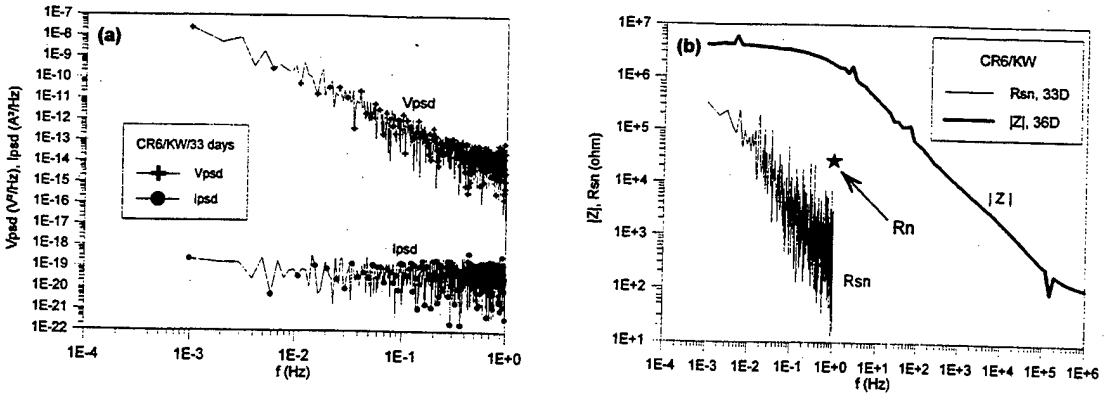


Figure 11. Potential and current PSD plots (Fig. 11 a) and comparison of impedance spectra (/Z/), spectral noise plots (R_{sn}) and R_n (Fig. 11 b) for CR 6 exposed at Key West (KW), FL for about one month.

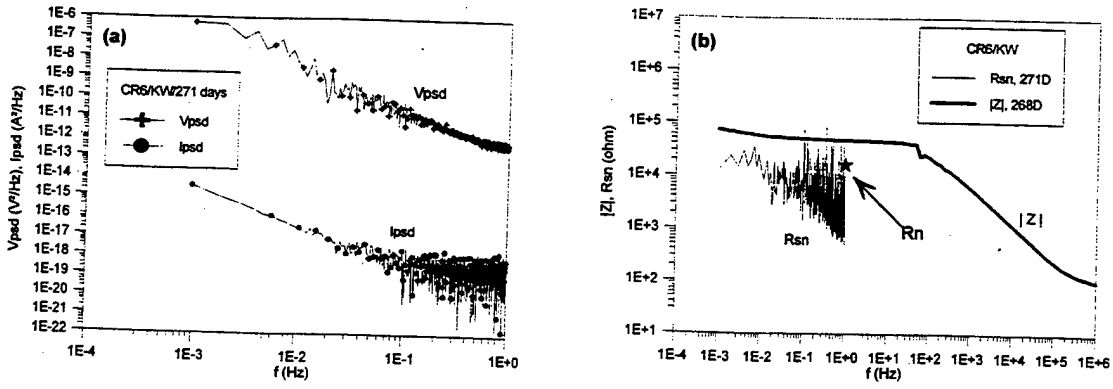
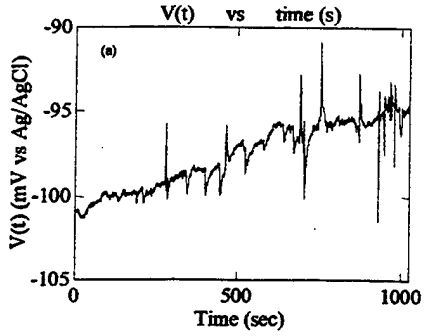
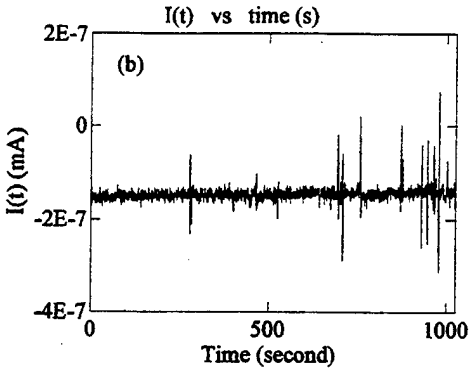
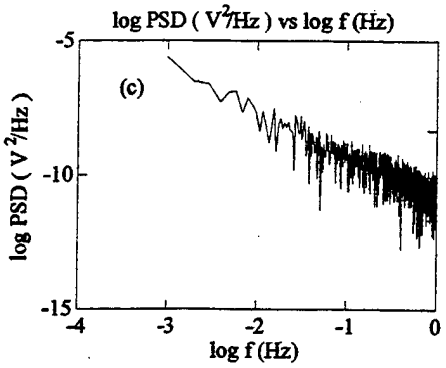
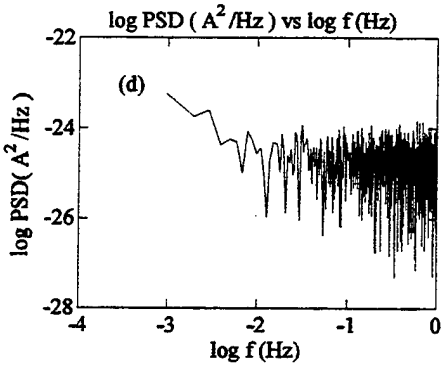


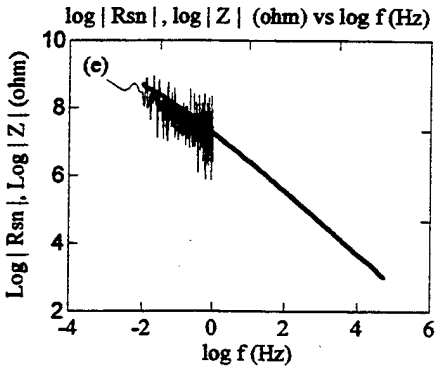
Figure 12. Potential and current PSD plots (Fig. 12 a) and comparison of impedance spectra (/Z/), spectral noise plots (R_{sn}) and R_n (Fig. 12 b) for CR6 exposed at KW for about nine months.











CR9, 780d, AS

mean potential:	E_{coup} = -0.0976	V
mean current:	I_{coup} = -1.462·10 $^{-10}$	A
SDev potential :	σV = 0.00199	V
SDev current :	σI = 1.602·10^{-11}	A
noise resistance :	R_n = 1.243·10^8	ohm
spectral noise resistance :	R^o_{sn} = 4.023·10^8	ohm
average of R_{sn} :	R_{snave} = 4.012·10^7	ohm

Figure 13. Analysis of electrochemical noise data for CR 9 exposed to AS for 780 days.

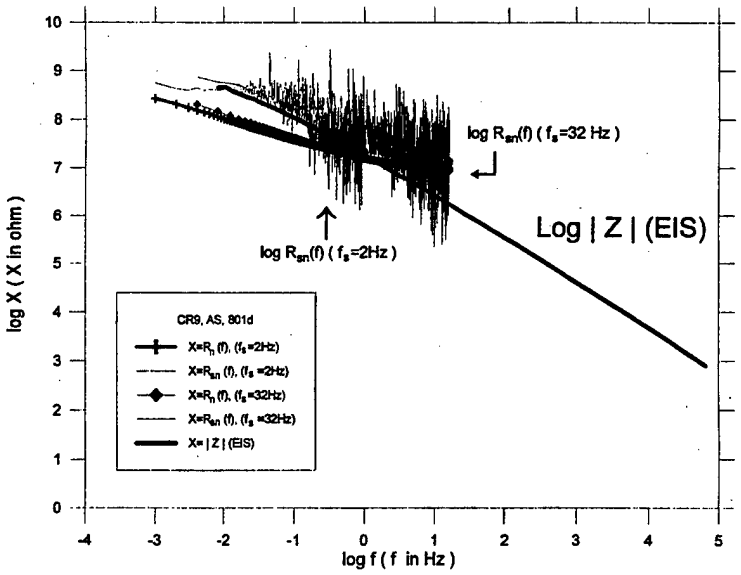


Figure 14. Comparison of impedance spectrum (|Z|), spectral noise plots ($R_{sn}(f)$) and $R_n(f)$ for CR 9 exposed to artificial seawater for 801 days.

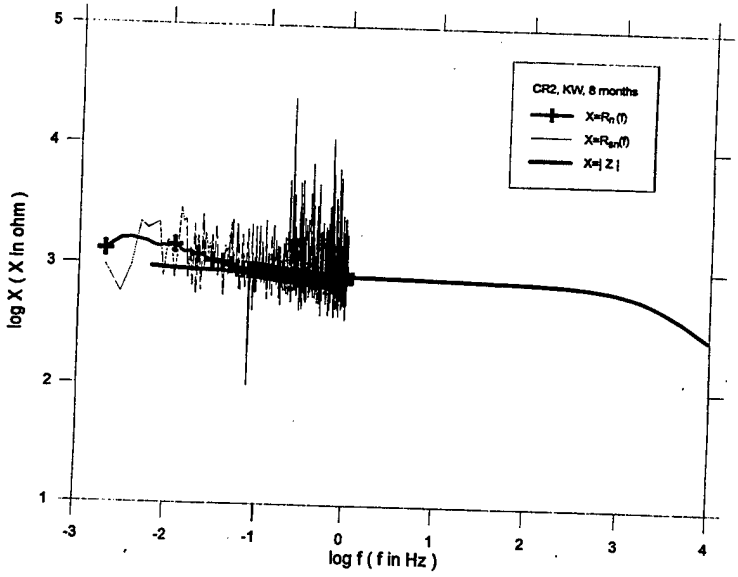


Fig. 15. Comparison of impedance spectrum (|Z|), spectral noise plots ($R_{sn}(f)$) and $R_n(f)$ for CR 2 exposed to natural seawater for 8 months.

Corrosion Testing in the U.S. Marine Corps

E. B. Bieberich and A.D. Sheetz
Carderock Division, Code 613
Naval Surface Warfare Center
9500 MacArthur Blvd.
West Bethesda , MD 20817-5700

ABSTRACT

Based on the high level of corrosion damage observed on vehicles returning from Southwest Asia (Desert Shield and Desert Storm), attention is being focused throughout the U.S. Marine Corps on improving corrosion prevention and control of combat and tactical equipment. The Naval Surface Warfare Center-Carderock Division Code 613 (Marine Corrosion Branch) is presently conducting both Research and Development (R&D) and Operations and Maintenance (O&M) programs for the United States Marine Corps. These programs support the Marine Corps Corrosion Prevention and Control (CPAC) program, which was established by the Corps to reduce corrosion of combat and tactical equipment and associated maintenance burdens.

INTRODUCTION

Based on the high level of corrosion damage observed on vehicles returning from Southwest Asia (Desert Shield and Desert Storm), attention is being focused throughout the U.S. Marine Corps on improving corrosion prevention and control of combat and tactical equipment.

For the past several years, the Marine Corps Systems Command (MARCORSYSCOM) has tasked the Naval Surface Warfare Center- Carderock Division (NSWCCD) to conduct both Research and Development (R&D) and Operations and Maintenance (O&M) programs which could reduce corrosion of USMC combat and tactical equipment and associated maintenance burdens. The R&D program is directed towards validation of existing corrosion prevention methods, identification of more corrosion resistant materials and coatings, and development of accelerated corrosion tests to permit rapid screening of better materials. The O&M program is directed toward identification of corrosion problems and their countermeasures, fleet implementation of corrosion prevention and repair, and in-service evaluation of new materials.

The purpose of this paper is to provide an overview of existing efforts in the following areas: Corrosion Surveys, Marine Atmosphere Corrosion Tests, Accelerated Corrosion Tests and Field Tests.

APPROACH

The overall result of the R&D and O&M tasks are the same; improving corrosion prevention and control of U.S. Marine Corps combat and tactical equipment. However, the individual task elements have their own methodology. The elements of this program related to corrosion tests, which will be discussed in this paper, are described below.

Corrosion Surveys

On-site inspections of equipment (surveys) permit the identification of common and widespread corrosion problems, and the related materials, maintenance and logistics issues. While the appearance of corrosion on different vehicles or weapon components may be similar, the causes can vary, including non-specification materials, inappropriate or poorly-applied coatings, exposure to unusually severe environments, or lack of required periodic maintenance. Sometimes, metallurgical failure analysis can provide a more exact identification of the causes of corrosion, thus permitting specific solutions to problems.

Marine Atmosphere Corrosion Tests

Atmospheric corrosion tests are being conducted on new materials and coatings to evaluate corrosion control methods for USMC vehicles and equipment. The tests consist of exposing specimens in a marine atmospheric environment, while monitoring their corrosion performance through periodic inspections. Using standard specimen types, various corrosion control methods will be tested concurrently so that comparative evaluations can be made.

The tests are being conducted at the Kure Beach test site of the LaQue Center for Corrosion Technology (LCCT) in North Carolina. The exposure site is a seaside lot 25 meters from the ocean. Due to the proximity of the ocean, test specimens are continually exposed to salt-laden air from the nearby surf. This site was selected because it is representative of the corrosive marine environment in which USMC vehicles operate, and because it has a historical data base covering over 40 years of marine atmosphere corrosion testing.

The test specimens are designed to have a similar configuration to the vehicle area or component that they are being used to evaluate. Where possible, actual vehicle components are used. A three year exposure duration with semiannual inspections is planned for all tests.. During these inspections, corrosion of the specimens is documented and relative performance of the various corrosion control options evaluated. This data is used in conjunction with field tests to recommend corrosion resistant alternatives for the present fleet of usmc vehicles and future acquisitions.

Accelerated Corrosion Tests

With the rapid development of new materials and coatings options, and the immediate need for improved materials specifications in procurement contracts, a method to compare new materials options with proven performers is required to permit rapid integration of new technology into impending procurements. A similar need has been forced by the US government

direction to use commercial standards instead of military specifications. Often, combat and logistic equipment is procured as a "non-developmental item" (NDI) or a commercial-of-the-shelf (COTS) acquisition, therefore, an accelerated test specified in the contract would permit the contractor to verify equal or better performance of his choices to a government-identified minimum performance standard.

In FY 96, NSWC began an evaluation of the GM9540P/ B accelerated corrosion test for Marine Corps applications. The accelerated corrosion performance was evaluated of some components and test panels for which field experience is reasonably well-documented, and/or for which marine atmosphere corrosion tests are being conducted. The tests were run for 120 days and evaluated for correlation with long term and field exposures.

In FY 97, a comparative evaluation of three different accelerated test methods, ASTM B117, ASTM G85 and GM9540 P/B, will be conducted to determine the best method for the Marine Corps to evaluate potential corrosion performance, and to provide a comparative basis for evaluation of commercially-proffered coatings and materials when data from one of those three tests is provided.

Field Tests

As corrosion testing and technology transfer efforts identify more corrosion resistant coatings, materials and designs for Marine Corps use, it is prudent to verify on fielded equipment that life-cycle performance payback is actually provided. Components or designs expected to provide significant savings are installed on appropriate vehicles, monitored, and compared to the performance of the standard materials. Upon installing the new corrosion control options on a set of vehicles, these vehicles are then returned to their normal unit to operate in typical environments. Units which deploy on amphibious ships and operate off LCACs are preferred because of the more severe environments. The vehicles will be tracked so that periodic inspections can be made to evaluate corrosion performance of the modified vehicle areas. Since the test areas will be exposed to actual vehicle environments, the field tests should provide the most accurate data on the service performance of the proposed corrosion control techniques. Field tests are used in conjunction with both the marine atmosphere and accelerated tests to identify the most effective corrosion control methods.

STATUS OF PROGRAM EFFORTS

Survey Results

Several vehicles from each vehicle classification identified by maintenance personnel as representative of their normal maintenance burden were surveyed at each of the three visited Marine Corps Bases; Camp Butler, Okinawa Japan, Camp Pendelton/ Twentynine Palms, California, and Camp LeJuene, North Carolina. This allowed survey of a large number of vehicles as well as a comparison of the corrosivity of the environments at each base. Overall, more corrosion problems were found on vehicles at Camp Butler in Okinawa than the other bases.

Conversely, few corrosion problems were found at Twentynine Palms. Although the severity of corrosion varied between the bases, the problem areas (type of corrosion and location) were similar.

The results of the corrosion surveys for a wide variety of Marine Corps combat systems has been reported previously[1]. Since a high similarity of problem areas was seen in the surveys, a matrix of marine atmospheric and accelerated corrosion tests was developed to evaluate potential corrosion resistant upgrades. The specific materials tested and results for both of these tests are detailed below.

Marine Atmosphere Corrosion Tests

As stated previously, marine atmospheric tests are conducted at the LCCT Kure Beach exposure site with progress reports from the site detailing the condition of each set of test specimens every six months. A complete list of materials in test is contained in Table 1. In the summer of 1996, Hurricanes Bertha and Fran made landfall sufficiently close to the test site to slightly affect some of the tests. Where specimens were lost or damaged, comment will be made in the following sections. Although the exposure tests are scheduled to last for three years, significant conclusions about the relative performance among the different materials can be made in several instances. A short summary of the present status of the corrosion performance of the various efforts follows:

CARC Coatings & Primers- Four primers topcoated with solvent-base CARC and a water-base camouflage coating (WBCC) were applied to structural steel, armor steel, and aluminum. After eighteen months, LCCT evaluated the performance of the panels by non-destructive visual observation, using the expected results from ASTM inspection standards D-610 and D-1654 as a guide. ASTM D-1654 requires scraping the scribed panels, which will not be done until test completion; however, an estimate of the coated area expected to fail upon scraping was made instead. Table 2 provides that evaluation.

Based on performance of the primers and topcoats at the scribed area of the panels, the best-to-worse performance of the primers on steel substrates (structural or armor) is zinc silicate (IC-531), zinc molybdate (F-84), the Army epoxy (MIL-C-52192) and the Mare Island Type IV epoxy (MIL-P-24441). Both the zinc silicate and zinc molybdate primers virtually eliminated undercutting of coating next to the scribe by corrosion; the zinc silicate almost completely stifled corrosion even at the bare scribe area. Coating performance on the aluminum panels had similar rankings. Even though the early-formulation water-base CARC was difficult to apply (the final coating had some runs and minor blisters), in concert with the primers tested, it appeared to provide superior anti-corrosion protection compared to the standard CARC topcoat, although the desert-tan standard CARC used in this test is said to perform poorly compared to the other colors in the field.

Electrical Connector Coatings & Alternate Materials- Four specimens each of the standard cadmium-coated aluminum connectors are in marine atmosphere exposure, along with six different coatings, an electroless nickel-plated aluminum connector with and without

Amlguard coating, and uncoated stainless steel and composite connectors. The thin film coatings, Amlguard, Tectyl 846 and Cortec VCI-368 are all presently-specified[2,3] coatings per MIL-C-16173D for Marine Corps use.

Based on the twelve month LCCT report, the following observations are made. No degradation in electrical conductivity has been measured in any connector. The standard cadmium-plated aluminum connectors show very little corrosion of the outside shell and base. Also, of the thin corrosion prevention compounds (CPC's) specified for Marine Corps use, performance is similar; preliminary indications are that the solvent-cutback types VCI-368 (both forms) and the Tectyl 846 appear to be out-performing the water-displacing corrosion prevention compound Amlguard. The two thick-film coatings are intact; the Dow 3140 is transparent, and has no associated corrosion; the PR-1773 is opaque. Provided that the Dow 3140 can be easily removed after some time in service, it would be the preferred thick coating to use. This coating was easiest to apply and permits visual inspection without removing the coating. The electroless nickel plated aluminum connectors have coating failure and the nickel coating is now accelerating corrosion of the aluminum substrate. The exterior of the stainless steel connector shows uniform surface rust. The lighter-colored portions of the composite connectors are deteriorating in a fashion that looks like surface corrosion.

Based on exposure tests so far, it is suggested that the extent of electrical connector corrosion observed during surveys in the fleet may be related to maintenance practices. It is recommended that Marine Expeditionary Forces apply coatings specified in maintenance documents[4,5] to electrical connectors, especially on the outside of vehicles, every six months or at least once per year. Solvent cutback CPC's have performed well.

Fasteners and Fastener Coatings- The fastener test basically consists of four of each fastener type bolted through each of two different aluminum armor materials, for a total of eight bolts (one set) of each type tested. One set of bare steel HHCS Grade-8 ½-13X1" bolts, five sets with different coatings (including the standard cadmium), and one set of stainless steel bolts were exposed in the marine atmosphere.

The performance of the fasteners and fastener coatings is noted as follows. The standard bare fasteners are heavily corroded. The stainless steel fasteners are in excellent condition. Of the sacrificially-coated fasteners (cadmium-plated, zinc-plated, zinc-nickel and Sermetel), all suffered some minor coating removal on one side due to sandblasting during Hurricane Bertha. Since, during normal usage, bolts and nuts get coating damage from wrenches, the test is not invalid. The degree of erosion from the wind and sand indicate coating factors such as adhesion, hardness, and thickness. The electroless zinc-nickel fasteners are in the best condition with only minor edge corrosion, followed by the zinc and then cadmium plated fasteners. (The Sermetel fasteners were performing excellently at six months, but were lost in Hurricane Fran; that set of coated fasteners will be reinitiated in test.) The inert Xylan 5214-coated fasteners show extensive coating breakdown and corrosion of the bolts. One set was lost in the hurricane.

Several other fastener coatings have recently gone into test, a replacement set of Sermetel fasteners, two sets of Dacromet-coated fasteners (Dacromet 320 / Plus L & Dacromet 320 /

Dacrokote 105), and Xylan 5252. They will be mounted through plastic panels rather than aluminum.

It probably should be noted that, with the exception of the (more expensive) stainless steel fasteners, all of the coated fasteners are beginning to show some corrosion after 18 months exposure. Therefore, except in the most benign environments, most fasteners will probably require some additional corrosion protection, either the selected primer for the subject vehicle, or periodic treatment with corrosion prevention compounds.

Aluminum Armor- Seven plates (4"X8"X ¼") each of aluminum alloys 5083 and 2519 were exposed in the fastener tests with four coated bolts bolted through the middle of each plate. After 18 months of marine atmosphere exposure, the following results are evident. Alloy 5083 is essentially unattacked with minor surface pitting around some of the bolts, especially the standard steel bolts, where it appears that pitting initiated under steel corrosion products. Alloy 2519 shows uniform pitting on entire surface of each panel.

Inorganic Coatings- Two sets of panels were placed into marine atmosphere exposure, Table 1, a set of flat, coated steel panels with a slanting milled scribe through the coating, and a set of KTA Tator specimens, a thicker steel panel with a steel "U" skip-welded to one face of the plate. The scribed panels could represent the sides of a cab and other sheet-metal sections, while the milled scribe is sufficiently wide enough to indicate whether the sacrificial coatings "throw" protection to areas not actually covered by the coating itself, as in a scratch. However, it should be noted that the company which scribed the panels cut the scribe deeper than desired; it was requested that the coating be removed, however, the company cut up to 1/32" deeper. While the deeper scribe makes it harder to evaluate the panels, it does not invalidate the test. The KTA panels are to test the capability to fill or stop corrosion in crevices, as well as offer a more difficult surface to coat. After six months exposure, the status of the panels is:

Scribed Panels- LCCT evaluated the performance of the scribed panels by non-destructive visual observation, using ASTM standards D-610 and D-1654 as a guide. ASTM D-1654 requires scraping the scribed panels, which will be done at test completion; however, an estimate of the coated area expected to fail upon scraping was made instead.
Table 3 provides that evaluation for each type of panel with the results noted below.

For the thermal spray aluminum topcoated with CARC or WBCC both sets of panels show evidence of cathodic protection of the scribed area (reduced corrosion). However, the corroding aluminum is causing creepage of the coating back from the scribe. The WBCC panels have marginally less creepage than the standard CARC panels.

For the zinc silicate panels, all three types are performing very well, with no undercutting of any coatings at the scribe area. Of those topcoated with WBCC, the Briner and Bruder panels have less corrosion in the scribe than the Ganicin panels. In discussions with Mr. Vince Pucco, resident chemist of Bruder Co, he stated that Bruder recently discontinued production of the MAB 24-A-190, because their major purchaser of the product (HiSteel Corp) experienced blistering of the zinc silicate when it was topcoated with acrylic latex topcoats. The company

supposedly also used other manufacturer's products (Porter, PPG, & DuPont products), and they all had similar blistering problems. No problems have been experienced with polyurethane topcoats of CARC or WBCC over zinc silicates in our test programs, however, so we will continue evaluation of these products for military use.

The electrocoated G-90 panels are corroding in the scribe and at panel edges. The hot-dip panels have almost entirely suppressed corrosion at the scribe; however, the coatings are not adhering well to the galvanizing.

KTA Panels- Performance of the KTA panels is summarized for each of the panel types as follows. For panels with the standard army primer with CARC, corrosion has started at welds around the "U" and edges of panels.

The thermal spray aluminum topcoated with CARC are in excellent condition, with one minor rust spot in weld of one of four panels, and indications of aluminum corrosion products at the base of the "U" in all four specimens.

For the zinc silicate panels, the 4 Ganicin panels have corrosion on the sides of the "U"s and 2 have corrosion on the edges. Four Briner panels have some attack on sides of "U". CARC-topcoated panels from both sets have minor rust bleed on sides of "U". Both sets may have suffered some sandblasting (on sides of U) during Hurricane Bertha. The Bruder panels are all in excellent condition, no corrosion, with or without topcoat.

The hot-dipped galvanized panels are all in excellent condition, no corrosion. However, there is significant coating loss from sandblasting in Hurricane Bertha and scratches from Hurricane Fran. It is suggested that poor adhesion of primer on galvanize made panels more susceptible to coating loss.

Headlamps- Steel headlamps are presently used on HMMWVs and five-ton trucks. They typically have corrosion of the frame and internal parts. Headlamps of the original steel material, electrogalvanized steel, and 3003 aluminum alloy were fabricated by the original manufacturer for evaluation in marine atmosphere and accelerated corrosion tests.

Results from the six month inspection of marine atmospheric tests can be summarized as follows; there is some rusting starting at holes, screws and edges of the steel headlamps and the galvanized and aluminum headlamps have not started showing signs of corrosion.

Fuel Lines- Previous observations have documented corrosion of steel fuel and brake lines. Potential alternatives, stainless steel fuel lines and steel fuel lines using two different electrodeposited coatings (Zincroterne and Procoat 2000), are being tested in marine atmospheric exposure at LCCT as potential replacements. The marine atmospheric exposure tests are being run concurrently with field tests on Marine Corp vechicles.

On 27 Febuary 1996, twelve fuel lines were placed on marine atmospheric exposure at LCCT. The material and coating specifications for the fuel lines and the number of samples exposed are summarized in Table 1.

Results of the first visual inspection show the performance after eight months of cumulative exposureare as follows. All of the steel specimens show areas of rust and loss of the coating. Both of the coatings are begining to show breakdown. Neither of the coatings is performing better than the other. There is no indication of corrosion on the stainless steel fuel lines.

Exhaust Components- On 23 July 1996, two HMMWV mufflers and six fording kits were placed on marine atmospheric exposure at LCCT. The mufflers are constructed of aluminized 409 stainless steel coated with a heat resistant paint which meets military specification MIL-P-14105 (Paint, Heat-Resisting [for steel surfaces]). The six fording kits are three sets of duplicate specimens, constructed of three material combinations which are painted with two different paints, providing both a cross comparison for the coatings and materials. Table 4 shows the materials and paints used in this test. A three year evaluation is planned with six month inspection intervals.

Radiators- Four nylon candidate replacement HMMWV radiators and one standard radiator were exposed at LCCT. The tests of the nylon and standard radiator materials were initiated on 15 December 1994 and biyearly inspections have been conducted to evaluate corrosion performance. The test design consists of sections of each radiator material placed in open wooden boxes with fans placed behind them to draw salt-laden air between the fins. In the nylon radiator test, two of the four nylon radiator sections are shielded from UV light with the other two directly exposed.

Currently, the two year exposure interval has passed and the following observations are noted. There is no difference in the performance of the nylon radiators in either direct or indirect UV exposure. There is corrosion occurring in the crevices formed by the welds of the aluminum frame and along the frame itself which encases the nylon radiators. Within one year of exposure there was extensive loss of the coating on the fins and tubes of the standard radiator. Coating loss has allowed the copper fins and tubes to form a uniform green patina. There does not appear to be pitting of the material thus far. Coating loss and subsequent corrosion of the steel frame of the standard radiator has occurred. A reinforcing element in one corner of the frame has corroded to the point of failure.

Marine Atmospheric exposure testing of one stainless steel AAV radiator at LCCT was initiated on 3 January 1996. The manufacturer provided the following compositions: sides/tanks - 304 stainless steel, internal tubes - bronze alloy 2613, fins - continuous solder-coated copper plate and washers/fasteners - 304 stainless steel. During the first six months of exposure the radiator received some damage to the factory-applied exterior coating due to blowing sand from Hurricane Bertha. This does not appear to have adversely affected the corrosion performance of the radiator.

After six months of marine atmospheric exposure, the following observations are made. The stainless steel body of the radiator is performing well, even in areas of coating loss and possible substrate damage. Some of the fasteners used to assemble segments of the radiator together are steel. These fasteners are corroding heavily. Other fasteners used in assembling the radiator which are stainless steel show no signs of corrosion. A uniform green patina is forming on the copper fins and brass tubes of the radiator with no indication of pitting of either of these materials at this time.

Frame Rails- One HMMWV frame rail which is galvanized was recently obtained for marine atmospheric exposure. Initiation of the test began in January 1997 with a three year test duration planned.

Crevice Coatings- During FY 97, an evaluation will be initiated of various coatings which could be applied to the crevices formed by assembled components which would normally not be disassembled during vehicle repair. The tests will be conducted for three years at the LCCT, Kure Beach North Carolina, 25m marine atmospheric exposure lot and are in support of CPAC tasks. They will be conducted in parallel with a six-month accelerated evaluation of crevice coatings at the Naval Research Laboratory, Key West Florida. The test matrix consists of a total of 19 crevice treatments plus one set of untreated standards. The crevice coatings to be used in this test are of three types - conversion, zinc-rich and ultra-thin film - and range from aerosols to brush-on application. The specific coatings to be used and the number of samples is defined in Table 5.

The test specimens consist of two 3" x 6" x 1/16" cold rolled SAE 1018 low carbon steel panels which are bolted together with stainless steel bolts to form a crevice, Figure 1. The top approximately 0.75" of one panel will be folded out to form an opening to the crevice. Prior to coating application all surfaces are to be sandblasted to a 2-3 mil profile. The exposed (non-mating) surfaces are to be coated with a water-reducible Army epoxy primer (MIL-P-53030) to a dry film thickness of 2-3 mils. The specimens will then be topcoated with Waterborne Camouflage Coating (WBCC, MIL-C-29475) to a minimum dry film thickness of 2-3 mils. The mating surfaces of the test specimens will not be coated. The panels will then be bolted together and precorroded. Precorrosion is to consist of dipping the panels in natural seawater followed by six weeks of marine atmospheric exposure.

Following the precorrosion period, the specimens will be removed from exposure, rinsed and allowed to dry for 24 hours indoors. Then the opening leading into each specimen will be coated with one of the nineteen crevice coatings. All crevice coatings will be applied in accordance with manufacturers recommendations. The crevice coatings will be tested as applied to two sets of precorroded steel specimens: one with a topcoat, and one without. The topcoat applied over the crevice coating will be the same MIL-P-53030 primer and WBCC used on the exterior of the specimens

There will also be sixteen "standard" specimens in test. These specimens will receive no crevice coating. Following precorrosion, eight of these specimens will be coated with the MIL-P-

53030 primer and MIL-C-29475 topcoat, whereas the other eight will have no coating in the crevice.

The specimens will be inspected and documented before test initiation and upon application of the crevice coatings. Once the crevice coatings have been applied, the panels will be placed back in marine atmospheric exposure. The specimens will be positioned at 30° to the horizontal facing the ocean with the crevice opening on the frontside and facing upwards. The specimens will be inspected every six months with photographic documentation provided. Half-way through the test period, one sample from each test configuration will be removed, disassembled and photographed.

Upon the completion of the test, the specimens will be disassembled and corrosion in the crevice areas of each specimen evaluated including color photographs. The specimens will be cleaned and weight loss measurements calculated. Average and maximum depths of corrosion are also to be measured in the crevice areas of each specimen.

Accelerated Corrosion Tests

Phase I - Capability of GM 9540 to Produce Corrosion Similar to Service

The primary purpose of the accelerated corrosion tests was an evaluation of the GM 9540 P test[6] method to determine whether this test could emulate the corrosion attack which occurs on Marine Corps equipment in the field. This report will summarize the general appearance of the test components with respect to early test results in the marine atmosphere (although the comparison will not be completely validated until three years of exposure have been logged), and provide comment on comparative appearance of accelerated test performance versus USMC field performance. The tests were run for 120 days, with a visual inspection at 80 days. These time periods coincide with possible test criteria now being considered by the Army for procurement. Table 6 lists the materials and components tested.

While the primary purpose of the accelerated corrosion test is to determine whether the general corrosion appearance of metals and coated metals used on USMC vehicles can be generated in a short time, the results of this first test may also indicate improved performance of some new materials. Improved performance will be discussed, especially where marine atmosphere tests indicate improved performance as well. Finally, the length of test period required to produce a reasonable level of corrosion (80 vs. 120 days) will be discussed.

The accelerated tests were run on plates and components made of steel (structural, hot-dip and electro-galvanized), aluminum (alloys 2519, 5083 and 6061) and stainless steel (alloy 304). Coatings on steel and aluminum included zinc and aluminum rich paints on steel brake lines; zinc-silicates, epoxy primers and urethane topcoats on steel; epoxy primer and urethane topcoats and cadmium plating on aluminum. The corrosion and coatings performance of the plates and components are summarized in Tables 7 through Table 13. Results will be discussed by the categories displayed in Table 6..

Headlamps- Steel, electrogalvanized steel and aluminum headlamps were tested in triplicate using the GM 9540 P test[6]. Table 7 provides a written summary of the appearance of the nine test headlamps after 80 and 120 days. At 80 days the difference in corrosion resistance of each material is evident with the steel headlamp retaining ring showing coating failure and corrosion of the substrate. At 120 days the headlamp assemblies were taken apart. The general appearance and coating failure mode of the steel headlamp is very similar to those seen in the field. The aluminum headlamp assembly performed better in the accelerated corrosion test than the other material types. The use of aluminum headlamp assemblies should be pursued as a replacement of the current steel headlamps. Also of note from this test is the condition of the mounting hardware from the aluminum headlamp assembly. Use of steel mounting hardware with this material was inappropriate. For future use, stainless steel mounting hardware should be substituted. The overall performance ranking of the headlamps is summarized in Table 7.

Electrical Connectors- Three cadmium-plated and three stainless steel electrical connectors were tested in the GM 9540 P test[6] to compare to marine atmosphere and field performance. Table 8 summarizes the results of 80 and 120 days of exposure. After 80 days of exposure the cadmium-plated connectors showed corrosion around the edges of the connector mount. After 120 days the corrosion at the connector mount was greater. Though the nature of the corrosion product and the degradation of the cadmium coating were similar to the results seen in the field, different locations were attacked. Further comparison will be made after 3 years of marine atmosphere exposure is available. The stainless steel connectors showed no difference from 80 to 120 days. The connectors performed very well through this test but did show some minor signs of corrosion in crevices.

Brake Lines- Steel brake lines with the same undercoat and two differing topcoats, and a stainless steel brake line were tested in triplicate using the GM 9540 P test[6]. Table 9 summarizes the results of those tests. After 80 days of exposure both coated steel brake lines had begun to fail. The Pro-Kote system had completely failed while some of the Zyncroterne system was still intact. The stainless steel brake lines showed no signs of corrosion on bold surfaces but did have pitting which initiated from corrosion of the springs. The galvanized springs and nuts had severely corroded on all specimens. No value is seen for the use of the protective springs, and it is recommended that their use be discontinued. After 120 days both coating systems on the steel brake lines had completely failed. The corrosion of the substrate for one of the brake lines using the Pro-Kote system was so severe that it fractured under its own weight. The stainless steel brake line was pitted underneath the spring. To reduce susceptibility to pitting, 316 stainless steel should be considered in place of 304 stainless steel.

Scribed Panels- Five types of coatings were applied to steel panels in triplicate. Three of the coatings were zinc silicates and the other two were CARC and CARC with a galvanized undercoat. A 1/8" scribe was milled in each panel along the diagonal to within one inch of the edge. Table 6 shows each coating type and its corresponding manufacturer or specification. Table 10 summarizes the results of the 80 and 120 day observations for all the panels. The zinc silicate coated panels performed much better in test than the CARC coated panels. After 120 days of accelerated exposure the zinc silicate coatings were intact and had very little delamination along the scribe. The best performing zinc silicate coating, MAB 24-A-190, still provided some

degree of protection to the scribe area. The CARC coatings did not perform well. The CARC coating with a galvanized undercoating showed heavy corrosion in the scribe and blistering and delamination of the coating after 80 days. Table 11 provides a rating of the scribe test panels appearance after 120 days of exposure.

KTA Crevice Panels- The accelerated corrosion test KTA crevice corrosion test panels were coated with the same coatings as used in the scribe test with the addition of a water-based CARC coating system. Table 6 summarizes the coatings applied and their respective manufacturer or specification. This specimen configuration was used to test the coatings ability to protect areas of uneven surface profile such as welds and areas where water can be trapped. The addition of the water-based CARC coating was to evaluate this product as a potential replacement to the current CARC coatings for which there are environmental concerns. The Bruder MAB 24-A-190 coating performed the best, providing excellent corrosion protection to the surface with only very minor area of pinhole corrosion in the weld areas. The other zinc silicate coatings in this test performed moderately. In this test the CARC coating with a galvanized undercoat also performed very well. This performance appears to be a function of the galvanizing and not the coating. The other CARC coatings performed poorly. In both the CARC and the water-based CARC, there is blistering of the coating and heavy corrosion in the U-channel. Table 12 provides a rating of the KTA crevice test panels appearance after 120 days of exposure.

Steel Panels- The main emphasis of this portion of the test was to validate the results of the GM9540 P test[6] versus marine atmospheric exposure. For an accelerated corrosion test to be an accurate predictor of future performance, the corrosion mechanism which is accelerated must be the dominant process which would normally occur. As a means to verify the results of the accelerated tests, three uncoated panels each of structural steel and hot-dipped galvanized steel were tested.

The bare steel panels were all heavily corroded by the 80 day visual inspection. The 120 day inspection of the bare steel panels did not reveal any changes in the panels. Visual inspections at 80 and 120 days for the bare steel panels were consistent with results seen for marine atmospheric exposure. This would indicate that for bare structural steel, 80 days of accelerated corrosion testing could simulate marine atmospheric exposure. The galvanized panels showed heavy scaling of the galvanizing and some small areas of rust bleed through at 80 days. At 120 days, the panels show similar results. Table 13 shows the visual observations for both the bare and galvanized steel panels for 80 and 120 days. The results of the accelerated corrosion testing for the galvanized steel panels produced interesting results. The nature of the corrosion product and the sacrificial manner by which the zinc provides protection to the steel substrate are consistent with marine atmospheric exposure. The rate of corrosion of the zinc was high. The scaling and aggressive corrosion of the zinc draw the question as to whether the corrosion mechanism which was accelerated in this test is the corrosion mechanism which would normally occur in-service.

Aluminum Armor- Similar to the atmospheric exposure, aluminum alloys 2519 and 5083 were exposed in triplicate using the GM 9540 P/B test[6]. The evaluation of these alloys was twofold: first, a comparison of the corrosion resistance of the two alloys as a function of

exposure time; secondly, to evaluate the time needed to replicate performance noted in marine atmospheric exposure as compared to the bare steel panels.

Table 13 summarizes the results of the 80 and 120 day observations for the aluminum panels. In terms of a direct comparison of the alloys, alloy 5083 performed far better than the alloy 2519. Alloy 5083 showed only very minor signs of signs of corrosion after 120 days of exposure. Alloy 2519, on the other hand, did not perform well. At 80 days, the panels showed signs of pitting on all surfaces which was particularly heavy on the backside. At 120 days, the level of corrosion was heavier.

The results of the testing of the aluminum panels shows the time variant factor in accelerated corrosion testing. Materials of interest which have increased corrosion performance are going to take longer exposure times in order to make any reasonable life cycle analysis. The results of the testing on the bare and galvanized steel panels indicate 80 days of exposure would produce results which are similar or more aggressive than marine atmospheric exposure. However, the results of the accelerated corrosion testing of the aluminum armor alloys show that a longer period of testing is required to achieve results similar to marine atmospheric testing. Particularly with the use of more corrosion resistant alloys, such as 5083, exposure periods up to 120 days should be used with the GM 9540 P/B test[6].

Phase II - Comparison of Three Accelerated Corrosion Tests to Marine Atmosphere

Metals and coatings companies often provide accelerated corrosion test data (from a variety of tests) to show how well their material would perform. Often, these tests have not been correlated with marine atmosphere performance to permit any indication of adequate service for the marine environment. Therefore, three accelerated corrosion tests will be comparatively evaluated in FY 97 at the Naval Research Laboratory, Key West Florida. Results from each test will be compared to performance in marine atmospheric exposure at the LaQue Center for Corrosion Technology, Wrightsville Beach North Carolina. The tests are cyclic corrosion tests using the GM9540P/B[6] test, ASTM G85 (prohesion)[7] and ASTM B117 (salt fog)[8] methods. The test matrix for the three accelerated corrosion tests includes four different substrates (sets of bare metal coupons to be evaluated for corrosion rate and mode) and an array of six primers and three topcoats on steel coupons, all to be evaluated using the three cyclic corrosion test methods. Both the coated and uncoated coupons are to be tested in the same test chamber during cycling of one of the given test methods. The tests will be described below in greater detail.

Each of the cyclic corrosion test methods is different in electrolyte composition and cycle, therefore the results obtained for each method will be compared against the others to determine the test which is the best predictor of marine atmospheric exposure.

The ASTM B117 (salt fog) test method consists of a continuous spray of 5% sodium chloride solution at 35°C which has a pH between 6.5 and 7.2. The ASTM B117 test will be run for up to 3000 hours with evaluations of the coupons and possible removal of failed samples at 1000 and 2000 hours.

The ASTM G85 (prohesion) test method runs on a two hour cycle, with one hour of salt fog at 25°C and one hour of dry off at 35°C. The electrolyte solution used in the prohesion test is more dilute than traditional salt fog and is made up of 0.05% sodium chloride and 0.35% ammonium sulfate at a pH between 5.0 and 5.4.

The GM9540P/B test method is more involved than either of the ASTM standard methods. This test utilizes a 24 hour cycle which is defined in Table 14. The solution used is more complex and consists of 0.9% sodium chloride, 0.1% calcium chloride and 0.25% sodium carbonate at a pH between 6.0 and 8.0.

Both the ASTM G85 and GM9540P/B tests will be run for up to 120 days. Coupons exposed in these tests will be evaluated at 40 and 80 days and similarly failed samples will be removed.

Corrosion Mode Tests- This test utilizes 4" x 6" x 1/8" uncoated coupons of four alloys, as specified in Table 15, in order to evaluate each of the cyclic corrosion test methods. Upon completion of cycling for each of the test methods the replicate coupons from each alloy will be evaluated as to the mode and degree of corrosion on the panel. The results from the cyclic corrosion tests will be compared against one another to determine if there is a distinct difference as to the means by which corrosion is accelerated by each of the tests. The results of the cyclic corrosion tests will also be compared against the results of extended marine atmospheric testing, as they become available, to determine which of the test methods best replicates it.

Corrosion Rate Tests- This test utilizes 2" x 3" x 1/8" uncoated coupons of four alloys, as specified in Table 16, in order to evaluate each of the cyclic corrosion test methods. A coupon of each alloy will be removed periodically from each of the three tests, cleaned and weighed, to determine the rate of corrosion[9] on the panel per ASTM G1. The results from the cyclic corrosion tests will be compared against one another to determine if corrosion is accelerated differently by each of the tests. The results of the cyclic corrosion tests will also be compared against the corrosion rate results in extended marine atmospheric testing, as they become available, to determine which of the test methods best replicate it.

Accelerated Corrosion Tests of Coatings- This test consists of 4" x 6" x 1/16" cold rolled SAE 1018 low carbon steel coupons coated with primers and topcoats as specified in Table 17. Prior to coating application, all surfaces are to be sandblasted to a 2-3 mil profile. Both the primer and topcoat are to be applied in accordance with manufacturer specifications. However, the minimum dry film thickness of any primer should not be less than 2-3 mils. Once the coatings are fully cured, the panels will be scribed[10] per ASTM D1654. Upon completion of cycling for each of the test methods, the replicate coupons from each primer/ topcoat combination will be evaluated with respect to the amount of scribe creepage. The panels will also be evaluated for the degree of blistering[11] and rusting[12], using ASTM standards D714 and D610 respectively. The results from the cyclic corrosion tests will be compared against one another, to determine if there is a distinct difference between the types of coating failure which occurred in each of the tests or if a coating failed in one test but not in others. The results of the cyclic corrosion tests will also

be compared against the results of extended marine atmospheric testing, after three years exposure, to determine which of the test methods best replicate marine atmosphere exposure.

Field Tests

Two field tests of improved corrosion control materials have recently been initiated: a demonstration of new materials and coatings on HMMWVs and M939 trucks and an exhaust system materials and coatings evaluation on HMMWVs and M939 trucks. A third field test of the relative performance of galvanized frame rails versus standard frame rails has been initiated.

SUMMARY

This report has covered the status of various research and development tests in corrosion presently being conducted for the Marine Corps by the Corrosion Branch, Carderock Division Naval Surface Warfare Center. The status and interim results of marine atmosphere tests of various metals, coatings and components are presented. An ongoing evaluation of accelerated corrosion tests is discussed, with the intention of identifying useable screening or referee methods for the comparative evaluation of promising corrosion prevention materials for the fleet. Concurrent field tests of selected materials and parts on Marine Corps vehicles are discussed.

For emphasis, some specific recommendations are reiterated. Aluminum headlamp assemblies have performed better in the accelerated corrosion test than the other material types, and initial indications of marine atmosphere performance support that conclusion. Based on those tests, the use of aluminum headlamp assemblies should be pursued as a replacement of the current steel headlamps on HMMWVs and five ton trucks. Although already installed on HMMWVs and trucks for a field test, the next step would be production discussions with the manufacturer. For future use, stainless steel mounting hardware should be substituted for the presently used steel.

Based on exposure tests so far, it is suggested that the extent of electrical connector corrosion observed during surveys in the fleet may be related to maintenance practices. It is recommended that Marine Expeditionary Forces apply coatings specified in maintenance documents to electrical connectors (especially on the outside of vehicles) every six months or at least once per year. Solvent cutback CPC's have performed well.

With the exception of the (more expensive) stainless steel fasteners, all of the coated fasteners are beginning to show some corrosion, after 18 months marine atmosphere exposure. Except in the most benign environments, then, in the fleet, most fasteners will probably require some additional corrosion protection, either the selected primer for the subject vehicle, or periodic treatment with corrosion prevention compounds.

Based on the performance of the seamless 304 stainless steel fuel lines in both Marine Atmosphere (12 Months) and the GM 9540 Accelerated Corrosion tests, it is highly recommended that the smaller diameter brake lines for HMMWVs be procured in a seamless 316

stainless steel product for field testing. The galvanized "protector" springs and nuts had severely corroded on all fuel line specimens. No value is seen for the use of the protective springs, and it is recommended that their use be discontinued for all vehicle types.

An evaluation on Marine Corps components in the field of a zinc-silicate primer topcoated with the water base camouflage coating (WBCC) (also see Inorganic Coatings section) is recommended. Either the Bruder (if available) or Ganicin coatings could be used. Possible candidates for application are the Rough Terrain Container Handler (RTCH), 25 or 30 Ton Cranes, HMMWVs, skip-weld areas on 5 ton truck beds, fenders and frames on potable-water "buffaloes", or various types of trailers.

In the GM 9540 P/B test, the results of the accelerated testing on the bare and galvanized steel panels indicate 80 days of exposure would produce results which are similar or more aggressive than marine atmospheric exposure. However, the results of the accelerated corrosion testing of the aluminum armor alloys show that a longer period of testing is required to achieve results similar to marine atmospheric testing. Particularly with the use of more corrosion resistant alloys, such as 5083 aluminum, exposure periods to 120 days should be used with the GM 9540 P/B test.

ACKNOWLEDGEMENTS

The authors would like to express their appreciation for the excellent support provided by Mr. Stan Pickul of the Laque Center for Corrosion Technology in the conduct of the marine atmosphere tests, and Mr. Rick Foster of the Naval Research Laboratory in the conduct of the accelerated corrosion tests.

Table 1. Marine Atmosphere Test Matrix

Test	Number Of Specimens	Substrate Specification	Test Materials	Coating Specification	Comments	Date Initiated	Inspections
CARC Coating	96 total	aluminum (5083)	2 CARCS Standard	MIL-C-46168 TYPE II		12/09/94	6 mo
		steel MIL-S-22698	Water-Base Camoflage Coati	MFD by NILES & CO.			12 mo
		armor steel per	4 Primers				18 mo
	4 per coating-substrate combination	MIL-A-46100D 4"X6"X1/8" panels	Std Army primer Std Navy primer Inorganic zinc, IC-531 zinc molybdate	MIL-P-52192 COMP G MIL-P-24441 zero-VOC Zn silicate TTP-645B	plates scribed diagonally		24 mo
Electrical Connector Coatings & Alternate Materials	44 total	MIL-C-38999 connectors Al w/ Cd plate	Amlguard Tectyl 846 Courtald Aerospace PR 1773 Dow 3140 RTV Cortec VCI-368 (spray) Cortec VCI-368 (brush-on)	MIL-C-85054 (AS) Ty 1 Cl MIL-C-16173D Gr 4 polysulfide-based MIL-A-46146B MIL-C- 16173B Grl Cl I MIL-C- 16173B Grl Cl I	tests include electrical resistance measurements	08/08/95	6 mo 12 mo
		QQ-A-591	Aluminum with Cd plate	standard connectors	controls	08/08/95	6 mo
		QQ-A-591	Aluminum with Ni plate	proprietary			
		QQ-A-591	Ni-plate Al w/ Amlguard	MIL-C-85054 (AS) Ty 1 Cl B			12 mo
			Passivated stainless steel Composite shell	proprietary 300 series proprietary			
Fastener Coatings & Alternate Materials	56 total	grade 8 steel 1/2" fasteners SAE J429	Uncoated Cadmium Zinc (alkaline cyanide bath) Electroless nickel Sermatel Xylan 5214 316 stainless	SAE J429 QQ-P-416F Ty II Cl III ASTM B 633-85 Ty II AMS 2417 Ty II Cl II Ceramically-bonded Al ctg Flouroploymer ASTM A 493	4 fasteners of each specimen type bolted into a plate of each aluminum armor material	05/26/95	6 mo 12 mo 18 mo
Aluminum Armor	14 total	ASTM B-209 MIL-A-46192	Alloy 5083 Alloy 2519		combined with fastener tests	05/26/95	6 mo 12, 18 mo
Radiator Materials	4 plastic 1 control 1 stainless		Plastic Standard HMMWV Stainless AAV		2 plastic exposed to UV, 2 plastic shielded from UV test includes air flow	12/15/94 03/03/96 (SS)	6,12,18 24 mo (6 mo)
Inorganic Coatings: Scribed Panels	48 total	steel panels ~4" X 6" X 1/8"	Thermal Spray Al w/ std CAR TS Al w/ Water-Base Camo C Zinc silicate MO-ZINC 2 (Mobile) 24-A-190 (Bruder) V-65 (Briner) Galvanized G90 w/ CARC Hot dip galvanized w/CARC	MIL-STD-2138A (SH) MIL-STD-2138A (SH) low-VOC Zinc Silicate low-VOC Zinc Silicate low-VOC Zinc Silicate ASTM A 879-92 ASTM A 123-89a	milled scribe 4 - no topcoat 2 - topcoated with WBCC	02/02/96	6 mo
Inorganic Coatings: KTA Panels	4 4 6 6 6 4	MIL-S-22698 steel specimens 4" X 6" X 3/16" with welded "U"	Standard CARC Thermal spray Al w/ CARC MO-ZINC 2 (Mobile) 24-A-190 (Bruder) V-65 (Briner) Hot dip galvanize w/ CARC	MIL-C-46168 TYPE II MIL-C-46168 low-VOC Zn Silicate low-VOC Zn Silicate low-VOC Zn Silicate ASTM A 123-89a	TS: MIL 2138A (SH) two each of the zi silicates topcoated with CARC	02/02/96	6 mo
Headlamp Brackets	4 4 3	QQ-S-698 QQ-S-698 ASTM B209	Steel Electrogalvanized Steel 6061 Aluminum	Std HMMWV ASTM 879-92		02/02/96	6 mo
Fuel Lines	12 total 4 per material	SAE 1010 SAE 1010	Steel with Zyncroterne Steel w/ Superterne & Pro-Kote 304 Stainless steel	Zn-rich paint Galfan Al-rich paint	Superterne (Pb-12%Sn)	02/27/96	6 mo
Exhaust Components	6 total 2 per material	ASTM A176 ASTM A176	Aluminized steel 409 stainless steel (SS) Aluminized 409 SS	ASTM A463 ASTM A463	ambient temperature only	03/01/96	6 mo
Frame Rails	1		Galvanized, E-coated			N/A	

Table 2. Evaluation of Painted Test Panels, Marine Atmosphere, 25 m lot

Exposure Date: 12-9-94 Orientation: 30' facing ocean
Inspection Date: 6-12-96 Exposure Period: 18 months

Primer		Mare Island Type IV									
Top Coat →		Standard CARC (per MIL-C-46168, Type II)					Niles Company, Low VOC, CARC				
Base Plate ↓	Plate #	Panel (1) Rust Grade	(Notes)	Scribe Creepage (2) min	mea	max	Panel (1) Rust Grade	(Notes)	Scribe Creepage (2) min	mea	max
Aluminum	1	3		10	10	8	4		10	10	3
	2	3		10	10	0	10		10	10	3
	3	3		10	10	0	4		10	10	2
	4	6		10	2	1	5		10	2	2
Avg		**3.8**		**10.0**	**8.0**	**2.3**	**5.8**		**10.0**	**8.0**	**2.5**
Mild Steel	1	10	3	10	1	0	10		10	5	3
	2	9	3	10	3	1	10		9	5	3
	3	10	3	2	0	0	10		10	7	6
	4	10	3	2	2	0	10		10	7	3
Avg		**9.8**		**6.0**	**1.5**	**0.3**	**10.0**		**9.8**	**6.0**	**3.8**
Armor Plate	1	10	3	10	7	4	10	3	10	10	6
	2	10	3	10	2	0	10	3	10	10	6
	3	10	3	10	4	3	10	3	10	10	7
	4	9	3	10	8	7	9	3	10	10	7
Avg		**9.8**		**10.0**	**5.3**	**3.5**	**9.8**		**10.0**	**10.0**	**6.5**

Primer		Standard Army Primer 52192									
Top Coat →		Standard CARC (per MIL-C-46168, Type II)					Niles Company, Low VOC, CARC				
Base Plate ↓	Plate #	Panel (1) Rust Grade	(Notes)	Scribe Creepage (2) min	mea	max	Panel (1) Rust Grade	(Notes)	Scribe Creepage (2) min	mea	max
Aluminum	1	7		10	10	0	7	4	10	3	0
	2	6	4	10	10	3	7	4	10	3	3
	3	5	4	10	0	0	7	4	10	10	4
	4	5	4	10	2	0	6	4	10	2	0
Avg		**5.8**		**10.0**	**5.5**	**0.8**	**6.8**		**10.0**	**4.5**	**1.8**
Mild Steel	1	10	3	9	3	0	10	3	10	8	6
	2	10	3	10	1	0	10	3	10	9	7
	3	10	3	2	0	0	10	3	10	6	5
	4	10	3	9	5	1	10	3	10	7	5
Avg		**10.0**		**7.5**	**2.3**	**0.3**	**10.0**		**10.0**	**7.5**	**5.8**
Armor Plate	1	3	spR (3)	10	5	4	5		10	5	4
	2	4	spR (3)	10	4	3	6		10	5	4
	3	4	spR (3)	10	5	4	6		10	5	4
	4	4	spR (3)	10	4	3	6		10	5	4
Avg		**3.8**		**10.0**	**4.5**	**3.5**	**5.8**		**10.0**	**5.0**	**4.0**

Notes
(1) per ASTM D-610
(2) Per ASTM D-1654
(3) Rust at edge
(4) Underfilm corrosion at edge
(5) Topcoat peeling off primer
(6) 1pR = 1 pinpoint rust spot
(7) spR = several pinpoint rust spots
(8) fc = filiform corrosion

Table 3. Evaluation of Panels with Inorganic Coatings, Marine Atmosphere, 25 m lot

Exposure Date: 02-26-96 Orientation: 30° facing ocean
Inspection Date: 08-27-96 Exposure Period: 6 months

Primer		Standard Army Epoxy (MIL-P-53022)								
Top Coat →		Chemical Agent Resistant Coating,CARC (MIL-C-46168)					Waterborne Camouflage Coating, WBCC (MIL-C-29475)			
Base Plate ↓	Panel #	Panel (1) Rust Grade	(Notes)	Scribe Creepage (2) min	mea	max	Panel (1) Rust Grade	(Notes)	Scribe Creepage (2) min	mea	max
Steel Thermal Sprayed with Aluminum	1	10	(3)	10	6	4	10		10	6	2
	2	10	(3)	10	6	4	10		10	7	5
	3	10	(3)	10	6	2	10		10	10	4
	4	10	(3)	10	7	5	10		10	10	4
Avg		**10.0**		**10.0**	**6.3**	**3.8**	**10.0**		**10.0**	**8.3**	**3.8**

Primer		Gancin 347 WB								
Top Coat →		None					Waterborne Camouflage Coating, WBCC (MIL-C-29475)			
Base Plate ↓	Panel #	Panel (1) Rust Grade	(Notes)	Scribe Creepage (2) min	mea	max	Panel (1) Rust Grade	(Notes)	Scribe Creepage (2) min	mea	max
Bare Steel	1	10		10	10	10	10		10	10	10
	2	10		10	10	10	10		10	10	10
	3	10		10	10	10					
	4	10		10	10	10					
Avg		**10.0**		**10.0**	**10.0**	**10.0**	**10.0**		**10.0**	**10.0**	**10.0**

Primer		Briner V65								
Top Coat →		None					Waterborne Camouflage Coating, WBCC (MIL-C-29475)			
Base Plate ↓	Panel #	Panel (1) Rust Grade	(Notes)	Scribe Creepage (2) min	mea	max	Panel (1) Rust Grade	(Notes)	Scribe Creepage (2) min	mea	max
Bare Steel	1	10		10	10	10	10		10	10	10
	2	10		10	10	10	10		10	10	10
	3	10		10	10	10					
	4	10		10	10	10					
Avg		**10.0**		**10.0**	**10.0**	**10.0**	**10.0**		**10.0**	**10.0**	**10.0**

Primer		Bruder MAB 24-A-190								
Top Coat →		None					Waterborne Camouflage Coating, WBCC (MIL-C-29475)			
Base Plate ↓	Panel #	Panel (1) Rust Grade	(Notes)	Scribe Creepage (2) min	mea	max	Panel (1) Rust Grade	(Notes)	Scribe Creepage (2) min	mea	max
Bare Steel	1	10		10	10	10	10		10	10	10
	2	10		10	10	10	10		10	10	10
	3	10		10	10	10					
	4	10		10	10	10					
Avg		**10.0**		**10.0**	**10.0**	**10.0**	**10.0**		**10.0**	**10.0**	**10.0**

Primer		Standard Army Epoxy (MIL-P-53022)								
Top Coat		Chemical Agent Resistant Coating,CARC (MIL-C-46168)					Waterborne Camouflage Coating, WBCC (MIL-C-29475)			
Base Plate	Panel #	Panel (1) Rust Grade	(Notes)	Scribe Creepage (2) min	mea	max	Panel (1) Rust Grade	(Notes)	Scribe Creepage (2) min	mea	max
Hot Dipped Galvanized Steel	1	10		10	10	10	10		10	10	10
	2	10		10	10	10	10		10	10	10
	3	8	(3)	10	10	5	10		10	10	10
	4	10	(3)	10	6	3	10		10	10	10
Avg		**9.5**		**10.0**	**9.0**	**7.0**	**10.0**		**10.0**	**10.0**	**10.0**

Notes
(1) Per ASTM D-610
(2) Per ASTM D-1654
(3) Scribe undercutting more severe at bottom where moisture accumulates

Table 4. Exhaust Components Test Matrix

COMPONENT	MATERIAL	COATING	NOTES
fording kit	aluminized steel	Dexter Hi-Heat 383	flat green, meets Mil-P-14105
fording kit	aluminized 409 SS	Dexter Hi-Heat 383	gloss green, meets Mil-P-14105
fording kit	aluminized 409 SS	Amerloc 892	silver, does not meet MIL-P-14105
muffler	aluminized 409 SS	Dexter Hi-Heat 383	flat green, meets Mil-P-14105

Table 5. Crevice Coatings Test Matrix

Corrosion Preventive Primers	Steel Precorroded w/ Overcoat	Steel Precorroded w/o Overcoat
Conversion Coatings:		
Vactan	4	4
PlastiKote Rust-Not High-Build	4	4
Rust-O-Leum Rust Reformer	4	4
Loctite Extend Rust Treatment 754	4	4
Phoscote	4	4
RDP	4	4
Corroseal	4	4
Neutrarust	4	4
Cortex 420	4	4
Rusteco Corrosion Treatment	4	4
Zinc-rich coatings:		
ZRC/Galvalite	4	4
Allied Signal Acqua 220	4	4
International Zn WB-18	4	4
M.A. Bruder 24-A-190	4	4
Thin-film coatings:		
Fluid-Film (Aerosol)	4	4
Dri-Touch IRP1	4	4
Permastoprust	4	4
NWAC Hardwax	4	4
NWAC A-120	4	4
Standard:	8	8

Table 6. Accelerated Corrosion Test Matrix - Phase I, GM 9540 P/B

Test	Material Description	Substrate Specification	Coating Specification	Number Of Specimens	Comments
Headlamps	Steel	QQ-S-698	MIL-C-46168 TYPE II	3	Std CARC
	6061 Aluminum	ASTM B209	MIL-C-46168 TYPE II	3	Std CARC
	Galvanized Steel	QQ-S-698	ASTM G90/MIL-C-46168 TYII	3	Std CARC
Electrical Connectors	Cd-plated Aluminum	QQ-A-591		3	
	300 series stainless steel			3	
Brake Lines	Steel with Superterne & Zyncroterne	SAE 1010	Zn-rich paint	3	Superterne is (Pb-12%Sn)
	Steel with Superterne & Pro-Kote		Galfan Al-rich paint	3	
	304 Stainless steel			3	
Scribed Panels	Ganicin 347WB	Steel	DuPont	3	Zn Silicate
	Briner V-65		Briner Paint Co.	3	Zn Silicate
	MAB 24-A-190		M.A. Bruder & Sons, Inc	3	Zn Silicate
	CARC		MIL-C-46168 TYPE II	3	
	Galvanized w/ CARC		MIL-C-46158 TYPE II	3	
KTA Crevice Panels	Ganicin 347WB	Steel	DuPont	3	Zn Silicate
	Briner V-65		Briner Paint Co.	3	Zn Silicate
	MAB 24-A-190		M.A. Bruder & Sons, Inc	3	Zn Silicate
	Water Base Carc		MIL-P-29475	3	
	CARC		MIL-C-46168 TYPE II	3	
	Galvanized w/ CARC		MIL-C-46168 TYPE II	3	
Uncoated Panels	**Steel**				
	Bare Steel, Structural	ASTM A36		3	
	Hot-dip Galvanized Steel	ASTM A361		3	
	Aluminum Armor				
	Alloy 5083	ASTM B-209		2	AAV
	Alloy 2519	MIL-A-46192		2	AAAV

Table 7. GM 9540 P/B Phase I Test Results for Headlamps

Component & Material	GM 9540 P Test	
Headlamps	**80 days**	**120 days**
Steel	heavy corrosion and paint failure	General corrosion of outside bracket heaviest at edges (+ initiate at edges) lots of scaling Outer bolt (No corrosion) holding front bracket is stainless or nickel alloy Inside body has some corrosion in crevice with bracket Backside relatively free of corrosion Steel bolt materials HEAVILY rusted especially mounting bolts on backside - all came off in glued area Took apart #3 Inside mounting alignment ring was uncoated electrogalvanized or Cd-plate Signs of Zn corrosion and rusting of steel especially at outer edges - heaviest at bottom Backside bracket looks good on inside except for mounting brackets which are heavily rusted
6061 Aluminum	no corrosion - mounting studs are steel and corroding (specify stainless steel in future)	No corrosion at general surfaces Some Al corrosion products apparent at some edges and mostly under rubber mounting pads on back piece and under stainless bolts on front bracket (1 assembly (#2) is much worse than others) Took apart #3 Outer bracket has some minor corrosion at bottom on inside where water could collect Alignment ring - uncoated Al General surfaces uncorroded except for some light etching on bottom and 1 light area of minor corrosion at edge. Crevice corrosion at bolt areas where stainless bolts mounted into some brackets
Galvanized Steel	some corrosion starting at edges and in crevices	Outside surfaces mostly rust free except for some minor corrosion at edges. Also white Zn corrosion products at edges and under bolts. Inside crevice of outer brackets - signs of corrosion and rust bleed at bolts. Bolt materials same problems as steel head lamps. Took Apart # 3 Inside outer bracket some corrosion of Zn and rusting of steel at bottom Bolt material for outer bracket no corrosion - stainless or nickel alloy Inside alignment ring electrogalvanized and some corrosion of Zn and steel like steel headlamps Same appearance as steel on mounting bolts/etc. but a little less corrosion. Spring material no corrosion Corrosion has clam shell - type propagation appearance at bottom
Overall Performance		
	best to worse:	Aluminum > Electrogalvanized >> Steel

Table 8. GM 9540 P/B Phase I Test Results for Electrical Connectors

Component & Material	GM 9540 P Test Results	
Electrical Connectors	**80 days**	**120 days**
Cd-plated Aluminum	Some minor general corrosion on outside	Male base mounts have heavy attack, especially at edges (white-blue/green corrosion products primarily) Female plugs look good, only very minor corrosion at edges or crevices <u>Inside</u> Minor corrosion at outer thread on both male and female portions No corrosion of any internals beyond threads
300 series Stainless Steel	No general corrosion on outside, some Corrosion in crevices.	External areas look good with no corrosion. Corrosion seen inside crevices, mostly of female portion <u>Inside</u> Corrosion on threads orange/black corrosion products Also corrosion further inside on tube around pins No corrosion inside tube around pins or of pins
Overall Performance	Neither are recommended:	Al- general corrosion problem SS-crevice corrosion problem

Table 9. GM 9540 Phase I Test for Brake Lines

Component & Material	GM 9540 P Test Results	
Brake Lines	**80 days**	**120 days**
Steel with Superterne & Zyncroterne	Coating starting to fail. Spotty surface rust	Heavy corrosion on entire exposed surfaces including heavy scaling Compression nut - heavily corroded/scaled Protective spring heavily corroded and cracked (can peel right off of surface) No zinc left on spring brake line underneath corroded with darker corrosion products (mostly black)
Steel with Superterne & Pro-Kote	Coating starting to fail. Spotty surface rust	Very heavy corrosion on exposed surfaces plus scaling and peeling (more corrosion products than Zyncroterne) 2 lines entirely corroded through and broke off at base during testing Compression nuts and spring look same as controls
304 Stainless Steel	Corrosion on compression nuts and spring, some pitting on lines under springs	Exposed areas look good on top, bottom has staining from spring corrosion that leaked down Compression nuts and spring same as controls with slightly less corrosion- harder to "peel" off like others Under spring stained black - pitting has initiated on stainless caused by corrosion of springs
By 80 days, galvanized springs had corroded on all specimens (galvanizing failed and steel corroding).		
Overall Performance	best to worse:	Stainless >> Zincroterne > Procoat

Table 10. GM 9540 P/B Phase I Test Results for Scribed Panels

Component & Material	GM 9540 P Test Results	
X-Scribe	**80 days**	**120 days**
Ganicin 347WB	Corrosion of scribe and edges	Entire scribe rusted. rust creepage 1/4 - 1/2" from scribe. corrosion at edges mostly on top edge)(some entire top edge). 1 panel with pin hole rust spots on front (0.1%). 1 backside no rusting
Briner V-65	Entire scribe lightly corroded	Entire scribe rusted. rust creepage 1/8 - 1/4" from scribe. a couple rust spots on top edge. general surfaces rust free
Bruder MAB 24-A-190	Some light corrosion in part of scribe / not all	2 panels have ~1/3 of scribe rust free. 1 panel - scribe is entirely rusted, creepage 0 - 1/8" from scribe
All zinc silicate specimens have white corrosion products on most surfaces		
CARC	Failing at scribe and edges (1 panel failing on face)	Very heavy corrosion in scribed area (more corrosion product than G90). creepage of rust mostly 3/4" - 1" on 2 specimens except bottom of plate on 1/2 of specimen. 1 specimen entire front side rusted in edges (mostly top and bottom) moderately rusted.
Galvanized w/ CARC	Steel corroding at scribe and heavy blistering with corrosion at scribe	Heavy corrosion at scribe. creepage of rust and blistering of coatings over 1" from scribed area. edges and sides lightly corroded. backside general surfaces mostly rust free

Table 11. General Rating of Panel Appearance

(0-10) 0=bad and 10= excellent (no rust)

Scribed	Bruder	Briner	Ganicin	CARC	G90	
	9	8	6	2	2	
KTA	Bruder	Briner	Ganicin	CARC	Hot dip	WBCC
	9	6	6	2	9	1

Table 12. GM 9540 P/B Phase I Test Results for KTA Crevice Panels

Component & Material	GM 9540 P Test Results	
KTA	80 days	120 days
Ganicin 347WB	Some light corrosion at U-weld and edges	General surfaces rust free. couple rust areas at edges (mostly a top corner of 2 specimens) U- channel Entirely rusted in weld/crevice areas (rust creepage 1/4" outside U area). Entirely rusted on surface where water would collect (upward facing surface of U)
Briner V-65	Some light corrosion at U-weld	General surfaces rust free. light rust at couple areas of top edge and side on 2 specimens U channel Weld/crevice areas rust initiated on all specimens (rust creepage 1/4" outside U). 2 specimens much heavior rusting. Upward facing surfaces entirely rusted on 2 specimens. 1 specimen lighter with tiny rust spots on 50%. Corrosion also on edges (1 specimen almost all surfaces 80% rusted)
Bruder MAB 24-A-190	No corrosion of steel.	General surfaces and edges rust free. U channel Some initiation at sides of channel in weld/crevice areas. No creepage on outside crevices
Water Base CARC		Middle of plates OK but corrosion creeping much further inward from sides than CARC. Sides/edges very heavy corrosion with heaviest on bottom U channel Heavy attack on all surfaces and crevices
CARC	Failing at edges and U channel	Middle of plates look ok with a few rust spots. sides/edges have heavy corrosion with heaviest attack on bottom backside of plate U channel Heavy corrosion in crevice areas. most of sides and edges also corroded
Galvanized w/CARC	Some white corrosion products at edges and U-channel	General surfaces and edges rust free U channel Some corrosion crevices - mostly on upward facing bottom where water collects. appears hot-dip sealed up crevices. edges/sides/bottom look good

Table 13. GM 9540 P/B Phase I Test Results for Uncoated Standards

Component & Material	GM 9540 P Test Results	
Standard Plates	80 days	120 days
Steel ASTM A36	Heavy general corrosion	Heavy corrosion products (black/orange) on all surfaces and heavy scaling at edges and blisters of corrosion product
Galvanized Steel ASTM A361	Galvanizing corroded, some spots of rust	Front side - thick white corrosion product on all surface. Some spotty (appears very minor) rust showing thru backside-thinner layer of white corrosion product on most of surface-some clean areas 5-10%. Some spotty rust near edges but mostly rust free
Alloy 5083	Very minor pitting at edge	Front and back may have some "pin-point" pits but mostly looks good and free of corrosion. Top edge has some pits.
Alloy 2519	Minor pitting on all surfaces, heavier on back	Front side - lots of tiny pits on most of surface with a few larger pits. Backside and edges - larger pitted areas white - blue green corrosion products primarily

Table 14. GM9540P/B (modified) Cycle for Accelerated Corrosion Tests

Step 1	Subcycle Step 2-3 Repeat 4x	
Step 2	Fog Mist at 25°C	15 Minutes
Step 3	Dry-Off at 25°C	105 minutes
Step 4	Humidity at 49°C (95-100% RH)	8 Hours
Step 5	Dry-Off at 60°C	7 Hours
Step 6	Dry-Off at 25°C	1 Hour
Step 7	Final Step	Go to Step 1

Table 15. Corrosion Mode Test Matrix

Bare Coupons:	Material Specification	ASTM B117 salt fog	GM9540P/B cyclic corr.	ASTM G85 Prohesion	LCCT marine atm.
1015 Steel	ASTM A569	4	4	4	4
6061 Aluminum	ASTM B209	4	4	4	4
304 Stainless	ASTM A269	4	4	4	4
Monel 400	ASTM B127	4	4	4	4

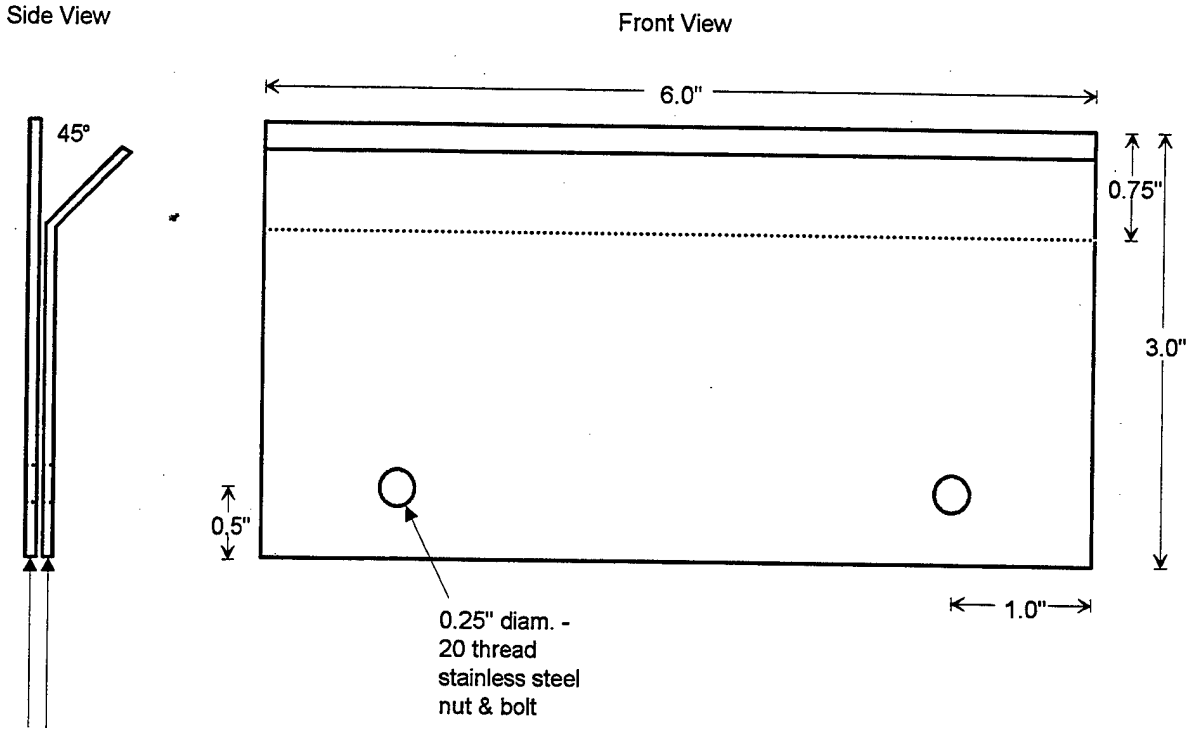
Table 16. Corrosion Rate Test Matrix

Bare Coupons:	Material Specification	ASTM B117 salt fog	GM9540P/B cyclic corr.	ASTM G85 prohesion	LCCT marine atm.
1015 Steel	ASTM A569	6	6	6	6
6061 Aluminum	ASTM B209	6	6	6	6
304 Stainless	ASTM A269	6	6	6	6
Monel 400	ASTM B127	6	6	6	6

Table 17. Accelerated Corrosion Test Matrix of Candidate Coating Systems

1018 Steel Coupons Coated With:		Number of Specimens Per Test Condition			
Primer	Topcoat	ASTM B117 salt fog	GM9540P/B cyclic corr.	ASTM G85 prohesion	LCCT marine atm.
Epoxy (MIL-P-53022)	Aliphatic Polyurethane CARC (MIL-C-46168)	4	4	4	4
Water Reducible Epoxy (MIL-P-53030)	Aliphatic Polyurethane CARC (MIL-C-46168)	4	4	4	4
Water Reducible Epoxy (MIL-P-53030)	Waterborne Camouflage Coating (MIL-C-29475)	4	4	4	4
Polyamide Epoxy (MIL-P-24441)	Waterborne Camouflage Coating (MIL-C-29475)	4	4	4	4
Zinc Molybdate (TT-P-645 [F-84])	Waterborne Camouflage Coating (MIL-C-29475)	4	4	4	4
Zinc Silicate (MAB 24-A-190)	Waterborne Camouflage Coating (MIL-C-29475)	4	4	4	4
Zinc Silicate (WB-18)	Waterborne Camouflage Coating (MIL-C-29475)	4	4	4	4
Water Reducible Epoxy (MIL-P-53030)	Alkyd Resin Enamel (NSN 8010-00-298-2295)	4	4	4	4
Zinc Molybdate (TT-P-645 [F-84])	Alkyd Resin Enamel (NSN 8010-00-298-2295)	4	4	4	4

USMC Crevice Specimens



Material: 1/16" thick cold rolled SAE 1018 low carbon steel or 1/16" thick 6061 aluminum as determined by test matrix.

Notes: All surfaces sandblasted to a 2-3 mil profile.
Front and backside of crevice specimen coated with MIL-P-53 primer with a topcoat of MIL-C-29475.
Mating (crevice) sides of plates should be left bare.

Figure 1. Crevice Specimen Configuration

REFERENCES

1. Bieberich, E. B., T. J. Jackovic and R. M. Janeczko, "USMC Corrosion Reduction Program: Vehicle Corrosion Surveys at Camp LeJeune, Camp Pendelton and Twenty-nine Palms Marine Corps Bases", Proceedings of the 1994 Tri-Service Conference on Corrosion, 21-23 June 1994

2. USMC TM 3080-12, "Corrosion Prevention and Control for Marine Corps Equipment" March 1992.

3. USMC TM 3080-50, "Corrosion Control Procedures, Depot Maintenance Activities for Marine Corps Equipment," December 1989

4. USMC TM 3080-12, "Corrosion Prevention and Control for Marine Corps Equipment" March 1992.

5. USMC TM 3080-50, "Corrosion Control Procedures, Depot Maintenance Activities for Marine Corps Equipment," December 1989

6. GM9540P, Accelerated Corrosion Test", General Motors Engineering Standards, July 1991

7. ASTM G 85-94, "Standard Practice for Modified Salt Spray (Fog) Testing", American Society for Testing and Materials, Philadelphia, Pa., 1990

8. ASTMB 117-90. "Standard Test Method of Salt Spray (Fog) Testing", American Society for Testing and Materials, Philadelphia, Pa., 1990

9. ASTM G 1 -90, "Standard Practice for Preparing, Cleaning, and Evaluating Corrosion Test Specimens", American Society for Testing and Materials, Philadelphia, Pa., 1990.

10. ASTM D 1654 -92, "Standard Test Method for Evaluation of Painted or Coated Specimens Subjected to Corrosive Environments", American Society for Testing and Materials, Philadelphia, Pa., 1992

11. ASTM D 714 -87, "Standard Test Method for Evaluating Degree of Blistering of Paints", American Society for Testing and Materials, Philadelphia, Pa., 1987

12. ASTM D 610-95, "Evaluating Degree of Rusting on Painted Surfaces", American Society for Testing and Materials, Philadelphia, Pa., 1995

Initial Studies of Electrochemical Comparison of Coating Performance in Flowing vs Stationary Electrolyte

Carol S. Jeffcoate, Gordon P. Bierwagen, N Davis and Sebastien Touzain

Polymers and Coatings Dept., North Dakota State University
Fargo, ND 58105

Abstract:
Initial studies of coating performance while immersed in a flowing electrolyte have shown a drastic drop in performance when compared to similar samples monitored in immersion in a stationary electrolyte. The study has included variation in electrolyte flow rate and electrolyte concentration. Performance monitoring techniques included electrochemical impedance spectroscopy and electrochemical noise methods. The coatings used in this preliminary study were Navy epoxy coatings typically used in below-waterline service. Our data indicates that immersion in a flowing electrolyte apparently degrades the coating/metal system more rapidly than static immersion. These results are shown by EIS, ENM and DC resistance measurements. Some preliminary interpretation of these results is given.

Introduction

Electrochemical methods have long been utilized to assess the corrosion protective performance of coatings. Although the earlier work was with DC resistance[1], recent work has concentrated on more sophisticated techniques[2,3,4]. The methods used in this study are electrochemical noise measurement (ENM)[5,6,7] and electrochemical impedance spectroscopy (EIS)[8,9].

The primary advantage of ENM is that it is a non perturbing technique i.e. the spontaneous current and voltage fluctuations are measured between two nominally identical panels, with no external potential or current applied[7]. The method can be applied as a semi-continuous monitoring technique and with time gives an indication of the overall coating performance. EIS gives more detailed information about the coatings electrical properties but at the sacrifice of perturbing the electrochemical system by applying a scan of AC potentials over a range of frequencies.[9]

This work has been designed to test typical marine coating systems for corrosion protection performance in a laboratory environment. The function of a marine coating is two fold. The primary requirement for a coating, of this type, is to provide corrosion resistance. The coating is the primary method for corrosion protection with cathodic protection being used as a secondary method[10].

In an attempt to have a more 'realistic' laboratory assessment, the flowing electrolyte has been added to the testing scheme. The typical laboratory test set-up includes a conductive

electrolyte (usually containing chloride) in 'stationary' contact with the test panels. This work investigates, via electrochemical testing, the effect of a flowing electrolyte on the degradation of marine coatings.

Experimental

Sample Preparation

The test samples were three layer marine coatings on mild steel. The layers were combinations of three primers: an alkyd (A), a zinc silicate (Z) and a green epoxy (MIL-P 24441 type 1 F-150) (G). The two top coats were a haze gray epoxy (MIL-P 24441 type F-151) (H) and a silicon alkyd (S). Each of the three layers were of approximate equal thickness and gave an average total coating thickness of 200±10μm.The primer/topcoat combinations tested in this investigation were (from substrate interface to electrolyte) AAS, ZAS and GHS. The GHS and AAS combinations were chosen as typical barrier type marine coating systems currently in service. The zinc silicate in the ZAS system works mainly by a sacrificial mechanism, and is non-common for this application. The electrical contact was made through wires which were attached to the test samples. The back and edges of each sample were coated with a colophony rosin / beeswax mixture (3/1) to act as an effective inert, high resistance protective coating. The exposed surface area of the test panel was 50 cm^2 (0.005 m^2).

Cell Design

For both the flowing and the stationary electrochemical cell, a solution of 3% sodium chloride (NaCl, analytical grade) in distilled deionized water was used as the conductive electrolyte. Solutions in both cells were open to the laboratory air and changed monthly to minimize algae growth. The reference electrode for ENM was a saturated Calomel electrode, and for the EIS measurements a platinum secondary electrode was also used.

The cell containing the flowing electrolyte was constructed from a 35x25x25 cm high density polyethylene (HDPE) tank with three 26 cm baffles to obtain a total path length of approximately 95 cm, as shown in figure 1. A constant volume of 10 liters of electrolyte was maintained and a pump circulating at 35 liters/minute provided a flow rate of approximately 0.055$m.s^{-1}$ (3.33 $m.min^{-1}$), ensuring laminar flow over the surface of the samples. The stationary electrolyte electrochemical cell consisted of a circular glass dish 18 cm in diameter and 10 cm deep with sufficient electrolyte to cover the exposed surface of the samples. A slotted polystyrene sheet held the samples in position vertically (the pairs facing each other, with a gap of 2 cm between them). For the flowing electrolyte cell, the electrochemical measurements were taken after the pump was switched off and flow stopped. A picture of the tank is included in Figure 1.

Sample Pairing for Noise Studies

Three nominally identical panels of each of the three types of paint system were immersed into the flowing cell. By cross pairing sample the three panels of each type, it was possible to maximize the number of possible electrode pairs. By cross pairing the three single

panels (A, B, C) this allowed three pairs of panels for the electrochemical noise (ENM) studies (AB, AC, BC) for statistical validity.

Experimental Methodology

EIS and ENM measurements were taken right after immersion in the test cells and then at recorded intervals during the immersion time. The fluid pump was switched off during measurements to ensure static conditions, because fluid flow effects will interfere with the ENM and EIS measurements.

ENM measurements on the nominally identical panels (paired by AB, AC, BC) were taken on first immersion and at intervals of 15 to 20 days during the extended exposure. Sample acquisition rate for the simultaneous raw potential and raw current data was made at a frequency of once every 2 seconds (0.5 Hz). The noise resistance (R_n) was calculated[7] using the standard deviations of the raw potential (σ_V) and the raw current noise (σ_I) as in equation 1.

$$R_n = \frac{\sigma_V}{\sigma_I} \qquad (1)$$

Calculations of the standard deviation were made by taking 10, 40 and 128 values in each data set points and variations in the resultant R_n values recorded.

For the EIS measurements the frequency range was from 65500 to 0.02 Hz and the applied AC voltage was 10 mV RMS.

Results and Discussion

Electrochemical Noise Method

The variation of raw data sample size, i.e. the number of raw data points used to calculate the standard deviation of the simultaneously measured current and potential values, for the calculation of R_n gave varying results, an example of which is given in Table 1. The smaller sample size of 10 raw data points taken over a time period of 20 seconds gave, at several time intervals, a divide by zero error, i.e. a steady state current was measured over a 20 second sampling period therefore producing a zero standard deviation. The variable R_n observed for the 128 raw data point (taken over 256 seconds) sample size is worthy of caution because the σ_V and σ_I values may be artificially high due to any uncorrected DC drift occurring during the measurement time-span. Because of the possibility of DC drift (non-stationarity of the system when "relaxing " from the flow conditions), the sample size o f40 points was used.

The noise resistance (R_n) vs. time (130 days) plots for all sample pairs immersed in the flowing electrolyte is shown in figures 2 and 3. The trend of R_n for the three samples of each coating type is shown to be very reproducible. The alkyd (AAS) samples show an initial drop of R_n followed by a reasonably steady state reading for the majority of the exposure period. A slight, further, decrease is seen in all the pairs after 96 days. Epoxy sample pairs showed a similar trend. An initial very high value of R_n sharply decreased from 1.1×10^{10} to 6.8×10^{8} Ωcm^2 after 10 days of immersion, followed by a relatively constant R_n value for 60 days. The rapid decrease in R_n observed in all the sample systems, on initial immersion, is due to water uptake

and consequent swelling of the films. The last of the test systems, ZAS, exhibited slightly different behavior. The initial, immersion, value of R_n ($4.8x10^7$ Ωcm^2) was lower with a sharp decrease to R_n values close to values expected for a bare steel electrode after 10 days of immersion.

A similar effect is observed with the samples immersed in the stationary electrolyte. Average R_n values vs. time plots for samples in the stationary electrolyte is shown in figure 4. On immersion in the stationary electrolyte all the coating types exhibited high values of R_n, in the range of 10^9 - $10^{11}\Omega cm^2$. The AAS samples maintained a high R_n value, above $10^8\Omega cm^2$, for the duration of the test. The GHS also maintained the average R_n value above 10^8 Ωcm^2 for the monitoring time. ZAS again proved to be the exception, showing a large drop in R_n value after only 10 days of immersion. After the 70 day immersion time the R_n value dropped further to 10^5 Ωcm^2, similar to that of the flowing electrolyte case.

It is seen that although the initial (on immersion) R_n values were similar for all three coating systems, for both types of test, the R_n value after a period of 1 month was found to be consistently lower for all samples in the flowing environment. Figure 5 shows a direct comparison of the two cases. Of the three coating systems investigated the most marked difference is seen with the AAS coating system. A variation of nearly three orders of magnitude between the flowing and the stationary R_n values was observed. The GHS samples in the flowing cell showed a drop of R_n values by two orders over the values obtained from stationary electrolyte samples. This reduction in the R_n value for a 'good' coating in the stationary cell re-classifies the coating to 'fair' when the flowing system is considered. The results from both of the ZAS sample sets indicate a presence of conductive pathways to the metal surface.

R_n values for both the flowing and stationary electrolyte are shown in table II

Electrochemical Impedance Spectroscopy

The impedance spectra were viewed with regard to the shape (one or two time constants) and the value for the maximum stable impedance modulus ($|Z|_{max}$). The $|Z|_{max}$ value gives an indication of the barrier properties of the film, the higher this value, the better the barrier type protection for a given coating system.

Monitoring the $|Z|_{max}$ value over an extended period of time gives observations similar to noise data. Samples in the flowing electrolyte gave values of $|Z|_{max}$, after an immersion of one month, significantly lower than those obtained from the samples immersed in the stationary electrolyte. Table III lists the $|Z|_{max}$ values obtained from the EIS measurement for the flowing and the stationary cells.

The initial $|Z|_{max}$ values for all the panels were, within an order of magnitude as compared with R_n values obtained from the noise measurements. After immersion in their respective environments for three months the $|Z|_{max}$ values results from the flowing cell were significantly lower than the values for the stationary electrolyte. An exception to this is where the ZAS system, $|Z|$ and R_n values show the same trend in both environments. The ZAS coating system protects the steel substrate by acting in a sacrificial manner. Sacrificial coatings are usually

designed and formulated above the critical pigment volume concentration (CPVC) and would therefore be porous in nature. This type of formulation leads to a direct electrolyte connection through the open porous structure of the coating system. As expected, low R_n and $|Z|_{max}$ values were observed and extensive blistering occurred in both the flowing and stationary electrolyte.

In all there is a good correlation (within an order of magnitude) between the R_n and the $|Z|_{max}$ values with the exception of the stationary AAS which produced higher R_n values. The flowing environment, although still maintaining laminar flow, is much more aggressive than the stationary cell.

We also calculated capacitance values from our impedance data, assuming a simple Randle's Equivalent Circuit in our analysis. From these values, diffusion coefficients for the individual systems were calculated.

Conclusions

When calculating R_n from raw potential and raw current data, the number of data points in the sample size needs to be chosen carefully. An uncompensated DC drift in the potential data results in an artificially high R_n value, conversely a drift in the current signal produces a depressed value of R_n.. Too small a sample size, especially for good coating systems, produces divide by zero errors periodically, reducing the effective data size and possibly leads to inaccurate estimations of the coating performance.

The introduction of a flowing electrolyte into an electrochemical experimental set up has a marked effect upon the performance of a coating system. For the coating systems tested the R_n and $|Z|_{max}$ value were significantly lower in the flowing cells, when compared with the values obtained from similar panels in a 'stationary' electrolyte. The reduction in effectiveness of these barrier type coatings reduces the ranking of both the AAS and the GHS from 'good' to 'fair'(*1*) coatings. The $|Z|_{max}$ values obtained from EIS measurements show a good correlation to within one order of magnitude, with the R_n, values obtained from the ENM method.

Acknowledgments

This work was carried out under the auspices of the Office of Naval Research, Grant No. N00014-95-1-507, and the National Science Foundation - Industry / University Coatings Research Center. Portions of this work are to be published in the book, *Corrosion Control by Coatings,* G.P.Bierwagen, ed., ACS Books, Symposium Series.

Days	R_n, σ of 10 Data Points	R_n, σ of 40 Data Points	R_n, σ of 128 Data Points
0	Divide by Zero Error	1.22×10^{11}	1.28×10^{11}
4	3.25×10^{7}	3.20×10^{7}	3.19×10^{7}
10	3.32×10^{7}	3.16×10^{7}	2.90×10^{7}
25	2.26×10^{7}	2.25×10^{7}	2.17×10^{7}
42	Divide by Zero Error	2.35×10^{7}	2.83×10^{7}
66	7.09×10^{6}	1.17×10^{7}	1.37×10^{7}
76	5.18×10^{5}	2.12×10^{5}	2.19×10^{5}

Table 1 Typical noise resistance values for AAS pair 1, calculated using the standard deviation of 10, 40 and 128 raw data points.

	AAS R_n, Ωcm^2	GHS R_n, Ωcm^2	ZAS R_n, Ωcm^2
Stationary on Immersion	2.97×10^{11}	6.11×10^{9}	6.91×10^{9}
Stationary after 22 days	5.79×10^{9}	4.09×10^{8}	2.69×10^{7}
Stationary after 70 days	1.33×10^{8}	3.77×10^{8}	2.79×10^{5}
Flowing on Immersion	4.08×10^{10}	1.07×10^{10}	4.82×10^{7}
Flowing after 25 days	3.42×10^{7}	2.53×10^{7}	4.29×10^{6}
Flowing after 76 days	2.03×10^{6}	3.4×10^{6}	1.31×10^{4}

Table II Average noise resistance values, with time, obtained from the flowing and the stationary electrolyte tests.

	AAS $\lvert Z\rvert_{max}$, Ωcm^2	GHS $\lvert Z\rvert_{max}$, Ωcm^2	ZAS $\lvert Z\rvert_{max}$, Ωcm^2
Stationary, on Immersion	3.9×10^{10}	7.5×10^{9}	5.5×10^{9}
Stationary, after 28 days	2.2×10^{7}	6×10^{9}	4×10^{6}
Stationary, after 96 days	2.0×10^{7}	2×10^{8}	7×10^{5}
Flowing, on Immersion	2.4×10^{10}	2.7×10^{10}	2.8×10^{10}
Flowing, after 35 days	8×10^{6}	1×10^{7}	3×10^{6}
Flowing, after 110 days	3.5×10^{5}	1.4×10^{6}	4.2×10^{4}

Table III : Comparison of EIS Data obtained from Stationary and Flowing Electrolytes.

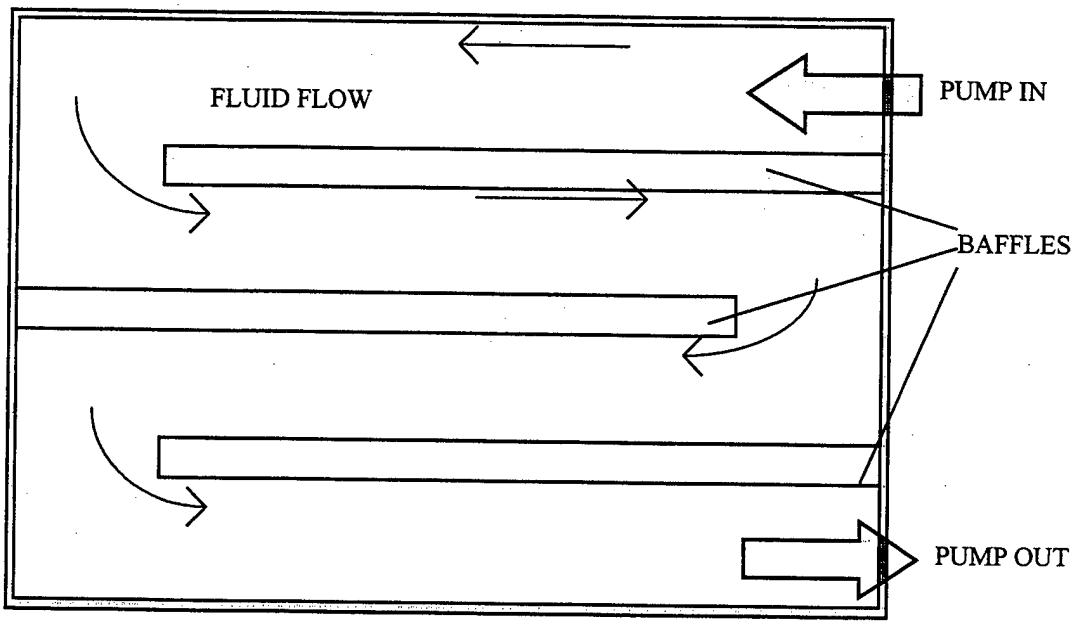


Figure 1. Schematic of the flowing electrolyte electrochemical cell, showing the baffles and fluid flow pattern.

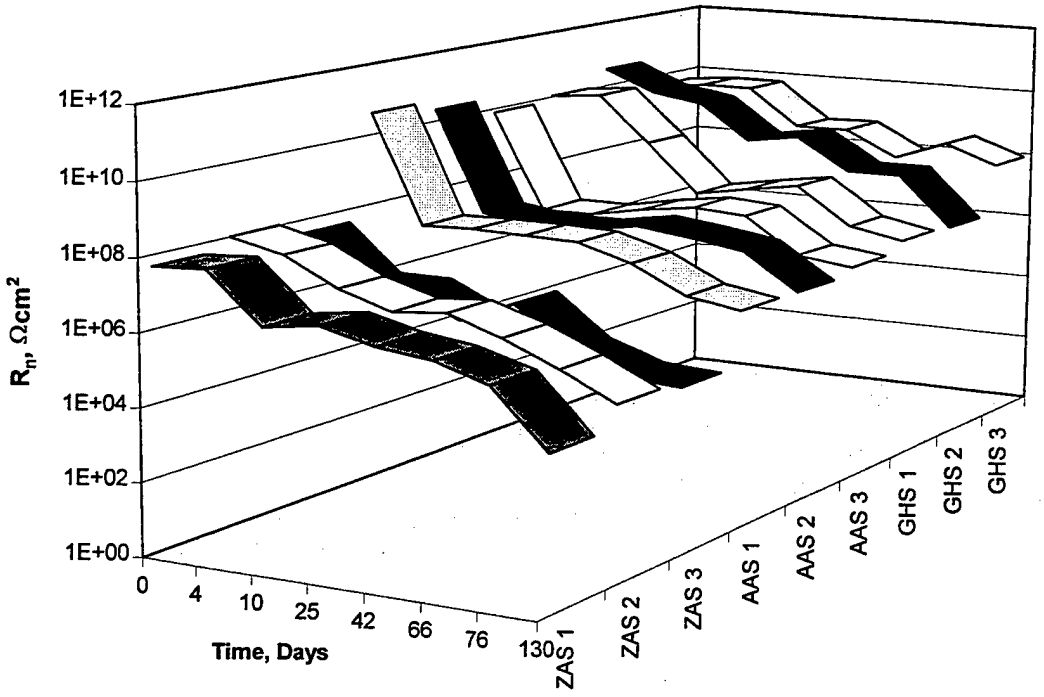


Figure 2 Ribbon graph of noise resistance vs. time, showing the reproducibility between the pairs of panels with identical coatings

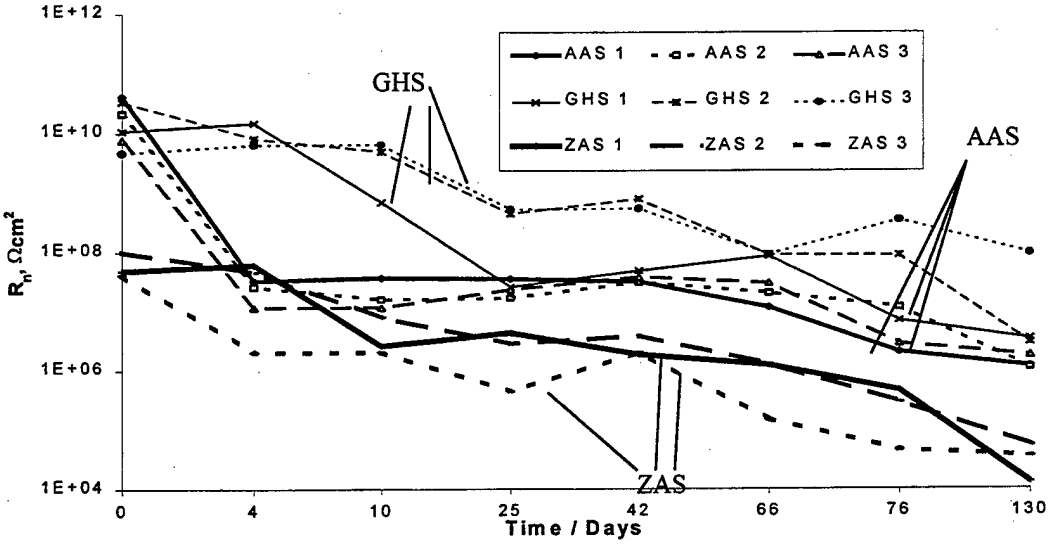


Figure 3 Line graph of noise resistance vs. time, showing the reproducibility between the pairs of panels with identical coatings

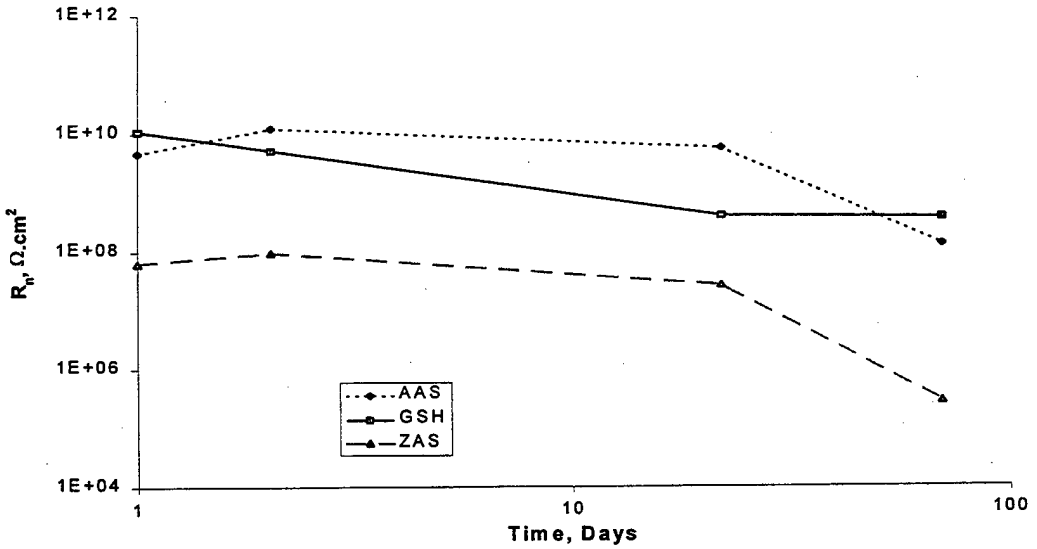


Figure 4 Noise resistance vs. time plot, for the stationary electrolyte electrochemical cell, showing the poor performance of the ZAS compared to the performance of the AAS and GHS panels

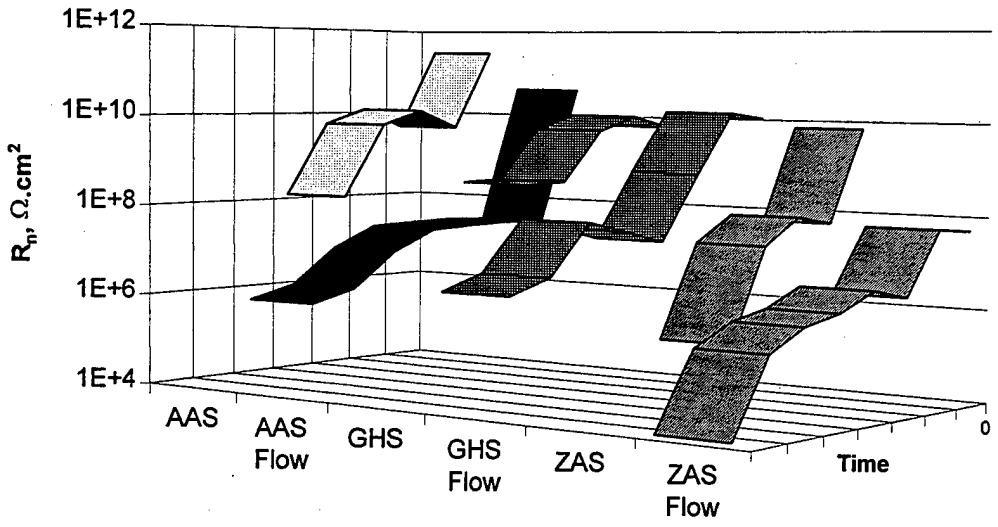


Figure 5 Ribbon graphs showing the difference in noise resistance values for the flowing and the stationary electrolyte electrochemical cell

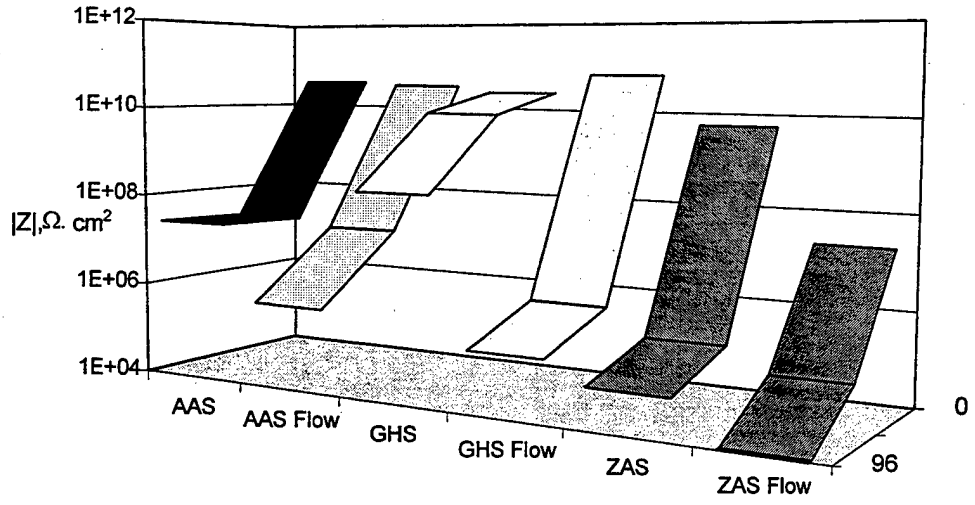


Figure 6 Ribbon graphs showing the difference in impedance modulus values for the flowing and the stationary electrolyte electrochemical cells. As in the previous figure note the large difference in $|Z|_{max}$ values between the flowing and the stationary electrolyte for the AAS and the GHS systems.

Appendix A

To analyze the results of our experiments on flowing electrolyte effects in coating degradation, we have struggled with the proper way to interpret the data. Since we observe results that indicate a acceleration of coating failure due to liquid flow, we conclude that mass transfer effects of some type are involved. The simplest interpretation is that the agitation involved in flow somehow increases the O_2 concentration n the solution by aerating it, much like bubbling air through a solution might accelerate reactions involving O_2. This does not seem likely, because it is unlikely the O_2 concentration is rate limiting unless the surface of the coating is bare. A similar consideration of flow effects would let one analyze a decreased diffusion boundary layer present at the coating/electrolyte solution interface if mass transfer from the electrolyte is the rate limiting step in the coating degradation. If we assume that the diffusion from the solution to the film takes place across a diffusion boundary layer, (δ) and that we can describe the flux (Q) of the diffusant from the solution to the film following a Nernst-like process, the ratio of the fluxes of material with and without stirring will be given by [see V.G.Levich, *Physicochemical Hydrodynamics,* Prentice-Hall, Englewood Cliffs, NJ.(1962) ch.II; and R.A. Probstein, *Physicochemical Hydrodynamics*, Butterworths, NY (1989) ch. 2]

$$\frac{Q_{stirred}}{Q_{static}} = \frac{\delta_{static}}{\delta_{stirred}} = 1.333\sqrt{u}\left(\frac{\rho}{D\eta}\right)^{1/3}.$$

Q = flux
D = Diffusion Coefficient
ρ = density
η = viscosity
δ = diffusion layer thickness

Again, this does not seem to make any sense, because the species that might diffuse across the boundary are the electrolyte ions and O_2, both of which should not be rate limiting in the coatings as we picture them.

What else might cause the effects we see in the work we have just described? One possibility is that there is a component diffusing out of the coating and into the bulk immersion electrolyte solution that, when lost from the coating, severely diminishes the coating's protective/resistance or barrier properties. The kinetics of the loss of this unknown material may possibly be matched by the modeling of diffusion limited dissolution of a minor constituent in the coating. Another possible effect which might give the results we have reported above is the presence of moving, swollen boundary of electrolyte saturated coating film, the motion of which is controlled by both diffusion and the kinetics of polymer reorganization and plasticization. The swollen, plasticized film would have a much lower barrier properties than the original coating film. When the swollen boundary reaches the metal/coating interface, the protection/barrier properties of the film are drastically diminished, and failure is more rapid. We are now examining the possibility of running model calculations of these two effects.

References

[1] Bacon R.C., Smith J. J., Rugg F. M., *Ind. Eng. Chem.* **1948**, *40*, pp. 161-167
[2] Skerry B.S., Eden D.A, *Prog.Org. Coatings* **1987**, *15*, pp. 269-285
[3] Skerry B.S., Eden D.A., *Prog. Org. Coatings* **1991**, *19*, pp. 379-396
[4] Chen C.T., Skerry B.S., *Corrosion***1991**, *47*, pp. 598-611
[5] Mills D.J., Bierwagen G.P., Skerry B.S., Tallman D.E., *Proc. of the 12th international Corrosion Congress*, **1993**, *Vol 1* pp. 184

[6] Bierwagen G. P., Mills D. J., Tallman D. E., Skerry B. S., *Proc. of Symposium on Corrosion and Corrosion Prevention in Seawater Environments*, E.C.S., Oct. **1993**, Abstract No 81
[7] Bierwagen G. P., *J. Electrochemical Soc.*, **1994,** *141*, pp. L155-157
[8] Electrochemical Impedance, Scully J.R.; Silverman D.C.; Kendig M.W., Eds.; Special Tech. Publ. 1188, ASTM, Philadelphia, PA, **1993**
[9]Impedance Spectroscopy, MacDonald J.R., Ed.; Wiley-Interscience, New York, NY, **1987**
[10] Callow, M. *Chemistry and Industry*, **1990**, pp 123

Laboratory Evaluation of an In Situ Coating Process for Mitigation of Lead and Copper in Drinking Water

Vincent F. Hock, Erik Kirstein, Kent W. Smothers, Jeremy L. Overmann
U.S. Army Corps of Engineers
Champaign, IL 61826, USA
217-373-6753

ABSTRACT

Water pipe failures (leaks) within buildings are an ongoing problem at many large installations such as military bases, universities, and industrial complexes. Such failures can cause severe, costly damage to building interiors, personal property, and electronic equipment. Most failures in metallic potable water pipes may be induced by certain constituents in the water and/or poor workmanship practices. Water temperatures, pressures, and velocities are also factors in the corrosion process. In order to mitigate water-side corrosion and comply with the 1986 Safe Drinking Water Act and the National Primary Drinking Water Regulations for lead and copper, 40 CFR 141.82, an alternative to chemical treatment was developed. The preliminary results of in situ pipe coatings for small diameter building plumbing are presented.

INTRODUCTION

Army installations must comply with the increasingly stringent drinking water quality standards enacted at the Federal level and enforced by State regulations. The Safe Drinking Water Act (SDWA) of 1974 required the U.S. Environmental Protection Agency (USEPA) to develop a list of maximum contaminant limits (MCLs) for inclusion in the National Primary Drinking Water Regulations (NPDWR).[1] A September 1986 amendment to the SDWA banned the use of lead in public water system pipes, solder, and flux. On 7 June 1991, the USEPA finalized these regulations with a requirement of an MCL for lead concentration of 0.015 mg/L measured in the ninetieth percentile taken from cold water kitchen faucets following a 6- to 8-hour stagnation time. In September 1992, the USEPA finished Volume II of the Lead and Copper Rule (LCR), which is the guidance manual on corrosion control treatment.[2]

Much attention has focused on the costly remediations required when the lead action level is exceeded. This issue plays a significant role in the national debate over unfunded environmental mandates, and more specifically, in the search for cost-effective ways to ensure that drinking water at Army installations meets all standards for quality and compliance with applicable laws. Two possible strategies to ensure that drinking water meets current standards are by chemical treatment and by application of coatings or linings to pipes or tubes to mitigate corrosion or

plumbosolvency. In addition to plumbsolvency, copper tubes and fittings fail by pitting corrosion, concentration cell corrosion and galvanic corrosion as a result of both water chemistry and workmanship. Chemical treatment alone will not mitigate corrosion induced failure where poor workmanship has been identified as the primary cause of failure. The use of an in-situ coating or lining can be utilized as an alternative to chemical treatment to mitigate these types of corrosion induced failure. An example of corrosion induced water-side pipe failure within building plumbing systems that could be mitigated by in-situ coating is shown in Figure 1. This study was undertaken to evaluate the effectiveness of an in situ epoxy coating in comparison with a proven chemical treatment for potable water.

The purposes of this study were to initiate operation of the Water Treatment Test Facility (WTTF), and to execute a 12-week test program. This study evaluated the effectiveness of an in situ epoxy coating for the mitigation of lead and copper corrosion in comparison to both a control and a proven, effective chemical treatment (zinc orthophosphate) for potable water.

EXPERIMENTAL PROCEDURE

The initial phase of the laboratory investigation was to determine whether a coating or lining could be applied in-situ to existing small diameter (1"-2") pipes or tubes. The experimental procedures consisted of fabricating copper pipe specimens, abrasively cleaning the interior surface followed by either blowing through or depositing the 100% solids epoxy coating. The coating application loop is represented in Figure 2. The epoxy coating was then air cured. The evaluation consisted of sectioning the specimens and measuring the coating thickness to determine uniformity of each application technique, in addition to taking weekly water analysis samples to determine lead ion contents.

The water entering the water treatment test facility can be altered mechanically and chemically to produce a water with the desired concentrations of hardness, alkalinity, pH, calcium, etc. Several different water qualities (up to four) can be evaluated during each daily cycle by using a computer to control sequencing of valves, pumps, etc. Provisions have been made for testing up to four different chemical treatments for each of the water qualities. Figures 3, 4, and 5 provide detailed schematics of various elements of the WTTF.

This study employed only two water qualities. One was softened water (<2.0 mg/L hardness as $CaCO_3$) with an alkalinity of ~200 mg/L and a flowing pH of approximately 7.0, and the second was a hard water (municipal supply, ~80 mg/L as $CaCO_3$) with an alkalinity of 200 mg/L and a flowing pH of 7.5. The original intent was to operate the hard water system with a pH of 8.0, but the water pH was not stable in that range. The incoming municipal water has a nominal pH of 8.8 to 9.0, so the pH is first lowered and the alkalinity neutralized by the addition of sulfuric acid. Soft water test loops are first passed through a water softener to remove most of the hardness. After the acid addition, solutions of first sodium bicarbonate and then sodium hydroxide are injected into the test loop to raise the alkalinity and pH to the desired levels. There were three water treatment schemes, a control with no coating, in situ epoxy coating, and zinc

orthophosphate. The two flow rates employed were 5 and 3 feet per second (fps).[3] Each of the water qualities (WQ) were tested at two velocities (3 and 5 fps), the maximum for copper pipe in a typical building flow is 4 fps. This resulted in four designated water qualities:

1. WQ 1, hard water, 5 FPS
2. WQ 2, soft water, 5 FPS
3. WQ 3, hard water, 3 FPS
4. WQ 4, soft water, 3 FPS

Water flowed through each of the 12 legs for 2 hours each day. Each of the twelve legs in operation had a 3½-in. long copper specimen with ½-in. coating of 50/50 tin-lead solder with a thickness of .03" ± .005"and 3 in. long copper specimens. Since the loops are constructed of PVC pipe, these pipe specimens are the only potential source of lead and copper in the system except the incoming city water.

Samples were taken weekly following an 8-hour standing time from each of the twelve legs and analyzed for lead, copper, total organic carbon (TOC), orthophosphate, zinc, methyl orange alkalinity (M-alkalinity), hardness, pH, and temperature. Source water for the loops was Champaign-Urbana tap water (Northern Illinois Water Corporation). This was monitored weekly for copper, TOC, orthophosphate, and zinc. The soft and hard water supplied to the legs was monitored for background concentrations in all of the species listed above. Oxygen and temperature levels during operation were recorded by on-line instruments. The uncoated copper specimens were removed for corrosion weight loss measurements.

DISCUSSION OF RESULTS

Analytical Data

One concern with the use of the in situ epoxy coating was the possible decomposition of the coating, which might result in the release of organic compounds. The supply water was monitored for background TOC levels, and the average value for the 12-week period was 1.8 mg/L. The average for the four legs that used the in situ epoxy coated specimens was 1.7 to 1.9 mg/L, indicating no significant decomposition of the epoxy coating. Neither the flow rate (5 fps and 3 fps), nor the water quality had any apparent impact on the lead or copper concentrations. The temperature was relatively constant throughout the course of the experiment, with a range of 16.9 to 20.3 °C, and an average value of 17.9 to 18.6 °C in the individual legs. The pH for the standing samples in all of the legs was constant at approximately 7.0 (±0.3).

Lead corrosion was obviously controlled by water treatment by using a zinc orthophosphate inhibitor, since very few of the samples contained lead concentrations above the detection limit. Copper concentrations were measurable for all 12 weeks in each of the four legs using zinc orthophosphate. The average concentration of copper was highest (0.51 mg/L) in the soft water,

3 fps leg. The average concentration of copper in the other three legs was very consistent at 0.41, 0.43, and 0.44 mg/L. None of the copper concentrations exceeded the USEPA 1.3 mg/L MCL. The average TOC concentration in these four legs was very similar to the coated specimen legs, ranging from 1.7 to 2.0 mg/L. Zinc concentrations averaged between 0.86 and 0.96 mg/L, and the average orthophosphate concentrations ranged from 1.52 to 1.91 mg/L. The zinc orthophosphate treatment provided satisfactory corrosion inhibition of lead and copper.

Corrosion rates for both lead and copper was highest in the control legs. The soft water, 5 fps leg, had the lowest lead levels, averaging 1.04 µg/L. The other three legs were more consistent with each other, averaging 2.10 to 2.74 µg/L. Hard water showed higher Pb corrosion rates than soft water for lead at both flow rates. However, the average copper concentrations were more consistent, ranging from 1.03 to 1.26 mg/L for the four control legs. Copper concentrations exceeded the MCL of 1.3 mg/L in 41 percent of the samples from these legs.

Once again, TOC concentrations were comparable in both the in situ epoxy coated specimen legs and the zinc orthophosphate treated legs, ranging from 1.8 to 2.0 mg/L. Champaign-Urbana tap water was used as the supply for these loops, and was monitored for copper, TOC, orthophosphate, and zinc. Zinc and copper concentrations were below instrument detection limits for all of the samples analyzed. The TOC concentrations averaged 1.8 mg/L for the duration of the test run. Trace amounts of orthophosphate recorded in two samples, which may have been due to system pH upsets that resulted in a release were of phosphate from existing deposits on the distribution piping.

Flowing water samples from the hard and soft water supply loops were analyzed during most of the 12-week period for the same analyses as the legs. Oxygen concentrations averaged 3.6 mg/L in the soft water loop and 3.8 mg/L in the hard water loop. The temperatures were, as expected, much lower in the flowing samples, averaging near 10 °C for both loops. The copper, zinc, and lead concentrations in the loop were found to be at or below the detection limit.

Weight Loss Data

Corrosion weight loss measurements were conducted on the 3-in. copper specimens installed in the zinc orthophosphate and control loops. The corrosion rate was somewhat higher for the soft water than the hard water for both velocities in the control and treated legs. The 5 fps velocity legs had higher corrosion rates than the comparable 3 fps legs for three of the four water quality/velocity combinations. The soft water legs treated with zinc orthophosphate had the same corrosion rates for both the 3 and 5 fps legs. The effect of velocity on the corrosion rate of copper was obvious in the control legs. The copper corrosion rate in MPY (millimeters penetration/year) for the 5 fps legs in both the hard and soft waters was almost 20 percent higher than in the 3 fps legs. The recommended maximum velocity for copper tube in potable water systems is 4 fps; flow rates higher than that can cause an increase in corrosion rates. The copper corrosion rates for the four legs using zinc orthophosphate ranged from 0.34 to 0.49 MPY, and

the corrosion rates in the control legs were 0.95 to 1.19 MPY. Copper corrosion rates of 1.0 MPY are much higher than desired for potable water systems, the desired corrosion rate is less than 0.5 MPY. Corrosion weight loss determinations were not performed on the 3½ in. specimens since ½ in. of the inside is coated with 50/50 tin-lead solder, and it would be difficult to determine how much weight loss was attributable to copper and how much was lead or tin.

Wilcoxon Signed Rank Test

The Wilcoxon Signed Rank Test (Wilcoxon) is a nonparametric statistical analysis comparing two related (dependent) samples. The Wilcoxon takes into account the size of the rank order differences within pairs of data, as opposed to the numerical values of the differences. Paired data were examined among three different water treatment conditions (epoxy coating, zinc orthophosphate, and control) under four different water quality conditions. Table 1 summarizes the water treatments and qualities. The Wilcoxon was applied to look for differences among the three different water treatments.

In this experiment, copper, lead, and total organic carbon (TOC) values in water were recorded. The Wilcoxon was performed separately for each of these three elements. For the purpose of reading the tables, water quality is denoted by WQ, and water treatment is denoted by WT. The numbers corresponding to the water treatments and qualities are designated in Tables 1 and 2. The Wilcoxon tables are broken down into three sections:

1. Counts of Differences: This section presents the number of times element values from a given WQ and WT (listed along the left-hand column) are greater than the values for one of the other WTs (listed along the top row).

2. Z: This section presents the sum of the signed ranks divided by the square root of the sum of the squared ranks. This statistic is given meaning by the probability value obtained in statistical tables.[4]

3. Two-Sided Probabilities: The statistical significance to the corresponding Z-value is given in this section. A probability of 1.000 means the paired rankings are indistinguishable from one another and the differences between them are insignificant. A probability of 0.001 means there is a 99.9 percent probability the paired rankings are distinguishable and significantly different.

Table 2 summarizes the Wilcoxon for copper, lead, and TOC values.

Table 3 summarizes the results shown in Table 2, and ranks the water treatments for the reduction of each element. The data in Table 3 shows that the epoxy coating was the most effective for reducing copper concentrations in the pipe loop. Both the epoxy coating and the zinc orthophosphate were effective in reducing lead values, and both seemed to work equally well in comparison with the control. However, all three water treatments were statistically

indistinguishable from one another in reducing TOC values. None of the water treatments stood out as a good agent for the reduction of total organic carbon in water.

Visual Observations

Visual observations were made for all of the 3½-in. and 3-in. specimens after completing the test run, and before making any weight loss determinations. The exterior surface of each specimen was discolored, indicating there had been some seepage of water between the specimen and the holder. The specimens designated by C are the 3-in. copper specimens and those designated by P are the 3½-in. copper and tin-lead solder specimens. Table 4 lists the visual observations.

CONCLUSIONS

The results of this study clearly indicate that the in situ epoxy coating provides an effective alternative to conventional chemical treatment for the prevention of lead and copper metal release in a system modeled to simulate a home plumbing system. Lead concentrations were lower than the USEPA MCL for all of the samples, but this was probably due to the very small surface area of lead available. The control samples had measurable lead concentrations in most samples (>80 percent), with three of the legs averaging more than 2 µg/L lead for the standing samples. The zinc orthophosphate and in situ epoxy coating legs all had only occasional (<20 percent) lead concentrations above the detection limits. Copper concentrations were very high in the control legs, having average copper concentrations near the USEPA MCL of 1.3 mg/L (1.03–1.26 mg/L) for each leg, with ~41 percent of the samples exceeding the MCL. The zinc orthophosphate exhibited a significant improvement in the copper concentrations found in the standing samples for all water qualities, with none of the samples exceeding the MCL. The average copper concentrations varied from 0.41 to 0.51 mg/L. The in situ epoxy-coated legs showed an even more dramatic reduction of copper levels than the zinc orthophosphate treatment, with only one of the 48 samples having a copper concentration (0.030 mg/L) above the detection limit of 0.006 mg/L.

This study also initiated operation of the WTTF, and determined its viability as a test facility to simulate a variety of water qualities in a home plumbing system. The WTTF operated reliably over the course of the 12-week study, which gathered valuable information on operating procedures. Comprehensive information on the operation of the loop, computer programs, and equipment specifications can be found in the Army Water Treatment Test Facility Operation Manual.

[1] "Minimization of Lead Corrosion in Drinking Water," *Materials Performance* (August 1990), pp 45-49.

[2] U.S. Environmental Protection Agency (USEPA), *Lead and Copper Rule Guidance Manual Volume II: Corrosion Control Treatment*, EPA 811-B-92-002 (USEPA, September 1992).

[3] 1 ft = 0.305 m; 1 in. = 25.4 m.

[4] Vincent F. Hock, Henry Cardenas, Kent W. Smothers, and Eric D. Zelsdorf, *Control of Plumbosolvency in Building Plumbing Supplies*, Technical Report (TR) 96/74/ADA315200 (U.S. Army Construction Engineering Research Laboratories [USACERL], July 1996).

Table 1. Sample Identifications

Sample Identification	Water Quality	Water Treatment	Treatment
A-1	1	1	Coating
I-1		2	Zinc Orthophosphate
R-1		3	Control
D-3	2	1	Coating
L-2		2	Zinc Orthophosphate
S-1		3	Control
F-1	3	1	Coating
M-1		2	Zinc Orthophosphate
V-1		3	Control
G-1	4	1	Coating
P-2		2	Zinc Orthophosphate
W-1		3	Control

Table 2. Summaries of the Wilcoxin for copper, lead, and TOC values.

Water Quality	Copper	Lead	TOC
WQ1: "hard" water, 5 fps.	WT1 was the best treatment for this WQ, having a 99.8 percent significance over WT2 and WT3. WT2 ranked second, also having a 99.8 percent significance over WT3.	The results for comparing WT1 and WT2 were not distinguishable. However, both WT1 and WT2 were significantly better than WT3 (over 99 percent).	There was no significant difference between WT1 and WT2, as well as between WT2 and WT3. The results for WT1 and WT3 were 96.5 percent distinguishable, with WT1 prevailing.
WQ2: "soft" water, 5 fps.	The results for WQ2 were almost identical to WQ1. WT1 had over a 99 percent significance over WT2 and WT3. WT2 had a 99.7 percent significance over WT3.	The results were similar to the WQ1 results. WT1 and WT2 were not distinguishable, but both WTs prevailed over WT3.	None of the three water treatments were statistically distinguishable from one another for this water quality.
WQ3: "hard" water, 3 fps.	The results were exactly identical to the results obtained for WQ1. WT1 was the best, followed by WT2 and WT3.	In this case, WT1 and WT2 were distinguishable, with WT2 having a 95.7 percent significance over WT1. Both WT1 and WT2 were significantly better than WT3 (over 95 percent).	The results for WQ3 were the same as for WQ2. None of the three water treatments were statistically distinguishable from one another.
WQ4: "soft" water, 3 fps.	Once again the results were similar to WQ1. Order of performance: WT1, WT2, WT3.	WT1 had a slight significant edge over WT2 (92 percent), and WT3 had the most number of larger lead values, placing it last among the three water treatments.	For WQ4, WT2 was slightly significantly different over WT1 (91.9 percent). The remaining results were not distinguishable.

Table 3. Wilcoxon signed rank test results.

Water Quality	Copper Water Treatment Rank			Lead Water Treatment Rank			TOC Water Treatment Rank		
WQ1	WT1	WT2	WT3	WT1, WT2	WT3	—	WT1, WT2, WT3	—	—
WQ2	WT1	WT2	WT3	WT1, WT2	WT3	—	WT1, WT2, WT3	—	—
WQ3	WT1	WT2	WT3	WT2	WT1	WT3	WT1, WT2, WT3	—	—
WQ4	WT1	WT2	WT3	WT1	WT2	WT3	WT1, WT2, WT3	—	—

Table 4. Visual observations on all 3-in. and 3½-in. specimens after the test run.

	In Situ Epoxy coating		Zinc Orthophosphate		Controls	
	Specimen	**Observation**	**Specimen**	**Observation**	**Specimen**	**Observation**
Hard water, 5 fps	C11	Very thin, yellow-tan colored deposit on epoxy coatng	C06	Very thin, soft, surface deposit with a harder, blue-green and gray deposit underneath.	C13	Very thin, soft, surface deposit and a harder, yellow-tan deposit beneath, which increases in thickness near the stamped end of the specimen.
	P11	Very thin, soft, surface deposit with a harder orange-tan deposit beneath, and an orange-tan colored stain on epoxy coating.	P06	Very thin, soft, yellow-gray deposit on solder. Very thin, soft, tan-brown deposit on the copper surface.	P13	Very thin, soft, surface deposit with a harder, yellow-tan deposit on the solder and copper surfaces.
Soft water, 5 fps	C14	Tan colored stain on epoxy coating.	C09	Very thin, soft, surface deposit with a harder blue-green and yellow-tan deposit underneath.	C01	Very thin, soft, surface deposit with a harder, yellow-tan deposit underneath.
	P14	Very thin, yellow-tan deposit and yellow-tan colored stain on epoxy coating.	P09	Very thin, soft, surface deposit with a harder, gray and yellow-tan deposit on solder. Very thin, soft, surface deposit with a harder yellow-tan and tan-brown deposits on copper surfaces	P01	Very thin, soft, surface deposit with a harder, yellow-tan deposit on the solder. Very thin, hard, tan deposit on copper.
Hard water, 3 fps	C10	Very thin, yellow-tan colored deposit on epoxy coating.	C07	Very thin, soft, surface deposit with a harder, blue-green and tan deposit beneath.	C02	Very thin, soft, surface deposit with a harder, yellow-tan deposit near the stamped end, dark discoloration of the interior surface near the other end.
	P10	Very thin, yellow-tan deposit and yellow-tan colored stain on epoxy coating.	P07	Very thin, soft, gray deposit on solder. Very thin, tan deposit on copper.	P02	Very thin, soft, surface deposit with a harder, yellow-tan deposit on solder. Very thin, hard, yellow-tan deposit on copper.
Soft water, 3 fps	C12	Light yellow-tan colored deposit on epoxy coating.	C08	Very thin, soft, surface deposit with a harder, blue-green and yellow-tan deposit underneath.	C03	Very thin, soft, surface deposit with a harder, tan deposit beneath.
	P12	Very thin, light tan deposit and light yellow tan-colored stain on epoxy coating.	P08	Very thin, soft, surface deposit with a harder, gray deposit on solder. Very thin, soft, surface deposit with a harder, tan-brown deposit beneath on the copper.	P03	Very thin, soft, surface deposit with a harder, yellow-tan and gray deposit on solder. Very thin, hard, yellow-tan deposit on copper.

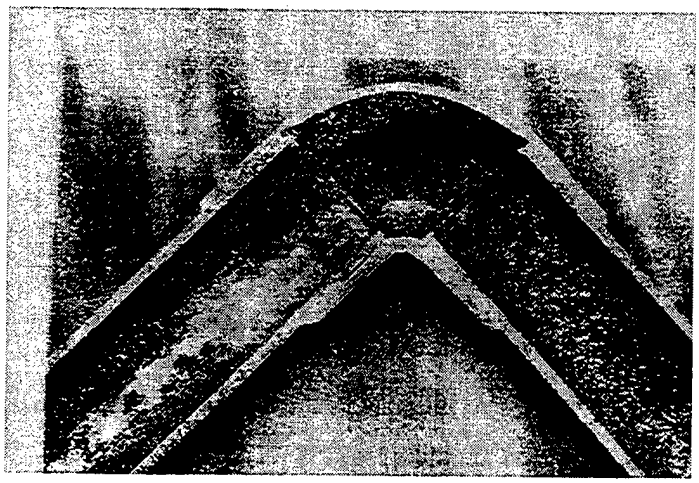


Figure 1. Copper tube showing workmanship defect, i.e., unreamed tube ends, solder globs, and excess solder flux.

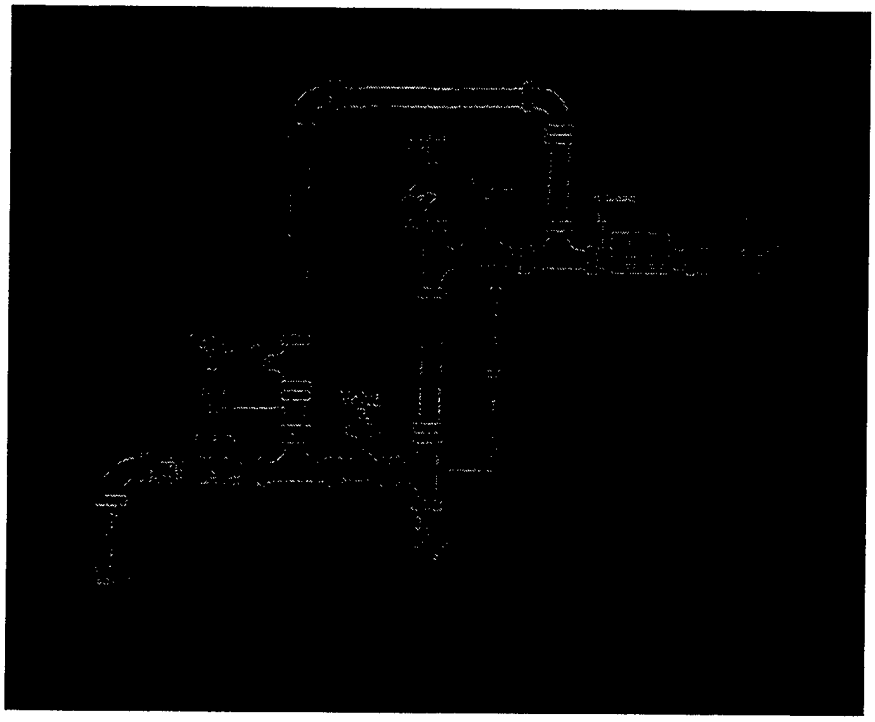


Figure 2. In-situ coating application loop.

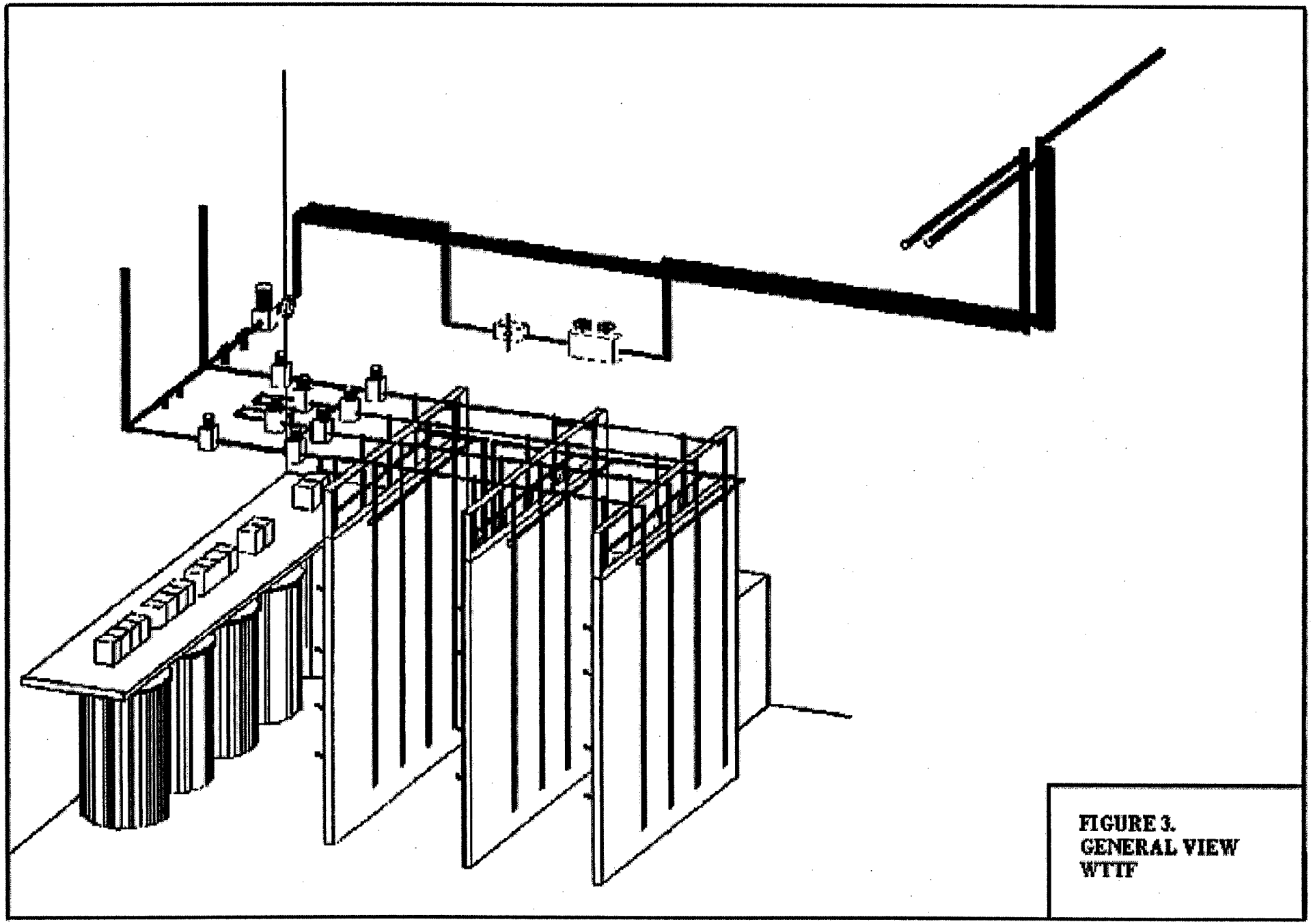


FIGURE 3.
GENERAL VIEW
WTTF

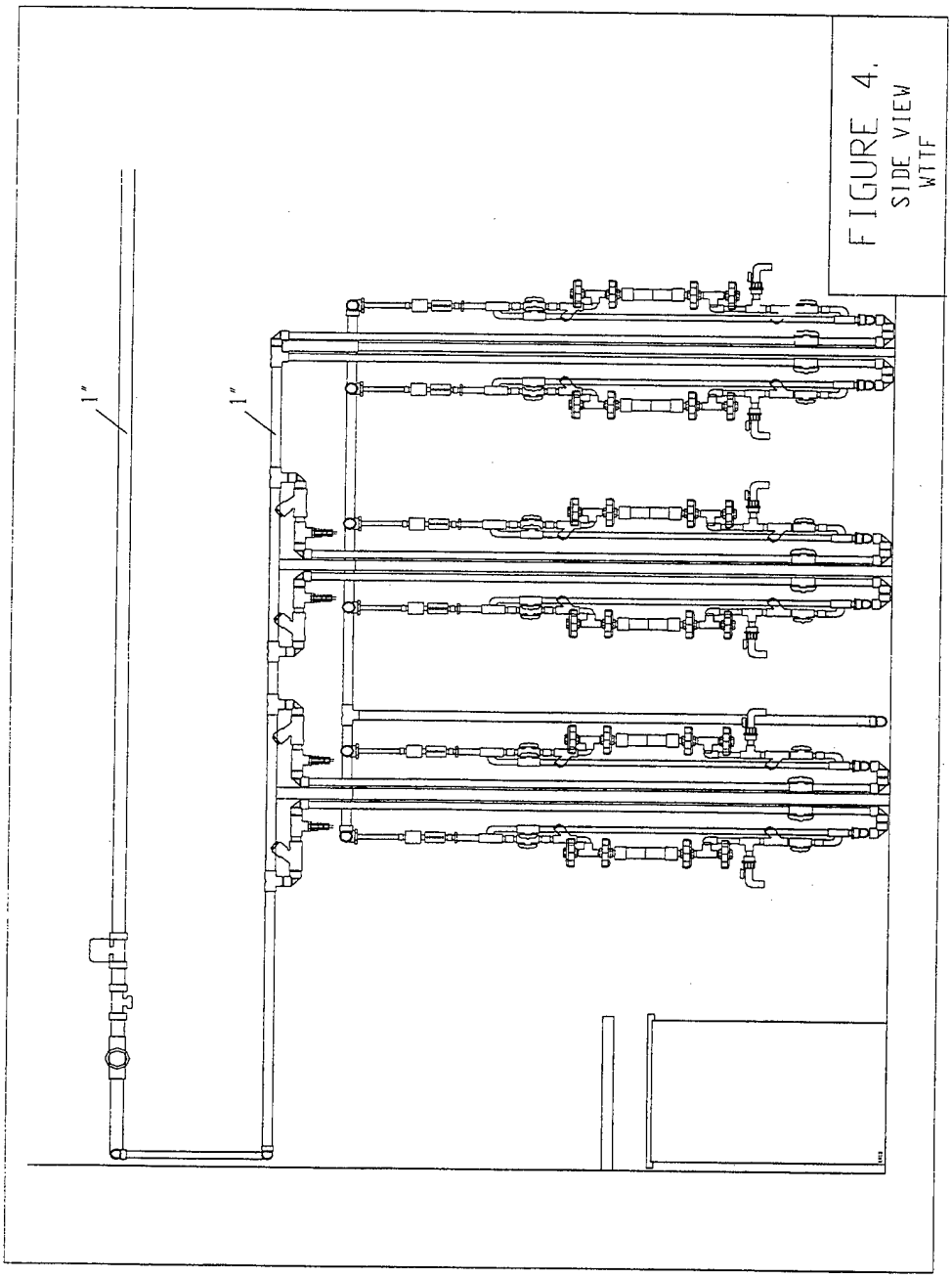


FIGURE 4.
SIDE VIEW
WTTF

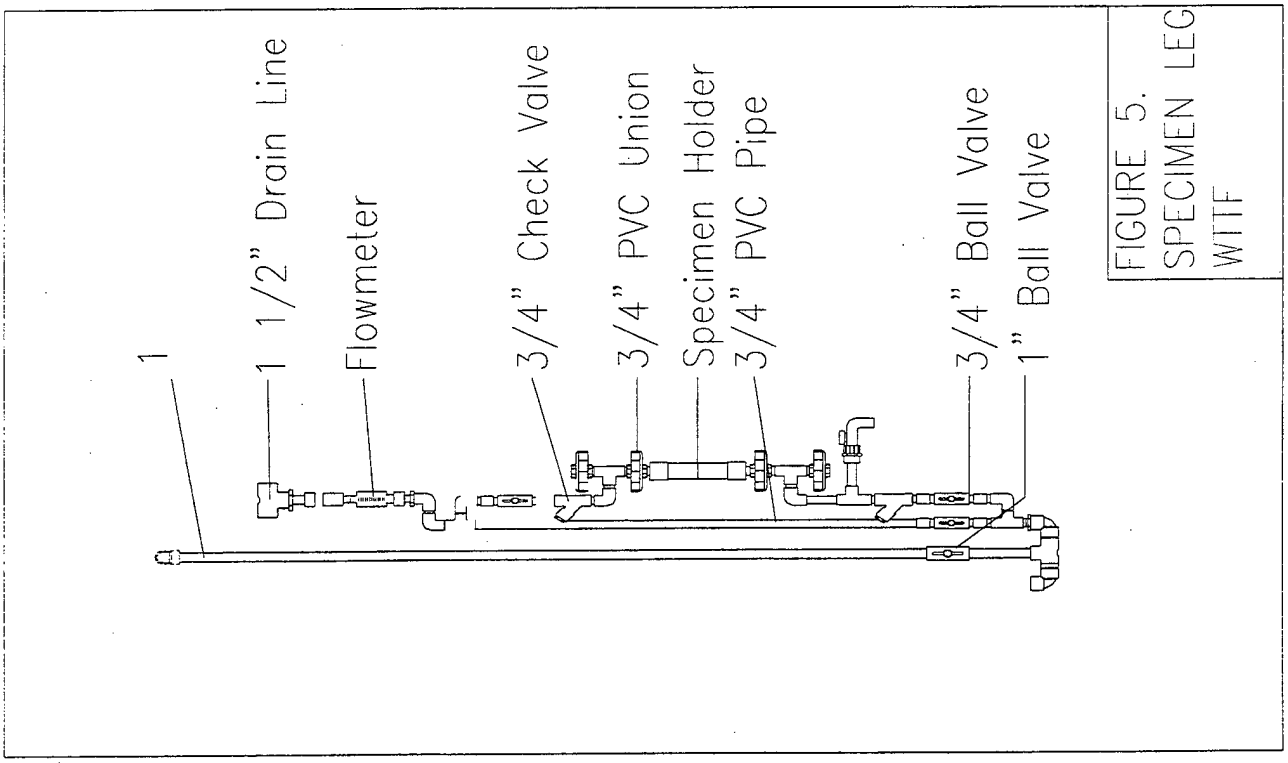


FIGURE 5.
SPECIMEN LEG
WITF

Evaluating Anti-Galling Thread Treatments for Beta-C Titanium Fasteners Exposed to Marine Environments

R.K. Conrad, A. Sheetz and C. Bowles
Naval Surface Warfare Center- Carderock Division
Corrosion Technology Group- Code 683
9500 MacArthur Blvd.
West Bethesda, MD 20817-5700

R. Simmons
SBB Technologies Inc.
13851 S.W. 37th Ct.
Davie, FL 33330

ABSTRACT

Fasteners for top-side applications on Naval ships have historically been steel fasteners. These fasteners when exposed to marine environments suffer extensive corrosion. Alternatives such as high strength stainless steel, nickel alloy and titanium alloy fasteners are being considered. While these alternative materials offer better corrosion resistance than steel, they can suffer from thread galling when used in the uncoated and/or unlubricated condition. Solid film lubricants such as molybdenum disulfide-impregnated epoxy polyimide have shown anti-galling properties. Additionally, anti-seize compounds such as copper loaded grease have also shown anti-galling properties. In a paper on titanium as alternative fasteners[1], K. Faller compares titanium fasteners to steel and high strength alternative materials. In this study, Beta-C titanium fasteners are investigated as an alternative fastener for Naval use. Galvanic interactions and thread galling are evaluated to identify candidate coatings or lubricants so that Beta -C titanium fasteners can be utilized for top-side applications.

INTRODUCTION

Make/break testing was performed on 15 solution treated titanium Beta-C (YS~120 ksi) ½"-13UNC hex-cap screws to evaluate anti-galling thread treatments. Each make/break torque test measured torque behavior to reveal any galling or galvanic corrosion tendencies. Titanium Beta-C was supplied by RMI Titanium Company, of Niles, Ohio to Mr. Kurt Faller of B & G Manufacturing of Hatfield, PA, for the production of ½" diameter fasteners. Alloy composition, physical and mechanical properties are shown in Tables 1, 2 and 3 respectively. Initial make/breaks of some of the fasteners were performed by Mr. Faller. The test fixture with the fasteners was delivered to the Naval Surface Warfare Center Carderock Division (NSWC CD), Corrosion Technology Group, Code 683, Ft. Lauderdale Marine Corrosion Test Site in December 1993.

EXPERIMENTAL PROCEDURE

The test fasteners without washers were tightened with a torque wrench in a steel plate with through hole (Figure 1) to two-thirds of the materials' yield strength to simulate a stress state of service. Monthly make/break testing was performed on 15 titanium Beta-C ½"- 13UNC hex-cap screws. Table 4 lists the three conditions in which the fasteners were tested. The anti-galling materials listed in Table 4 were applied to the fasteners only at the beginning of the test. All of the nuts were untreated.

Test Environment

The fasteners were subjected to periodic seawater wetdown for nine months. The fasteners were attached to seawater wetdown test racks located 30 feet from the Port Everglades channel, 400 feet from the ocean, and approximately 8 feet above sea level. The seawater wetdown system operates on a continuous cycle where the test fixture is sprayed with seawater for a period of 10 minutes and allowed to air dry for 50 minutes. Figure 2 shows the test rack and spray system. This test was designed and developed with close adherence to the American Society for Testing and Materials (ASTM) G33[2] , G44[3], G50[4], and G52[5]. Although the seawater spray wetdown is not an ASTM standard, it closely simulates the top side environment of Naval ships. After the ninth month the seawater wetdown was stopped and the samples were exposed to the marine atmosphere for 7 months in accordance with ASTM G50[4].

Make/Break Procedures

Prior to delivery, Mr. Faller performed 17 make/break tests per fastener on nine of the 15 fasteners. The remaining six fasteners had three make/breaks each performed. After delivery to the test facility the following procedure was performed every month on each fastener:

a) Length of the fastener was measured under load and recorded to the nearest thousandth of a inch.
b) Maximum torque needed to loosen the nut (i.e. break torque) was determined and recorded.
c) Fastener was removed from the fixture, and the length of the fastener under no-load was measured and recorded.
d) Threads of the fastener were visually inspected for galling.
e) Fastener was replaced in fixture and torqued to 10 ft-lbs.
f) Length of fastener was measured and recorded.
g) Fastener was torqued to 50 ft-lbs in 10 ft-lbs increments, measuring length of the fastener at each step.
h) Test fixture was placed back into the test environment.

Statistical Analysis

Statistical analysis of the breakloose torque[6] values was performed to determine the difference in performance between the three types of fastener anti-galling coatings. The method

used was a two-factor analysis of variance. This technique analyzes the variance of the breakloose torque over the exposure period for each bolt in the sample group using the inverse F-test which is based on the variance of the differences sample groups (also known as treatment levels).

RESULTS

From the monthly make/break testing of these fasteners, it was found that all of the uncoated control fasteners had seized in the steel test fixture due to galvanic corrosion occurring between the steel and the titanium Beta-C. Thread galling had also occurred under the nuts on the control fasteners. The molybdenum disulfide epoxy-polyimide coated fasteners were also seized in the test fixture. However, they could be removed from the test fixture using a slight amount of force. The breakloose torques of the FelPro C-5A coated fasteners were lower than the controls and molybdenum disulfide coated fasteners. The breakloose torque values were identical to the initial installation torque values for those fasteners. After loosening the FelPro C-5A graphite grease coated fasteners, they were found to be loose in the holes and could be easily removed from the test fixture. No galling of the thread area was observed.

Two-Factor Analysis of Variance

The two-factor ANalysis Of VAriance (ANOVA) method analyzes the variance of the breakloose torque as both a function of each specimen and the period of exposure for each bolt with the same anti-galling treatment. Using the inverse F-test allows for the treatment levels to be analyzed even though their average values are different. The values of the breakloose torque and the corresponding ANOVA for each condition are listed in Tables 5, 6, and 7. All ANOVA is performed at the 99.9999% confidence level. Analysis of the ANOVA performed on the data from the molybdenum disulfide epoxy-polyimide coated fasteners, Table 5, verifies that there is a significant changes from the initial torque values as a function of exposure time since the F value (16.484) calculated is greater than the critical F value (6.999). There is no difference between the specimens (F value < Fcrit) which indicates that the change in the torque values occurred for all specimens equally. Analysis of the ANOVA for the FelPro C-5A graphite grease coated fasteners, Table 6, indicates no difference in the breakloose torque values between specimens and there is no significant change in the breakloose torque values as a function of exposure time. This is indicated by both F values being less than their respective Fcrit values. Also, for the titanium Beta-C uncoated fasteners, Table 7, there is no difference in the breakloose torque values between specimens and there is no significant change in the breakloose torque values as a function of exposure time. This is indicated by both F values being less than their respective Fcrit values.

The two-factor ANOVA is able to distinguish changes in the breakloose torque values as a function of time on exposure. However, this analysis does not allow for discrimination between the anti-galling treatments. Therefore one more step was taken. A pairwise comparison of the treatment levels was performed. This analysis is based on the confidence interval of the means. Any confidence interval which contains zero is considered not to vary from the standardized mean significantly. The comparisons were calculated at the 95% confidence level and are shown in

Table 8. The results of this analysis show that there is very little difference between the molybdenum disulfide and the control samples. There is, however, a difference between the FelPro C-5A graphite grease and the molybdenum disulfide and control fasteners.

SUMMARY

The methodology and results of this test are more severe than would normally be expected for either fasteners or thread treatments. However, the combination of the highly corrosive test environment along with the monthly make/break cycle more accurately reflect fastener life cycle aboard a Naval surface combatant. After nine months of seawater spray and seven months of marine atmospheric exposure the following has been noted:

- The control titanium Beta-C fasteners seized in the steel test fixture due to galvanic corrosion. These fasteners also had galling occurring within the threads and the nuts.

- The molybdenum disulfide-impregnated epoxy polyimide solid film lubricant coated fasteners had galling occurring between of the threads of the fasteners and nut, and the fasteners are tight in the test fixture. Statistical analysis of the make/break testing indicates that these fasteners perform no better than the control fasteners.

- Beta-C fasteners coated with the FelPro C-5A Graphite Grease anti-galling compound performed the best. The fasteners are easy to remove from the test fixture and no thread galling had occurred.

- The ANOVA results reinforce the conclusions drawn from the visual observations. The main variation in the data occurs as a function of exposure time for the molybdenum disulfide-impregnated epoxy polyimide solid film lubricant coated fasteners.

- The results of this testing indicates the need for a better way of galvanically insulating the Beta-C from less noble materials. Titanium Beta-C fasteners offer more corrosion resistance but because it is so noble could cause severe galvanic corrosion of the substrate if care is not taken.

ACKNOWLEDGEMENTS

The authors wish to thank the AEGIS PMS 400 AP/SC Program Office and Mr. Randy Fortune for their support of this work.

REFERENCES

1. K. Faller, W. A. Edmonds, "The Incentives for Titanium Alloy Fasteners in Navy/Marine Environments," 1991 Ship Maintenance in the 21 Century Symposium, Virginia Beach, VA October 21-22 1991, American Society of Naval Engineers, Alexandria, VA.

2. American Society for Testing and Materials: 1991 Annual Book of ASTM Standards, "Vol. 03.02, Wear and Erosion; Metal Corrosion", G33-88, "Practice for Recording Data From Atmospheric Corrosion Tests of Metallic-Coated Steel Specimens", p.116, 1991.

3. American Society for Testing and Materials: 1991 Annual Book of ASTM Standards, "Vol. 03.02, Wear and Erosion; Metal Corrosion", G44-88, "Practice for Alternate Immersion Stress Corrosion Testing In 3.5% Sodium Chloride Solutions", p. 162, 1991.

4. American Society for Testing and Materials: 1991 Annual Book of ASTM Standards, "Vol. 03.02, Wear and Erosion; Metal Corrosion", G50-76(1984), "Recommended Practice for Conducting Atmospheric Corrosion Testing on Metals", p. 186, 1991.

5. American Society for Testing and Materials: 1991 Annual Book of ASTM Standards, "Vol. 03.02, Wear and Erosion; Metal Corrosion", G52-88, "Practice for Exposing and Evaluating Metals and Alloys in Surface Seawater", p. 193, 1991.

6. MIL-STD-1312-31, "Fastener Test Methods, Method 31, Torque", July 1985

TABLE 1
TITANIUM BETA-C ALLOY COMPOSITION

Composition	wt%
Al	3.0 - 4.0
Va	7.5 - 8.5
Cr	5.5 - 6.5
Mo	3.5 - 4.5
Zr	3.5 - 4.5
Fe	0.30 max
N	0.03 max
C	0.05 max
O	0.12 max
H	0.02 max
Other Total	0.40 max
Titanium	Remainder

TABLE 2
TITANIUM BETA-C PHYSICAL PROPERTIES

Density, g/cm^3	4.82
Betal Transus, °C	732
Thermal Coeff. of Expansion, (20-482 °C) STA*	9.7×10^{-6}
Modulus of Elasticity, Mpa Tension (Annealed)	96.5×10^6
Tension (STA*)	106.2×10^6
Compression (STA*)	102.0×10^6
Modulus of Rigidity- Torsion (STA*), MPa	40.7×10^6
Melting Point (approx.), °C	1650

* Solution Treated and Aged

TABLE 3
TITANIUM BETA-C MECHANICAL PROPERTIES

Size	Condition	Ultimate Tensile Strength*	Yield Strength*	% Elongation*	% Reduction of Area*
12-76 mm	Solution Treated	827 MPa	793 MPa	15 %	25 %

* Longitudinal Direction

TABLE 4
MATRIX OF ANTI-GALLING MATERIAL TESTED ON TITANIUM BETA-C FASTENERS

Anti-Galling Material	Number Tested
Control (No Anti-Galling Material)	3
Molybdenum disulfide-impregnated Epoxy Polyimide solid film lubricant	6
FelPro C-5A Graphite Grease	6

TABLE 5
MOLYBDENUM DISULFIDE EPOXY-POLYIMIDE COATED FASTENERS
BREAKLOOSE TORQUE VALUES (FT-LB) AND ANOVA RESULTS.

DATE	A5	A6	A7	A8	A9	A10
Mar 94	60	65	65	62	57	60
Jun 94	52.5	60	60	67.5	55	62.5
Sep 94	60	72.5	65	72.5	57.5	70
Dec 94	60	50	55	50	50	50
Feb 95	57.5	52.5	57.5	52.5	50	50
Apr 95	50	50	50	50	50	45
May 95	52.5	52.5	50	47.5	47.5	50

ANOVA: Two-Factor Without Replication

SUMMARY	Count	Sum	Average	Variance
3/1/94	6	369	61.5	9.9
6/1/94	6	357.5	59.58333	28.54167
9/1/94	6	397.5	66.25	41.875
12/1/94	6	315	52.5	17.5
2/1/95	6	320	53.33333	11.66667
4/1/95	6	295	49.16667	4.166667
5/1/95	6	300	50	5
A5	7	392.5	56.07143	18.45238
A6	7	402.5	57.5	75
A7	7	402.5	57.5	39.58333
A8	7	402	57.42857	97.11905
A9	7	367	52.42857	15.86905
A10	7	387.5	55.35714	80.05952

ANOVA

Source of Variation	SS	df	MS	F	F crit
Date of Test	1501.155	6	250.1925	16.4837	6.999471
Specimen	137.9048	5	27.58095	1.817146	7.63248
Error	455.3452	30	15.17817		
Total	2094.405	41			

TABLE 6
FELPRO C-5A GRAPHITE GREASE COATED FASTENERS BREAKLOOSE TORQUE VALUES (FT-LB) AND ANOVA RESULTS.

DATE	B1	B2	B3	B4	B5	B6
Mar 94	45	42	45	42	45	40
Jun 94	45	42.5	50	45	42.5	45
Sep 94	50	45	45	45	45	47.5
Dec 94	50	47.5	52.5	50	50	50
Feb 95	45	42.5	50	47.5	47.5	50
Apr 95	50	42.5	42.5	40	45	45
May 95	30	42.5	40	30	45	45

ANOVA: Two-Factor Without Replication

SUMMARY	Count	Sum	Average	Variance
3/1/94	6	259	43.16667	4.566667
6/1/94	6	270	45	7.5
9/1/94	6	277.5	46.25	4.375
12/1/94	6	300	50	2.5
2/1/95	6	282.5	47.08333	8.541667
4/1/95	6	265	44.16667	11.66667
5/1/95	6	232.5	38.75	49.375
B1	7	315	45	50
B2	7	304.5	43.5	4.083333
B3	7	325	46.42857	20.53571
B4	7	299.5	42.78571	42.65476
B5	7	320	45.71429	5.654762
B6	7	322.5	46.07143	12.20238

ANOVA

Source of Variation	SS	df	MS	F	F crit
Date of Test	443.8333	6	73.97222	6.04756	6.999471
Specimens	75.67262	5	15.13452	1.237315	7.63248
Error	366.9524	30	12.23175		
Total	886.4583	41			

TABLE 7
TITANIUM BETA-C UNCOATED (CONTROL) BREAKLOOSE TORQUE VALUES (FT-LB) AND ANOVA RESULTS.

DATE	C1	C2	C3
Mar 94	55	75	60
Jun 94	50	40	50
Sep 94	47.5	60	52.5
Dec 94	65	60	65
Feb 95	55	52.5	52.5
Apr 95	52.5	52.5	52.5
May 95	50	50	47.5

ANOVA: Two-Factor Without Replication

SUMMARY	Count	Sum	Average	Variance
3/1/94	3	190	63.33333	108.3333
6/1/94	3	140	46.66667	33.33333
9/1/94	3	160	53.33333	39.58333
12/1/94	3	190	63.33333	8.333333
2/1/95	3	160	53.33333	2.083333
4/1/95	3	157.5	52.5	0
5/1/95	3	147.5	49.16667	2.083333
C1	7	375	53.57143	33.03571
C2	7	390	55.71429	118.1548
C3	7	380	54.28571	36.90476

ANOVA

Source of Variation	SS	df	MS	F	F crit
Date of Test	757.7381	6	126.2897	4.086677	13.56238
Specimens	16.66667	2	8.333333	0.269663	21.85698
Error	370.8333	12	30.90278		
Total	1145.238	20			

TABLE 8
PAIRWISE COMPARISON OF CONFIDENCE INTERVALS

	max	min
Molybdenum disulfide-FelPro C-5A	13.6791	8.5828
FelPro C-5A - Control	12.7279	6.4863
Molybdenum disulfide - Control	4.6446	-1.5970

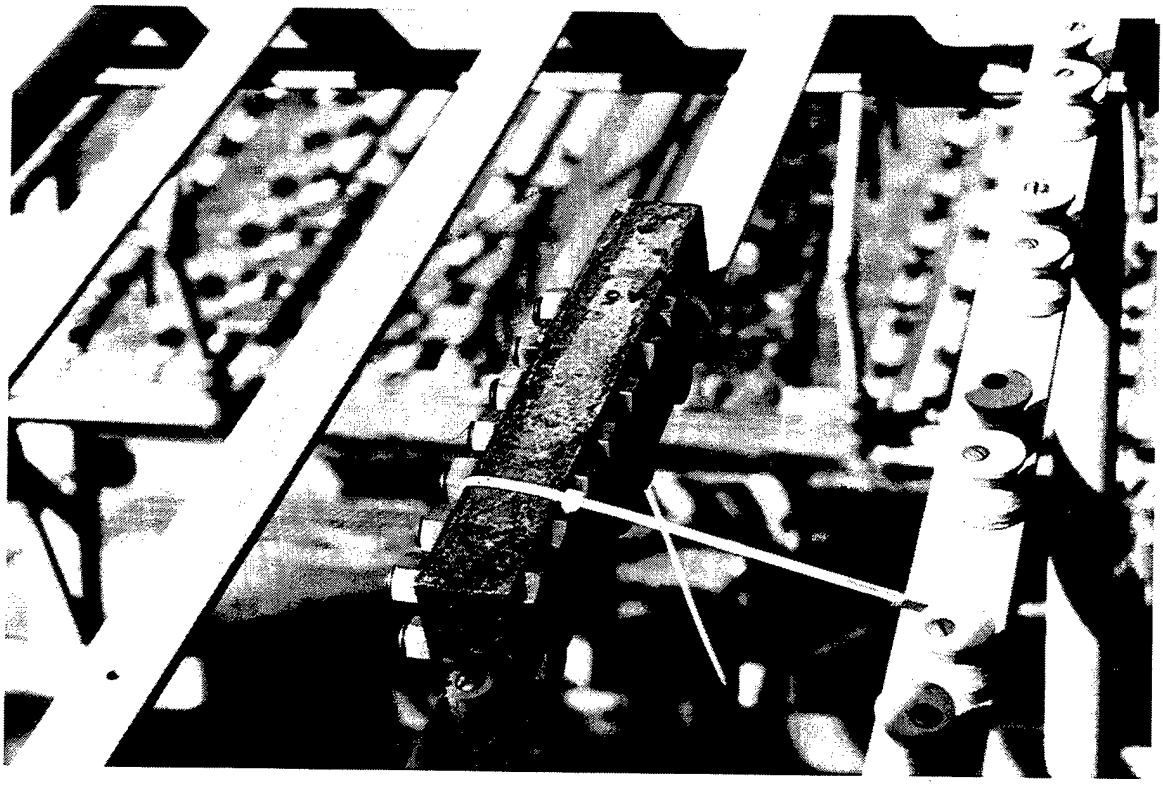


FIGURE 1 - Steel Test Fixture with Titanium Beta-C Fasteners

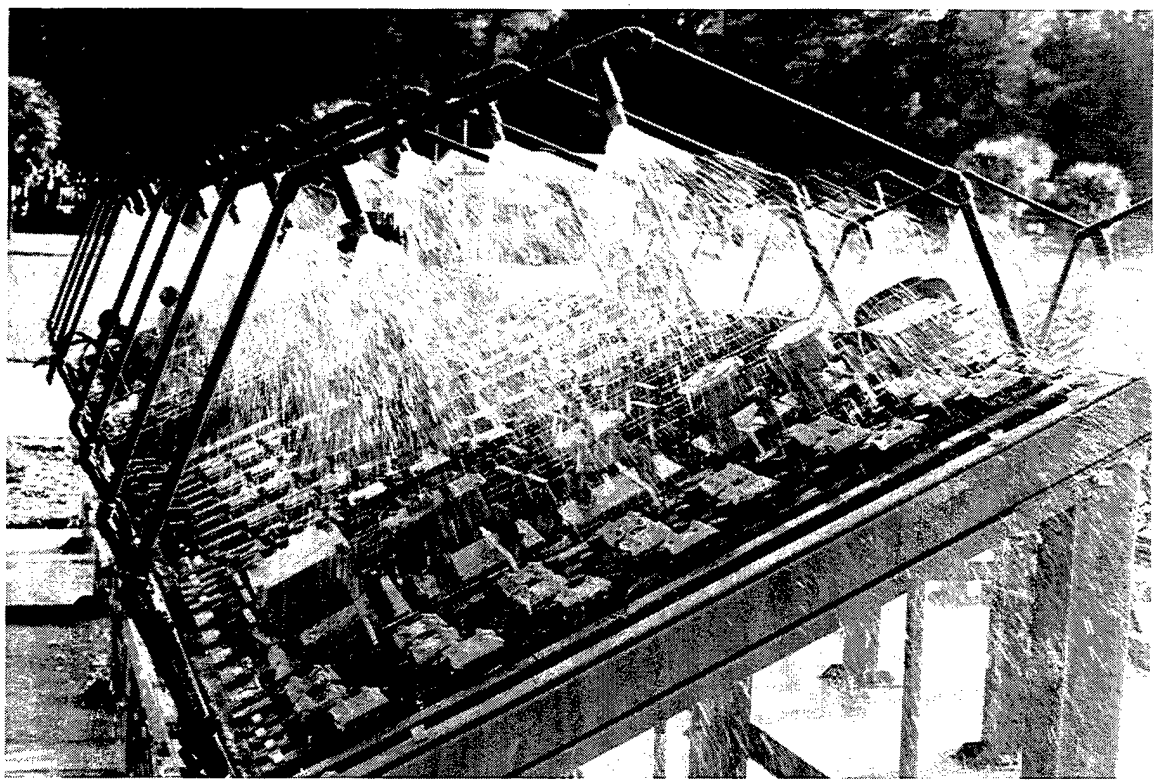


FIGURE 2 - Seawater Wetdown Test Facility

Marine Coatings

A. G. Holder and J.A. Montemarano
Code 641
Naval Surface Warfare Center, Carderock Division
9500 MacArthur Blvd.
Carderock, MD 20817-5700

ABTRACT

All ships and boats are constructed of materials that need protection from the corrosive marine environment. Paints and coatings have been the preferred method of preservation, because of cost, ease of application and the availability of materials. Initially coal-tar and natural gums were used, followed by synthetic polymers, namely, modified alkyds and solution materials like chlorinated rubber and vinyls. When epoxy resin technology became cost effective with excellent anticorrosive properties, it replaced most of these materials as the anticorrosive coating system of choice for marine applications. Advances in zinc, polyurethane, and powder coating technology have resulted in these coatings being evaluated for long term service life. Zinc, due to its cathodic protection, performs satisfactorily in the marine environment. Polyurethanes, especially aliphatics, are being accepted for exterior use due to their corrosion resistance in thin coats which are aesthetically pleasing. Powder coatings with no volatile compounds meet the most stringent environmental regulation. Today, the requirements for an acceptable marine coating system goes beyond performance. The material must be in compliance with all local, state and federal environmental regulations. The cost of compliance can be formidable when the life cycle of the coating system is considered.

INTRODUCTION

Advances in coating technology today are driven by environmental regulations. The coating industry faces a challenge in complying with a variety of governmental rules while trying to provide the customer with high performance products. How to meet ever increasing and stringent environmental demands, while producing a coating with equal or improved performance properties is the concern. A recent article in *Chemical Week* estimates that 75% of the research and development effort in the coating industry is focused on developing coatings that are "environmentally friendly," i.e., comply with present or future environmental regulations (1). These resources would normally have been directed to improving coating product performance through advancements in coating technology.

ENVIRONMENTAL REGULATIONS

Environmental regulations address the management of natural resources in terms of conservation, protection and restoration. It is these regulations that are driving coating

technology today. In the United States, the Clean Air Act (CAA) requires that all areas be in compliance with ambient air quality standards and hazardous air pollutants (HAPs). The Environmental Protection Agency (EPA) as well as state and local agencies enforce air pollution regulations that affect the use of paints and coatings. Solvents used in the coating industry are the main focus of air pollution regulations. Solvents are viewed as volatile organic compounds (VOCs) which are regulated since VOC emissions contribute to formation of ground-level ozone or smog. Control techniques guidelines (CTGS) are established to reduce VOC emissions. Under Coatings for Miscellaneous Metal Parts, one of the earliest categories of coatings to be regulated, painting in shops and other enclosed stationary facilities are covered. In the United States, states are required to have implementation plans which at a minimal, meet CAA regulations. California with 14 Air Quality management Districts (AQMDS) is the most active in the regulation of VOC emissions for coatings (2). California regulations established general VOCs requirements for air dried (340 g/L) and baked (275 g/L) coatings as well as for special coating application. The VOC limit for specialty coatings vary according to the best available technology. In addition to reduced VOCs, a coating formulator today must select from a narrower choice of solvents due to the HAPs list.

In addition hazardous wastes generated during coating application or removal processes are also regulated. & waste is considered hazardous or toxic if it meets certain levels of reactivity, ignitability, corrosivity or toxicity as defined by the Resource Conservation and Recovery Act (RCRA). Presently 450 hazardous wastes are listed by RCRA. Reducing the volume and toxicity of these wastes is required by RCRA. Hazardous waste minimization or HAZMIN is required of facilities which generate more than 100 kilograms of hazardous waste (or 220 pounds which is equivalent to 1/2 drum) or 1 kilogram of acute hazardous wastes per month. The chemical waste generator is responsible for chemical waste disposal from "cradle to grave (3).

THE MARINE ENVIRONMENT

The marine environment is particularly aggressive and the selection of a coating depends on what area of the ship the coating is applied since the service conditions vary - underwater hull, boottop (waterline area), topsides, decks, interior, and tanks (4). Conventional coatings are normally barrier coatings which act as physical barriers between the seawater (the electrolyte) and the metal substrate. For a specific marine application a coating system is specified in terms of an anticorrosive coating (usually 2 coats) followed by a topcoat. Conventional anticorrosion coatings for splash-zone and immersion applications are epoxy, chlorinated rubbers. Above the waterline where the coating requirements are less severe, modified alkyds, vinyls and chlorinated rubbers are used (5, 6) . Coatings used for exterior application above the waterline are parallel to heavy duty' maintenance paints. Urethane coatings and water borne paints are increasingly being used for exterior superstructure application due to their durability, and gloss retention and resistance to cracking, respectively.

TYPES OF COATINGS

Alkyds Coatings

Alkyds are polyesters derived from the reaction of polyhydric alcohols and a polybasic acid in the presence of a drying oil (7). These coatings were the first synthetic resins developed in the early 1930's and have been the workhorse for maintenance coatings during the 1900's (8). Alkyd coatings are frequently modified to improve their physical properties by reacting or mixing with vinyl, silicone, or urethanes. Alkyds are typically one component systems suitable for use as anticorrosive primers and topcoats in interior applications and as topcoats over primers in exterior applications. Current environmental regulations has driven the development of water reducible air dry alkyd coatings which used water-miscible cosolvents (glycol ethers or alcohols) with VOCs ranging form 300 to 350 g/L. In addition, high solids alkyd coatings have been developed as baked finishes for decorative use.

Epoxy Coatings

Epoxy coatings for marine applications are two component systems based on bisphenol A type resins cured with amines, amine adducts, or polyamide resins. For over 30 years these-coatings have been the mainstay for industrial applications. Besides reduced VOCs, raw materials utilized in epoxy coating formulations have been identified as toxicologically unacceptable (9). Lower VOCs have driven the development of high solids epoxy formulations. The first solventless coatings were high solid epoxies based on liquid diglycidyl ether of bisphenal-A type resins and liquid polyamines. Improvements in the curing agents, the use of reactive diluents and the development of new, lower-viscosity epoxy resins are the focus of current epoxy high solids technology (10) . High build, high solids epoxy coatings specially tailored for rusty surfaces has been an outgrowth of high solids coating developments. These are normally brush applied to wire brushed surfaces (11). Water borne epoxy technology is emerging technology for high performance, industrial maintenance applications (i.e., primers for structural steel and industrial machinery). Water based coating systems face two inherent problems - slow drying or cure time, and poor water and chemical resistance. Utilization of higher functionality epoxy resins and water-reducible amine adducts are representative of current water borne epoxy technology (12). For both high solids and water borne coatings airless spray is required for productive application speed and high build films (13). High solids coatings normally require high air volume and air pressures as well as larger orifice tips for airless systems. Compressed air, including high-volume, low-pressure (HVLP) are acceptable. HVLP offers high transfer efficiency which reduces coating waste and VOC emissions (14).

Urethane Coatings

Urethane coatings are relatively new for marine applications above the waterline (boottop, topside, weather deck, superstructure area). These are normally two component system based on the reaction of a resin containing isocyanate groups with hydroxyl groups found in the curing agent. Polyurethanes are known for their toughness, durability, and abrasion resistance. Development of economically acceptable aliphatic isocyanates have resulted in excellent,

nonyellowing, high gloss, urethane topcoats (15). High solids technology for two component polyurethanes focused on producing polyisocyanates with low viscosity and high equivalent weight. Incorporation of a reactive diluent (aliphatic diols, urethane diols, ketimines, or hindered diamines) which replaces part of the hydroxy-terminated resin in a two component urethane coating also reduces VOCs (16).

Zinc-Rich Coatings

Zinc rich coatings which originated in the 1940's are sacrificial coatings versus barrier coatings. These coatings contain a high zinc dust content (75 to 95 percent) in either an organic or inorganic vehicle which corrodes in preference to the steel substrate (17). The high zinc content is necessary in order to provide contact between the zinc particles throughout the film from the exposed surface to the steel substrate (18). Zinc rich coatings are normally topcoated with barrier coatings and find use on weather decks, the superstructure and off-shore structures. The organic zinc rich coatings can be applied to a commercial-grade blast, whereas the inorganic coatings require a near-white blast cleaned surface. Epoxies are the most commonly used organic binders and ethyl silicates are the traditional inorganic binder.

Water Borne Coatings

VOC regulations are the drivers for the development of water borne coating technology. As these become more restrictive the use of water borne coatings will increase. Water reducible resins, typically acrylics, form the basis for these coatings. In the neutralized resin solution, pigments are dispersed, followed by the addition of a crosslinker and additives and then, the coating is diluted with water to application viscosity. Water reducible coatings containing 20% organic solvents can generally meet current VOC requirements. Evaporation of the water results in film formation. Single component water borne coatings find use as cosmetic topcoats over anticorrosive coatings and are not applicable to immersion service. Over the last decade water borne coatings have been applied to ferries, cruise ships, salvage vessels, and crude oil carriers in interior areas such as bulkheads, hangars, and on exterior areas such as the superstructure and topsides. The application of these coatings is limited to above 5°C.

Powder Coatings

The coating industry, under environmental pressure to produce 100% solids paint (98% for powder) and to increase transfer efficiency (90-95% for powder) has developed powder coatings which are today one of the fastest growth areas in the paint industry (19). Ease of application and the high quality finish of powder coatings make them attractive as finishes. Powder coatings were first developed in the 1950's, however, not until the development of compounding paints by an extruder and the development of electrostatic spray in the 1960's was the application of powder coatings practical for large scale industrial application (20). Epoxy powders were developed first but had a chalking problem in exterior applications due to ultraviolet degradation. The development of polyester and acrylic powders followed to addressed this problem. Thermoset powders (epoxy, polyester, acrylic) can be applied 1.0-3.5 mils thick followed by heat cure for approximately 20 minutes. Vent screens, telephone boxes, electrical

boxes, light fixtures and lockers are typical applications for powder coatings for the U.S. Navy (21).

Antifouling Coatings

Unique to marine coatings is antifouling coating technology. Marine fouling which is the growth of marine organisms on an underwater hull results in economic costs to the ship owner. For a 250 ton tanker, five percent fouling is estimated to result in increase fuel costs of more than one million dollars a year (22). In order to prevent fouling a pesticide is used to either kill or deter fouling organisms. This approach has been used for more than a century. However, the use of pesticides in antifouling coatings are also restricted by environmental regulations. Traditionally copper based antifouling coatings have been the paint of choice. However, copper as an antifoulant gives variable performance. In the 70's, organotin based antifouling coatings were developed which were extremely effective against a broad spectrum of marine fouling organisms and provided long term service life. However, the use of organotins have been restricted by world wide legislation (23). Current developments address the addition of cabiocides to booster the performance of copper base paints, exploration of natural antifoulants (substances found in coral and sponges which prevent fouling) as environmentally safe pesticides and the use of easy release coatings. The last alternative is based on silicone coating technology which allows the attached fouling to be easily removed.

TEST METHODOLOGY

The emerging high performance coating technologies require test methodologies to characterize paint film properties. These tests may be done to predict the performance of the coating under actual use (in field exposure or accelerated laboratory tests) and to evaluate materials properties. The latter tests are normally standardized test methods (commonly, American Society for Testing and Materials, ASTM) which define the composition of the coating as well as identify its chemical and physical properties. Physical properties of a coating are characterized by volatile content, solids content by volume, pigment content, viscosity and sprayability. Common performance parameters that are measured are film hardness, adhesion, impact, flexibility, gloss retention, salt spray resistance, solvent resistance, abrasion resistance, and accelerated weathering. The selection of these tests depends on the service environment the coating will experience.

CONCLUSIONS

Environmental regulations are the drivers for current research and development in compliant coating technology. These environmental restrictions are constantly changing to more stringent limits, e.g., reduced VOCs and minimal hazardous materials. The coating producer needs to comply with these regulations utilizing the best available control technology (BACT), but still produce a quality coating meeting the required service life. High solids and water borne coating technologies are currently being exploited to meet increasingly demanding environmental

restrictions. The development of these technologies is a credit to the coating formulators who have creatively answered these environmental challenges.

REFERENCES

I. M. Coeyman, Chemicalweek (October 13, 1993): p. 30.

2. M. Chan, Journal of Protective Coatings & Linings (February 1989): p. 40.

3. L. Martin, Modern Paint and Coatings (April, 1988): p. 59.

4. S. Paul, Surface Coatings Science and Technology, (New York; John Wiley & Sons, 1985), p.553.

5. G. Weismantel (ed), Paint Handbook, (New York; McGraw-Hill Inc.,1981), p. 14-18.

6. Steel Structures Painting Council, "Performance Testing of Marine Coatings: New Test and Evaluation Procedures," SSPC Publication /90-02, June 1990.

7. H. R. Bleile and S. Rodgers, "Marine Coatings," Federation of Societies for Coatings Technology, March 1989.

8. C. H. Hare, Journal of Protective Coatings and Linings, 11 2(1994); p. 87.

9. M.A. Jackson, Surface Coatings Australia, 30 3 (1993): p.6.

10. A. Wilson, J.W. Nicholson and H.J. Prosser (eds.), Surface Coatings-1, (New York; Elsevier Applied Science, 1987), p. 89.

11. I.K. Baxter, Surface Coatings Australia, 30 8 (1993): p. 12.

12. J. Gniecko and D. Helfand, Modern Paint and Coatings (March 1994): p. 26.

13. J.P.. Hund, Journal of Protective Coatings & Linings, 10 11 (November 1993): p. 44.

14. L. Snowden-Swan and P. Worner, "Transfer Efficiency and VOC Emissions of Spray Gun and Coating Technologies in Wood Finishing," Proceedings: Pollution Prevention Conference on Low- and NO-VOC Coating Technologies, EPA-600/R-94-022, February 1994.

15. F.L. LaQue, Marine Corrosion Causes and Prevention, (New York: John Wiley & Sons, 1975), p. 307.

16. Z. Wicks, Jr., F. Jones, and S.P. Pappas, Organic Coatings: Science and Technology,

Volume 11, (New York: John Wiley & Sons, Inc., 1994), p. 204.

17. M. Henthorne, "Corrosion Causes and Control," Chemical Engineering, 1971-1972.

18. E.V. Schmid, Exterior Durability of Organic Coatings, (England: FMJ International Publications Limited, 1988), p. 35.

19. F. Folkerman, R. Haegeman, A. Porro, P. Thornton and N. Whitehouse, "Practical Guide to Powder Coating, " European Community Sprint project No. RA 165, 1992.

20. D.A. Bate, The Science of Powder Coatings, Volume I, (London, United Kingdom; Selective Industrial Training Associates Limited, 1990).

21. A. Holder, "Advantages of Powder Coatings, Proceedings: Pollution Prevention Conference on Low- and NO-VOC Coating Technologies, EPA-600/R-94-022, February 1994.

22. J.A. Lewis, Surface Coatings Australia,- 29 4 (April 1992): p. 20.

23. E. B. Kajaer, Progress in Organic Coatings, 20 (1992): p. 339.

Investigation of Corrosion Protection of Steel by Electrically Conductive Polyaniline Coating

Youngun Pae[†], Gordon P. Bierwagen[†], Guoling Chen*, Dennis E. Tallman*

Department of Polymers & Coatings[†]
and
Department of Chemistry*
North Dakota State University
Fargo, ND 58105

ABSTRACT

Polyaniline coatings on steel were studied by using Electrochemical Impedance Spectroscopy (EIS) and Electrochemical Noise Methods (ENM). EIS of the polyaniline sample was obtained for increasing time of immersion. An increase in charge transfer resistance (R_{ct}) was observed in Nyquist and Bode plots. Our ENM data showed that active electrochemical changes occurred during the early stages of immersion. The mean potential displayed a tendency toward positive potential. The mean current exhibited a drastic increase during the early stage. Noise resistance (R_n) values showed initial fluctuations, followed by a general increase from 10^3 to 10^5 $\Omega \cdot cm^2$. As R_n has been closely identified with R_{ct}, this is consistent with the EIS results. Our electrochemical data suggests that the passivation of the steel surface occurs during immersion. The surface structure characterization before and after immersion by AFM is also part of our continuous research effort.

INTRODUCTION

Electrically Conductive Polymers (ECPs) are polymers with a highly conjugated backbone structure, which can be transformed to polymers with metallic properties through electrochemical/chemical oxidation or reduction.[1] This reversible conversion is accomplished by doping the polymer with appropriate ionic species, which enables charges to move freely along the polymer chain. ECPs have been the subject of enormous interest from both scientific and practical points of view. Their unique electronic and optical properties along with processability of polymers show promising prospects for numerous potential applications. The list of possible applications include rechargeable batteries, electrochromic devices, sensors, antistatic shielding materials, etc.[2]

One of the recent potential uses of ECPs has been in the area of corrosion resistant coatings, which possesses an immense significance regarding the urgency to replace environmentally non-compliant, yet effective, chromate conversion pretreatment of metal substrates and chromate pigments.[3] Polyaniline, in particular, has attracted considerable scientific attention that has generated encouraging results for anticorrosive coating purposes. The advantages of polyaniline over other ECPs are: easy polymerization with high yield, inexpensive monomer, environmental

stability, high level of conductivity (up to 10^2 S/cm), and facile conversion from non-conductive to conductive state. The major obstacle lies on its intractability and brittleness, and hence difficulty in generating adherent coatings with uniform film thickness. A wide range of research has been conducted over the past decade to enhance the solubility of polyaniline. The development of water-soluble polyaniline products has been achieved with a fair amount of success, by the addition of appropriate functional groups such as sulfonic acid.[4] The processability of polyaniline can also be enhanced by the formation of stable colloidal dispersions with polymeric stabilizers[5,6] , or by utilizing polymer blends with thermoplastic[7,8] or thermosetting systems.[9]

Corrosion studies carried out by NASA and Los Alamos National Laboratory have indicated that the steel panels coated with doped polyaniline primer and epoxy topcoat showed outstanding performance over the sample without the polyaniline primer. Similar results were obtained for the sample with polyurethane topcoat. Samples with polyaniline showed no trace of corrosion when the coating was scratched and immersed in acidic and NaCl solution.[10] Kinlen et al have shown that certain coating formulations with polyaniline could tolerate scratches although further optimization is required to compete against zinc-based primers.[11]

The corrosion protection of metals provided by polyaniline appears to be electrochemical in nature. It has been proposed that polyaniline may function as a redox catalyst to form passivating metal oxide layers on exposed metal surfaces. Smyrl et al have demonstrated that conductive polymers could maintain stable passivity of a metal by a redox reaction coupled with O_2 reduction on the film.[12] XPS analysis indicates the formation of passive oxide layers consisting of γ-Fe_2O_3 and Fe_3O_4 in the metal/coating interface.[13] Alumunum surfaces coated with polyaniline also showed a significant decrease in corrosion rate.[14, 15]

EIS and ENM are techniques commonly used for evaluating the corrosion protective properties of coating systems. Corrosion is an electrochemical phenomenon, therefore these two techniques can provide quantitative data on the degree and mechanism of film degradation (barrier properties of coatings, passivation, etc.) and corrosion activities.

Electrochemical noise is known as spontaneous fluctuations in the voltage and current that arise from the onset and continuing process of corrosion. The analysis of current and voltage time series data can be evaluated by the calculation of noise resistance (R_n) value, shown in equation [3], which can be obtained by dividing the standard deviation of the potential by the standard deviation of the current.[16] The main advantage of ENM over EIS is that it is non-perturbing. However, frequency dependent parameters are more easily obtained in EIS.

Current noise: $I = I(t) \rightarrow \sigma I(t)$ [1]

Potential noise: $V = V(t) \rightarrow \sigma V(t)$ [2]

Noise Resistance: $$R_n = \frac{\sigma_V(t)}{\sigma_I(t)}$$ [3]

Electrochemical impedance is measured by applying a small sinusoidal potential at varying frequencies to the electrochemical cell, and by detecting the current response through the cell. Despite numerous impedance studies of conducting polymers that have been undertaken by various research groups, the theoretical model that is appropriate for conducting polymers has not been well established. The generalized transmission line equivalent circuit has been successfully used to model the impedance behavior of conducting polymers. However, further research is needed to establish a clearer theoretical foundation.[17, 18] Traditional techniques such as salt spray (ASTM B-117) or Prohesion tests can generate qualitative data for the ranking of coatings; however, the interpretation of the data can be subjective.

In our experiment, EIS and ENM techniques were used to study the electrochemical phenomena related to the corrosion protection of cold-rolled steel in 3% NaCl provided by polyaniline coating solution. The data was collected from samples under continuous immersion in the electrolyte solution.

EXPERIMENTAL

Sample Preparation for EIS & ENM

The polyaniline (XICP) used in the experiment was received from Monsanto. XICP is a soluble conducting polyaniline polymer dissolved in xylene and butyl cellosolve. A thin film of polyaniline was cast on cold-rolled steel 3"X12" panels by using a draw bar, and cured at 100°C for about 1 hour. The coated panels were cut into 3"X6" panels. The film thickness ranged between 40 and 50 μm which was measured with an Elcometer®. A PVC pipe was glued onto the coated surface of the panel to hold in the electrolyte solution. The area of the coating exposed to the electrolyte solution was approximately 12.6 cm^2.

Electrochemical Impedance Spectroscopy

Test samples for impedance measurements were prepared as shown in figure 1. A platinum mesh and saturated calomel electrode (SCE) were used as the counter and the reference electrode respectively. The electrolyte solution used for impedance measurements was 3% NaCl solution. The EIS instrument consisted of a Gamry potentiostat and an 8-channel multiplexer, both controlled by Gamry CMS 100 software. Impedance measurements were carried out with 10 mV applied potential between the frequency range of 0.01 Hz and 5000 Hz.

Electrochemical Noise Method

Electrochemical noise equipment called Denis, manufactured by Capcis March Limited (CML), is used for Noise Resistance (R_n) measurements. Denis electrochemical noise system is an automated digital instrument that can monitor up to 12 probes. A schematic diagram is illustrated in figure 2. Two nominally identical coated panels function as working electrodes which are connected together both electrically and electrolytically during measurements via a zero resistance ammeter. These two panels along with a saturated calomel reference electrode and a salt bridge comprise one probe. Each probe is monitored for about 8.5 minutes. The monitoring continues on to the next probe, and returns to the first probe at the end of the cycle.

The monitoring is essentially continuous and data can be gathered over days, weeks, or months. Each R_n value was calculated by collecting data (i.e. voltage and current) every two seconds for a total of 8.5 minutes to gather a total of 256 data points. These 256 data points were averaged and the standard deviation of the potential was divided by the standard deviation of the current to render one R_n value. Noise resistance, R_n, values can be used to rank the protective properties of various coating systems. Typically R_n values above 10^7 ohms is indicative of good barrier property of a coating. In addition to calculating R_n, the instrument also generates a value of the mean voltage (V_m) and the mean current (I_m) during each 8.5-minute sampling period. Some encouraging results have been obtained for a wide range of anticorrosive coatings.[19,20] This technique can be used to differentiate coatings in terms of the extent and the mechanism of corrosion.

Atomic Force Microscopy

Atomic force microscopy (AFM) is a powerful, high-resolution imaging technique for determining the structure of surfaces. AFM was used to examine the corrosion resistance of polyaniline coated on steel substrate by checking the interfacial change of the samples before and after the immersion test. The solution used for the immersion test was 3% NaCl solution. The immersion time was 10 days. The interface was obtained by separating the polymer film and the substrate after soaking in water for 40 minutes. The specimens were cut into disks with diameter equal to 1.3 cm. AFM experiments were performed with a Nanoscope III (Digital Instruments, Inc.) using a 100μm cantilever with a Si_3N_4 tip and a J scanner in the standard contact mode.

RESULTS & DISCUSSION

Electrochemical Impedance Spectroscopy

Electrochemical impedance was used to investigate the electrochemical response of the polyaniline coated steel panels to sinusoidal perturbations about the open circuit potential. The electrolyte solution of 3% NaCl was used to imitate the marine environment. Impedance data was collected for increasing time of immersion in the electrolyte solution.

The Nyquist plot in figure 3 shows two regions of distinct electrochemical response. At low frequencies (lower limit = 0.01 Hz), the response is limited by the diffusion process within the polyaniline film. This process is readily apparent from the long diffusion tail represented by a straight line with 45° angle with respect to the real axis. In terms of passive circuit elements, the diffusion tail is referred to as Warburg impedance. At higher frequencies, the kinetics of a charge transfer process at the electrode surface can be measured. This is characterized by a semicircle, and one can extract the value for charge transfer resistance, R_{ct}, solution resistance, R_s, and double layer capacitance, C_{dl}. Charge transfer resistance arises as a result of a kinetically controlled electrochemical reaction, such as electrons travelling to the metal while metal ions diffuse out of the metal during the corrosion process.[21]

The interesting aspect of our Nyquist plot is the tendency of the semicircle to increase as a function of immersion time. On the first day of immersion, a semicircle with a small diameter appears at the high frequency end of the impedance spectrum. However, the semicircle increases

in diameter gradually as the sample is continuously immersed in the solution. The maximum increase in the semicircle is achieved after 35 days of immersion. The increase in semicircle diameter is indicative of rising charge transfer resistance value. Theoretically, charge transfer resistance is an important parameter for assessing the corrosion protection because corrosion rate can be extracted. Higher charge transfer resistance can be related to better corrosion protection. The result we obtained indicates that the system appears to become more protective or noble as it is exposed to corrosive environment.

The equivalent circuit for a kinetic and diffusion controlled model shown in figure 4 was used to calculate the charge transfer resistance. The real axis intercept at the highest frequency in Nyquist plot corresponds to the solution resistance R_s, and the real axis intercept at lower frequency gives $R_s + R_{ct}$. The non-linear fit using the CMS 100 software was carried out, and R_{ct} values for increasing immersion time were calculated. The charge transfer resistance in figure 5 shows a gradually increasing trend up to day 35, but a decreasing trend for immersion time longer than 35 days. The polyaniline coating appears to provide passivation effect that raises R_{ct} at early stages of immersion. The immersion of polyaniline sample beyond 50 days caused blistering, followed by visibly orange rust products on the surface. Previous studies by Elsenbaumer et al have indicated that the corrosion rate was reduced by polyaniline, and that a passivating oxide layer comprised of Fe_2O_3 and Fe_3O_4 was formed on steel panels.13 Based on their UV/VIS analysis, Wessling et al have suggested that polyaniline may function as a redox catalyst for passivating oxide formation, and provided a probable passivation mechanism.[22] Therefore, the rise in R_{ct} might be related to the process of passive oxide layer formation. The oxide layer may hinder the electron transfer process at the interface, and consequently raise R_{ct}. The steady rise in R_{ct} is also clearly evident in the Bode plot where impedance modulus is plotted against frequency as shown in figure 6. The change in phase angle in figure 7 also indicates that the system undergoes changes as the immersion time increases. Another possibility is that the reduction of doped polyaniline may contribute to changes in R_{ct}. The reduced form of polyaniline is less permeable to ions and electrons in comparison to the doped polyaniline, which is a polyelectrolyte.

Electrochemical Noise

The advantage of using electrochemical noise is that it is a non-perturbing method of monitoring samples under immersion. The spontaneous fluctuations of voltage and current that arise between two nominally identical samples are measured, and the noise resistance value is calculated based on Ohm's Law.

The plot of noise resistance, R_n, vs. immersion time for the polyaniline sample is shown in figure 8. The values of R_n stayed close to 10^4 and 10^5 $\Omega \cdot cm^2$. In the early stages of immersion, oscillatory behavior of R_n values is observed. The polyaniline sample appears to exhibit a markedly different behavior from barrier type coatings. Good barrier type coating systems have high R_n values. Typically, low R_n is any value below 10^5 Ω and high R_n is any value above 10^6 Ω. Therefore polyaniline does not appear to function as a good barrier. In fact, polyaniline is a polyelectrolyte with charges that would allow facile penetration of water and ions through the coating.

The mean current pattern as a function of immersion time is plotted in figure 9. At the beginning of immersion, the current demand increases drastically over a 1.5 day period and reaches a maximum value. Subsequently, a steady tapering of current flow about zero current axis follows a rapid decrease in current demand. The initial rise in negative current demand may be caused by the oxidation of Fe into Fe^{2+}, which is the ionic product needed to form iron oxide. However the current flow appears to diminish as the passivating oxide layer is formed. From the mean current data, we can assume that the passivation process is most active during the initial 5 days of immersion.

The mean potential vs. immersion time is plotted in figure 10. After one day of immersion, the potential increases and reaches a peak. A short decrease and subsequently a steady rise in potential are observed. The continuous rise in potential toward a noble region appears to indicate that the system is becoming increasingly passivating as the immersion time increases.

Atomic Force Microscopy

The Polyaniline film coated on steel was very smooth before immersion as illustrated in figure 11(a), but the morphology of polyaniline changed considerably after immersion as shown in figure 11(b). The surface structure of bare steel without the polyaniline coating is shown in figure 11 (c). The interface structure obtained by carefully peeling off the coating in the absence of immersion is shown in figure 11(d). Changes in surface structure did not seem to have occurred when (c) and (d) were compared. Both (c) and (d) illustrate fine granular structures. However, the surface granules became bulkier when the interfacial structure was characterized after a week of immersion as shown in figure 11(e). These morphology changes are consistent with the formation of a passivating oxide layer.

CONCLUSIONS

The mechanism of corrosion protection by polyaniline has been a subject of great interest, and various explanations have been proposed. Although none of them have found widespread acceptance, corrosion protection of steel by polyaniline definitely does not appear to lie on its barrier property. Impedance data showed low R_{ct} values, which subsequently increased as a function of immersion time. Contrary to good barrier type coatings[19, 20], polyaniline samples showed low R_n values according to the electrochemical noise data. From the plot of mean potential vs. time, we observed that the potential of the polyaniline sample rises steadily, which indicates the system is driven to a more noble state.

Our EIS and ENM results provide good evidence that polyaniline may protect against corrosion of steel by a passivation mechanism, and we speculate that anodization of metal substrate is the primary protection mode. AFM results showed that the surface morphologies of the steel substrate and polyaniline film have been modified after immersion.

ACKNOWLEDGMENTS

This work was supported by the Office of Naval Research, Grant No. N00014-95-1-507. We would also like to thank Dr. Kinlen for a valuable discussion, the Monsanto Co. for providing the soluble conducting polyaniline polymer sample, Jeremy Daum and Juleen Berg for their assistance in sample preparation and data analysis.

REFERENCES

[1] Huang, W. S., Humphrey, B.D., MacDiarmid, A. G., "Polyaniline, a Novel Conducting Polymer", *J. Chem. Soc., Faraday Trans. 1*, 82, 2385 (1986)

[2] Reprints from *"Chemical Engineering"*, McGraw-Hill Companies Inc., July 1996

[3] Sitaram, S. P., Stoffer, J. O., O'Keefe, T. J., "Application of Conducting Polymers in Corrosion Protection", *J. Coat. Tech.*, 69, 866, 65 (1997)

[4] Kathirgamanathan, P., Adams, P. N., Quill, K., Underhill, A. E., "Novel Conducting Soluble Co-polymer of Aniline", *J. Mater. Chem.*, 1, 1, 141 (1991)

[5] Liu, J-M., Yang, S. C., "Novel Colloidal Polyaniline Fibrils by Template Guided Chemical Polymerization", *J. Chem. Soc., Chem. Commun.*, 1529 (1991)

[6] Aldissi, M., Armes, S. P., "Colloidal Dispersions of Conducting Polymers", *Progress in Organic Coatings*, 19, 21 (1991)

[7] Goh, S. H., Chan, H. S. O., Ong, C. H., "Miscibility of Polyaniline/Poly(vinyl acetate) blends", *Polymer*, 37, 13, 2675 (1996)

[8] Abraham, D., Bharathi, A., Subramanyam, S. V., "Highly Conducting Polymer Blend Films of Polyaniline and Nylon 6 by Cosolvation in an Organic Acid", *Polymer*, 37, 23, 5295 (1996)

[9] Kathirgamanathan, P., "Curable Electrically Conductive Resins with Polyaniline fillers", *Polymer*, 34, 13, 2907 (1993)

[10] Thompson, K. G., Bryan, C. J., Benicewicz, B. C., Wrobleski, D. A., "Corrosion Resistant Coatings from Conducting Polymers", *ACS Polymer Preprints*, 35, 1, 265 (1994)

[11] Kinlen, P. J., Silverman, D. C., Jeffreys, C. R., "Corrosion Protection Using Polyaniline Coating Formulations", *Synthetic Metals*, 85, 1327-1332 (1997)

[12] Deng, Z., Smyrl, W. H., White, H. S., "Stabilization of Metal-Metal Oxide Surfaces Using Electroactive Polymer Films", *J. Electrochem. Soc.*, 136, 8, 2152 (1989)

[13] Lu, W. K., Elsenbaumer, R. L., Wessling, B., "Corrosion Protection of Mild Steel by Coatings Containing Polyaniline", *Synthetic Metals*, 71, 2163 (1995)

[14] Racicot, R., Clark, R. L., Liu, H-B., Yang, S.C., "Thin film conductive Polymers on Aluminum Surfaces: Interfacial Charge-transfer and Anti-corrosion Aspects", *SPIE*, 2528, 251 (1995)

[15] Racicot, R. J., Clark, R. L., Liu, H-B., Yang, S.C., Alias., M. N., Brown, R., "Anti-corrosion Studies of Novel Conductive Polymer Coatings on Aluminum Alloys", *Materials Research Society Proceedings Preprint*, (1996)

[16] Bierwagen, G. P., "Calculation of Noise Resistance from Simultaneous Electrochemical Voltage and Current Noise Data", *J. Electrochem. Soc., 141, L155-157* (1994)

[17] Albery, J. W., Mount, A. R., "Dual Transmission Line with Charge-transfer Resistance for Conducting Polymers", *J. Chem. Soc. Faraday Trans.*, 90, 8, 1113-1119 (1994)

[18] Ren, X., Pickup, P. G., "An Impedance Study of Electron Transport and Electron Transfer in Composite Polypyrrole + Polystyrenesulphonate films", *J. Electroanal. Chem*, 420, 251 (1997)

[19] Chen, C.T., Skerry, B. S., "Assessing the Corrosion Resistance of Painted Steel by AC Impedance and Electrochemical Noise Techniques", *Corrosion*, 47, 598 (1991)

[20] Mills, D. J., Bierwagen, G. P., Skerry, B. S., Tallman, D. E., "Investigation of Anticorrosive Coatings by the Electrochemical Noise Method", *Materials Performance*, 34, 5, 33-38 (1995)

[21] Amirudin, A., Thierry, D., "Application of Electrochemical Impedance Spectroscopy to Study the Degradation of Polymer-coated Metals", *Progress in Organic Coatings*, 26, 1-28 (1995).

[22] Wessling, B., Schroder, S., Gleeson, S., Merkle, H., Schroder, S., Baron, F., "Reaction Scheme for the Passivation of Metals by Polyaniline", *Materials & Corrosion*, 47, 439-445 (1996)

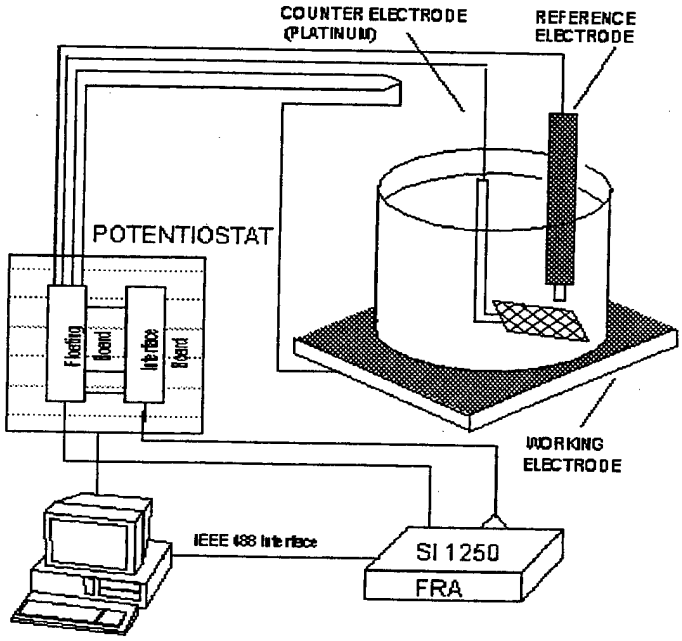


Figure 1. Schematic diagram of the EIS sample setup

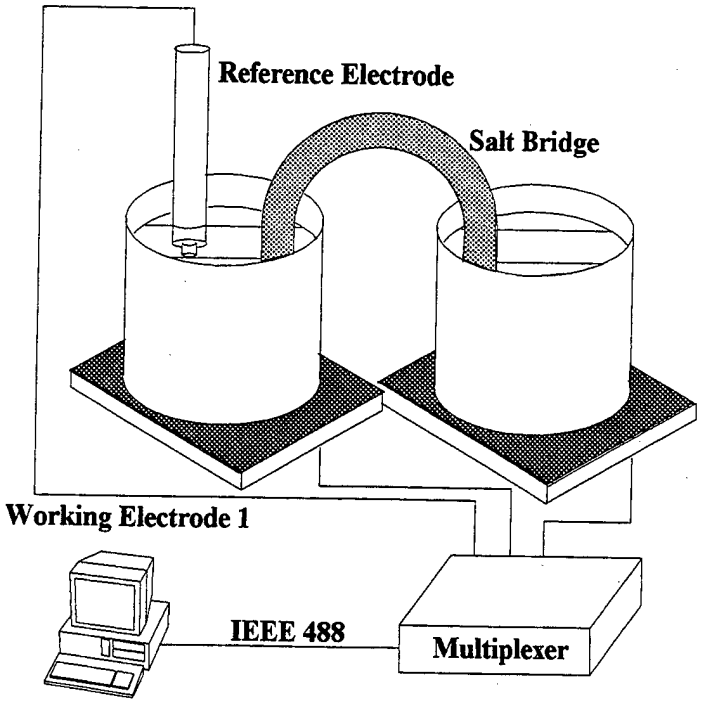


Figure 2. Schematic diagram of the ENM sample setup

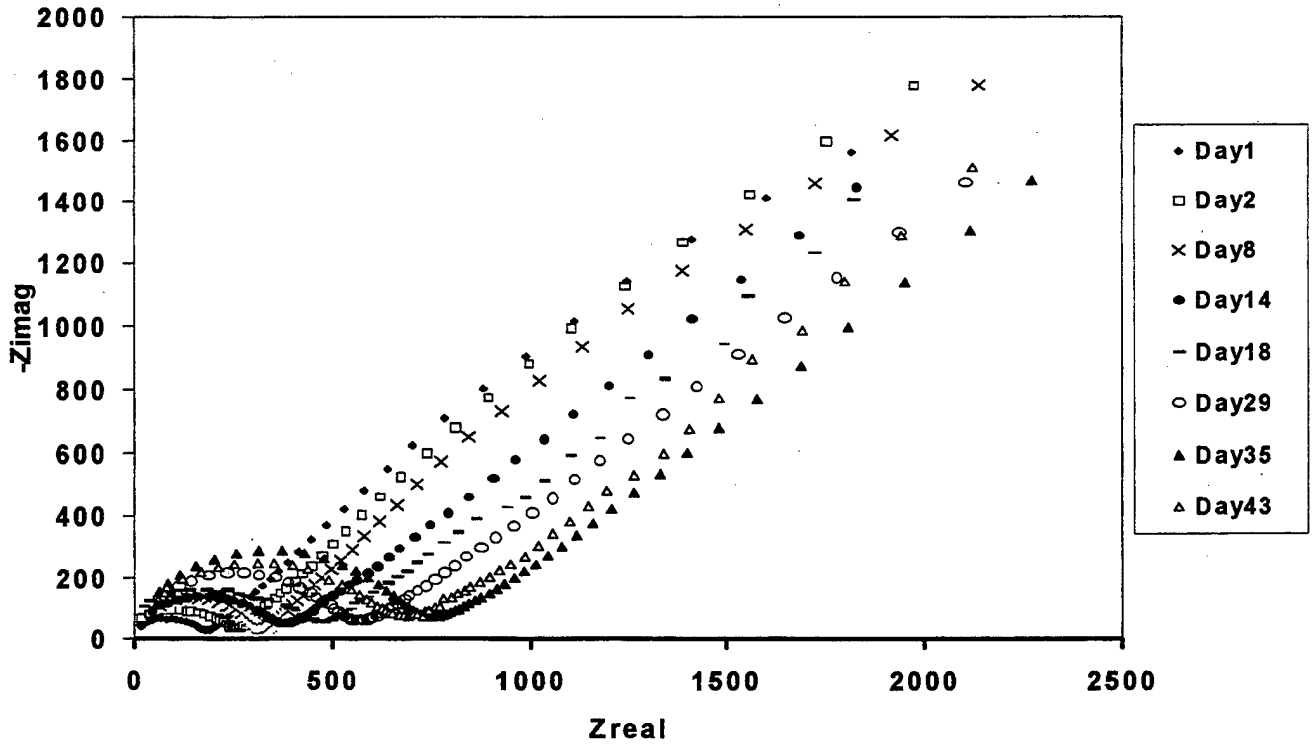


Figure 3. Nyquist plot for polyaniline coated steel sample for increasing immersion time

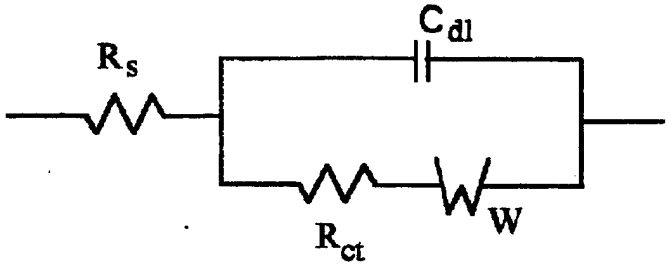


Figure 4. The equivalent circuit used to calculate R_{ct} of polyaniline sample

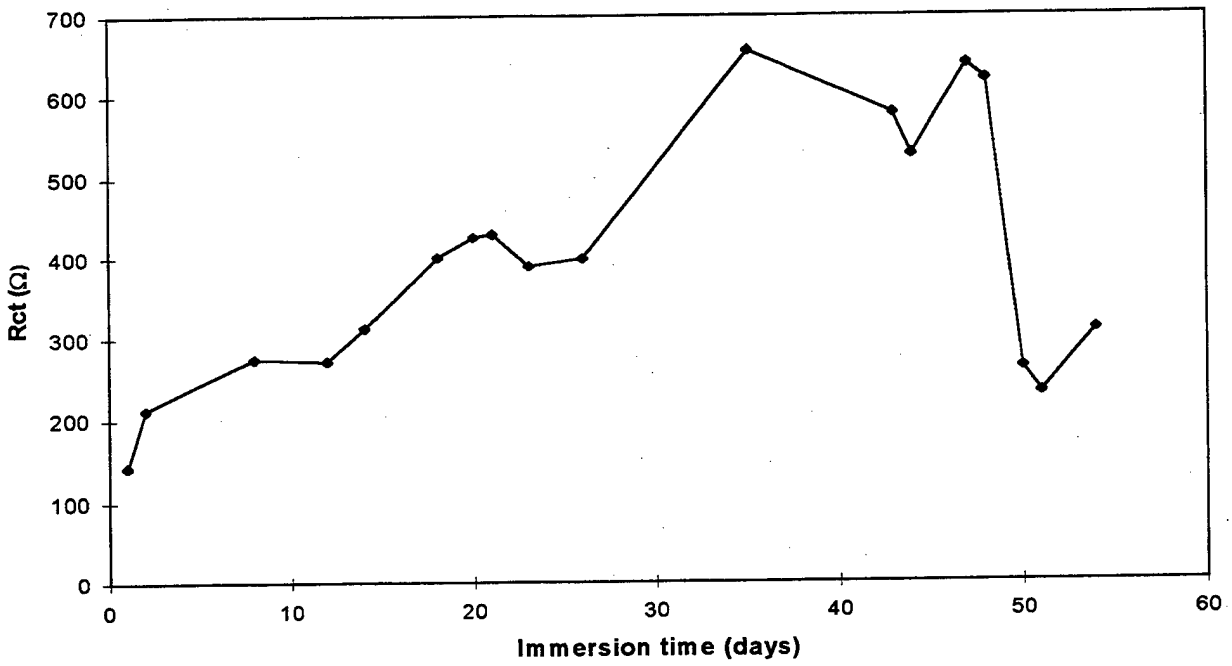


Figure 5. The plot of Rct vs. immersion time for polyaniline sample

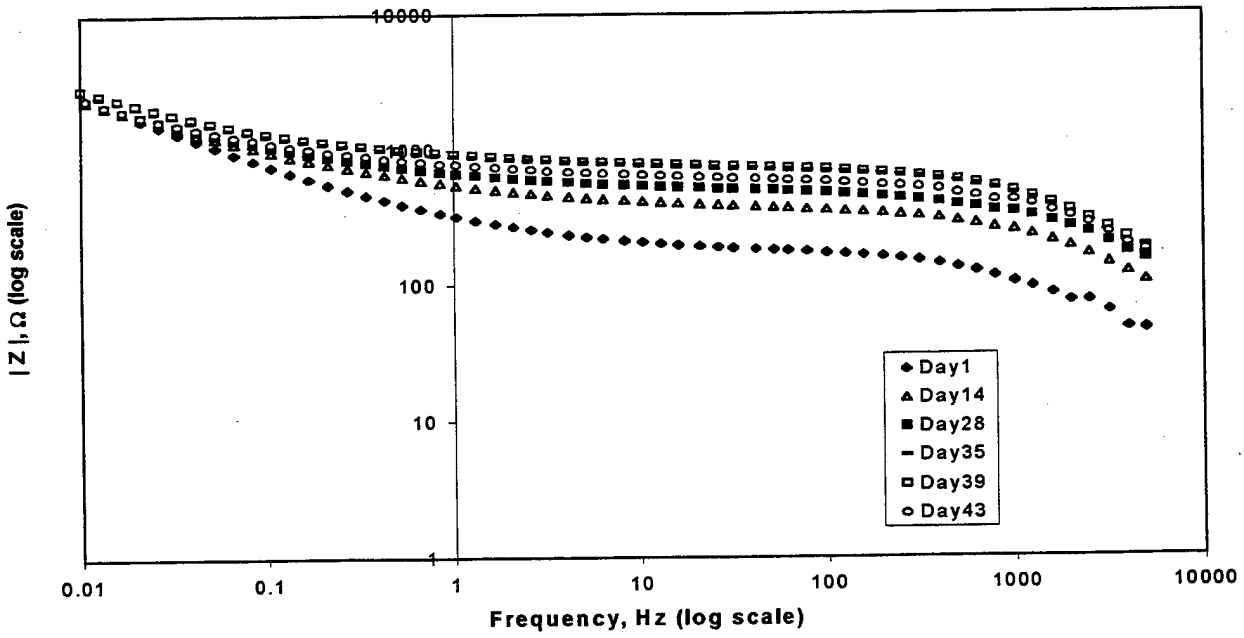


Figure 6. Bode plot of impedance modulus (|Z|) vs. frequency for increasing immersion time

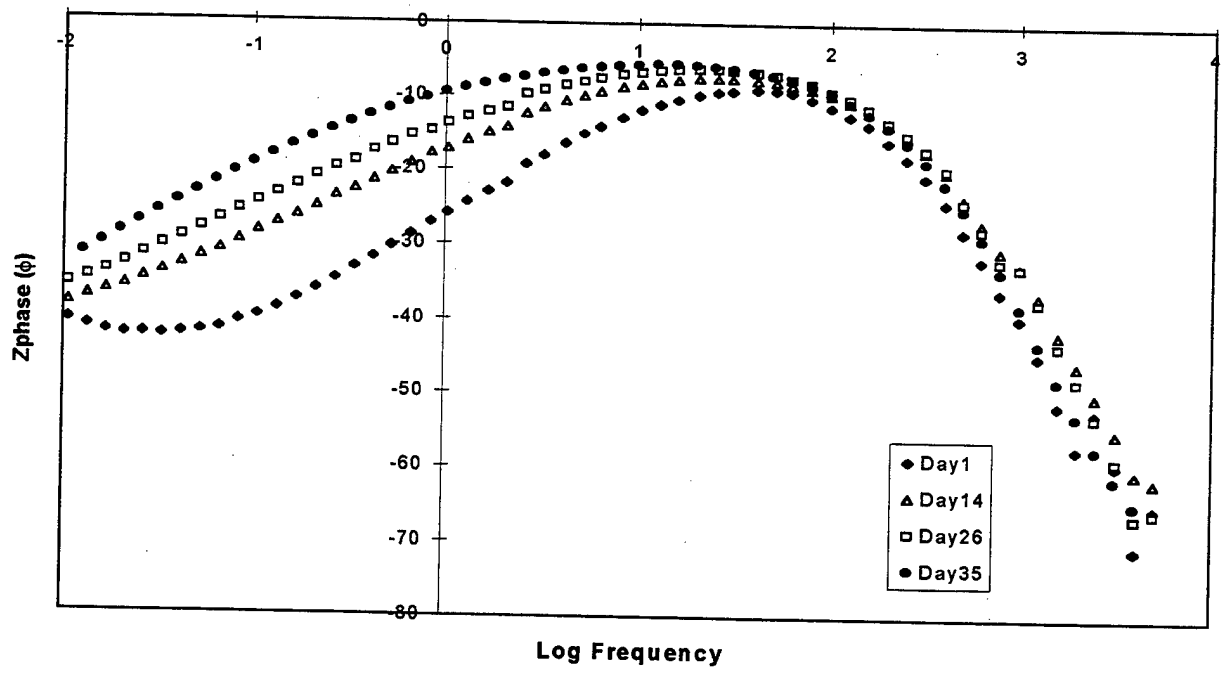


Figure 7. Bode plot of phase angle (ϕ) vs. log of frequency for increasing immersion time

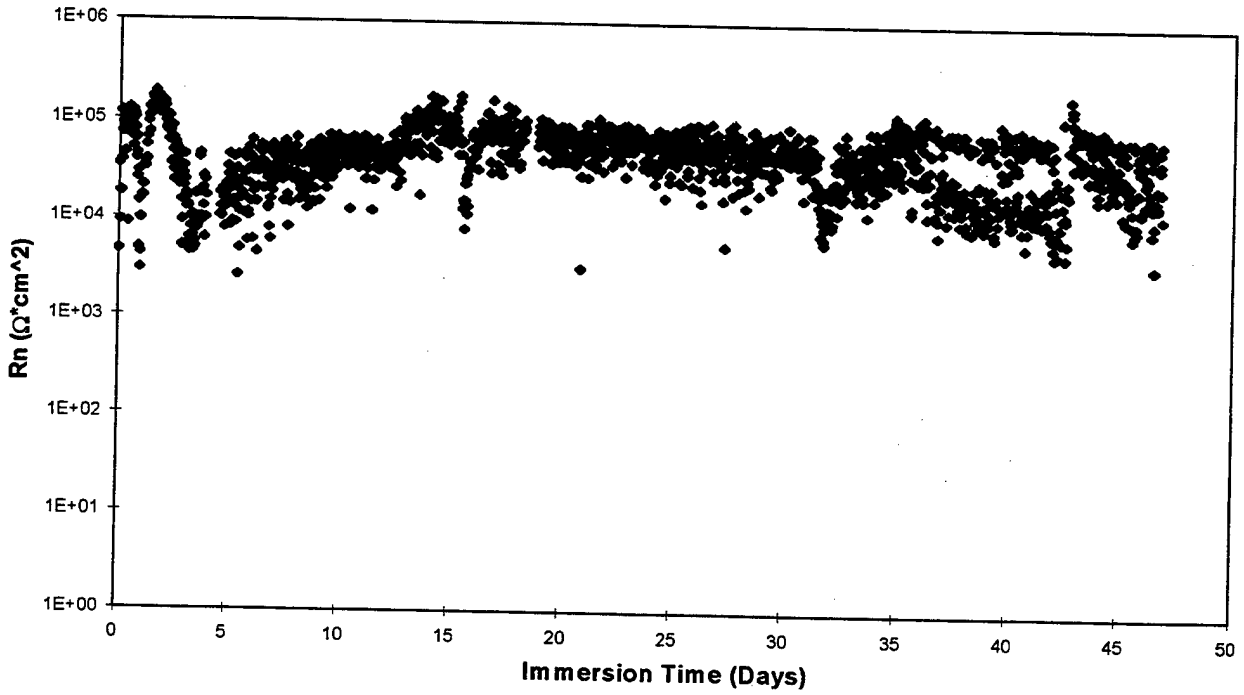


Figure 8. The plot of Noise resistance vs. immersion time for the polyaniline sample obtained from ENM

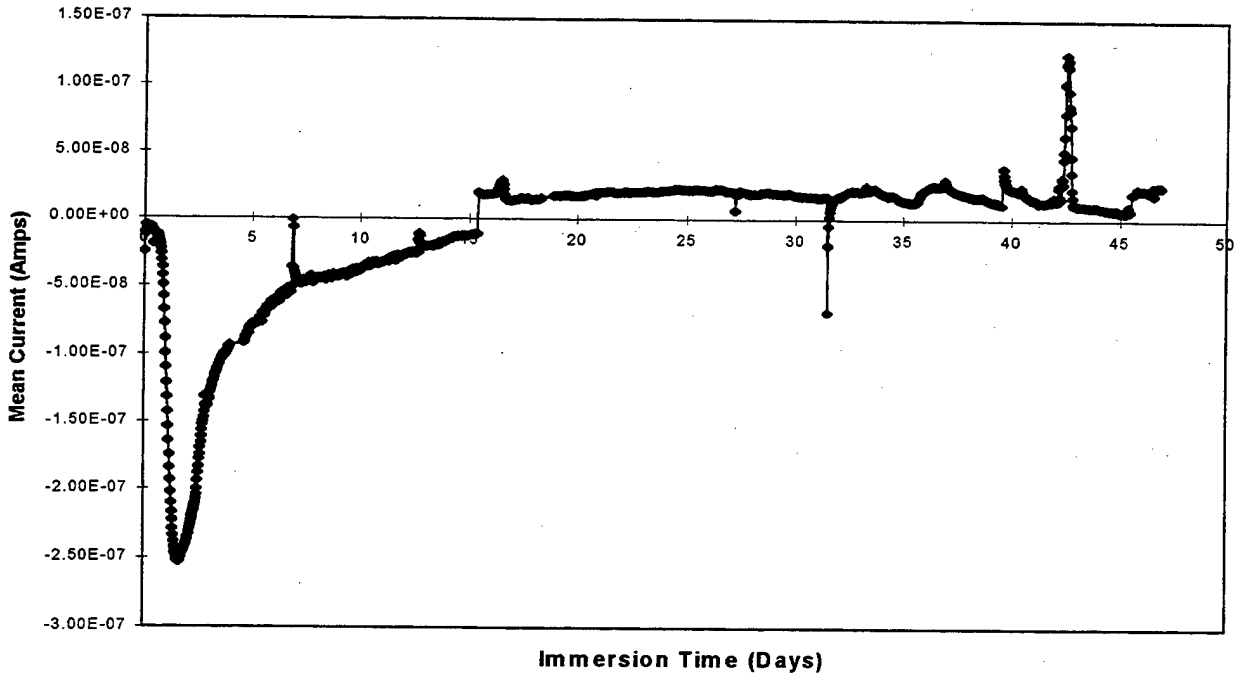


Figure 9. The mean current vs. immersion time for the polyaniline sample obtained from ENM

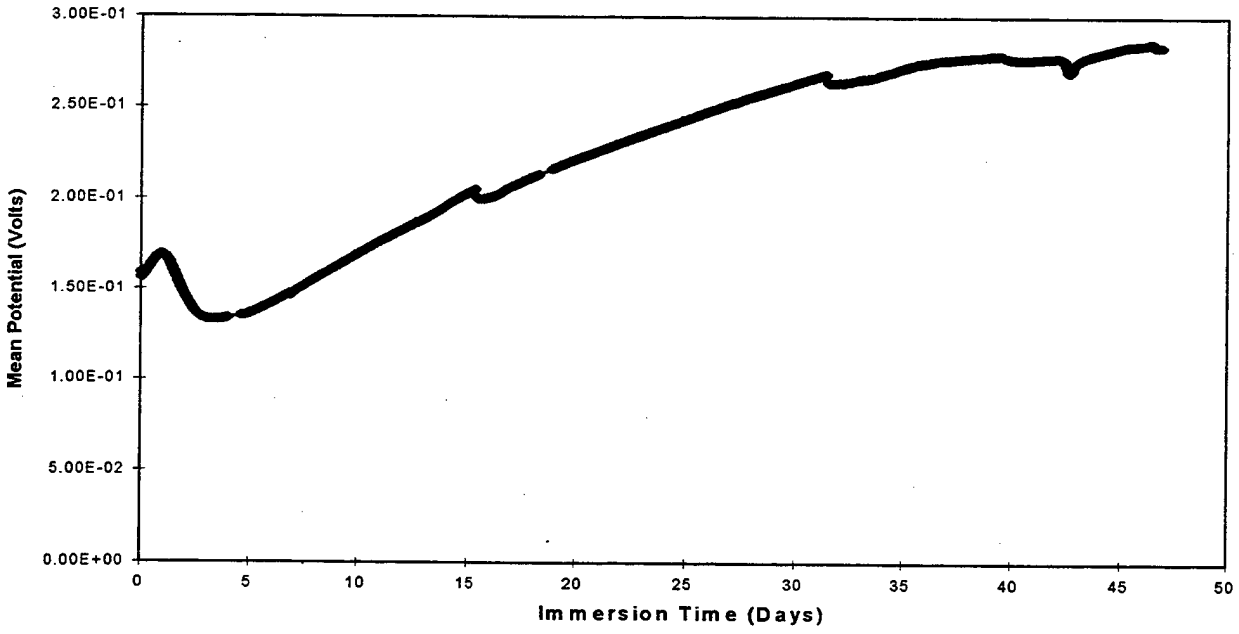
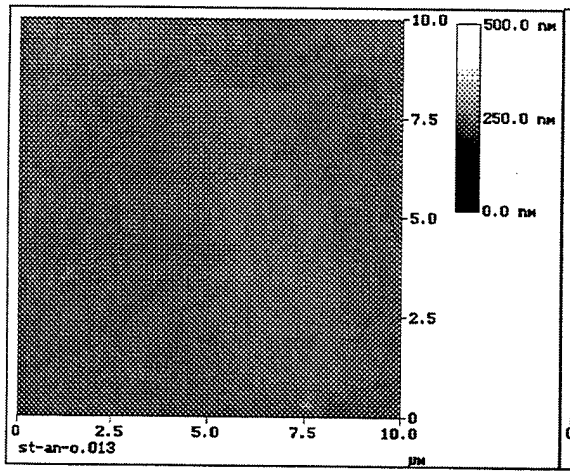
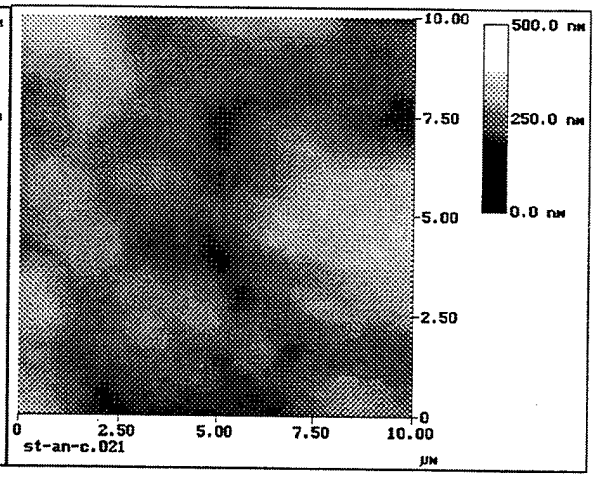


Figure 10. The mean potential vs. immersion time for the polyaniline sample obtained from ENM

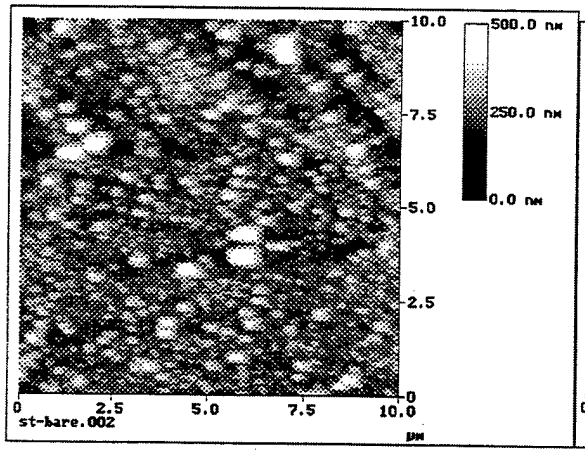
(a) Polyaniline coating surface before immersion



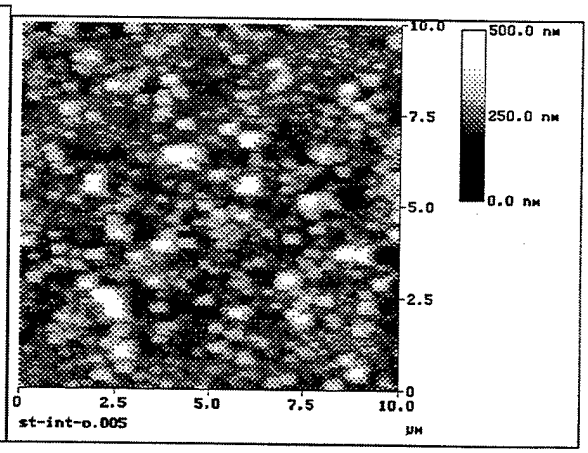
(b) Polyaniline coating surface after immersion



(c) Bare steel surface



(d) Steel/polyaniline interface before immersion



(e) Steel/polyaniline interface after immersion

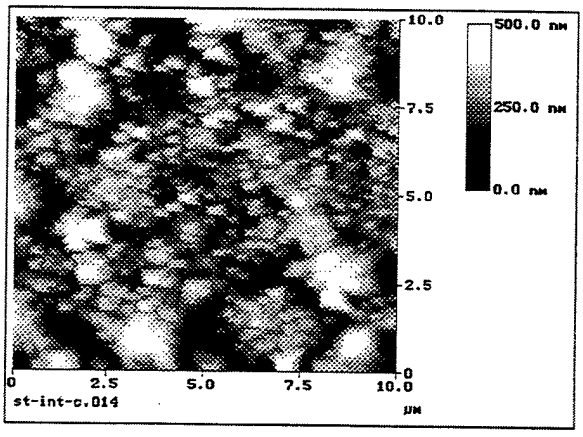


Figure 11. Surface structures characterized by atomic force microscopy

An Acoustic Emission Method for the Evaluation of Environmentally Assisted Cracking

Paul F. Buckley, Kevin Baldwin, Michael J. Ehrlich and
James W. Wagner

Abstract

Acoustic emission measurements were performed on a 7039-T6 aluminum alloy undergoing environmentally assisted cracking (EAC) in a 50/50 by volume respectively 3.5% NaCl and 3% H_2O_2 solution at STP. A fiber optic laser heterodyne interferometric measuring system was evaluated against a pinducer measuring system for sensitivity and fidelity. An array of six pinducers was used to determine the sources of the acoustic emissions during the cracking processes. Using theoretical compressive wave radiation patterns for a force dipole source, a double monopole source, a dilitation source, two shear sources and a microcrack source the experimentally obtained waveforms were compared to the different sources after adjusting for source receiver angles and surface interactions. It was determined that force dipoles were the predominant acoustic emission source, corresponding to anodic dissolution of $MgZn_2$ precipitates and subsequent ligament fracture.

Introduction

Environmentally assisted cracking (EAC) is a significant problem in modern structures. The combination of a susceptible material, an adverse environment and mechanical stress can lead to unexpected failure of a structure by catastrophic crack growth. The mid-air failure of the aluminum alloy bulkhead as shown in figure 1, and the subsequent loss of life on a Aloha Airlines flight on April 28, 1988 illustrates this fact. Additionally, the operating environment of the US Army contributes to premature failure of structures such as aluminum alloy armor, high strength steel armor and high strength steel control components on Army helicopters [1]. These failures not only endanger life but they also seriously hamper the fighting readiness of U.S. forces because of equipment down time for inspection and repair of faulty components. Work has been performed to better characterize EAC resistance in high strength aluminum armor alloys [2]. These high strength alloys are particularly prone to failure in a chloride environment, an environment encountered in most of the world. If we plan to avoid such failures, we must better understand the EAC phenomena and more diligently detect growing cracks before they become critical in length. One characterization technique that promises to serve well both as a laboratory tool for understanding EAC and as a field device for detecting EAC is acoustic emission evaluation. This promise is borne of the inherent nature of cracking phenomena. When a material cracks, even on a microscopic level, it releases energy in the form of mechanical waves. These waves travel throughout the structure. Acoustic emission (AE) is the science of monitoring these waves and determining the nature and significance of the event that caused them. We see that the usefulness of AE depends on three general abilities. First, can we measure our surface disturbance

accurately? Second, can we understand how the mechanical wave is transformed on its journey from source to receiver? Third, can we accurately describe the source of the mechanical wave given the previous abilities coupled with our theoretical know-how? If we are able to answer these questions sufficiently, we will find AE useful in characterizing and preventing EAC in engineering structures. This is the goal of this research endeavor.



Figure 1. Picture of the April 18, 1988, Aloha Airlines bulkhead immediately after landing.

Theory

A fundamental understanding of environmentally assisted cracking, acoustic emission sources, propagation and sensing as well as source location algorithms must be established before we actually apply this technology.

Environmentally Assisted Cracking

Environmentally assisted cracking reduces the working strength of many engineering alloys. Aluminum armor alloys, like many high strength alloys, are susceptible to EAC. Basically, environmentally assisted cracking occurs when three conditions occur simultaneously. The combination of a mechanical stress, an aggressive environment, and a susceptible material can lead to premature failure of a component by crack growth and eventual fracture. The specific mechanisms vary with the diversity of the three prerequisite conditions. In some polymeric materials such as polycarbonate, the material fails in the presence of alcohol by a crazing phenomenon [3]. Optical fibers made of silica are known to crack in the presence of water and tensile stress by a mechanism of bond rupture [4]. In high strength steels, the material can fail due to crack growth in the presence of tensile stress and hydrogen because of a bond-weakening mechanism [5]. In aluminum armor alloys, there is debate as to the mechanism of crack growth. Burleigh presents an excellent review of postulated mechanisms of EAC in 7000 series aluminum [6]. In this review, he cites numerous supporters of the hydrogen embrittlement theory. Hydrogen enters into the alloy at cathodic sites during the corrosion process. This monatomic hydrogen diffuses to the crack tip area and embrittles the material leading to rapid and localized crack growth as illustrated in Figure 2a. Others believe the mechanism to be brittle rupture of the passive film at the crack tip as shown in Figure 2b. The crack tip corrodes in solution and forms a passive film. Under stress, this film fractures leading to rapid and localized crack growth. Fresh metal is exposed and repassivates, leading to the next cycle. Other researchers believe the EAC mechanism to be anodic dissolution as

shown in Figure 2c. The crack tip area is under a stress while corroding and continues to grow through a combination of corrosion and stress. The corroding phase could either be the bulk material or the precipitate. Any characterization technique that can monitor certain physical parameters during the cracking process can be used in determining the exact cracking mechanism in the alloy of interest. Acoustic emission is a candidate technique for this task. First, we must establish the necessary technology for accurate assessment of EAC in aluminum armor.

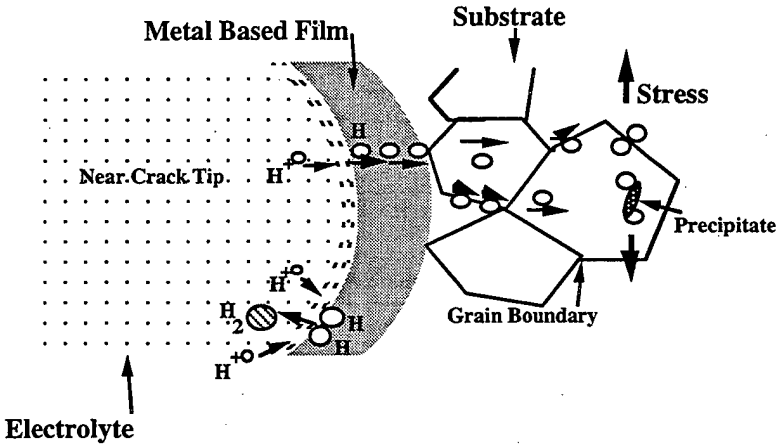


Figure 2a. A schematic of the region near a crack tip experiencing hydrogen embrittlement.

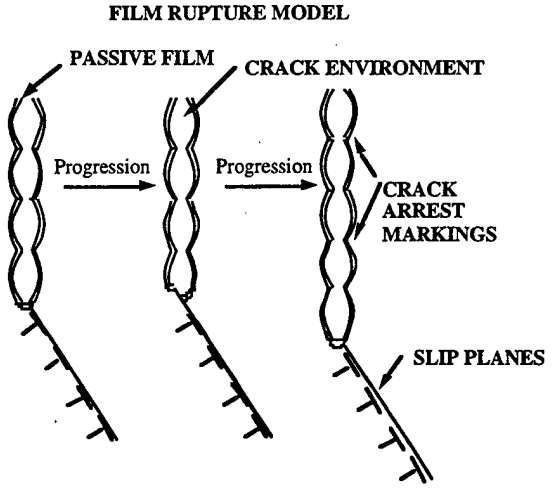


Figure 2b. A schematic of the film rupture mechanism for EAC.

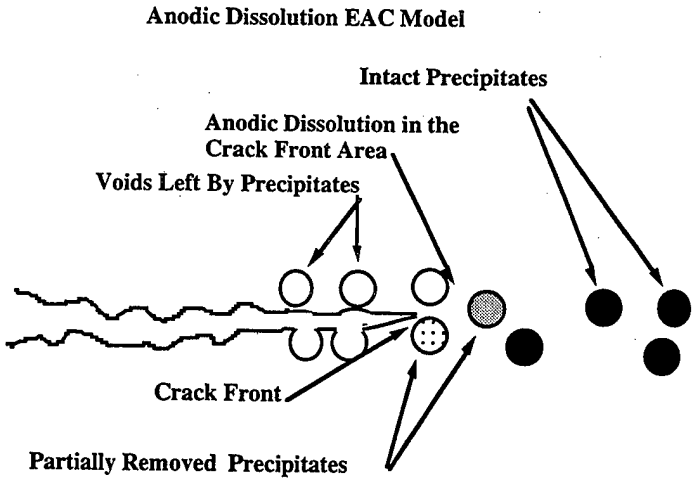


Figure 2c. A schematic for the anodic dissolution model of EAC.

Acoustic Emission Generation and Propagation

Scruby et al.[9] have laid out a concise and workable basis for quantitative acoustic emission analysis. This discussion basically follows that already established in Scruby's paper. As described earlier acoustic emission results form elastic waves released in a material when there are sudden localized changes in the stress state. The more dramatic the change the greater likelihood that the wave thus generated will be detectable. Often it is reasonable to model the source of these waves as a point given the relatively long distance of wave propagation compared with the size of the source itself. Assuming that all parts of the source radiate simultaneously with the same time dependence, the source can be represented as displacement discontinuities, $U_j(t)$ or a combination of forces, $f_j(t)$. This source produces a wave that will travel throughout the material until detection at some point , x', and some time, t'. The displacement at the detection point , Ui(t'), can be predicted theoretically by convolution of the source function with the transfer function affecting the elastic wave in the given material. This function written for a delta function source in time and space is known as the Green's function. Thus, for the displacement at point x' and time t', the equation is presented as shown in Equation 1.

$$U_i(t')=G_{ij}\,(x',t'-t;x)\,f_j(t) \qquad (1)$$

In which $G_{ij}\,(x',t'-t;x)$ is the Green's function describing displacements in the i=1,2,3 directions at point x' at time t' generated by a force, $f_j(t)$, applied at point x in the i=1,2,3 directions at time t. If we assume that the displacement measurements are made at a considerable distance from the source we can eliminate terms dependent on $(x'-x)^{-n}$ where n>1. This Green's function for a semi-infinite isotropic body simplifies to the following [8]:

$$G(x',t'-t;x)=\frac{1}{4\pi\rho v_p^2}\gamma_i\gamma_j\frac{1}{r}\delta(t'-t-\frac{r}{v_p})-\frac{1}{4\pi\rho v_s^2}(\gamma_i\gamma_j-\delta_{ij})\frac{1}{r}\delta(t'-t-\frac{r}{v_s}) \qquad (2)$$

This equation expresses the far field compression and shear waves terms respectively, material density, ρ, compression and shear wave velocities, v_p and v_s, x to x' direction cosines, γi, the distance between x and x', r and the delta function, δ. This Green's function is only valid given that the waves reach the detection site without interacting with any phase boundaries. We avoid this if we only look at the first arrival of the compression waves and we account for the interaction at the stress-free phase boundary where the measurement is made. The stress-free boundary conditions create reflection and mode conversions dependent on the angle of incidence of the wave, ϕ. The transformed displacement is calculated according to Equation 3.

$$U_i'(x') = U_i(x')R(\phi) \tag{3}$$

Here, U'i(x') is the transformed perpendicular surface displacement, Ui(x') is the compression wave displacement at x' and R(f) is the receiver function according to Equation 4 [9].

$$R(\phi) = \frac{2k^2(k^2 - 2\sin^2\phi)\sqrt{(1-\sin^2\phi)}}{(k^2 - 2\sin^2\phi)^2 + 4\sin^2\phi\sqrt{(1-\sin^2\phi)(k^2-\sin^2\phi)}} \tag{4}$$

In which k is the ratio of the compression wave velocity to the shear wave velocity and we are considering the elastic wave to be a plane wave. Not only do we need to consider the propagation of the elastic wave, but we must also address the theory of the generation of the wave or the source. As stated previously, we can assume a point source. Also, we can assume that this point source is self equilibrating. Therefore, the point sources must be some sort of force dipole. The following sources are considered for this work: double monopole, dipole, dilatation, shear dislocation and microcrack.

Double Monopole

The double monopole consists of two equal and opposite point forces. This might exist in a growing crack that was still joined by a ligament. Upon fracture of the ligament, the two fracture surfaces will separate and act as two half spaces with their respective equal and opposite point forces creating elastic waves. The compression wave amplitude thus generated will have an angular dependence according to Equation 5.

$$U(x') \propto \cos(\theta) \text{ for } x_2>0, \qquad U(x') \propto -\cos(\theta) \text{ for } x_2<0 \tag{5}$$

In where the crack is in the x_1x_3 plane at $x_2=0$ and θ is with respect to the $+x_2$ direction.

Dipole

A single force dipole with forces moving in the x_2 direction the angular dependence of the compression wave amplitude in relation to the x_2 axis is according to Equation 6.

$$U(x') \propto \cos^2(\theta) \tag{6}$$

Dilatation
The compression wave amplitude is constant with angle of propagation for a dilatation source as expressed in Equation 7.

$$U(x') \propto \text{constant.} \tag{7}$$

Shear Dislocation
A shear source with a primary shear plane at 45^0 to the crack plane will show one of the angular relationships shown in Equation 8, where Ψ is the angle with the x_1 axis.

$$U(x') \propto \cos^2(\theta)\text{-}\cos^2(\Psi)\sin^2(\theta)$$

$$U(x') \propto \cos^2(\theta)\text{-}\sin^2(\Psi)\sin^2(\theta) \tag{8}$$

Microcrack
A microcrack can be expressed as a combination of a dilatation source and a 45^0 shear source. The radiation pattern is given by Ohstu in Equation 9 [9], where ν is Poisson's ratio.

$$U(x') \propto 2\cos^2(\theta) + 2\nu/(1\text{-}2\nu) \tag{9}$$

These equations are graphically depicted in Figure 3 a-e.

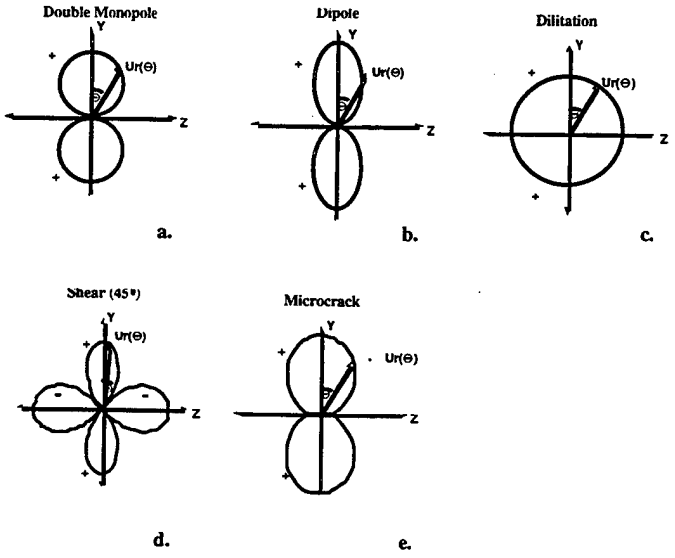


Figure 3. Radiation patterns for five different sources, $U(\theta)$ is the theoretical displacement from the compression wave.

Source Location

Before we can use any of our theory on elastic wave sources and propagation, it is important to know where our source is located. In this work, source location was calculated using a error minimization algorithm. Given that the location of at least four receivers is known and given that we have relative arrival times for all four receivers we can set up a relationship of at least four equations to solve for our four unknowns, x1,x2,x3 and time. The following equations were used.

$$dt2 = \frac{\sqrt{[(x_s - x_{T2})^2 + (y_s - y_{T2})^2 + (z_s - z_{T2})^2]}}{v_p} - \frac{\sqrt{[(x_r - x_{T2})^2 + (y_r - y_{T2})^2 + (z_r - z_{T2})^2]}}{v_p} \quad (10)$$

$$dt3 = \frac{\sqrt{[(x_s - x_{T3})^2 + (y_s - y_{T3})^2 + (z_s - z_{T3})^2]}}{v_p} - \frac{\sqrt{[(x_r - x_{T3})^2 + (y_r - y_{T3})^2 + (z_r - z_{T3})^2]}}{v_p} \quad (11)$$

$$dt4 = \frac{\sqrt{[(x_s - x_{T4})^2 + (y_s - y_{T4})^2 + (z_s - z_{T4})^2]}}{v_p} - \frac{\sqrt{[(x_r - x_{T4})^2 + (y_r - y_{T4})^2 + (z_r - z_{T4})^2]}}{v_p} \quad (12)$$

$$Error = \sqrt{\Sigma(dti_{actual} - dti_{calculated})^2} \quad (13)$$

Here, dt2, dt3 and dt4 in equations 10-12 are the differentials of the time of flight for the first compression or "p" wave arrival from the source to the respective transducer versus the time of flight from the source to the reference transducer, transducer 1. The locations of the transducers are denoted as x_{T2}, y_{T2} and z_{T2} for transducer 2, x_{T3}, y_{T3} and z_{T3} for transducer 3, etc. The source location is denoted as x_S, y_S and z_S. The compression wave velocity is v_p. The source location is incrementally adjusted until Equation 13 is minimized. Thus a best guess with respective error is established for the source location. Once the source location is known we can use our understanding of compression wave propagation and amplitude radiation patterns previously discussed to make a best guess at the type of source we have. Of course, this is assuming that we have a high fidelity transducer that accurately and consistently measures the surface disturbances.

Experimental Considerations

System Calibration

All testing was conducted on a double cantilever beam sample shown in Figure 4. Samples were machined from 50.8 mm 7039-T6 aluminum plate. A starter crack was introduced by torqueing the loading bolts until the critical stress intensity was exceeded. Six Valpey-Fisher Model 97 pinducers were arranged according to Figure 5.

Prior to actual testing, calibration was performed by pulsing the specimen with a YAG laser at the location marked in Figure 5. This laser produced an 8-ns pulse of 25 mJ with a footprint of approximately 15 mm^2. The target area was marked with a optically black marker in order to produce ablation at the site. Signals from the

pinducers were collected using three Gage two-channel 50 MHz boards inserted in a Gateway 2000 4DX2-66 personal computer using LabVIEW software.

Typical waveforms resulting from the laser ablation site are shown in Figure 6. These waveforms were used to calculate the relative sensitivities of each transducer measurement system. Using the known source location and transducer locations along with the correction for mode conversion at the transducer sights according to equation 3, the measured amplitude of the first compression arrival was compared with the predicted amplitudes from a monopole source with the known source-receiver angular relation. The predicted amplitudes and the measured amplitudes were normalized to channel 1. The sensitivity ratios as well as the measured and predicted amplitudes are shown in Table I.

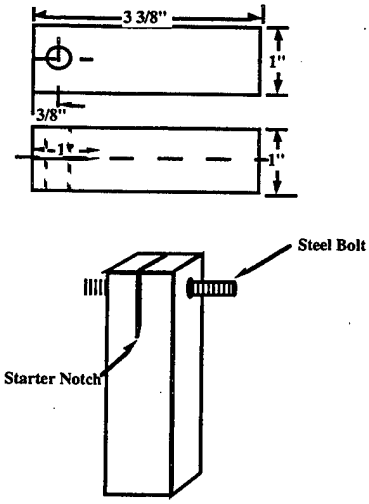


Figure 4. The double cantilever beam specimen used to produce EAC in the 7039-T6 aluminum alloy.

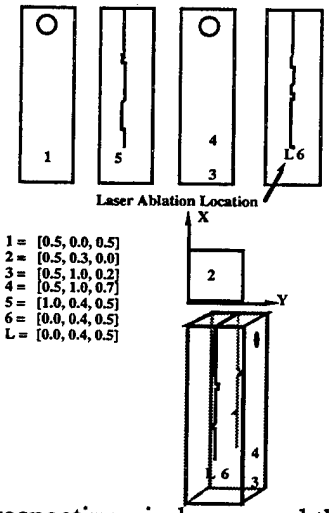


Figure 5. The location of the respective pinducers and the laser ablation site on the double cantilever beam specimen.

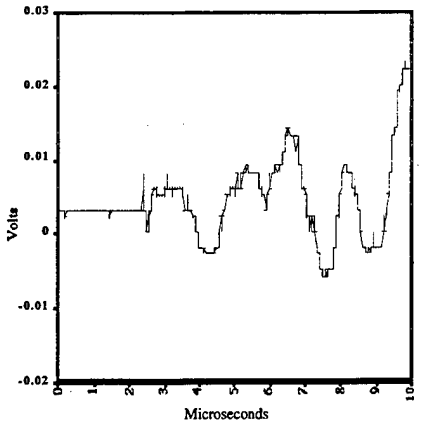


Figure 6a. A typical response to the laser ablation event as recorded by Pinducer 1.

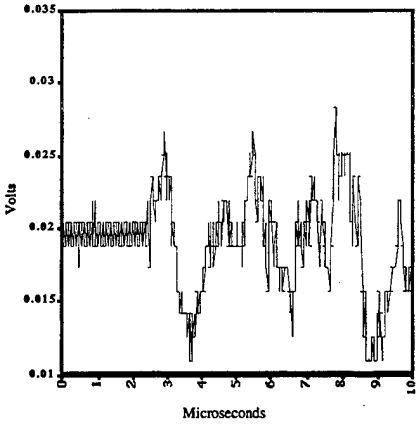


Figure 6b. A typical response to the laser ablation event as recorded by Pinducer 2.

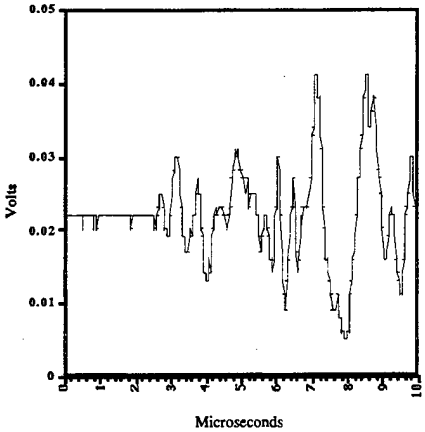


Figure 6c. A typical response to the laser ablation event as recorded by Pinducer 3.

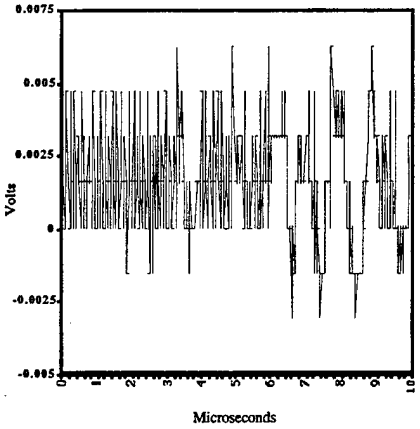


Figure 6d. A typical response to the laser ablation event as recorded by Pinducer 4.

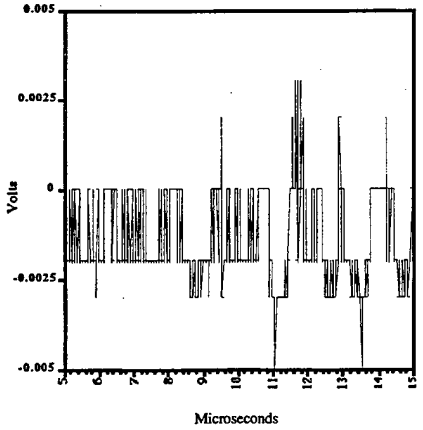


Figure 6e. A typical response to the laser ablation event as recorded by Pinducer 5.

Experimental Procedure

Immediately after initial calibration, a mixture of 50% by volume 3.5% NaCl and 50% by volume 3% H_2O_2 was added drop-wise into the crack area. Acoustic measurements were recorded over a 50-hr time period in which the crack grew approximately 2 inches. All procedures were conducted in an ambient laboratory environment on top of pneumatically stabilized optical benches.

Results & Discussion

Waveforms As Received

Typical waveforms recorded while the crack grew under EAC conditions are shown in Figure 7. All of the first arrival compression waves exhibited positive amplitudes.

Source Location

Source location was performed on events 40 through 120. These locations were obtained using the error minimization algorithm in three dimensions as shown in Equations 16-19. The results from this algorithm are shown in Table II. Only those locations having an error less than 10% were used. Figure 8 shows the locations and the respective numbers of the waveforms. This figure indicates the crack grew as expected, with a fairly uniform spread in space of recordable emissions. These correctly located sources then were used for determining the angular relations between pinducers and sources and hence the necessary adjustments of the recorded amplitude according to Equation 4.

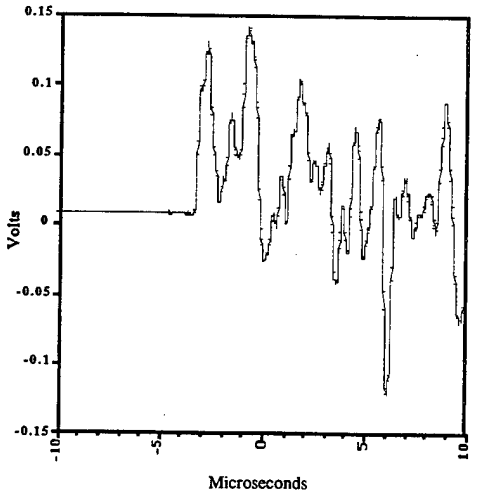


Figure 7a. A typical response to an EAC event as recorded by Pinducer 1.

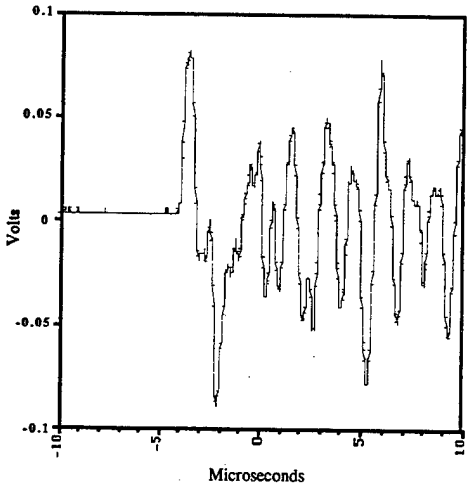


Figure 7b. A typical response to an EAC event as recorded by Pinducer 2.

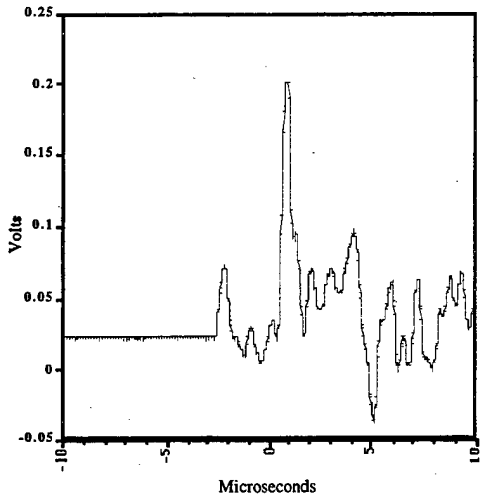


Figure 7c. A typical response to an EAC event as recorded by Pinducer 3.

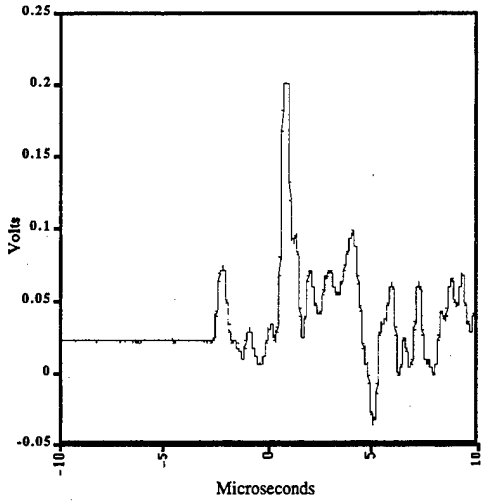


Figure 7d. A typical response to an EAC event as recorded by Pinducer 4.

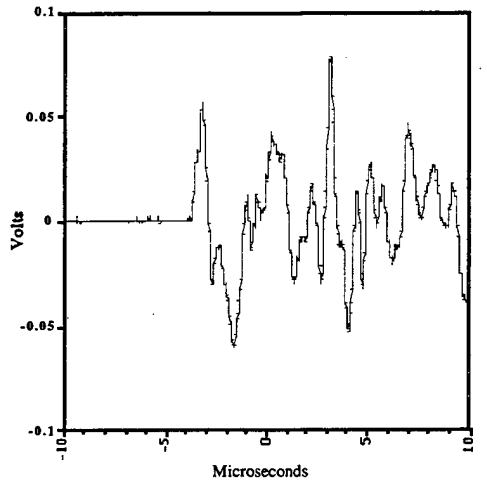


Figure 7e. A typical response to an EAC event as recorded by pinducer 5.

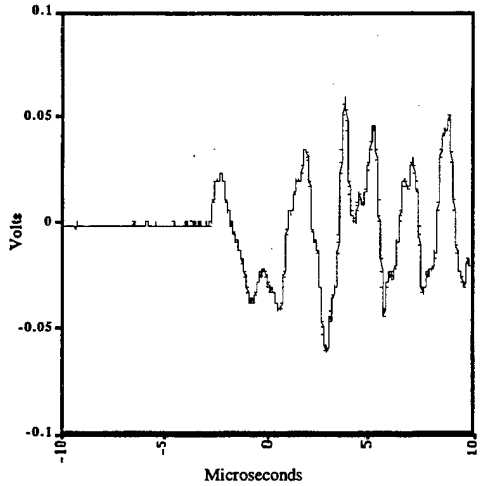


Figure 7f. A typical response to an EAC event as recorded by pinducer 6.

Amplitude Analysis

More than 125 events were record over a period of 48 hours. This represented a crack growing from the starter notch in figure 4 to within 1/2 inch of the bottom of the specimen. All recorded events were subjected to the source location algorithm. The events where the crack front was most equidistant from all transducers were numbers 90 through 121; therefore, these were used in the final analysis. The calabration data were used to produce normalized longitudinal amplitudes, shown in Table II. When one converts these to the respective normalized theoretical amplitudes, accounting for surface interactions, we can clearly see, as shown for typical cases in Table III, that the dipole source demonstrates the least cumulative error according to the following equation.

$$Error = \frac{\Sigma}{n}\sqrt{(\frac{AA_i - TAA_i}{TAA_i})^2} \qquad (14)$$

In which AA_i is the actual adjusted amplitude, TAA_i is the theoretical adjusted amplitude, and n is the number of measurements. Of 25 events analyzed, 14 are dipole sources, 8 are microcrack sources, 3 are dilitation sources. The dipole sources show an average error of 14%, the microcrack sources show an average error of 17%, the dilitation sources show an average error of 95%.

Hit	X	Y	Z
90	0.68	0.459	0.328
91	0.094	0.478	0.545
93	0.075	0.494	0.54
98	0.11	0.481	0.498
102	0.131	0.478	0.45
103	0.927	0.5	0.428
107	0.913	0.497	0.417
105	0.882	0.49	0.393
110	0.878	0.5	0.379
104	0.837	0.484	0.354
99	0.763	0.454	0.332
101	0.749	0.459	0.331
96	0.75	0.45	0.327
97	0.704	0.431	0.322
95	0.278	0.441	0.308
109	0.296	0.405	0.3
115	0.301	0.422	0.278
92	0.48	0.464	0.271
94	0.521	0.444	0.258
117	0.344	0.422	0.235
100	0.436	0.449	0.206
121	0.36	0.458	0.183
118	0.582	0.458	0.173
120	0.373	0.462	0.166
119	0.386	0.455	0.16
113	0.42	0.442	0.139

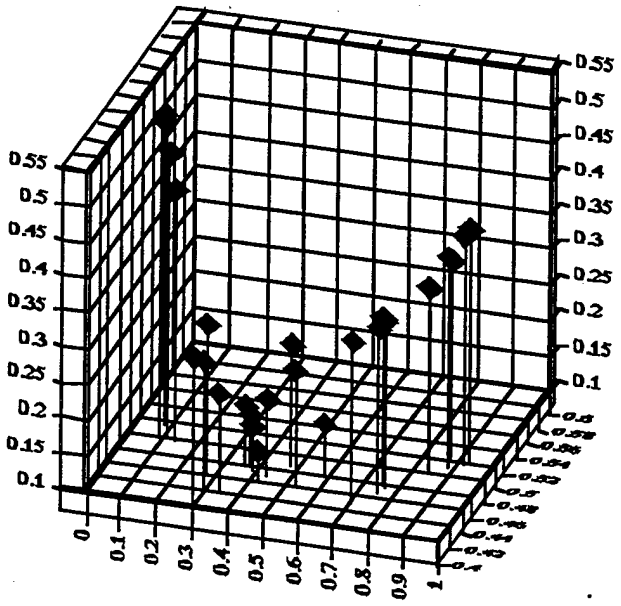


Figure 8. The source locations for events 90 through 121 as determined by the error minimization algorithm. Units are in inches using the axes established in figure 18 .

Table I. Theoretical Responses of Pinducers

Hit	Pinducer1	Pinducer 2	Pinducer 3	Pinducer 4	Pinducer5	Pinducer6
0	0.0110	0.0408	0.0110	0.0064	0.0080	0.0000
1	0.0100	0.0408	0.0110	0.0064	0.0080	0.0000
2	0.0065	0.0160	0.0060	0.0048	0.0050	0.0000
3	0.0110	0.0400	0.0120	0.0080	0.0060	0.0000
4	0.0100	0.0160	0.0070	0.0048	0.0400	0.0000
Average Amplitude	0.0097	0.0307	0.0094	0.0061	0.0134	0.0000
Adjusted to Surface Interactions, Theory	0.0077	0.0130	0.0046	0.0076	0.0240	0.0000
Normalized to Pinducer1	1.0000	1.6914	0.6022	0.9916	3.1273	0.0000
Theoretical Response	0.8824	1.5567	1.2921	0.5242	1.2604	1.4534

Table II. Normalized Amplitudes

Hit	Pinducer 1	Pinducer 2	Pinducer 3	Pinducer 4	Pinducer 5	Pinducer 6
90	27.7721	9.2997	22.4420	10.4733	4.0127	2.0146
91	11.4436	4.2290	22.1465	7.7517	1.8094	10.5121
92	11.0261	5.0770	5.3034	3.6811	1.2210	0.7495
93	22.9874	6.5872	38.2149	12.7261	3.9906	13.5013
94	19.8165	9.8912	7.2645	6.8007	2.0784	1.7389
95	35.1729	11.3990	27.3403	12.7715	3.7988	5.6436
96	-0.0349	-0.1813	0.1988	-0.0412	0.1225	9.6512
97	6.0133	2.9242	4.8557	2.9149	1.1967	0.4848
98	3.4254	1.5633	4.2154	2.1999	0.6827	1.6306
99	8.6435	3.4117	7.0999	3.2348	1.2782	0.7313
100	10.4548	8.3075	3.1272	4.1185	1.1906	0.9728
101	9.9906	3.7803	8.2408	3.8575	1.5103	0.9735
102	13.4884	4.1514	19.1009	9.6976	2.5992	4.1965
103	23.6119	7.8454	25.9213	13.6265	4.9801	3.3066
104	20.0038	5.5193	17.1403	8.1795	2.8033	2.4528
105	6.5578	1.8408	7.0326	3.2555	1.6166	0.8237
107	10.8293	2.5751	11.5132	5.3126	2.0692	1.4040
109	43.5449	23.2274	34.5883	23.4108	8.5208	8.3652
110	9.0905	3.2600	9.1217	3.9779	1.6850	1.1493
113	3.0622	4.5938	3.7303	1.8523	0.5810	0.4502
115	41.4588	10.2724	-0.1351	20.1993	7.7367	7.0523
117	3.7181	1.9645	3.8914	1.5823	0.7567	0.6690
118	5.0666	13.7480	4.5034	2.0677	0.7477	0.6551
119	3.4588	2.6688	4.9704	1.6652	0.5389	0.3815
120	4.3172	3.1141	5.7743	2.0371	0.9517	0.6308
121	120.6404	1.6918	2.5361	1.2998	0.7292	0.2540

Table III . Normalized Theoretical Amplitudes

	U1	U2	U3	U4	U5	U6	Error
Hit 99	8.64	3.41	7.10	3.23	1.28	0.73	
normalized	1.00	0.39	0.82	0.37	0.15	0.08	
double monopole	1.00	0.56	-1.04	-0.88	0.41	0.33	0.57
dipole	1.00	0.31	1.07	0.77	0.17	0.11	**0.13**
dilitation	1.00	1.00	1.00	1.00	1.00	1.00	0.22
Shear Ia	1.00	-0.11	1.12	0.63	-0.34	-0.44	0.40
Shear Ib	1.00	-0.11	1.12	0.63	-0.34	-0.44	0.40
Microcrack	1.00	0.63	1.04	0.88	0.55	0.52	0.16
Hit 100	10.45	8.31	3.13	4.12	1.19	0.97	
normalized	1.00	0.79	0.30	0.39	0.11	0.09	
double monopole	1.00	0.83	-1.20	-0.88	0.26	0.20	0.48
dipole	1.00	0.69	1.43	0.78	0.07	0.04	0.26
dilitation	1.00	1.00	1.00	1.00	1.00	1.00	0.24
Shear Ia	1.00	0.41	1.82	0.58	-0.78	-0.84	0.53
Shear Ib	1.00	0.41	1.82	0.58	-0.78	-0.84	0.33
Microcrack	1.00	0.85	1.21	0.89	0.55	0.54	**0.25**
Hit 101	9.99	3.78	8.24	3.86	1.51	0.97	
normalized	1.00	0.38	0.82	0.39	0.15	0.10	
double monopole	1.00	0.57	-1.04	-0.87	0.43	0.35	0.57
dipole	1.00	0.32	1.07	0.76	0.19	0.12	**0.13**
dilitation	1.00	1.00	1.00	1.00	1.00	1.00	0.22
Shear Ia	1.00	-0.09	1.12	0.62	-0.31	-0.41	0.41
Shear Ib	1.00	-0.09	1.12	0.62	-0.31	-0.41	0.41
Microcrack	1.00	0.63	1.04	0.87	0.56	0.53	0.16
Hit 102	13.49	4.15	19.10	9.70	2.60	4.20	
normalized	1.00	0.31	1.42	0.72	0.19	0.31	
double monopole	1.00	0.45	-0.91	-0.90	0.86	0.85	0.75
dipole	1.00	0.21	0.82	0.81	0.74	0.72	0.17
dilitation	1.00	1.00	1.00	1.00	1.00	1.00	0.21
Shear Ia	1.00	-0.20	0.73	0.71	0.60	0.57	0.35
Shear Ib	1.00	-0.20	0.73	0.71	0.60	0.57	0.35
Microcrack	1.00	0.55	0.90	0.89	0.85	0.84	**0.17**

Linkage to Real Phenomena

The results of the previous analysis leads one to ask "What are the mechanisms that would create acoustic sources best modeled by a force dipole?" Carpenter et al.[11] found that in 7075 aluminum the primary acoustic source in fatigue was from precipitate separation [11]. Scruby argues for microcracking as the chief mechanism in his work [9]. Although these analyses were done on fatigue crack growth, we can expect some of the same mechanisms. Both hydrogen embrittlement and brittle film rupture are capable of producing such microcracking emissions, but this is not the primary emission in this study. These phenomena also are capable of producing a source modeled by a force dipole, the most common source in this study, given that the plastic zone ahead of the crack front produced some local decohesion. However, one would expect a correspondent heavy amount of microcracking with this type of fast brittle crack growth. A more likely scenario is a crack growing in the presence of anodic dissolution. Corrosion would weaken areas at the crack tip, leaving ligaments behind that would preferentially fracture as depicted in Figure 9. This weakened area in 7039 would be composed of material left behind after the dissolution of the anodic precipitate, $MgZn_2$. Fortunately, others concur. Landkof et al.[12] concluded in their work on 7039 that ductile rupture of the bridges between cavities left by the corroded $MgZn_2$ was an important mechanism in the environmentally assisted cracking of 7039 aluminum. Therefore, this mechanism of anodic dissolution and crack advance through the remaining ligaments is responsible for producing the emissions classified as force dipoles, the primary emissions in this work.

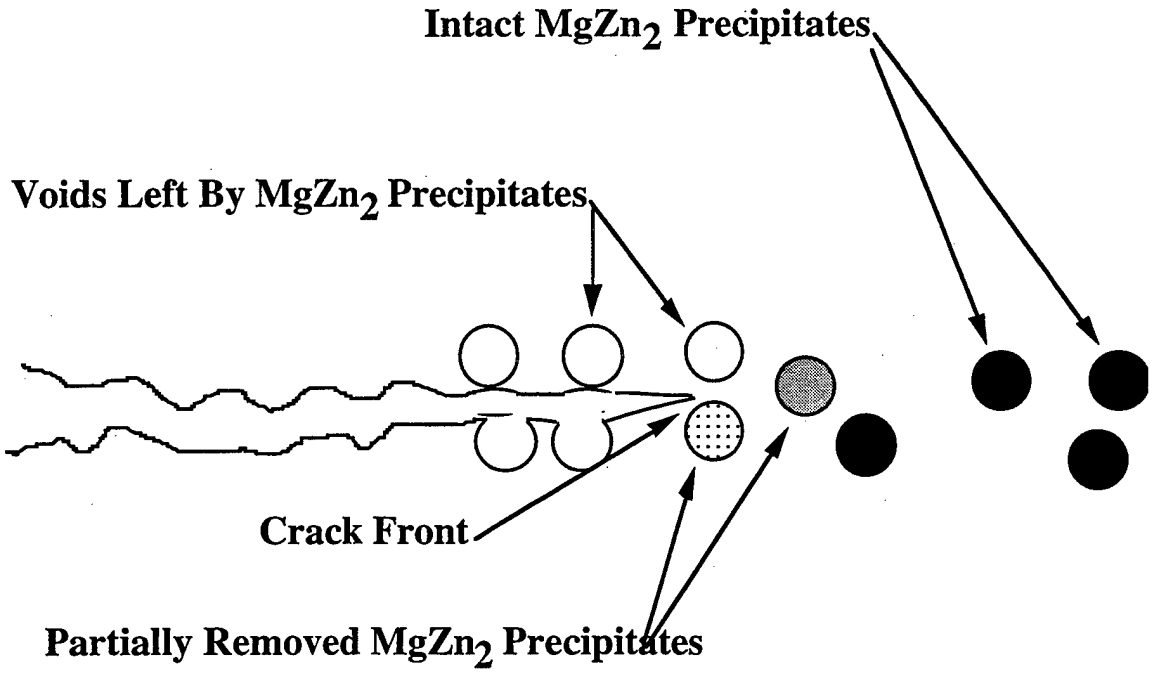


Figure 9. The proposed mechanism for production of a dipole source.

Conclusions

This study leads to the following conclusions. First, from the preceding section, anodic dissolution is a primary mechanism in the EAC of 7039-T6. Other mechanisms may be present but they do not produce any significant acoustic emissions. Secondly, acoustic emission analysis yields quantitative results regarding sources given that the measuring system is well characterized and the elastic wave propagation theory is well understood. Finally, acoustic emission radiation patterns are a practical and simple way to apply well-established but complex acoustic theory.

References

1.Milton Levy, Paul Buckley, John Beatty, Richard Brown, Robert Huie, June 1992, "Failure Analysis of the Main Rotor Retention Nut From The AH-64 Helicopter," MTL TR 92-39.

2. Eugenio DeLuca, Albert A. Anctil, Walter Czyrklis, Nancy D. Kackley, April 1986, "Laminate Armor For Combat Vehicles," MTL TR 86-14, pp. 129-141.

3. J. Donovan, Personal conversation and class notes from Environmental Degradation of Polymers, MTL, Boston, MA, 1987.

4. P. Ostojic, 1995, "Review: Stress Enhanced Environmental Corrosion and Lifetime Prediction Modeling In Silica Optical Fibers," Journal of Materials Science, 30, pp. 3011-3023.

5. Robb Thompson, Ing-Hour Lin, 1985, "Cracking and Failure Mechanisms," in Hydrogen Degradation of Ferrous Alloys, Oriani, Hirth and Smialowski Eds., Noyes Publications, Park Ridge, NJ, pp. 454-509.

6. T.D. Burleigh, 1991, "The Postulated Mechanisms for Stress Corrosion Cracking of Aluminum Alloys," Corrosion, Vol. 47, No. 2, pp. 89-98.

7. Robert D. Huber, 1993, "Optical Detection of Stress Waves From Glass Fiber Reinforced Polymer Matrix Composite Material," Doctoral Thesis, Johns Hopkins University, 1993.

8. Ian G. Scott, 1991, Basic Acoustic Emission, from Non-Destructive Testing Monographs and Tracts, Warren J. McGonnagle Ed. Gordon and Breach Science Publishers, New York, NY.

9. D.J. Buttle, C.B. Scruby, 1990, "Characterization of Fatigue of Aluminum Alloys by Acoustic Emission, Part I - Identification of Source Mechanism," Journal of Acoustic Emission, Volume 9, Number 4, pp. 243-254.

10. C.L. Pekeris, 1955, "The Seismic Surface Pulse," Geophysics, Vol. 41, pp. 469-480.

11. Steve H. Carpenter, Michael R. Gorman, 1994, "A Waveform Investigation Of The Acoustic Emission Generated During The Deformation And Cracking of 7075 Aluminum," Progress in Acoustic Emission VII, pp. 105-111.

12. M. Landkof, L. Gal-Or, 1980, "Stress Corrosion Cracking of Al-Zn-Mg Alloy AA-7039," Corrosion, Vol. 36, No. 5, 1980, pp. 241-246.

Evaluation of Vapor Phase Corrosion Inhibitors and Dehumidification As Corrosion Control Methods For Advanced Double Hull Naval Ships

C. Bowles, A. Sheetz, H. Hack[1] and K. L. Vasanth
Naval Surface Warfare Center, Carderock Division
9500 MacArthur Blvd.
West Bethesda, MD 20817-5700

R. Simmons
SBB Technologies, Inc.
13851 S.W. 37th Ct.
Davie, FL 33330

ABSTRACT

Two vapor phase corrosion inhibitors (VCIs) and one industrial desiccant wheel (DEW) dehumidifier are evaluated in small-scale advanced double hull (ADH) compartments exposed to the marine environment in Dania, Florida. The steel compartments were fabricated to simulate the environmental conditions likely to be encountered in service. Steel weight loss coupons and galvanic couples of steel/copper-nickel 90-10, steel/stainless steel 304, and steel/aluminum alloy 6061-T6 were installed in each compartment, along with atmospheric corrosion probes, thermocouples, and relative humidity probes. Six and 12 month weight loss, corrosion rate, temperature and humidity data are presented. Results indicate that the dehumidifier is providing the best environmental and corrosion control. The VCIs show promise under ideal environmental conditions but are unable to provide adequate protection under worst case conditions.

INTRODUCTION

The primary objective of the test is to evaluate the effectiveness of vapor corrosion inhibitors (VCIs) and dehumidification as corrosion control methods in steel test chambers designed to simulate the compartments of advanced double hull (ADH) naval ships. The test chambers, referred to as boxes, are exposed to the marine environment at the Naval Surface Warfare Center, Carderock Division, (NSWCCD) Marine Corrosion Test Site in Dania, Florida. The six and 12 month sample evaluations, referred to as sample pulls, involved the removal of bare commercial grade (c.g.) steel coupons from each of 20 test chambers for the purpose of visual examination and weight loss measurements. Additionally, the bare interior walls of the steel test chambers were examined and photographed, along with galvanic couples suspended in each box. The galvanic couples consist of

[1] current address: Northrop Grumman Corporation
Electric Sensors and Systems Division
P.O. Box 1488
Annapolis, MD 21404

two coupons (1" x 1") of dissimilar alloys attached to each other with nylon fasteners. Three galvanic couple configurations are under test: c.g. steel/aluminum alloy (AA) 6061-T6 (UNS A96061), c.g. steel/stainless steel (SS) 304 (UNS S30400), and c.g. steel/90-10 copper-nickel (UNS C70600).

Two proprietary VCI formulations, referred to as VCI A and VCI B, are being evaluated in ADH boxes. VCI A is a mixture of Cortec Corporation VCI products, including VCIs 307 and 609. VCI B is CCI Powder, manufactured by Corroless Corporation, Ltd. VCI 307 and CCI Powder are marketed as multi-metal inhibitors intended to protect various alloys, including steel, stainless steel, aluminum alloys, and copper alloys, from atmospheric corrosion. VCI 609 is intended to protect ferrous and aluminum alloys but is not recommended for copper-based alloys, which may be attacked by an ammonia compound contained in the VCI. VCIs, in general, achieve corrosion protection in enclosed compartments through adsorption of the inhibitor on bare metallic surfaces. The applied VCI powders are transported to the metallic surfaces to be protected through vaporization.[1] When the equilibrium vapor pressure of the VCI is attained, the vapors condense, and an adsorbed molecular inhibitor layer forms on the metallic surface. In order to maintain corrosion protection, the equilibrium vapor pressure must be maintained; the VCI layer will readily desorb and dissipate if the equilibrium vapor pressure is not maintained.[2] Nonetheless, Miksic[1] asserts that VCIs do not require tightly sealed compartments and are capable of performing well in routinely opened compartments.

An industrial silica gel desiccant wheel (DEW) dehumidifier is also being evaluated in ADH boxes. The dehumidifier under test is a Model HC-150-I DEW system manufactured by Munters Cargocaire Engineering Corporation. A DEW dehumidification system operates by forcing the process air through three-fourths of a wheel that contains the active desiccant. The last one-fourth of the wheel is used for reactivation, or drying out, of the desiccant. Dehumidification can effectively stop the atmospheric corrosion of iron and steel by preventing the formation of a thin layer of water on the surface of the alloy. This water layer serves as an electrolyte through which corrosion can occur. Drying the air to a relative humidity (RH) below 40% prevents the formation of the water layer, so that corrosion cannot occur.[3]

The effectiveness of the three corrosion control methods (VCI A, VCI B, and DEW dehumidifier) is evaluated relative to controls (chambers with no corrosion control) for each environmental test condition, as applicable. Three types of boxes were designed to simulate the environmental conditions likely to be encountered in actual ADH compartments. Sealed boxes were designed to simulate air- and water-tight ADH compartments containing ambient humid air. Seawater pool boxes were designed with shallow seawater pools covering the entire floor to simulate spilling or leaking of seawater into a compartment. Baffle boxes were designed with end covers containing air holes and baffles to allow humid air ingress while preventing rain entry; these boxes were intended to simulate a compartment with an air leak. Table 1 shows the environmental conditions and corrosion control methods used in each box. Table 1 also shows the sensors installed in each of the boxes to monitor interior temperature (surface and air), relative humidity (RH), and corrosion rate during the test period.

The VCIs and DEW dehumidification system were selected for testing based on the findings of a feasibility analysis[4] in which various environmental modification methods were considered for corrosion protection of ADH compartments on tankers and combatants. Inhibitors, oxygen

scavengers, inert gas purging, and dehumidification were evaluated as alternatives to painting the interiors of steel ADH compartments. In the evaluation of these alternative methods, the ADH compartments were assumed to be dry (versus seawater ballast tanks). The study evaluated the corrosion abatement capabilities of candidate systems along with environmental, health, and safety issues, installation and maintenance logistics, storage requirements, remote monitoring capabilities, survivability, and cost. VCI A, VCI B, and the DEW dehumidifier were identified as feasible corrosion control methods and were recommended for field testing.

EXPERIMENTAL PROCEDURE

Test Chamber Fabrication and Sample Installation

Test chambers (3' x 1' x 1') were designed and fabricated to simulate ADH compartments on a small scale. The chambers, referred to as boxes throughout this report, and steel coupons (3" x 3" panels) were fabricated from hot rolled c.g. steel sheet. Each box was constructed by welding two L-shaped steel sections together to form an open-ended rectangular column. The interior surfaces of each box were sand blasted to a white metal surface during construction. Flanges were machined from hot rolled c.g. steel sheet and welded to the ends of each box. Square end covers were fabricated from transparent ultraviolet (UV) resistant acrylic sheet, and an o-ring groove was machined around the outer perimeter of each cover. Through holes were machined in the flanges and end covers to allow fastening using screws and nuts. The exterior of each box was blasted and painted with epoxy polyamide primer (MIL-P-24441) and silicon alkyd topcoat (MIL-S-24635). This coating system was selected to simulate the coatings most likely to be used on the outer hulls of ADH naval ships.

Extreme care was taken to ensure that the bare metallic surfaces of the boxes and coupons remained clean and free of corrosion until test initiation. After assembly and painting of the boxes, the interior walls and machined flange surfaces were wiped with methanol to remove machining oils. The c.g. steel coupons (3" x 3" and 1" x 1") were degreased in acetone and sand blasted to white metal. The copper-nickel (Cu-Ni) 90-10, SS 304 and AA 6061-T6 coupons were degreased in acetone prior to assembly of the galvanic couples. Rubber gloves were worn at all times when handling the coupons or touching the interior walls of the boxes. Silica gel desiccant packs were placed inside of the sealed boxes for storage and shipping to Dania, Florida. The coupons were stored in desiccators or ziploc bags containing silica gel packs until installation and test initiation.

Each box was designed to accommodate samples in four quadrants, established by dividing the box into fourths along its length from front to back, as shown in Figure 1. Steel coupons were installed in each quadrant in the following four locations (shown in Figure 1): on the bottom of the box, on the side wall, on the top wall, and hanging from a plastic rod spanning the width of the box. The samples installed on the top and side walls are held in place by plastic sample holders. A total of 16 steel coupons were installed in each box. They were installed in these positions in distinct quadrants to allow up to four sample pulls, in which coupons are removed from a specified quadrant, corresponding to the exposure time, in each box. Thus, the bottom, side, top, and hanging coupons in the first quadrant of each box were removed during the first (i.e. six month) sample pull. In a similar manner, the four samples in the second quadrant of each box were removed during the 12 month sample pull. The samples in the third and fourth quadrants remain in the boxes for future sample

pulls. In addition to the bare steel coupons, six galvanic couples (two of each configuration) were installed in each box by suspending them from the plastic rods in the second and third quadrants. The three couples (one of each configuration) hanging in the second quadrant were examined and photographed during the six and 12 month sample pulls. During the 12 month sample pull, several couples were removed from their boxes for several minutes to allow closer examination.

Just prior to installation of the samples in the test chambers, the 3" x 3" steel coupons were removed from the desiccator and weighed. The coupons were visually examined and any pre-existing corrosion or staining was noted. At the initiation of the field test, the steel coupons and galvanic couples were installed in the locations previously described. The boxes were then closed, sealed, and placed on wooden test racks, as shown in Figure 2, located approximately 200 feet from the ocean. Atmospheric corrosion probes (described below) were installed in 10 of the 20 boxes. The steel sensor elements of the probes were exposed and initiated at the same time that the coupons were installed. After placing the boxes on the racks, thermocouples and RH sensors (described below) were installed in each of the boxes, VCIs were applied, and the DEW unit was activated. Installation of the VCIs was performed using compressed air to blow the VCI powder into the boxes. It should be noted that VCI A was installed at approximately 300% the recommended dosage, based on vendor recommendations, while VCI B was applied at 100-150% the recommended dosage. To seal the boxes, a silicone rubber o-ring was installed between the end covers and flanges of the boxes. The covers were attached to the flanges with SS 304 and SS 316 (UNS S31600) screws and nuts. Silicone sealant was applied at the interface between the covers and the flanges. Acetic acid free RTV was applied around the probes (thermocouple, RH sensors) which were inserted through holes in the test chamber walls and end covers.

Commercially available atmospheric corrosion probes were installed in one of the duplicate boxes representing each test condition, as indicated in Table 1. The probes selected for testing were Mode 2000 Corrosometer probes manufactured by Rohrback Cosasco Systems, Inc. The probes were installed on the east side of each box (same side as the side-mounted coupons), centered along the length and height of the box. Corrosion rate readings are taken from the probes on a daily basis using a portable meter to collect and download the data. The probes monitor atmospheric corrosion by measuring changes in electrical resistance due to metal loss as the element corrodes. In order to provide meaningful corrosion rate data, the probe element material should be as close in composition as possible to the material of the structure or hardware which is being monitored. The probes purchased for the field test contain sensing elements made of carbon steel, similar in composition to the box and coupon material. Two types of probe elements were selected based on the expected corrosion rates in the boxes. One of the elements, referred to as type 1, consists of a strip of steel which can detect metal loss up to a penetration depth of 1 mil (.001"). Type 1 elements were selected for boxes with the lowest expected corrosion rates where greater sensitivity was desired. The other elements, referred to as type 2, consist of steel tubes which can measure penetration depths up to 2 mils (.002"). Type 2 elements were selected for boxes with higher expected corrosion rates, where longer sensor life was desired. For comparison of probe sensitivity, both type 1 and type 2 probe elements were installed in the sealed, control box (Box 1).

Temperature and relative humidity sensors were installed in the boxes to enable on-line data collection throughout the test period. A data acquisition system is used to collect data from the RH sensors and thermocouples every two hours. All but one of the boxes (Box 14, DEW unit) contains a commercially available humidity probe, consisting of a polymer film humidity sensor at the end of a

duct-mountable probe (wand) and a weather-proof box containing the probe electronics. The probes were inserted into the boxes through the east wall (side with steel coupons) just above the corrosion probes (halfway down the length of the box). The polymer film sensors provide relative humidity data by measuring changes in the polymer capacitance. During the third month of the test, an additional RH sensor was installed to monitor the outside ambient RH. Additionally, all of the boxes contain two thermocouples: an air temperature probe and a surface mounted thermocouple. The air temperature probes (wands) were inserted into the boxes through the south end covers. The probes were positioned with the thermocouple as close to the center of the box as possible. The self-adhesive surface mount thermocouples were attached directly to the west walls (opposite the sides with the steel coupons) of the boxes, as close to the center as possible.

Sample Removal and Evaluation

Four samples were removed from the first and second quadrants of each box for the six month and one year sample pulls, respectively. An end cover was removed from each box to allow retrieval of the coupons and examination of the box interior and galvanic coupons. Attempts were made to minimize the amount of time that each box remained open; in most cases, the end covers were replaced within 10 minutes of opening. Prior to closing the seawater pool boxes, fresh seawater was added to the pool on the bottom of the box. Equivalent amounts were added to each of the seawater pool boxes. During the six month pull, 50 ml of seawater was added to each box, and 800 ml was added to each box during the 12 month pull.

Black finger-like corrosion products were observed on the steel walls of the boxes containing seawater pools. The fingers were found to be brittle and crumbled easily. Intact samples were removed for analysis using an environmental scanning electron microscope (ESEM) and energy dispersive x-ray (EDX) analysis.

Prior to chemically cleaning the coupons, the optimum solution concentration was determined using the method described in ASTM G1[5]. A solution composed of 125 ml HCl, 875 ml reagent water, and 3.5 g hexamethylenetetramine was found to give an acceptable rate of dissolution of the base steel. Dissolution rate data were obtained by immersing a bare steel 3" x 3" coupon in this solution for the following consecutive time increments: 1, 1, 2, 4, 8, 16, 32, 64, 128, and 256 minutes. After each of these immersion periods, the bare steel coupon was rinsed in reagent water, dried with a hairdryer, and weighed. The weight loss data were plotted versus immersion time to obtain a substrate loss calibration curve for up to 512 minutes of total cleaning time in the HCl solution.

The solution described above was used to chemically clean the six and 12 month steel coupons according to ASTM G1[5]. Samples were immersed in the HCl cleaning solution in an ultrasonic bath for as long as necessary to remove as much visible rust as possible. Cleaning times ranged from two minutes to 64 minutes for the six month samples, and up to 212 minutes for the 12 month samples. In some cases, small amounts of rust remaining at the edges of samples were ignored. Upon removal from the solution, samples were rinsed in reagent water and dried with a hairdryer. Flash rusting during drying was unavoidable. Some of the samples showing no visible rust (i.e. sealed box samples) were cleaned in ethanol for one minute rather than in the HCl solution.

To calculate the corrosion rates of the six month samples according to the formula in ASTM G1[5], the dimensions of each coupon were measured using calipers and recorded. Nominal

dimensions (3" x 3") were used to calculate the 12 month corrosion rates. Comparison of corrosion rates calculated using actual dimension to corrosion rates calculated using nominal dimensions showed no appreciable difference

RESULTS AND DISCUSSION

Weight Loss and Corrosion Rate Data

The weight loss and corrosion rate of the six and 12 month steel coupons were calculated according to ASTM G1.[5] The results are given in Tables 2 and 3. The sample labeling scheme used in Tables 2 and 3 is as follows:

NPQ where: N is the number of the box (1-20)
P is the position of the sample (B, H, S, or T) where:
B indicates a bottom sample
H indicates a top sample
S indicates a side sample
T indicates a hanging sample
Q is the quadrant (1-4) in which the sample is located (Q=1 for the six month pull, Q=2 for the 12 month pull)

The average corrosion rates determined from corrosion probes installed in half of the boxes are included in Tables 2 and 3.

Weight loss data are plotted in Figures 3-6 for the sealed, seawater pool, baffle, and DEW boxes, respectively. Examination of the data in Figure 3 show that the weight loss is very low, ranging from nil to 0.10 g for the sealed boxes. This indicates that for short-term exposures up to 12 months, corrosion rates are so low under ideal conditions (i.e. sealed with no leaks) that the benefit of applying a VCI to a sealed ADH compartment is negligible.

Comparison of Figures 3 and 4 shows that the maximum weight loss values in the seawater pool boxes were significantly higher than the maximum losses in the sealed boxes. After 12 months of exposure, one of the side-mounted control, seawater pool coupons (4S2) lost 10 g, which corresponds to a corrosion rate of 3.8 mils per year (mpy). These were the highest observed weight loss and corrosion rate values of all of the weight loss coupons. In the VCI, seawater pool boxes, the maximum 12-month exposure weight loss values were 1.9 g for VCI A (coupon 10B2) and 4.2 g for VCI B (coupon 18B2), corresponding to corrosion rates of 0.7 mpy and 1.6 mpy, respectively. Both of these coupons were submerged beneath the seawater pool and received little protection from the VCI. Thus, the mass loss of these bottom samples does not directly reflect the corrosion abatement capabilities of the VCIs; the side, top, and hanging coupons provide more meaningful data for the VCIs than the bottom coupons. Looking at the side, top and hanging samples in the VCI, seawater pool boxes and considering both the six and 12 month sample pulls, a maximum corrosion rate (based on weight loss measurements) of 1 mpy was observed for both VCI A and VCI B; the coupons (10S1 and 17S1, respectively) corresponding to this maximum value were both side-mounted coupons removed during the six month sample pull.

In duplicate seawater pool boxes, the weight loss data and calculated corrosion rates for replicate side and bottom coupons tended to vary significantly for both the six and 12 month sample pulls. The weight loss data and calculated corrosion rates for the top and hanging coupons did not show such variability, and their corrosion rates were generally low (less than 0.1 mpy). The observed variability in the weight loss data for the side and bottom coupons was found to be consistent with the appearance of the samples. The amount of corrosion product observed on these samples was extremely variable, ranging from only light rust and small pits to regions of continuous corrosion product in the form of nodules or finger-like deposits (discussed later in this report). The two side-mounted VCI, seawater pool coupons (10S1 and 17S1) which corroded at a rate of 1 mpy were both located within regions of continuous corrosion product extending from the surface of the seawater pool up the side walls of the boxes. The weight loss data and calculated corrosion rates for the side and bottom seawater pool coupons reflect the extremely variable conditions within these boxes and indicate that measurable corrosion may occur under such conditions even in the presence of a VCI.

Figure 5 shows the weight loss data for the baffle boxes. Although the maximum losses for the coupons in the baffle boxes were lower than those observed for the seawater pool boxes, it is worth noting that the bottom coupons from the baffle boxes required the longest cleaning times. The bottom coupons were covered with an extremely adherent, continuous layer of rust. The 12 month bottom coupons from the control baffle box required roughly 3.5 hours to clean in the HCl solution. In all six of the baffle boxes, including those with VCIs, the bottom coupons were the most heavily corroded coupons in each box. The weight loss data for the six baffle boxes show similar values for duplicate coupons; much less scatter was observed in the data for replicate baffle box coupons than was observed in the data for replicate seawater pool coupons (bottom and side). Overall, the maximum weight loss values observed for coupons from the VCI, baffle boxes are lower than those observed for coupons from the control, baffle boxes. For replicate VCI A, baffle, bottom coupons (11B and 12B), the weight loss values for the 12 month coupons are only marginally higher than the weight loss values for the six month coupons, resulting in lower corrosion rates for 12 months than for six months. In comparison, the replicate bottom coupons in both the control, baffle and VCI B, baffle boxes showed significantly higher weight losses after 12 months than after six months. The corrosion rates for the control, baffle, bottom coupons (5B and 6B) were nearly the same after six and 12 months while the corrosion rates for the VCI B, baffle, bottom coupons (19B and 20B) were higher after 12 months than after six months.

Figure 6 shows the weight loss data for the DEW boxes. Like the other sealed boxes, the DEW boxes showed no measurable weight loss.

Plots of the data obtained from the atmospheric corrosion probes for the first 12 months of the test are provided in Figures 7-10. In these figures, metal loss is plotted as a function of time, so that the slope of the curves gives the corrosion rate. Figures 7-10 include the raw data obtained from the corrosion probes as well as predicted values obtained by performing a linear regression on raw data. It should be noted that the discontinuous curve for Box 17 (VCI B, seawater pool) in Figure 8 is the result of premature failure and replacement of a defective probe element at approximately 260 days. The probe in Box 17 failed prematurely due to crevice corrosion at the base of the steel element, as discussed further at the end of this section. The corrosion rates obtained from the corrosion probes are plotted along with the corrosion rates calculated from the weight loss coupons in the same boxes in Figures 11-13. It should be noted that Figures 11-13 show the corrosion rate data for the ten boxes with corrosion probes (i.e. odd numbered boxes). The corrosion rates calculated from the weight loss

coupons from the other ten boxes (i.e. even numbered boxes) is not plotted, but is included in Tables 2 and 3.

Comparison of the average corrosion rate data collected from the corrosion probes to the data obtained from the weight loss coupons (12-month samples) leads to some interesting observations. Figure 11 shows that in the sealed boxes containing probes, the coupon-based and probe-based corrosion rates are extremely low (nil to 0.04 mpy) and compare reasonably well. For the seawater pool boxes and baffle boxes containing probes, the agreement between the coupon-based and probe-based corrosion rates is not as good, as seen in Figures 12 and 13. Since the probes were installed on the sides of the boxes approximately half way up the wall, one would expect the probes to correlate most closely with the side coupons. Comparison of the bars corresponding to the "S coupon" and "Probe" in Figures 12 and 13, however, shows measurable differences between the two. The corrosion rate obtained from the probe exceeds the corrosion rate of the side coupon by 0.11 to 0.50 mpy (up to 1500%) in the seawater pool and baffle boxes. As a general rule, the bottom coupons in each box had the highest corrosion rates, except for the previously noted disparities in the seawater pool boxes. In the baffle boxes, the average corrosion rate calculated from the probe data was found to exceed the corrosion rates of the bottom coupons. In the seawater pool boxes, the probe-based corrosion rates fell between the corrosion rates of the side and bottom coupons.

As previously noted, the corrosion probe in Box 17 failed after approximately 8.5 months due to crevice corrosion at the base of the element, at the point where the steel element is embedded in a ceramic disk. This failure was deemed by the manufacturer to be premature, due to the severity of the environment within the seawater pool boxes. The failed type 1 probe element was replaced with a new, longer-life type 2 probe element. The probes under test are designed to measure metal loss due to uniform corrosion; they cannot account for rapid, localized penetrations due to crevice corrosion. For this reason, the corrosion rate obtained for Box 17 is considered a best approximation based on the skewed data from the defective probe and the data from the replacement probe. The corrosion rate obtained from the linear regression performed on the two curve segments (0-260 days and 265-360 days) shown in Figure 8 for Box 17 is 0.24 mpy. Linear regressions performed for the data obtained from 0-90 days and 265-360 days yielded corrosion rates of 0.11 mpy and 0.33 mpy. Comparison of these data and consideration of trends observed in other boxes suggest that 0.24 mpy is a reasonable approximation of the corrosion rate for Box 17. Additionally, it should be noted that a second probe failed prematurely in Box 3 (control, seawater pool) just after 12 months of exposure. Again, the cause of failure was crevice corrosion at the steel element/ceramic disk interface. The failed type 2 element was replaced with a new type 2 element. Premature failure of two of the three probes in the seawater pool boxes suggests that the probe design, specifically at the interface of the probe element and the ceramic disk, is not suitable for the severe conditions present in these boxes.

Appearance of Box Interior and Steel Coupons

In general, the condition of the interior walls of the boxes was well reflected by the coupons. A few general points warrant noting. In the sealed cells, very little corrosion was observed on the walls. In some of the boxes, corrosion was seen in the weld areas or in small localized areas. Some of this rust may have occurred during fabrication and shipping of the boxes, despite efforts to prevent such corrosion. During the six and 12 month sample pulls, the layer of VCI A powder remaining on the bottom of the sealed boxes contained numerous browned spots. Discussions with the manufacturer of VCI A revealed that the powder may discolor if it is exposed to temperatures greater

than 50° C for extended periods. Temperature data obtained from thermocouples installed in the VCI A sealed boxes indicated that surface and air temperatures within the boxes exceeded 50° C on several occasions. Alternatively, the discoloration may have resulted from high temperature exposure of the powder prior to installation in the boxes.

In the seawater pool boxes, all three conditions (control, VCI A, VCI B) contained regions of black, finger-like corrosion product on the side walls. This corrosion product originated near the surface of the seawater pool and extended approximately one third to one half way up the side of the wall. Figure 14 shows this type of corrosion, as seen in Box 3 (control, seawater pool) during the six month sample pull. A close-up view of one of the fingers removed for analysis during the six month sample pull is given in Figure 15. Continued growth of the fingers between the six and 12 month samples pulls was evident. The presence of black, nodular corrosion product on several of the weight loss coupons significantly affected the weight loss data. As a general rule, the region of nodular or finger-like product was observed to extend higher up the side walls in the first quadrant, near the north end cover (see Figure 1), than in the second quadrant of any given box. Thus, the first quadrant (six month) side-mounted weight loss coupons samples were more likely to fall within regions of continuous nodular or finger-like corrosion product than the second quadrant (12 month) side-mounted coupons. The surface of the walls above the black finger-like corrosion product was covered with scattered spots of red rust. The seawater pool contained a viscous, sludge-like layer that was rust and/or black in color. A white, crystalline growth was observed on the surface of the seawater pool in Box 17 (VCI B) during the 12 month sample pull.

The interior surfaces of the baffle boxes were covered with varying degrees of corrosion product. After six months of exposure, the bottoms of the baffle boxes for all three conditions (control, VCI A, and VCI B) were covered with a continuous layer of tenacious corrosion product. Chemical cleaning of the bottom coupons from the control baffle boxes required approximately 1 hour for the six month samples and approximately 3.5 hours for the 12 month samples. For both sample pulls, these were the longest required cleaning times. The top and side walls of these boxes were covered with scattered areas of corrosion, as were the top, side, and hanging coupons. In general, the coupons exposed in the control baffle box were more heavily rusted than either of the VCI baffle boxes after both six and 12 months. After six months of exposure, the side, top, and hanging coupons removed from the VCI A baffle boxes contained regions of red and black corrosion product. Similar coupons removed from the VCI B baffle boxes after six months of exposure contained only red corrosion product. After 12 months, the coupons removed from the VCI A baffle boxes contained a higher ratio of red corrosion product to black corrosion product than the six month coupons from the same boxes. The 12 month VCI B coupons again contained only red corrosion product. Additionally, it was observed during the 12 month sample removal that only red corrosion product had formed between months six and 12 on a small area of bare steel in one of the VCI A baffle boxes. Removal of the bottom coupon during the six month pull exposed the underlying bare steel that had been shielded from corrosion for the first six months. This area was covered with only red rust at the time of the 12 month pull, while the rest of the bottom of the box contained a mixture of black and red rust. Discussions with the manufacturer of VCI A revealed that the formation of the black corrosion product on steel exposed to VCI A is not well understood at this time. It should also be noted that very little white VCI powder was visible in the VCI A and VCI B baffle boxes after six months; however, more VCI B powder was visible as piles or clumps on the bottom of the box than VCI A powder.

Appearance of Galvanic Couples

The galvanic couples (c.g. steel/SS 304, c.g. steel/AA 6061-T6, and c.g. steel/90-10 Cu-Ni) suspended from rods in the second quadrant of each box were visually observed and documented during the six and 12 month pulls. In all of the sealed boxes (control, VCI A, VCI B, and DEW), the galvanic couples showed virtually no corrosion, as expected.

In the seawater pool boxes, rust spots were observed scattered across the surface of the steel sample in each of the galvanic couples. The steel samples in the galvanic couples in the VCI A and VCI B, seawater pool boxes appeared to have fewer rust spots than those in the control seawater pool boxes. The Cu-Ni 90-10 sample in the second quadrant c.g. steel/Cu-Ni 90-10 couple in Box 9 (VCI A) was observed to have green corrosion product on its edge during both the six month and 12 month sample pulls. During the 12 month pull, corrosion was also observed on the second quadrant Cu-Ni 90-10 sample in Box 17 (VCI B); green corrosion product formed in the region between the nylon screws. The galvanic couples in the two VCI A, seawater pool boxes were covered with a brownish film of VCI powder which made visual observations difficult. Wiping of the film from one corner of the steel/Cu-Ni 90-10 couple revealed visible pitting beneath the VCI film. VCI A did not remain powdery on the surface of the couples. Rather, it formed a continuous film that was difficult to rub off and required a solvent to remove. As previously noted, VCI A contains an ammonia-based component that may cause attack of copper-based alloys such as Cu-Ni 90-10. Moisture retained by a desiccant component in the VCI A layer covering the suface of the Cu-Ni could exacerbate this effect. In contrast to VCI A, VCI B remained light and powdery on the surfaces of the galvanic couples and did not discolor.

In the control baffle boxes, the steel samples in the couples were heavily covered with rust spots. The couples in the VCI A and VCI B baffle boxes, in comparison, showed only light rusting of the steel samples in the couples. As previously noted, most of the powder appears to be gone in the VCI baffle boxes, but more VCI B powder is visible as piles or clumps on the bottom of the box than VCI A.

Environmental Scanning Electron Microscope (ESEM) and Energy Dispersive X-ray (EDX) Analysis of Corrosion Product

Intact samples of the black finger-like corrosion products observed on walls of the seawater pool boxes were analyzed during the six month pull using an ESEM and EDX. As a basis for comparison, the same analysis was performed on a control sample which had the same cleaning and blasting treatment as the boxes and weight loss coupons prior to exposure. The results of the EDX analysis of the finger-like corrosion product indicated that the composition of the product is in similar proportion to the control sample. The corrosion product does, however, show the presence of a significant amount of chloride ion as compared to the other detectable trace elements of the base material. EDX of the control specimen indicated a high proportion of silicon ions, which is an indication of the presence of impinged blast media.

Photographs and the location and orientation of the finger-like corrosion product suggest that they were formed due to condensation on the sides of the boxes. The EDX analysis of the corrosion product is consistent with water droplets condensing on the side of the boxes containing chloride ions and iron ions in suspension. Upon the next heating cycle of the box, these ions in suspension would

plate out at the droplet condensation site. The fingers were notably longer after 12 months than after six months.

Temperature and Relative Humidity (RH) Data

The data collected from the RH sensors and thermocouples were reduced by calculating the average (mean), maximum, and minimum values for each 10-day interval during the 360 day (12 month) period. The average, maximum, and minimum values of RH, air temperature, and surface temperature were plotted for each box. Representative plots for selected boxes are provided in Figures 16-21.

RH Data for Control Boxes - The RH data collected from the control boxes throughout the first 12 months of exposure met expectations. Representative plots of the RH data are provided for Box 2 (control, sealed), Box 3 (control, seawater pool) and Box 5 (control, baffles) in Figures 16, 17, and 18, respectively. The RH data (maximum, average, and minimum curves) for the control, seawater pool boxes were notably higher than the RH data for the control, sealed boxes. This trend may be observed by comparing the plots for Box 2 (Figure 16) and Box 3 (Figure 17). The difference between the maximum and minimum RH curves for the control, baffle boxes was greater than the difference between the control, sealed boxes. In addition, the average and maximum RH values for the control, baffle boxes were notably higher than the respective values for the control, sealed boxes, due to ingress of ambient humid air into the baffle boxes. Comparison of the data for Box 2 (Figure 16) and Box 5 (Figure 18) reveals these trends. In the following discussion, the difference between the maximum and minimum RH curves for a given box will be referred to as the RH envelope. Several meaningful observations can be made based on comparison of the RH data for the VCI and DEW boxes to the control boxes.

RH Data for VCI A Boxes - The RH data for the VCI A boxes was found to be significantly lower than the RH data for the control boxes. Additionally, the size or width of the RH envelope was observed to be smaller for the VCI A boxes than for the controls. This trend was observed across the board for all three environmental test conditions, with the sealed boxes showing the most pronounced effect. A representative plot of the RH data obtained from Box 8 (VCI A, sealed) is provided in Figure 19. Comparison of RH data for Figure 19 to Figure 16 shows that the average RH curve for Box 8 lies 5-15% RH below the average RH curve for Box 2 (control, sealed). Additionally, the width of the RH envelope for Box 8 varies from 15-20% RH, while the RH envelope for Box 2 varies from 40-50% RH. Similar trends are observed when comparing the VCI A and control baffle boxes and seawater pool boxes. The seawater pool boxes showed the least reduction in RH due to VCI A; the average, maximum, and minimum RH curves for the VCI A boxes were shifted nominally 10% lower than the controls while the RH envelope was roughly the same (10-15% RH) for both conditions. It should be noted that the seawater pool boxes saw the highest humidity levels, with the maximum RH value reaching 100% in nearly all of the intervals. The observed reduction in RH due to VCI A was confirmed by the manufacturer to be due a desiccant in the powder.

RH Data for VCI B Boxes - Comparison of the RH data for VCI B and control boxes shows little to no decrease in the average RH and only a slight reduction in the size of the RH envelopes for the VCI B boxes. The average RH curve for Box 16 (VCI B, sealed), shown in Figure 20, tracks below or just slightly above the average RH curve for Box 2 (control, sealed), shown in Figure 16, for the first 250 days. The increase in humidity observed in Box 16 at the 260 day point was due to a

leak that developed around one of the sensors. After the leak was repaired, the RH began to decrease. The width of the RH envelope for Box 16 is on average only 5-10% smaller than the RH envelope for Box 2. Similar trends are seen for the VCI B baffle boxes and seawater pool boxes.

RH Data for DEW Unit - As expected, the RH data obtained from Box 13 (DEW unit), shown in Figure 21, remained stable around 30% RH throughout the 12 month period. The slight increase in maximum RH in the last interval was caused by the brief opening of the box in August to remove the 12 month samples. The size of the RH envelope for Box 13 varied from 2-5% RH.

Temperature Data - Comparison of the temperature data for all of the boxes did not reveal any significant trends. Two minor points are, however, worth noting. First, in most cases, the surface temperature and air temperature curves for the boxes are very close in magnitude, and they show similar trends. Although the maximum temperature curves in some of the boxes show more scatter than the mean and minimum temperature curves, as primarily seen in the maximum surface temperature curves, these deviations are not thought to be significant and are believed to have emerged as a result of the data reduction performed over 10-day intervals. Representative plots of temperature data are provided for Boxes 2 and 13 in Figures 16 and 21, respectively. Second, the width of the air temperature envelopes for the DEW unit (Boxes 13 and 14) was observed to be notably smaller than the width of the envelopes for the other boxes. See Figure 21. This is likely due to continuous recirculation of warmed process air through the DEW unit.

CONCLUSIONS

The following conclusions are reached, based on 12 months of ADH field test data.

1. All of the sealed boxes are performing well, as evidenced by low corrosion rates and little to no visible rusting of the coupons and box walls. In the ideal case of air filled, sealed compartments, corrosion rates remained so low throughout the 12 month period that the presence of a VCI made little difference. The effect of a VCI may become evident over longer exposure periods.

2. The DEW unit is performing extremely well and is maintaining a stable relative humidity of 30%. No corrosion has been observed on the coupons or box walls, and the corrosion rates are negligible. The DEW unit is currently being evaluated only in the sealed box condition; thus, the outstanding performance reported for the DEW system applies only to ideal (sealed) compartments.

3. Compared to controls, the presence of the VCIs in the seawater pool and baffle boxes was found to reduce the maximum observed corrosion rates. In the baffle boxes, the presence of the VCIs reduced the maximum corrosion rates from 0.4 mpy (control) to 0.2 mpy (VCI A) or 0.3 mpy (VCI B). In the seawater pool boxes, the VCIs reduced the maximum corrosion rate (excluding submerged bottom coupons) from 4 mpy (control) to 1 mpy (VCIs A and B). Although the corrosion rates were reduced, neither of the VCIs under test was able to adequately protect bare steel under the extreme conditions within the seawater pool and baffle boxes. Significant amounts of corrosion were observed on the coupons and interior walls of the seawater pool and baffle boxes with VCIs. Furthermore, comparison of the maximum

corrosion rates observed for VCIs A and B in the baffle and seawater pool boxes indicate little if any difference between the two inhibitor formulations.

4. Conditions within the seawater pool boxes are extremely variable and lead to the highest observed corrosion rates. Side-mounted coupons showed extreme variability, with corrosion rates ranging from 0.2 mpy to 4 mpy in the control boxes and 0.06 mpy to 1 mpy in the VCI A and B boxes. Top and hanging coupons within the control and VCI boxes showed very low or negligible corrosion rates, with values ranging from 0.03 to 0.08 mpy for the controls, 0.02 to 0.04 mpy for VCI A, and 0.01 to 0.06 mpy for VCI B. Finger-like corrosion products were observed in all seawater pool boxes, including those containing VCI A and VCI B.

5. Corrosion of the Cu-Ni 90-10 sample coupled to c.g. steel was observed in both VCI A and VCI B seawater pool boxes. This may become an issue if Cu-Ni hardware or piping is to be installed in ADH compartments.

6. VCI A was observed to reduce the relative humidity within the boxes and to maintain a more stable humidity level (i.e. smaller RH envelope) over time. This trend was observed in all of the VCI A boxes (sealed, seawater pool, and baffles) and has been attributed to a desiccant in the powder. The data for VCI B showed only a slight reduction in relative humidity in only some of the boxes. To the knowledge of the authors, VCI B does not contain a desiccant. Despite their reduced humidity levels, boxes containing VCI A showed little difference in maximum corrosion rates than boxes containing VCI B.

7. Corrosion rate data collected from the commercial atmospheric corrosion probes does not correlate well with corrosion rates calculated from the weight loss coupons. Additionally, two of the 11 probes under test have failed prematurely due to crevice corrosion at the base of the element. Both of the failed probes were used to monitor seawater pool boxes. The observed limitations of the probes indicate a need for further investigation of alternative sensing devices for remote monitoring of corrosion within ADH compartments.

ACKNOWLEDGMENTS

The authors wish to acknowledge the Naval Sea Systems Command (NAVSEA) Code O3P4 as the sponsors of this effort. The authors thank Cortec Corporation and Corroless International Ltd for providing free samples of their products for testing.

REFERENCES

1. B. A. Miksic, "Some Aspects of Metal Protection by Vapor Phase Inhibitors," Anticorrosion Methods and Materials, 22, 3 (March 1975).

2. G. E. Fodor, "The Inhibition of Vapor-Phase Corrosion: A Review," Belvoir Fuels and Lubricants Research Facility, Southwest Research Institute, San Antonio, Texas, 1985.

3 . M. Ohaly and C. J. Moench, Jr., "Long-Term Mothballing of Production Facilities in a Marine Environment," SPE 15987, Fifth SPE Middle East Oil Show (Richardson, TX: SPE, 1987) pp. 709-715.

4. H. Hack et. al., "Corrosion Control on Advance Double-Hull Commercial Tankers and Combatants," Naval Surface Warfare Center, Carderock Division, Technical Report, NSWCCD-TR-61-95/13, March 1996.

5. American Society for Testing and Materials (ASTM) Standard G1-90, "Standard Practice for Preparing, Cleaning, and Evaluating Corrosion Test Specimens," Annual Book of ASTM Standards, 03.02 (1991): pp. 35-41.

Table 1. ADH Test Chamber Matrix

Box No.	Environment/Condition	Surf. T Sensors	Air T Sensors	RH Sensors	Corrosion Sensors
1	Control, Sealed	1	1	1	2 (type 1 & 2)
2	Control, Sealed	1	1	1	
3	Control, Seawater Pool	1	1	1	1 (type 2)
4	Control, Seawater Pool	1	1	1	
5	Control, Baffles (air vents)	1	1	1	1 (type 2)
6	Control, Baffles (air vents)	1	1	1	
7	VCI A, Sealed	1	1	1	1 (type 1)
8	VCI A, Sealed	1	1	1	
9	VCI A, Seawater Pool	1	1	1	1 (type 1)
10	VCI A, Seawater Pool	1	1	1	
11	VCI A, Baffles (air vents)	1	1	1	1 (type 2)
12	VCI A, Baffles (air vents)	1	1	1	
13	DEW, Sealed	1	1	1	1 (type 1)
14	DEW, Sealed	1	1		
15	VCI B, Sealed	1	1	1	1 (type 1)
16	VCI B, Sealed	1	1	1	
17	VCI B, Seawater Pool	1	1	1	1 (type 1)*
18	VCI B, Seawater Pool	1	1	1	
19	VCI B, Baffles (air vents)	1	1	1	1 (type 2)
20	VCI B, Baffles (air vents)	1	1	1	
	Outside			1	

*replaced with type 2 element after 8.5 months

Table 2. Six Month Mass Loss and Corrosion Rate Data (Boxes 1-10)

Box ID	Sample ID	Wt. Loss for 6 mo. (g)	Corrosion Rate calc. from wt. loss (mpy)	Corrosion Rate from sensor data (mpy)
1	1B1	-0.003	-0.002	0.012 0.010
	1H1	-0.004	-0.003	
	1S1	0.001	0.001	
	1T1	-0.004	-0.003	
2	2B1	0.061	0.047	no sensor
	2H1	0.019	0.014	
	2S1	-0.007	-0.005	
	2T1	-0.003	-0.002	
3	3B1	2.198	1.707	0.956
	3H1	0.100	0.076	
	3S1	0.315	0.238	
	3T1	0.058	0.044	
4	4B1	2.337	1.767	no sensor
	4H1	0.074	0.056	
	4S1	0.270	0.203	
	4T1	0.055	0.041	
5	5B1	0.566	0.427	0.619
	5H1	0.262	0.198	
	5S1	0.117	0.090	
	5T1	0.238	0.179	
6	6B1	0.553	0.417	no sensor
	6H1	0.221	0.167	
	6S1	0.126	0.095	
	6T1	0.280	0.211	
7	7B1	0.023	0.018	-0.002
	7H1	-0.008	-0.006	
	7S1	-0.008	-0.006	
	7T1	-0.010	-0.008	
8	8B1	-0.006	-0.005	no sensor
	8H1	-0.012	-0.009	
	8S1	-0.009	-0.007	
	8T1	-0.010	-0.008	
9	9B1	0.511	0.385	0.247
	9H1	0.036	0.027	
	9S1	0.077	0.058	
	9T1	0.039	0.029	
10	10B1	1.129	0.851	no sensor
	10H1	0.026	0.020	
	10S1	1.395	1.053	
	10T1	0.043	0.032	

Table 2. Six Month Mass Loss and Corrosion Rate Data (Boxes 11-20)

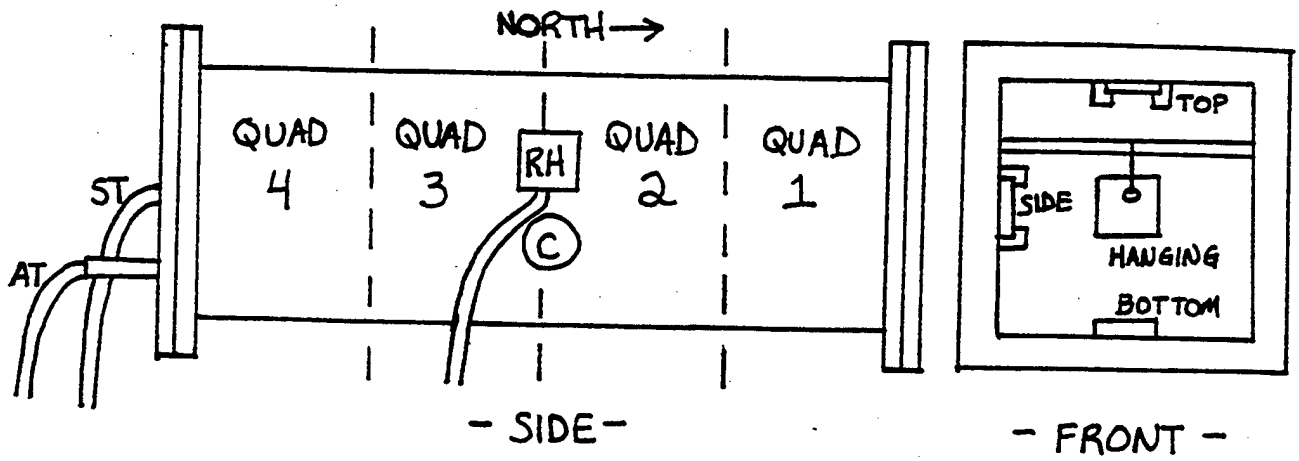
Box ID	Sample ID	Wt. Loss for 6 mo. (g)	Corrosion Rate calc. from wt. loss (mpy)	Corrosion Rate from sensor data (mpy)
11	11B1	0.309	0.233	0.125
	11H1	0.124	0.093	
	11S1	0.045	0.034	
	11T1	0.097	0.073	
12	12B1	0.404	0.305	no sensor
	12H1	0.134	0.103	
	12S1	0.041	0.031	
	12T1	0.071	0.054	
13	13B1	-0.011	-0.008	0.037
	13H1	-0.011	-0.008	
	13S1	-0.005	-0.004	
	13T1	-0.011	-0.008	
14	14B1	-0.011	-0.008	no sensor
	14H1	-0.005	-0.004	
	14S1	-0.008	-0.006	
	14T1	-0.011	-0.008	
15	15B1	-0.008	-0.006	0.011
	15H1	-0.007	-0.005	
	15S1	-0.006	-0.005	
	15T1	-0.003	-0.002	
16	16B1	-0.007	-0.005	no sensor
	16H1	0.001	0.001	
	16S1	0.001	0.001	
	16T1	0.000	0.000	
17	17B1	0.893	0.673	0.480
	17H1	0.033	0.025	
	17S1	1.277	0.964	
	17T1	0.075	0.057	
18	18B1	1.122	0.846	no sensor
	18H1	0.063	0.048	
	18S1	0.108	0.082	
	18T1	0.060	0.045	
19	19B1	0.260	0.197	0.305
	19H1	0.091	0.069	
	19S1	0.049	0.037	
	19T1	0.059	0.044	
20	20B1	0.257	0.193	no sensor
	20H1	0.068	0.051	
	20S1	0.057	0.043	
	20T1	0.088	0.066	

Table 3. Twelve Month Mass Loss and Corrosion Rate Data (Boxes 1-10)

Box ID	Sample ID	Wt. Loss for 12 mo. (g)	Corrosion Rate calc. from wt. loss (mpy)	Corrosion Rate from sensor data (mpy)
1	1B2	0.028	0.011	-0.002 0.005
	1H2	0.036	0.014	
	1S2	0.049	0.019	
	1T2	0.028	0.011	
2	2B2	0.031	0.012	no sensor
	2H2	0.030	0.012	
	2S2	0.029	0.011	
	2T2	0.019	0.007	
3	3B2	3.280	1.258	1.132
	3H2	0.089	0.034	
	3S2	2.251	0.863	
	3T2	0.218	0.084	
4	4B2	5.926	2.273	no sensor
	4H2	0.089	0.034	
	4S2	10.027	3.845	
	4T2	0.124	0.047	
5	5B2	0.990	0.379	0.548
	5H2	0.208	0.080	
	5S2	0.157	0.060	
	5T2	0.433	0.166	
6	6B2	1.057	0.405	no sensor
	6H2	0.245	0.094	
	6S2	0.213	0.082	
	6T2	0.581	0.223	
7	7B2	-0.002	-0.001	0.005
	7H2	0.094	0.036	
	7S2	0.015	0.006	
	7T2	0.017	0.007	
8	8B2	0.018	0.007	no sensor
	8H2	0.027	0.010	
	8S2	-0.001	0.000	
	8T2	0.015	0.006	
9	9B2	1.762	0.676	0.146
	9H2	0.108	0.042	
	9S2	0.090	0.035	
	9T2	0.110	0.042	
10	10B2	1.916	0.735	no sensor
	10H2	0.070	0.027	
	10S2	0.125	0.048	
	10T2	0.080	0.031	

Table 3. Twelve Month Mass Loss and Corrosion Rate Data (Boxes 11-20)

Box ID	Sample ID	Wt. Loss for 6 mo. (g)	Corrosion Rate calc. from wt. loss (mpy)	Corrosion Rate from sensor data (mpy)
11	11B2	0.411	0.158	0.183
	11H2	0.140	0.054	
	11S2	0.045	0.017	
	11T2	0.132	0.050	
12	12B2	0.508	0.195	no sensor
	12H2	0.126	0.048	
	12S2	0.037	0.014	
	12T2	0.101	0.039	
13	13B2	-0.016	-0.006	-0.004
	13H2	-0.012	-0.005	
	13S2	-0.006	-0.002	
	13T2	-0.011	-0.004	
14	14B2	-0.006	-0.002	no sensor
	14H2	0.018	0.007	
	14S2	-0.009	-0.003	
	14T2	0.045	0.017	
15	15B2	0.051	0.020	0.014
	15H2	0.019	0.007	
	15S2	0.047	0.018	
	15T2	0.025	0.010	
16	16B2	0.016	0.006	no sensor
	16H2	-0.019	-0.007	
	16S2	0.004	0.002	
	16T2	0.020	0.008	
17	17B2	1.538	0.590	0.238
	17H2	0.030	0.012	
	17S2	0.161	0.062	
	17T2	0.049	0.019	
18	18B2	4.158	1.594	no sensor
	18H2	0.111	0.043	
	18S2	1.090	0.418	
	18T2	0.073	0.028	
19	19B2	0.782	0.300	0.337
	19H2	0.079	0.030	
	19S2	0.052	0.020	
	19T2	0.094	0.036	
20	20B2	0.673	0.258	no sensor
	20H2	0.116	0.044	
	20S2	0.024	0.009	
	20T2	0.136	0.052	



KEY: RH = RELATIVE HUMIDITY PROBE
C = CORROSION (METAL LOSS) PROBE
ST = SURFACE TEMPERATURE THERMOCOUPLE
AT = AIR TEMPERATURE THERMOCOUPLE

Figure 1. Schematic of an ADH Box (Side and Front Views)

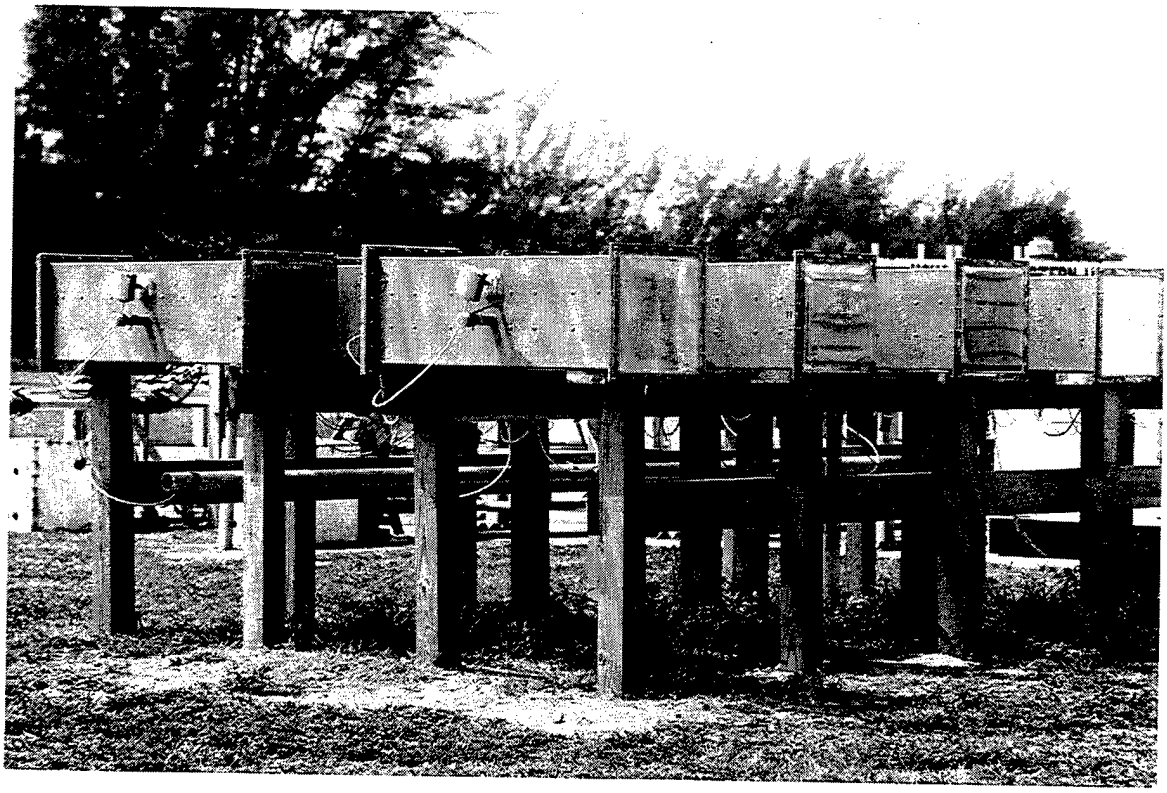
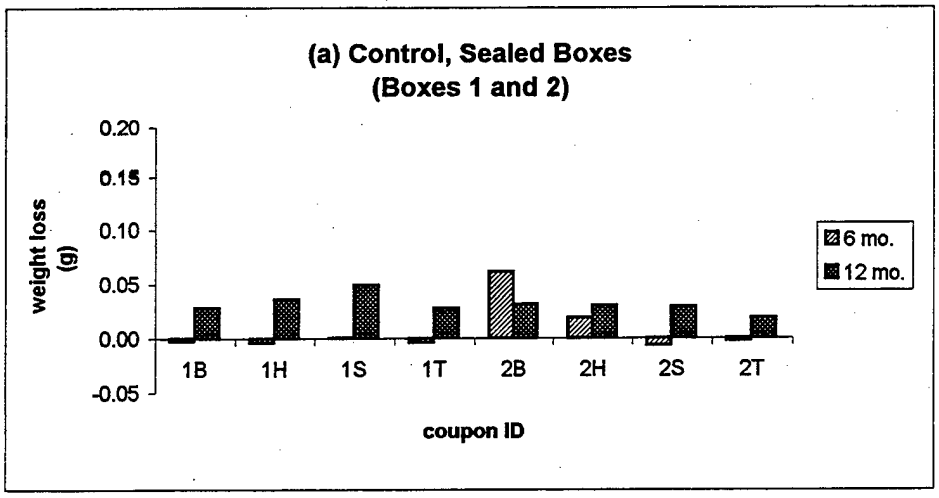
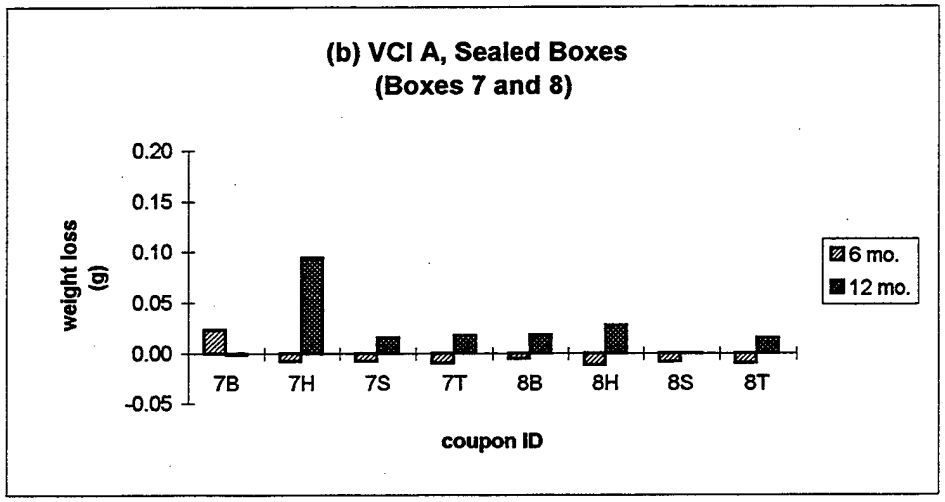


Figure 2. ADH Boxes on Test Racks at the Marine Corrosion Test Site





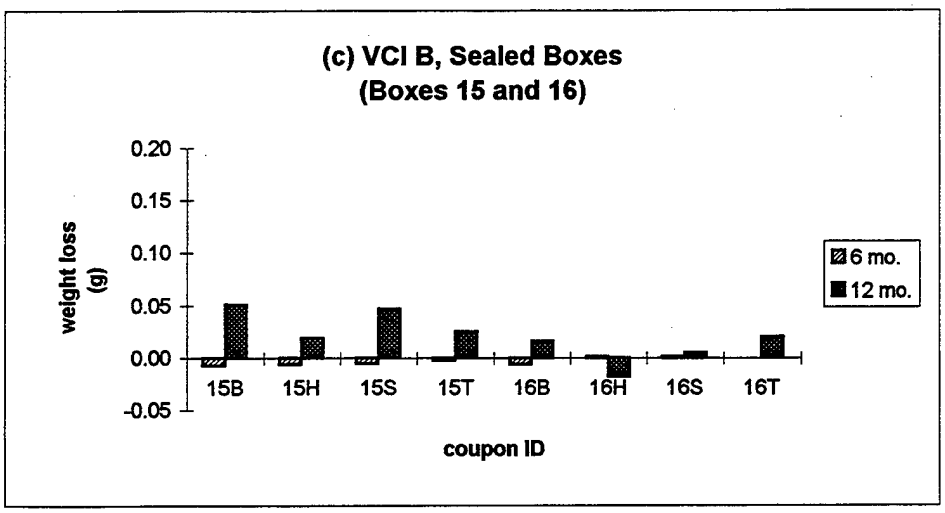
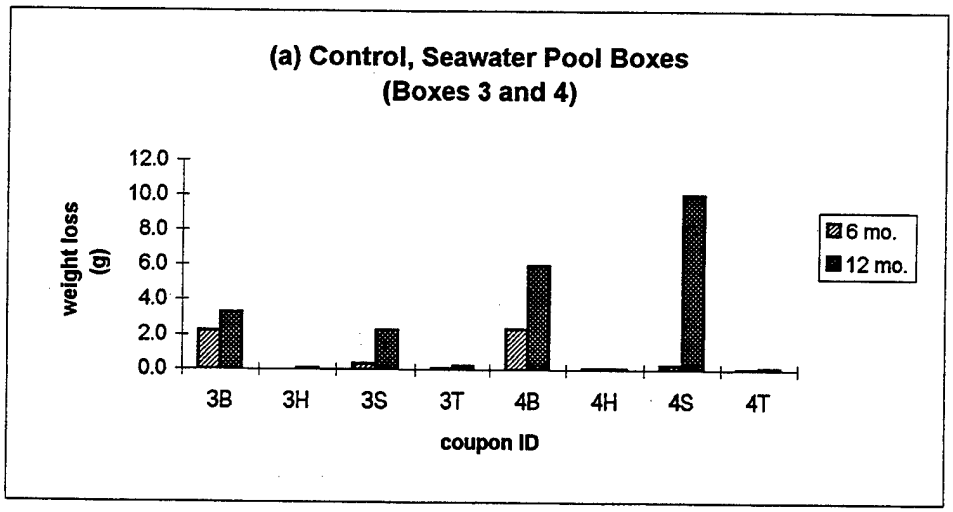
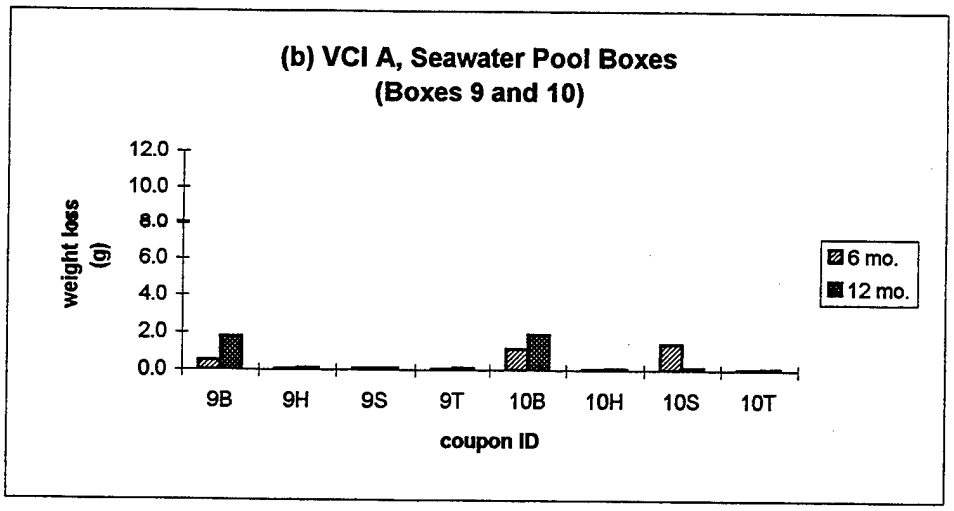


Figure 3. (a-c) Weight Loss Data for Sealed Boxes





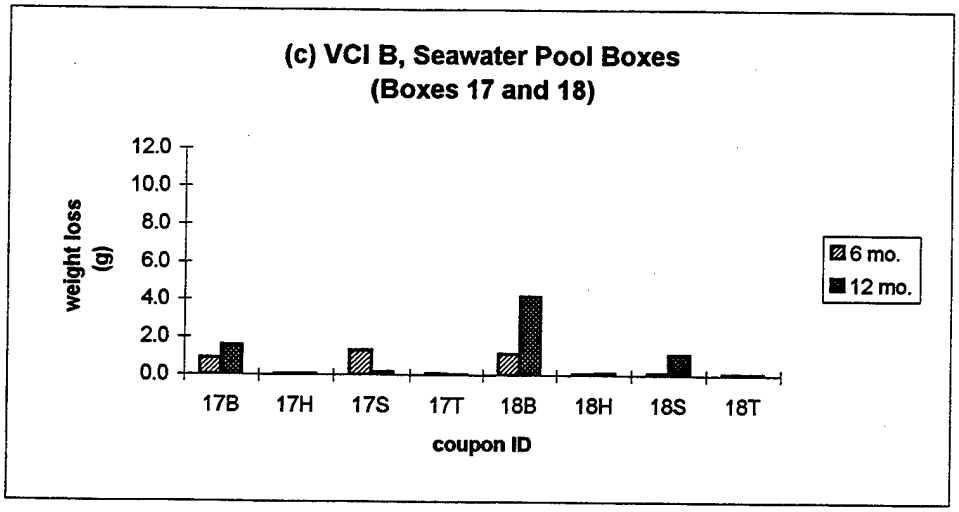
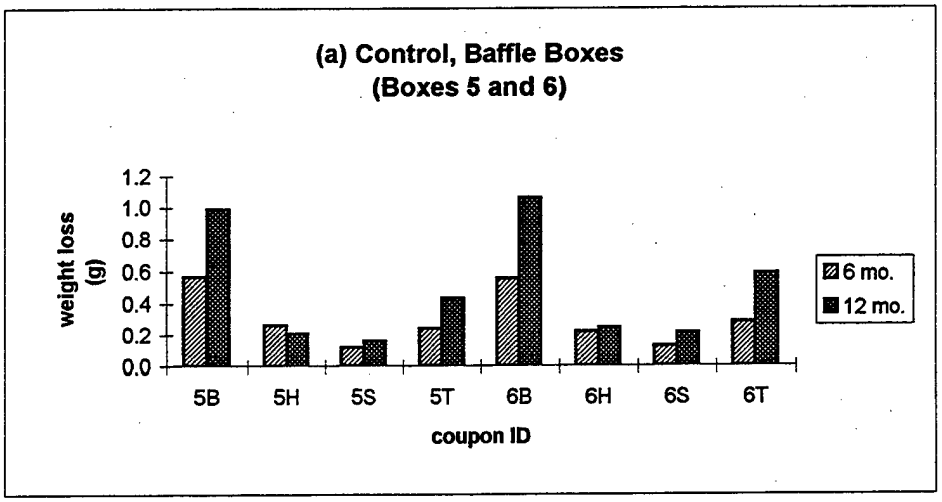
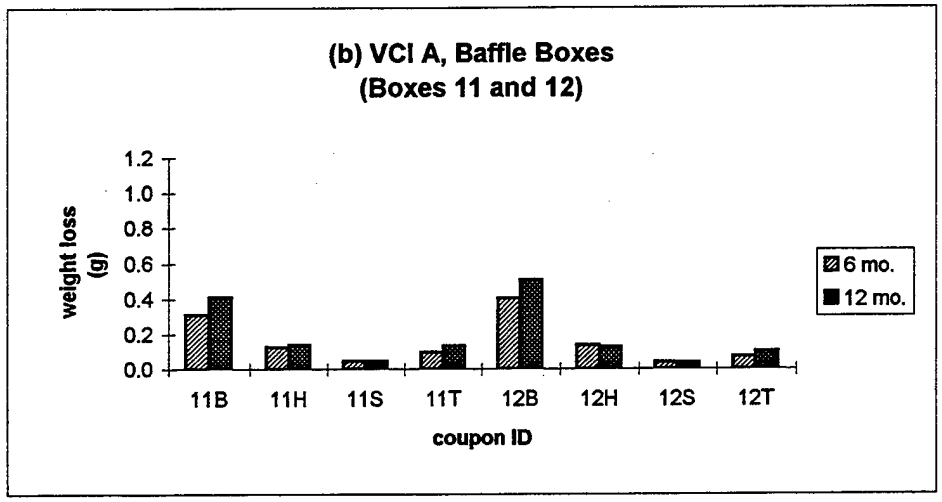


Figure 4. (a-c) Weight Loss Data for Seawater Pool Boxes





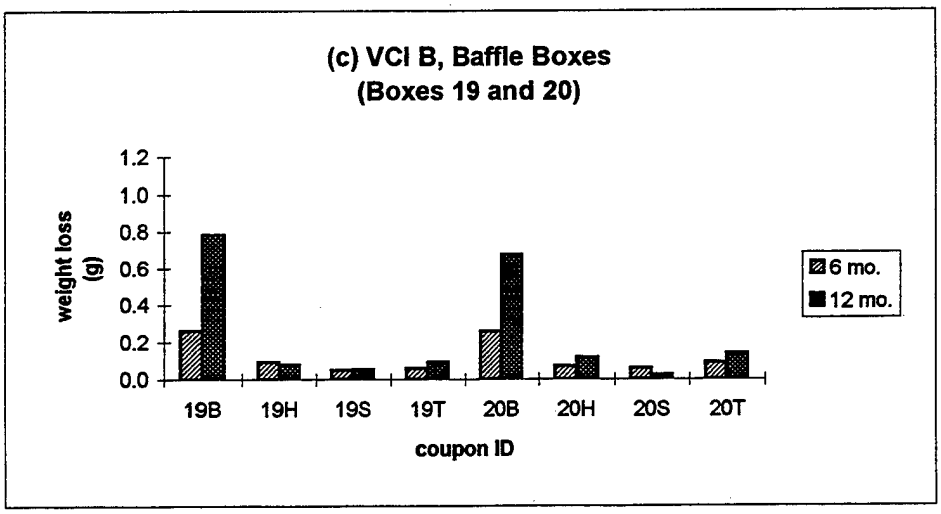


Figure 5. (a-c) Weight Loss Data for Baffle Boxes

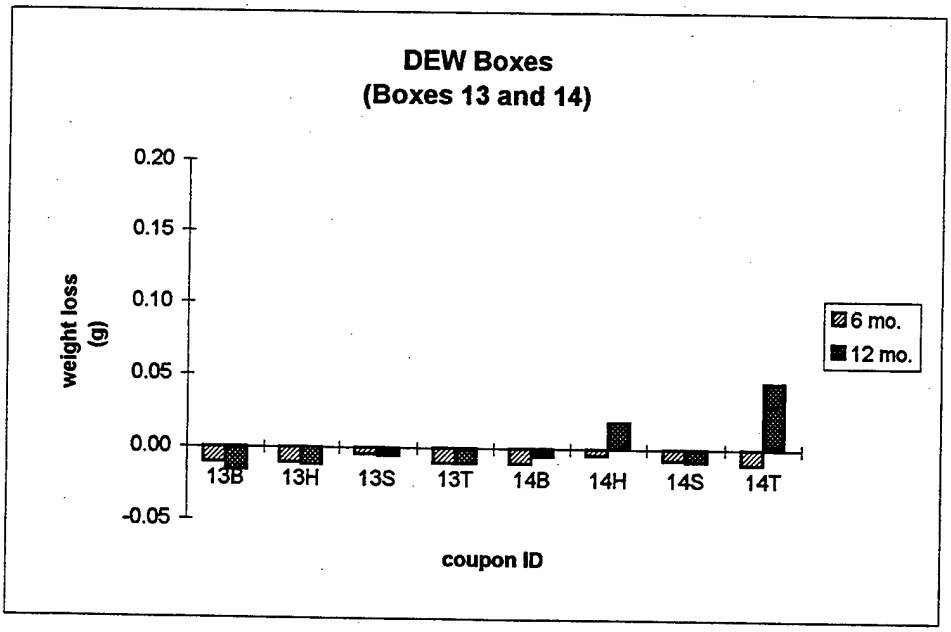


Figure 6. Weight Loss Data for Dew Unit Boxes

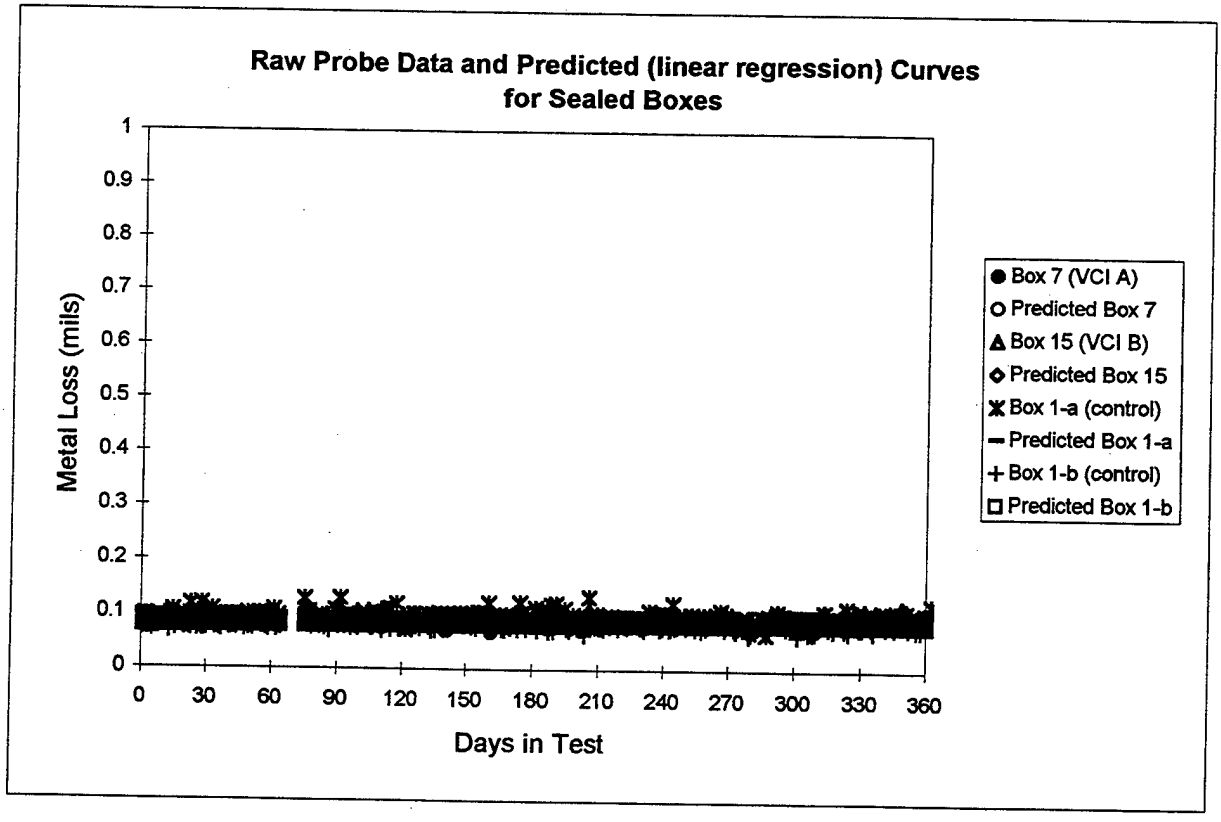


Figure 7. Atmospheric Corrosion Probe Data for Sealed Boxes

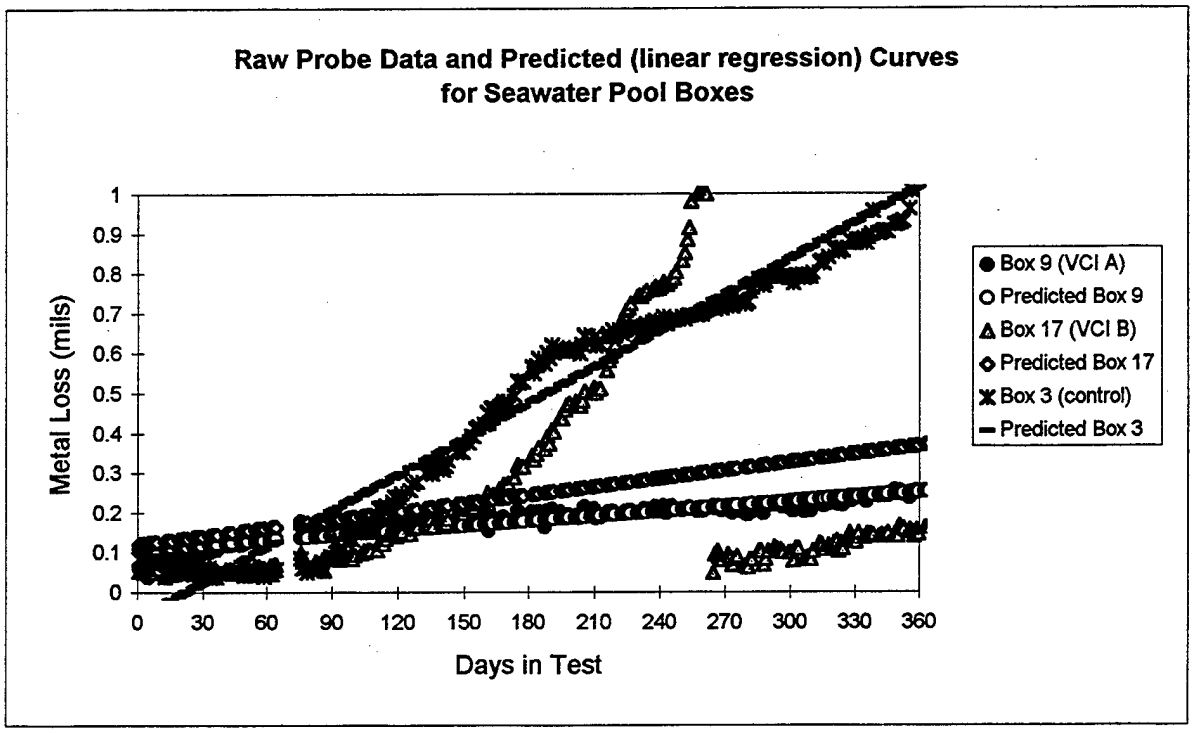


Figure 8. Atmospheric Corrosion Probe Data for Seawater Pool Boxes

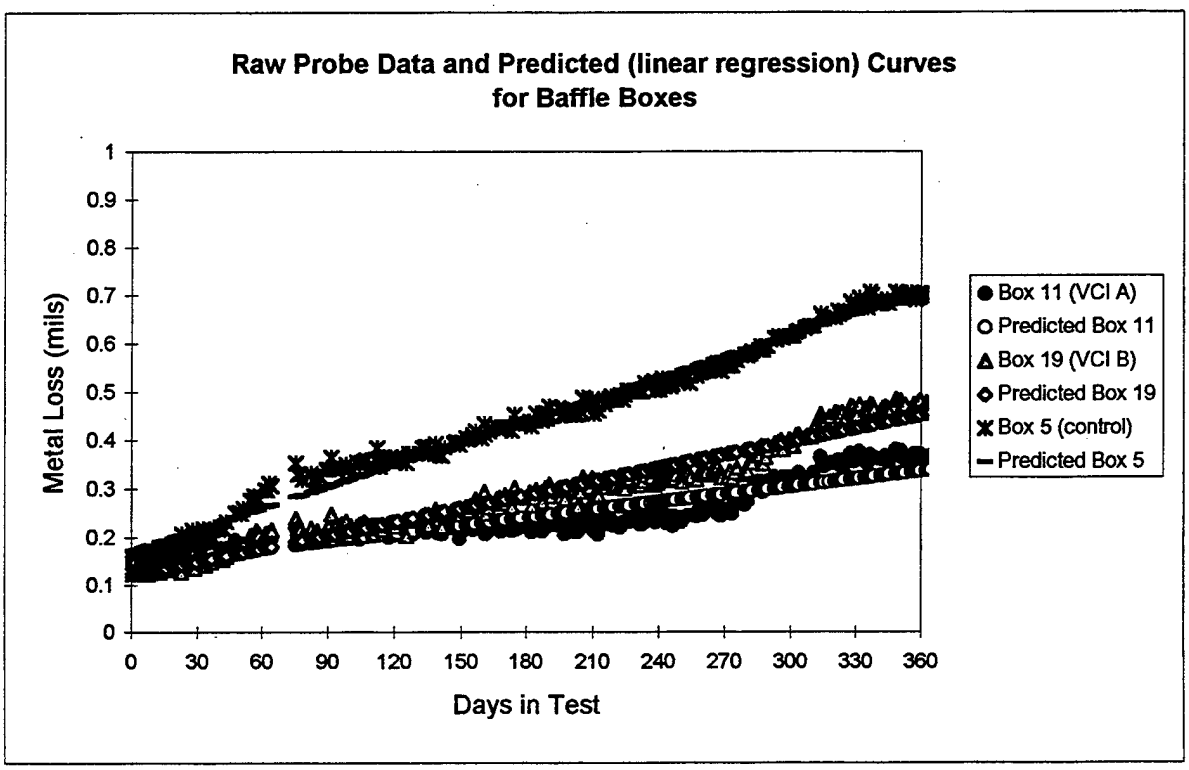


Figure 9. Atmospheric Corrosion Probe Data for Baffle Boxes

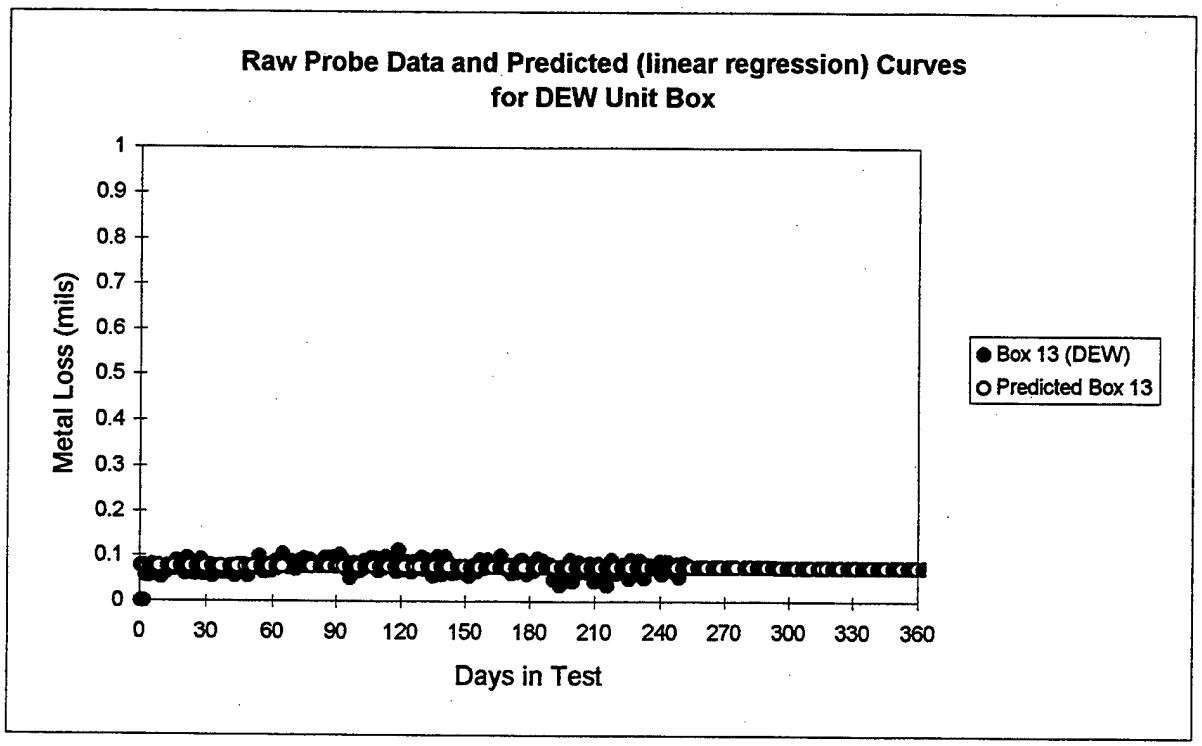


Figure 10. Atmospheric Corrosion Probe Data for DEW Unit Box

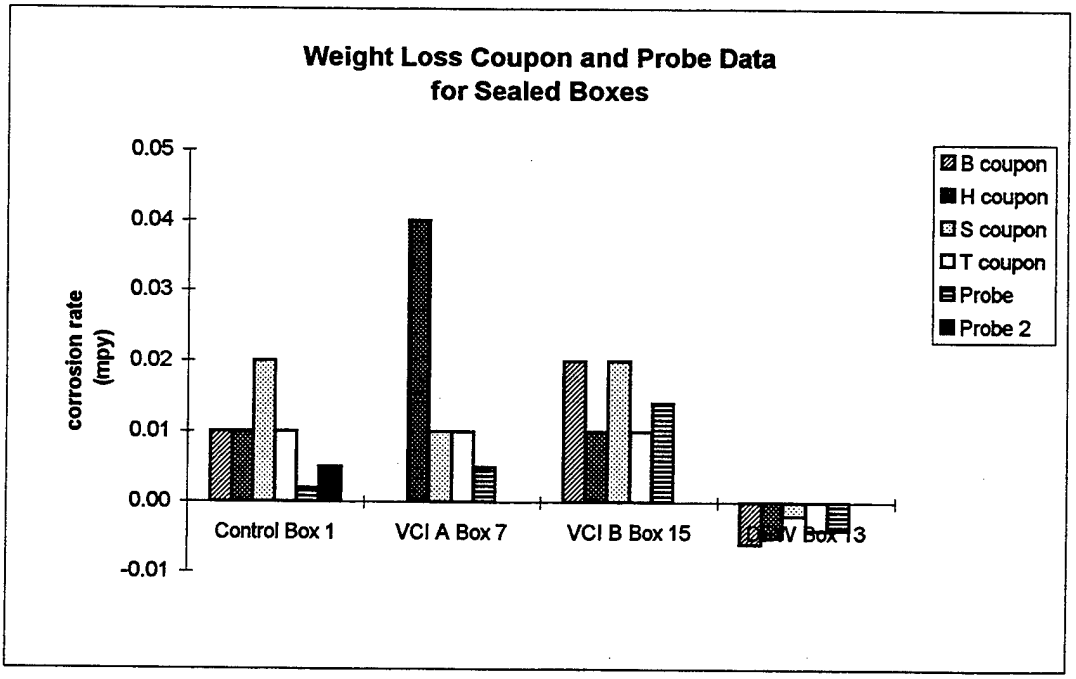


Figure 11. Calculated Corrosion Rates for Sealed Boxes (based on 12 month data)

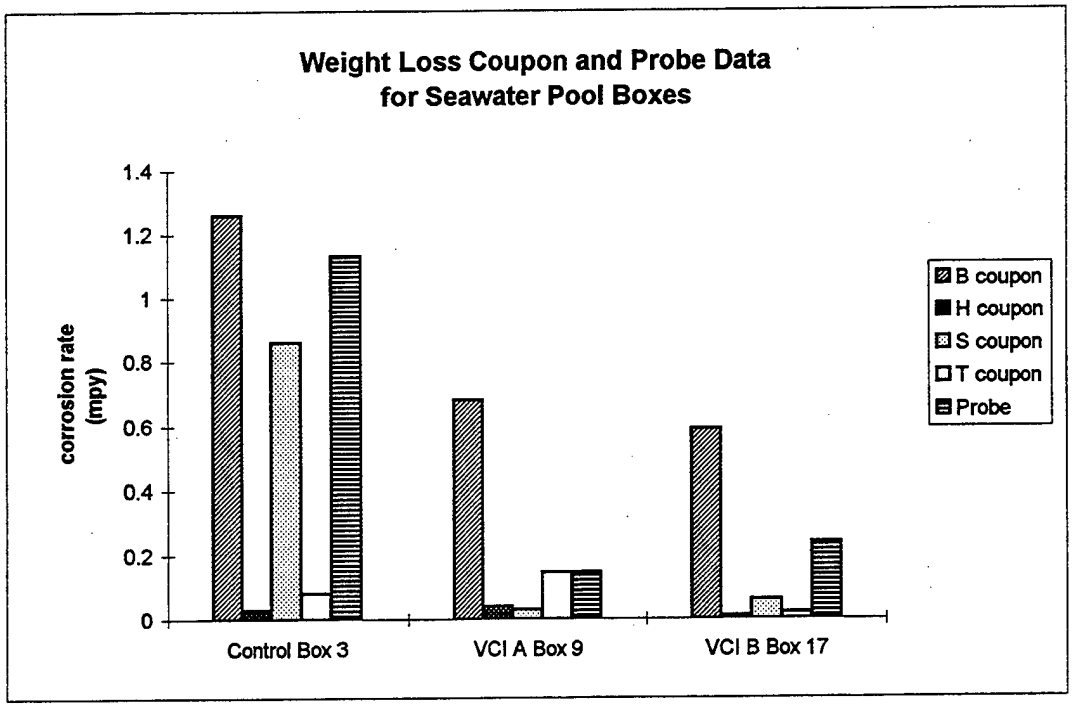


Figure 12. Calculated Corrosion Rates for Seawater Pool Boxes (based on 12 month data)

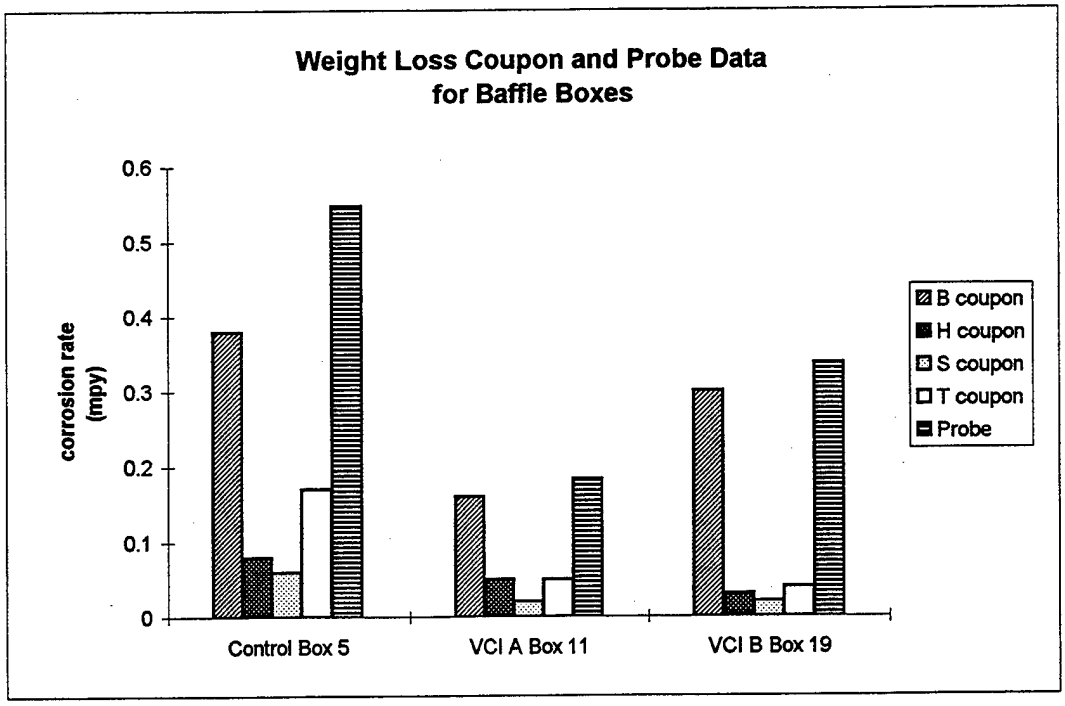


Figure 13. Calculated Corrosion Rates for Baffle Boxes (based on 12 month data)



Figure 14. Finger-like Corrosion Product in Box 3 (Control, Seawater Pool)

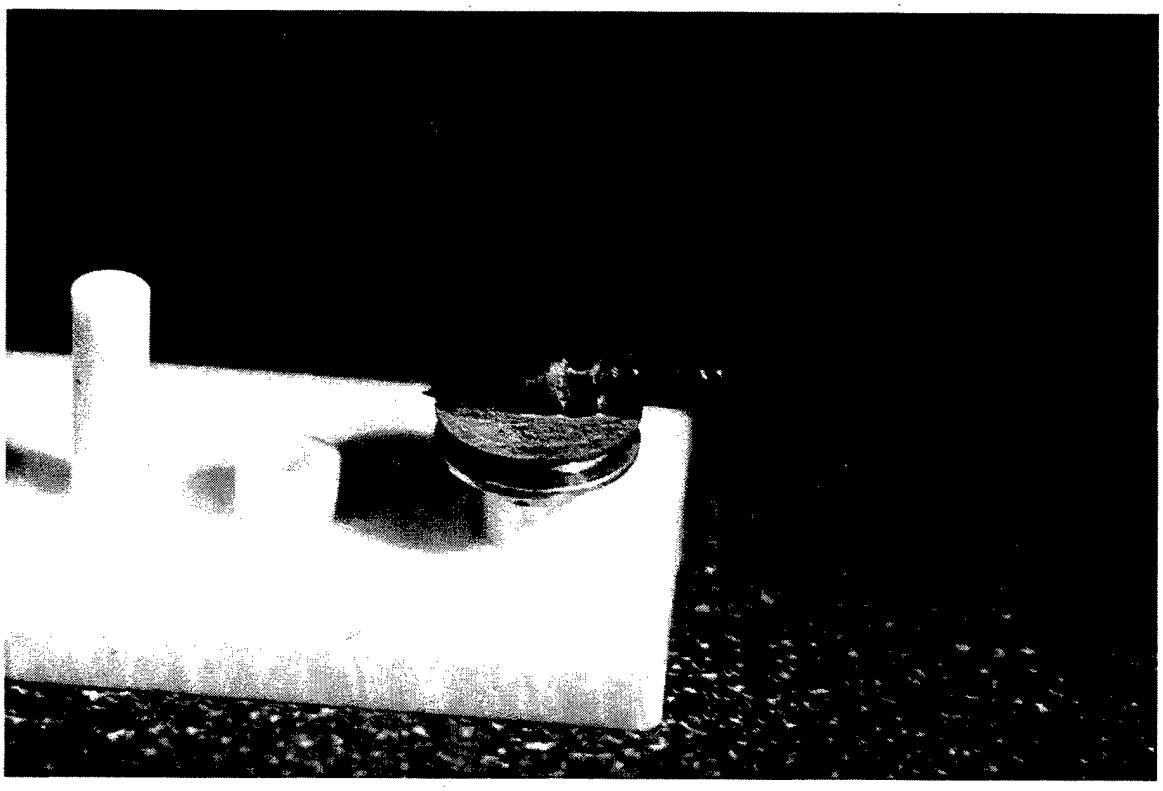
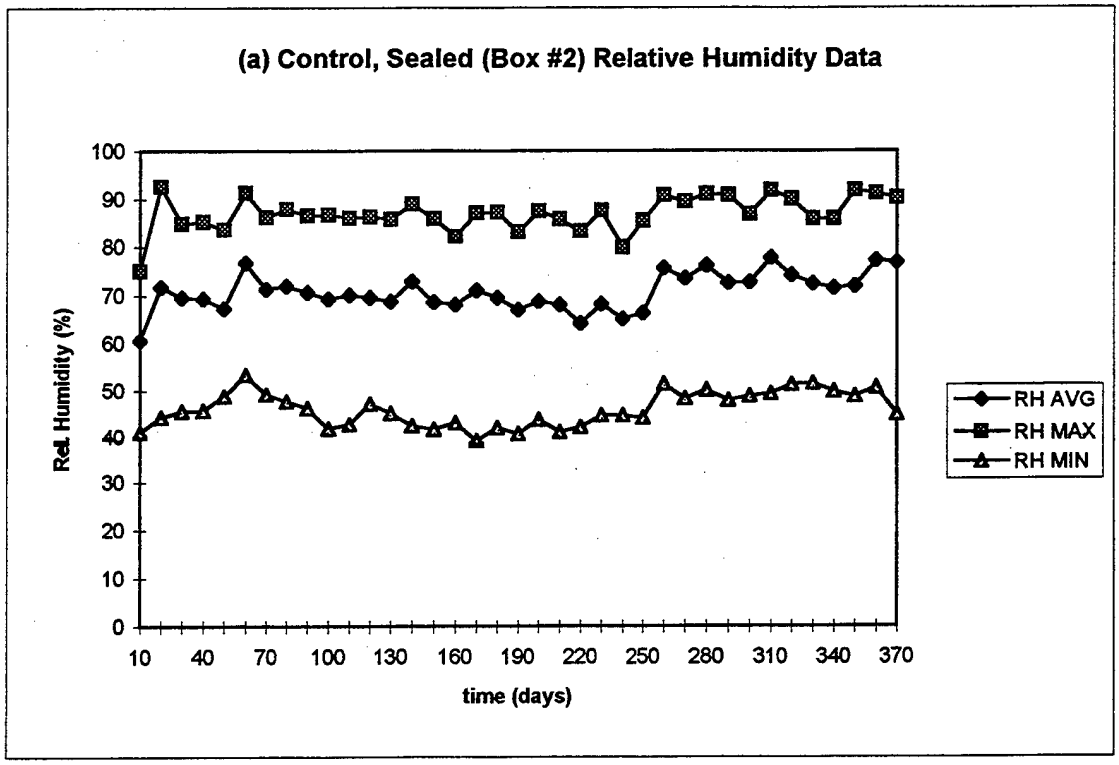


Figure 15. Close-up of Finger-like Corrosion Product



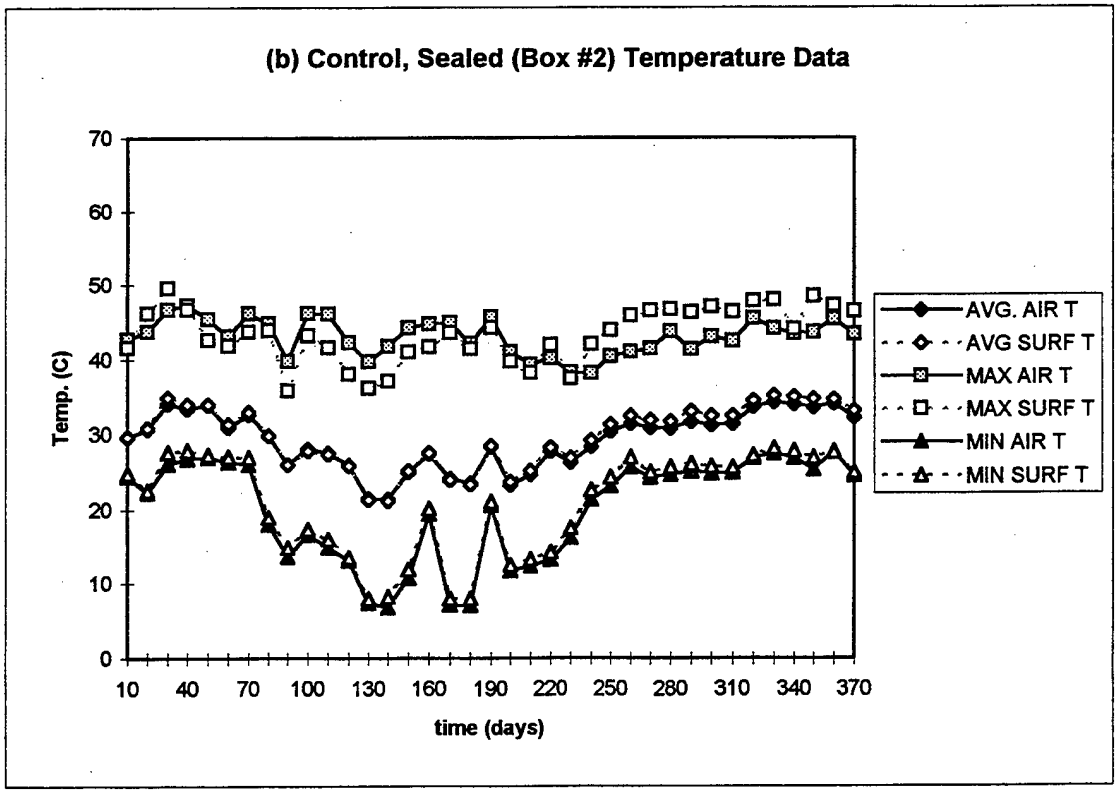


Figure 16. (a-b) Relative Humidity and Temperature Data for Box 2

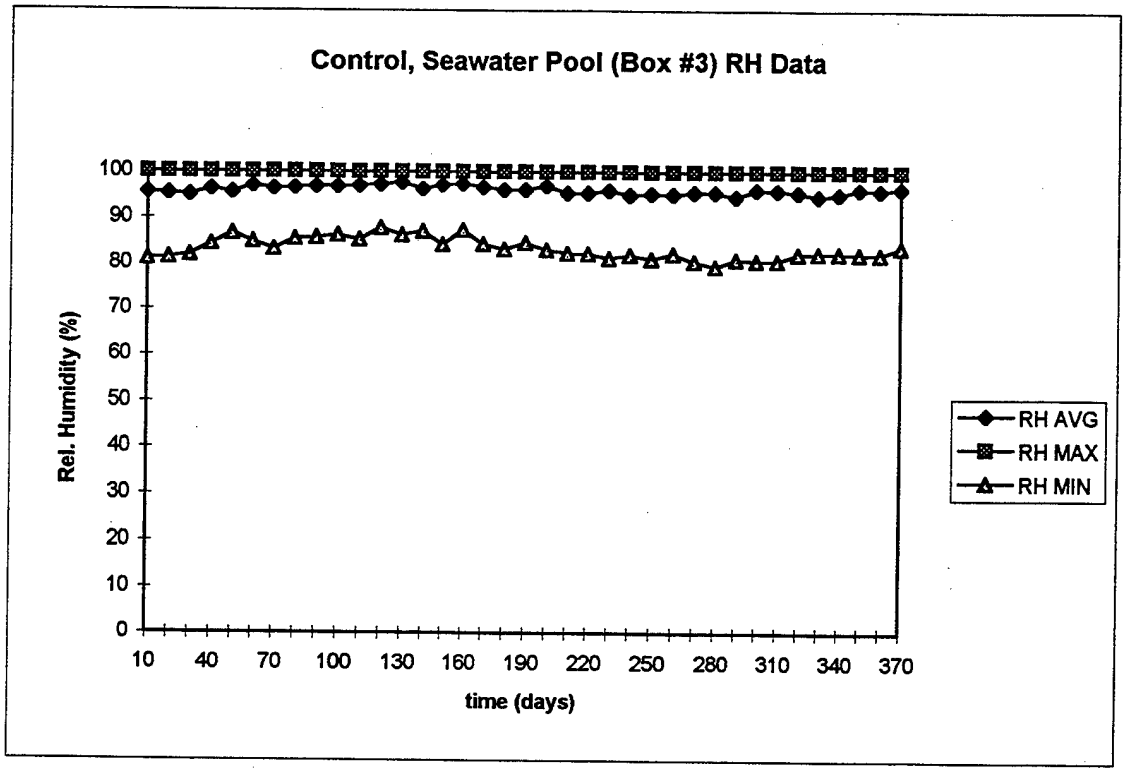


Figure 17. Relative Humidity Data for Box 3 (Control, Seawater Pool)

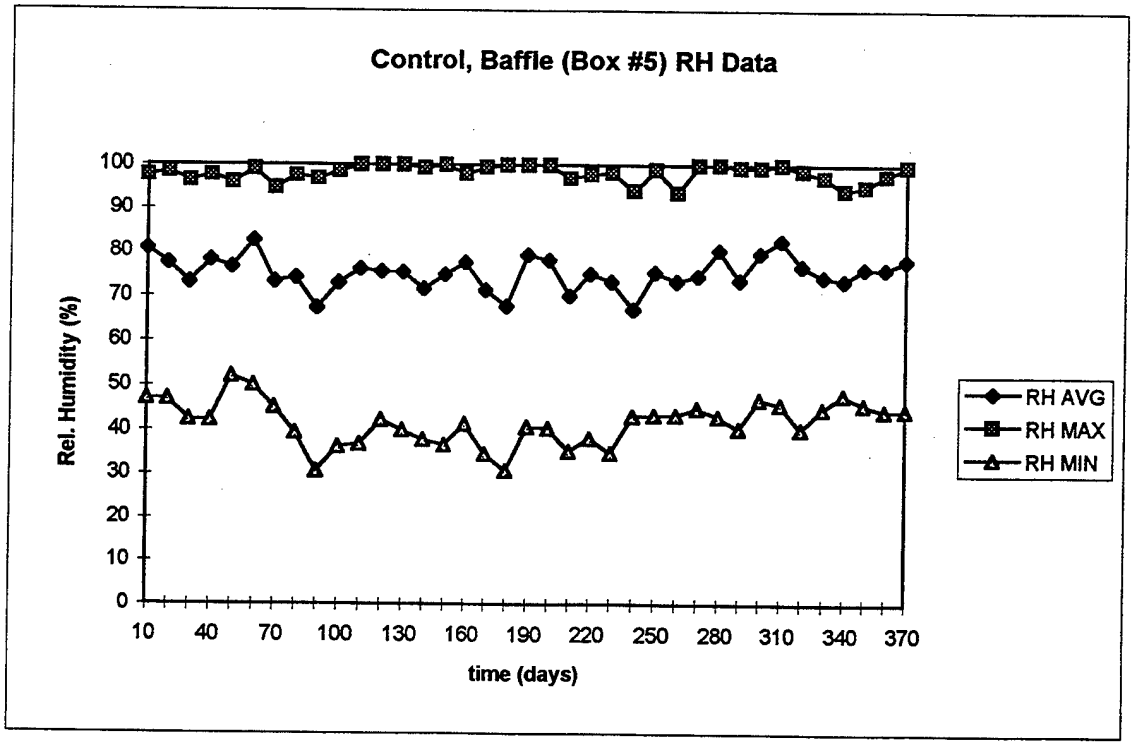


Figure 18. Relative Humidity Data for Box 5 (Control, Baffle)

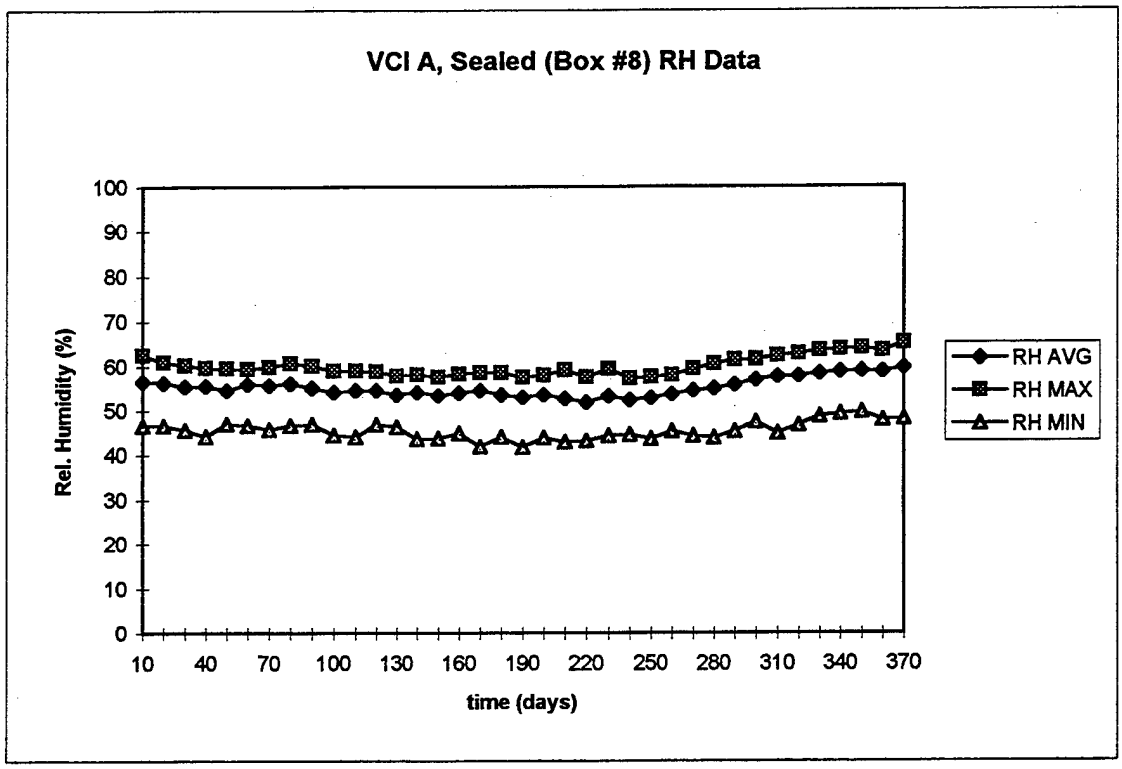


Figure 19. Relative Humidity Data for Box 8 (VCI A, Sealed)

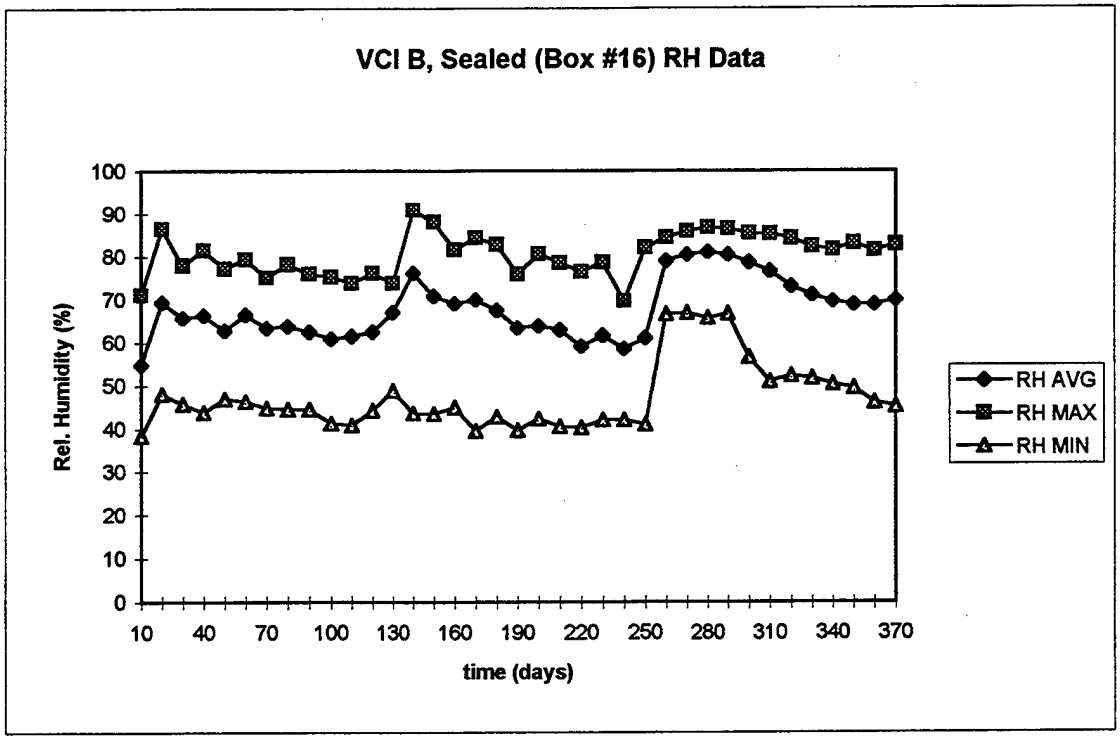
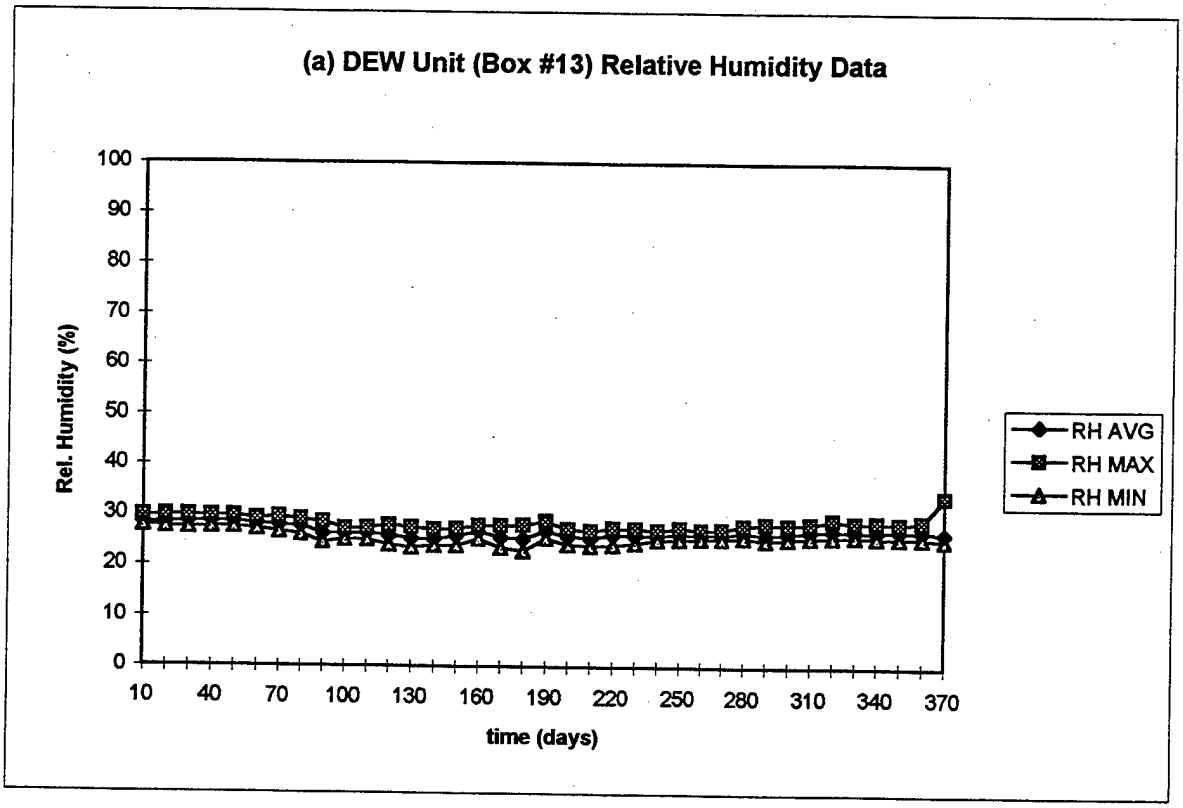


Figure 20. Relative Humidity Data for Box 16 (VCI B, Sealed)



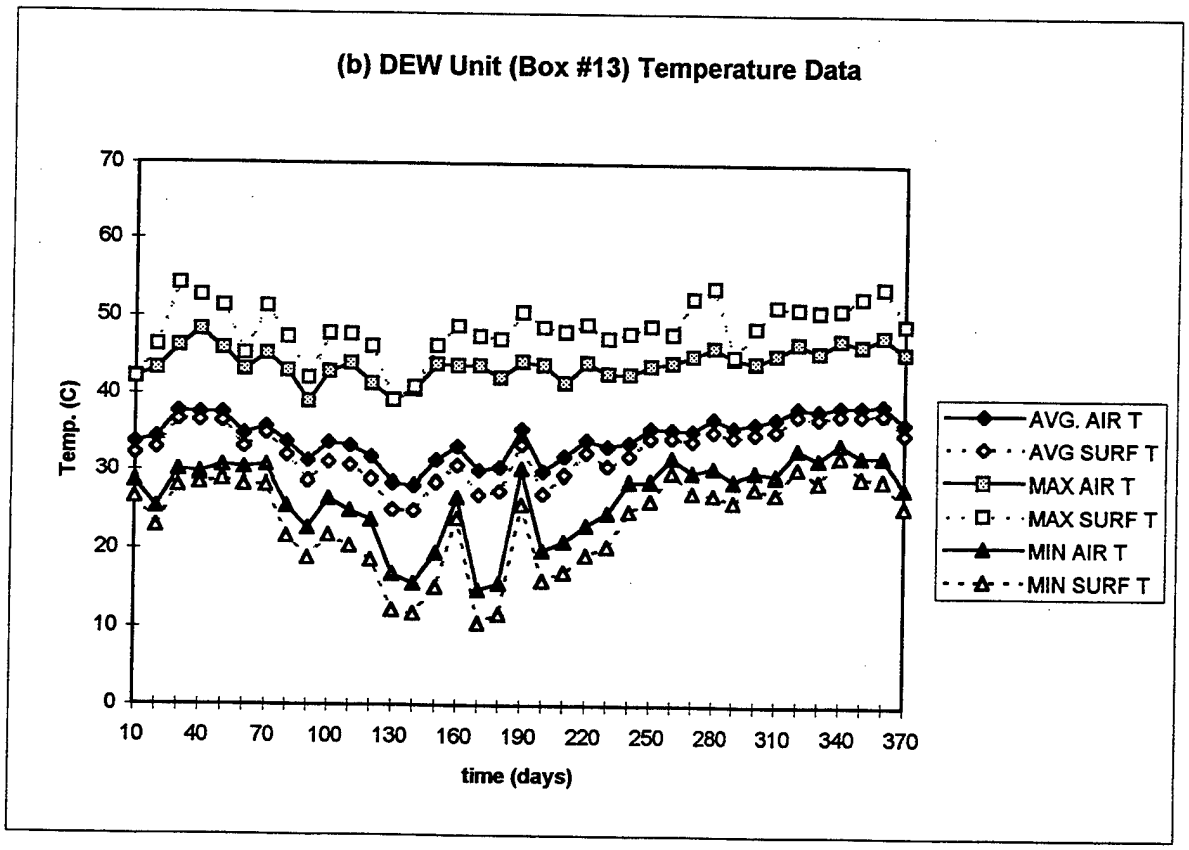


Figure 21. (a-b) Relative Humidity and Temperature Data for Box 13

Preservatives Testing for Cargo/Weapons Elevators

Thomas McCammon
Naval Surface Warfare Center
Carderock Division - Ship Systems Engineering Station
Code 9770 Philadelphia, PA 19112-5083

ABSTRACT

Shipboard cargo/weapons elevators use a system of steel guide rails to guide the lifting platform throughout the trunk. These rails have machined surfaces which make contact with steel guide rollers mounted on the platform. Planned maintenance procedures are in place to prevent the corrosion of these rails. Testing was recently conducted on several preservatives in an effort to reduce the frequency of application. A corrosion preventative was identified that allowed the maintenance periodicity to be increased from quarterly to annually.

INTRODUCTION

Originally, shipboard cargo/weapons elevator guide rails were preserved using grease. Repeated applications of grease however, created problems with build-up in the elevator safety devices. In 1980, turbine oil was chosen to replace grease and the frequency of application increased from quarterly to monthly. A monthly periodicity meant that the crew of a typical underway replenishment ship with 7 elevators was performing this maintenance 84 times annually equating to over 250 manhours in an effort to keep the guide rails from corroding. Performing maintenance in an elevator trunk is inherently dangerous and necessary safety precautions result in increased time and cost. The recent maintenance strategy has been to reduce or eliminate in-trunk maintenance whenever practical in an effort to reduce the cost and potential for mishaps. NSWCCD looked at cargo/weapons elevator guide rail maintenance with the objective of reducing its frequency of accomplishment.

PRELIMINARY ACTION

Several commercial elevator companies were contacted to compare maintenance practices. It was found that most maintenance schedules do not require guide rail lubricants or preservatives if the elevator uses guide rollers. Lubrication is necessary for the sliding gib configurations. Corrosion prevention, as opposed to lubrication, was the purpose of oiling Navy shipboard elevator guide rails. The commercial companies that do oil guide rails for preservation purposes, do so generally on a semiannual to annual basis. When the decision was made in 1980 to go to oil from grease, the frequency of application was increased from quarterly to monthly based on the difference in viscidity. No testing was accomplished to support it.

In 1994, NSWCCD issued an In Service Engineering advisory directing all cargo/weapons elevator guide rail maintenance be accomplished quarterly. Afloat commands and elevator support units were encouraged to report conditions of evolving corrosion. Although a few were reported, the manhour savings resulting from the change outweighed any negative effects. Maintenance personnel were also directed to increase the frequency of application for any chronic problem areas. Efforts then turned to finding a preservative that would allow the frequency of application to be reduced even further.

TESTING

Phase I: Salt Fog

Several corrosion preventatives and lubricants were identified through contact with materials specialists, Mil-Spec review, trade shows, manufacturers and technicians experienced on missile launchers and other equipment using rails. In three separate tests, a total of 13 materials (including the turbine oil as a control specimen for relative comparison purposes) were applied to 1 foot long mild steel A36 guide rail test specimens and placed in a salt fog chamber for approximately 72 hours. This test is in accordance with ASTM B 117-94. It uses 100% humidified air to aspirate a 5% salt water solution in a chamber which is kept at near 100 degrees Fahrenheit. This creates a dense fog of moisture which condenses directly on samples creating a highly corrosive environment. Coating thicknesses varied based on the manufacturer's recommendations for the level of protection desired. Each material's corrosion prevention performance was rated on a scale of 0 to 6, with 3 being the oil coated control sample rating. Refer to Table 1.

The turbine oil coated sample (M.) was the first to corrode and the most corroded test sample. This was in part due to the mist like quality of the air in the salt fog chamber causing the oil to run off. The oil also tends to run down the guide rails to a lesser degree when applied on the elevators. Of the vegetable oil based preservatives (G.-J.), only J. performed well enough to consider for further testing. The solid film lubricant (A.) and molycoat (D.) performed somewhat better. By comparison, both the Petroleum 00 (E.) and the Teflon based (F.) greases allowed significantly less corrosion. The corrosion preventative compounds grades 1 (B.) and 5 (C.) also performed very well. The superior performers by far however, were the 2 wools wax or lanolin based corrosion preventatives, (K.) and (L.). The test samples coated with the lanolin based corrosion preventatives exhibited no corrosion at all after the 72 hour test cycle. The difference in performance between these 2 materials and all others in the test was profound. It was the most telling result of all of the testing accomplished for this project.

Phase II: Land Based Elevator

NSWCCD accomplishes new design testing for shipboard cargo/weapons elevator components at a Land Based Engineering Site (LBES) in Philadelphia PA. A full scale, 6 level elevator similar to those installed on the AOE-6 class of ships is installed at this site. All of the elevator components, including the 4 guide rails, are the same as those typically installed aboard ship. In several tests, each of the LBES' 4 guide rails were coated with a different test material and the elevator was run and the safety devices set. This was performed to demonstrate the effects of guide roller and safety roller pressure on each material. The same rating system as was used in the salt fog test was applied here. Refer to Table 2.

All of the materials which dried to a solid film or semi-solid coating could not withstand the friction and pressure of the guide rollers and either flaked or wore off. These included the Solid Film Lubricant MIL-L-23398 Type 1 (A.), Corrosion Preventative Compound MIL-C-16173 Grade 1 (B.), Dry Molycoat (D.), and vegetable oil based corrosion preventative (J.). While the Corrosion Preventative Compound MIL-C-16173 Grade 5 (C.) actually performed very well in both the salt fog and LBES tests, it was not recommended for shipboard use after a product safety and health review. LBES testing of materials E., F., J., K. and L. also included the spraying of salt water directly into the guide roller paths. This, like the salt fog test, is a more aggressive exposure than would be found in most shipboard elevator environments. All but the lanolin based corrosion preventative (L.) developed corrosion in the roller path.

Phase III: Shipboard Testing

USS SEATTLE (AOE-3) was selected as a test platform for 4 selected materials. This particular ship was chosen because it has multiple (7) elevators, was conveniently located to facilitate monitoring and was representative of the fleet's cargo/weapons elevators in general. While not directly weather exposed, this ship's elevators do not use watertight doors and are heavily used. Ship's Force reported operations consisting of over 3,000 total elevator lifts during the 1 year test cycle. This test commenced concurrently with the final round of LBES testing. The vegetable oil based corrosion preventative (J.), Teflon based grease (F.) and the two lanolin based corrosion preventatives (K.) and (L.) were tested aboard ship.

With the exception of the vegetable oil based corrosion preventative (J.), the differences in performance between materials was not as profound in this test as in the preliminary tests. Material J. flaked off and created a problem by fouling the guide rollers as it also did on the LBES. Although the Teflon based grease (F.) and lanolin based corrosion preventative (K.) both kept a wet protective coating for the test cycle, they were a heavier consistancy which had some undesirable effects. The grease (F.) tended to sling off of the rails after it was first applied and the elevator was run (USS SEATTLE's elevators run 50% faster than the LBES). They both (F. and K.) tended to collect on the edges of the roller paths rather than stay evenly spread across the surfaces they were protecting. Lanolin based corrosion preventative (L.) is described as a semi-liquid. It was better self healing than the other materials and provided an even wet coating for the entire test cycle. The rails coated with this material kept a clean, shiny finish with no evidence of corrosion for the full 1 year test cycle.

CONCLUSIONS AND RESULTING ACTION TAKEN

The lanolin based corrosion preventative (L.) was the superior performer of all tested materials. It is not only desirable based on test results, it is also environmentally safer and requires no solvents to remove. It is removed using clean, dry rags only which causes much of the material to become ingrained in the metal, actually improving its performance over time. It was recommended for shipboard use and is available through the Navy stock system under NSNs 8030-01-386-3871 (1 gallon) and 8030-01-387-1070 (5 gallon). NSWCCD issued In Service Engineering Advisory no. 008-97 via message NAVSURFWARCEN SHIPSYSENGSTA PHILADELPHIA PA 151230Z MAY 97. This advisory directs the fleet's cargo/weapons elevator maintenance personnel to replace turbine oil with the lanolin based corrosion preventative (L.) as a guide rail preservative. It extends the maintenance periodicity from quarterly to annually which will result in a maintenance cost savings estimated at over $150,000 annually for the fleet. Formal documentation changes in progress.

ACKNOWLEDGMENTS

The author would like to thank the sponsor of this project, Mr. Ken Brayton of NAVSEA 03W4 for his continued support; Mr. Jeff Duckworth of NSWCCD 624 for providing laboratory testing; Mr. Stephen Caplan of NSWCCD 9760 for his assistance during laboratory testing and providing LBES testing; the crew of USS SEATTLE (AOE-3) for the use of their elevators and their assistance during shipboard testing, Mr. Don Blankenship of Eureka Chemical Co. for reference material and material samples and Mrs. Suzanne Kralle of NSWCCD 9780 for copy editing.

OTHER MILITARY TESTING CONDUCTED

The following is a brief outline of some known military testing and applications of Lanolin Based Preservatives (LBP):

Army:

Field and laboratory testing of LBP vs. MIL-L-6340 cleaner, lubricant and preservative (CLP). Evaluation found LBP to be superior.

Air Force:

Conducted rust prevention testing in accordance with MIL-C-16173E. LBP exceeded requirements.

Study conducted by Purdue University found LBP to effectively protect against stress corrosion cracking. When applied prior to exposure of the protected surface to aggressive environment, LBP was most effective.

Marine Corps:

LBP field tested on Landing Vehicle Tank, Personnel (LVT-P-7). LBP subsequently incorporated into vehicle maintenance schedule.

Coast Guard:

Laboratory and field testing of LBP for use on Sikorsky HH3F helicopter demonstrated maintenance cost reduction could be achieved. LBP subsequently incorporated into maintenance schedules for several aircraft types.

Ratings Legend-	worse 0	1	2	oil 3	4	5	better 6

ASTM B 117-94
Salt Fog Test

TABLE 1

Material	Approx % Corroded	Rating
A. Solid Film Lubricant MIL-L-23398 Type 1	40	4
B. Corrosion Prevent. Comp. MIL-C-16173 Grade 1	5-10	6
C. Corrosion Prevent. Comp. MIL-C-16173 Grade 5	5-10	6
D. Aerolex Dry Molycoat	40	4
E. Shell 00 grease	20	5
F. Magnalube-G (Teflon based grease)	20	5
G. PreLube 19 (vegetable oil based)	90	3
H. PreLube 19HV (vegetable oil based)	90	3
I. PureLube (vegetable oil based)	90	3
J. MarineLube (vegetable oil based)	40	4
K. Fluid Film AR (lanolin based)	0	6+
L. Fluid Film NAS (lanolin based)	0	6+
M. Lub. oil, stm turb, MIL-L-17331, SYM 2190 TEP	90	3

LBES Test

TABLE 2

Material	Roller Path Corroded?	Rating
A. Solid Film Lubricant MIL-L-23398 Type 1	NA	0
B. Corrosion Prevent. Comp. MIL-C-16173 Grade 1	NA	0
C. Corrosion Prevent. Comp. MIL-C-16173 Grade 5	NA	3
D. Aerolex Dry Molycoat	NA	0
E. Shell 00 grease	Yes	2
F. Magnalube-G (Teflon based grease)	Yes	3
J. MarineLube (vegetable oil based)	Yes	0
K. Fluid Film AR (lanolin based)	Yes	3
L. Fluid Film NAS (lanolin based)	No	6
M. Lub. oil, stm turb, MIL-L-17331, SYM 2190 TEP	NA	3

The Salt-Spray Test as an Alternative to Long-Term Marine Exposure

Sharad P. Pednekar
Process and Properties Branch
Weapons and Materials Research Directorate
Army Research Laboratory, Aberdeen, MD 21005

ABSTRACT

Exterior coatings for military applications have to pass many tests designed to duplicate extreme conditions of environmental exposure. The requirement for weather resistance often is no cracking or loss of adhesion after twelve months of continuous marine exposure in Key West, FL (e.g., MIL-C-81904B(AS)). ASTM D 1014 similarly recommends outdoor exposure of appropriate type and duration. Such long test exposures are inconvenient and waste resources when the objective is to improve an existing product or to screen a number of promising products for further improvement. A test which is short in duration but is equivalent to long-term marine exposure will ease this search by providing a quick evaluation of formulation changes. With that objective, we compared archival atmospheric corrosion data for AISI 1020 carbon steel in the 800-foot (250-m) lot at Kure Beach, NC, with the nature and rate of corrosion of coupons of the same grade of steel in a salt-spray chamber. Results show that 24 days in a salt spray chamber cause the same amount and type of corrosion in steel as does one year in the marine environment.

INTRODUCTION

The Salt Spray chamber provides a uniform, easily controlled corrosive environment. As such, the practice, as described in ASTM B117, is widely used to gauge the relative corrosion resistance of metals and coatings. Further, because of the presence of sodium chloride, researchers often use exposure in the chamber to simulate corrosion, pitting, or stress corrosion cracking of metals observed in marine or chloride environments. For example, intergranular stress corrosion cracking observed in fasteners of nickel-base Inconel 718 alloy in the field was reproduced[1] by exposing stressed assemblies in the salt spray chamber. In spite of the wide use of the salt spray chamber for the above purposes and in spite of the conviction of researchers that the salt spray chamber environment provides an accelerated test for gauging the relative resistance of a material to a marine environment, no successful attempts have been reported to measure the extent of acceleration that the standard salt spray fog test provides over atmospheric exposure testing at a marine site.

For an ongoing program, we needed to test a number of coatings for their suitability for use onboard navy ships. A variety of prescribed tests needed to be conducted for measuring the resistance of these coatings to lubricating oil, impact, humidity, temperature shock, and weather, to determine this suitability. Most of these tests could be conducted in less than four weeks,

except the weather resistance test. This latter test required that two test panels of each coating be exposed continuously in Key West, FL, for twelve months mounted at 45° facing south before being examined for cracks or lack of adhesion. The client was willing to substitute the test with an accelerated test of a shorter duration, such as salt spray testing, if it would provide reliable, equivalent results. Data are available[2] in literature on corrosion rates of carbon steels and other metals in various coastal locations. These data could be used to calibrate the salt spray chamber if the mechanism and rate of corrosion of metals in it were the same as in coastal locations. This calibration was performed by determining the weight loss of carbon steel specimens in the salt spray chamber as a function of time and comparing it with time required for the same loss at coastal sites.

EXPERIMENTAL

Rectangular specimens of 1020 carbon steel (C 0.2, Mn 0.45, S 0.05, and P 0.04%) were cut from 1/16 inch thick hot-rolled and cold-drawn stock into 1-inch by 2-inch samples. The surface was smooth and free from scale as received and was not altered except for abrading the edges on a No. 180 grit paper to remove burrs. The specimens were then weighed, degreased in ethyl alcohol, and washed in de-ionized water before being placed in a salt spray chamber. The salt spray chamber was operated per ASTM B117 at a temperature of 95±2°F (35±1°C) using a 5% sodium chloride solution of pH 6.9±0.2. The specimens were arranged at an angle of 15° to the vertical. Care was taken to ensure that condensed spray did not collect in a pool on the surface or at the bottom edge of the specimens.

Specimens were removed from the chamber at suitable intervals, immediately rinsed with de-ionized water and then with ethyl alcohol, dried in cool air, and placed in a desiccator to be ready for removal of corrosion products from the surface at a later date. Corrosion products were removed by cathodic polarization of specimens in inhibited dilute sulfuric acid per ASTM G1-81, except for the use of a platinum anode instead of carbon or lead anode. Cleaned, washed, and dried specimens were weighed to 0.1 mg.

RESULTS

Within the first few hours after the specimens had been placed in the salt spray chamber, greyish black corrosion products began forming on their surface. With continued exposure, the surface area covered with the corrosion product grew in size. Specks of orange-yellow material appeared within the corrosion product film within the first twenty four hours. The corrosion product film never completely covered the specimen surface and was always grainy and loose in appearance. It was therefore apparent that the film was not protective. The colors of the corrosion products indicated[3] that the film consisted of α- and γ-FeOOH (yellow and orange, resp.,), α- and γ-Fe_2O_3 (brown and brick red to black, resp.), and perhaps, also, magnetite, Fe_3O_4 (black). Electrolytically cleaned specimens showed uneven corrosion with grooves and shallow, wide pits. This appearance was almost identical to that in photographs presented by Baker and Lee[4] of iron specimens (C 0.02, Mn 0.05, Cu 0.066) exposed in the 80-foot (25 m) lot at Kure Beach, NC, for

one year either vertically or at 30° from the horizontal. Photographs of specimens from the 800-foot (250 m) lot are not available in literature, but it may be assumed these specimens had a similar appearance after one year even though their corrosion rate was at least 10 times lower.

The weight loss data are summarized in Table 1. It is seen that the corrosion rate ranged from 16 to 26 mils per year (mpy) and averaged 22 mpy (1.5 μm/d). The average calculated depth of attack in mils is shown in Figure 1 as a function of time. It is seen from Figure 1 that the data can be represented by a straight line . Dotted lines give the 95% confidence limit for these data.

DISCUSSION

A large volume of data on corrosion rates of carbon steel in marine environments are available and have been recently summarized[5] . However, most of the data were collected nearly fifty years ago, were obtained on different grades of steel in different locations, are now readily available only in secondary sources such as References 2, 4, and5, and appear to have been misquoted occasionally. The test material, AISI Grade 1020 carbon steel, for the present test program was chosen for two reasons: 1) Alloying elements that might influence the passive oxide layer on steels, such as copper, nickel, and chromium, are present in this plain carbon steel at very low levels and only as residuals from the steelmaking practice. Consequently, corrosion rates measured in the salt spray chamber would provide a measure of the severity of the environment directly without having to account for the presence of any alloying elements in retarding that corrosion; 2) The easy and wide availability of this steel would enable us and other researchers to obtain comparable data in other environments in future, and 3) Data are available[2,4,5] for this grade of steel exposed to marine atmosphere at Kure Beach, NC for periods up to 7.5 years.

The average reduction of thickness for carbon steel exposed in a lot 800 feet away from the shore at Laque Corrosion Center in Kure Beach, NC, as reported by Fink and Boyd[4] is presented in Figure 1. The carbon steel was of AISI 1020 composition and contained (C 0.16, Mn 0.42, P 0.013, S 0.021, Si 0.01, Cu 0.02, Ni 0.02, and Cr 0.01%. It is seen that the data fall on a straight line with an average corrosion rate of 1.7 mpy. The presence of as little as 0.05% copper resulted in the steel forming a more resistant corrosion product film on the surface, and corrosion slowed down with time. This is seen in Figure 1 in the curve for carbon steel (C 0.24, Mn 0.48, P 0.04, S 0.027, Si 0.008, Cr 0.03 Ni 0.051 and Cu 0.08%) tested at a US Naval Research Laboratory site in Cristobal, Panama (data taken from Table 12 in Reference 5). The stabilized average corrosion rate for the carbon steel at this site was about 1 mpy (0.07 μm/d). It is to be expected that corrosiveness of the marine atmosphere will be different at different locations around the world. For carbon steel (apparently, of composition similar to 1020), corrosion rates ranged[2] from 0.62 mpy (0.043 μm/d) in Halifax, Nova Scotia to 17.3 mpy (1.2 μm/d) in Colombo, Sri Lanka. In Kure Beach itself, corrosion rate jumped to 47 mpy (3.2 μm/d) in a lot 80 feet (25 m) from the shore, no doubt due to the higher moisture content of the air, a longer time of wetness, and a greater salt content of air than in the 800-foot (250 m) lot.

In developing a correlation between salt-spray and marine exposures, we chose the 800-foot

(250 m) Kure Beach data for copper-free 0.2% C carbon steel and our corrosion rates for AISI 1020 carbon steel in Figure 1. It was noted earlier that the appearance of corrosion coupons before and after removal of the corrosion product film was similar for the salt-spray carbon steel specimens and the 80-foot and, by analogy, probably for the 800-foot Kure Beach iron panels. Weight loss or other corrosion data for carbon steel in the 80-foot lot, having been published nearly fifty years ago[6], were not available to us in the original, but Baker and Lee[4] present data for exposure times up to about 1200 h for both the 80- and 800-foot lots. Both plots are nearly linear with time with corrosion rates of 21 and 6 mpy (1.4 and 0.4 μm/d), respectively. The corrosion product film on both the Kure-beach iron and carbon steel specimens and our Grade 1020 carbon-steel specimens was noncontinuous and porous. It is not surprising, therefore, that corrosion was linear with time in all these cases. This linearity allows one to conclude from the two sets of data in Figure 1 that one year of exposure in the 800-foot (250 m) lot at Kure Beach, NC, is equivalent to 24$\pm$3 days in a salt-spray chamber for plain-carbon steel.

Baker and Lee[4] report a linear corrosion rate of 28.5 mpy (1.9 μm/d) for carbon steel in a salt-spray chamber using a 3% NaCl solution for spray. Considering the scatter generally obtained in weight-loss corrosion measurements, the agreement in magnitude and linearity of their data with ours is good. For reasons that seem unconvincing, Baker and Lee however did not think a calibration was possible from their data.

The corrosion of metals in a marine environment is influenced by the high moisture and salt content and mild temperature fluctuations of the air. The anodic reaction is:

$$Me \rightarrow Me^{n+} + ne^{-}. \qquad (1)$$

The cathodic reaction, because of the near-neutral pH of condensed moisture in the general absence of carbon dioxide and sulfur-bearing gases, is the oxygen reduction reaction:

$$H_2O + \tfrac{1}{2}\, O_2 + 2e^{-} \rightarrow 2(OH)^{-}. \qquad (2)$$

For identical reasons, these same reactions would occur also in the salt-spray chamber. The presence of a continuous salt spray and a uniformly high temperature only accelerate the rates of the anodic and cathodic reactions but not their nature. The linearity of the salt-spray and Kure-Beach data in Figure 1 show that such indeed was the case.

It is emphasized that the linearity of the data is necessary only for setting up a correlation between the two environments. It need not mean that the correlation is only good for plain carbon steel. As long as the factors influencing the corrosion of a metal are the same in the two environments, the same correlation of 24 days in a salt-spray chamber to one year in the 800-foot lot at Kure Beach should apply. In fact Baker and Lee's data[4] show that their zinc specimens corroded about 17 times faster in the 3% NaCl salt-spray chamber (~21 mpy or 1.4 μm/d) than in the 800-foot lot (~1.3 mpy or 0.1 μm/d), nearly the same as the acceleration shown by plain carbon steel, 15 times over exposure in the 800-foot (250 m) lot. The reasoning used above may

be extended also to cases where uniform corrosion of a metal in the marine environment is followed by formation and propagation of pits, for example, as in the case of low-alloy steels or stainless steels. Pits initiate at sites of local destruction of the passivation layer by chloride ions and propagate because of acidification of the pit solution due to hydrolysis of dissolved iron[7]. The mechanism will be the same in the two environments, only accelerated in the salt-spray chamber. One should therefore expect the same extent of acceleration as in the case of plain-carbon steels or zinc.

The salt-spray chamber also may be used to accelerate the effects of a marine environment on the metal substrate of coatings for the same reasons as were advanced above for metallic materials. Salt-spray exposure, of course, will not simulate the effect of outdoor electromagnetic radiation, and additional tests such as ASTM G26 for accelerated weathering will need to be conducted to qualify a coating for outdoor marine applications.

CONCLUSIONS

1. Loss due to corrosion of 1020 carbon steel in salt-spray chamber exposure conducted per ASTM B117 was linear with time as are literary data for the same steel exposed in the 800-foot (250 m) lot at Kure Beach, NC.

2. A year of exposure in the 800-foot (250 m) lot at Kure Beach, NC, for 1020 carbon steel is equivalent to a 24-day salt-spray chamber exposure conducted per ASTM B117.

3. Tests conducted per ASTM B117 on coated and noncoated metallic materials accelerate marine exposure in the 800-foot lot at Kure Beach, NC, by a factor of ~15.

REFERENCES

1. Champagne, V. K., G. Wechsler, M. S. Pepi, and K. J. Bhansali, *Failure Analysis of an Alloy 718 Barrel Nut from an Army Attack Helicopter,* in Superalloys 718, 625, 706, and Various Derivatives, E. A. Loria Ed., TMS, 1997, pp. 813-824.

2. Fink, F. W. And W. K. Boyd, The Corrosion of Metals in Marine Environments, Defense Metals Information Center, 1970, pp. 10-11.

3. Strauss, M. B. and M. C. Bloom, J. Electrochem. S., 107, 2, 73-79, 1960.

4. Baker, E. A. and T. S. Lee, *Calibration of Atmospheric Corrosion Test Sites*, in Atmospheric Corrosion of Metals, S. W. Dean and E. C. Rhea, Eds., ASTM STP 767, ASTM, 1982, pp. 250-266.

5. *Marine Corrosion*, R. H. Heidersbach, Ed., in Metals Handbook, 9th Edition, ASM, 1987, 893-926.

6. LaQue, F. L., in Proceedings ASTM, 51, 1951, p. 495, as quoted by Baker and Lee in Reference 4.

7. Fontana M. G. and N.D. Greene, Corrosion Engineering, 2nd Edition, McGraw-Hill, 1978, pp. 48-58.

Table 1. Corrosion Rates for 1020 Carbon Steel in Salt-Spray Chamber per ASTM B117

Specimenl #	Area, cm2	Exposure, days	Initial Weight, g	Final Weight, g	Weight loss, g	Corr. Rate, mpy	loss, mil
12	24.98	4	14.4481	14.3625	0.0856	15.66	0.17
11	25.20	4	14.2076	14.1051	0.1025	18.59	0.20
10	25.34	7	14.5048	14.3239	0.1809	18.65	0.36
9	25.12	7	14.6241	14.3643	0.2598	27.02	0.52
8	24.91	11	14.4452	14.1276	0.3176	21.19	0.64
7	25.85	11	14.4328	14.1305	0.3023	19.43	0.59
6	24.90	18	14.5298	13.9158	0.614	25.04	1.23
5	24.94	18	14.5105	13.8811	0.6294	25.63	1.26
4	25.51	20	14.4371	13.7547	0.6824	24.46	1.34
3	25.23	20	14.5205	13.801	0.7195	26.07	1.43

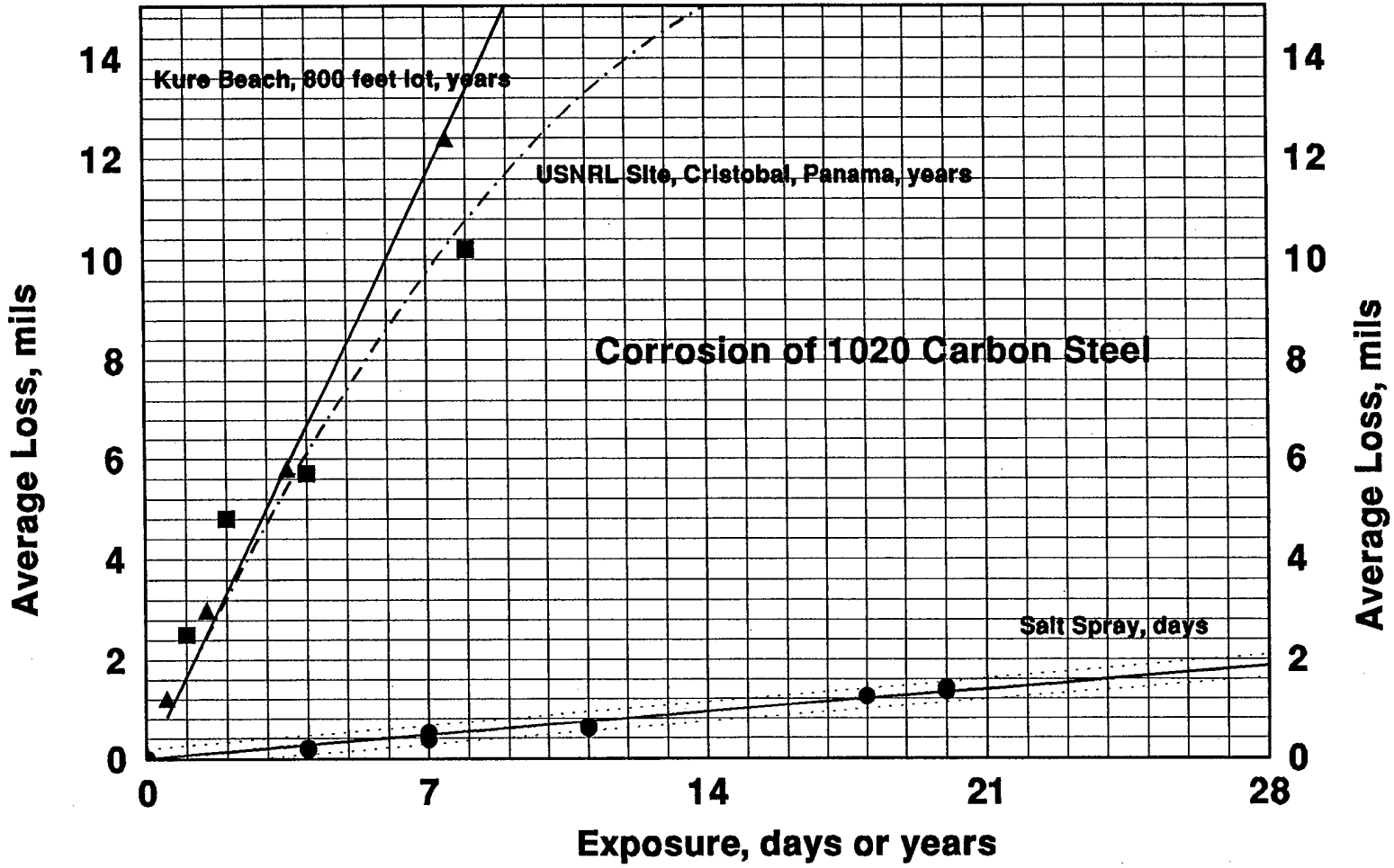


Figure 1. Reduction in Thickness for Carbon Steel in Salt Spray Chamber and at Two Marine Sites

Stress Corrosion Cracking of Naval Structural Steels

R.A. Hays[1], D.A. Davis[2], and D.M. Aylor[2]

[1]Proteus Engineering
301 Pier One Rd., Suite 200
Stevensville, MD 21666

[2]Naval Surface Warfare Center,
Carderock Division
Corrosion Branch, Code 613
9500 MacArthur Blvd
West Bethesda, MD 20817-5700

ABSTRACT

Stress corrosion cracking can be defined as cracking caused by the simultaneous presence of tensile stress and a specific environment. As such, this definition can include many types of cracking in corrosive mediums including those caused by hydrogen embrittlement. The term "hydrogen embrittlement" is used to characterize the near room temperature effects of hydrogen on materials. Among the effects of this form of attack are loss of ductility, loss of load carrying capability, delayed cracking, and loss of true stress at fracture. As a result, hydrogen embrittlement is a persistent concern affecting the use of a broad range of structural materials exposed to marine environments.

The hydrogen embrittlement susceptibility of high strength martensitic "HY" steels (MIL-S-16216K) is compared to that of the high strength, low alloy "HSLA" steels (MIL-S-24645A). The performance of weldments in both alloy systems is also discussed along with the influence of cathodic protection level, yield strength, and microstructure on susceptibility.

INTRODUCTION

Stress corrosion cracking (SCC) can be defined as cracking caused by the simultaneous presence of tensile stress and a specific environment [Fontana (1986)]. As such, this definition can include many types of cracking in corrosive mediums including those caused by hydrogen embrittlement. It is generally accepted that high strength steels in seawater under cathodic protection suffer from hydrogen embrittlement as opposed to other forms of stress corrosion cracking.

Hydrogen embrittlement is a persistent concern affecting the use of a broad range of ferrous and non-ferrous structural materials exposed to marine environments. The term hydrogen embrittlement is used to characterize the near room temperature effects of hydrogen on materials. Among these effects are loss of ductility, loss of load carrying capability, delayed cracking, and loss of true stress at fracture. Although there is an incomplete understanding of the mechanisms

of hydrogen related failures, the evidence indicates there is no single dominant mechanism operative over a broad range of materials. In fact, several mechanisms may operate even within a single system. Various mechanisms have been offered to explain the role of hydrogen in the degradation of material properties. These may be grouped into five categories :

- Formation of molecular hydrogen at preexisting microcracks and voids in the metal resulting in very high internal pressure [Zapffe and Sims (1941)];
- A weakening of the cohesive force between metal atoms by the presence of hydrogen [Troiano (1960)];
- The adsorption of hydrogen on crack surfaces [Petch and Stables (1952)];
- Hydrogen enhancing localized plastic deformation [Beachem (1972)];
- Formation of hydrides [Westlake (1972)].

Increasing performance requirements have led designers to consider the use of higher strength steels in advanced marine structures. Since the susceptibility of high strength steels to hydrogen embrittlement is generally considered to be directly proportional to yield strength (i.e., susceptibility increases with increasing yield strength) for a given alloy class [Fontana (1986), Pressouyre (1982)], the need to characterize the performance of these steels and their associated welding systems is critical.

There are a wide variety of test techniques which have been used to characterize the susceptibility of materials to stress corrosion cracking and hydrogen embrittlement. In general, they fall into three major categories:

- Constant displacement techniques such as bent-beam, U-bend, wedge-open loading, and proving ring tests. In these tests, specimens are loaded to some fixed displacement and then exposed to the corrosive environment. Initiation of cracking causes the stress to be relieved, thus causing crack arrest. These tests tend to be plagued by a high degree of scatter and in many cases do not result in a useful design parameter.

- Rising load techniques such as the slow strain rate test [Parkins, (1993)]. In this technique, specimens are subjected to a rising stress, typically applied by a screw-driven testing machine. These tests tend to produce conservative results (i.e. materials which show susceptibility in these tests may not show susceptibility in service) in a relatively short period of time. This conservatism may result from the fact that engineering structures are rarely loaded in this fashion. As such, these tests are typically used only to relatively rank susceptibility of materials.

- Load controlled techniques such as the cantilever beam test. In these tests, specimens are dead-weight loaded to produce the desired stress. Any cracks which initiate, grow into an increasing stress field resulting in failure of the specimen. Unfortunately, these tests are time-consuming and costly. However, a critical linear elastic stress intensity

factor can be obtained from these tests and this parameter can subsequently be used in design or to determine the flaw tolerance of an engineering structure.

While researchers have tried all of the methods discussed above (as well as various combinations thereof), the test method most frequently used by the U.S. Navy for determining the stress corrosion cracking susceptibility of high strength structural alloys is the cantilever beam test. Results from these tests can be used to calculate the threshold linear elastic stress intensity parameter, K_{Iscc}. K_{Iscc} is the plane-strain, linear elastic stress intensity factor describing the stress and crack size threshold below which subcritical cracks will not propagate under conditions which promote stress-corrosion cracking. The purpose of this paper is to summarize the cantilever beam stress corrosion cracking data developed by the Navy over the last 15 years and compare the susceptibility of the HY and HSLA steel systems.

EXPERIMENTAL PROCEDURE

The cantilever beam technique utilizes long term static load testing of fatigue precracked single-edge notched beam specimens (SEN-B) manufactured to guidelines designed to produce plane-strain SCC data [Novack and Rolfe (1970)]. Test durations range from several hours to over 10,000 hours. The 10,000 hour runout time is preferred to ensure sufficient time for crack incubation (hydrogen entry and transport to the crack tip region in the case of hydrogen embrittlement) without being excessively long. The specimens are often cathodically polarized to potentials more negative than the metal being tested using either sacrificial anodes or a potentiostat. Time-to-failure for a series of specimens loaded to various applied stress intensity (K_{app}) levels is recorded. For a given test series, K_{Iscc} is defined at the highest K_{app} level below which no failures occurred prior to completion of the test duration (runout).

Materials

The "High Yield" or "HY" family of steels HY-80, HY-100, and HY-130 are high strength, quenched and tempered, martensitic steels. They were developed in the mid 1950's and early 1960's as tough, weldable steels for Navy ship and submarine construction. While these steels have been used successfully for many years, the opportunity to realize significant cost savings and efficiency gains with the elimination of weld pre-heating requirements led to the development of the high strength, low alloy (HSLA) steels, HSLA-80 and HSLA-100. These steels are low carbon for weldability and strengthened primarily by copper precipitation. The microstructure of HSLA-80 tends to be acicular or polygonal ferrite depending on gage while the microstructure of HSLA-100 is primarily bainitic. Composition and mechanical properties for the base materials are provided in Tables (1) and (2). The HSLA steels were developed such that they could use the same welding consumables as their counterpart HY steel (i.e., HY-80 and HSLA-80 use the same welding consumbles, etc.).

Cantilever Beam Testing

The American Society for Testing and Materials (ASTM) is currently working on standardizing a test method for environmentally assisted cracking characterization of metallic alloys using the cantilever beam specimen (ASTM E1681, Standard Test Method for Determining the Threshold Stress Intensity for Environment-Assisted Cracking of Materials Under Constant Load). Although the work summarized herein was performed by different researchers over a period of approximately 15 years, the test methodology contained in the current draft of the standard was generally followed in all cases. The test methodology is described below and significant deviations from the draft ASTM standard are noted.

Cantilever beam SCC tests are conducted using specimens with the nominal dimensions shown in Figure (1). The specimens are deadweight loaded in a cantilever configuration, Figure (2). The desired applied stress intensity (K_{app}) is converted to a moment for loading using the following equation:

$$M = \frac{K_I B(W)^{\frac{3}{2}}}{4\left[\frac{1}{\alpha^3} - \alpha^3\right]^{\frac{1}{2}}} \qquad \text{..... (1)}$$

where:

α = $1 - (a_o/W)$
K_I = crack tip stress intensity
a_o = fatigue precrack length
B = specimen thickness
W = specimen width
M = applied moment

Prior to testing, the machined notch is sharpened under fatigue loading. This fatigue pre-cracking is typically accomplished in a standard hydraulic test stand in three- or four-point bending following the general procedures outlined in ASTM Standard E 399-90. The notable exception to those procedures has been the recent use of reverse bending to condition welded specimens prior to precracking. This technique has been used in an attempt to produce straight fatigue crack fronts in specimens containing residual stress gradients such as those resulting from multi-pass welds since approximately 1990 [Kirk (1992)]. During the initial loading of the specimens for testing, the fatigue precrack length is estimated from specimen compliance.

Test Environment

Environmental conditions are established by attaching a 0.5 liter polyethylene container around the crack tip and filling it with ambient temperature natural seawater which is filtered to remove hard fouling organisms, Figure (3). Seawater is drip-fed at a flow rate resulting in complete container solution replacement every hour which is sufficient to avoid metal-ion buildup or depletion of cations due to calcareous reactions on the specimen surface. Specimens can be tested under freely corroding conditions or under cathodic polarization using sacrificial anodes or potentiostatic control.

Test Duration

One of the biggest variables in the Navy's cantilever testing has been test duration. The draft test method, ASTM E1681, recommends 10,000 hour duration for runouts and this is typical of the Navy's testing as well. However, pressure to limit costs and obtain results has occasionally led to the early termination of tests. While specimen failures are uncommon after the first 500 hours, a sufficient number occur between 5,000 and 10,000 hours that test series conducted with runout periods less than 10,000 may be non-conservative. That said, test durations longer than 10,000 hours do not appear necessary.

Post-Test Specimen Handling

When specimens fracture during testing, the fracture surfaces are cleaned, rinsed in alcohol, and dried. Data is recorded as time-to-failure (to the nearest hour) and applied moment. The draft ASTM E1681 test method requires the physical measurement of initial crack length at the center of the specimen and at points midway between the center and edge on both sides of the specimen. These three measurements are then averaged and used to calculate K_{app}. However, this measurement procedure may not accurately describe highly irregular crack fronts. As a result, Navy researchers measure initial crack lengths using the procedure described in ASTM E 813-89. This procedure requires crack length measurements on nine equally spaced points about the specimen centerline. The crack length is determined by averaging the two measurements taken at the specimen surfaces, combining this result with the other seven measurements, and taking an average. This average crack length is then used to calculate the actual K_{app}.

Selected specimens are examined using light or scanning electron microscopy (SEM) to determine fracture morphology. To facilitate the fractography, fracture surfaces are saw-cut from the specimen and cleaned for examination. Regions of the fracture surfaces including the precrack area, areas just ahead of the precrack tip, and areas well removed from the precrack can then be characterized at higher magnification.

RESULTS AND DISCUSSION

HY-80 and HSLA-80

In general, steels with yield strengths below 100 ksi (690 MPa) are not considered susceptible to hydrogen embrittlement cracking in seawater at cathodic potentials typically used to mitigate general corrosion (-1.0 V versus Ag/AgCl and more electropositive) [Pressouyre (1982)]. As a result, only minimal, confirmatory work has been done on base plates at the 80 ksi (551 MPa) yield strength level. In work done with wedge-open loading (WOL) specimens, K_{Iscc} was found to exceed 125 ksi$\sqrt{in}$ (137 MPa$\sqrt{m}$) for HY-80 base plate polarized to -1.000 V versus Ag/AgCl. Although test results are not available for HSLA-80 base plate, the highly refined microstructure and toughness of this alloy indicate SCC resistance at least as good as HY-80.

Since overmatching yield strength welding is often used in naval construction, there has been more concern regarding the SCC susceptibility of weld metals used to join the 80 ksi (552 MPa) yield strength materials, and more recently, heat affected zones of welds. The weld metals exhibit excellent SCC resistance with K_{Iscc} for HY-80 gas metal arc (GMA) welds measured at 133 ksi$\sqrt{in}$ (146 MPa$\sqrt{m}$) and K_{Iscc} for HY-80 shielded metal arc (SMA) welds measured at 125 ksi$\sqrt{in}$ (137 Mpa$\sqrt{m}$). While these measurements were made using WOL and step-loaded cantilever beam techniques respectively, the high K_{Iscc} values and excellent service experience indicate minimal susceptibility for HY-80 welds.

An ongoing Navy program is investigating the effects of high heat inputs on the SCC resistance of HY-80 and HY-100 heat affected zones (HAZ). The HAZ is of particular importance since portions of this region can be have high hardness leading to increased SCC susceptibility. The limited data available to date for HY-80 GMA weld HAZ's welded with a nominal heat input of 113 kJ/in. indicate K_{Iscc} to be between 70 ksi$\sqrt{in}$ (77 MPa$\sqrt{m}$) and 80 ksi$\sqrt{in}$ (88 MPa$\sqrt{m}$). It should be noted that, due to the relatively large size of the cantilever beam specimen, measurement of SCC properties in areas where large gradients in properties occur over small distances (such as HAZ's) is difficult. Repeatable placement of the crack tips for multiple specimens in the same metallurgical region of a given weldment is nearly impossible and therefore a large amount of scatter is typically seen in the data.

HY-100 and HSLA-100

Figure (4) presents stress intensity versus time to failure data for HY-100 and HSLA-100 base plate. The tests were conducted in natural seawater at various cathodic potentials. Table (3) summarizes the K_{Iscc} data for these materials and test conditions. While K_{Iscc} for both the HY-100 and HSLA-100 exceed the ASTM validity criteria, the identical specimen size and the nominally equivalent strength levels for the two materials make comparisons between them valid. Interestingly, these results show K_{Iscc} for HY-100 at open circuit (approximately -0.650 V vs. Ag/AgCl for steels) and at a polarization level of -1.000 V vs. Ag/AgCl to be essentially equivalent. This is contrary to the notion that more electronegative potentials produce greater

SCC susceptibility due to higher concentrations of hydrogen at the cathodic surface. The probable explanation for this result is that the stress intensity levels are so high that the region surrounding the crack tip is highly plastic and the specimens tested at the open circuit potential failed by simple overload. Of course, it is possible that the specimens tested under open circuit conditions could suffer from a form of stress corrosion cracking called anodic path dissolution. Results such as these reinforce the need to perform fractography on the failed specimens to positively identify failure modes.

The comparison between HY-100 and HSLA-100 base metals is of greater importance to the designer and user of these materials. Strict interpretation of the test data show a K_{Iscc} of 122 ksi$\sqrt{in}$ (134 MPa$\sqrt{m}$) for HY-100 and 113 ksi$\sqrt{in}$ (124 MPa$\sqrt{m}$) for HSLA-100 polarized to -1.00 V vs. Ag/AgCl. However, since no failures occurred in the HSLA-100 test series, the difference in K_{Iscc} is more likely an artifact of the limited number of specimens than a true difference in SCC resistance. In an effort to produce an SCC failure in HSLA-100 base plate, three specimens were tested at a cathodic potential of -1.500 V vs. Ag/AgCl. Fracture surfaces of the failed specimens were characterized by low ductility and secondary cracking, Figure (5). This fracture mode is similar to the "quasi-cleavage" fracture mode exhibited by the HY steels.

Figure (6) plots the results for several series of HY-100 and a single series of HSLA-100 weld metal tests. There are several points that can be made regarding the figure. First, the scatter associated with SCC testing of weld metals is very large. Possible sources of scatter are as follow:

- Metallurgical variability within a given weldment and between weldments (even those made with nominally the same welding parameters);
- Residual stresses;
- Non-uniform crack fronts (resulting from residual stresses and metallurgical variability;
- Number of specimens within a test series;
- Duration of tests.

Multi-pass welds have a complex microstructure and significant changes in hardness and other mechanical properties can be observed over distances (such as the weld bead width) which are small compared to the dimensions of a cantilever beam specimen. As a result, the crack front sits in a nonhomogeneous material with respect to mechanical properties and SCC resistance. Residual stresses can act to shield the crack from, or be additive to, the applied stress creating uncertainty with respect to the true value of K_{app}. Both of the previous items also cause difficulty in fatigue precracking leading to the testing of specimens with highly non-uniform fatigue cracks, Figure (7). Non-uniform fatigue precracks result in a variable K_{app} as a function of position along the crack front making interpretation difficult. Since cantilever beam tests are relatively costly and time consuming, there is continuous pressure to minimize both the number of specimens and test duration. Limiting the number of test specimens reduces the accuracy and resolution with which K_{Iscc} can be determined. It also increases the risk that all the specimens of a given series will fail and result in an invalid test. The longer the test duration, the greater the chance that the concentration of available diffusible hydrogen has reached equilibrium at critical sites near the tip

of the crack. Although most specimens that fail do so within 500 hours, many fail after several thousand hours making the 10,000 hour runout duration important.

In spite of the large amount of scatter in the data, Figure (6) shows a general trend of increasing SCC susceptibility with increasing yield strength. Submerged arc and gas-metal arc welds appear to have similar SCC susceptibility. The increased resistance of the gas-tungsten arc weld relative to the other weld types can be attributed to the more refined grain structure [Zanis et al. (1980)]. Not surprisingly, the submerged arc weld in the HSLA-100 appears similar in resistance to the HY-100 welds since the same filler metals are used for both alloys.

Based on the limited data available, the SCC resistance of HY-100 heat affected zones is influenced strongly by the weld heat input, Table (3). At the moderate heat input of 55 kJ/in, the HAZ SCC resistance is slightly below that of the base plate. At 113 kJ/in, the HAZ SCC resistance is lower than that of the weld metal. The HAZ SCC resistance in HSLA-100 is similar to that of the base plate at a heat input of 85 kJ/in.

HY-130

K_{Iscc} data from long-term cantilever beam tests in natural seawater as a function of cathodic potential for HY-130 base plate, GMA weld, and HAZ are plotted in Figure (8) and summarized in Table (3). The trend toward decreasing SCC resistance with more electronegative potentials can clearly be seen for all three materials. The base plate is the most resistant of the materials and shows the least sensitivity to changes in potential while the weld metal is the most susceptible of the materials and shows the most sensitivity to changes in potential. The fact that the HAZ falls between the base metal and weld data may indicate that a mixture of base plate and weld metal were tested rather than the true heat affected zone. Again, attempting to investigate metallurgical features which occur over relatively small areas is difficult with the standard cantilever beam specimen.

Decreases in SCC resistance at increasingly electronegative potentials were also seen for HY-130 base plate and GMA weld metal in slow strain rate tests [Klein and Hays (1993)] and in SMA, GMA, and GTA welds tested using step-loaded cantilever beams in a 3.5% NaCl environment [Fujii (1981)]. The slow strain rate specimens had the advantage of being small enough to be thermally treated to simulate microstructural features (i.e. tempered or untempered weld beads, heat affected zones, etc.) and the work confirmed the greater sensitivity of the weld metal to changes in cathodic potential. However, the results of these tests could only be used to relatively rank the various material conditions. All the K_{Iscc} values reported in the step-loaded cantilever beam study were significantly higher for each potential than those for the long-term study, presumably due to a lack of time for hydrogen to diffuse to critical locations.

SUMMARY AND CONCLUSIONS

It is generally accepted that high strength steels under cathodic protection in seawater can undergo a form of stress corrosion cracking known as hydrogen embrittlement. Quantifying this susceptibility is important to designers and maintainers of marine structures. The U.S. Navy typically uses the cantilever beam technique which comprises a fracture mechanics specimen under deadweight loading in a marine environment to assess susceptibility of high strength steels to stress corrosion cracking. Properly performed, this technique will yield a critical stress intensity for initiation of stress corrosion cracking (K_{Iscc}) which can then be used in design and flaw tolerance analyses.

A survey of available cantilever beam stress corrosion cracking data for the "HY" and "HSLA" steels was performed. Based on the results of the survey, the following conclusions are made.

- HY-80 base and weld metals are highly resistant to stress corrosion cracking under conditions typical of marine use (i.e. seawater immersion under -1.0 V versus Ag/AgCl cathodic protection). Some limited susceptibility was seen for HY-80 heat affected zones at very high (>100 kJ/in) weld heat inputs. Although test results are not available for HSLA-80 base plate, the highly refined microstructure and toughness of this alloy indicate SCC resistance at least as good as HY-80.
- The SCC data for HY-100 base plate and welds shows a high degree of scatter. However, a general trend of increasing susceptibility with increasing yield strength is apparent. The limited data for HSLA-100 indicate that it is at least as resistant to SCC as HY-100.
- As expected, HY-130 is the most susceptible to SCC of the alloy families surveyed. Increasingly electronegative potentials increased the susceptibility of the base plate, GMA weld, and heat affected zone.
- While long term cantilever beam testing has the benefit of producing a design parameter under loading and environmental conditions similar to those experienced by marine structures, the technique can result in a large degree of scatter if:
  - ⇨ Large gradients in properties occur in the material over small distances relative to the key specimen dimensions of width, thickness, and crack length;
  - ⇨ An insufficient number of specimens is used;
  - ⇨ Inadequate test durations are used;
  - ⇨ Residual stress levels are high.

ACKNOWLEDGEMENTS

The authors would like to thank those at the Naval Sea Systems Command (NAVSEA) and the Office of Naval Research (ONR) who provided the funding for the work summarized here. The assistance of the NSWCCD and LaQue Center for Corrosion Technology personnel who participated in the preparation, testing, and analysis of specimens is greatly appreciated.

REFERENCES

Beachem, C.D., "A New Model for Hydrogen Assisted Cracking (Hydrogen Embrittlement)," Met. Trans. Vol. 3, p 437 (1972).

Fontana, M.G., Corrosion Engineering, McGraw-Hill, Inc., New York (1986).

Fujii, C.T., "Factors Influencing Stress-Corrosion Cracking of High-Strength Steel Weld Metals," Met. Trans. A, Vol. 12A, pp. 1099-1105, June, 1981.

Kirk, M.T., "A Cyclic Reverse Bending Technique for Fatigue Precracking from Shallow Notches in SE(B) Specimens," Fracture Mechanics: Twenty-Second Symposium (Volume I), ASTM STP 1131, H.A. Ernst, A. Saxena, and D.L. McDowell, Eds., American Society for Testing and Materials, Philadelphia, PA (1992).

Klein, P.A. and R.A. Hays, "The Hydrogen Cracking Susceptibility of a High Strength Steel Weldment," Slow Strain Rate Testing for the Evaluation of Environmentally Induced Cracking, Research and Engineering Applications, ASTM STP 1210, R.D. Kane, ed., American Society for Testing and Materials, Philadelphia, PA, 1993.

Novak, S.R. and S.T. Rolfe, "Comparison of Fracture Mechanics and Nominal Stress Analyses in Stress Corrosion Cracking," Corrosion, Vol. 26, No. 4, (Apr 1970).

Parkins, R.N., "Slow Strain Rate Testing - 25 Years Experience," Slow Strain Rate Testing for the Evaluation of Environmentally Induced Cracking, Research and Engineering Applications, ASTM STP 1210, R.D. Kane, ed., American Society for Testing and Materials, Philadelphia, PA, 1993.

Petch, N.J. and P. Stables, "Delayed Fracture of Metals Under Static Load," Nature, Vol 169, pp 842-843 (1952).

Pressouyre, G.M., in Current Solutions to Hydrogen Problems in Steels, C.G. Interrante and G.M. Pressouyre eds., ASM Metals Park, OH, p. 18 (1982).

Troiano, A.R., "The Role of Hydrogen and Other Interstitials in the Mechanical Behavior of Metals," Trans. ASM, 52 (1), p 54-80 (1960).

Westlake, D.G., Trans. ASM, Vol 3, No. 2, p. 437 (1972).

Zanis, C.A., P.W. Holsberg, and E.C. Dunn, Jr., "Seawater Subcritical Cracking of HY-Steel Weldments," Welding Research Supplement, American Welding Society, Dec. 1980.

Zapffe, C.A. and C.E. Sims, "Hydrogen Embrittlement and Defects in Steel," Trans AIME, Vol 145, pp. 225-261 (1941).

Table (1). HY and HSLA Steel Compositions

Material	Composition (weight %) - Maximum Unless Range Specified										
	C	Ni	Cr	Mo	Cu	Mn	P	S	Si	Cb	V
HY-80 Steel MIL-S-16216K	0.13-0.18	2.50-3.50	1.40-1.80	0.35-0.60	0.25	0.10-0.40	0.015 max	0.008	0.15-0.38	---	---
HSLA-80 Steel MIL-S-24645A	0.06	0.70-1.00	0.60-0.90	0.15-0.25	1.00-1.30	0.40-0.70	0.020	0.006	0.40	0.02-0.06	---
HY-100 Steel MIL-S-16216K	0.14-0.20	2.75-3.50	1.40-1.80	0.35-0.60	0.25	0.10-0.40	0.015	0.008	0.15-0.38	---	---
HSLA-100 Steel MIL-S-24645A	0.06	3.35-3.65	0.45-0.75	0.55-0.65	1.45-1.75	0.75-1.05	0.020	0.006	0.40	0.02-0.06	---
HY-130 MIL-S-24371A	0.12	4.75-5.25	0.40-0.70	0.30-0.65	0.25	0.60-0.90	0.010	0.010	0.15-0.35	---	0.05-0.10

Table (2). Mechanical Properties of HY and HSLA Steels

Grade	Specification	Yield Strength		Tensile Strength		Elongation in 2-in.	Reduction of Area	Charpy V-Notch	Dynamic Tear	Comment
		(ksi)	(MPa)	(ksi)	(MPa)	(%)	(%)	(ft-lb)	(ft-lb)	
HY-100	MIL-S-16216K	100-120	690-827	120 typ.	827 typ.	18	45	60 @ 0 F 40 @ -120 F	500 @ -40 F	> 3/4-in. Plate
HY-80	MIL-S-16216K	80-99.5	552-686	105 typ.	724 typ.	20	50	60 @ 0 F 35 @ -120 F	450 @ -40 F	<= 1.25-in. Plate
HSLA-100	MIL-S-24645A	100-125	690-862	120 typ.	827 typ.	18	45	80 @ 0 F 60 @ -120 F	record @ -40 F	> 3/4-in. Plate
HSLA-80	MIL-S-24645A	80-100	552-690	100 typ.	690 typ.	20	50	60 @ -120 F	record	<= 1.25-in. Plate
HY-130	MIL-S-24371A	130-145	896-1000	142 typ.	979 typ.	15	50	60 @ 0 F 60 @ 70 F	---	2-in. Plate

Table (3). Summary of HY and HSLA Steel Stress Corrosion Cracking Data

Material	Potential	Yield Strength		KIscc		Comment
	(V vs. Ag/AgCl)	(ksi)	(MPa)	(ksi√in)	(MPa√m)	
HY-80 Base Plate	-1.000	80	552	>125	>137	WOL Test
HY-80 GMAW	-1.000	82	565	133	146	WOL Test
HY-80 SMAW	-1.000	85	586	125	137	WOL Test
HY-80 HAZ	-1.000	---		70	77	Heat Input 113 kJ/in
HSLA-100 Base Plate	-1.000	118	814	113	124	
HSLA-100 Base Plate	-1.500	106	731	90	99	
HSLA-100 SAW	-1.000	110	758	99	109	
HSLA-100 HAZ	-1.000	---		121	133	Heat Input 85 kJ/in
HY-100 Base Plate	-0.650	109	752	123	135	
HY-100 Base Plate	-1.000	112	772	122	134	
HY-100 GMAW	-1.000	119	821	112	123	
HY-100 GMAW	-1.000	120	827	62	68	
HY-100 GMAW-P	-1.000	132	910	87	96	
HY-100 GMAW-P	-1.000	124	855	85	93	
HY-100 GMAW-P	-1.000	125	862	90	99	
HY-100 GMAW-P	-1.000	133	917	85	93	
HY-100 GMAW-P	-1.000	131	903	95	104	
HY-100 GMAW	-1.000	104	717	110	121	
HY-100 SMAW	-1.000	124	855	98	108	
HY-100 GTAW	-1.000	128	883	109	120	
HY-100 HAZ	-1.000	---		101	111	Heat Input 55 kJ/in
HY-100 HAZ	-1.000	---		60	66	Heat Input 113 kJ/in
HY-130 Base Plate	-0.650	137	945	110	121	
HY-130 Base Plate	-0.850	137	945	96	106	
HY-130 Base Plate	-1.000	137	945	90	99	
HY-130 GMAW	-0.850	145	1000	50	55	
HY-130 GMAW	-1.000	140	965	30	33	
HY-130 HAZ	-0.850	---		75	82	Heat Input 30-50 kJ/in
HY-130 HAZ	-1.000	---		45	49	Heat Input 30-50 kJ/in

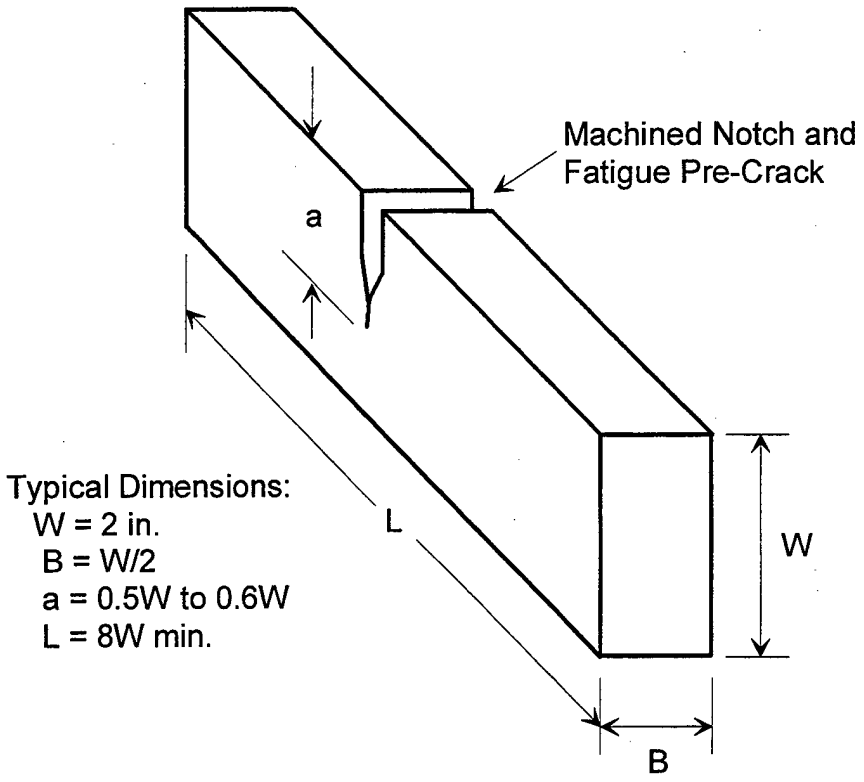


Figure (1). Schematic of Cantilever (Single Edge Notch) Beam SCC Specimen

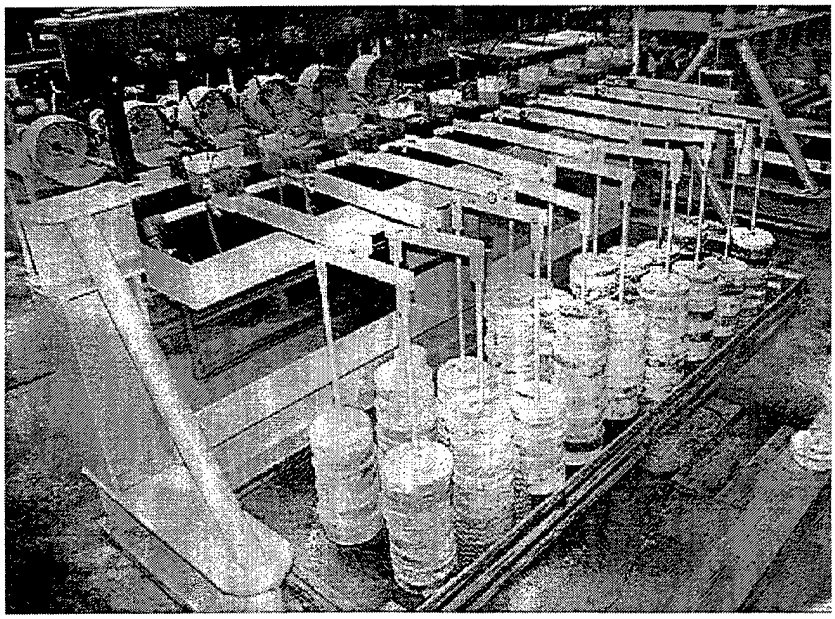


Figure (2). Typical Cantilever Beam Test Rack Showing Deadweight Loading

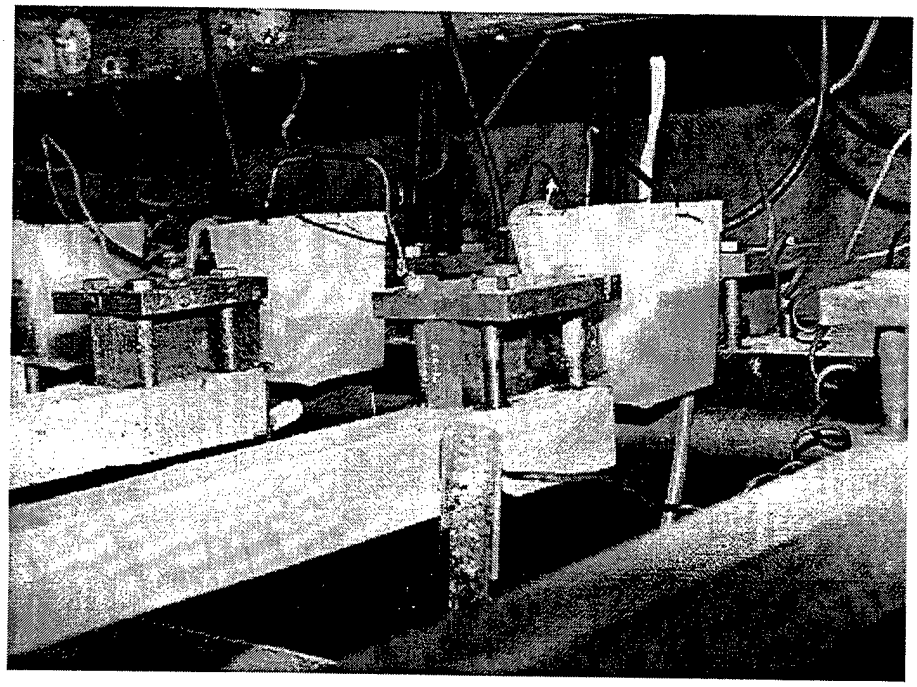


Figure (3). Close Up Cantilever Beam Test Area with Seawater-Filled Container Surrounding Crack Tip

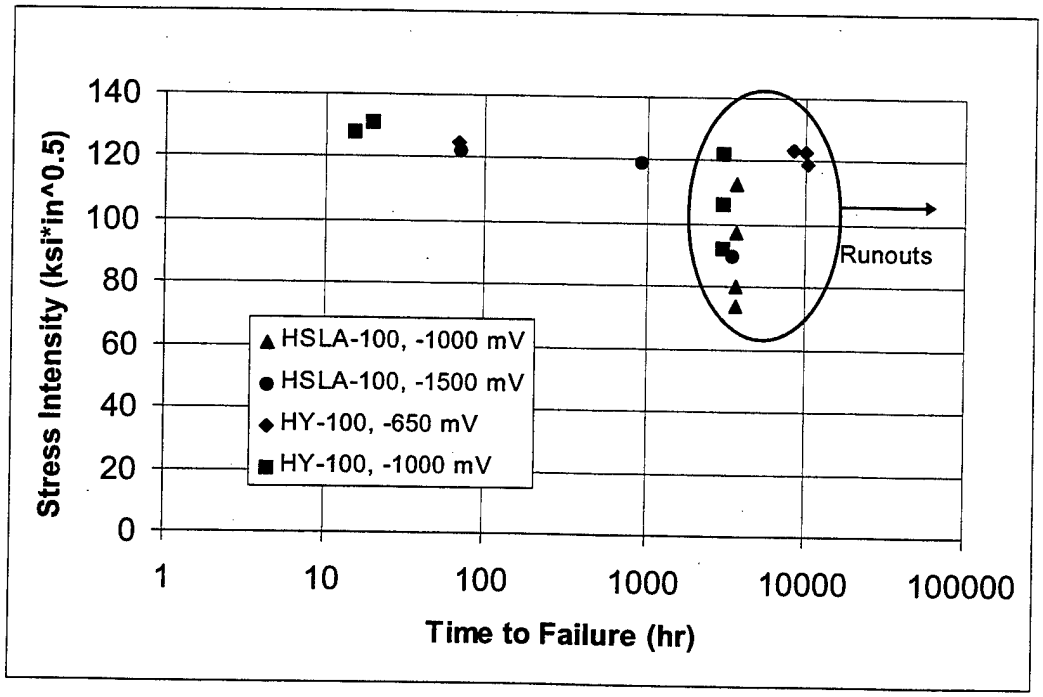


Figure (4). Stress Intensity versus Time to Failure for HY-100 and HSLA-100 Base Plate

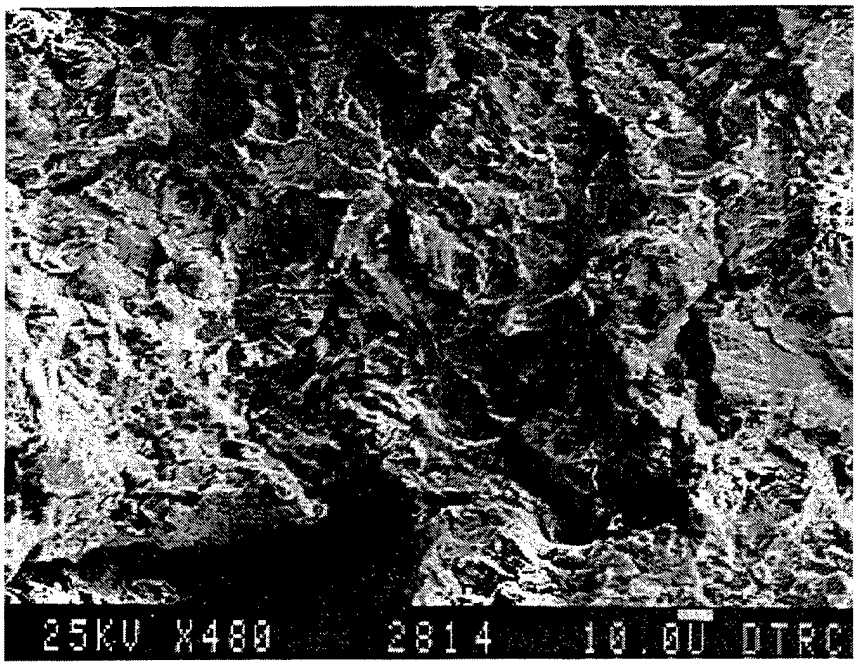


Figure (5). SCC Fracture Surface of HSLA-100 Steel Tested at -1.5V versus Ag/AgCl.

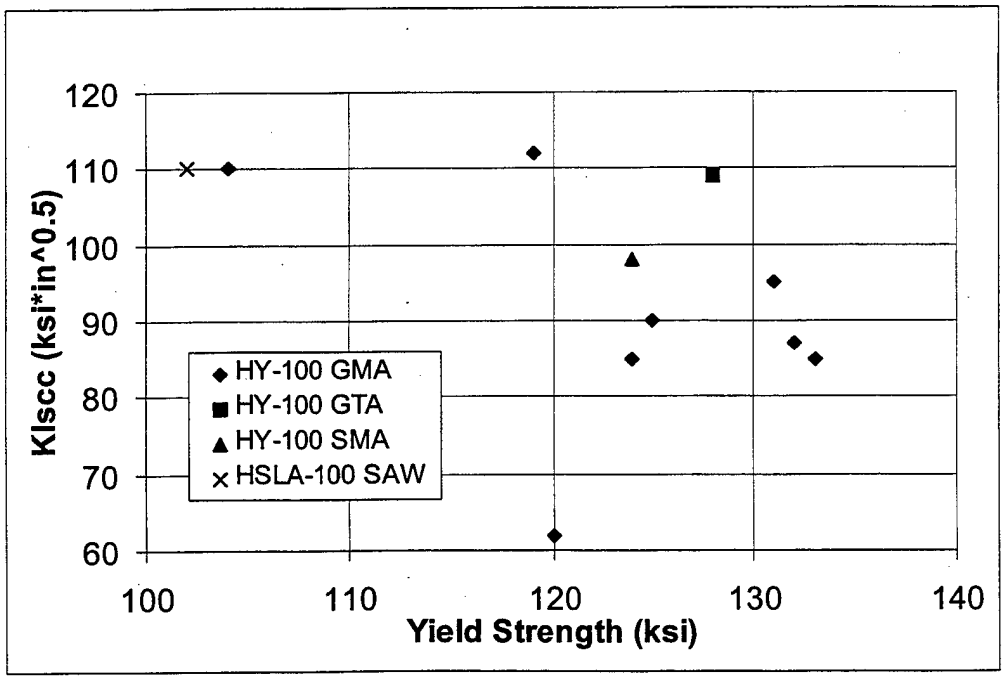


Figure (6). K_{Iscc} Data for HY-100 and HSLA-100 Welds

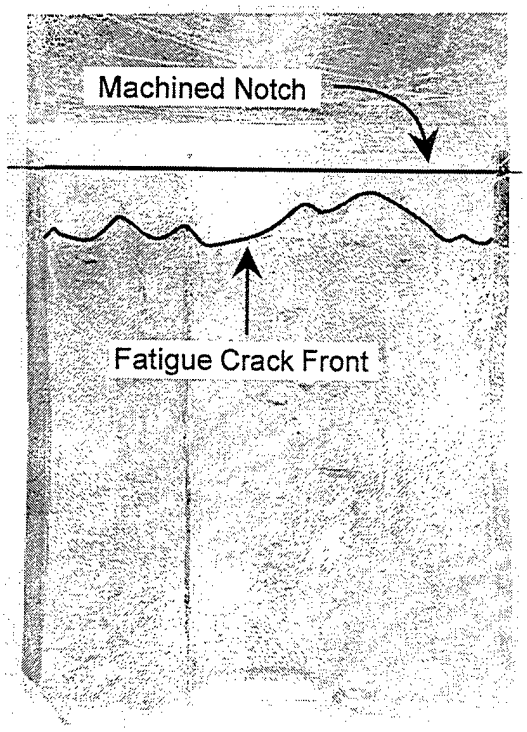


Figure (7). Non-Uniform Crack Front in HY-100 Weld

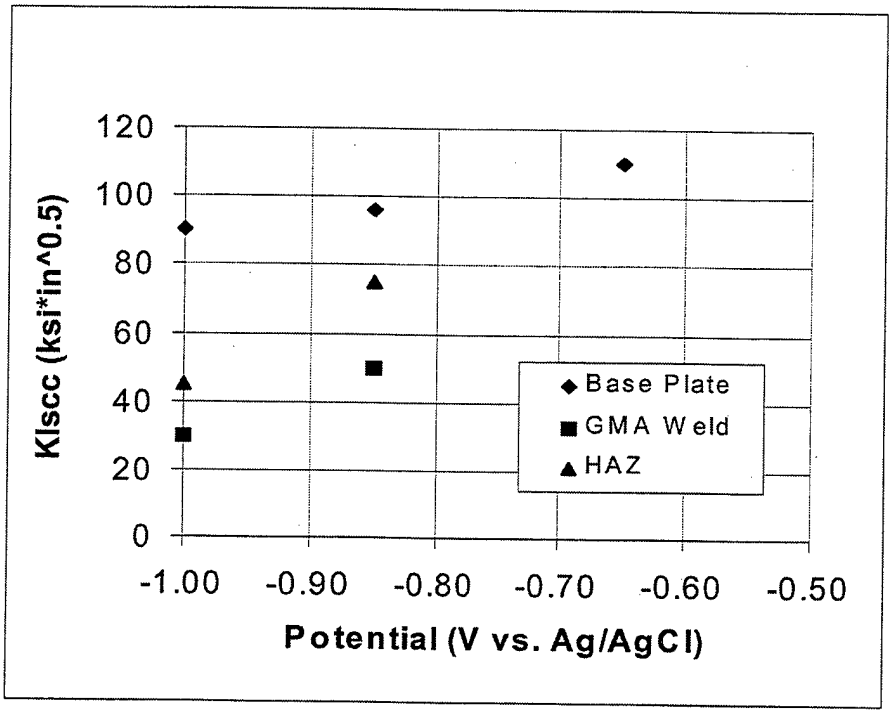


Figure (8). K_{Iscc} Data for HY-130 Steel as a Function of Cathodic Potential

The Effect of Heat Treatment on Hydrogen Trapping in AerMet 100 and Alloy K-500

B. G. Pound
SRI International
333 Ravenswood Ave.
Menlo Park, CA 94025

ABSTRACT

The effect of heat treatment on irreversible hydrogen trapping was investigated for AerMet 100 and alloy K-500. A potentiostatic pulse technique was used to determine irreversible trapping constants (k) and H entry fluxes. Irreversible trapping in AerMet 100 varies with aging temperature. The order of k values for AerMet 100 and other high-strength steels inversely parallels their threshold stress intensities for stress corrosion cracking. The type of heat treatment used for alloy K-500 can also produce marked differences in irreversible trapping. The values of k for annealed-aged and direct-aged specimens were found to correlate with their observed resistances to hydrogen embrittlement.

INTRODUCTION

Various high-strength alloys are used by the Navy for fasteners and aircraft components such as landing gear and arresting hooks. These alloys must meet stringent requirements with respect not only to strength but also to resistance to environmentally assisted cracking. One of the alloys developed for aerospace applications is a martensitic steel—AerMet 100—that is strengthened by precipitation of M_2C carbides (M = Mo and Cr, with Fe also being identified in one study).[1,2] This steel is reported to have a higher resistance to hydrogen-assisted cracking in 3.5% NaCl than 18Ni maraging steel, 300M, and AISI Types 4340 and H11 steel.[3,4] However, precipitation-hardened, martensitic iron-base alloys as a group tend to be rather prone to hydrogen embrittlement (HE).[5,6]

Another type of alloy, the age-hardenable Ni-Cu alloy K-500, is used extensively for seawater applications where strength is a critical factor. However, aging can render the alloy more susceptible to HE, depending on the type of heat treatment.[7] Tests on cold worked alloy K-500 have shown that the ultimate tensile strength of annealed and aged (AA) specimens which were cathodically precharged for 16 days decreased by 35%, whereas the strength of the direct-aged (DA) alloy actually increased slightly. Thus, alloys, such as the high-strength steels and alloy K-500, that are of interest in their aged conditions continue to be of considerable concern regarding the possibility of HE.

The resistance of an alloy to HE is strongly affected by the interaction of hydrogen (H) with microstructural defects that act as H traps.[8] The local concentration of H trapped at a defect must reach some critical level (C_k) for cracks to be initiated.[8,9] The magnitude of C_k depends on factors such as the size and location of the defect. Thus, the type of defect can play a crucial role in determining an alloy's intrinsic susceptibility to HE, with large irreversible (high binding energy) traps typically imparting a high susceptibility.[9,10]

Over the last few years, H trapping in various high-strength alloys has been investigated at SRI by using a potentiostatic pulse technique.[11-15] The alloy of interest is cathodically charged with H at a constant potential for a given time. The potential is then stepped in the positive direction, so that H diffuses back to the entry surface and is reoxidized. The resulting anodic current transients obtained for different charging times are analyzed by using a diffusion/trapping model to determine values of the irreversible trapping constant (k) and H entry flux (J). The results show, for most of the alloys studied, a correlation between the intrinsic susceptibility, as represented by k, and the actual resistance to HE observed in mechanical tests. This correlation applies only to the specific alloys tested in their particular thermomechanical conditions and may not extend to these alloys at lower yield strengths or to other alloys. Exceptions to the correlation can occur, for example, when the entry flux is so low that it becomes the primary factor in determining the resistance to HE.

The correlation appears to apply to a range of alloys, including steels, Ni-base alloys, and Cu-Ni alloys. However, it has not been determined to what extent this correlation applies, particularly with respect to an alloy that is heat treated under different conditions. In the present work, the pulse technique was used to investigate the effect of heat treatment on irreversible trapping in AerMet 100 and alloy K-500. The variation in k was examined as a function of yield strength for AerMet 100 and type of heat treatment (direct aging versus annealing and aging) for alloy K-500. AerMet 100 extends the range of high-strength steels (4340, H11, and 18Ni) examined previously,[11, 12, 15] while alloy K-500 with different heat treatments provided a comparison with specimens of this alloy that had already been studied.[14, 15] The results were intended to characterize the intrinsic susceptibility of AerMet 100 and alloy K-500 to HE in terms of their irreversible trapping constants and to elucidate whether heat treatment has a large influence on the resistance of these alloys to HE.

ANALYSIS

Trapping Constants

The current transients obtained by the pulse technique were analyzed using a model that allows for the effect of trapping on diffusion for cases involving either a constant concentration or a constant flux at the input surface.[11, 16] In contrast, most, if not all, models for permeation methods are based solely on an input boundary condition of constant concentration. The permeation models thus strictly apply only for charging conditions without any entry limitation.

The constant flux model for analyzing the pulse data has been found to apply to all alloys studied to date. In this model, the rate of H ingress is controlled by diffusion, but the entry flux of H is restricted, which results in interface-limited diffusion control. Solution of the diffusion equation for a constant flux condition gives the following expression for the anodic charge (C m^{-2}):

$$q'(\infty) = FJ\, t_c\{1 - e^{-R}/(\pi R)^{1/2} - [1 - 1/(2R)]\mathrm{erf}(R^{1/2})\} \qquad (1)$$

where F is the Faraday constant, J is the entry flux in mol m^{-2} s^{-1}, $R = k_a t_c$, and k_a is an apparent trapping constant measured for irreversible traps in the presence of reversible traps. The charge $q'(\infty)$ is equated to the charge (q_a) passed during the experimental anodic transients. q_a can be associated entirely with absorbed H, because the adsorbed charge is almost invariably negligible.

For the constant flux model to apply, it must be possible to determine a value of k_a for which J is independent of charging time at each potential. Also, the model requires that k_a be independent of charging potential (except when a change in trapping behavior occurs), because the trapping characteristics should be unaffected by electrochemical conditions unless the traps become filled to a significant extent.

Intrinsic Susceptibility to HE

k_a is related to the irreversible trapping constant (k) by kD_a/D_L, where D_a is the apparent diffusivity and D_L is the lattice diffusivity of H. The magnitude of k depends on the density of particles or defects (N_i) providing irreversible traps, the radius (d) of the trap defects, the diameter (a) of the metal atom, and D_L:[17]

$$k = 4\pi d^2 N_i D_L / a \qquad (2)$$

The term d^2N_i can be used to represent the trapping capacity and thus provides a basis for proposing k as an index of an alloy's intrinsic susceptibility to HE. It has long been recognized that the susceptibility is affected by a wide range of factors, but some of them would be expected to exert a greater influence than others and so be primarily responsible for determining the susceptibility. The correlation observed between k and the actual resistance to HE suggests that k contains enough key parameters to be effective as an index of susceptibility for the alloys studied to date at their respective yield strengths. Parameters other than those above may well assume a greater role at low yield strengths, such that k becomes inadequate as an index of susceptibility.

Trap size is a particularly important parameter because of the strong influence that it has on the critical concentration. At C_k, the trapped hydrogen causes enough of an increase in the induced and applied stresses and/or the hydrogen pressure to overcome the cohesive strength, which itself may be decreased.[18] The capability of large irreversible traps to impart a high intrinsic susceptibility results from their relatively high probability of being located in a crack-sensitive region and therefore of being associated with low values of C_k.[8] In contrast to large traps, irreversible traps that are finely and homogeneously distributed may delay the onset of cracking.[9] However, small irreversible traps can also be detrimental—that is, have a low C_k—if they lie in a vulnerable region such as a grain boundary.

Hydrogen is generally distributed within an alloy over a range of metallurgical sites with different interaction (and binding) energies.[19] However, these energies tend to fall into reasonably well-defined groups. In steels, for example, the interaction energy is ≤29.9 kJ/mol for most solute elements, dislocations, and grain boundaries; 53.1-58.9 kJ/mol for high angle grain boundaries; but somewhat higher for particle-matrix interfaces associated with MnS, Fe_3C, and TiC (up to 94.6 kJ/mol for incoherent particles). Thus, in terms of irreversible traps, only a few types of microstructural heterogeneities are usually important, these being primarily particle-matrix interfaces. More importantly, within a group of irreversible traps of similar interaction or binding energies, the relative contribution of each type of heterogeneity to k is determined by its size and density.

The effect of small irreversible traps on the value of k is a critical issue with respect to HE susceptibility. Homogeneously distributed, small particles (<<1 μm for α-Fe) that are irreversible

traps can be beneficial in terms of delaying crack initiation, as noted above. Because of their small size, these particles are more likely to be associated with high values of C_k.[20] Moreover, the particles are supposedly small enough to limit their concentration of trapped H such that it cannot reach C_k. Thus, the presence of small particles would not be expected to increase the intrinsic susceptibility (as determined by the irreversible traps) or, as a consequence, decrease the observed resistance to HE. Accordingly, k will not reflect the intrinsic susceptibility correctly when *only* small traps are present; the relationship between k and $N_i d^2$ implicitly applies to particles that are large enough for C_H to reach C_k. Neverthless, it should be noted that the presence of irreversible traps alone does not necessarily result in a high trapping constant; since k (and k_a) is proportional to d^2, small particles and other heterogeneities, even if numerous, may be associated with a relatively low value of k.

Previous results obtained with the pulse technique indicated that k is generally a reliable index of intrinsic susceptibility for engineering alloys containing a *range* of irreversible traps. In practice, most irreversible traps are characterized by large specific saturabilities, as noted by Gibala and DeMiglio.[21] The majority of the engineering alloys in the pulse tests contained carbides, carbonitrides, or sulfides that were in the form of large particles (>1 μm and typically several micrometers). Because of their density and size, these particles would be expected to have the predominant influence on the value of k. The trap density calculated using Eq. (2) was in fact found to be in good agreement with the actual concentration of particles for a number of the alloys, which indicated that it was these large particles that provided the *principal* irreversible traps.[13] Such particles are known to increase the extent of H damage in an alloy, particularly if they are distributed heterogeneously.[9] Thus, the addition of large traps gives a higher k value and is expected to cause a corresponding decrease in the actual resistance to HE, which fits with the observed correlation. Although a range of traps may be present in the alloys, the ability of the carbides and other particles to accumulate large amounts of H makes them likely sites for crack initiation.

The contribution of small particles to k in the case of most engineering alloys appears to be overwhelmed by that of larger particles, such that k correlates with the observed resistance to HE. However, this correlation may not hold for some alloys because the effect of large detrimental traps on the resistance to HE is delayed by a slow rate of H accumulation, which in turn is caused by either a restricted H entry into the alloy or the presence of a high density of small, homogeneously distributed, reversible or irreversible, trap heterogeneities.

EXPERIMENTAL PROCEDURE

Alloys

Table 1 shows the compositions of AerMet 100 and the other steels—4340, H11, and 18Ni. The AerMet 100 was supplied as 1.36-cm-diameter rod in an annealed/overaged (677°C/16 h) condition. A section of rod was subsequently solution treated at 885°C for 1 h, air cooled to 66°C over 1-2 h, further cooled to -73°C for 1 h, and finally aged for 5 h at temperatures of 270°, 370°, and 482°C, which is the standard aging temperature.

The microstructure of AerMet 100 was not examined in this study, because it has been investigated in detail by other workers.[1,2] The alloy has an Fe-Ni lath martensite structure. Fe_3C precipitates were found in alloy aged between 316° and 482°C but not at 204°C, which suggests

that they can be formed somewhere in the range from 204° to 316°C. Aging at temperatures above 454°C causes precipitation of coherent M_2C carbides within the martensite, as noted above. Novotny found that the M_2C carbides produced by a 482°C/5 h age are well-dispersed, very fine, rod-shaped precipitates with an average length of 9.1 nm.[2] Similar observations were made by Ayer and Machmeier, who reported the carbides as having a length of ~8 nm and a diameter of ~3 nm.[1] Ayer and Machmeier found that the M_2C carbides contained Cr, Mo, and Fe and that there was no Fe_3C, at least at the grain boundaries, in a 482°C-aged sample. In contrast, Novotny reported that only Mo and Cr constituted the metallic components in the M_2C carbides and that rod-shaped Fe_3C precipitates (40 nm long × 5 nm wide) were present. AerMet 100 also contains ~3 vol.% austenite as quenched and when aged for 5 h at temperatures from 93° to 468°C. Aging at 482°C increased the amount of austenite slightly to 4 vol.%. The austenite is present as a thin film (~3 nm) at the martensite lath boundaries.

Table 1 also gives the compositions of cold drawn (CD) alloy K-500 and the annealed and aged alloy (in two heats, denoted as AA-1 and AA-2)(1) used previously.[15] AA-1 and AA-2 were supplied as sections of bar that had been solution-annealed and aged at 607°C for 16 h to give a yield strength in the range 689-724 MPa. The alloys had a similar bulk composition, but the AA-2 alloy exhibited a moderate amount (~20%) of graphitic C at the grain boundaries, whereas the AA-1 alloy contained only a small amount (1-3%) of grain boundary C.[22]

The CD alloy K-500 was supplied as a 1.27-cm-diameter rod, which was direct aged (DA) in the previous work to give a yield strength of about 1096 MPa. The aging treatment followed the procedure recommended for CD rods ≤3.8 cm in diameter: Heat at 600°C for 8 h and then cool to 480°C at a rate of 11°C/h.[23] In the present work, the CD alloy was annealed at 982°C and, where relevant, aged at 600°C. The alloy was tested in four conditions: (1) annealed for 0.5 h, (2) annealed for 0.5 h and aged for 8 h, (3) annealed for 0.5 h and aged for 16 h, and (4) annealed for 0.25 h and aged for 8 h. These conditions are denoted as 0.5h-A, 0.5h-AA, 0.5h-AA-16h, and 0.25h-AA, respectively. During aging, particles of $Ni_3(Ti,Al)$ are precipitated throughout the matrix of alloy K-500.[23]

Electrochemical Tests

Details of the electrochemical cell and instrumentation have been given previously.[11] The test electrodes consisted of a 1.27-cm length of rod press-fitted into a polytetrafluoroethylene sheath so that only the planar end surface was exposed to the electrolyte. The surface was polished before each experiment with SiC paper followed by 0.05-μm alumina powder. The electrolyte contained 1 mol L^{-1} acetic acid and 1 mol L^{-1} sodium acetate (pH 4.8) with 15 ppm As_2O_3 and was deaerated continuously with argon before and throughout data acquisition. The potentials were measured with respect to a saturated calomel electrode (SCE). All tests were performed at 22° ± 1°C.

The test electrode was cathodically charged with H at a potential E_c for a time t_c, after which the potential was stepped anodically to a value 10 mV negative of the open-circuit potential E_{oc}. Anodic current transients were obtained over a range of charging times, typically from 5 to 60 s, at different overpotentials ($\eta = E_c - E_{oc}$). The open-circuit potential of the test electrode was measured immediately before each charging time and was also used to monitor the stability of the alloy surface.

(1) Provided by Dr. M. Natishan, University of Maryland, while at the David Taylor Research Center, Department of the Navy.

RESULTS

For alloy K-500 and aged AerMet 100, Eq. (1) could be fitted to the experimental data for q_a to obtain values of k_a and J where J was independent of charging time. For overaged AerMet 100, q_a increased linearly with t_c, indicating that $k_a = 0$ and therefore that irreversible trapping was negligible. Tables 2 and 3 show the number of tests and range of overpotentials used for AerMet 100 and alloy K-500, respectively. Also listed are the number of k_a values and the mean k_a obtained for each test.

The values of k_a for aged AerMet 100 are presented in Figure 1. In all the tests, k_a was independent of charging potential, as is required for the model to be valid. The aged alloy, in contrast to the overaged alloy, exhibited moderately high values of k_a, which were indicative of pronounced irreversible trapping. However, raising the aging temperature from 270° to 370°C did not have a significant effect on k_a, whereas it was increased considerably by aging at the standard temperature of 482°C. The overall mean value of k_a for each aging temperature is given in Table 4, which shows that k_a for the 482°-aging is 50% higher than the value for the two lower aging temperatures.

The values of k_a for alloy K-500 in each condition are given in Figure 2. k_a was independent of charging potential also for this alloy. Annealing increased k_a, with the unannealed DA alloy having the lowest value, followed by the 0.25-h-annealed alloy and then the 0.5-h-annealed alloy. The overall mean values of k_a listed in Table 4 show that k_a is more than doubled by a 0.25-h anneal and is tripled by a 0.5-h anneal. In contrast, k_a was essentially independent of aging time (such that it was the same within experimental uncertainty) for all conditions involving a 0.5-h-anneal.

DISCUSSION

Irreversible Trapping Constants

Irreversible trapping constants (k) were calculated from the mean values of k_a by correcting for the effect of reversible traps. The correction is made using diffusivity data for the "pure" alloy to obtain the lattice diffusivity (D_L) and for the actual alloy to obtain the apparent diffusivity (D_a). From the viewpoint of diffusivity, the "pure" alloys were assumed to be 65Ni-35Cu for alloy K-500 and Fe-11Ni-3Cr for AerMet 100. (Although Co is a prominent alloying element in AerMet 100, it is regarded as an anti-trap in Fe[8] and has been shown to have little effect on the diffusivity[24]). Minor elements (either in their atomic form or as intermetallics precipitated during aging) in the actual alloys were treated as reversible traps and in fact were assumed to be primarily responsible for reversible trapping.

For body-centered cubic (bcc) Fe, elements such as Cr can have a marked effect on the diffusivity of H.[25] For example, the addition of 5 at% Cr to Fe decreases the diffusivity by over two orders of magnitude at 27°C. Although AerMet 100 differs in having a martensitic lattice and in Cr being considered one of the its major elements, minor elements that act as reversible traps could also be expected to have significant but smaller effects in this alloy. Moreover, based on the case of Cr, even these reduced effects are likely to be large enough to dominate those from microstructural defects such as dislocations. The austenite present at lath boundaries may provide

reversible traps in the actual alloy, but the small amount (3-4 vol%) suggests that the effect of the austenite should be small enough to ignore, particularly for a martensitic lattice. The contribution of the martensitic lattice itself is discussed below.

For face-centered cubic (fcc) alloys, defects such as vacancies or edge dislocations were presumed to make a negligible contribution to reversible trapping, because the binding energy of H to such defects is considerably smaller than the activation energy for diffusion.[26,27] Thus, reversible trapping in alloy K-500, which has an fcc lattice, should be influenced more by composition than by microstructural defects.

AerMet 100 — The diffusivity was not available for martensitic Fe-11Ni-3Cr, so a value was estimated for D_L from data for ferritic Fe-3Cr.[25] The diffusivity for Fe-3Cr is $(7.5 \pm 0.5) \times 10^{-11}$ $m^2 s^{-1}$, which approaches the diffusivities for quenched and tempered martensitic steels (even with reversible traps) such as 4340 (1.4×10^{-11} $m^2 s^{-1}$)[28] and thus suggests that the decrease caused by the Cr is enough to effectively incorporate that resulting from the martensitic lattice of AerMet 100. The effect of Ni on the diffusivity for Fe is much smaller than that of Cr; for example, 5Ni decreases the diffusivity by a factor of only 1.3 compared with ~140 for 5Cr.[25,29] Hence, it was assumed that the effect of 11Ni on the diffusivity could be neglected. The presence of two phases (α and γ) in Fe-Ni alloys containing between 10 and 33% Ni[30] was ignored for the purposes of estimating data for a martensitic steel. Thus, D_L was taken simply as the diffusivity for Fe-3Cr.

Diffusivity data were also not available for AerMet 100. However, the diffusivity for another high-strength steel—D6AC with a yield strength of 1550 MPa—has been studied[28] and, although this steel contains only 1.08 Cr, was considered to provide the most appropriate value of D_a. The diffusivity obtained from electrochemical permeation measurements for D6AC is $(7.8 \pm 0.5) \times 10^{-12}$ $m^2 s^{-1}$. Thus, a value of 9.6 was obtained for D_L/D_a and was used to calculate values of k for AerMet 100, as given in Table 4. The same value of D_L/D_a was assumed to apply to the overaged alloy and the partially and standard (482°C) aged alloy, because the Fe_3C and M_2C particles precipitated during aging were considered irreversible traps[19] (discussed below) and therefore should not affect D_a as measured when only reversible traps are effective (irreversible traps being saturated).

Alloy K-500 — The lattice diffusivity was determined by interpolation of data for a range of binary Cu-Ni alloys and was found to be $(3.0 \pm 0.1) \times 10^{-14}$ $m^2 s^{-1}$ for 65Ni-35Cu at 25°C.[31] The level of Cu differs slightly between the 65Ni-35Cu alloy and actual alloy K-500 (30Cu), but the error in using the diffusivity of the 35Cu alloy for D_L was considered negligible. The apparent diffusivity for AA alloy K-500 (assumed to be at ambient temperature) is 1.90×10^{-14} $m^2 s^{-1}$, which is only slightly higher than the value of 1.48×10^{-14} $m^2 s^{-1}$ for the DA alloy.[7] These data were used to calculate values of k for the AA and DA alloys, as given in Table 4.

No data were available for the diffusivity for the annealed (unaged) alloy, so D_a was estimated from the values for the aged alloy. The intermetallic particles precipitated during aging appear to have little effect on D_a compared with that of the minor alloying elements in solid solution: D_a for the DA alloy was only about a factor of 2 smaller than D_L. Because most solutes introducing an electron vacancy provide reversible traps that could largely account for this factor, the intermetallics must be presumed to add little to the effect of the minor elements. Hence, it was assumed that D_a for the annealed alloy could be approximated to that for the AA alloy. By using this value and the D_L above, k was calculated for the annealed alloy (Table 4).

Susceptibility to HE

AerMet 100 — The trapping constants for AerMet 100 are compared with those for the three other steels (4340, H11, and 18 Ni) in Table 4. AerMet 100 has the lowest k value and is therefore considered to have the lowest intrinsic susceptibility to HE of the four steels. The order of the k values for these steels inversely parallels typical values of their threshold stress intensities for stress corrosion cracking (K_{ISCC}) in 3.5% NaCl[3, 4] (Figure 3); that is, a lower value of k corresponds to a higher value of K_{ISCC}. This trend is underscored by the similarity in k values matching the similarity in K_{ISCC} values for the two most susceptible steels—4340 and H11. The k values indicate that the intrinsic susceptibility may actually be a little lower for H11. The order of this difference is consistent with test results showing that, for these two steels in distilled water, the failure times at various applied stress intensities were longer for H11.[32] Furthermore, the value of k for H11 is consistent with that for 18Ni steel in terms of the degree of embrittlement observed in electrolytic charging tests.[33]

The parallel between k and K_{ISCC} supports the general view that hydrogen plays the predominant role in stress corrosion cracking of martensitic steels.[34] Thus, for these four steels, k can be correlated with the observed resistance to HE, as represented by K_{ISCC}. This correlation provides additional support for the concept of k as an index of intrinsic susceptibility for high-strength alloys. In addition, it implies that the intrinsic susceptibility is a primary—possibly the predominant— factor determining the observed resistance of these high-strength steels to HE.

Figure 4 compares the dependence of k on aging temperature with a typical dependence of yield strength, as reported by the alloy producer.[35] k clearly follows the general trend in yield strength, exhibiting an initial increase before leveling off and then increasing more sharply. The changes in the two curves match reasonably well with respect to aging temperature, bearing in mind that the yield strength curve is not specific to either the form or size of alloy used in these tests. The increase in k with aging temperature, particularly between 370° and 482°C, implies that the observed resistance to HE should decrease based on the correlation between k and K_{ISCC}. Such a decrease would be consistent with the decreases in HE resistance observed for 4340 steel and 18Ni maraging steel as their yield strengths are increased.[6, 36] Bernstein and Thompson have shown, however, the resistance to HE to be more directly an effect of microstructure than of strength.[34, 37] Thus, k would not necessarily be expected to show a correlation with yield strength. Clearly, the more appropriate comparison is between k and the microstructural changes that occur during aging.

Figure 5 shows the variation in k and carbide size with aging temperature. The increase in k occurs in two stages. The first stage corresponds to Fe_3C precipitation and the second stage corresponds to M_2C precipitation. The arrest in k between 270° and 370°C coincides with the aging temperature range where the Fe_3C particles do not change in size. Furthermore, the subsequent steep increase in k occurs with the transition in carbides from Fe_3C to M_2C and evidently reflects the sharp increase in size of the M_2C particles. Possibly, the lath boundary austenite provides irreversible traps and hence that the higher k at 482°C resulted from the increase in austenite. However, the increase was only from 3 vol% to 4 vol%, and also k~0 for the unaged alloy with its 3 vol% austenite.(1) Another possibility is that impurities such as S and P segregate to grain boundaries during aging, thereby causing an increase in the irreversible trapping capability. Nevertheless, the M_2C particles remain most likely responsible for the increased k at

(1) Any additional reversible trapping caused by the slightly higher level (1 vol.%) of austenite in the standard aged alloy would decrease D_a and hence increase k. Hence, the effect of aging would appear even more pronounced.

482°C. Thus, irreversible trapping in AerMet 100 appears to involve the carbides primarily, with Fe_3C particles providing the principal traps for lower aging temperatures and M_2C particles filling that role for higher aging temperatures.

The M_2C particles in AerMet 100 aged at 454°C are coherent with the matrix,[(1)] but at least some of them appear to lose coherency at 482°C.[1] The particles are therefore expected to become more irreversible as traps for higher aging temperatures.[19] Lee has shown that stress corrosion cracking in AerMet 100 proceeds intergranularly,[38] which implies that the loss of coherency must occur preferentially at grain boundaries, if the resistance to HE is governed by irreversible trapping (as indicated by the correlation with k) and if the less coherent M_2C particles are the principal irreversible traps produced by aging at 482°C.

Alloy K-500 — The values of k for the different heat treatments are presented graphically in Figure 6. Clearly, alloy K-500 can exhibit a marked difference in irreversible trapping, depending on the type of heat treatment. Annealing caused a large increase in k for CD alloy K-500 and thus is deemed to greatly heighten the instrinsic susceptibility of this alloy. In fact, the values of k for all the 0.5-h-annealed specimens—unaged or aged—were more than twice as large as that obtained for the direct-aged CD specimen. Even halving the annealing time to 0.25 h resulted in a k double that of the DA alloy and only about 20% lower than the value obtained for the full (0.5-h) annealing time. Addition of the 0.5-h-annealing step before aging the CD alloy gave the same k values as those for the annealed and (16-h) aged alloy (AA-1 and AA-2) that was obtained from two other heats and tested previously. The effect of 8-h aging on k was negligible for the annealed alloy and relatively small for the unannealed alloy. Doubling the aging time to 16 h for the annealed alloy did not affect k. Thus, the annealed alloy had similar values of k in the unaged and the aged (at least up to 16 h) conditions.

The results show that differences in irreversible trapping observed previously between the DA specimens and the AA-1 and AA-2 specimens resulted from the differences in heat treatment. Moreover, they indicate that the key factor is the annealing step rather than the aging time and that annealing has quite a pronounced effect on the irreversible trapping characteristics of alloy K-500. Lee and Latanison have shown that graphite precipitation occurs at grain boundaries in Ni 200 (≤0.15 C) aged for 24 h at 450° to 650°C.[39] The AA-1 and AA-2 specimens, however, differed in heat treatment only with respect to annealing time yet exhibited different levels of grain boundary C, which implies that annealing renders alloy K-500 more prone to graphite precipitation during aging. Thus, the higher k values for the annealed and aged alloy appears to be determined by the amount of grain boundary graphitic C.

Tensile tests on alloy K-500, as noted above, showed a difference in ultimate tensile strength between DA and AA specimens cathodically precharged for 16 days.[7] The decrease (35%) in strength of the AA alloy together with the slight increase for the DA alloy indicated that the AA alloy is less resistant to HE. The order of the k values for the two types of aged alloy K-500 thus correlate with their observed resistances to HE, implying that the decrease in the resistance to HE produced by annealing is caused, at least in part, by changes in the irreversible H traps.

---

(1) Coherent particles are likely to be more reversible in terms of trapping.[19] If the coherent M_2C particles were reversible traps, D_a would be expected to decrease as the aging temperature is increased above 454°C, and so k would increase still more sharply with aging temperature.

The yield strength of alloy K-500 also varies with the type of heat treatment and should therefore be considered as a possible factor in the resistance to HE. However, the order of the yield strengths for the AA specimens (689-724 MPa) and the DA specimen (1096 MPa) was opposite to that of their k values, which suggests that the difference in HE susceptibility does not result from yield strength.

SUMMARY

- AerMet 100 exhibited a large difference in irreversible trapping between overaged (annealed) and aged specimens. In contrast to the overaged alloy, the aged alloy displayed significant irreversible trapping, which appears to be associated with Fe_3C particles at low aging temperatures and M_2C particles at high aging temperatures. The intrinsic susceptibility (as represented by k) of AerMet 100 to HE increases with aging temperature, particularly from 370° to 482°C.

- AerMet 100 in its standard aged (482°C) condition has a lower value of k than three other high-strength steels, 4340, H11, and 18Ni maraging steel. Hence, AerMet 100 has the lowest intrinsic susceptibility to HE of the four steels, whereas H11 and 4340 steel are the most susceptible. For these four steels, the observed resistance to HE, as represented by K_{ISCC}, can be correlated with the intrinsic susceptibility defined by k.

- Irreversible trapping in CD alloy K-500 can depend strongly on the type of heat treatment. Marked differences in k between DA and AA specimens can be attributed to the annealing step rather than to aging time. The intrinsic susceptibility to HE (k) is increased considerably by annealing, whereas aging has a negligible effect for the annealed alloy and only a modest effect for the unannealed alloy.

- The intrinsic susceptibilities for AA and DA alloy K-500 can be correlated with the observed resistances to HE. Thus, the decrease produced in the HE resistance by annealing appears to result to a large extent, if not entirely, from a change in the number or the type of irreversible traps. Differences in the grain boundary chemistry resulting from heat treatment could account for changes in the type of irreversible traps.

ACKNOWLEDGEMENT

Financial support of this work by the Office of Naval Research under Contracts N00014-91-C-0263 and N00014-95-C-0313 (Dr. A. J. Sedriks, Program Officer) is gratefully acknowledged.

REFERENCES

1. R. Ayer and P. M. Machmeier, *Metall. Trans.* **24A**, 1943 (1993).
2. P. M. Novotny, in *Proc. Gilbert R. Speich Symposium: Fundamentals of Aging and Tempering in Bainitic and Martensitic Steel Products* (ISS, Warrendale, PA, 1992), p. 215.
3. T. J. McCaffrey, *Advanced Mater. Proc.* **9**, 47 (1992).
4. P. M. Novotny and J. M. Dahl, in *Proc. 32nd Conf. on Mechanical Working and Steel Processing*, Vol. XXVIII (ISS, Warrendale, PA, 1991), p. 275.
5. A. W. Thompson, *Metall. Trans.* **4**, 2819 (1973).

6. D. P. Dautovich and S. Floreen, in *Proc. Conf. on Stress Corrosion Cracking and Hydrogen Embrittlement of Iron-Base Alloys*, eds. R. W. Staehle, J. Hochman, R. D. McCright, and J. E. Slater (NACE, Houston, TX, 1977), p. 798.
7. J. A. Harris, R. C. Scarberry, and C. D. Stephens, *Corrosion* **28**, 57 (1972).
8. I. M. Bernstein and G. M. Pressouyre, in *Hydrogen Degradation of Ferrous Alloys*, eds. R. A. Oriani, J. P. Hirth, M. Smialowski (Noyes Publications, Park Ridge, NJ, 1985), p. 641.
9. G. M. Pressouyre and I. M. Bernstein, *Acta Metall.* **27**, 89 (1979).
10. G. M. Pressouyre and I. M. Bernstein, *Metall. Trans.* **9A**, 1571 (1978).
11. B. G. Pound, *Corrosion* **45**, 18 (1989).
12 B. G. Pound, *Acta Metall.* **38**, 2373 (1990).
13. B. G. Pound, in *Proc. Fifth Int. Conf. on Hydrogen Effects on Material Behavior*, eds. N. R. Moody and A. W. Thompson (TMS, Warrendale, PA, 1996), p. 115.
14. B. G. Pound, *Corrosion* **50**, 301 (1994).
15. B. G. Pound, "Characterization of Hydrogen Ingress in High Strength Alloys," Final Report, Office Of Naval Research, Contract No. N00014-91-C-0263 (1995).
16. R. McKibbin, D. A. Harrington, B. G. Pound, R. M. Sharp, and G. A. Wright, *Acta Metall.* **35**, 253 (1987).
17. B. G. Pound, R. M. Sharp, and G. A. Wright, *Acta Metall.* **35**, 263 (1987).
18. G. M. Pressouyre and I. M. Bernstein, *Metall. Trans.*, **12A**, 835 (1981).
19. G. M. Pressouyre, *Metall. Trans.* **10A**, 1571 (1979).
20. G. M. Pressouyre, in *Current Solutions to Hydrogen Problems in Steels*, eds. C. G. Interrante and G. M. Pressouyre (ASM, Metals Park, OH, 1982), p. 18.
21. R. Gibala and D. S. DeMiglio, in *Proc. 3rd Int. Conf. on Effect of Hydrogen on Behavior of Materials*, eds. I. M. Bernstein and A. W. Thompson (TMS, Warrendale, PA, 1980), p. 113.
22. M. E. Natishan, E. R. Sparks, and M. L. Tims, in *ISTFA '90: Proc. Int. Symposium for Testing and Failure Analysis* (ASM, Materials Park, OH, 1990), p. 385.
23. Monel Nickel-Copper Alloys, 4th ed. (Huntington Alloys, Huntington, WV, 1981).
24. K. W. Lange and H. J. Koning, in *Proc. Second Int. Conf. on Hydrogen in Metals*, eds. P. Azou, paper 1A5 (1973).
25. J. O'M. Bockris, M. A. Genshaw, and M. Fullenwider, *Electrochim. Acta* **15**, 47 (1970).
26. W. D. Wilson and S. C. Keeton, in *Advanced Techniques for Characterizing Hydrogen in Metals*, eds. N. F. Fiore and B. J. Berkowitz (TMS, Warrendale, PA, 1981), p. 3.
27. J. Y. Lee and S. M. Lee, *Metall. Trans.* **17A**, 181 (1986).
28. C. S. Kortovich and E. A. Steigerwald, *Eng. Fract. Mech.* **4**, 637 (1972).
29. W. Beck, J. O'M. Bockris, M. A. Genshaw, P. K. Subramanyan, *Met. Trans.* **2**, 883 (1971).
30. R. E. Ogilvie, *Trans. TMS-AIME* **223**, 2083 (1965).
31. H. Hagi, *Trans. Jpn. Inst. Metals* **27**, 233 (1986).
32. W. D. Benjamin and E. A. Steigerwald, *Metall. Trans.* **2**, 606 (1971).
33. T. P. Groeneveld, E. E. Fletcher, and A. R. Elsea, *A Study of Hydrogen Embrittlement of Various Alloys*, Summary Report, Contract NAS8-20029 (NASA, Huntsville, AL, 1966).
34. A. W. Thompson and I. M. Bernstein, in *Advances in Corrosion Science and Technology*, eds. R. W. Staehle and M. Fontana (Plenum Press, New York, 1979), p. 53.
35. Alloy Data: AerMet 100 Alloy, Alloy Steels 6 (Carpenter Tech. Corp., Reading PA, 1992).
36. G. Sandoz, *Metall. Trans.* **3**, 1169 (1972).
37. I. M. Bernstein and A. W. Thompson, *Int. Met. Rev.* **21**, 269 (1976).
38. E. U. Lee, *Metall. Mater. Trans.* **26A**, 1313 (1995).
39. T.S.F. Lee and R. M. Latanision, *Metall. Trans.* **18A**, 1653 (1987).

Table 1. Alloy Composition (wt%)

Element	AerMet 100	H11	4340	18Ni	K-500 CD	K-500 AA-1	K-500 AA-2
Al	0.005		0.031	0.13	2.92	2.95	2.95
B				0.003			
C	0.24	0.41	0.42	0.009	0.16	<0.17	<0.14
Co	13.47			9.15			
Cr	3.00	4.88	0.89	0.06			
Cu		0.03	0.19	0.11	29.99	29.53	29.8
Fe	71.00	bal	bal	bal	0.64	<0.85	<0.74
Mn	0.01	0.30	0.46	0.01	0.72	<0.70	<0.58
Mo	1.19	1.32	0.21	4.82			
Ni	11.07	0.04	1.74	18.42	64.96	65.29	65.1
P	0.002	0.011	0.009	0.004			<0.002
S	<0.0005	0.003	0.001	0.001	0.001	<0.001	<0.001
Si	<0.01	0.88	0.28	0.04	0.15	<0.05	<0.15
Ti	0.009			0.65	0.46	0.46	0.44
Other	<0.0010 N	0.45 V	0.005 N	0.01 W			
	<0.0010 O		0.001 O	0.05 Ca			
				0.02 Zr			

Table 2. Apparent Trapping Constants for Aged AerMet 100

T_{age} (°C)	Test no.	η range (V)	No. of k_a values	k_a (s^{-1})
270	1	-0.05 to -0.20	4	0.044 ± 0.005
	2	-0.10 to -0.25	2	0.044 ± 0.001
	3	-0.10 to -0.15	2	0.049 ± 0.002
	4	-0.10 to -0.20	2	0.049 ± 0.002
370	1	-0.10 to -0.20	3	0.045 ± 0.005
	2	-0.05 to -0.20	4	0.047 ± 0.002
482	1	-0.10 to -0.25	4	0.069 ± 0.006
	2	-0.20 to -0.25	2	0.069 ± 0.001

Table 3. Apparent Trapping Constants for Alloy K-500

Condition	Test no.	η range (V)	No. of k_a values	k_a (s^{-1})
0.5h-A	1	-0.30 to -0.40	3	0.065 ± 0.002
	2	-0.30 to -0.45	4	0.063 ± 0.005
	3	-0.30 to -0.40	3	0.066 ± 0.001
0.5h-AA	1	-0.25 to -0.45	5	0.064 ± 0.002
	2	-0.25 to -0.40	4	0.064 ± 0.004
0.25h-AA	1	-0.25 to -0.55	7	0.052 ± 0.004
	2	-0.25 to -0.50	3	0.051 ± 0.004
0.5h-AA-16h	1	-0.30 to -0.40	3	0.061 ± 0.001
	2	-0.30 to -0.40	3	0.066 ± 0.003

Table 4. Trapping Parameters for High-Strength Steels and Alloy K-500

Alloy	Condition	k_a (s^{-1})	D_L/D_a	k (s^{-1})
Steels				
AerMet 100	Annealed	0.000 ± 0.001	9.6 ± 1.3	0.00
	270°C-aged	0.046 ± 0.003	9.6 ± 1.3	0.44 ± 0.09
	370°C-aged	0.046 ± 0.004	9.6 ± 1.3	0.44 ± 0.10
	482°C-aged	0.069 ± 0.004	9.6 ± 1.3	0.66 ± 0.13
4340	HRC 53	0.008 ± 0.001	500	4.0 ± 0.5
H11	HRC 51	0.080 ± 0.004	43.3 ± 6.2	3.5 ± 0.7
18Ni (2068)*	482°C-aged (4 h)	0.005 ± 0.002	300 ± 90	1.50 ± 1.05
Alloy K-500				
	0.5h-A	0.065 ± 0.003	1.6	0.104 ± 0.008
	0.5h-AA	0.064 ± 0.003	1.6	0.102 ± 0.008
	0.25h-AA	0.052 ± 0.004	1.6	0.083 ± 0.009
	0.5h-AA-16h	0.063 ± 0.003	1.6	0.101 ± 0.008
	AA-2 (aged 16 h)	0.063 ± 0.003	1.6	0.099 ± 0.008
	AA-1 (aged 16 h)	0.060 ± 0.006	1.6	0.095 ± 0.013
	DA	0.021 ± 0.003	2.0	0.042 ± 0.007
	CD-Unaged	0.017 ± 0.003	2.0	0.034 ± 0.007

* Nominal yield strength in MPa.

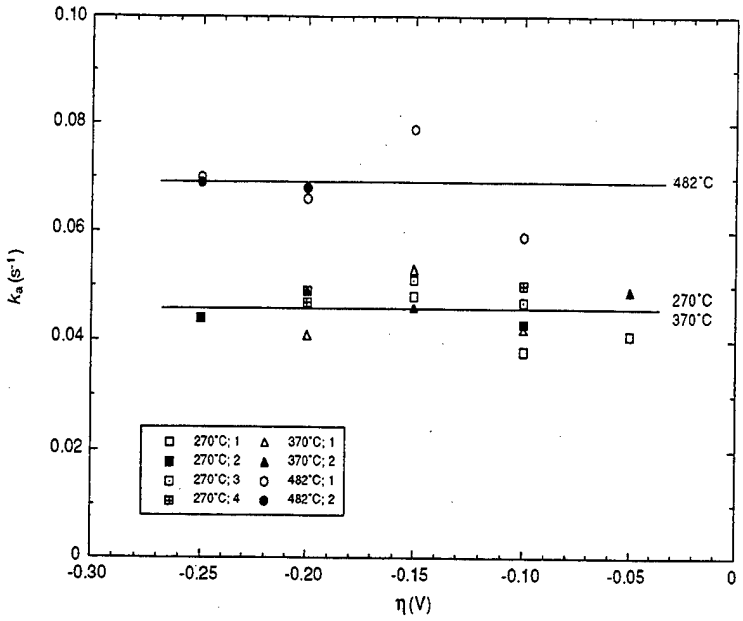


Figure 1. Values of k_a for aged AerMet 100 at various overpotentials. Each symbol is identified by the aging temperature and a test number for that temperature.

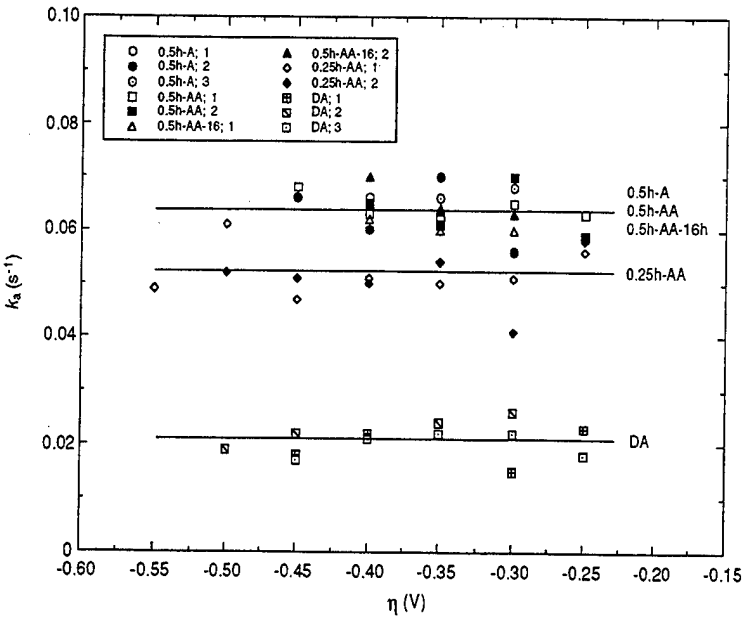


Figure 2. Values of k_a for alloy K-500 at various overpotentials. Each symbol is identified by the heat treatment and a test number for that treatment.

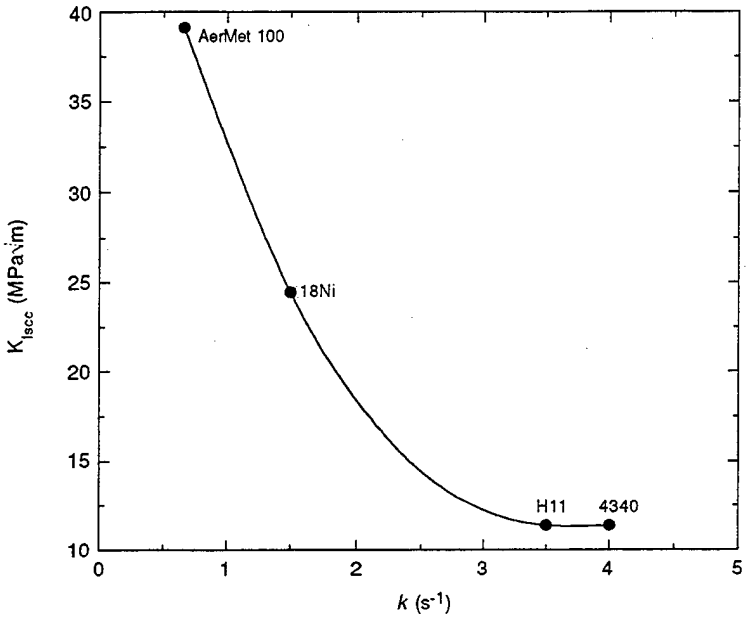


Figure 3. Variation of K_{ISCC} with k for high-strength steels. The value of K_{ISCC} for 18Ni pertains to the 1723 MPa (250 ksi) grade.

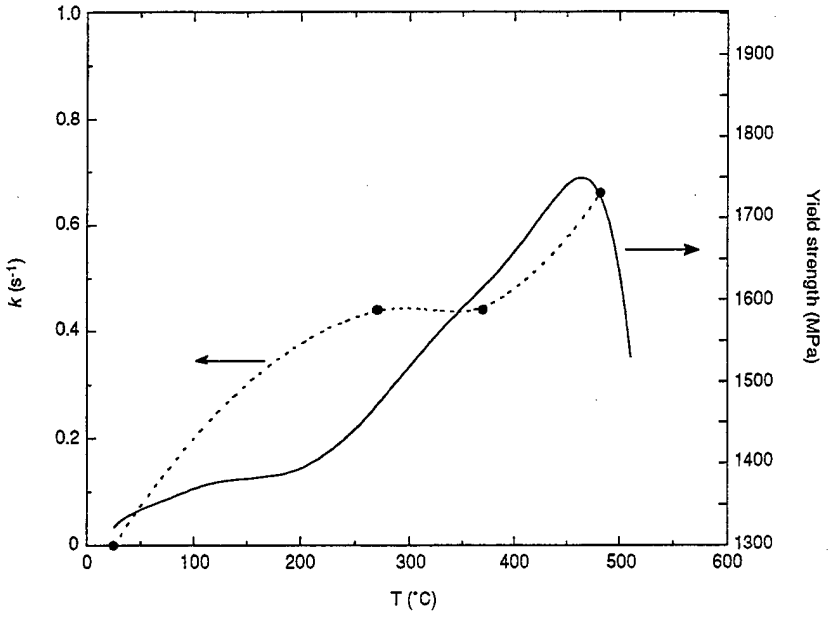


Figure 4. Variation of k and yield strength with aging temperature for AerMet 100.

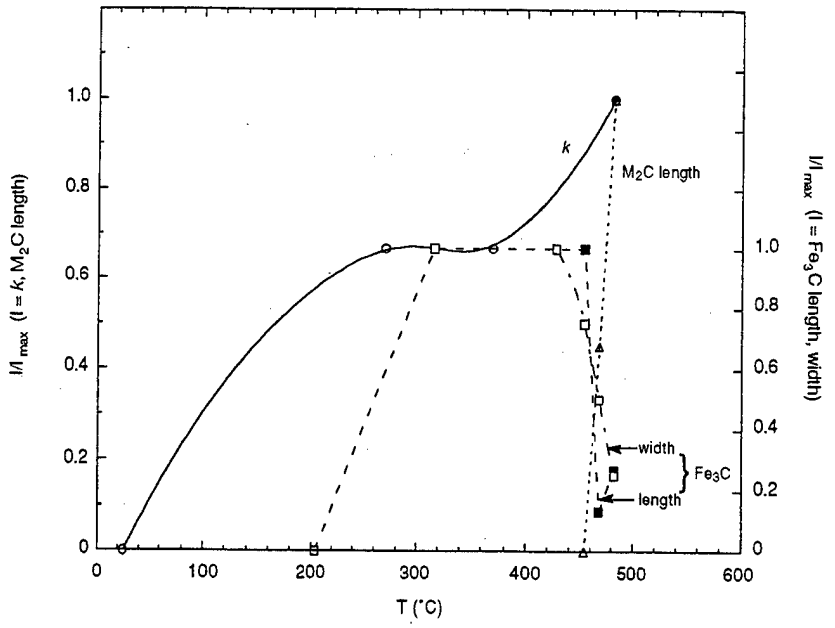


Figure 5. Variation of k and carbide size with aging temperature for AerMet 100.
The dimensions of the carbides were obtained from Ref. 2.

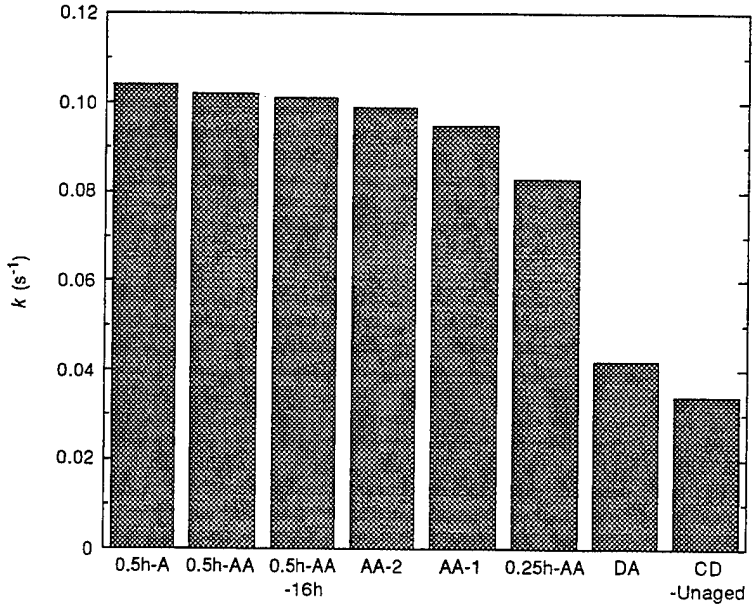


Figure 6. Variation in k for different heat treatments of alloy K-500.

Environment Assisted Fatigue Cracking of AerMet 100 Steel

Eun U. Lee, Kenneth George and William E. Frazier
Naval Air Warfare Center, Aircraft Division
Patuxent River, Maryland 20670

ABSTRACT

The fatigue cracking behavior of AerMet 100 steel was studied at various stress ratios and frequencies in gaseous dry nitrogen, distilled water and aqueous 3.5% NaCl solution. In the Paris regime, the environment assisted fatigue crack growth was faster for a more aggressive environment and a lower frequency. In the near-threshold fatigue crack growth regime, raising stress ratio increased the crack growth rate but decreased the threshold stress intensity range, ΔK_{th} in a 3.5% NaCl solution. The stress ratio effect diminished with increasing fatigue crack growth rate.

INTRODUCTION

Advanced aircraft landing gear and other fracture critical components demand strong and tough materials to achieve higher performance and greater reliability. In the past, 300M and AF1410 steels were accepted as the materials for aircraft landing gear because of the high strength of 300M steel and the great fracture toughness of AF1410 steel. In 1990, a new steel, AerMet 100, was developed to have a good combination of high ultimate tensile strength (UTS), 1930-2070 MPa, and high fracture toughness, K_{IC}, exceeding 120MPa$\sqrt{m}$. The UTS and K_{IC} are similar to and much greater than those of 300M steel, 2000 MPa and 65 MPa$\sqrt{m}$, respectively. On the one hand, they are greater and less, compared to those of AF1410 steel, 1585-1724 MPa and 165 MPa$\sqrt{m}$, respectively. Therefore, AerMet 100 steel can replace 300M steel to increase damage tolerance and AF1410 steel to achieve weight reduction.

Recently, AerMet 100 steel has been employed more and more for fracture critical components, such as aircraft landing gear, arresting gear shank, horizontal stabilizer spindle, wingfold transmission and wing pivot pin. Those AerMet 100 steel components, especially carrier-based aircraft components, are exposed to aggressive environments and are subjected to fluctuating loads. However, the environment assisted fatigue cracking data for AerMet 100 steel are rather sparse, and its behavior has not been fully understood. This study aims at characterizing and understanding the environment assisted fatigue cracking behavior of AerMet 100 steel in aggressive environments. Since the environment assisted fatigue crack growth rate is affected by environment and loading frequency, their roles are evaluated. In addition, as there has been a rapidly increasing need for near-threshold crack growth rate data, particular emphasis is placed on the near-threshold crack growth in an aggressive environment.

EXPERIMENTAL PROCEDURE

The specimen material, AerMet 100 steel, was supplied by Carpenter Technology Corp., Reading, PA in the form of a forged slab of 38.1 x 114.3 x 330.2 mm (1.5 x 4.5 x 13 in). The chemical composition is shown in Table 1. The slab was subjected to a heat treatment: preheating at 593°C (1,100°F) for 1.25 hours in an argon atmosphere, solution treatment at 885°C (1,625°F) for 1.25 hours in an argon atmosphere, cooling in a nitrogen atmosphere, freezing in dry-ice and alcohol
(-73°C) for 2 hours and aging at 482°C (900°F) for 5 hours in air. This heat treatment resulted in hardness R_c 54 and the microstructure shown in Figure 1. Subsequently, compact tension C(T) specimens, 12.7 mm (0.5 in) thick and 50.8 mm (2 in) wide, were prepared in the L-T orientation by Electro Discharge Machining, Figure 2.

For the fatigue test, two closed-loop servo-hydraulic mechanical test machines were used. One was a 490 KN (110 kip) conventional vertical MTS machine fitted with a Plexiglas environmental chamber for a fatigue test in a gas environment. The other was a horizontal mechanical test machine for a fatigue test in a liquid medium. The latter consisted of a 44.5 KN (10 kip) actuator, a 22.25 KN (5 kip) load cell, a supporting frame and a liquid container, in which a specimen was partly immersed. A liquid medium was constantly circulated between the liquid container and a 3.8 liter (1 gallon) reservoir by a pump. Each test machine was suitably interfaced with a laboratory computer system for automated monitoring of fatigue crack growth, using either compliance or d-c potential drop technique.

The fatigue crack growth tests for the investigation of environment and loading frequency effects were conducted under load control in tension-tension cycling of a sinusoidal waveform with frequencies 0.1, 1, and 10 Hz and stress ratio 0.1 at ambient temperature. The test environments were gaseous dry nitrogen, distilled water and aqueous 3.5% NaCl solution. The fatigue testing in gaseous dry nitrogen was carried out in the vertical MTS machine with a Plexiglas environmental chamber, The chamber totally enclosed a C(T) specimen, and gaseous dry nitrogen constantly flowed through to maintain an inert reference environment. Oil free gaseous nitrogen was dried to 5% relative humidity by passing through Drierite ($CaSO_4$) prior to entering the environmental chamber. The environment assisted fatigue testing was performed with a C(T) specimen in the horizontal mechanical test machine, The notch tip and crack of the specimen was immersed in a liquid medium: distilled water or aqueous 3.5% NaCl solution. The fatigue crack length was continuously monitored with a computer system, using compliance technique. The fatigue loading procedure was K-decreasing (load shedding) and K-increasing for the crack growth rates below and above 2.54×10^{-5} mm/cycle (10^{-6} in/cycle), respectively.

The fatigue crack growth tests for the investigation of the near-threshold crack growth in an aqueous 3.5% NaCl solution were carried out with the horizontal mechanical test machine at frequency 1 Hz and stress ratios (R = minimum stress/maximum stress), ranging from 0.1 to 0.9. The other test conditions were identical to those described above.

RESULTS

Environment Effect

The variation of fatigue crack growth rate da/dN with stress intensity range ΔK is illustrated in Figure 3(a) for the fatigue test at frequency 10 Hz in two environments: distilled water and aqueous 3.5% NaCl solution. This figure also includes the curve of da/dN vs ΔK for the fatigue test at frequency 1 Hz in gaseous dry nitrogen. Above 2.54×10^{-5} mm/cycle (1×10^{-6} in/cycle) or in the Paris regime*, the fatigue crack growth rates are similar in the three environments, indicating absence of environment effect on fatigue crack growth rate at frequency 10 Hz. On the other hand, the near-threshold fatigue crack growth rate is least in aqueous 3.5% NaCl solution, intermediate in distilled water, and greatest in gaseous dry nitrogen. The threshold stress intensity for fatigue crack growth ΔK_{th} appears to be greatest in aqueous 3.5% NaCl solution, intermediate in distilled water, and least in gaseous dry nitrogen. In other words, a more aggressive environment slows down the near-threshold fatigue crack growth and raises the ΔK_{th} more.

Figure 3(b) shows the da/dN vs ΔK curves for frequency 1 Hz in the three environments. Above 2.54×10^{-5} mm/cycle (1×10^{-6} in/cycle) or in the Paris regime, the aggressive environments, aqueous 3.5% NaCl solution and distilled water, accelerate the fatigue crack growth rate. This indicates that environment assisted acceleration of fatigue crack growth occurs at frequency 1 Hz. The near-threshold fatigue crack growth rate is least in aqueous 3.5% NaCl solution, intermediate in distilled water, and greatest in gaseous dry nitrogen. Correspondingly, the ΔK_{th} is greatest in aqueous 3.5% NaCl solution, intermediate in distilled water, and least in gaseous dry nitrogen.

Figure 3(c) shows the da/dN vs ΔK curves for frequency 0.1 Hz in the three environments. da/dN is greater in aqueous 3.5% NaCl solution than in distilled water and gaseous dry nitrogen for much of the da/dN region investigated. Furthermore, da/dN is greater in distilled water than in gaseous dry nitrogen above 1×10^{-5} mm/cycle (4×10^{-7} in/cycle), and the reverse is true below 1×10^{-5} mm/cycle (4×10^{-7} in/cycle). This indicates that the environment assisted fatigue cracking is more obvious than at frequency 1 Hz.

Frequency Effect

In gaseous dry nitrogen, the fatigue crack growth rates are nearly identical at two different frequencies, 0.1 and 1 Hz, Figure 4(a), indicating frequency-independent fatigue crack growth.

In distilled water, the fatigue crack growth rate is greatest at 0.1 Hz, intermediate at 1 Hz, and least at 10 Hz above 2.54×10^{-5} mm/cycle (1×10^{-6} in/cycle) or in the Paris regime, Figure 4(b). Below 2.54×10^{-5} mm/cycle (1×10^{-6} in/cycle) or in the near-threshold fatigue crack growth regime, the reverse seems to be true.

---

* the regime in which there is a linear log-log relation between da/dN and ΔK

In aqueous 3.5% NaCl solution, the fatigue crack growth rates at three different frequencies, 0.1, 1 and 10 Hz, are similar above 1×10^{-3} mm/cycle (4×10^{-5} in/cycle), Figure 4(c). Similar fatigue crack growth rates are still observable at 1 and 10 Hz below 1×10^{-3} mm/cycle (4×10^{-5} in/cycle) but above 2.54×10^{-5} mm/cycle (1×10^{-6} in/cycle), while they are lower than that at 0.1 Hz. Below 2.54×10^{-5} mm/cycle (1×10^{-6} in/cycle), the da/dN is greatest at 0.1 Hz, intermediate at 10 Hz, and least at 1 Hz. This observation evidences a diminishing frequency effect on fatigue crack growth with increasing da/dN in aqueous 3.5% NaCl solution.

Stress Ratio Effect

The variation of fatigue crack growth rate da/dN with stress intensity range ΔK is shown for stress ratios R = 0.1, 0.5, 0.7 and 0.9 in Figure 5(a) and for R = 0.2, 0.3 and 0.8 in Figure 5(b). These figures indicate that raising stress ratio increases the near-threshold fatigue crack growth rate and reduces the threshold stress intensity range ΔK_{th}. The variations of threshold stress intensity range ΔK_{th} and maximum stress intensity $K_{max} = \Delta K_{th}/(1-R)$ with stress ratio R are shown in Figure 6. With increasing R, ΔK_{th} decreases between R = 0.1 and 0.3, levels off between R = 0.3 and 0.6, and decreases again between R = 0.6 and 0.9. On the one hand, K_{max} increases little between R = 0.1 and 0.4 but increases steeply between R = 0.4 and 0.9. ΔK_{th} is plotted against K_{max} in Figure 7. Such a plot, called fundamental threshold curve.[1] provides interrelation between the two parameters ΔK_{th} and K_{max} defining regimes, where fatigue crack grows (above the curve) and where it does not (below the curve). In other words, the curve delineates a boundary where fatigue crack growth starts for a given K_{max} and indicates the resistance to threshold fatigue crack growth.

Crack Path

Figure 8 shows a crack path in a specimen, which was subjected to a fatigue test in distilled water. The environment assisted fatigue crack follows a path, which is partly intergranular and partly transgranular. Crack branching occurs along prior austenite grain boundaries. A similar crack path is also observable in a specimen that was subjected to a fatigue test in an aqueous 3.5% NaCl solution.

DISCUSSION

Fatigue Crack Growth in Other Steel

Figure 9 compares the variations of fatigue crack growth rate with stress intensity range for AerMet 100 and AF1410 steels, which were subjected to identical fatigue loadings of stress ratio 0.1 and frequency 1 Hz in aqueous 3.5% NaCl solution.[2] The two curves of da/dN vs ΔK nearly overlap each other, indicating similar environment assisted fatigue crack growth rates of these two steels, despite the difference in the fracture toughness (151.7 MPa$\sqrt{m}$ for AerMet 100 steel and 164.9 MPa$\sqrt{m}$ for AF1410 steel), yield strength (1,744.4 MPa for AerMet 100 steel and 1,516.9 MPa for AF1410 steel), and ultimate tensile strength (1,896.1 MPa for AerMet 100 steel and 1,654.8 MPa for AF1410 steel).

Environment Effect

The experimental results show that the rate of environment assisted fatigue crack growth in an AerMet 100 steel is greater for a more aggressive environment and a lower loading frequency in the Paris regime but the reverse is true in the near-threshold fatigue crack growth regime. Similar behavior was observed in
2 1/4Cr-1 Mo steels, rotor steels and a 4340 steel, and the threshold fatigue crack growth behaviors of these steels were attributed to oxide-induced crack closure.[3-7]

The observed absence of loading frequency effect on fatigue crack growth behavior of an AerMet 100 steel in gaseous dry nitrogen confirms the observations for a 7075-T651 alloy and a 4340 steel in inert environments.[8,9]

Stress Ratio Effect

The variation of threshold stress intensity range for fatigue crack growth ΔK_{th} and maximum stress intensity K_{max} with stress ratio R in an aqueous 3.5% NaCl solution is compared with that in gaseous dry nitrogen.[10] Figure 6. Since the crack plane orientations for the fatigue tests in a 3.5% NaCl solution (L-T) and in gaseous dry nitrogen[10] (C-R) are different, a direct comparison of those data is not quite valid. However, some distinct features of those results may be detected by examining both data. From Figure 6 , it is evident that ΔK_{th} and K_{max} values are greater in an aqueous 3.5% NaCl solution than in gaseous dry nitrogen for a stress ratio less than 0.8.

The fundamental threshold curves of ΔK_{th} vs K_{max} for the fatigue tests in an aqueous 3.5% NaCl solution and gaseous dry nitrogen[9] are compared in Figure 7. These two curves indicate that the resistance to threshold fatigue crack growth is greater in an aqueous 3.5% NaCl solution than in gaseous dry nitrogen for a stress ratio less than 0.8. This must be associated with the corrosion product at the crack tip in an aqueous 3.5% NaCl solution.

CONCLUSIONS

1. The environment assisted fatigue crack growth in AerMet 100 is faster for a more corrosive environment (aqueous 3.5% NaCl solution) and a lower frequency in the Paris regime.

2. Raising stress ratio R for AerMet 100 increases the near-threshold fatigue crack growth rate but decreases the threshold stress intensity range for fatigue crack growth ΔK_{th} in an aqueous 3.5% NaCl solution.

3. With increasing R, the AerMet 100 ΔK_{th} decreases between R = 0.1 and 0.3, levels off between R = 0.3 and 0.6, and decreases again between R = 0.6 and 0.9. On the one hand, K_{max} increases little between R = 0.1 and 0.4, but increases steeply between R = 0.4 and 0.9.

4. The resistance of AerMet 100 to threshold fatigue crack growth appears to be greater in an aqueous 3.5% NaCl solution than in gaseous dry nitrogen for a stress ratio less than 0.8. This must be associated with the corrosion product at the crack tip in an aqueous 3.5% NaCl solution.

5. The fatigue crack path for AerMet 100 is partly intergranular and partly transgranular in distilled water and an aqueous 3.5% NaCl solution.

ACKNOWLEDGMENTS

This study was supported by the F/A-18E/F Project, F/A-18E/F Landing Gear Fatigue, AIRTASK E4HP-1300, NAVAIR Work Unit No. A5304B-24.

Thanks are due to Messrs. D. Cadman and S. Bettadapur for helpful and stimulating technical discussions.

REFERENCES

1. Vasudevan, A. K. and Sadananda, K., "Classification of Fatigue Crack Growth Behavior," Metallurgical and Materials Transactions A, 1995, vol. 26A, pp. 1221-1234.

2. Pawlik, M.: "Improved Landing Gear Steels," McDonnel Douglas Corp. Report MDC 91B0357, 1 July 1991.

3. Ritchie, R. O., Suresh, S. and Moss, C. M.: "Near-Threshold Fatigue Crack Growth in 2 1/4Cr-1Mo Pressure Vessel Steel in Air and Hydrogen," Journal of Engineering Materials and Technology, 1980, vol. 102, pp. 293-299.

4. Suresh, S., Zaminski, G. F. and Ritchie, R. O.: "Oxide-Induced Crack Closure: An Explanation for Near-Threshold Corrosion Fatigue Crack Growth Behavior," Metallurgical Transactions A, 1981, vol. 12A, pp. 1435-1443.

5. Stewart, A. T.: "The Influence of Environment and Stress Ratio on Fatigue Crack Growth at Near-Threshold Stress Intensities in Low-Alloy Steels," Journal of Engineering Fracture Mechanics, 1980, vol. 13, pp. 463-478.

6. Liaw, P. K., Leax, T. R. and Donald, J. K.: "Fatigue Crack Growth Behavior of 4340 Steels, " Acta Metallurgica, 1987, vol. 35, no. 7, pp. 1415-1432.

7. Wei, R. P.: "On Understanding Environment-Enhanced Fatigue Crack Growth - A Fundamental Approach," Fatigue Mechanisms, ASTM STP 675, American Society for Testing and Materials, 1979, pp. 816-840.

8. Wei, R. P. and Landes, J. D.: "The Effect of D_2O on Fatigue-Crack Propagation in a High-Strength Aluminum Alloy," International Journal of Fracture Mechanics, 1969, vol. 5, pp.69-71.

9. Hutin, J. P.: "Sub-Critical Crack Growth in AISI 4340 Steel in Water and Water Vapor," M. S. Thesis, Lehigh University, Bethlehem, PA, 1975.

10. Lee, Eun U., "Load Ratio Dependence of Fatigue Threshold in AerMet 100 Steel," Report NAWCADPAX--96-250-TR, Naval Air Warfare Center Aircraft Division, Patuxent River, MD, 2 October 1996

TABLE 1
Chemical Composition of AerMet 100 Steel Slab

Element	Weight %
C	0.23
Mn	0.03
Si	0.03
P	0.003
S	0.0009
Cr	3.03
Ni	11.09
Mo	1.18
Co	13.44
Cu	0.01
Fe	bal

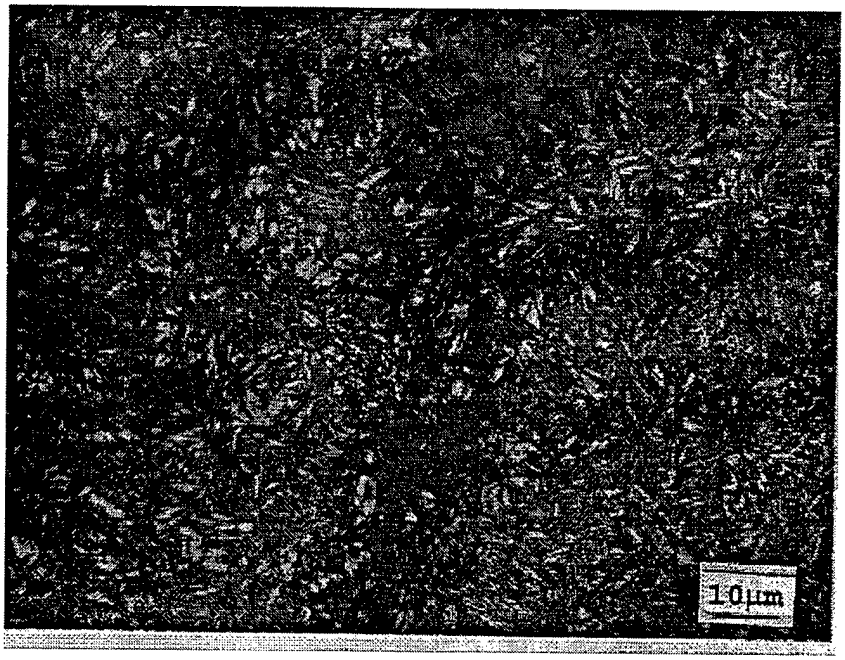
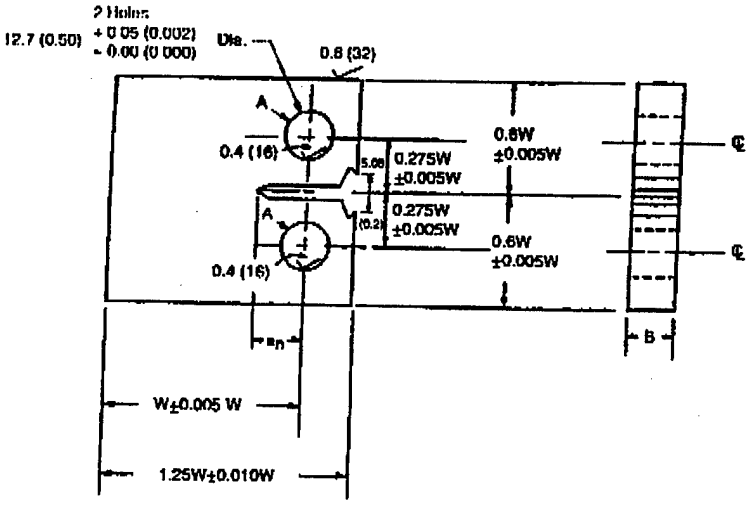


Figure 1. Microstructure of AerMet 100 Steel



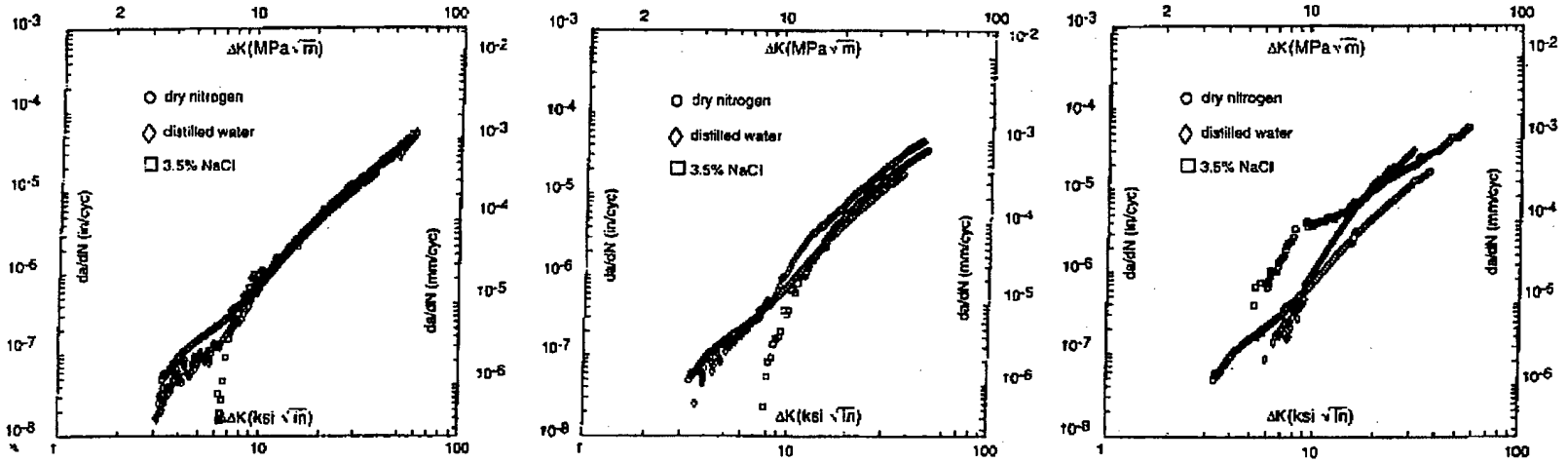
(*) Dimensions are in millimeters (inches).

W = 58.74 (2 5/16)

B = 12.70 (1/2)

a_n = 16.00 (0.63)

Fig. 2. Compact Tension Specimen

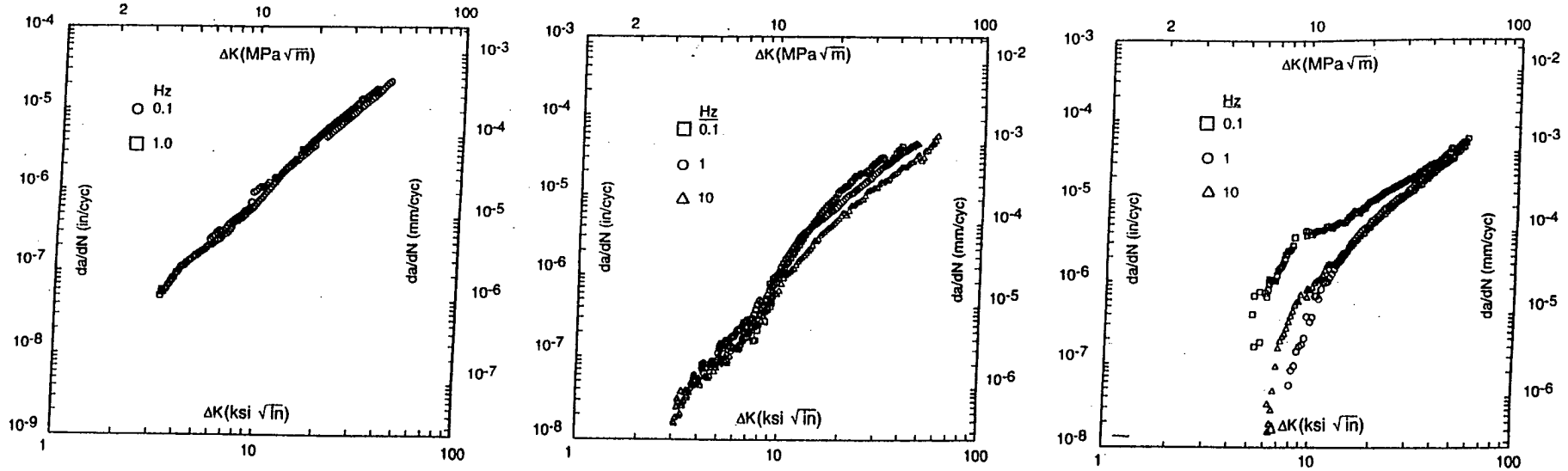


(a) f = 1 Hz for Dry Nitrogen
f = 10 Hz for Distilled Water
and 3.5% NaCl Solution

(b) f = 1 Hz for Three Environments

(c) f = 0.1 Hz for Three Environments

Fig. 3. AerMet 100 Environment Effect on Fatigue Crack Growth Rate at Different Frequencies

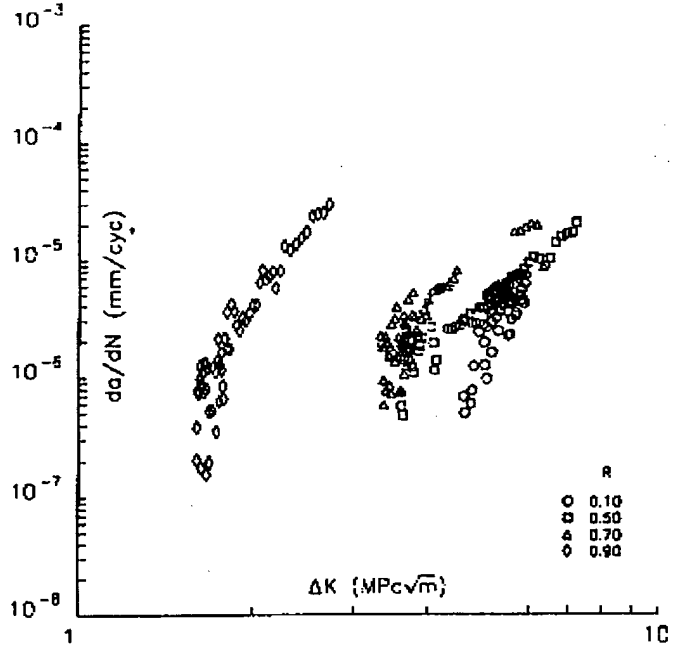


(a) Dry Nitrogen

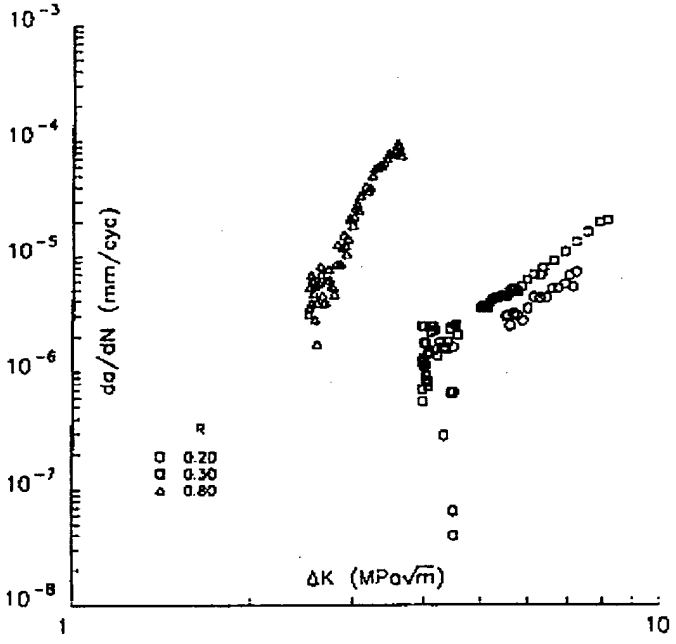
(b) Distilled Water

(c) 3.5% NaCl Solution

Fig. 4. AerMet 100 Frequency Effect on Fatigue Crack Growth Rate in Different Environments



(a) R = 0.10, 0.50, 0.70 & 0.80



(b) R = 0.20, 0.30 & 0.80

Fig. 5. AerMet 100 Stress Ratio Effect on Fatigue Crack Growth Rate in Aqueous 3.5% NaCl Solution

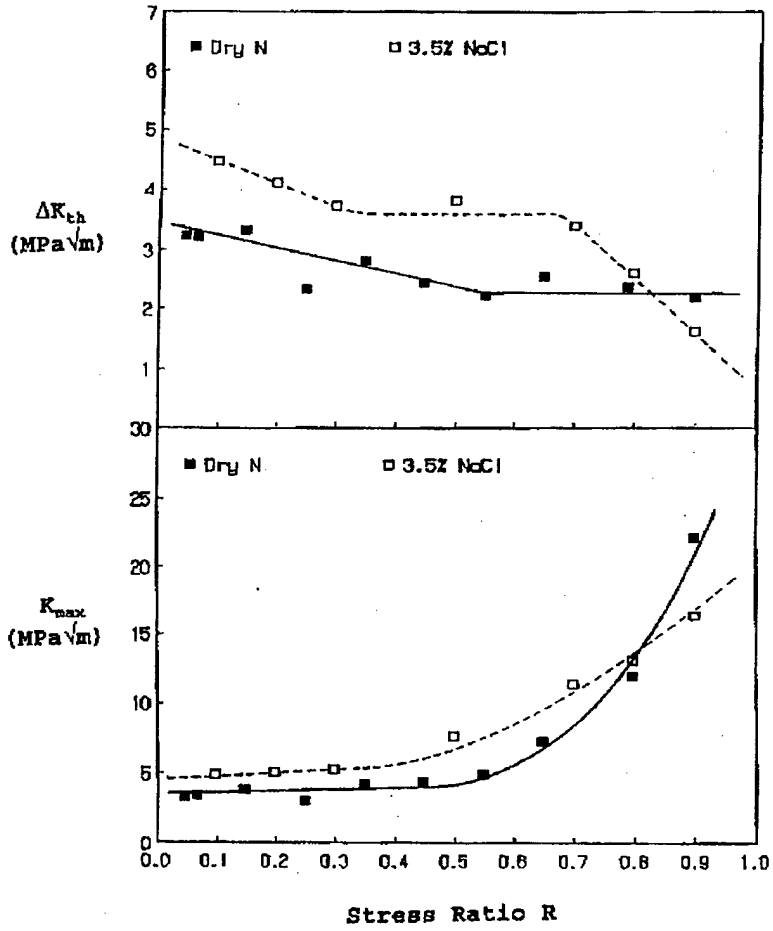


Fig. 6. Variation of AerMet 100 Alternating and Maximum Stress Intensities at Threshold, ΔK_{th} and K_{max}, with Stress Ratio R

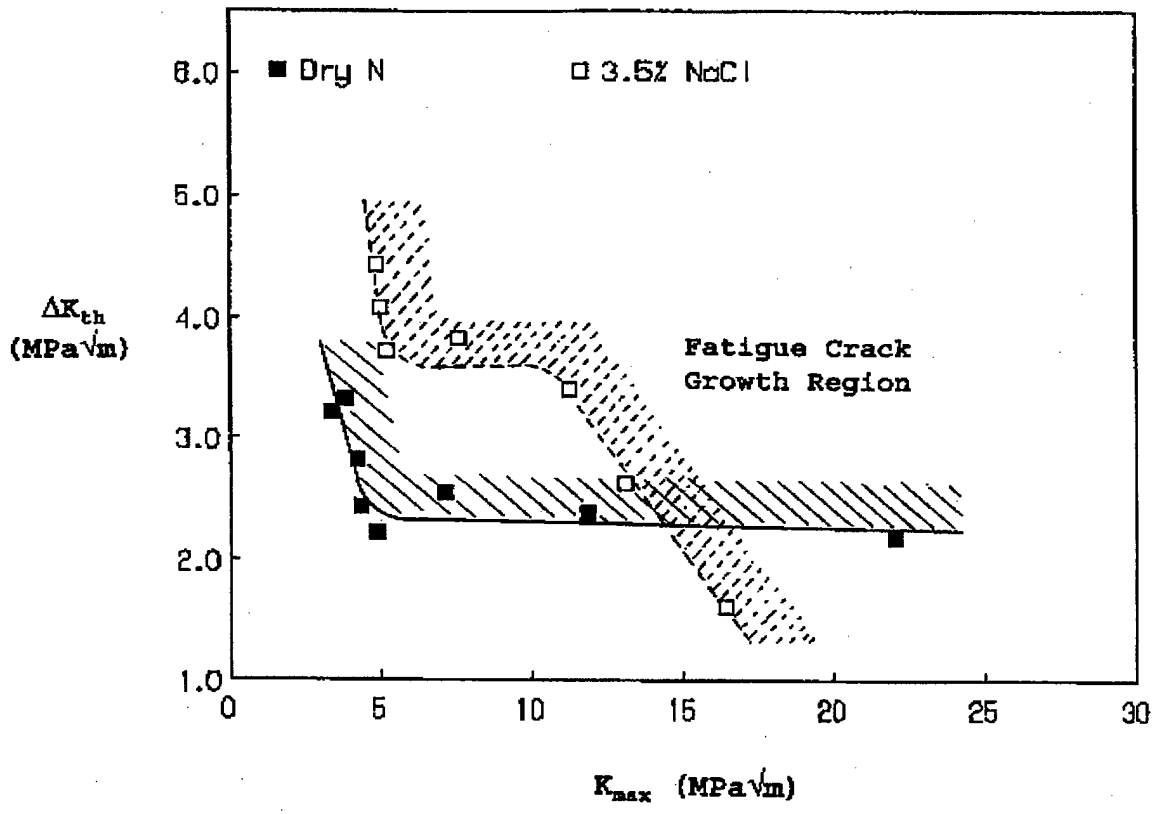


Fig. 7. Fundamental Threshold Curves of ΔK_{th} vs K_{max}

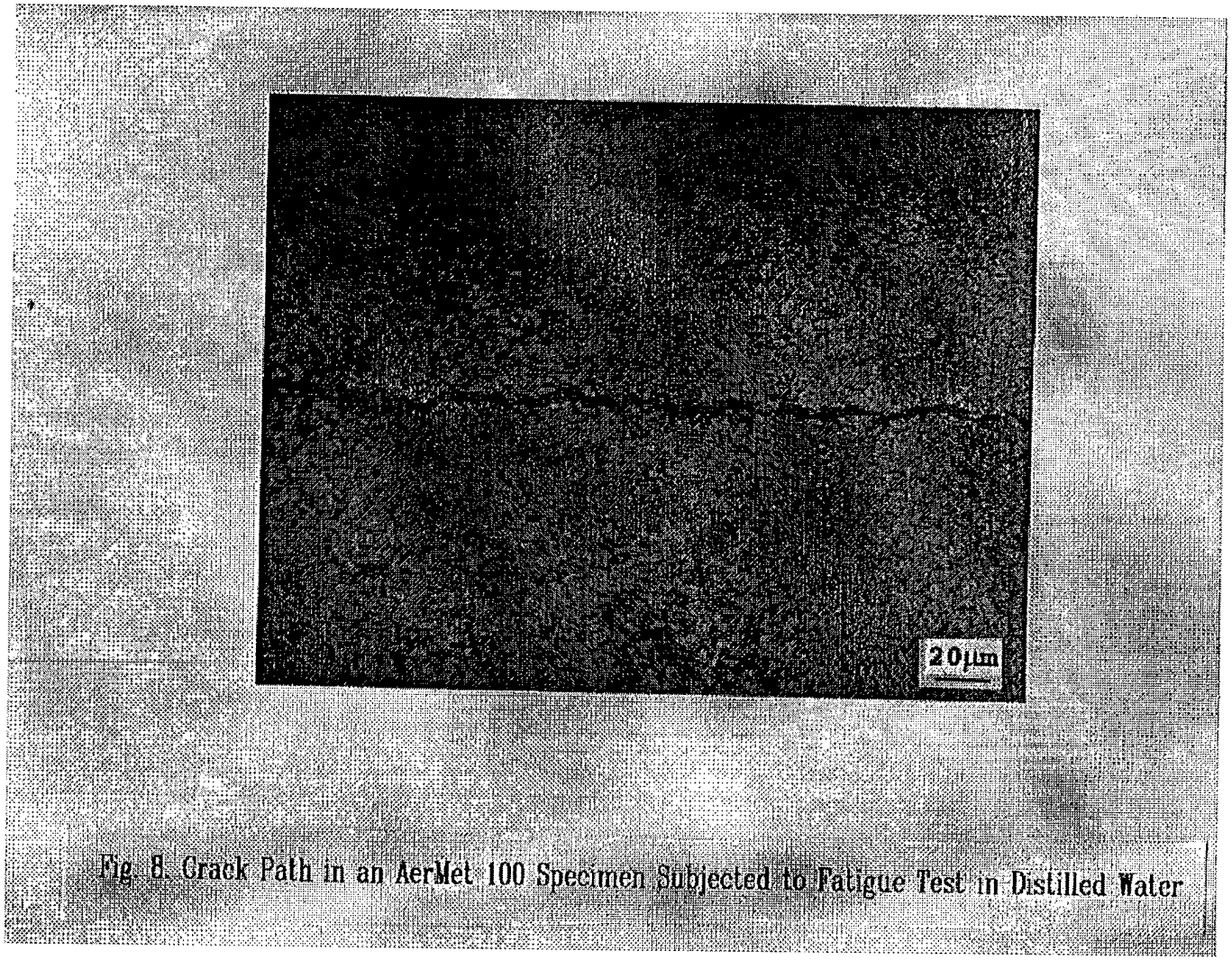


Fig. 8. Crack Path in an AerMet 100 Specimen Subjected to Fatigue Test in Distilled Water

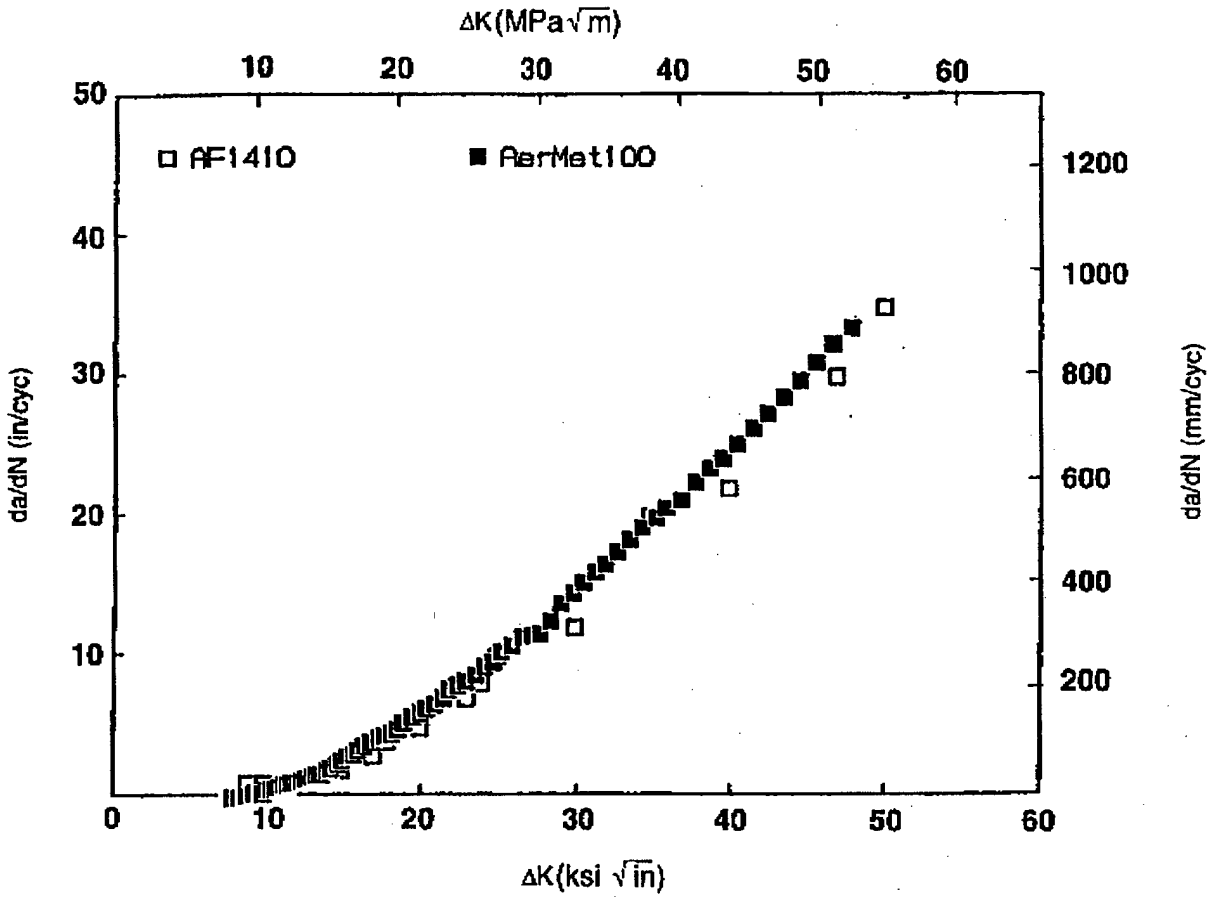


Fig. 9. Fatigue Crack Growth Rates of AerMet 100 and AF1410 Steels in Aqueous 3.5% NaCl Solution

Ripple-Load Cracking Sensitivity in Engineering Alloys

P.S. Pao, S.J. Gill, and R.A. Bayles

Naval Research Laboratory, Washington, D.C. 20375-5343

and

G.R. Yoder

Office of Naval Research, Arlington, VA 22217-5000

ABSTRACT

If very small amplitude cyclic (or "ripple") loads perturb an otherwise constant load condition in an aggressive environment, life prediction based solely on the static stress-corrosion cracking threshold (K_{ISCC}) may prove nonconservative, as the ripple-load effect may produce fracture in a structural alloy at stress-intensity levels less than 50% of K_{ISCC}. By approaching ripple-load cracking as an extreme case of high stress-ratio fatigue, a predictive framework for the ripple-load effect and a new ripple-load cracking parameter, K_{IRLC}, are developed based on the descriptive parameters used in SCC and corrosion fatigue characterization. Critical conditions required for the occurrence of ripple-load effects are discussed.

INTRODUCTION

Stress-corrosion cracking (SCC) is a form of subcritical crack growth which will occur if a sensitive material is exposed to an appropriate environment under sufficient stress for a sufficient length of time. The SCC resistance is often evaluated in terms of the fracture mechanics parameter, K_{ISCC}, the threshold stress-intensity factor below which crack growth will not occur. In SCC, a constant load condition is always assumed.

However, in the real world, an absolutely constant load condition is rarely attainable. For example, the loading profiles experienced by offshore platform structures and steam turbine generator blades most likely involve the superposition of relatively small amplitude cyclic load perturbations on a substantially larger constant load. Though such perturbations might at first glance seem virtually insignificant on the basis of their amplitude, preliminary study has shown that their effect, described as the "ripple effect" by Speidel [1], can be sizable. Recent work at the Naval Research Laboratory on steels, titanium, and aluminum alloys has suggested that the presence of such ripple loads can produce fracture at stress-intensity levels significantly less than K_{ISCC} and thus shorten the life of a structure.[2-7] Parkins [8-9] and Endo and Komai et al [10-12] have also observed that small fluctuating loads may produce SCC at significantly lower stresses than those required under purely static loads. Thus, a design based solely on the static K_{ISCC}, without proper consideration of the ripple-load effect, may be nonconservative.

Not all materials, however, appear susceptible to the ripple-load effect. For instance, in the case of an HY-130 steel, a 60% ripple-load degradation was observed in a 3.5% NaCl solution, yet absolutely no degradation was found in a 4340 steel under similar ripple-load conditions.[2-3] Similar observations of the lack of ripple-load sensitivity have been made for materials in other families of structural alloys as well.

The purpose of this paper is to show that diverse alloys, such as ferrous, titanium, and aluminum alloys, may exhibit substantial degradation from the ripple-load effect (RLE) in SCC conditions, yet, more importantly, to demonstrate that the sensitivity of a specific material to ripple-load degradation is predictable. Critical conditions for ripple-load cracking and a methodology for quantitative prediction can be obtained if the ripple-load effect is approached as an extreme case of high stress-ratio fatigue. A new ripple-load cracking threshold, K_{IRLC}, which marks the onset of ripple-load crack growth, can be identified to predict material resistance to ripple-load degradation.

MATERIALS AND EXPERIMENTAL PROCEDURES

To study the effect of ripple loads on the SCC resistance, we selected at least one SCC-susceptible alloy and one or more SCC-resistant alloys from each of the three major engineering alloy families. From the ferrous family, AISI 4340 (σ_{ys} = 1240 MPa) and 5Ni-Cr-Mo-V (HY-130, σ_{ys} = 900 MPa) steels were selected to represent, respectively, the SCC-susceptible and SCC-resistant materials. Similarly from the aluminum family, the SCC-susceptible, short-transverse (ST) oriented peakaged 7075-T651, which is well known for its low K_{ISCC}, and the SCC-resistant ST and longitudinal (LT) overaged 7075-T7351 were selected for study. And from the titanium family, a recrystallization-annealed (RA) Ti-6Al-4V (an α–β alloy), a duplex-annealed (DA) Ti-8Al-1Mo-1V (a near α alloy), and a peakaged TIMETAL®21S (a metastable β alloy) were selected as relatively SCC-susceptible alloys. The SCC-resistant titanium alloys were beta-annealed (BA) Ti-6Al-4V, BA Ti-8Al-1Mo-1V, Ti-15V-3Cr-3Al-3Sn (a β–α alloy), and overaged TIMETAL®21S. Specific chemical analysis, product form, and mechanical properties for these alloys are available from previous publications.[2-7]

For steels, time-to-failure data under SCC and ripple-load conditions were directly measured in a 3.5% NaCl solution at ambient temperature using precracked cantilever-beam specimens. For ripple-load cracking, the frequency of the ripple loading was 0.10 Hz (6 cpm), with a skewed triangular waveform and stress ratios (minimum/maximum), R, ranging from 0.975 to 0.90 (which correspond to 1.25 to 5 % ripple loading). The AISI 4340 steel was tested at the freely corroding potential while the 5Ni-Cr-Mo-V steel was tested at a potential of -1.0 V.

For the aluminum and titanium alloys, high stress-ratio corrosion fatigue experiments with R = 0.90 (corresponding to 5% ripple-load amplitude), a haversine waveform, and a frequency of 5 Hz were conducted to simulate a ripple-load condition, using WOL-type compact specimens. After first acquiring the fatigue crack growth rate (da/dN) data in a 3.5% NaCl, a time-to-failure curve for the WOL-sample geometry is obtained via numerical integration of the da/dN data. For aluminum and titanium alloys, all salt water tests were conducted at the freely corroding potential. Slow strain-rate tests with a loading rate of 10^{-4} MPa$\sqrt{m}$/s were used to determine the K_{ISCC} in a 3.5% NaCl aqueous solution, using fatigue precracked WOL-type specimens. Crack lengths were determined using a compliance related CMOD technique.[13] Details of the ripple-load cracking experimental procedures and the specimen configurations have been published elsewhere.[2-7]

RESULTS

Analysis of Ripple Load Cracking

An example of a ripple-load profile is shown in Fig. 1, which shows a cyclic ripple load with an amplitude equal to 5% of the substantially larger constant load upon which it is superposed. This ripple-load profile is equivalent to that of fatigue at a high stress ratio R = 0.90. Similarly, smaller ripple loads with amplitudes equal to 1.25% and 2.5% of the sustained load are treated as high stress-ratio fatigue with R = 0.975 and R = 0.95, respectively. In the context of a "ripple" load, the stress ratio is presumed to be $R \geq 0.90$, although such a stipulation does not affect the generality of the treatment which follows.

To begin with, the critical conditions and the predictive methodology for ripple-load effects involve the interface between SCC and corrosion-fatigue cracking behavior. The relationship between the small amplitude stress-intensity range associated with ripple loading, ΔK^{RL}, the threshold for fatigue crack growth, ΔK_{th}, the maximum stress intensity, K_{max}, and the threshold stress-intensity factor, K_{ISCC}, are considered. In particular, our attention is focused on the regime below K_{ISCC} where propagation of existing cracks and failure are not expected under a constant load condition. Thus, with the presence of small ripples superimposed on a large sustained load, the maximum stress intensity in the ripple-load cycle, K^{RL}_{max}, is equal to or less than K_{ISCC}. That is, the first condition for ripple-load cracking can be set as:

$$K^{RL}_{max} \leq K_{ISCC} \tag{1}$$

Next, from fatigue considerations, crack propagation will not occur during ripple loading unless ΔK^{RL} in the ripple cycle equals or exceeds ΔK_{th} or:

$$\Delta K_{th} \leq \Delta K^{RL} \tag{2}$$

$$\text{or} \quad \frac{\Delta K_{th}}{1-R} \leq K^{RL}_{max} \tag{2a}$$

Thus, a new parameter, K_{IRLC}, the ripple-load cracking threshold below which ripple-load cracking does not occur, can be defined as:

$$K_{IRLC} = \frac{\Delta K_{th}}{1-R} \tag{3}$$

Combining (1), (2a) and (3), the conditions for a material to exhibit a ripple-load cracking are:

$$K_{IRLC} \leq K_{max}^{RL} \leq K_{ISCC} \quad (4)$$

Relation (4) is schematically illustrated in Fig. 2. Figure 2 can be divided into three regions which are separated by K_{ISCC} and K_{IRLC}. In Region 3, the maximum applied stress intensity experienced during ripple loading is higher than both K_{ISCC} and K_{IRLC}. In this region, cracks will grow by both corrosion-fatigue and stress-corrosion cracking mechanisms, which can be addressed via the Wei and Landes superposition model.[14] Since crack growth of alloys under constant loading is well recognized, structural failures in this region are less likely. At the other end of the spectrum -- in Region 1, the maximum applied stress intensity is lower than both K_{ISCC} and K_{IRLC}. Under this loading condition, existing cracks in the structure will be non-propagating, even with the presence of ripple loads.

Region 2, which is upper-bounded by K_{ISCC} and lower-bounded by K_{IRLC}, is more interesting. This region can be called the "window of susceptibility" in which the ripple-load effect would be anticipated, and is the focus of this study. The narrower the window, the less susceptible the material is to ripple-load cracking. In the extreme case where K_{IRLC} approaches K_{ISCC}, the susceptibility window is completely closed and no ripple-load effect is expected. In Region 2, because the maximum applied stress intensity is lower than K_{ISCC}, cracking under constant load SCC mechanisms is not expected. However, the applied stress intensity is higher than K_{IRLC} and, therefore, cracks will grow under ripple-load conditions.

If one considers the difference between the threshold for ripple-load cracking, K_{IRLC}, and K_{ISCC}, then the maximum extent of ripple-load degradation can be defined as:

$$\% \text{ degradation} = (1 - K_{IRLC} / K_{ISCC}) \times 100 \quad (5)$$

Finally, the ripple-load cracking time-to-failure curve can be obtained from a simple piecewise numerical integration of the corrosion-fatigue crack growth rate data, for the particular structural geometry of concern -- as detailed in a previous publication.[3]

Ripple-Load Degradation and Stress-Corrosion Cracking in Steels

At the Naval Research Laboratory, studies of ripple-load cracking commenced with the work of Crooker, Hauser, and Bayles[2], which reported the contrasting ripple-load cracking sensitivities in 5Ni-Cr-Mo-V and AISI 4340 steels. Figures 3 and 4 show the time-to-failure data for 5Ni-Cr-Mo-V steel and Fig. 5 for AISI 4340 steel, under SCC and ripple-load conditions in a 3.5% aqueous NaCl solution.

For the 5Ni-Cr-Mo-V steel, a static K_{ISCC} was established at 110 MPa$\sqrt{m}$ based upon multiple long-term tests exceeding 10,000 hours. Ripple-load cracking data for 1.25%, 2.5%, and 5% ripple-load amplitudes (corresponding to respective R values of 0.975, 0.95, and 0.90) were obtained and presented in Fig. 3. As shown in Figure 3, a 1.25% ripple loading did not cause any degradation and the apparent cracking threshold equaled the static K_{ISCC}. However, as the

amplitude of the ripples was increased to 2.5% and 5% of the sustained load, ripple loading significantly reduced the values of time-to-failure and the apparent cracking threshold. For instance, at the initial stress intensity of 90 MPa$\sqrt{m}$, which is well below the K_{ISCC} of 110 MPa$\sqrt{m}$, SCC failure will not occur under static loading. However, when small ripple loads with amplitude equal to 2.5% of the static load were added, the test specimen failed in about 1600 hours. For a 5% ripple loading, the failure time was further reduced to only 180 hours. Based on 4000-hour tests, the apparent cracking thresholds for 2.5% and 5% ripple loading were estimated to be 80 and 44 MPa$\sqrt{m}$, respectively. As we will see from application of predictive analysis, even these thresholds derived from 4000-hour exposures appear to be nonconservative.

Because ripple-load cracking is approached as high stress-ratio fatigue, the time-to-failure curve can be predicted efficiently by numerical integration of the fatigue crack growth rate data corresponding to the particular ripple loading in a similar environment. Fatigue crack growth kinetics of the same type 5Ni-Cr-Mo-V steel in a 3.5% NaCl aqueous solution at R = 0.90 previously published by Vosikovsky[15] were numerically integrated to obtain the predicted time-to-failure curve for the same cantilever geometry employed in the direct experimental determination. This predicted time-to-failure curve is shown in Fig. 4. As shown in Fig. 4, the predicted time-to-failure curve based on Vosikovsky's data at R = 0.90 is in excellent agreement with the actual experimental data. Furthermore, Vosikovsky reported a ΔK_{th} value of 3.10 MPa$\sqrt{m}$ for R = 0.90. Thus, according to Eq. 3, the ripple-load cracking threshold, K_{IRLC}, would be 31 MPa$\sqrt{m}$. This predicted K_{IRLC} is significantly lower than the 44 MPa$\sqrt{m}$ threshold derived from 4000-hour tests. To obtain the predicted K_{IRLC} of 31 MPa$\sqrt{m}$ experimentally, it is estimated that about 30,000 hrs (~ 3.5 yrs) would be required. For 5Ni-Cr-Mo-V steel, the 4000-hr duration for the direct experimental determination of the ripple-load threshold is inappropriately short and the threshold obtained is nonconservative.

Vosikovsky also proposed an analytical expression to predict the ΔK_{th} values corresponding to various stress ratios in a 3.5% NaCl solution.[15] Using his expression, the ΔK_{th} for 2.5% ripple loading (that is at R = 0.95) is estimated to be 2.95 MPa$\sqrt{m}$. Using Eq. 3, the ripple-load cracking threshold under a 2.5% ripple loading would be 59 MPa$\sqrt{m}$, which is again substantially below the 80 MPa$\sqrt{m}$ measured from 4000-hour tests. Thus, with a 2.5% ripple loading, the threshold stress intensity decreases from 110 to 59 MPa $\sqrt{m}$, a 46% reduction. The predicted K_{IRLC} (under 5% ripple loading) and the measured K_{ISCC} are compared in Table 1, along with the data obtained from other alloys. As shown in Table 1, under a larger 5% ripple loading, the ripple effect causes an even bigger 72% reduction as the threshold stress intensity is lowered to 31 from 110 MPa$\sqrt{m}$.

Figure 5 shows the SCC and ripple-load test results for AISI 4340 steel in a 3.5% NaCl solution. The SCC threshold, determined from long-term static tests, is established at 33 MPa$\sqrt{m}$. The two 5% ripple loading tests (corresponding to R = 0.90) produced results that fell directly on the static SCC time-to-failure curve. That is, even under a fairly large 5% ripple loading, AISI 4340 steel does not exhibit any ripple-load effect. It is also safe to predict, based on the experience with 5Ni-Cr-Mo-V steel, that AISI 4340 steel is not likely to demonstrate any ripple-load degradation if the size of the ripple is smaller than 5% of the sustained load.

The corrosion-fatigue cracking threshold, ΔK_{th}, for AISI 4340 steel was determined to be 3.3 MPa$\sqrt{m}$ from corrosion-fatigue tests performed at R = 0.90 (corresponding to 5% ripple loading) in a 3.5% NaCl solution. Again using Eq. 3, the ripple-load cracking threshold, K_{IRLC},

will be 33 MPa$\sqrt{m}$, which is equivalent to K_{ISCC}. Therefore, according to Eq. 4, the susceptibility window is nonexistent and no ripple-load effect is expected on this SCC-prone steel. Ripple-load cracking data shown in Fig. 5 indeed support this prediction.

Ripple-Load Degradation and Stress-Corrosion Cracking in Aluminum Alloys

In the case of 5Ni-Cr-Mo-V steel, we have shown that ripple-load cracking in a 3.5% NaCl solution can be successfully approached as high stress-ratio corrosion fatigue. The predictive time-to-failure curve obtained by numerical integration of the corrosion-fatigue crack growth rate data agrees well with the actual ripple-load cracking test results. We also demonstrate that the analytical procedure renders a more conservative estimate of the ripple-load cracking threshold. Moreover, the analytical procedure can establish the time-to-failure curve much more efficiently because one needs to determine experimentally only the corrosion-fatigue curve corresponding to the particular ripple-load condition in a similar environment instead of the many laborious long-term actual ripple-load cracking tests at various stress intensity levels. With this perspective, high stress-ratio corrosion-fatigue is used to simulate ripple-load cracking in aluminum and titanium alloys.

The aluminum alloys included in the ripple-load cracking studies are ST 7075-T651, ST 7075-T7351, and LT 7075-T7351. The SCC resistance of high strength Al 7075 alloy varies, of course, with orientation and aging condition. Of these three aluminum alloys, ST 7075-T651 is most susceptible to SCC and has the lowest K_{ISCC} while LT 7075-T7351 is the most SCC-resistant. Figure 6 shows the corrosion-fatigue crack growth rate data for ST 7075-T651 and ST 7075-T7351 at R = 0.90 in a 3.5% NaCl solution. These data reveal similar crack growth rates at any given stress-intensity as well as identical ΔK_{th}. Similar corrosion-fatigue crack growth rate data were determined for LT 7075-T7351 at R = 0.90 in a 3.5% NaCl solution.

The SCC threshold, K_{ISCC}, determined by slow-strain rate tests, and the ripple-load cracking threshold, K_{IRLC}, derived from corrosion-fatigue crack growth tests and Eq. 3 are tabulated in Table 1. As shown in Table 1, the SCC-susceptible ST 7075-T651 exhibits a very low K_{ISCC} of 11 MPa$\sqrt{m}$ while the SCC-resistant ST 7075-T7351 has a higher K_{ISCC} value of 27 MPa$\sqrt{m}$. It is interesting to note that overaging, while substantially increasing the K_{ISCC}, has no significant effect on K_{IRLC} in ST 7075. For LT 7075-T7351, which is expected to have the highest K_{ISCC} value, SCC test specimens do not exhibit subcritical crack growth and fail only when the fracture toughness is reached. Therefore, K_{ISCC} for LT 7075-T7351 cannot be determined from the slow-strain rate tests. Instead, a K_{ISCC} of 32.0 MPa$\sqrt{m}$ reported in the literature for LT 7075-T7351 is used in Table 1.[16] Otherwise, K_{ISCC} values determined in this study agree well with those found in the literature.[17-18]

The predicted time-to-failure curves under 5% ripple loading in a 3.5% NaCl solution for ST 7075-T7351 and ST 7075-T651, obtained by numerical integration of corrosion-fatigue rate data shown in Fig. 6, are presented in Figs. 7 and 8 together with the window for ripple-load cracking susceptibility. As shown in Fig. 7, the SCC-resistant ST 7075-T7351 has a much larger potential for degradation by ripple-load effects. The ripple-load cracking threshold for ST 7075-T7351 is as much as 59% lower than the corresponding static K_{ISCC}. A similarly large 59% (Table 1) ripple-load degradation is expected for LT 7075-T7351. However, for the peakaged ST 7075-T651 (Fig. 8), while well known for its low SCC-resistance and responsible for the bulk of reported SCC failures in high strength aluminum alloys, the ripple-load effect is

essentially nonexistent as the K_{IRLC} and K_{ISCC} are both about 11 MPa$\sqrt{m}$. Figures 7 and 8 suggest that while the lower bound of the susceptibility window defined by K_{IRLC} varies little for the three 7075 temper/orientation combinations, the upper bound, as determined by K_{ISCC}, differs significantly. Thus, the higher K_{ISCC} value for the SCC-resistant temper opens up the susceptibility window and causes the greater potential for ripple-load cracking degradation. That is, even though overaged 7075-T7351 offers excellent SCC resistance in both ST and LT orientations (as evidenced by the high K_{ISCC} values), this material nevertheless is very susceptible to ripple-load degradation. This behavior is consistent with the results for steel where the SCC-resistant 5Ni-Cr-Mo-V steel is more prone to ripple-load cracking degradation while the SCC-susceptible high strength AISI 4340 steel exhibits little or no ripple-load degradation.

Ripple-Load Degradation and Stress-Corrosion Cracking in Titanium Alloys

Seven titanium alloys, with different chemistry, microstructure, and SCC resistance, were investigated for their ripple-load cracking resistance. These include BA and RA Ti-6Al-4V, BA and DA Ti-8Al-1Mo-1V, Ti-15V-3Cr-3Al-3Sn, and peakaged and overaged TIMETAL®21S. In this group, BA Ti-6Al-4V, BA Ti-8Al-1Mo-1V, Ti-15V-3Cr-3Al-3Sn, and overaged TIMETAL®21S offer better SCC resistance.

A representative corrosion-fatigue crack growth rate curve taken at R = 0.90 in a 3.5% NaCl solution is shown in Fig. 9 for BA Ti-6Al-4V. The predicted time-to-failure curve, based on the numerical integration of these corrosion-fatigue data, is presented in Fig. 10. For BA Ti-6Al-4V, a static K_{ISCC} was established at 60 MPa$\sqrt{m}$. The ΔK_{th} is 2.8 MPa$\sqrt{m}$. From Eq. 3, the threshold value under a 5% ripple-load condition, K_{IRLC}, is analytically predicted to be 28 MPa$\sqrt{m}$. As shown in Fig. 10, a large susceptibility window bounded by K_{ISCC} and K_{IRLC}, representing a 53% ripple-load degradation, exists for this SCC-resistant titanium alloy. Separate ripple-load cracking experimental data (open circles in Fig. 10) illustrate a good agreement with the predicted time-to-failure curve.

The corrosion-fatigue crack growth rate and the predicted time-to-failure curves for other titanium alloys under 5% ripple load in a 3.5% NaCl solution were also determined.[4,6-7] The K_{ISCC}, K_{IRLC}, and the extent of ripple-load degradation for these titanium alloys are summarized in Table 1. As shown in Table 1, the K_{IRLC} for RA Ti-6Al-4V, which is less SCC resistant than the BA Ti-6Al-4V, is 39 MPa$\sqrt{m}$, which is about 9% lower than the static K_{ISCC}. The lower degree of ripple-load susceptibility appears partly due to the low static K_{ISCC} of this alloy, which defines the upper bound of the susceptibility window.

Following the trend set by BA and RA Ti-6Al-4V, the moderately SCC-resistant BA Ti-8Al-1Mo-1V exhibits a larger degree of ripple-load degradation (19%) while the less SCC-resistant DA Ti-8Al-1Mo-1V demonstrates no ripple-load degradation. Similarly, the more SCC-resistant overaged TIMETAL®21S beta titanium alloy exhibits higher ripple-load cracking susceptibility (67%) when compared to less SCC-resistant peakaged alloy (55%). For Ti-15V-3Cr-3Al-3Sn, with its excellent resistance to salt water stress-corrosion cracking, cracking can occur at stress intensities as much as 72% below the apparent K_{ISCC}, when this alloy is subjected to a 5% ripple loading.

DISCUSSION

It is significant to note that the ripple effect depends strongly on the size or amplitude of the ripple loads. As the fatigue crack growth threshold, ΔK_{th}, varies with the stress ratio, R, the ripple-load cracking threshold, K_{IRLC}, correspondingly varies with R according to Eq. 3. Thus, while a material may exhibit substantial ripple-load degradation with larger amplitude ripple loading, the same material may show less or even no ripple-load degradation if the existing ripples are smaller. Ripple load cracking experiments at various ripple sizes on 5Ni-Cr-Mo-V steel clearly demonstrate this important point. A separate study had also shown that ripple loads smaller than 2% of the sustained load had no effect on the stress-corrosion cracking resistance of peakaged TIMETAL®21S.[19]

The data in Table 1 indicate that materials which exhibit greater SCC resistance under static load conditions are far more susceptible to ripple-load degradation, as can be observed more readily from the illustration in Fig. 11. Without exception, we have demonstrated that in each of the three engineering material families, highly SCC-resistant alloys are more prone to ripple-load degradation than less SCC-resistant alloys. The more SCC-resistant alloys in each family, 5Ni-Cr-Mo-V steel, LT 7075-T7351, BA Ti-6Al-4V, and Ti-15V-3Cr-3Al-3Sn, experience reductions of more than 50% in apparent K_{ISCC} when they are subjected to 5% ripple-load amplitude. On the other hand, the less SCC-resistant alloys in each group, AISI 4340 steel, ST 7075-T651, and DA Ti-8Al-1Mo-1V, exhibit no ripple-load degradation. The significance of this finding is obvious, at least phenomenologically, as a structure designed to take advantage of the high K_{ISCC} of a highly SCC-resistant material may fail unexpectedly if ripple-load conditions exist. To circumvent this problem, it is suggested that the possibility of ripple loading in the operating environment should be considered early in the design process, and if a ripple condition does indeed exist, the ripple-load cracking threshold, K_{IRLC}, should be used instead of the static K_{ISCC} to determine the allowable stress and inspection intervals.

Alloy sensitivities to ripple-load degradation, as defined by the contrast in results found within each of the primary alloy families examined, poses both an intriguing dilemma to the engineer who must select structural materials for performance in a specific environment, as well as a complex challenge to the research community. It is clearly disconcerting to the engineer to observe that materials which exhibit the greater SCC resistance under static loads are the same materials which often exhibit the greater sensitivity to ripple-load degradation. For the specific materials and conditions examined in this work, the more SCC-resistant materials, from 5Ni-Cr-Mo-V steel to 7075-T7351 aluminum alloy and to BA Ti-6Al-4V are more prone to ripple-load degradation than the less SCC-resistant materials, from high strength AISI 4340 steel to 7075-T651 aluminum alloy and to RA Ti-6Al-4V.

There is a challenge to the research community to advance the theory of SCC and fatigue so that the influence of material variables can be predicted, perhaps from an atomistic viewpoint eventually. At present this predictability is grossly lacking, so that it is difficult to assess which material variables promote ripple-load degradation via Eqs. 3 or 4: the combination of high levels of K_{ISCC} and low levels of ΔK_{th}, or the optimal combination of both high K_{ISCC} and ΔK_{th}, with minimal ripple-load degradation. As yet, not even the role of yield strength is quantitatively predictable: in general, higher levels of K_{ISCC} tend to be associated with lower yield strength, higher toughness materials[20]. On the other hand, there is evidence that the lower levels of ΔK_{th} are related to higher yield strength[21-22]. Thus, interestingly, it would appear that strength level

may play competing roles relative to ripple-load degradation. To work toward the prediction of fatigue threshold, ΔK_{th}, much further understanding is required of crack growth kinetics (including temperature dependence), local crack tip chemistry (pH as a function of microstructure), stress-ratio effects, and the role of strain-rate effects. Moreover, beyond compositional effects, the role of other microstructural variables on SCC resistance needs to be firmly established. Hopefully, studies in areas such as these will help guide the evolution of the desired predictive capability.

CONCLUSIONS

- The presence of ripple loads can cause structural failure at a stress intensity significantly below the static K_{ISCC} threshold. To assure safety from the ripple effect, a new threshold parameter (K_{IRLC}), below which ripple-load cracking will not occur, is identified and recommended as a design consideration if ripple-load conditions are suspected.

- The extent of the ripple-load effect and K_{IRLC} depend on the size or the amplitude of the ripple. While a material may exhibit no ripple effect under a very small ripple amplitude (e.g. < 2.5 % of the maximum load), it may experience a significant ripple-load degradation when subjected to a larger one (e.g. > 5 % of the maximum load).

- In each of the Fe, Al, and Ti families, alloys which exhibit greater SCC resistance under static load conditions are the same materials which exhibit greater sensitivity to ripple-load degradation. On the other hand, SCC-susceptible alloys display little or no damaging ripple-load effects.

ACKNOWLDGMENTS

This work was funded by the Office of Naval Research, Corrosion Science Program, and monitored by Dr. A. J. Sedriks, Program Manager.

REFERENCES

1. M.O. Speidel, Corrosion Fatigue of Steam Turbine Blade Materials, (New York, NY: Pergamon, 1983), p. 1.
2. T.W. Crooker, J.A. Hauser II, R.A. Bayles, Environmental Degradation of Engineering Materials - III, (College Park, PA: The Pennsylvania State University Press, 1987), p. 521.
3. P.S. Pao, R.A. Bayles, and G.R. Yoder, J. Eng. Mat. & Tech. H113(1991), p. 125.
4. G.R. Yoder, P.S. Pao, and R.A. Bayles, Scripta Met. 24(1990), p. 2285.
5. P.S. Pao, S.J. Gill, R.A. Bayles, and G.R. Yoder, Scripta Met. 25(1991), p. 2085.
6. P.S. Pao, D.A. Meyn, R.A. Bayles, C.R. Feng, and G.R. Yoder, Scripta Met. 33(1995), p.497.
7. P.S. Pao, D.A. Meyn, R.A. Bayles, C.R. Feng, and G.R. Yoder, submitted to Scripta Met.
8. R.N. Parkins, B.S. Greenwell, Metal Sci. 8/9(1977), p. 405.
9. R.N. Parkins, P.M. Singh, Corrosion 46(1990), p. 485.
10. K. Endo, K. Komai, and M. Himejima, Trans. Japan Soc. Mech. Engrs. 37(1971), p. 2036.
11. K. Endo, K. Komai, and N. Imashiro, Trans. Japan Soc. Mech. Engrs. 42(1976), p. 2652.
12. K. Komai, K. Minoshima, H. Yukimachi, Japan Congr. Mater. Res. 20(1984), p. 57.

13. G.R. Yoder, L.A. Cooley, T.W. Crooker, Fatigue Crack Growth Measurement and Data Analysis, STP 738 (Philadelphia, PA: ASTM, 1981), p. 85.
14. R.P. Wei, J.D. Landes, Materials Research and Standards 9(1969), p. 25.
15. O. Vosikovsky, J. Testing and Evaluation 6(1978), p. 175.
16. Damage Tolerant Design Handbook, MCIC, Columbus, OH (1983).
17. M.S. Domack, Int. Conf. & Exh. on Fatigue, Corrosion Cracking, Fracture Mechanics,and Failure Analysis, 1985, Paper, 9P.
18. J.I. Dickson, P. Martin, and J.-P. Baïlon, Matl Sci. Eng. 58(1983), p. L5.
19. R.P. Gangloff and J.R. Scully, Annual Research Report, SEAS Report No. UVA/525464/MSE93/101, University of Virginia, Charlottesville, VA, 1992.
20. G. Sandoz, Stress-Corrosion Cracking in High Strength Steels and Aluminum and Titanium Alloys (Washington, D.C.: U.S. Government Printing Office, 1972), p. 79.
21. G.R. Yoder, L.A. Cooley, T.W. Crooker, Fracture Mechanics, vol. 1, ASTM STP 791 (Philadelphia PA: ASTM, 1983), p. 348.
22. S. Taira, K. Tanaka, M. Hoshina, Fatigue Mechanisms, ASTM STP 675 (Philadelphia PA: ASTM, 1979), p. 135.

Table 1 Summary of Measured K_{ISCC} and Predicted K_{IRLC} (Under 5% Ripple Loading) in 3.5% NaCl Solution

Material	K_{ISCC} (MPa$\sqrt{m}$)	K_{IRLC}	RL Degradation
5Ni-Cr-Mo-V Steel	110	31	72 %
AISI 4340 Steel	33	33	0 %
LT 7075-T7351	32	13	59 %
ST 7075-T7351	27	11	59 %
ST 7075-T651	11	11	0 %
BA Ti-6Al-4V	60	28	53 %
RA Ti-6Al-4V	43	39	9 %
BA Ti-8Al-1Mo-1V	43	35	19 %
DA Ti-8Al-1Mo-1V	25	25	0 %
Ti-15V-3Cr-3Al-3Sn	60	17	72 %
TIMETAL®21S (Overaged)	57	19	67 %
TIMETAL®21S (Peakaged)	33	15	55 %

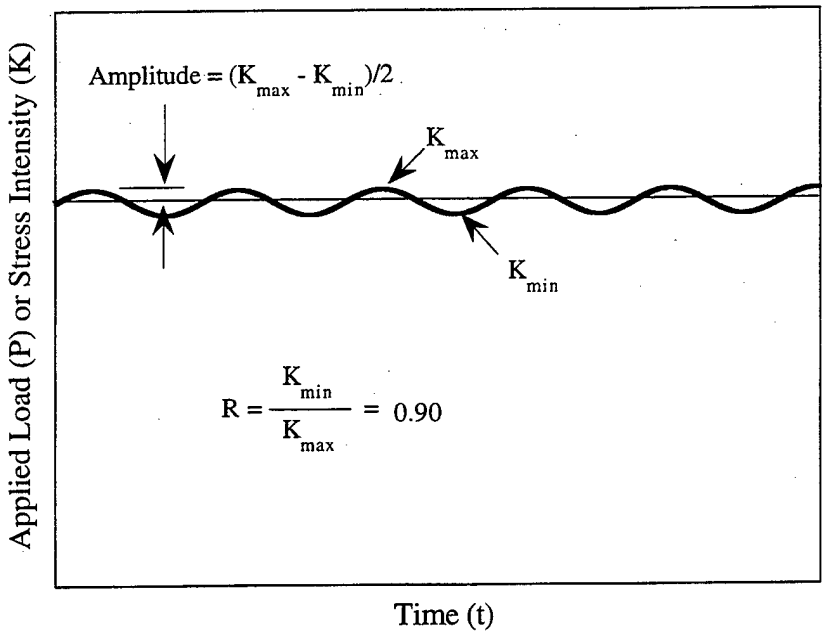


FIGURE 1. Ripple-load profile.

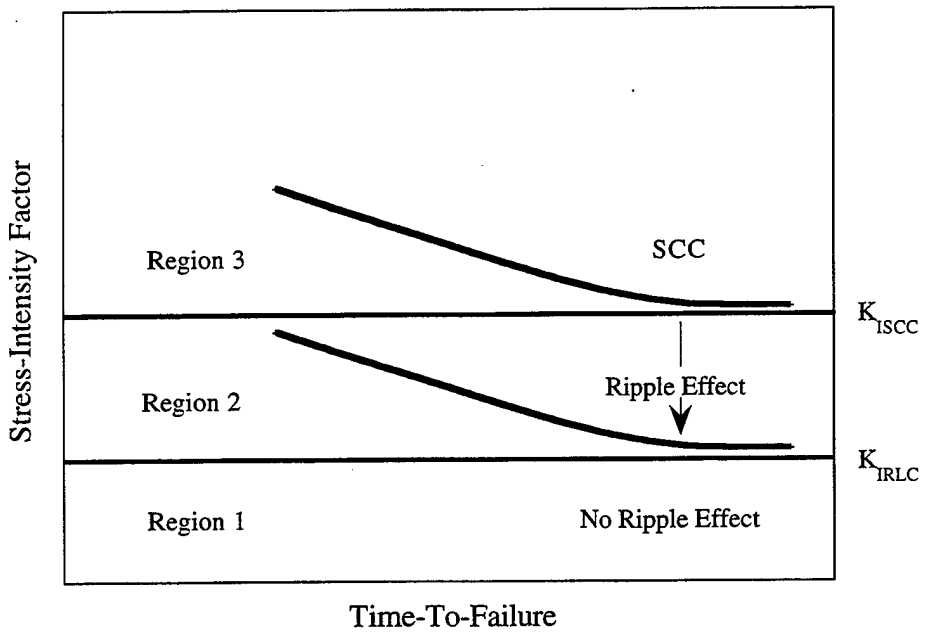


FIGURE 2. Schematic showing the ripple-load effect.

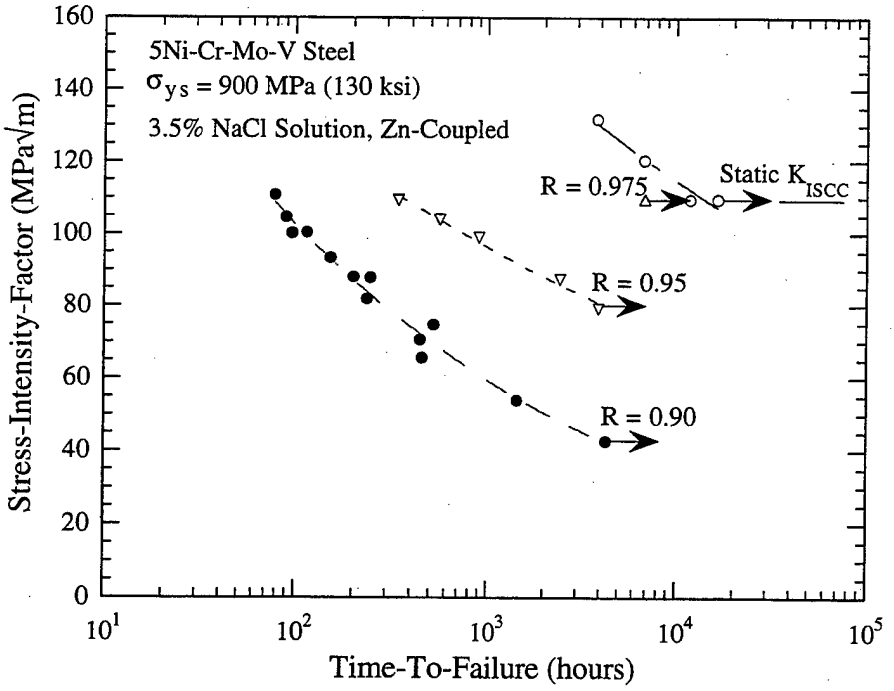


FIGURE 3. Ripple-load cracking (@ R = 0.975, 0.95, and 0.90) and stress-corrosion cracking of 5Ni-Cr-Mo-V steel in a 3.5% NaCl solution.

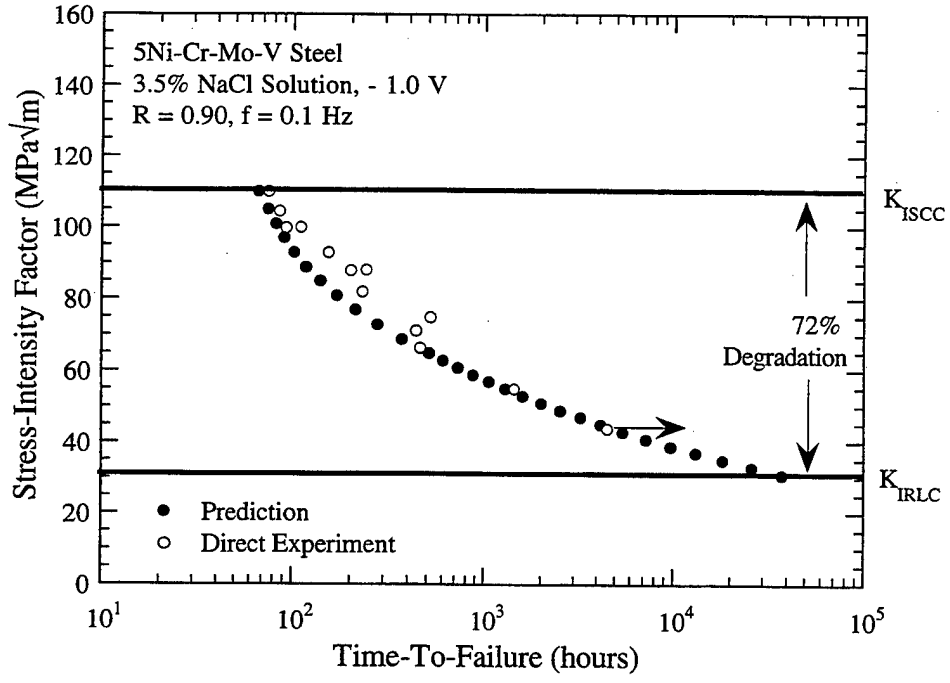


FIGURE 4. Ripple-load cracking of 5Ni-Cr-Mo-V steel in a 3.5% NaCl solution.

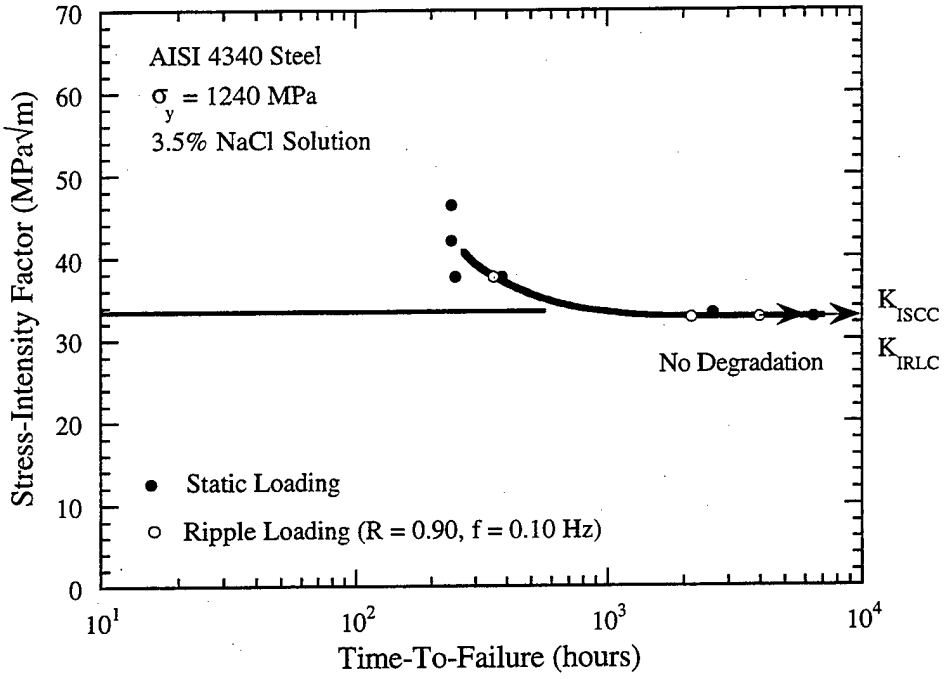


FIGURE 5. Ripple-load cracking and stress-corrosion cracking of AISI 4340 steel in a 3.5% NaCl solution.

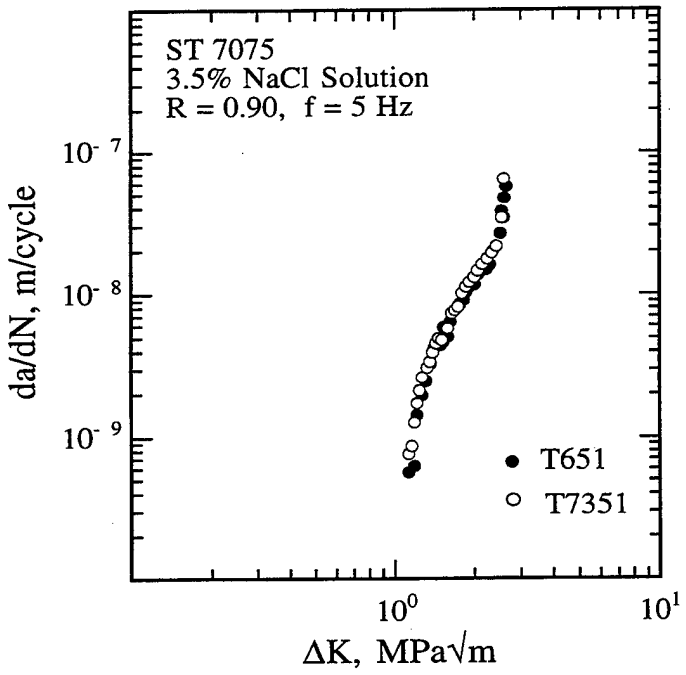


FIGURE 6. Fatigue crack growth of ST 7075-T651 and ST 7075-T7351 in a 3.5% NaCl solution at R = 0.90.

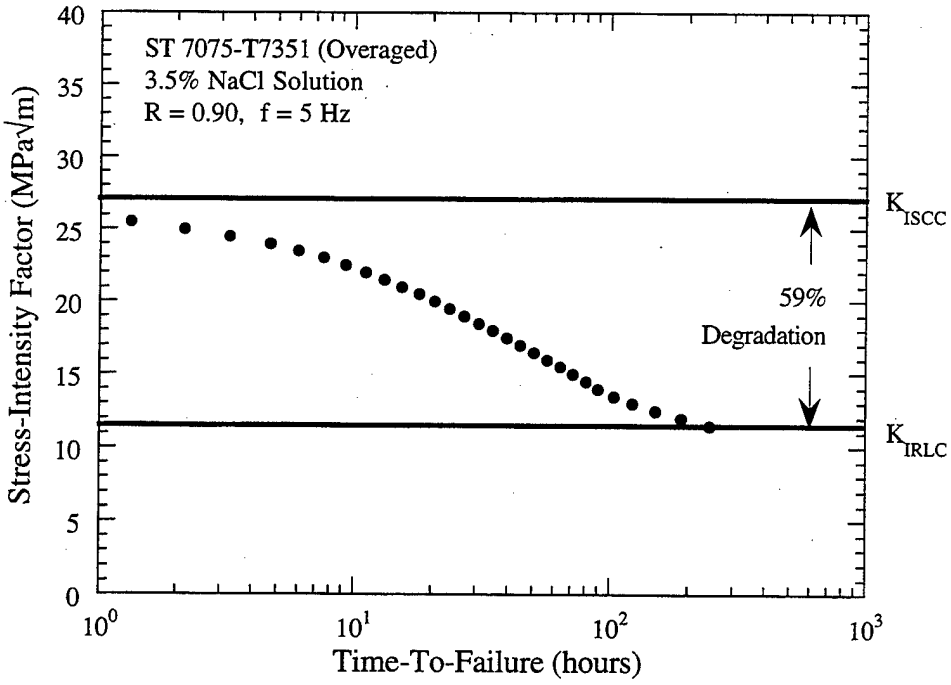


FIGURE 7. Ripple-load cracking of ST 7075-T7351 in a 3.5% NaCl solution.

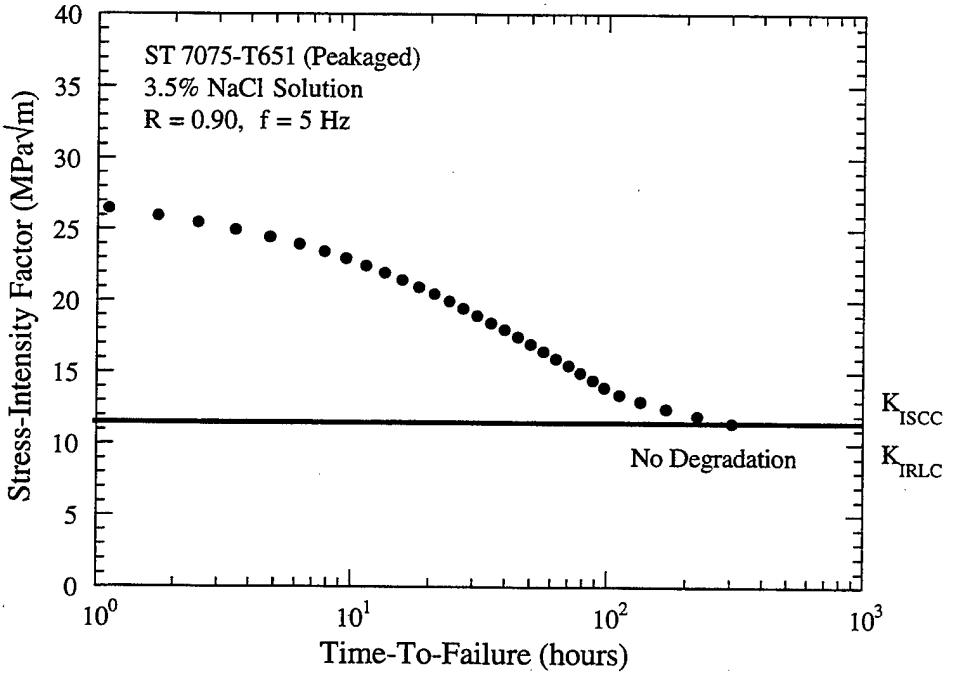


FIGURE 8. Ripple-load cracking of ST 7075-T651 in a 3.5% NaCl solution.

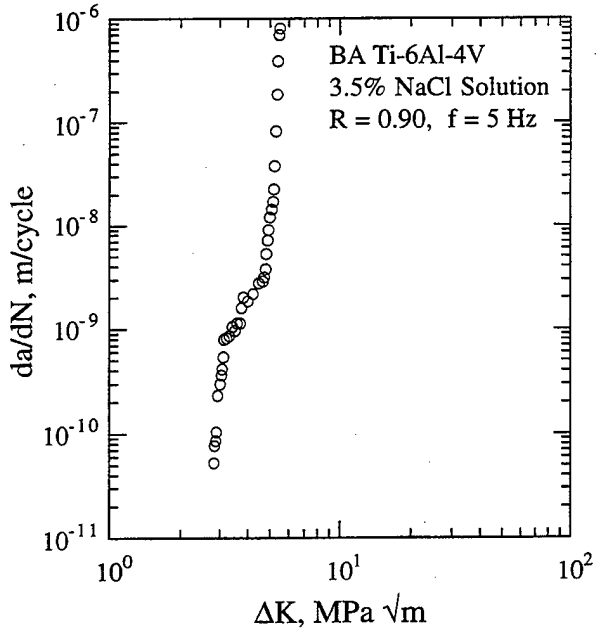


FIGURE 9. Fatigue crack growth of BA Ti-6Al-4V in a 3.5% NaCl solution at R = 0.90.

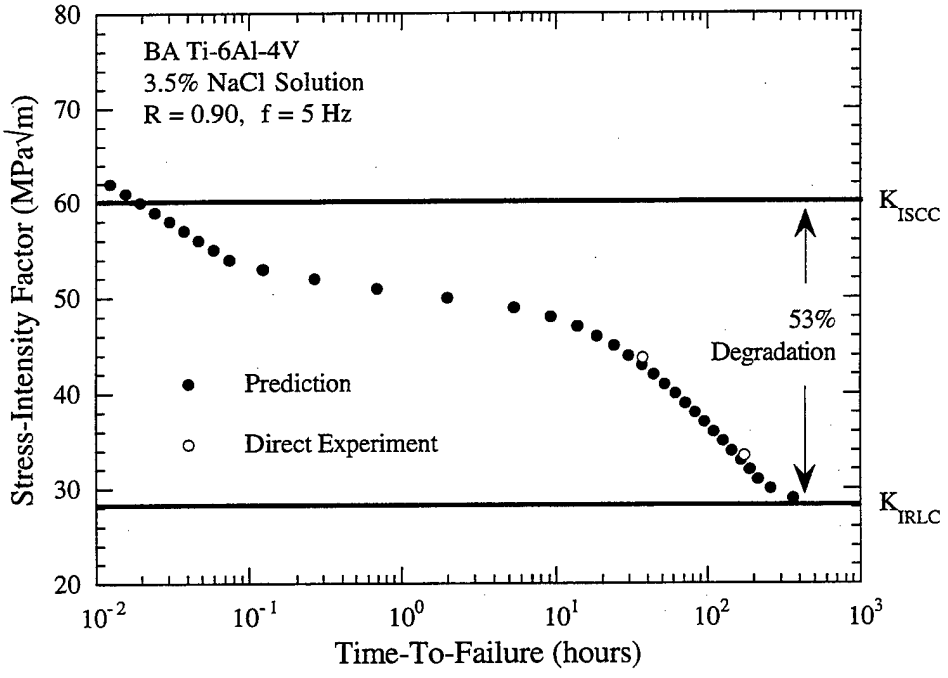


FIGURE 10. Ripple-load cracking of BA Ti-6Al-4V in a 3.5% NaCl solution.

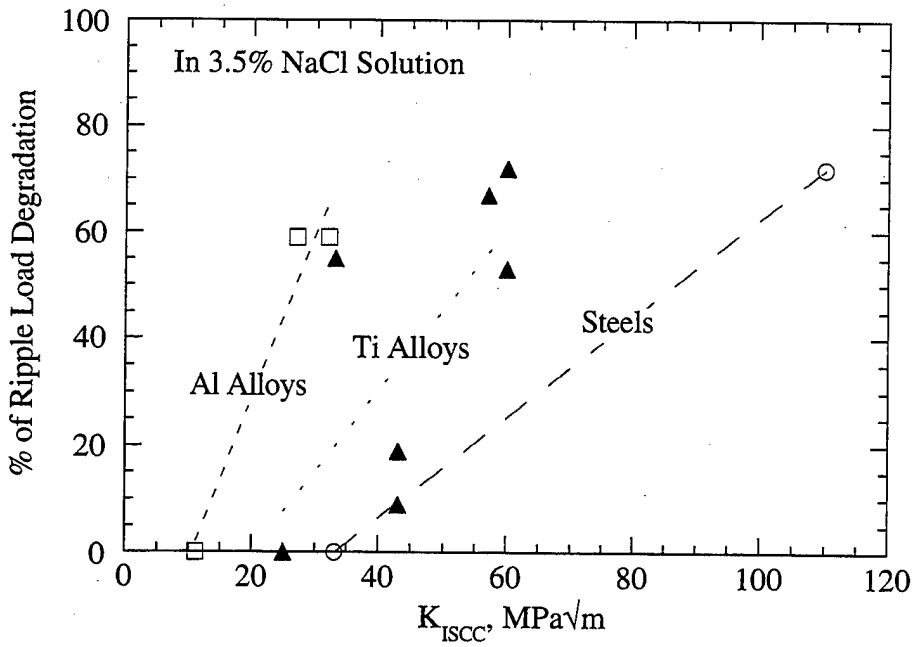


FIGURE 11. Relation of ripple-load susceptibility to stress-corrosion cracking threshold (all data for 5% ripple-load amplitude).

The Fatigue and Corrosion Fatigue Properties of Alloy 625 and 70/30 Copper-Nickel Alloy Electroslag Surfacing

Ernest J. Czyryca
Naval Surface Warfare Center
Carderock Division
West Bethesda MD 20817-5700

and

Robert B. Turpin
Oregon Graduate Institute of Science and Technology
Department of Materials Science and Engineering
Portland OR 97291-1000

ABSTRACT

Electro-slag surfacing (ESS) is a weld surfacing or cladding process capable of economically applying corrosion-resistant alloys on metal components. Fatigue and corrosion fatigue tests of Alloy 625 surfacing, applied as corrosion protection in a thin layer (6 mm) were conducted using flat plate, reversed bending tests. Also fatigue and corrosion fatigue tests of Alloy 625 and 70/30 Cu-Ni applied in thick, multi-layer build-up (25 mm) by ESS were conducted using rotating cantilever beam tests. The results showed that in thin layer Alloy 625 surfacing, a single-layer deposit by ESS and a two-layer deposit by gas metal-arc welding (GMAW) showed a similar corrosion fatigue strength of 15,000 psi. For thick Alloy 625 surface build-up (25 mm), a five-layer deposit by ESS showed a corrosion fatigue strength of 20,000 psi. The differences were primarily due to metallurgical factors (dilution, grain size, grain structure, etc.). Shot-peening was shown to improve the corrosion fatigue strength of Alloy 625 surfacing. The results for thick layer 70/30 Cu-Ni ESS showed a minor effect of saltwater on fatigue strength. The corrosion fatigue properties of 70/30 Cu-Ni ESS were comparable to those of centrifugal cast 70-30 Cu-Ni, with a corrosion fatigue strength of approximately 10,000 psi at 10^8 cycles.

INTRODUCTION

Electroslag surfacing (ESS) is a weld surfacing or cladding process capable of applying corrosion-resistant or wear-resistant alloys in thick layers. The ESS process has the following beneficial features: (1) high deposition rates, (2) low dilution of the surfacing alloy, (3) an arc-less process easily implemented in welding shops, and (4) ease of automation. The ESS process can deposit metallurgically sound cladding with only half the dilution and at twice the deposition rate of submerged arc surfacing.[1,2] The ESS process was investigated under a U.S. Navy-funded project as a cost-effective method for corrosion protection of propulsion shafts and as a alternate to removable, attached bearing and seal sleeves. Optimization of the ESS process was conducted for cladding propeller shafts with Alloy 625.[3] Subsequently ESS with 70/30 Cu-Ni was investigated for applications where existing Cu-Ni sleeves might be replaced without impact to ship corrosion protection systems.

The ESS process consists of the melting, deposition, and solidification of a consumable, metallic strip electrode. The process is shown schematically in Figure 1. The ESS head, mounted above the moving workpiece, feeds the strip through a leading layer of conductive, powder flux. Electric current passes through the flux surrounding the strip electrode and the surface of the component. Ohmic heating results in melting of the electrode occurs at the substrate surface along with a thin layer of the surface. Upon solidification, fusion is established between the cladding and substrate metal, and the solidified slag cleanly detaches from the metallic surfacing. ESS is a clean technology, since excess flux and solidified slag are removed by brushing, without the need for hazardous chemicals or mechanical removal methods.

Corrosion fatigue strength is a primary property considered in propulsion shaft design and may be the limiting criterion. The propeller shaft provides a rotating cantilever-beam support for the propeller, and the combination of gravity and cyclic bending forces develops cyclic bending stresses of relatively high magnitude, typically at shaft rotation frequency.[4] Thus, the evaluation of fatigue and corrosion fatigue properties of the ESS was conducted to support implementation of the process. Alloy 625 weld surfacing (variously called weld overlay or weld cladding) has been used as propulsion shaft corrosion protection since the 1970's. Primarily, Alloy 625 weld surfacing has been by gas metal-arc welding (GMAW) process, and the fatigue performance of Alloy 625 by ESS was compared to that of GMAW cladding.[5] Also surfacing and fatigue testing was conducted on submerged arc surfacing (SAS), a competitive process, for comparison. The fatigue performance of 70/30 Cu-Ni ESS was compared to centrifugal cast 70/30 Cu-Ni, the typical shaft sleeve alloy.

Scope

This paper describes fatigue and corrosion fatigue tests of thin Alloy 625 ESS corrosion protection layers (6 mm), thick Alloy 625 ESS sleeve replacement layers (25 mm), and thick 70/30 Cu-Ni alloy ESS sleeve replacement layers (25 mm).

MATERIALS INVESTIGATED

ESS was applied to sections of MIL-S-28234, Class 1 shaft steel, normalized and tempered, with composition and properties as shown in Tables 1 and 2, respectively. Arc sections were cut from the hollow shaft, forged into plate, and heat treated to conform to the specified mechanical properties. Each plate was no less than 3 inches thick and surfaces were prepared by Blanchard grinding and degreasing. The surfacing direction on the plates matched a circumferential welding pattern on the shaft.

The strip electrode alloys and ESS process parameters employed in the surfacing operations are provided in Tables 1 and 3, respectively. It should be noted that, with the exception of flux, all the materials and process parameters employed for ESS were essentially the same as those employed for submerged arc strip surfacing (SAS). Specimens for tensile and fatigue testing were extracted such that their longitudinal axes were perpendicular to the direction of surfacing (i.e. in the long axis of the original shaft). Tensile properties of the ESS and SAS deposited claddings used in fatigue tests are given in Table 2.

Surfacing was applied on steel substrate pieces of approximately 2 square feet area to provide material for fatigue specimens. As shown in Table 3, a preheat of 400 - 450 °F and an interpass temperature of 400 - 500 °F was controlled. A post-weld stress relief of 1050 °F for 2 hours was applied on some pieces to assess the effect of the required thermal treatment for propulsion shafts after welding. Single-layer welds were typically 0.25 inch and no less than 0.20 inch thick. Multi-layer ESS with Alloy 625 used 5 layers (passes) to provide a buildup of approximately one inch. The development of 70/30 Cu-Ni ESS process required that procedures be established to overcome the metallurgical incompatibilities between steel and Cu-Ni which inhibit welding. It was found that Cu-Ni ESS could be successfully applied to Class 1 shaft steel if a single, buttering layer of Ni-Cu (Monel metal) was deposited by ESS as an interlayer. The Cu-Ni ESS was deposited using this procedure. Test specimens were sectioned from the 4 layer Cu-Ni ESS buildup required for a one inch thick cladding.

EXPERIMENTAL METHODS

Fatigue and corrosion fatigue tests of Alloy 625 surfacing, applied as corrosion protection in a thin layer were conducted using Krouse-type, flat plate reversed bending tests, while fatigue and corrosion fatigue tests of Alloy 625 and 70/30 Cu-Ni in thick buildup (multiple layers) were conducted using McAdam-type rotating cantilever beam tests. In all cases, coupons were sawcut cut for fatigue specimens from the surfaced steel plate pieces, and all steel substrate was removed

by cutting and grinding (all Ni-Cu interlayer removed from 70/30 Cu-Ni ESS buildup. Thus the fatigue test specimens machined represented only the deposited surfacing.

Krouse-Type, Flat Plate Reversed Bending Tests

Krouse-type Model SP-150 plate-bending fatigue test machines were used for high-cycle fatigue and corrosion fatigue tests of the single-layer (thin layer) surfacing. The test specimens, Figure 2, and procedures are described in the ASTM *Manual on Fatigue Testing*.[6] Individual specimen identification was maintained by using a metal stamp to apply sample number and to maintain identification of the top surface of the weld deposit. Each sample was surface ground to thickness, then milled to the profile required for constant stress conditions in the test section (Figure 2). All grinding and machining marks were parallel of the length of the sample and the final edge preparation was accomplished by hand sanding with fine emery cloth to a 1/32 inch radius. Test frequency was 51.7 Hz and all tests were fully reversed (stress ratio R = - 1).

Corrosion fatigue tests were conducted in an artificial seawater produced in compliance with ASTM standard D 1141-90. The aerated, artificial seawater environment was maintained on the test section in an attached polyethylene container, Figure 3. The container was sealed and bonded to the test sample with a silicon-based marine adhesive. Failure was defined as complete fracture of the specimen.

McAdam-Type Rotating Cantilever Beam Tests

Fatigue and corrosion fatigue tests were conducted on the multi-layer (thick layer) surfacing using smooth and circumferentially notched rotating cantilever-beam (McAdam-type) specimens, Figure 4. The test specimens and procedures are also described in the ASTM *Manual on Fatigue Testing*.[6] Prior to fatigue testing, the smooth specimens were circumferentially and longitudinally polished to a metallographic grade finish, using a standardized polishing procedure.[6] The notch used was a machined, circumferential V-groove to result in a theoretical stress concentration factor, $K_t = 3.2$, as determined from the graphs of Peterson.[7] The notched specimens were tested in as-machined condition after optical inspection of the notch dimensions for conformity to requirements. In the fatigue tests, cyclic loading was obtained by applying a constant, deadweight load at the bearing end of the specimen while rotating at 1750 rpm. The maximum, nominal reversed stress was calculated from the applied deadweight load and the dimensions of the specimens, disregarding notch effects. The rotating cantilever-beam tests were performed in air and in saltwater, Figure 5, with the test section being continuously wetted with Severn River water, a brackish water having about one-third the salt content of natural seawater. All tests were conducted at an ambient room temperature. Failure was defined as complete fracture of the specimen.

FATIGUE DATA ANALYSIS

The results of the fatigue tests were analyzed to determine best-fit curves to data sets using statistical methods. In the analysis of the fatigue data, best-fit curves were calculated for sets of data using a modified log-log linear regression analysis by the following equation:

$$\log (S_a - S_e) = m \log N + b \qquad [1]$$

where

S_a = maximum nominal stress amplitude (psi);
S_e = stress which the best-fit curve approaches as an asymptote (psi);
m = slope;
b = intercept; and
N = cycles to failure.

The analysis program uses m, b, and S_e as fitting parameters, selecting values of S_e in increments of 100 psi to obtain an optimum correlation coefficient, r^2. The analysis uses a selected minimum and maximum stress over which S_e is fit. S_e is, in effect, an "endurance limit" or the fatigue strength for the test data at infinite life. For selecting the fitting range for S_e the following criteria were used:

1. Maximum value = highest stress amplitude used in fatigue test data set;
2. Minimum value = ½ the stress amplitude of the highest stress for which a runout was a result.

A fatigue test result is a runout when a test is discontinued after a predetermined "long life" without failure. A practical limit of exceeding 100,000,000 (or 10^8) cycles was used in this study.

RESULTS

The fatigue and corrosion fatigue strengths at 10^7 and 10^8 cycles, determined from best-fit curves to the data sets, are summarized in Table 4. The results for thin Alloy 625 ESS corrosion protection layers, thick Alloy 625 ESS sleeve replacement layers, and thick 70/30 Cu-Ni alloy ESS sleeve replacement layers are discussed in the following and compared to alloys used in similar applications.

Thin Layer Alloy 625 Surfacing

The results of the Krouse-type bending fatigue tests for single-layer Alloy 625 ESS on Class 1 shaft steel, in air and seawater environments, are given in Figures 6 and 7, respectively. Similarly, the results for single-layer Alloy 625 SAS on Class 1 shaft steel, in air and seawater environments, are given in Figures 8 and 9, respectively. For both processes, the fatigue

properties were not significantly different between the as-deposited and stress-relieved specimen series in each environment. The thermal stress-relief did not induce any significant microstructural change in the surfacing alloy that would affect the fatigue properties. For both SAS and ESS processes, the effect of the seawater environment was significant, showing reduction of fatigue strength in seawater versus fatigue strength in air. The corrosion fatigue strength at 10^8 cycles (Table 4) showed single-layer Alloy 625 deposit by ESS was 15 ksi and was equivalent to the application of two layers by GMAW, also 15 ksi.[5] Single-layer submerged-arc strip surfacing (SAS) was similar to both ESS and GMAW (16 ksi).

Examination of the fracture surfaces revealed a dull appearance at the fatigue crack initiation sites relative to the rest of the surface. The initiation sites were not located at any consistent distance from the specimen ends along the tapered, constant stress region. Fatigue crack initiation did not show any preferential site. Approximately half of the samples showed fatigue crack initiation from the surface originally near the substrate, while the rest showed initiation from the top surface.

Effect of Shot Peening on Alloy 625 ESS

Krouse-type corrosion fatigue tests in seawater were conducted using shot-peened single-layer Alloy 625 by ESS. The test section of the specimens (both sides and all edges) were shot-peened in accordance with MIL-S-13165, using Z-600 shot to an intensity of 0.008 to 0.012A, typically specified for critically stressed areas of cladding on Navy propulsion shafting.

Figure 9 provides the results of seawater corrosion fatigue tests of the shot-peened Alloy 625. The results to date indicate a corrosion fatigue strength at 10^8 cycles of 28 ksi. Thus, the effect of the shot-peening increased the corrosion fatigue strength above 15 ksi, the corrosion fatigue strength for the as-deposited Alloy 625 by ESS.

Thick, Multiple-Layer Alloy 625 Surfacing

Results of the McAdam-type rotating cantilever-beam fatigue tests of multi-layer Alloy 625 buildup by ESS are in air and saltwater are given in Figures 11 and 12, respectively. As in the single-layer tests previously discussed, thermal stress relief did not significantly affect the fatigue properties for all the conditions included in the study. The effect of the seawater environment was to cause a reduction of fatigue strength. The corrosion fatigue strength at 10^8 cycles (Table 4) of as-deposited, multi-layer Alloy 625 by ESS was 18 ksi and that for the stress relieved condition was 20 ksi. These values were higher than the corrosion fatigue strengths determined for the single-layer Alloy 625 by ESS.

The Krouse-type specimen used for the thin layer tests has a thin rectangular cross-section and a steep stress gradient in bending, whereas the McAdam-type specimen used for the multi-layer tests has a circular cross-section with stress gradient less than the Krouse-type. However, the results for tests in air for Alloy 625 ESS showed similar results for both types, Table 4. Thus,

it is suggested that the thin surfacing (single-layer) were affected by the seawater environment due to different chemical composition and solidification morphology than the multi-layer deposits. The level of iron dilution in the Alloy 625 surfacing decreases as the number of layers increases. The Krouse-type specimens used single-layer, the material with the highest dilution along its cross-section when compared to the multi-layer McAdam type specimens.

The fatigue notch reduction factor, K_f (the ratio of the fatigue strength for smooth specimens to the fatigue strength of notched specimens at a given cyclic life) ranged from 1.15 to 1.29, and was less than the theoretical value, $K_t = 3.2$, under all conditions. This indicated that the surfacing exhibits a low fatigue notch sensitivity.[7] The notch sensitivity was not affected by the saltwater test environment.

The corrosion fatigue strength of the multi-layer Alloy 625 cladding by ESS was less than half that of Alloy 625 plate, but greater than that of centrifugal cast Alloy 625, where tests were also conducted using McAdam-type, rotating cantilever-beam tests.

Effect of Cathodic Potential on Alloy 625 ESS

Corrosion fatigue tests of notched Alloy 625 ESS specimens were conducted with the test area given a coating of zinc applied by thermal spray (flame-spray) process. The objective of the tests was to determine if cathodic potential caused hydrogen damage detrimental to the corrosion fatigue properties of Alloy 625 ESS. Five notched specimens in the stress-relieved condition were prepared with the test area of each specimen was coated with zinc applied by flame-spray process, as shown in Figure 13. The surfaces outside the test area and the notch area (notch plus 0.1 inch to each side of the notch on the nominal diameter) were masked during surface preparation and spray deposition. The surfaces were grit-blasted for good coating adhesion. Specimens were preheated to 250 °F and a heavy layer of zinc was applied, nominally 0.050 to 0.100 inch thick on the nominal diameter. The zinc coating was then sealed with a polymeric sealant. The corrosion fatigue tests were conducted with the test area in a flowing stream of saltwater, where the masking was removed from the notch area. Post-test examination showed depletion of the zinc layer, it was assumed that the zinc was consumed by acting as sacrificial anode to the exposed, more noble notch area. No measurement of potential was conducted.

The corrosion fatigue results plotted in Figure 14, where the results and best-fit curve to the data for stress-relieved Alloy 625 ESS, freely corroding in saltwater, are shown. Note that the results for tests with cathodic potential provided via the zinc coating are within the scatter for tests in saltwater without zinc coating.

Thick, Multiple-Layer 70/30 Copper-Nickel ESS

The results for as-deposited 70/30 Cu-Ni by ESS, Figure 15, shows that the effect of saltwater on the fatigue strength was minor. The fatigue and corrosion fatigue strength of stress relieved 70/30 Cu-Ni ESS, Figure 16, was slightly higher than the as-deposited surfacing. The fatigue results are summarized in Table 4, where the fatigue strength at 10^8 cycles was follows

(highest to lowest): (1) stress relived in air, 13 ksi, (2) stress relived in saltwater, 12 ksi, (3) as-deposited in air, 11.5 ksi, and (4) as-deposited in saltwater, 10 ksi. The results indicated that the corrosion fatigue properties of 70/30 Cu-Ni by ESS were comparable to those of centrifugal-cast 70-30 Cu-Ni, where smooth specimens showed a saltwater corrosion fatigue strength of 11 ksi at 10^8 cycles.

SUMMARY AND CONCLUSIONS

The comparison of corrosion fatigue strengths at 10^8 cycles in this study showed that for thin Alloy 625 surfacing for corrosion protection, the single-layer deposit by ESS (15 ksi) was equivalent to the application of two layers by GMAW (15 ksi). Shot-peening can improve the corrosion fatigue strength of the thin Alloy 625 ESS to 28 ksi. Both ESS and SAS provide a more productive and economical means of surfacing ship propulsion shafting than GMAW for a corrosion resistant and damage resistant cladding.

For thick Alloy 625 surface build-up for sleeve replacement, the five-layer deposit by ESS showed a corrosion fatigue strength of 18 ksi, low notch sensitivity in way of grooves and slots used to fix seal components, and no sensitivity to hydrogen from cathodic protection systems. The corrosion fatigue strength was similar to that of centrifugal cast Alloy 625 (15 ksi). Although multi-layer 70/30 Cu-Ni ESS buildup for sleeve replacement does not exhibit the same production ease and economies of Alloy 625 ESS, the corrosion fatigue strength (12 ksi) was similar to that for centrifugal cast 70/30 Cu-Ni (11 ksi).

ACKNOWLEDGMENTS

The fatigue and corrosion fatigue study of Alloy 625 and 70/30 Cu-Ni ESS was in support of the Navy Manufacturing Technology project on Electroslag Strip Surfacing (ESS) Technology funded by the Office of Naval Research under Mr. S. Linder. The authors wish to thank the NSWCCD coordinators for the project, Mr. D.P. Rome and Mr. J.G. Mattern, for their assistance. The project was conducted by the Oregon Graduate Institute (OGI) under contract to National Center of Excellence for Metalworking Technology (NCEMT). For their continued help and interest during the fatigue studies and throughout the ESS project, the authors gratefully acknowledge the work of Drs. W. Wood and J. Develetian of OGI and Dr. F. Mollard of NCEMT.

REFERENCES

1. Yu, D.W., and J.H. Devletian, "Electroslag Surfacing: A Potential Process for the Rebuilding and Restoration of Ship Components," *Journal of Ship Production*, Vol.5, No. 2, May 1989, pp. 67-78.

2. Oh, Y.K., J.H. Devletian, and S.J. Chen, "Low-Dilution Electroslag Cladding for Shipbuilding," *Welding Journal*, August 1990, pp.37-44.

3. Devletian, J.H., Y.P. Gao, Q.H. Zhao, and W.E. Wood, "Strip Cladding of Propeller Shafts with Alloy 625 by Electroslag Surfacing," *Journal of Ship Production*, Vol. 9, No. 3, August 1993, pp. 173-180.

4. Heck, J.W., and E. Baker, "Marine Propeller Shaft Casualties," *Transactions of the Society of Naval Architects and Marine Engineers*, Vol. 65, 1963, pp. 682-702.

5. Hasson, D., C. Zanis, L. Aprigliano, and C. Fraser, "Surfacing of 3.25% Nickel Steel with Inconel 625 by the Gas Metal Arc Welding - Pulsed Arc Process," *Welding Research Supplement*, January 1978, pp. 1s-8s.

6. *Manual on Fatigue Testing*, ASTM STP 91, American Society for Testing and Materials, Phila., PA, 1949.

7. Peterson, R.E., *Stress Concentration Factors*, John Wiley & Sons, New York, NY,1974.

Table 1. Chemical compositions of materials used in surfacing.

	Chemical Composition (weight %)									
	C	**Mn**	**Si**	**Ni**	**Cr**	**Mo**	**Cu**	**Fe**	**Cb**	**Ti**
MIL-S-23284, Class 1 Steel	0.25	0.34	0.22	3.21	0.42	0.44	-	bal.	-	-
Alloy 625 Strip Electrode	0.005	0.03	0.04	bal.	22.5	9.30	-	0.95	3.70	0.2
70/30 Cu-Ni Strip Electrode	0.02	0.73	0.04	31.25	-	-	67.0	0.55	-	0.42
Ni-Cu Strip Electrode	0.02	3.54	0.17	65.1	-	-	28.64	0.52	-	1.98

Table 2. Tensile properties of surfacing deposits used in fatigue tests.

Material	Condition	Yield Strength (ksi)	Tensile Strength (ksi)	Elongation (%)	Reduction of Area (%)
MIL-S-23284, Class 1 Steel Shaft Substrate	Stress Relieved	89.4	109.3	21	62.5
Alloy 625 -- Single-Layer ESS	As Deposited	58.5	99.0	47	43
Alloy 625 -- Single-Layer ESS	Stress Relieved	56.0	97.4	43	45
Alloy 625 -- Single-Layer SAS	As Deposited	55.5	97.7	40	38
Alloy 625 -- Single-Layer SAS	Stress Relieved	56.0	99.8	41	42
Alloy 625 -- Multi-Layer ESS	As Deposited	58.5	95.3	47	46
Alloy 625 -- Multi-Layer ESS	Stress Relieved	58.1	96.0	49	45
70/30 Cu-Ni -- Multi-Layer ESS	As Deposited	28.1	50.9	29	22
70/30 Cu-Ni -- Multi-Layer ESS	Stress Relieved	32.6	56.7	27	23

Table 3. Process parameters used for ESS on Class 1 shaft steel.

	Alloy 625 ESS Single or Multipass	Ni-Cu Alloy Buttering Layer	70/30 Cu-Ni ESS Multipass
Current (A)	650	500	550
Voltage (V)	27	28 - 30	26 - 28
Machine Type	DCep constant voltage	DCep constant voltage	DCep constant voltage
Travel Speed (in/min)	7	6	6
Strip Feed Speed (in/min)	73	75	100 - 120
Bead-to-Bead Tie-In Overlap (in)	0.14	0.14	0.14
Strip Head Position	vertical	vertical	vertical
Strip Feed Angle	7° push	7 to 10° push	5 to 10° push
Contact Tip-to-Work Distance (in)	1.2	1.2	1.2
Flux	Type 59S	Type 59S	Type ESW9
Strip Size (mm)	30 X 0.5	30 X 0.5	30 X 0.5
Preheat / Interpass Temperature (minimum / maximum. °F)	400 / 500	400 / 500	400 / 500
Wire Brushing	no	no	after each pass
Grinding	no	no	after each layer
Post Surfacing Stress Relief Temperature (°F)	1200	1200	1200

Table 4. Summary of fatigue and corrosion fatigue of surfacing alloys and propulsion shaft sleeve alloys.

Process Description	Test Condition	Test Environment	Fatigue Strength at 10^7 cycles (ksi)	Fatigue Strength at 10^8 cycles (ksi)
Krouse-type Plate Bending Fatigue Tests Alloy 625 Thin Layer Surfacing				
ESS / 1 layer	as deposited / stress relieved	air	34	22
ESS / 1 layer	as deposited / stress relieved	seawater	23	15
ESS / 1 layer	stress relieved & shot peened	seawater	36	28
SAS / 1 layer	as deposited / stress relieved	air	31	19
SAS / 1 layer	as deposited / stress relieved	seawater	20.5	16
GMAW 2 layers	stress relieved	seawater	22	15
McAdam-type Rotating Cantilever-Beam Fatigue Tests Alloy 625 Thick Layer Surfacing				
ESS / 5 layers	as deposited	air	33	23
ESS / 5 layers	as deposited	notched / air	26	20
ESS / 5 layers	as deposited	SW	28.5	18
ESS / 5 layers	as deposited	notched / SW	23	15
ESS / 5 layers	stress relieved	air	33	25
ESS / 5 layers	stress relieved	notched / air	27	20
ESS / 5 layers	stress relieved	SW	31	20
ESS / 5 layers	stress relieved	notched / SW	24	16.5
ESS / 5 layers	stress relieved	notched / SW + Zn coating	24	16.5
Rolled Plate	hot rolled & annealed	SW	58	53
Casting	centrifugal cast & annealed	SW	26	15
McAdam-type Rotating Cantilever-Beam Fatigue Tests 70/30 Cu-Ni Thick Layer Surfacing				
ESS / 4 layers	as deposited	air	14	11.5
ESS / 4 layers	as deposited	SW	13.5	10
ESS / 4 layers	stress relieved	air	16.5	13
ESS / 4 layers	stress relieved	SW	15	12
Casting	centrifugal cast	SW	17	11

Note: SW = Severn River Water

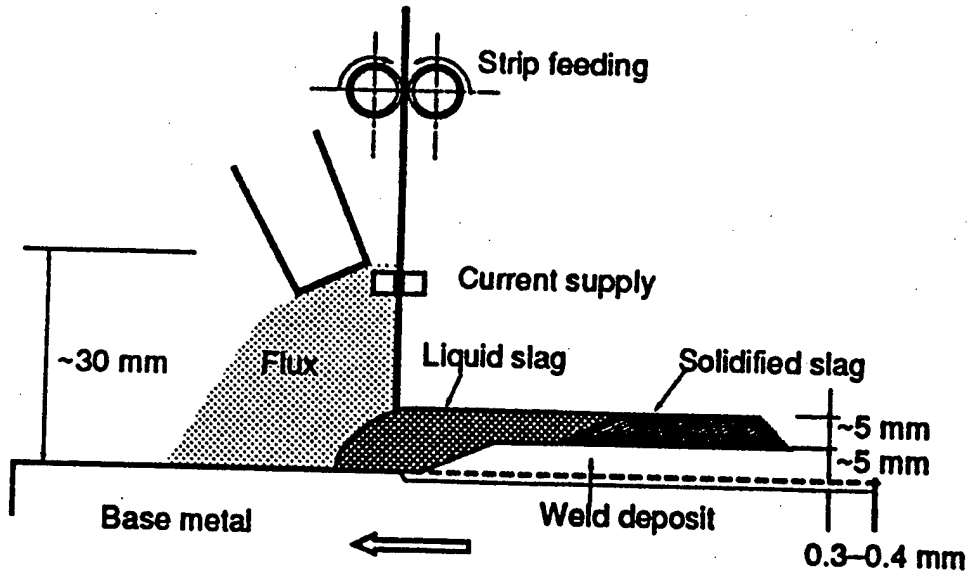


Figure 1. Schematic diagram of the electroslag surfacing (ESS) process.

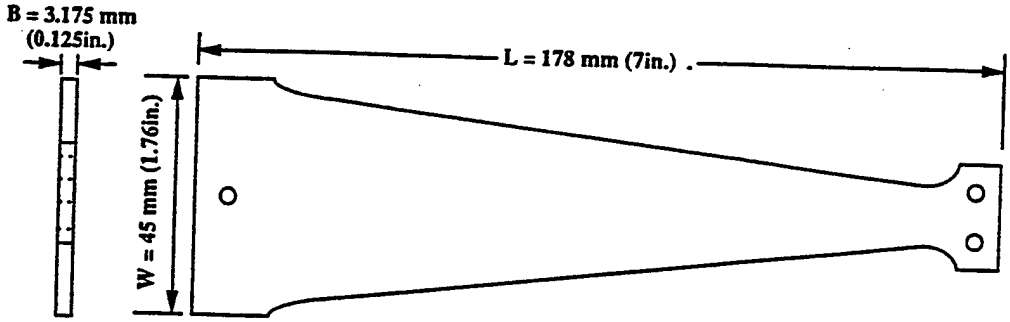


Figure 2. Krouse-type plate bending fatigue specimen.

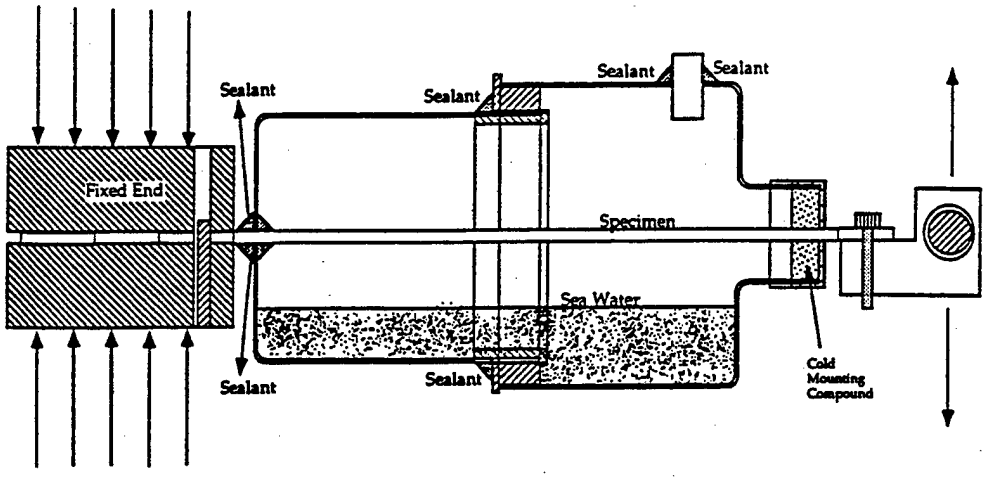


Figure 3. Containment cell attached to plate bending specimen for corrosion fatigue tests.

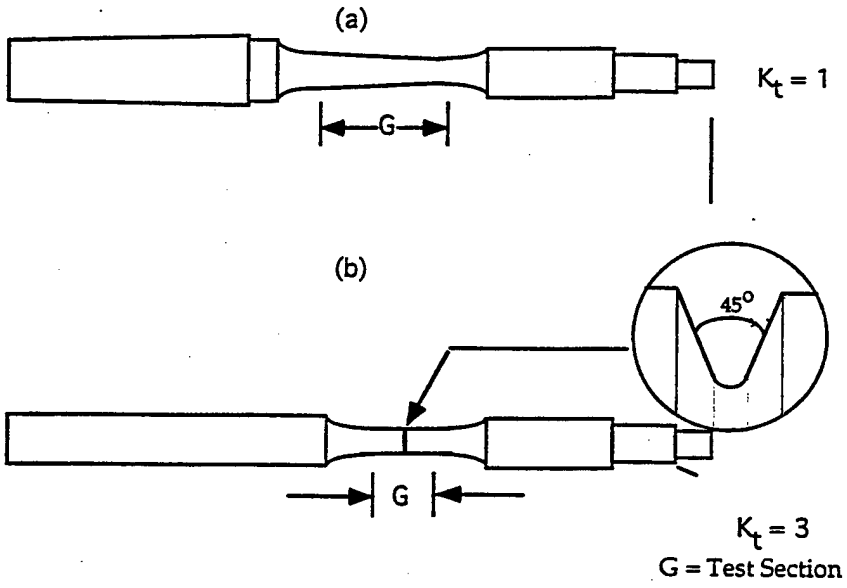


Figure 4. McAdam-type rotating cantilever-beam specimens: (a) smooth and (b) notched.

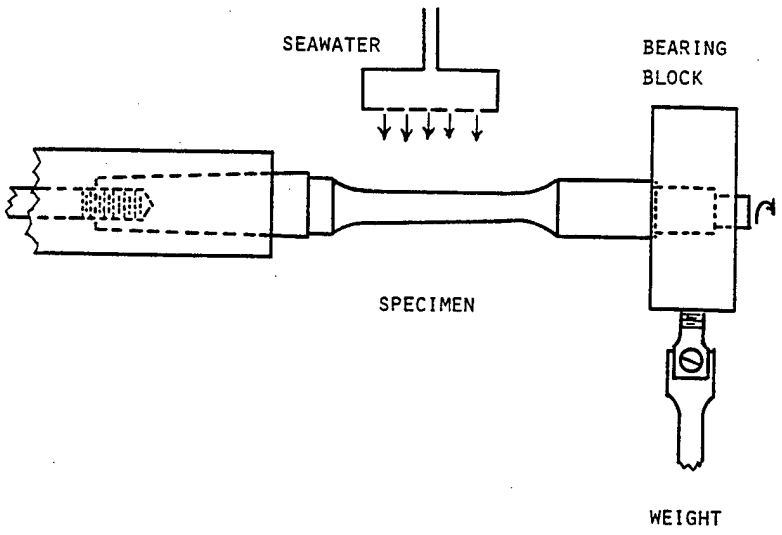


Figure 5. Schematic diagram of rotating cantilever-beam corrosion fatigue test set-up.

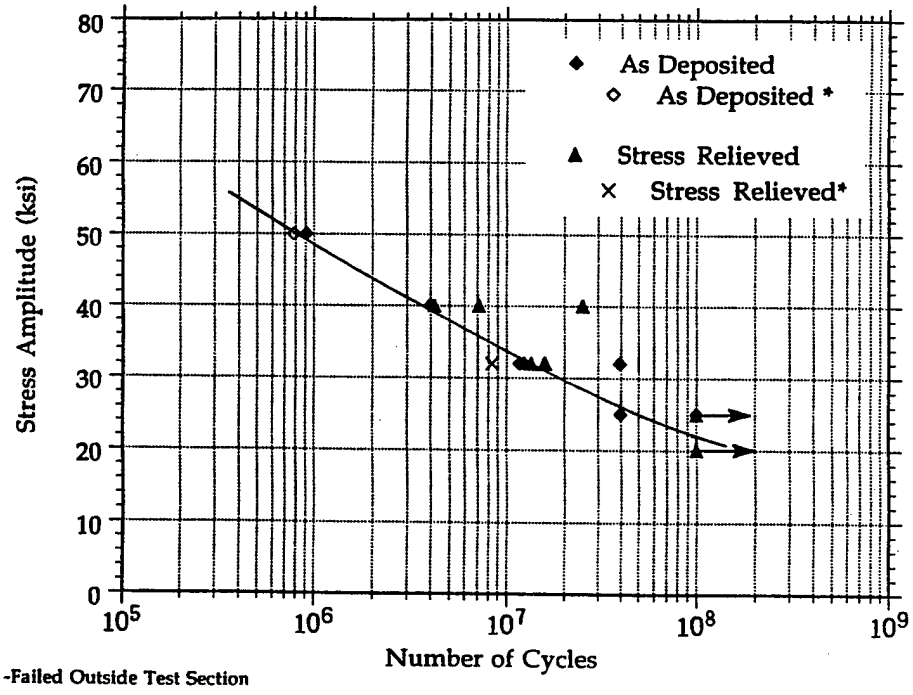


Figure 6. Results of Krouse-type bending fatigue tests in air for single-layer Alloy 625 ESS.

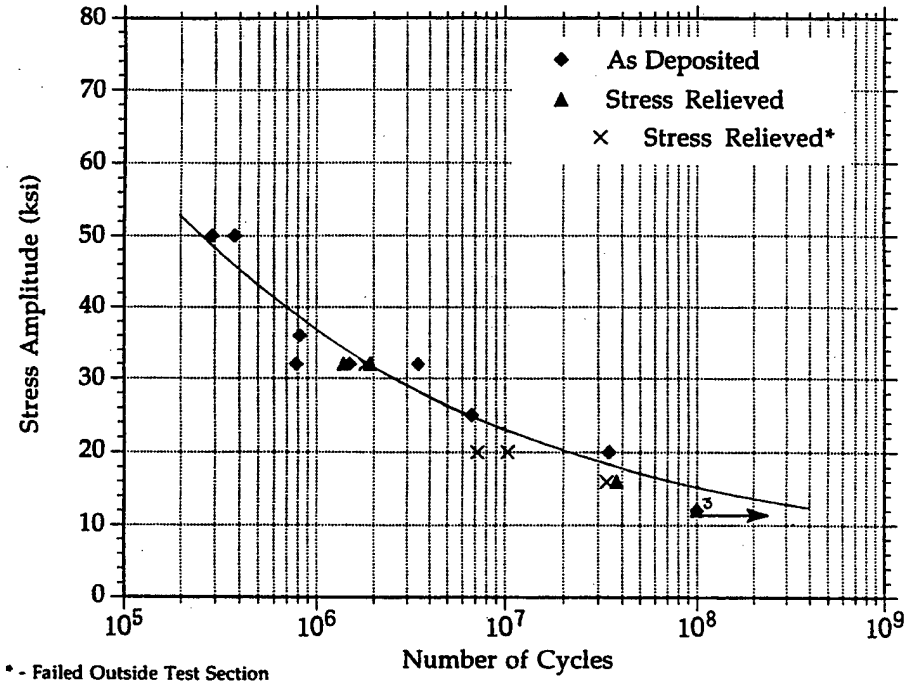


Figure 7. Results of Krouse-type bending fatigue tests in seawater for single-layer Alloy 625 ESS.

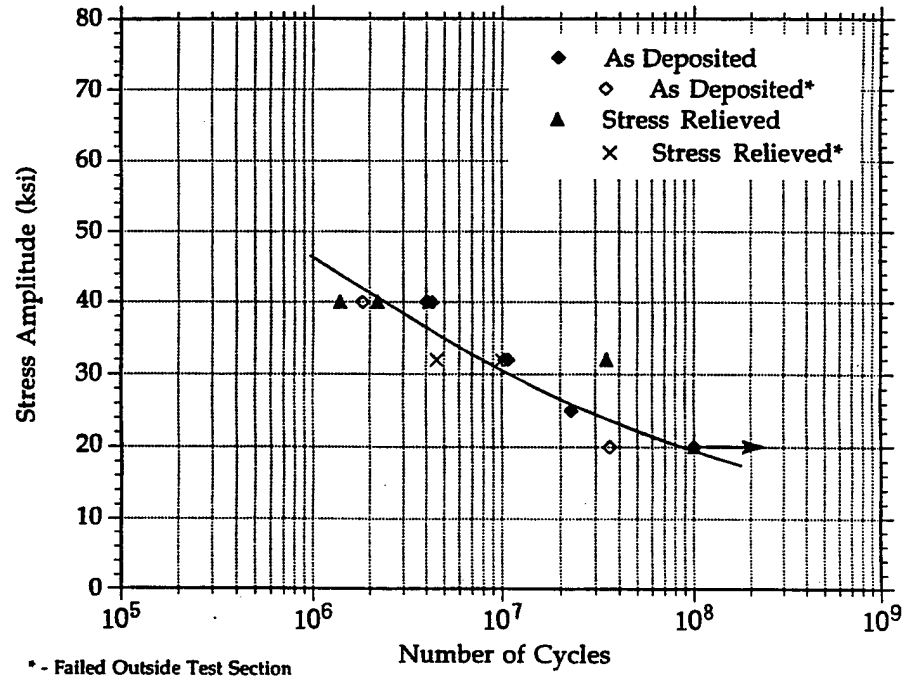


Figure 8. Results of Krouse-type bending fatigue tests in air for single-layer Alloy 625 SAS.

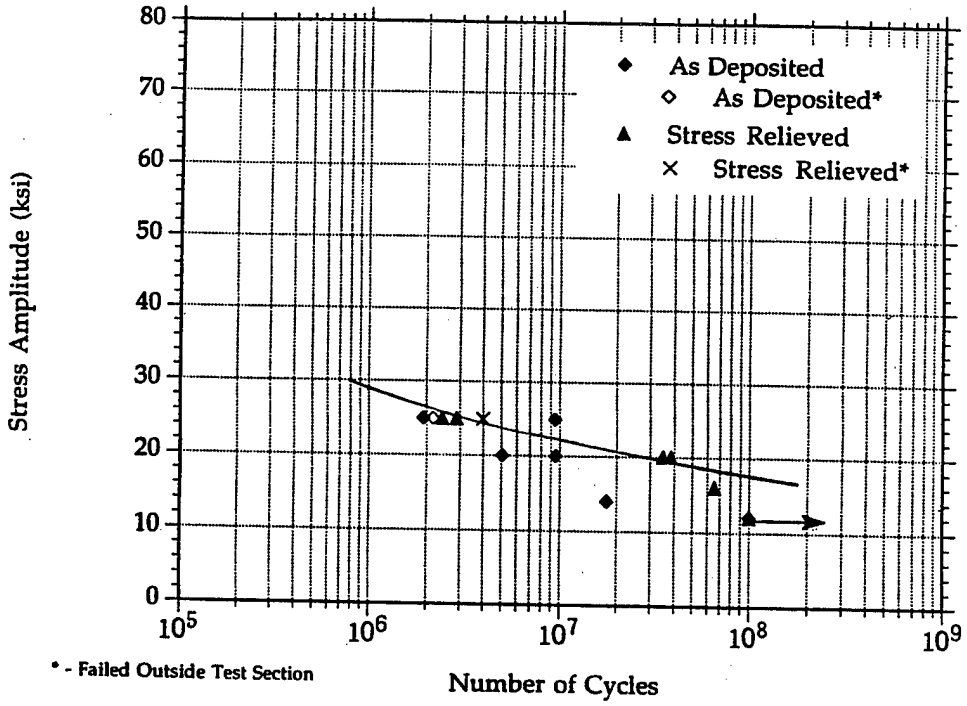


Figure 9. Results of Krouse-type bending fatigue tests in seawater for single-layer Alloy 625 SAS.

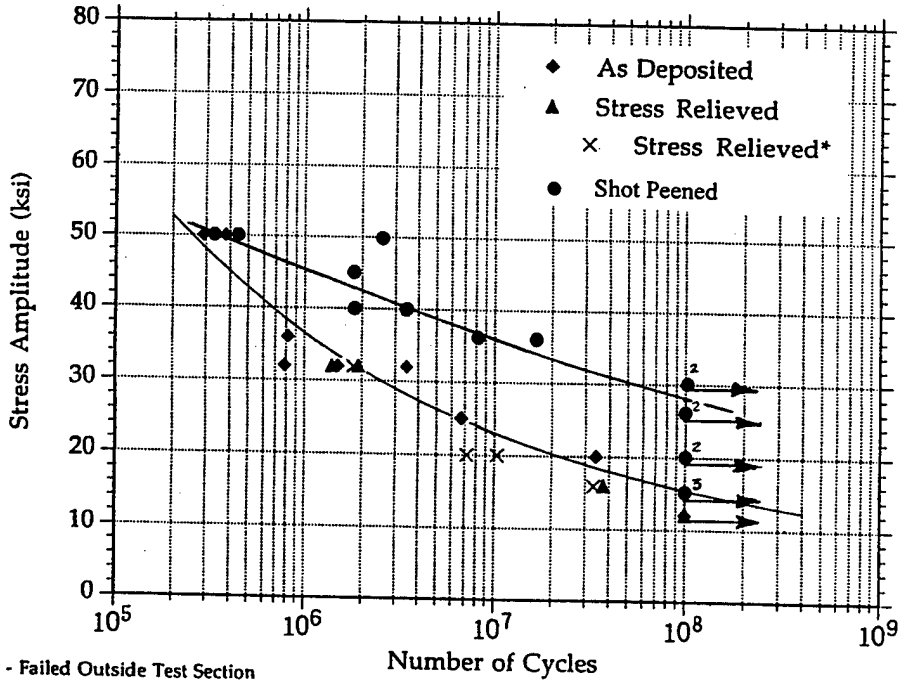


Figure 10. Results of Krouse-type bending fatigue tests in seawater for single-layer Alloy 625 ESS as deposited, stress relieved, and shot peened.

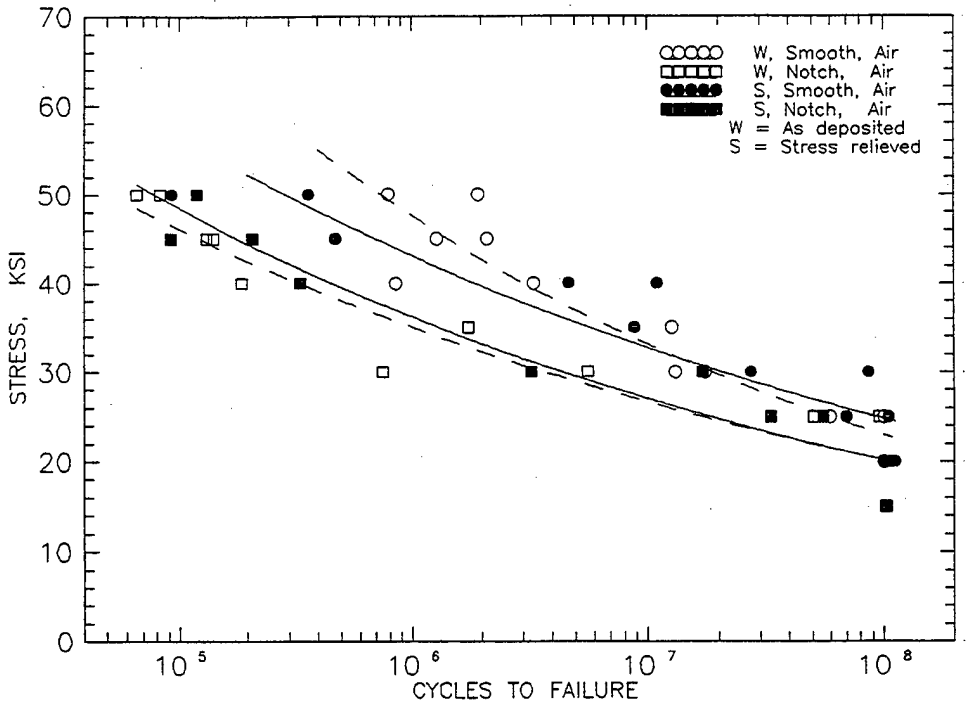


Figure 11. Results of McAdam-type rotating beam fatigue tests in air for multi-layer Alloy 625 ESS.

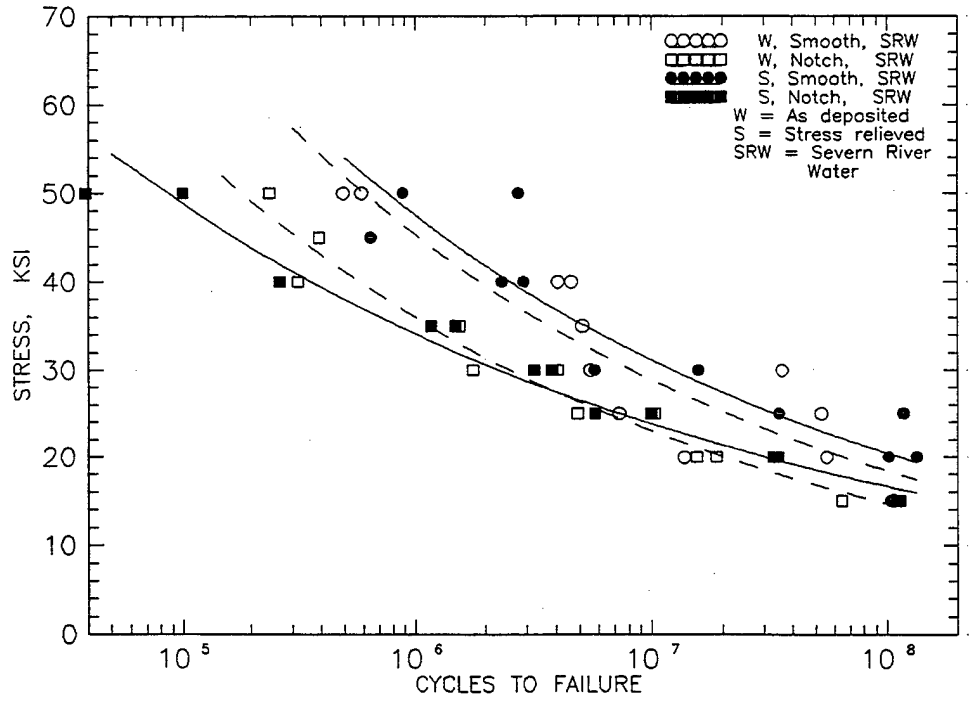


Figure 12. Results of McAdam-type rotating beam fatigue tests in seawater for multi-layer Alloy 625 ESS.

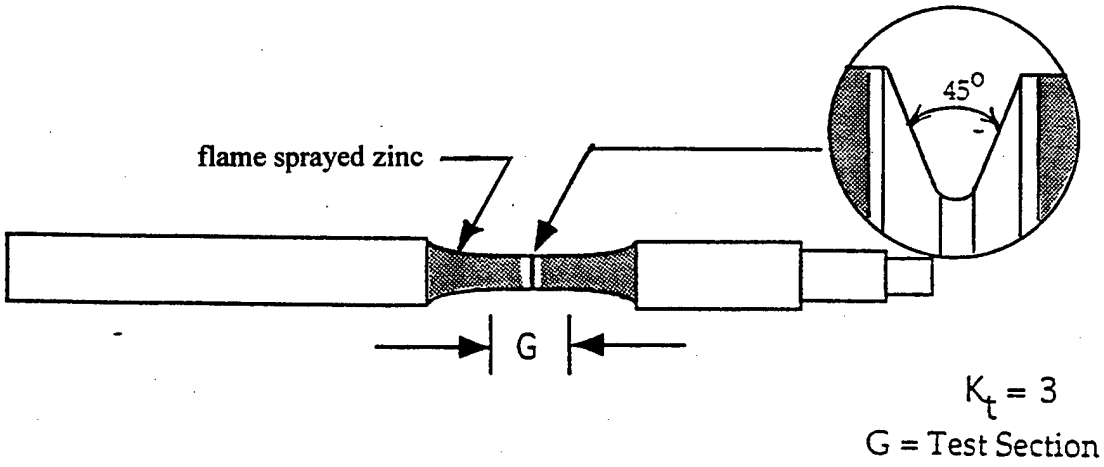


Figure 13. Notched McAdam-type rotating beam fatigue specimen of Alloy 625 ESS with flame-sprayed zinc in test section.

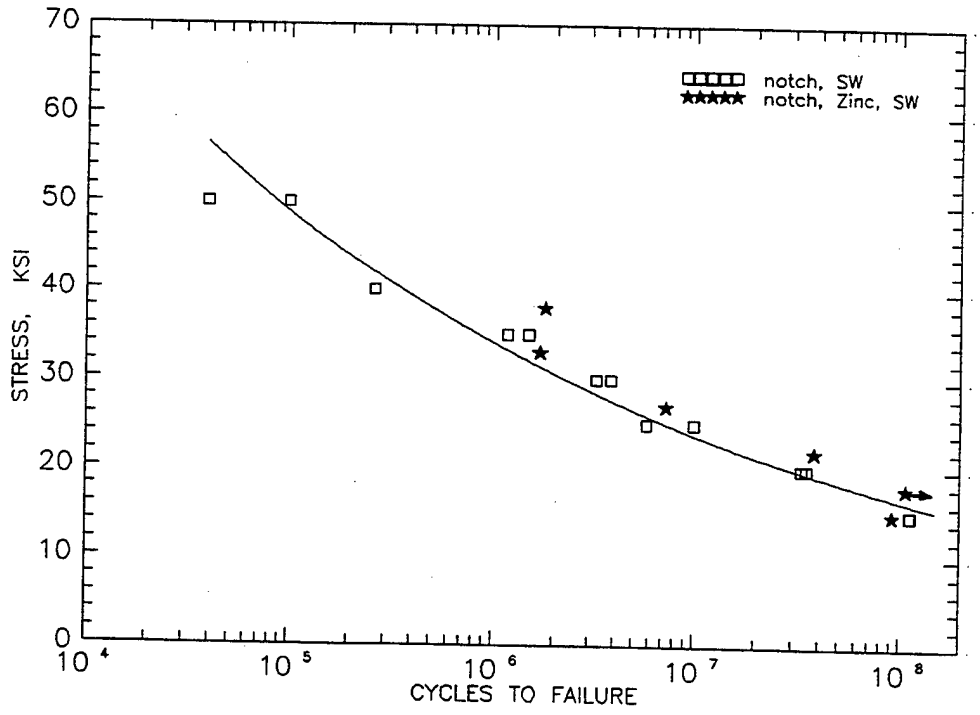


Figure 14. Results of notched McAdam-type rotating beam fatigue tests in saltwater for multi-layer Alloy 625 ESS, with and without cathodic protection.

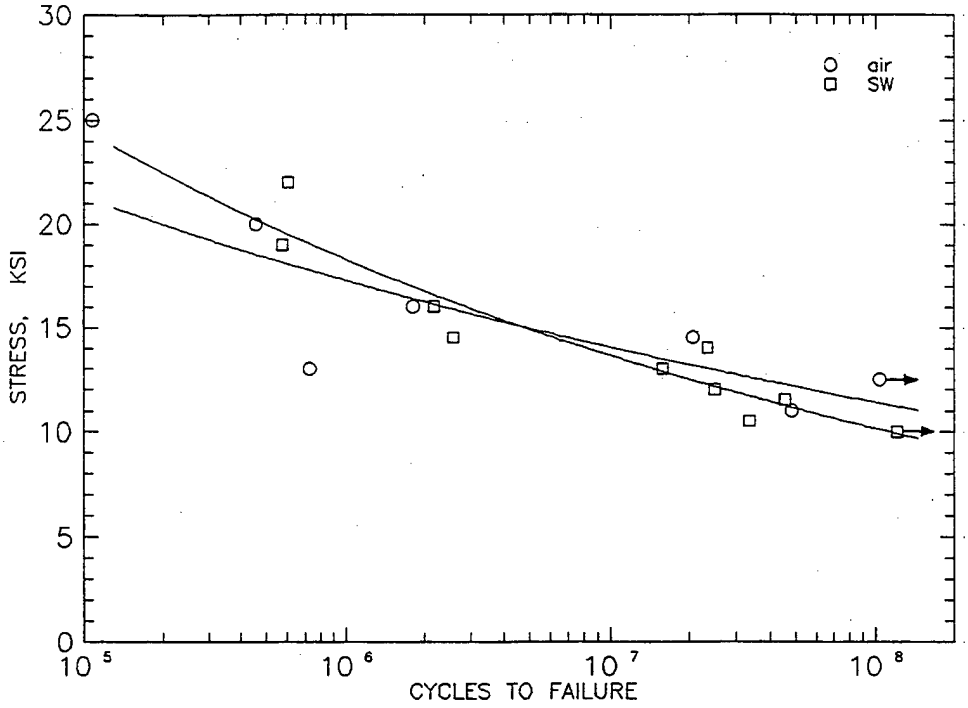


Figure 15. Results of McAdam-type rotating beam fatigue tests for as-deposited multi-layer 70/30 Cu-Ni ESS.

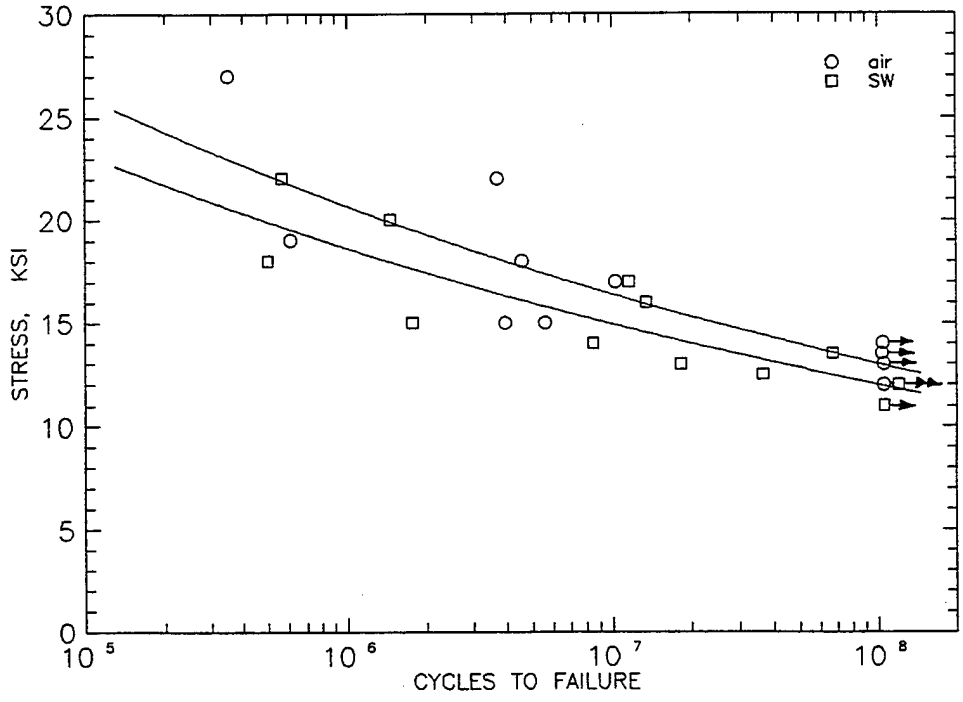


Figure 16. Results of McAdam-type rotating beam fatigue tests for stress relieved multi-layer 70/30 Cu-Ni ESS.

ROLE OF AQUEOUS ENVIRONMENT ON THE GROWTH OF LONG FATIGUE CRACKS

A. K. Vasudevan
Materials Division Code 332,
Office of Naval Research, Arlington, Virginia.22217

K. Sadananda
Materials Department Code 6323,
Naval Research Laboratory, Washington, D. C. 20375

ABSTRACT

The role of environment on fatigue crack growth is examined using the new concepts developed by earlier by the authors. The concepts are based on the finding that fatigue damage requires *two independent loading parameters* for an unambiguous description and that for a fatigue crack to grow there are two thresholds; one in terms of each loading parameter that must be satisfied simultaneously. These two thresholds can be uniquely described by the asymptotic limits in a plot of ΔK_{th} and K_{max} , defined as a *fundamental threshold curve.* The two thresholds depend on the environment and the metallurgical microstructure. Using these concepts, published fatigue crack growth data on several materials are examined and their subsequent behavior broadly classified into *five* groups. The relative roles of plasticity and environment are discussed for each of the cases using examples from the literature.

INTRODUCTION

It is recognized that the performance of materials can be degraded by the interactions of cyclic loading with the surrounding environment. The environment can be either chemical in nature such as NaCl or moisture, or it can be temperature. The general observation is that the environment can affect the fatigue characteristics either at near threshold regime or at higher growth rates. Commonly observed effects are that the cracks can accelerate, decelerate or even arrest depending on the nature and the degree of aggressiveness of the environment. Experimentally, these effects have been observed to be dependent on the load ratio and frequency. The degree of the environmental effects vary depending on the alloy microstructure, its strength and ductility. Specifically, such effects have been addressed with respect to a particular mechanism in a given environment [1,2].

One general experimental observation in fatigue crack growth is that the near threshold regimes can be markedly affected by the environment via the formation of corrosion debris or oxides. These in turn can retard or accelerate the crack growth rates depending on the aggressiveness of the environment. Retardation has been attributed to premature crack closure while acceleration to accentuated rupture of crack tip bonds by environmental interaction such as adsorption, absorption etc. For example, it is has been found that in the presence of an aggressive environment, the near threshold stress intensities decreased with increasing load ratio . This decreasing dependence on load ratio has been explained by the oxide or asperity induced closure by several investigators [1].

Recently, we have shown that the fatigue crack growth results (ΔK vs R) can be interpreted in terms of a *fundamental fatigue crack growth curve* : ΔK vs K_{max} [3-12]. We observe that ΔK and K_{max} gives a physically meaningful description of fatigue, than ΔK and R, since thare no such thing as a critical R below which there can be no crack growth. Such a ΔK-K_{max} curve has one important feature, in that, it gives two asymptotic values, ΔK^* & K^*_{max}, representing the two minimum values of ΔK and K_{max} at the threshold crack growth rates. Other critical values of ΔK and K_{max} can be obtained at higher crack growth rates. These are considered to be the two

independent crack tip driving forces that are necessary for a crack advance. This interpretation has an additional advantage, the method is independent of testing methods (hence the name fundamental fatigue curve). Thus, in its form, it reflects the *intrinsic behavior of fatigue*, requiring the two independent loading parameters to describe the cyclic deformation unambiguously. Their applicability has been shown clearly for various type of materials, ranging from monolithic to composites [3-10]. We have also shown that these two parameters ΔK & K_{max} are dependent on the microstructure, slip mode and environment [4,6,8,10,11,18].

The environmental effect on crack growth is manifested as a time dependent damage process that seems to have a marked impact on K_{max} relative to that on ΔK. K_{max} effect can be due to the slip initiation at lower stresses, or fracturing the crack tip oxide at a lower stress, etc. In general, the crack growth process can involve the role of plastic flow accomodation with slip to extend the crack tip. The overall crack growth will depend on the relative competition between the time dependent environmental effect with the rate of crack extension. Such environmental affects on fatigue characteristics depend on the test frequency and load ratio. The role of environment at higher growth rates, like in the Paris regime is usually small at moderate frequencies. However, as the frequency is decreased the effects can be pronounced at these higher growth rates. These topics are being analyzed and hence are not included in this article. The following brief discussion pertains to the role of environment that affects these two driving force parameters at ambient temperatures and at moderate frequencies. The discussions will focus on the relative role of slip character on the environmetal effect on fatigue. This would allow one to establish the basic role of ΔK & K_{max} parameters with microstructure in a given aqueous environment.

NEW INTERPRETATIONS OF FATIGUE CRACK GROWTH

The near threshold fatigue crack growth experimental results are conventionally plotted in terms of the variation in ΔK_{th} vs R. In general, most of the materials fatigue tested in an aqueous environment show a systematic linear reduction in ΔK_{th} with increase in R. Fig.1a shows such a result for a Ti-6Al -4V alloy for R varying between -2.0 to 0.9. On the

same plot K_{max} variation with R is also shown. The results indicate that ΔK_{th} decreased with R until R ~0.5 and then leveled off at R > 0.5. On the other hand, K_{max} was nearly independent of R till R = 0.5, then increased non-linearly with R.

In the new interpretation, we represent the raw fatigue data, from Fig.1a, in the form of a *fundamental fatigue crack growth curve*, ΔK_{th} vs K_{max} plots, as in Fig.1b. Such a curve then defines the two critical crack driving force parameters describing a *fatigue map* below which no fatigue cracks can grow. In the present case, for the Ti-6-4 alloy, the critical stress intensity values are: ΔK^*_{th} = 1.6 MPa$\sqrt{m}$ & K^*_{max} = 3.5 MPa$\sqrt{m}$, in lab air. For many materials with varying compositions, such a representation gives rise to two limiting values in ΔK_{th} and K_{max}, that are fundamental for the description of crack growth under fatigue damage, independent of testing methods.

The two stress intensity parameters , ΔK_{th} & K_{max}, depend strongly on the microstructure and environment [4]. The degree with which the effect has on these parameters depends on the slip mode of the material and the aggressiveness of the environment. In short, for a planar slip alloy, both ΔK_{th} & K_{max} can vary; while in a homogeneous/wavy slip material either ΔK_{th} or K_{max} can vary depending on the aggressiveness of the environment. To illustrate the first case, we look at an example from a 7075 aluminum alloy [4], tailor heat treated to give constant yield strengths in the underaged (UA: planar slip,YS = 456 MPa) and an overaged (OA: wavy slip, YS = 470 MPa). Such controlled microstructures in vacuum (in the absence of environment) causes a shift in both ΔK_{th} & K_{max} values significantly, as in Fig.2. Effect of environment is accentuated by the microstructure showing planar slip deformation than the homogeneous slip [4], although the yield strengths are nearly the same in both types of alloy microstructures.

In other alloys, depending on the environment, either ΔK_{th} or K_{max} can be affected. As an example, in a 304 stainless steel [14-16], going from somewhat an inert environment (such as low vacuum, silicon oil and liquid nitrogen) to a milder environment (such as argon & dry air), to a

relatively more aggressive one (such as moist air and NaCl) resulted in affecting the K_{max} more strongly relative to ΔK_{th}, as in Fig. 3. The aggressive environment seems to fall in between the inert and mild environment results, suggesting that there could be some crack tip interaction that affects the kinetics of crack growth process. Formation of a passive film at the crack tip, for example, can slow down the environmental interactions. The relative variations in K_{max} with different environment could be due to the relative ease to fracture the passive film thicknesses. Thinner films can be fractured at lower K_{max} than the thicker ones. Details of the mechanisms are not known.

In contrast to the behavior of 304 stainless steel, in rotor A542-3 type steels, the environment can affect the ΔK_{th} relatively more than the K_{max}, as shown in Fig. 4 [17]. The ΔK_{th} is relatively higher in the distilled water environment than in the moist air and H_2 & He environments. Also, in the moist air and H_2 & He, there are some deviations in ΔK_{th} - K_{max} curves which will be discussed in the later section. These examples, however, point out the main effects of environment on the microstructure through the mode of slip.

One can extend the two parametric description of fatigue crack growth to classify the overall fatigue crack growth data of different materials published in the literature. In the following discussion, we shall restrict ourselves to the near threshold fatigue crack growth phenomena. The basic concepts, however, are applicable to the fatigue behavior at all crack growth rates. We will also present most of the results in terms of ΔK_{th} vs K_{max} plots, since such plots outline clearly the important effects of environment. In order to analyze the fatigue data, we classify the entire fatigue behavior into several classes. This classification helps us recognize the individual fatigue mechanisms involved and makes it clear to recognize the role of environment on fatigue. We briefly describe the classifications in the following section; but for details reference can be made to the article [18].

CLASSIFICATION OF FATIGUE CRACK GROWTH

We have observed that most of the fatigue data on various alloy systems, tested in different environments, can be represented into *five* main classes. While the last, Class-V, belongs to polymeric systems, we will confine our discussions the first four main classes. This was conceived by hypothetically exploring the possibilities that can exist in terms of the ΔK vs R relationship, i.e. in terms of its slope and intercepts for all $R > 0$. The basic classification scheme is illustrated in Fig.5a, in terms of ΔK_{th} -R. Here Class-V is omitted.

To give reference to a commonly observed material behavior, labeled as a "normal" behavior, if the extrapolation of the linear portion of a ΔK_{th} vs R curve intersected the R-axis at $R = 1$ with $\Delta K_{th} = 0$. This class is designated as Class-III. When ΔK_{th} became independent of R for all $R > 0$, it is classified as Class-I behavior, with the slope of ΔK_{th} vs R tending to zero. If the ΔK_{th} intercept at $R = 1$ is greater than zero, it is termed Class-II. In Fig.5a, two different slopes are shown for Class-II (such as IIa, IIb). In the limit, Class-II converges to Class-I when the slope is zero and converges to Class-III when the intercept becomes zero. Class-IV (shown with two differing slopes IVa & IVb) corresponds to the type when the ΔK_{th} intercept at $R = 1$ is less than zero. Experimentally, the curves in Classes III and IV may level off before ΔK_{th} approaches zero. For the purpose of understanding, we extrapolate the curve to R=1 to give a basis for the classification scheme. Thus, as the degree of environmental effect increases, the slope of the ΔK_{th} vs R curve become steeper, moving from Class-I behavior (in an inert environment) towards a Class-IV that corresponds to aggressive environment(Fig.5a). Physics of the crack growth process can be influenced by the crack-tip environment of a material. For example, crack tip blunting process can affect K_{max} contributing to the slope of a ΔK_{th}-R curve, along with a positive intercept at R=1 contributes to the Class-II behavior. This factor becomes increasingly important with decreasing yield stress or increasing ductility. For example, Class-II behavior is exhibited by pure materials (low strength, high ductility) and some of the medium and high strength steels (with high ductility). Class-III behavior is common amongst aluminum alloys, in which ΔK_{th} and K_{max} are uniquely defined. Class-IV behavior is less common but has been observed in materials that show strong environmentally

controlled fatigue process such as in ceramic materials (popularly known in the ceramic community as static fatigue) and in materials that are susceptible to hydrogen-assisted crack growth (as in very high strength steels).

Fig.6a shows the decrease in ΔK_{th} with R, for rotor steels, with a plateau (with ΔK_{th} =3 MPa$\sqrt{m}$) occurring at R~0.5. When extrapolated to R =1, the linear portion of the curve intersects the R-axis at some R < 1(about R =0.8). Such a behavior falls under Class-IV, by definition [17,19]. The corresponding ΔK_{th} vs K_{max} plot (Fig.6b) shows two ΔK_{th} values for a given K_{max} less than K^*_{max} (shown by the arrow on the K_{max} axis). This non-uniqueness K_{max} is possibly related to the superposition of an additional environmentally induced mechanism superimposed during fatigue. One can speculate that the superimposed mechanisms are time dependent corrosion contributions. These processes can cause the fundamental threshold curves to develop a concave curvature, as shown in Fig 6b. While these deviations, with concave curvatures, are observed mostly at the threshold levels (or low growth rates where time is available for slow corrosion kinetic process can proceed); they, however, disappear at higher growth rates resulting in marked slope changes in the ΔK_{th} vs R curves transitioning the materials behavior to higher classes. This can be seen clearly in Fig.7a for one of the alloy discussed in Fig. 6b. Here, the classification moves from a Class-IV at the near threshold (da/dN=10^{-8} m/cycle) to Class-II at and above (da/dN) =10^{-6} m/cycle. Thus, the overall fatigue characteristics of the alloy, as described by the classification, depends on the relative kinetics of the fatigue crack growth vs the environmentally induced crack growth. Fig. 5 provides a list of possible fatigue and environmentally induced mechanisms that can affect the shape of the fundamental threshold curves. One can see that the Class-I, II & III materials are weakly dependent on the environment, while Class-IV materials are strongly dependent. Also Figs.1 & 3 show material behavior with classifications from Class-II, but slowly tending toward Class-III, where the behavior converges to a more perfect L-shape. On the other hand, Fig.4 illustrates the change in the behavior from Class-II to Class-IV behavior, as previously discussed with reference to Fig.7.

SUMMARY

We find that fatigue behavior involves two loading parameters that act as the two mechanical driving forces for cracks to advance. These two parameters have to be met *simultaneously* for crack growth to occur. These two parameters vary with microstructure and environment. We find that the overall fatigue behavior can be classified into *five* main groups that depends on the slip mode and environment. Examples from the literature are given to support the trends in the five classifications. Classification of materials behavior that distinguishes them into the different regimes becomes necessary for understanding (and for life prediction) the relative roles of mechanical and chemical crack tip driving forces. To achieve this, we recognize that systematic data acquisition at various R-ratios and over large variations in (da/dN) are necessary. Unfortunately, most available data in the literature are limited to a very narrow range of load ratios (mostly around R~0.1)and/or at intermediate crack growth rates. Conscientious efforts are needed to develop a systematic fatigue data base for the analysis. Most importantly, we have provided an alternate approach for the analysis of the fatigue behavior, classifying the relative roles of plasticity and environment that affect the fatigue crack growth. The above description provides the fundamental basis for an *intrinsic* fatigue deformation. The authors recognize the important aspect of frequency effects in corrosion fatigue which is omitted in the present article. This is being analyzed and to be published elsewhere.

REFERENCES

1. S. Suresh, Fatigue of Materials (Cambridge University Press), 1990.
2. R. P. Wei, Fracture Mechanics: Microstructure & Micro mechanisms, Eds. S. V. Nair et al. (ASM International, 1989), p.229.
3. A. K. Vasudevan, K. Sadananda & N. Louat, Scripta Metall. et Materialia, 27 (1992.)1673.
4. A. K. Vasudevan, K. Sadananda & N. Louat, Scripta Metall. et Materialia, 28 (1993) 65.
5. A. K. Vasudevan, K. Sadananda & N. Louat, Scripta Metall. et Materialia, 28 (1993) 837.

6. A. K. Vasudevan, K. Sadananda & N. Louat, FATIGUE '93, Eds. J. -P. Bailon & J. I. Dickson (EMAS Publn., 1993),vol.I, 565.
7. K. Sadananda, N. Louat & A. K. Vasudevan, FATIGUE '93, Eds. J. -P. Bailon & J. I. Dickson (EMAS Publn.,1993) vol.I, 571.
8 K. Sadananda & A. K. Vasudevan, Aspects of High Temperature Deformation & Fracture in Crystalline Materials, eds. Y. Hosoi et al.(JIM Publns.,1993), 551.
9. N. Louat, K. Sadananda, M. Duesbery & A. K. Vasudevan, Metall. Trans., vol. 24A (1993), 2225.
10. K. Sadananda & A. K. Vasudevan, ASTM STP-1220, 1995, 484.
11. A. K. Vasudevan, K. Sadananda & N. Louat, Matls. Sc. & Engg., vol. A188, (1994), 1.
13. R. A. Schmidt & P. C. Paris, ASTM STP-536, (1973), 79
14. S. Usami, Fatigue Thresholds, Proc. of the Ist Int. Conf. on Fatigue, Stockholm, Eds. J. Blacklund et al.(EMAS Publn., 1981), 203.
15. S. Usami, Y. Fukuda & S. Shida, Proc. of 4th Natl. Cong. on Pressure Vessel Tech., (ASME, 1983), 1.
16. S. Stanzl & E. Tschegg, Acta. Metall., vol.29 (1981), 21.
17. S. Suresh, G. F. Zaminski & R. O. Ritchie, Metall Trans., vol. 12A (1981), 1435.
18. A. K. Vasudevan & K. Sadananda, Metall. Trans., vol. 26A, (1995), 1221.
19. J. Denk, O. E. Lepik & G Ebi, Fatigue '93, Eds. J.-P. Bailon & J. I. Dickson, (EMAS Publns.,1993), vol.3, 1797.

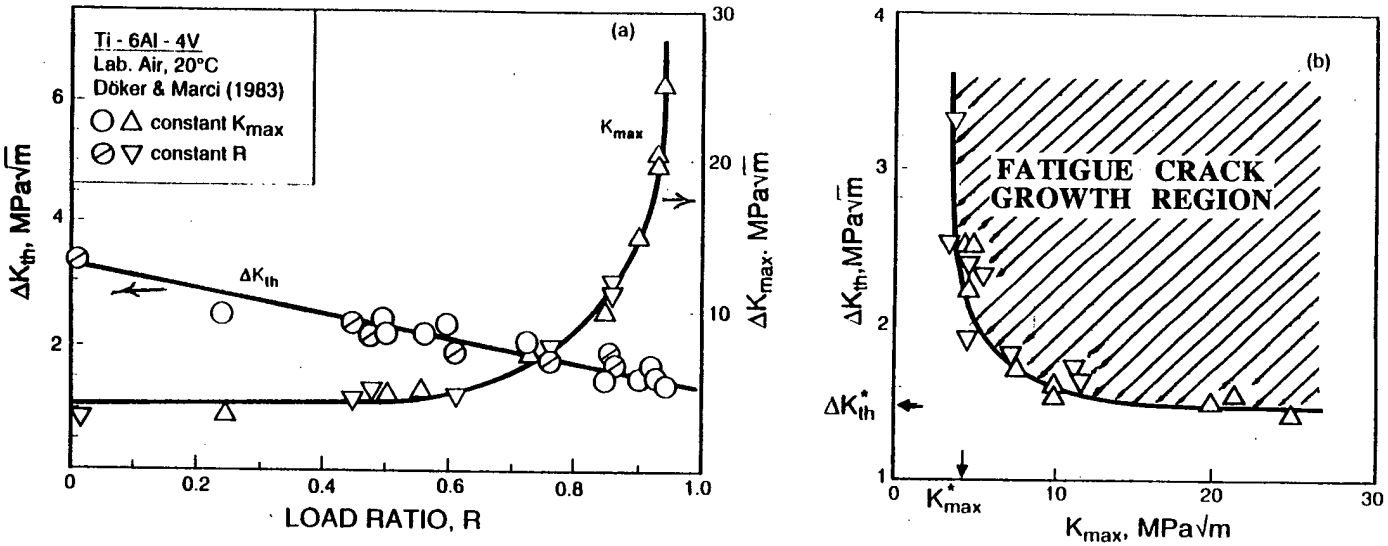


FIGURE 1. Near threshold fatigue crack growth data of Ti-6V-4Al alloy in lab air is presented : (a) variation in ΔK_{th} and K_{max} with load ratio R, and (b) a replot of (a) in terms of ΔK_{th} vs K_{max}, as a fatigue map

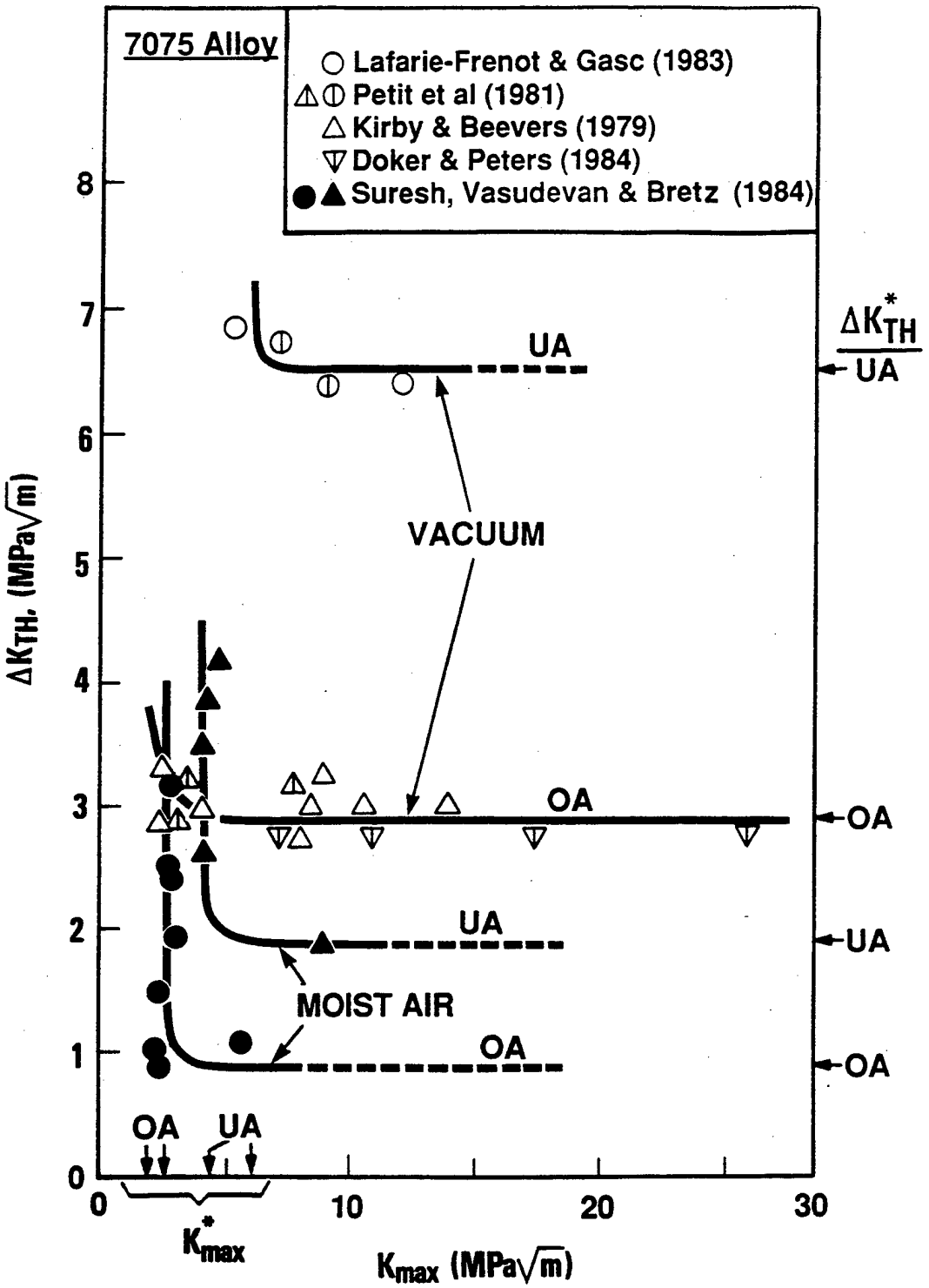


FIGURE 2. Fatigue crack growth map for a 7075 aluminum alloy with constant yield strength microstructures, in vacuum and in moist air environments.

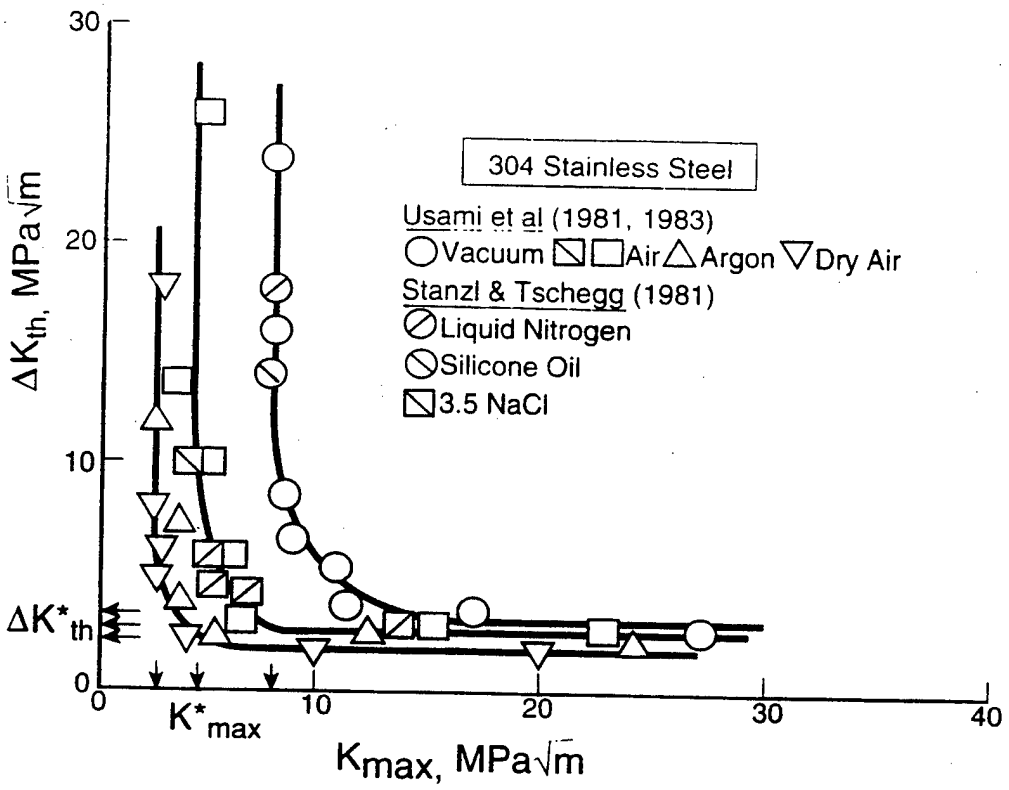


FIGURE 3. Fatigue crack growth map for a 304 stainless steel under various environments.

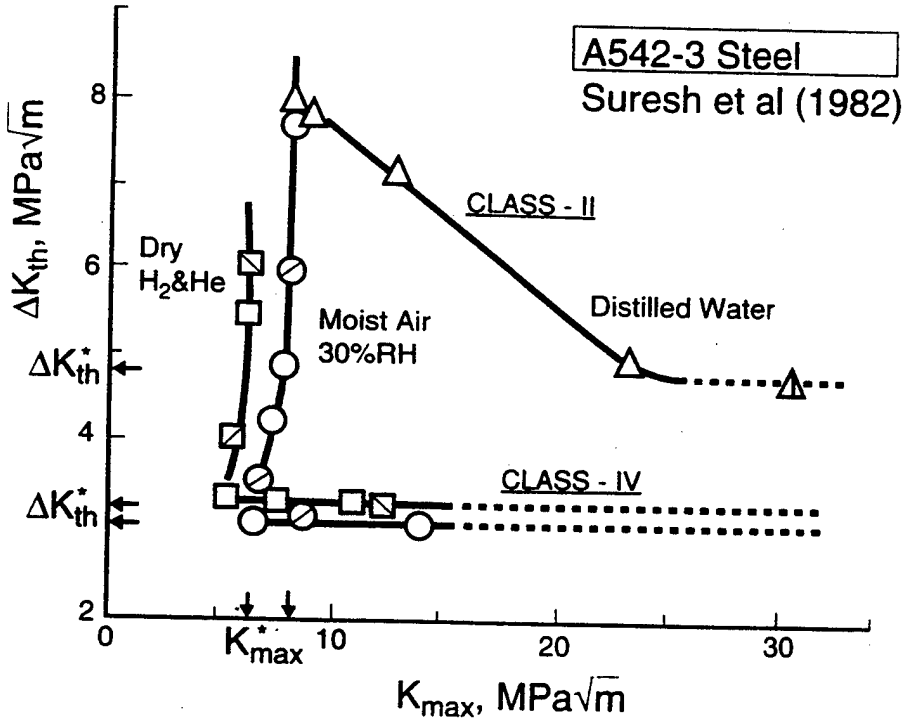


FIGURE 4. Fatigue crack growth map for a A542-3 steel in various environments.

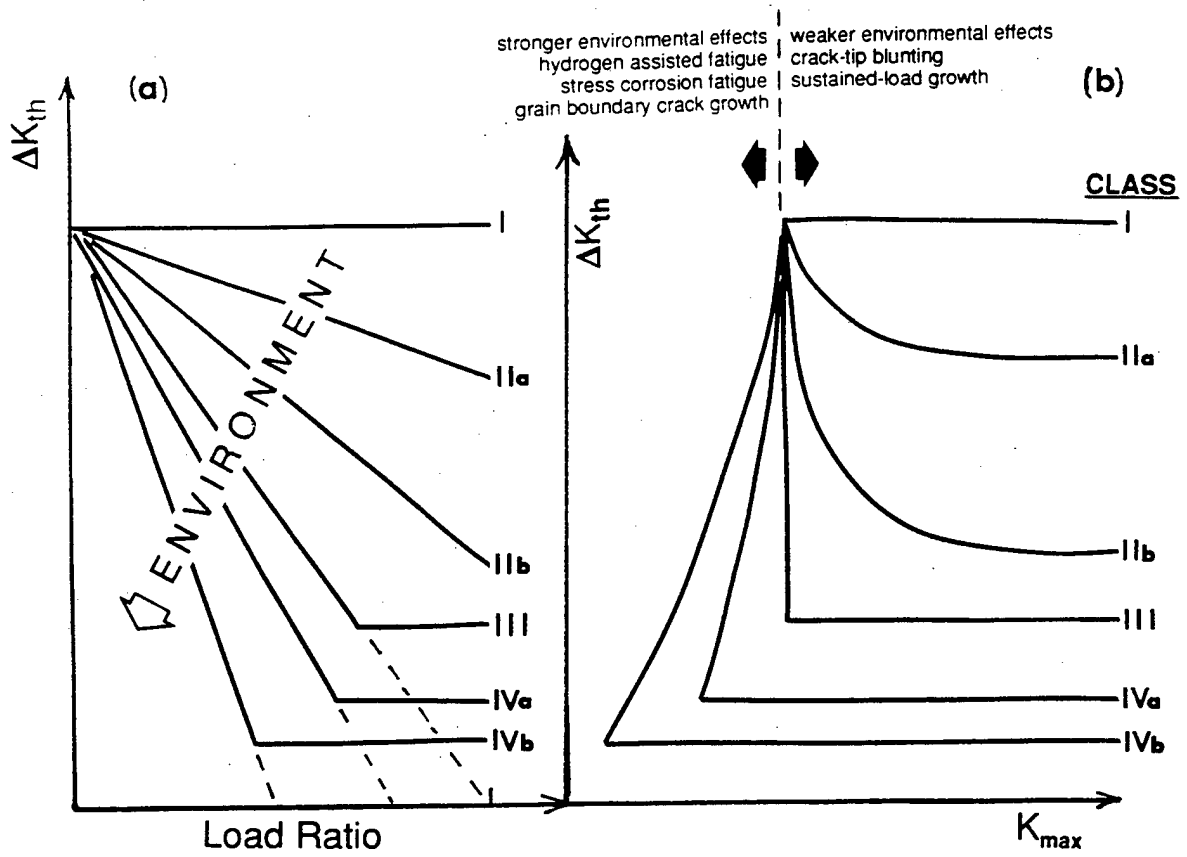


FIGURE 5. Schematic illustration of the overall fatigue mechanisms represented to show the four major classifications in terms of (a) ΔK_{th} vs R, and (b) ΔK_{th} vs K_{max}; along with the regions affected by the environment.

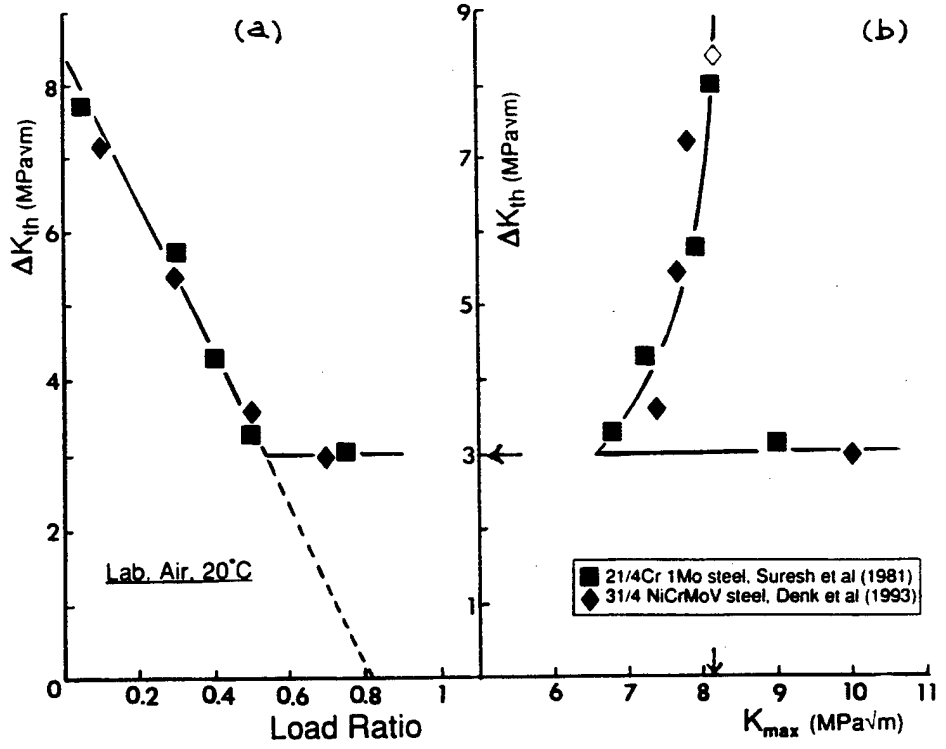


FIGURE 6. Example of a Class-IV behavior in steels shown in terms of (a) ΔK_{th} vs R, and (b) ΔK_{th} vs K_{max}.

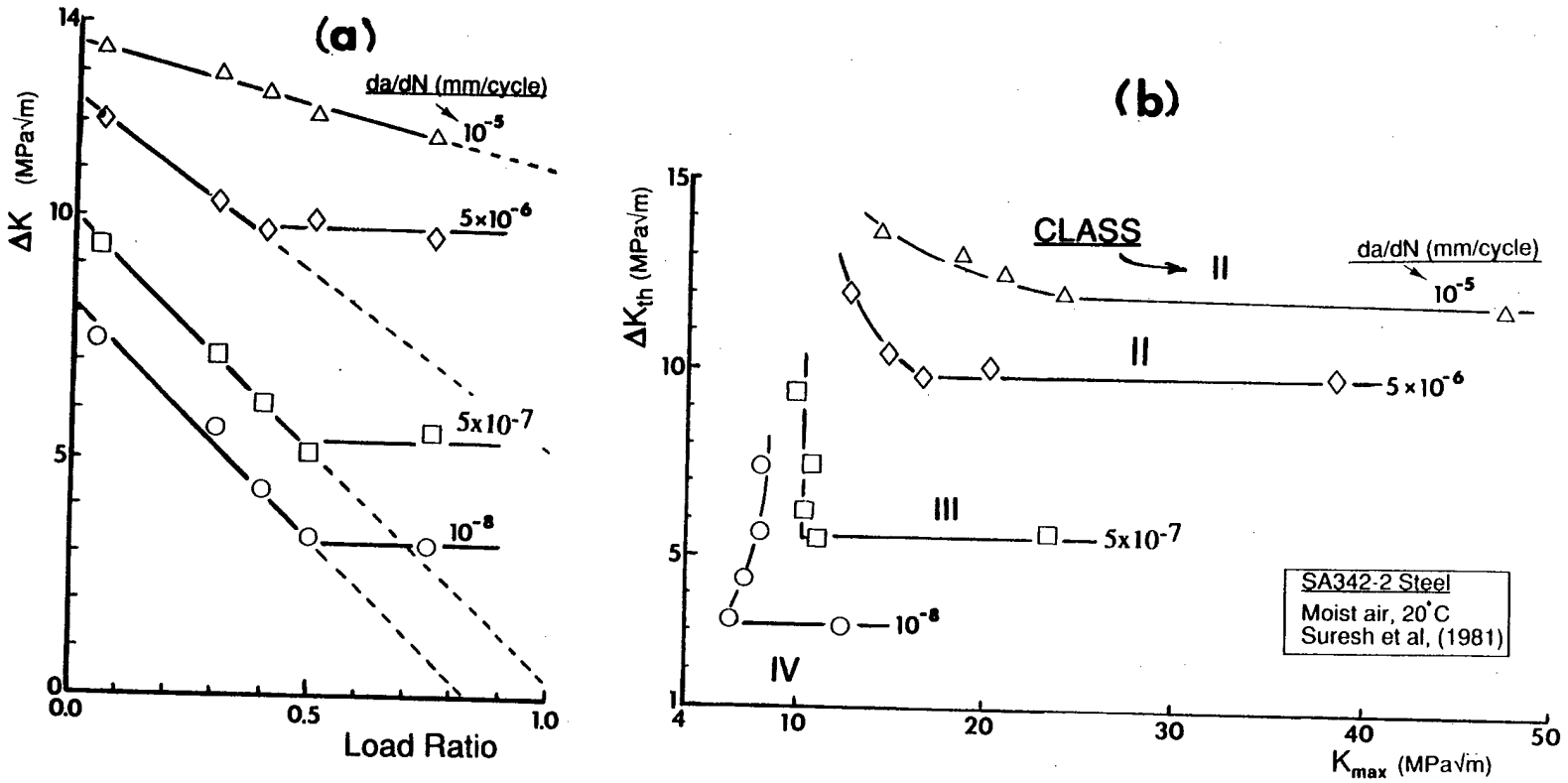


FIGURE 7.-Class-IV steel data, from FIG.6, extended to higher crack growth rates indicating the transitions from Class-IV to III to II.

High Strength Fasteners for Seawater Immersion Service

D.M. Aylor, C.A. Bowles, and R.L. Tregoning

Naval Surface Warfare Center, Carderock Division
9500 MacArthur Blvd.
West Bethesda, MD 20817-5000

ABSTRACT

Alloy K-500 is the currently used high strength alloy for Navy fastener applications in immersion service. Alloy K-500 has performed well as a fastener material in seawater but is susceptible to hydrogen cracking in areas of intense cathodic polarization and is galvanically incompatible with titanium and Alloy 625 components. Due to these inadequacies, it is necessary to identify alternate fastener materials that can suitably replace Alloy K-500. Numerous alloys that meet the minimum yield strength requirements of Alloy K-500 (90 ksi) have been considered. These include titanium-base, nickel-base, and stainless steel alloys. Data and guidelines on corrosion behavior, mechanical properties, fatigue behavior and other relevant material properties are currently being assembled into a high strength fastener handbook for 14 alloys. The technical information in the handbook will include data generated from in-house Navy programs as well as data reported in the literature by government and industry sources. Information included in the fastener handbook will be presented here, with particular emphasis on the applicability of specific alloys based on seawater corrosion behavior.

INTRODUCTION

In addition to meeting strength, ductility, and other mechanical property requirements, high strength fastener materials must provide adequate resistance to corrosion in the service environment of interest. High strength fasteners used on naval vessels are exposed to a variety of marine environments, including full immersion in seawater, intermittent seawater spray/marine atmosphere in topside areas, and alternate wetting in areas such as bilges. When assessing the corrosion resistance of a material, all applicable forms of corrosion must be considered. For naval fasteners, the forms of corrosion of concern include general, localized, and galvanic corrosion, along with environmentally assisted cracking (EAC), which includes hydrogen embrittlement (HE) and stress corrosion cracking (SCC). Sustained load cracking (SLC) resistance is also considered.

Corrosion data from laboratory and field tests performed on 14 alloys in simulated and natural seawater environments will be reviewed. The corrosion resistance of Alloy 725, Alloy 925, UNS N07716, Alloy 718, Rene 41, MP35N, Ti-6Al-4V (ELI), Ti 38-6-44, Ti 51111, Ti 16-2.5-3, Alloy A286, and 17-4 PH will be assessed relative to Alloy K-500, which is considered to be the baseline material for naval fasteners immersed in seawater.

Table 1 presents the nominal composition, recommended heat treatment, specification, and mechanical properties for each of the high strength fastener alloys. The recommended material condition for each alloy was defined based on the minimum strength requirements of Alloy K-500.

CORROSION PROPERTIES

Localized Corrosion Resistance

A summary of the maximum calculated pitting and crevice rates for the fastener alloys is provided in Table 2.

The nickel-base and stainless fastener alloys including Alloy K-500, Alloy 725, Alloy 925, UNS N07716, Alloy 718, Alloy A286, and 17-4 PH are susceptible to localized corrosion in quiescent and low velocity seawater conditions where adequate aeration is not available to maintain the passive surface film. Crevices formed by deposits such as barnacles or in fastener threads can promote initiation of localized corrosion. Components should be designed to minimize areas where seawater can collect, and a water-displacing lubricant or sealant should be applied to the fastener threads. Cathodic protection appears to be an effective method for minimizing localized corrosion of passive film forming alloys. An ongoing corrosion test of Alloy A286 bolts threaded into a titanium plate and immersed in quiescent, natural seawater is showing cathodic protection (zinc or iron anodes) to be effective in preventing localized corrosion of Alloy A286 within the tight crevices formed at the fastener thread-plate interfaces after six months.

Both Rene 41 and MP35N are highly resistant to localized corrosion in quiescent and low velocity seawater. Ti-6Al-4V (ELI) and Ti 38-6-44 are also highly resistant to localized corrosion in low and high velocity seawater as well as marine atmospheric, splash/spray, and tidal environments at ambient temperature. No localized corrosion information was found for Ti 51111 or Ti 16-2.5-3 alloys in ambient temperature seawater. These titanium alloys would be expected to have good localized corrosion resistance in this environment, since titanium alloys generally exhibit localized attack only within tight crevices while immersed in hot (>160°F) chloride solutions (14).

The crevice corrosion resistance of Alloy K-500, Alloy 725, Alloy 925, UNS N07716, Alloy 718, Alloy A286, and 17-4 PH is considered to be unacceptable for fasteners exposed to the marine environments of interest unless adequately protected. Rene 41, MP35N, Ti-6Al-4V (ELI), and Ti 38-6-44 are immune to both crevice corrosion and pitting in marine environments and are acceptable fastener candidates, based on localized corrosion resistance. Ti 51111 and Ti 16-2.5-3 alloys are also expected to be suitable fastener alloys in terms of localized corrosion resistance.

Galvanic Compatibility

The relative compatibility of the fastener alloys under consideration is summarized in Table 3.

Nickel-Base Alloys—Alloy K-500 was found to be galvanically incompatible with Alloy 625, and the extent of galvanic corrosion of Alloy K-500 increased substantially as the relative surface area of Alloy 625 was increased. Testing of K-500 coupled to Ti 6211 also showed K-500 to be galvanically incompatible with the Ti alloy, as evidenced by increased general corrosion and crevice corrosion rates of K-500. The extent of corrosion of K-500 became more severe as the surface area ratio of Ti 6211:K-500 was increased. Galvanic corrosion testing has shown Alloy 725 to be highly compatible with Alloy 625, with Alloy 725 cathodic to Alloy 625. It is recommended that Alloy 925:Alloy 625 couples only be utilized with corrosion control. Although the two alloys are galvanically compatible, severe localized corrosion of Alloy 925 will occur unless adequate protection is provided. The galvanic compatibility of UNS N07716 with Alloy 625 is considered marginal. In galvanic corrosion testing, the UNS N07716 was found to fluctuate from anodic to cathodic polarization with respect to Alloy 625 during the six month test period. Galvanic couple testing of Alloy 718 with various aluminum alloys showed marginal compatibility. The aluminum alloys exhibited slight to moderate corrosion. Alloy 718 compatibility with the aluminum alloys was judged to be better than that of Alloy A286 but less than that of Ti-6Al-4V with the same group of aluminum alloys. It is not recommended that Alloy 718 be used with Alloy 625 without corrosion control. Although the corrosion potentials of these alloys are similar and thus have good galvanic compatibility, severe localized corrosion of Alloy 718 will occur unless adequate protection is provided. MP35N has poor galvanic compatibility with Alloy K-500, 316 stainless, carbon steel, 7075-T6 Al, and 5456 Al. Coupling MP35N with these alloys causes their corrosion rates to be increased. 17-4 PH and MP35N are more galvanically compatible, but the 17-4 PH is susceptible to severe localized corrosion without protection. MP35N is galvanically compatible with both HY-130 and Ti-6Al-4V.

Titanium-Base Alloys—Galvanic corrosion testing of Ti-6Al-4V (ELI) with various materials including Alloy 625, titanium alloys, steel, iron, zinc, and fiberglass showed good galvanic corrosion resistance in all cases. The galvanic compatibility of Ti-6Al-4V with aluminum alloys was judged marginal to poor due to mild to severe corrosion of the aluminum alloys. Ti-6Al-4V coupled to Alloy A286 and to 17-4 PH has shown severe crevice corrosion of both of the stainless alloys. Ti 38-6-44 was found to be galvanically compatible with Alloy 625. No galvanic corrosion data were found for Ti 51111 or Ti 16-2.5-3, but it would be expected that these alloys would have similar compatibility as was found for Ti-6Al-4V (ELI).

Stainless Alloys—The galvanic compatibility of Alloy A286 with aluminum alloys was considered marginal due to moderate corrosion present on some of the aluminum alloy samples; overall, Alloy A286 was less compatible with aluminum alloys than either Alloy 718 or Ti 6Al-4V. Coupling Alloy A286 with either 17-4 PH or with Ti-6Al-4V is not recommended. The Alloy A286:17-4 PH couple resulted in minimal galvanic corrosion but severe localized corrosion of the 17-4 PH. The Alloy A286:Ti-6Al-4V coupling resulted in intense crevice corrosion and pitting observed on the Alloy A286 fasteners, which may have been enhanced by

anodic polarization resulting from galvanic coupling to Ti-6Al-4V. The Alloy A286: HY-130 couple exhibited good galvanic compatibility, with general corrosion only present on the HY-130 panels. Alloy 17-4 PH is not recommended for use with 2024-T4 Al, anodized steel, 304 stainless, or Ti 6211 based on galvanic corrosion data.

Methods to Control Galvanic Corrosion

Galvanic corrosion of fasteners exposed to marine environments can be minimized by following several general guidelines. First, when selecting a fastener alloy to join a dissimilar metal or alloy, the alloy selected for the fastener should be more noble (more cathodic) than the joint material(s). Use of a fastener that is cathodic to the joint material avoids unfavorable surface area ratios and minimizes galvanic corrosion of the fastener. The galvanic series in seawater (14) is useful for selecting a fastener material that is cathodic to the component material of interest. In some cases where fastener materials more anodic than the joint material have been used, external sources of cathodic protection such as anodes or impressed current have been relied upon to protect the fasteners from corrosion. It should be noted that electrical continuity is necessary to ensure cathodic protection of the fastener; the presence of dielectric films or coatings on the fastener or joint material may result in electrical isolation of the fastener. It is for this reason that fastener materials should also have inherently good general and localized corrosion resistance.

Second, fastener materials should be selected based on demonstrated galvanic compatibility with the joint material. As previously discussed, the galvanic series can be used to determine the anodic and cathodic member of the galvanic couple but has been shown to be a poor indicator of the extent or rate of corrosion (17). Galvanic corrosion has been observed on alloys with as little as 100 mV difference in potential. Experimental data, such as galvanic current measurements or weight loss measurements, are needed to accurately predict galvanic corrosion rates.

Third, to further minimize galvanic corrosion, the dissimilar metals may be electrically isolated. Nonmetallic sleeves and washers can be used in through-hole fastening systems to isolate the fastener from the joint material. A dielectric lubricant or antiseize may be applied to the fastener to isolate it from a joint material or nut, but complete coverage of the lubricant on the fastener is difficult to assure, especially when high installation torques are applied. Even dry film lubricants can be difficult to maintain on fastener threads subjected to repeated "make/break" cycles. Experimental evaluation of such products as galvanic insulators should be performed prior to their use in the field.

Environmentally Assisted Cracking (EAC) and Sustained Load Cracking (SLC) Resistance

The susceptibility of the high strength fastener alloys under consideration to EAC and SLC is summarized in Table 4.

Nickel-base Alloys—The susceptibility of Alloy K-500 to HE has been well-documented in the literature. The susceptibility threshold lies between -620 and -800 $mV_{Ag/AgCl}$. Based on the

limited data available for Alloy 725, UNS N07716, and Alloy 718 in the solution treated and dual aged condition, these Ni-Cr-Mo alloys offer little improvement over K-500. Rene 41, in the solution treated and aged condition, has shown a slight improvement in HE resistance over Alloy K-500. The slow strain rate test data for Rene 41 indicate resistance to HE at -850 mV_{SCE} and susceptibility at -1000 mV_{SCE}. Slow strain rate testing of Alloy 925 showed a HE susceptibility at -1250 mV_{SCE} and a ductile intergranular fracture mode in air, freely corroding, -850 mV, and -1000 mV_{SCE} environments. This intergranular fracture mode is indicative of a reduced load bearing capacity for this alloy, but the extent of the load reduction in service is not known. MP35N was the only nickel-base alloy with HE and SCC resistance. The HE and SCC data, however, are based on very limited testing.

SLC has not been detected in properly processed Alloy K-500 subjected to ambient temperatures. No data were available on the remaining nickel-base alloys; however, they are expected to exhibit a SLC resistance similar to K-500.

Titanium-base Alloys—Ti 38-6-44 has been shown to have good resistance to EAC in seawater in the solution annealed condition, which is the condition of interest for naval fastener applications. Ti 51111 (α-β forged) and Ti 16-2.5-3 (solution treated and overaged) also demonstrated good EAC resistance in chloride conditions. Annealed Ti-6Al-4V has been shown to have variable resistance to EAC, dependent on the composition and microstructure of the material, as well as the configuration and size of the specimen. The ELI grade, with less than 1200 ppm oxygen, has slightly improved resistance over higher-oxygen content specimens.

Testing of Ti-6Al-4V plate has shown this alloy to be susceptible to SLC under certain conditions. Some researchers have found interstitial content to play a key role in determining SLC susceptibility, while others have found no dependence of SLC on composition or processing. Texture has been found to markedly affect SLC of Ti-6Al-4V plate. Based on data obtained from plate, it can be said that Ti-6Al-4V bar stock may show degradation in fracture resistance under sustained loading conditions; relative degradation due to SLC may be assumed to be similar to that observed in plate. SLC testing of bar material in the condition of interest is needed to confirm these assumptions. Lack of sufficient data on SLC of Ti 38-6-44, Ti 51111, and Ti 16-2.5-3 also make predictions of SLC resistance equally difficult.

Stainless Alloys—Alloy A286 has shown good EAC resistance based on laboratory slow strain rate testing. A286 specimens were evaluated in both freely corroding seawater and in cathodically polarized conditions, where the potential was varied from -850 to -1250 mV_{SCE}. 17-4 PH is susceptible to EAC; however, the EAC resistance of this alloy significantly increases as the tempering temperature increases from 900 to 1100°F. At higher tempering temperatures (1050°F), limited data (61) suggest that a -600 to -1300 mV_{SCE} potential is required for protection of this alloy from the effects of EAC and localized corrosion. No information was found in the literature regarding the SLC resistance of Alloy A286 or 17-4 PH.

DISCUSSION

In addition to corrosion properties for these high strength fastener alloys, other properties must be considered. Issues specific to the successful use of a particular alloy will be briefly discussed. The high strength properties of MP35N are achieved by cold working this material. This, however, limits the finished fastener sizes that are capable of being produced. The size limitations result from the manufacturer's inability to cold work large diameter material or the inability to retain the cold work during hot forging of the bolt heads and nuts (62).

For all of the titanium alloys, room temperature creep and galling are of concern. Room temperature creep can occur at applied stresses ranging from 60% σ_{ys} up to the alloy's proportional limit. Limited data have suggested that a double fastener tightening procedure may be effective in preventing room temperature creep (63, unpublished data). Effective use of titanium alloys as fasteners will require anti-galling surface treatments, and specific treatments should be evaluated in the service environment to assess any adverse corrosion behavior due to the application of these products.

SUMMARY AND CONCLUSIONS

When assessing the corrosion resistance of an alloy, one must consider all forms of corrosion applicable to the end item and its expected service environment. In this paper, the localized and galvanic corrosion and environmentally assisted cracking susceptibilities of 14 fastener alloys have been evaluated for applicability as a fastener alloy in seawater. Obviously, when selecting an alloy for a high-strength fastener application, corrosion resistance is only one consideration; other material properties, such as mechanical and physical properties must also be considered.

Based solely on corrosion resistance, the data reviewed in this paper indicate that MP35N, Alloy A286, Ti-6Al-4V, Ti 38-6-44, Ti 51111, and Ti 16-2.5-3 are the most promising candidates for high strength fastener applications. MP35N has excellent localized corrosion and EAC resistance. While MP35N is resistant to galvanic attack when coupled with more anodic materials, attack of the more anodic material may be a problem. MP35N is galvanically compatible with HY-130 and Ti-6Al-4V, but may require a corrosion control method such as electrical isolation if used with Alloy K-500, steel, stainless steel, or aluminum alloys. For these galvanic couples, however, a small cathode (MP35N fastener) to large anode (joint material) area ratio will lessen the extent of corrosion occurring. Since the high strength of the MP35N alloy is achieved through cold working, there are size limitations for producing MP35N fasteners. This is due to the inability of a) cold working large diameter material or b) retaining the cold work during hot forging of the bolt heads and nuts. Alloy A286 is also recommended for high strength fastener use due to its excellent EAC resistance. This alloy is susceptible to localized corrosion, though, and would require cathodic protection for effective application in seawater.

Ti-6Al-4V and Ti 38-6-44 are essentially immune to localized corrosion, and Ti-6Al-4V is galvanically compatible with Alloy 625, other titanium alloys, steel, iron, zinc, and fiberglass.

Coupling Ti-6Al-4V with aluminum alloys may necessitate the use of a corrosion control method to prevent corrosion of the aluminum. Use of Alloy A286 or 17-4 PH with Ti-6Al-4V would require cathodic protection to prevent crevice corrosion of the stainless alloys. Ti 38-6-44 has shown good galvanic compatibility with Alloy 625. No other galvanic corrosion data were found for Ti 38-6-44, although this material should have a galvanic corrosion resistance similar to Ti-6Al-4V. Ti 38-6-44 in the solution annealed condition is resistant to hydrogen embrittlement and stress corrosion cracking. The resistance of Ti-6Al-4V to stress corrosion cracking has been found to vary, depending on the composition and processing of the material as well as the size and configuration of the specimen or end item. The low-oxygen ELI grade of Ti-6Al-4V has been found to generally improve the alloy's resistance to stress corrosion cracking. Ti-6Al-4V has also exhibited a susceptibility to SLC based on plate data only. Both Ti 51111 and Ti-16-2.5-3 have good EAC resistance in seawater environments. No seawater localized corrosion or galvanic compatibility data were found in the literature for these alloys, but they would be expected to have corrosion properties similar to Ti-6Al-4V.

Other concerns with effectively using titanium alloys as fastener materials include room temperature creep and galling. High strength titanium alloys are susceptible to room temperature creep at applied stresses varying from 60% σ_{ys} up to the alloy's proportional limit. A double fastener tightening procedure may be effective in eliminating room temperature creep in fastened joints. Anti-galling surface treatments are available for titanium alloys, but specific treatments should first be evaluated in the service environment that the fastener will be used since the use of such products can affect the corrosion behavior of the system.

REFERENCES

1. Niederberger, R.B., R.J. Ferrara, and F.A. Plummer, "Corrosion of Nickel Alloys in quiet and Low Velocity Sea Water," *Materials Protection and Performance*, Vol. 9, No. 8, 1970, pp. 18-22.

2. Lennox, T.J., Jr., M.H. Peterson, and C.W. Billow, "Corrosion Resistance and Response to Cathodic Protection of Advanced Alloys in Seawater," *Materials Performance*, June 1983, pp. 49-55.

3. Caplan, I.L. and H.P. Hack, "The Galvanic Effects of Titanium Coupled to Various Marine Alloys in Seawater", DTNSRDC/SME-80/54, Oct. 1980.

4. Kain, R.M., "Galvanic/Crevice Corrosion Resistance of Directly Coupled Incoloy alloy 925 and Inconel alloy 625 in Seawater: 6-Month Status Report," LaQue Center for Corrosion Technology, Inc. report for Inco Alloys International, Inc., September 1995.

5. Kain, R.M., "Galvanic Corrosion Testing of Inconel alloy 625 and Incoloy alloy 925 in Ambient Temperature Seawater," LaQue Center for Corrosion Technology, Inc. report for Inco Alloys International, Inc., January 1995.

6. Hack, H.P., "Mechanical, Corrosion, and Fatigue Properties of 15-5 PH, Inconel 718, and Rene 41 Weldments," NSRDC, Report 4528, May 1975.

7. Taylor, E., "Corrosion Resistance of Multiphase Alloys," *Materials Protection*, Vol. 9, No. 3, March 1970, p. 29-31.

8. Multiphase MP35N Alloy Technical Data, Latrobe Steel Company, 1994 revision.

9. Teel, R.B., "Performance of MP35N Ni-Co-Cr-Mo Wire Strand and Wire Rope in Marine Environments, " International Nickel Company Internal Report - Reference Nos. FLL2150.1, HIP 44544 and 4544A, December 27, 1972.

10. Hasson, D.F. and C.R. Crowe, "Titanium for Offshore Oil Drilling," *Titanium for Energy and Industrial Applications*, D. Eylor, Editor, AIME, 1981, pp. 65-82.

11. Uhlig, H.H. and A.I. Asphahani, "Corrosion Behavior of Cobalt Base Alloys in Aqueous Media," *Materials Performance*, Vol. 18, No. 11, November 1979, pp. 9-20.

12. Thomas, D.E., "Analysis of Cathodically Protected Ti-6Al-4V," R&D Tech Brief 87-3, RMI, February 1987.

13. Hack, H.P., "Seawater Corrosion of Fasteners in Various Structural Materials," DTNSRDC Report #76-0034, April 1976.

14. *Metals Handbook Vol. 13, Corrosion,* ASM International, Metals Park, Ohio, 1987.

15. Hibner, E.L. and R.H. Moeller, "Corrosion-Resistant Alloys UNS N09925 and N07725 for Oilfield Applications," OTC 7206, presented at the 25th Annual Offshore Technology Conference, Houston, TX, May 1993.

16. Thomas, E.D., E.A. Hogan, and K.E. Lucas, "Fasteners in Marine Service," Offshore Technology Conference, OTC 6585, 1991.

17. Mansfeld, F., D.H. Hengstenberg, and J.V. Kenkel, " Galvanic Corrosion of Al Alloys; I. Effect of Dissimilar Metals," *Corrosion*, Vol. 30, No. 10, Oct. 1974, pp.343-353.

18. Private communication with R.M. Kain of LaQue Center for Corrosion Technology, Wrightsville Beach, NC, 4 June 1996.

19. Taylor, E., "Galvanic Compatibility of Coated and Bare MP35N Bolts with 6Al-4V Ti, 7075-T6 Al and Cadmium Plated Steel Structures," SPS Steel Structures," SPS Report No. 5302 Revised, September 15, 1971.

20. "SRB Materials and Processes Assessment from Laboratory and Ocean Environmental Tests," NASA TM-78187, George C. Marshall Space Flight Center, Alabama, June 1978.

21. Hibner, E.L., "A New Age-Hardenable Corrosion Resistant Alloy for Deep Sour Gas Well Service," NACE Corrosion '90, Paper #50, 1990.

22. Thompson, S.D., B.L. White, and J.A. Snide, "Accelerated Corrosion Testing of Graphite/Epoxy Composites and Aluminum Alloy Mechanically Fastened Joints," AFWAL-TR-84-3115, June 1985.

23. Taylor, E., "Fastener Corrosion in Hydrospace," NACE Corrosion '74, Paper #79, Houston, TX, March 1974.

24. Joosten, M.W. and L.H. Wolfe, "Failures of Nickel-Copper Bolts in Subsea Applications," Offshore Technology Conference, OTC 5553, Houston, TX, April 1987.

25. Efird, K.D., "Failure of Monel Ni-Cu-Al Alloy K-500 Bolts in Seawater," *Materials Performance*, Vol. 24, No. 4, April 1985, pp. 37-40.

26. Harris, J.A., R.C. Scarberry, and C.D. Stephens, "Effects of Hydrogen on the Engineering Properties of MONEL Nickel-Copper Alloy K-500," *Corrosion*, Vol. 28, No. 2, February 1972, pp. 57-62.

27. Harris, J.A. and E.F. Clatworthy, "Hydrogen Embrittlement of Incoloy alloy 925, Monel alloy K-500, and Inconel alloy 625 by Slow Strain Rate Method," NACE Corrosion '86, Paper #150, Houston, TX, March 1986.

28. Aylor, D.M. "High Strength Alloys for Seawater Fastener Applications," Proceedings of the Tri-Service Corrosion Conference, Orlando, Florida, June 1994.

29. Aylor, D.M., "An Environmental Cracking Evaluation of Fastener Materials for Seawater Applications," NACE Corrosion '94, Paper #484, 1994.

30. Tregoning, R.L., D.M. Aylor, and I.L. Caplan, "High Strength Titanium Alloys for Naval Fastener Applications," Proceedings of the 8th World Conference on Titanium, Birmingham, England, October 1995.

31. Vassilaros, M. J., et al., "Environmental Slow Strain Rate J-Integral Testing of K-500," ASTM STP 1210, *Slow Strain Rate Testing for the Evaluation of Environmentally Induced Cracking*, 1993, pp. 123-133.

32. Wolfe, L.H., C.C. Burnette, and M.W. Joosten, "Hydrogen Embrittlement of Cathodically Protected Subsea Bolting Alloys," *Materials Performance*, Vol. 32, No. 7, July 1993.

33. Montano, J.W., "A Mechanical Property and Stress Corrosion Evaluation of MP35N Multiphase Alloy," NASA TM X-64591, Marshall Space Flight Center, Alabama, May 1971.

34. Taylor, E., "Multiphase Alloy Environmental Resistance," Standard Pressed Steel, Report No. 5817, Jenkintown, June 1976.

35. Yoder, G.R., C.A. Griffis, T.W. Crooker, "The Cracking of Ti-6Al-4V Alloys Under Sustained Load in Ambient Air," *Journal of Engineering Science and Mechanics*, Trans. ASME, October 1974, pp. 268-274.

36. Pound, B., "Evaluation of a Diffusion/Trapping Model for Hydrogen Ingress in High-Strength Alloys," Final Report, SRI International, October 1993.

37. Venkataraman, G. and A.D. Goolsby, "Hydrogen Embrittlement in Titanium Alloys from Cathodic Polarization in Offshore Environments and Its Mitigation," NACE Corrosion '96, Paper #554, 1996.

38. Schliecher, H. and U. Zwicker, "The Effects of Hydrogen in Titanium Alloys," *Z. Metalkund*, Vol. 47, No. 8, 1956, p. 570.

39. Brown, B.F., "Stress Corrosion Cracking Control Measures: 5. Titanium Alloys," American University Chemistry Department, report submitted to the Office of Naval Research, 1975.

40. Judy, R.W., Jr., and R.J. Goode, "Stress Corrosion Cracking Characteristics of Alloys of Titanium in Salt Water," NRL Report #6564, July 21, 1967.

41. Wald, G.G., "Effect of Heat Treatment on Salt Water Delayed Fracture of Titanium Alloys", presented at the 96th AIME Annual Meeting, Los Angeles, CA, 1967.

42. Beacham, D.C. and Meyn, D.A., "The Effect of Thickness Upon Sustained Load Crack Propagation Characteristics of Titanium Alloys," NRL Report 7449, August 8, 1972.

43. Hack, H.P., "Corrosion Considerations for the Use of Ti-6Al-4V in a Window Clamping System at the National Aquarium in Baltimore," report prepared for the National Aquarium.

44. Gerberich, W.W., et al., "Final Report on Evaluation of Selected Titanium Alloys as a Function of Environment and Heat Treatment," Aerojet-General Corporation Report for Annapolis Division, NSRDC, August 1987.

45. Puzak, P.P., et al., "Metallurgical Characteristics of High Strength Structural Materials: Eleventh Quarterly Report," NRL Report #6513, August 1966.

46. Link, F. and D. Munz, "The Initiation of Stress Corrosion Cracking in Ti-6Al-4V Alloy," *Corrosion Science*, Vol. 13, 1973, pp. 809-811.

47. Meyn, D.A., "Effect of Hydrogen on Fracture and Inert-Environment Sustained Load Cracking Resistance of α-β Ti Alloys," *Metallurgical Transactions*, Vol. 5, Nov. 1974, pp. 2405-2414.

48. Boyer, R.R. and W.F. Spurr, "Characteristics of Sustained-Load Cracking and Hydrogen Effects in Ti-6Al-4V," *Metallurgical Transactions A*, Vol. 9A, Jan. 1978, pp. 22-29.

49. Paton, N.E. and R.A. Spurling in *Metallurgical Transactions A*, Vol. 7A, 1976, p. 1769.

50. Williams, D.N. in *Metallurgical Transactions*, Vol. 5, 1974, p. 2351.

51. Williams, D.N. in *Materials Science and Engineering*, Vol. 18, 1975, p. 149.

52. Meyn, D.A., paper presented at TMS-AIME Fall Meeting in Niagra Falls, New York, September 1976.

53. LRA Labs, Inc., "Evaluation of Structural Properties of Grade 5, Grade 8, and Beta C Fasteners for DDG 51 Mast Bolt Applications," Final Report for NSWC/White Oak, 17 Feb. 1995.

54. Somerday, B.P., J.A. Grandle, and R.P. Gangloff, "Yield Strength and Solution Composition Effects on Aqueous Environmental Cracking of Ti-8V-6Cr-4Zr-4Mo-3Al (Beta C)," Proceeding of the Tri-Service Conference on Corrosion, 1994, pp. 375-392.

55. DeLuccia, J.J., "Electrolytic Hydrogen in Beta Titanium," Naval Air Development Final Report, 10 June 1976.

56. Dudik, A.S., "The Effect of Elevated Hydrogen Levels in the Beta C Titanium Alloy," Dynamet Technical Report, Washington, PA.

57. Gaudett, M.A. and J.R. Scully, "Hydrogen Interactions and Embrittlement in Metastable Beta Ti-3Al-8V-6Cr-4Mo-4Zr," in "Environmentally Assisted Cracking of High Strength Beta Titanium Alloys," Final Report, University of Virginia, Report No. UVA/525461/MSE95/102, November 1994.

58. Bavarian, B. and M. Zamanzadeh, "Corrosion Behavior of Beta-21S Titanium Alloy in Chloride-Containing Environments," NACE Corrosion '93, Paper #284, 1993.

59. Judy, R.W., C.T. Fujii, and R.J. Goode, "Properties of 17-4 PH Steel," Naval Research Laboratory, NRL Report No. 7639, 18 Dec 1973.

60. Carter, C.S., et al., "Stress Corrosion Properties of High Strength Precipitation Hardening Stainless Steels," *Corrosion*, Vol. 27, No. 5, May 1971, pp. 190-197.

61. Vreeland, D.C., "Precipitation Hardening Stainless Steel," *Materials Protection*, Vol. 9, No. 1, January 1970, pp. 32-35.

62. Roach, T.A., "Aerospace High Performance Fasteners Resist Stress Corrosion Cracking," *Materials Performance*, Vol. 23, No. 9, September 1984, pp. 42-45.

63. LRA Laboratories, Inc., "Titanium Beta-C, Annealed Titanium 6Al-4V ELI, and K-Monel Room Temperature Creep Test," LRA Report No. RMI 41111-0820, 10 May 1995.

Table 1. Mechanical Properties, Composition, and Recommended Heat Treatment Schedules for Fastener Alloys

Alloy	Nominal Composition	Recommended Heat Treatment	Specification or Standard	UTS ksi, min.	0.2% YS ksi, min.	% Elong., min.	% Reduction in Area
K-500	Ni-30Cu-3Al	Solution Treatment + Age (either Single or Dual Age)	FED SPEC QQ-N-286, MIL-S-1222	130	85	20	---
Alloy 725	Ni-21Cr-8Mo-8Fe-3.5Cb	Solution Treatment + Dual Age[a]	ASTM B805	165	120	20	35
Alloy 925	Ni-27Fe-20Cr-3Mo-2Ti-2Cu	Solution Treatment + Dual Age	None	168 TYP	110 TYP	27 TYP	45 TYP
UNS N07716	Ni-21Cr-8Mo-5Fe-3.5Cb	Solution Treatment + Dual Age[a]	ASTM B805	165	120	20	35
Alloy 718	Ni-19Cr-10Mo-10Co-5Fe-2Ti	Solution Treatment + Dual Age	ASTM B637	185	150	12	15
Rene 41	Ni-20Cr-11Co-10Mo-5Fe-3Ti	Solution Treatment + Age	AMS 5713	170	130	8	10
MP35N	35Ni-35Co-20Cr-10Mo	Solution Treatment + Cold Work + Age	AMS 5845	260	230	8	35
Ti-6Al-4V, Ti-6Al-4V ELI	Ti-6Al-4V	Recrystallization or Beta Anneal	MIL-H-81200, MIL-S-1222	115	105	12	20
Ti 38-6-44	Ti-3Al-8V-6Cr-4Mo-4Zr	Solution Treatment[b]	MIL-H-81200, MIL-T-9047	120	115	10	25
Ti 51111	Ti-5Al-1Sn-1Zr-1V-0.8Mo	α-β Forged (1750°F)	None	126 TYP	111 TYP	13 TYP	29 TYP
Ti 16-2.5-3	Ti-16Mo-2.5Nb-3Al	Solution Treatment + Overage	None	130 TYP	120 TYP	20 TYP	---
Alloy A286	Fe-26Ni-15Cr-2Ti-2Mn	Solution Treatment + Age	ASTM A453	130	85	15	18
17-4 PH H1100	Fe-16Cr-4Ni-4Cu	Solution Treatment + Age	ASTM A693	140	115	14	35

[a]: identical to Age process in ASTM B805 except for furnace cooling rate; for optimum results, furnace cool at 100°F/hour.

[b] :identical to solution treatment process in MIL-H-81200 except for temperature range (1400-1700°F in MIL-H-81200); for optimum results, heat within 1500-1550°F.

Table 2. Summary of Localized Corrosion Resistance Data in Quiescent and Low Flow Natural Seawater (6 Month to 2 Year Exposure Periods)

Alloy	Max. crevice corrosion rate, metal to metal (mm/yr)	Max. crevice corrosion rate, metal to nonmetal (mm/yr)	Max. pitting corrosion rate (mm/yr)
K-500	0.29-0.72[a] (1, unpublished data)	0.03-0.50[a,b] (2, unpublished data)	0.32-0.51[a,c] (1,3)
Alloy 725	0.10-0.13[d] (unpublished data)	0.36[d] (unpublished data)	no data found
Alloy 925	susceptible (4); rates not available	susceptible[a,b] (5); rates not available	susceptible (4); rates not available
UNS N07716	0.05-0.08 [d] (unpublished data)	0.08-0.51[d] (unpublished data)	no data found
Alloy 718	2.09[a] (1)	0.51-0.97[b] (2)	negligible[a,b] (1,6)
Rene 41	immune [b,e] (1,6)	immune[e] (6)	immune [b,e] (1,6)
MP35N	immune[b,f](7-9,10)	immune[f] (2,10)	immune[f] (2,10,11)
Ti-6Al-4V, TI-6Al-4V ELI	immune[b] (unpublished data,12)	immune[b] (unpublished data,2,12)	immune[c] (3)
Ti 38-6-44	immune [b] (unpublished data)	immune [b] (unpublished data)	no data found
Ti 51111	no data found	no data found	no data found
Ti 16-2.5-3	no data found	no data found	no data found
Alloy A286	susceptible (13); rates not available	insufficient data	susceptible (13); rates not available
17-4 PH	susceptible (13); rates not available	no data found	0.98-1.70[c] (3)

[a]: annealed and aged
[b]: annealed
[c]: wrought
[d]: ST and dual-aged
[e]: annealed and overaged
[f]: cold worked (50% or more)

Table 3. Summary of Galvanic Compatibility in Marine Environments

Candidate Alloy	Dissimilar Alloy	Relative Compatibility of Candidate Alloy with Dissimilar Alloy[a]	References
K-500	Alloy 625	Poor; severe corrosion of K-500, especially for high 625:K-500 surface area ratios; anodic to 625	2,3,15,16, unpublished data
K-500	Ti-6211	Poor; general and localized corrosion rates of K-500 are increased, especially for high Ti-6211:K-500 area ratios	
Alloy 725	Alloy 625	Good; little to no corrosion, cathodic to Alloy 625	2
Alloy 925	Alloy 625	Poor; galvanically compatible, but severe localized corrosion of Alloy 925 unless cathodically protected	unpublished data
UNS N07716	Alloy 625	Marginal; little to no corrosion, but potential may fluctuate and remain anodic to 625	unpublished data
Alloy 718	aluminum alloys	Marginal; slight to moderate corrosion of the aluminum alloys; Alloy 718 compatibility with aluminum alloys > Alloy A286 but < Ti-6Al-4V	17,18
Alloy 718	Alloy 625	Poor; corrosion potential data suggests galvanic compatibility, but severe localized corrosion of Alloy 718 unless cathodically protected	
Rene 41		No data found	

[a]Good indicates no significant corrosion of either the candidate or dissimilar alloy.
Marginal indicates slight to moderate corrosion of one or both of the coupled alloys.
Poor indicates severe of one or both of the coupled alloys due to galvanic coupling, crevice corrosion, or general corrosion.

Table 3. (continued)

Candidate Alloy	Dissimilar Alloy	Relative Compatibility of Candidate Alloy with Dissimilar Alloy[a]	References
MP35N	Alloy K-500	Poor; corrosion rate of K-500 increased	7,13,19
MP35N	316 stainless	Poor; corrosion rate of 316 increased	
MP35N	carbon steel	Poor; corrosion rate of carbon steel increased	
MP35N	7075-T6 Al, 5456 Al	Poor; corrosion rate of aluminum alloys increased	
MP35N	17-4 PH	Poor; although little galvanic corrrosion, severe 17-4 PH crevice corrosion	
MP35N	HY-130	Good; slight corrosion of HY-130	
MP35N	Ti-6Al-4V	Good; no corrosion	

[a]Good indicates no significant corrosion of either the candidate or dissimilar alloy.
Marginal indicates slight to moderate corrosion of one or both of the coupled alloys.
Poor indicates severe corrosion of one or both of the coupled alloys due to galvanic coupling, crevice corrosion, or general corrosion.

Table 3. (continued)

Candidate Alloy	Dissimilar Alloy	Relative Compatibility of Candidate Alloy with Dissimilar Alloy[a]	References
Ti-6Al-4V ELI	Alloy 625	Good; no corrosion of Ti-6Al-4V, cathodic to 625	3,12,13,17, 20,21, unpublished data
Ti-6Al-4V	aluminum alloys	Marginal to Poor; no corrosion of Ti-6Al-4V, but mild to severe corrosion of aluminum alloys	
Ti-6Al-4V	titanium alloys	Good; no corrosion	
Ti-6Al-4V	stainless steel	Poor; no corrosion of Ti-6Al-4V, but severe crevice corrosion of Alloy A286 and 17-4 PH	
Ti-6Al-4V	steel, iron	Good; mild corrosion of HY-130	
Ti-6Al-4V	zinc	Good; no corrosion	
Ti-6Al-4V	fiberglass	Good; no corrosion	

[a]Good indicates no significant corrosion of either the candidate or dissimilar alloy.
Marginal indicates slight to moderate corrosion of one or both of the coupled alloys.
Poor indicates severe corrosion of one or both of the coupled alloys due to galvanic coupling, crevice corrosion, or general corrosion.

Table 3. (continued)

Candidate Alloy	Dissimilar Alloy	Relative Compatibility of Candidate Alloy with Dissimilar Alloy	References
Ti 38-6-44	Alloy 625	Good; no corrosion, cathodic to 625	unpublished data
Ti 51111		No data found but expected to be similar to Ti-6Al-4V	
Ti 16-2.5-3		No data found but expected to be similar to Ti-6Al-4V	
Alloy A286	aluminum alloys	Marginal; moderate corrosion of aluminum alloys (less compatible than Alloy 718 or Ti-6Al-4V with aluminum alloys)	13,17,22,23
Alloy A286	17-4 PH	Poor; although little galvanic corrosion, coupling not recommended due to severe crevice corrosion of 17-4 PH	
Alloy A286	HY-130	Good; no increased corrosion of HY-130 due to coupling	
Alloy A286	Ti-6Al-4V	Poor; severe crevice corrosion of Alloy A286	
17-4 PH	2024-T4 Al, anodized steel, 304 stainless	Poor	3,13
17-4 PH	Ti 6211	Poor; increased 17-4 PH corrosion	

[a]Good indicates no significant corrosion of either the candidate or dissimilar alloy.
Marginal indicates slight to moderate corrosion of one or both of the coupled alloys.
Poor indicates severe corrosion of one or both of the coupled alloys due to galvanic coupling, crevice corrosion, or general corrosion.

Table 4. Summary of EAC and SLC Resistance in Seawater

Alloy and Condition	EAC and SLC Susceptibility	Supporting Data	References
Alloy K-500 (Solution treated and aged)	Susceptible to HE (at or electronegative to -800 $mV_{Ag/AgCl}$); resistant to SLC at service temperatures of interest	Slow strain rate, J_{Ic}, long-term exposure (7 mo. to 2 yr.), failure analyses	1,24-31
Alloy 725 (Solution treated and dual aged)	Susceptible to SCC and to HE (at or electronegative to -850 mV_{SCE}); SLC unknown	Slow strain rate, long-term exposure (1.2 yr.)	unpublished data
Alloy 925 (Solution treated and dual aged)	Susceptible to HE at -1250 mV_{SCE}; reduced load bearing capacity evident in air, freely corroding, -850, and -1000 mV_{SCE} conditions; SLC unknown	Slow strain rate	28
UNS N07716 (Solution treated and dual aged)	Resistant to SCC; susceptible to HE (at or electronegative to -850 mV_{SCE}) ; SLC unknown	Slow strain rate, long-term exposure (7 mo., 1.2 yr.)	28,29
Alloy 718 (Solution treated and dual aged)	Resistant to SCC; susceptible to HE (at or electronegative to -850 mV_{SCE}); SLC unknown	Slow strain rate	32,unpublished data
Rene 41 (Solution treated and aged)	Resistant to SCC; susceptible to HE at or electronegative to -1000 mV_{SCE}; SLC unknown	Slow strain rate	28
MP35N (Solution treated and aged)	Resistant to HE and SCC; SLC unknown	C-rings, bolts stressed to varying 0.2% YS levels, three-point bend	33,34

Table 4. (continued)

Alloy and Condition	EAC and SLC Susceptibility	Supporting Data	References
Ti-6Al-4V, Ti-6Al-4V ELI (Solution Treated and Annealed)	Variable susceptibility to HE and SCC (dependent on composition, microstructure); lower oxygen of ELI grade improves EAC resistance; susceptible to SLC (based on plate data)	Slow strain rate, K_{Ith}, long-term exposure (7 mo. to 1.8 yr.)	28-30,35,36-46,47-52
Ti 38-6-44 (Solution Treated and Annealed)	Resistant to HE and SCC; SLC unknown	Slow strain rate, K_{Ith}, long-term exposure (7 mo., 1.2 yr.)	28-30,32,36, 53-57
Ti 51111 (As-forged)	Resistant to HE and SCC; SLC unknown	Slow strain rate	30
Ti 16-2.5-3 (Solution Treated and Overaged)	Resistant to HE and SCC; SLC unknown	Slow strain rate, U-bends	29,30,58
Alloy A286 (Solution Treated and Aged)	Resistant to HE and SCC; SLC unknown	Slow strain rate, three-point bend	28,32
17-4 PH (Solution Treated and Aged)	HE and SCC resistance increases as tempering temperature increases from 900 to 1100°F; at higher tempering temperatures (1050°F), a -600 to -1300 mV_{SCE} potential required for protection; SLC unknown	Bent beam, cantilever beam	59-61

Kinetics of Pitting Corrosion and Effects on Fatigue Behavior of Aluminum Alloy 7075-T6

K. K. Sankaran, B. Johnson(1) and R. Perez
The Boeing Company, Mail Code S1111041, POBox 516, St. Louis MO 63166

and

K. V. Jata
Wright Laboratory/Materials Directorate, WL/MLLM, WPAFB, OH 45433

ABSTRACT

Localized corrosion provides sites for fatigue crack initiation, and for accurate life prediction of aging aircraft, the early stages of corrosion and transition to fatigue cracks under simulated service environments must be characterized. The pitting kinetics of bare 7075-T6 aluminum alloy sheet (commonly used in airframe construction) was studied following exposure for up to 1,536 hours in a prohesion cyclic salt spray chamber and measuring pitting damage evolution as a function of time. The pit depth was observed to increase with time in accordance with a power law, and as expected, pitting significantly reduced the fatigue lives of the 7075-T6 alloy. The measured fatigue lives were also found to be in general agreement with those calculated analytically using the pit dimensions as sizes of equivalent crack initiating initial flaws.

INTRODUCTION

The most significant part of the total maintenance cost for the United States Air Force results from corrosion damage to aging aircraft. This cost problem is becoming more critical as budgetary constraints require aircraft life extensions far beyond that intended by the initial design. State-of-the-art practices prevalent during the design and manufacture of these aging aircraft allowed dry assembly methods and spot welded joints without sealants protecting the faying surfaces. Corrosion resistant aluminum alloys and heat treatment tempers were also not available for use. The resulting crevice corrosion in joints where fatigue damage also tends to accumulate provides fatigue crack initiation sites and accelerates crack propagation. A need thus exists for a quantitative assessment of the effects of corrosion on the structural integrity of these aging aircraft. The issues of aging aircraft corrosion and the approach planned by the US Air Force to perform structural studies and to develop analytical methods for quantifying the effects of corrosion have been summarized in a recent article by Groner[1].

To understand and predict the combined effects of corrosion and fatigue on structural integrity, quantitative measures of corrosion damage must be developed and validated in analytical models of life prediction. The effect of corrosion on fatigue life has been determined by

(1) Currently student at the University of Illinois, Urbana

Harmsworth[2] for aluminum alloy 2024-T4 by conducting S-N fatigue tests on pre-corroded specimens, and the fatigue life has been shown to decrease with increasing corrosion pit depth.

Fracture mechanics based approaches being developed and validated to quantify corrosion damage approximate corrosion by thickness loss to account for exfoliation and local stress concentration to account for pitting[3]. In a recent study, Perez[4] found good correlation of measured fatigue lives of etched (corroded) aluminum alloys 2124-T851 and 7050-T7451 with the lives predicted from analytical models using the size of the crack initiating pit as an equivalent initial flaw size (EIFS). Probability models for predicting corrosion and corrosion fatigue life are being developed by studying the growth of pits to a critical size for fatigue crack nucleation[5].

The purpose of the present study is to determine the pitting corrosion kinetics parameters that can be used as inputs for validating analytical life prediction models. These parameters will also provide the extent of pitting that can be allowed before maintenance/repair activities on in-service aircraft are undertaken. Preliminary results of pitting kinetics measurements on aluminum alloy 7075-T6 and the effects of pitting on fatigue behavior are reported in the following sections.

EXPERIMENTAL PROCEDURE

Rectangular test coupons, 150 mm x 75 mm (6 in. x 3 in.), were prepared from 2 mm (0.080 in.) thick bare 7075-T6 aluminum alloy sheet stock. The side with the 75 mm (3 in.) dimension was parallel to the rolling direction. The coupons were exposed to dilute electrolyte cyclic fog/dry (prohesion) spray per ASTM Standard G85, Annex 5 for varying lengths of time up to 1,536 hours. Three coupons were exposed for each test duration. The prohesion electrolyte is a solution of 0.05% NaCl and 0.35% $(NH_4)_2SO_4$ with a pH between 5.0 and 5.4. The test consists of alternating cycles of 1 hour fog at room temperature and 1 hour drying period at 35°C (94°F).

Spray tests were chosen in this study because of the ability to obtain progressively increasing pitting corrosion damage under controlled conditions in relatively simple tests. Exposed coupons are also amenable to ease of fabrication of fatigue test specimens. Additionally, the prohesion test combines wet-dry cycles with a relatively dilute mixed salt spray (in comparison with the more commonly used 5% NaCl) solutions thus better simulating natural service conditions.

Pits on specimens exposed to the prohesion cyclic spray were characterized by using a metallurgical microscope with a fine focus knob calibrated to 1 μm. Pit depths were measured by focusing on the specimen surface first at the lip of the pit and then at the bottom of the pit, with the difference in the fine focus knob reading being the pit depth. Two hundred randomly chosen pits were examined in various locations in each of the exposed coupons to determine the pit dimension (length, width and depth) distribution.

Fatigue test specimens with 38 mm (1.5 in.) long and 13 mm (0.5 in.) wide constant gage section were fabricated from the coupons exposed in the prohesion test chamber for 1,536 hours. The overall length of the specimens was 150 mm (6 in.). Three specimens were fabricated from

The overall length of the specimens was 150 mm (6 in.). Three specimens were fabricated from each of three identically exposed coupons for a total of nine specimens. Constant amplitude S-N fatigue tests were conducted at various maximum stress levels up to 415 MPa (60 ksi) in laboratory air environment using an R ratio of 0.02 and a frequency of 10 Hz. Tests were also conducted on uncorroded 7075-T6 specimens to generate comparative baseline S-N fatigue data. The fatigue lives of corroded specimens were also calculated from analytical life prediction models using the size of the crack initiating pit as an equivalent initial flaw size. The predicted fatigue lives were compared to the measured lives in a manner similar to that reported in a recent study by Perez[4].

RESULTS

Pitting Characteristics of 7075-T6

The microstructure of 7075-T6 and the typical appearance of the pits on the corroded surface of the specimens are shown in Figures 1 and 2, respectively. The pits were irregular in shape with the longer pit dimension almost always in the rolling direction. Figure 3 shows the histograms of the pit aspect ratio (length/width ratio where length is measured in the rolling direction) for 200 randomly chosen pits each in specimens exposed to varying lengths of time. This data clearly indicates preferential pit growth in the rolling (grain flow) direction. Additionally, increasing the exposure (increasing pit size) reduces the shape anisotropy of the pits.

Figure 4 shows the histograms of the pit depth for the 200 pits each in specimens exposed to varying lengths of time. The data indicates an increase in the mean depth of the pits (Figure 5) with increasing corrosion exposure. For exposures up to 192 hours, the maximum pit depth remains the same, between 30 and 40 μm. The maximum pit depth increases to between 50 and 60 μm for 384 hours exposure and to between 80 and 85 μm for 1,536 hours exposure indicating continued pit growth and further sub-surface pit nucleation. The maximum pit depth for specimens exposed for 768 hours is however only between 30 and 40 μm and the reason for this anomaly is not yet clear. Additional experiments are being conducted to verify this behavior.

The pitting factor (defined in the ASTM Standard G46 as the ratio of the maximum pit depth to the mean depth) is shown in Figure 6. An increasing uniformity of pitting with time is indicated by this data.

Corrosion pitting behavior data was fit to a 3 parameter Weibull distribution and good curve-fits were obtained. Early time data was skewed to smaller pit sizes, and as time progresses the distributions became more normal. Characteristic pit depth values from these Weibull distributions are plotted in Figure 7 as a function of exposure time. Data from the specimen exposed for 768 hours has been excluded from this plot owing to the anomalous nature of the data. Regression analysis shows that the pit depth increases with time in accordance with a power law with a time exponent of 0.4. This compares well with the very limited amount of published data available on the pitting kinetics of aluminum alloys wherein exponents of 1/3 and 1/2 have been reported.

Pitting in aluminum alloys such as 7075 is known to be associated with the constituent particles and occurs from the galvanic corrosion and dissolution of the aluminum matrix from the coupling with these particles. The observed maximum pit size (depth) of between 30 and 40 μm for exposures up to 192 hours can thus be explained on the basis of the maximum constituent particle size of about 20 μm observed in the alloy (Figure 1). At longer exposures, sufficient pits come into contact with sub-surface constituent particles causing further corrosion and increase of pit depth.

A detailed statistical analysis of the pit characteristics data is in progress. Confidence bands are being generated for the Weibull plots to assist in determining the effects of reducing the data collection required from each specimen. It is also important that the accelerated corrosion tests such as the spray tests used in this study simulate as closely as possible real time aging aircraft environments. To accomplish this, future tests are planned under corrosive environments that simulate the chemistry[6] of aging aircraft lap splice joints using specimens designed to simulate aircraft lap joints[7].

Effect of Pitting on the Fatigue Properties of 7075-T6

The results of the constant amplitude fatigue tests conducted on uncorroded baseline 7075-T6 specimens and on specimens machined from coupons exposed for 1,536 hours in the prohesion chamber are shown in Table 1 and Figure 8. Also shown are the fatigue lives of corroded specimens calculated from analytical life prediction models using the size of the crack initiating pit as an equivalent initial flaw size. The Boeing developed model is a fracture mechanics and crack growth analysis software which computes the life based on the number of cycles needed to grow an initial flaw to a critical crack size for catastrophic failure. Crack growth rates for common materials such as 7075-T6 are available in the software. The model independently computes crack growth on the surface (using pit length as twice the initial crack length) as well as through the thickness (using the pit depth as the initial crack length). Fatigue life is determined by the time for the first crack to reach the critical size.

The results of the fatigue tests clearly show the significant decrease (by a factor of 6 to 8 for the data shown) in the lives caused by the pitting corrosion damage. The measured lives are also in close agreement with the predicted lives assuming an equivalent initial flaw corresponding to a pit of average measured length and depth. Of course, the predicted life would be lower if the initial flaw corresponds to the pit with the largest length and depth. This is shown by the data in Table 1. A detailed examination of the fracture surfaces is in progress to identify the fracture initiating flaw (pit) and to understand the reasons for the excellent correlation of the measured and predicted lives when the average pit length and depth are used for the analysis.

These preliminary results suggest that the approach used in this study has the potential for the systematic development and validation of accelerated corrosion tests for determining the kinetics of corrosion and its effects on the life of aging aircraft structures. Further work, particularly correlation with actual damage in aged/corroded aircraft structures, is necessary for achieving this validation.

CONCLUSIONS

1. Standardized spray corrosion tests are well suited for measuring the kinetics of corrosion in aircraft structural materials such as 7075-T6.

2. The kinetics of pitting corrosion in 7075-T6 measured in spray tests obeys a power law with a time exponent of 0.4 which is in agreement with those measured from more conventional immersion and electrochemical tests.

3. Pit nucleation occurs at the constituent particles. The pitting kinetics data shows that the depth of the pits increases by the interconnection of the pits that have nucleated at constituent particles at various depths through the thickness of the exposed panels.

4. Pitting degrades the fatigue properties of 7075-T6. There is very good agreement between measured and predicted fatigue lives of the corroded alloy when the average pit size is used as the size of the initial crack initiating flaw.

ACKNOWLEDGMENTS

This program is funded by the AFOSR Third Millennium Initiative on Aging Aircraft through the contract F33615-96-D-5835, managed by the Wright Laboratory/Materials Directorate.

REFERENCES

1. D. J. Groner, "US Air Force Aging Aircraft Corrosion", Current Awareness Bulletin, Structures Division, Wright Laboratory/FIBD, Aerospace Structures Information and Analysis Center, WPAFB, OH.

2. C. L. Harmsworth, "Effect of Corrosion on the Fatigue Behavior of 2024-T4 Aluminum Alloy", ASD Technical Report 61-121, 1961, Aeronautical Systems Division, Air Force Systems Command, WPAFB, OH.

3. M. T. Doerfler, A. F. Grandt, Jr., R. J. Bucci and M. Kulak, "A Fracture Mechanics Based Approach for Quantifying Corrosion Damage", Proc. of the Tri-Services Conference on Corrosion, Orlando, FL, June 21-23, 1994, pp. 433-444.

4. R. Perez, "Metrics Exploration and Transformation Development for Corrosion/Fatigue", Final Report, Delivery Order 0005, US Air Force Contract F33615-95-D-3216, November 1996.

5. D. G. Harlow and R. P. Wei, "Probability Approach for Prediction of Corrosion and Corrosion Fatigue Life", AIAA Journal, Vol. 32 (No. 10), October 1994, p. 433.

6. R. S. Piascik, R. G. Kelly, M. E. Inman and S. A. Willard, "Fuselage Lap Splice Corrosion", Proc. of the US Air Force Structural Integrity Program Conference, San Antonio, TX, November 28-30, 1995.

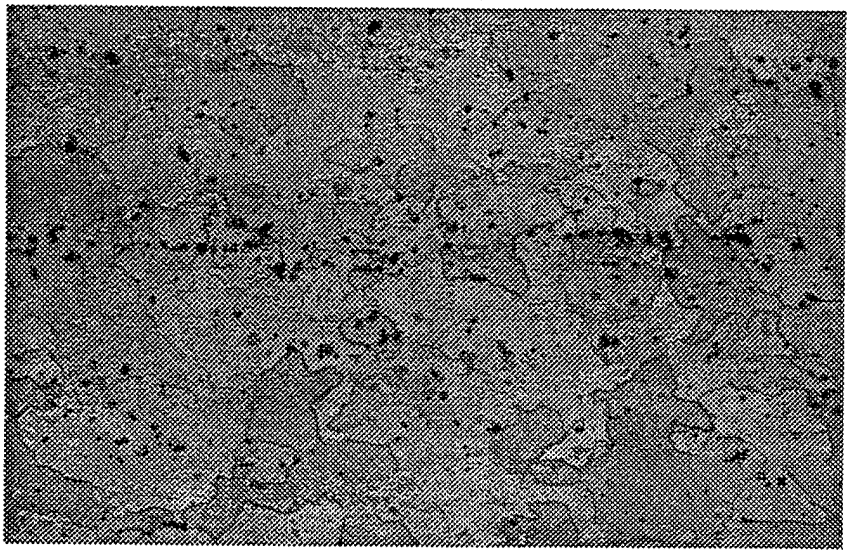
7. R. J. Bucci, H. J. Konish and B. J. Shaw, "Lap-Splice Corrosion Simulation - A Case Study", US Air Force 3rd Aging Aircraft Conference, Dayton, OH, Sept. 26-28, 1995.

Table 1

Measured and Predicted Fatigue Life Data for 7075-T6
(Note: Pit dimensions used in the analysis for life prediction correspond to the length and depth of the pit)

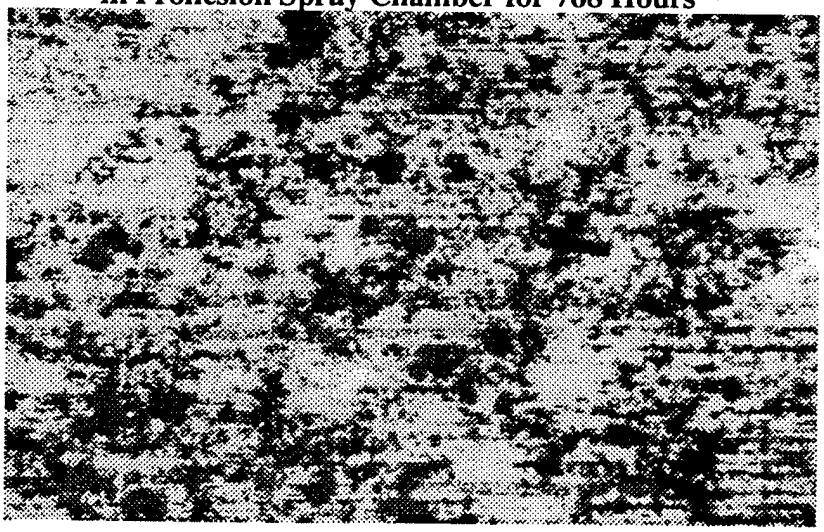
Maximum Stress MPa (ksi)	Measured Fatigue Life, Cycles Baseline Uncorroded 7075-T6	Measured Fatigue Life, Cycles Corroded 7075-T6 (1,536 hours in Prohesion Test)	Predicted Fatigue Life, Cycles Initial Flaw Size = Average Dimension Of Pits	Predicted Fatigue Life, Cycles Initial Flaw Size = Maximum Dimension of Pits
240 (35)		30,950 39,380	87,078	12,977
275 (40)		22,950	28,525	7,498
310 (45)		18,830 15,130	13,767	5,043
345 (50)	87,140 38,290 82,120		8,260	3,625
380 (55)	39,270 45,800	6,040 6,852	5,630	2,831
415 (60)	33,900 40,620	4,510	4,150	2,245
450 (65)	12,230 26,870		3,217	1,820

Figure 1
Optical Micrograph Showing Microstructure of 7075-T6
(LT Plane Representative of Surface Exposed to Corrosion Spray)



100 μm

Figure 2
SEM Micrograph Showing Typical Corrosion Pits Formed by Exposure in Prohesion Spray Chamber for 768 Hours



200 μm

Figure 3

Histograms of Pit Aspect ratio

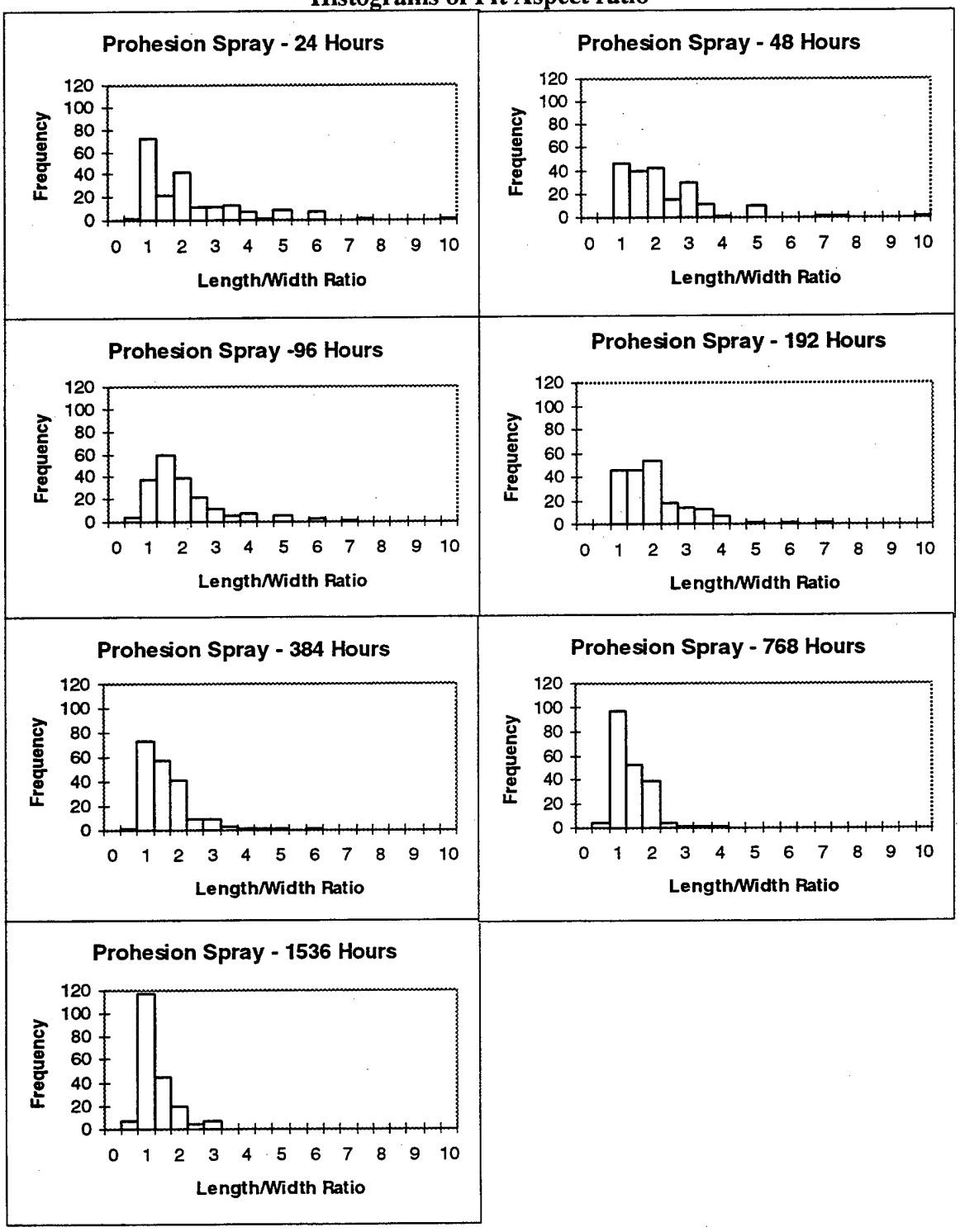


Figure 4

Histograms of Pit Depth

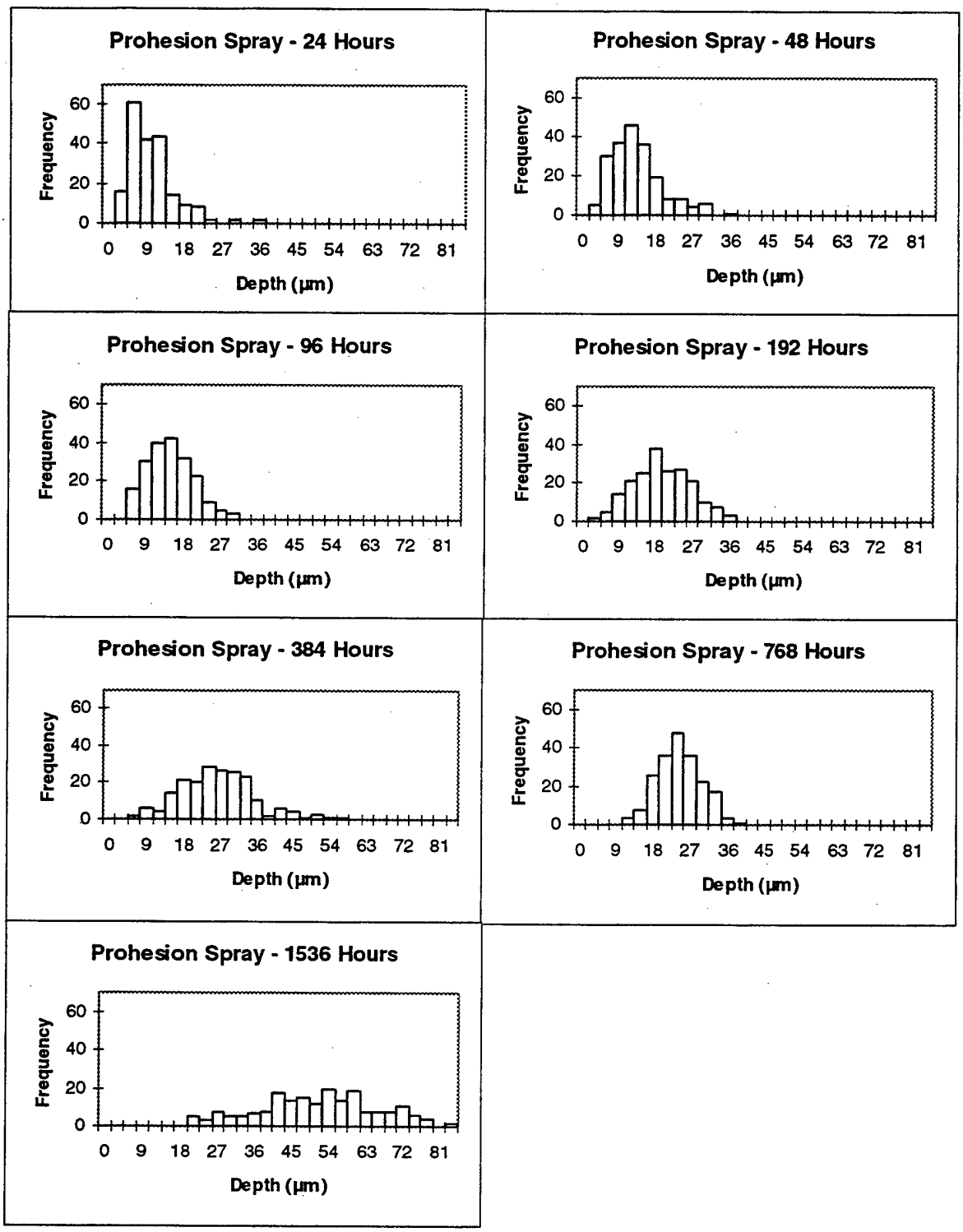


Figure 5

Mean Pit Depth

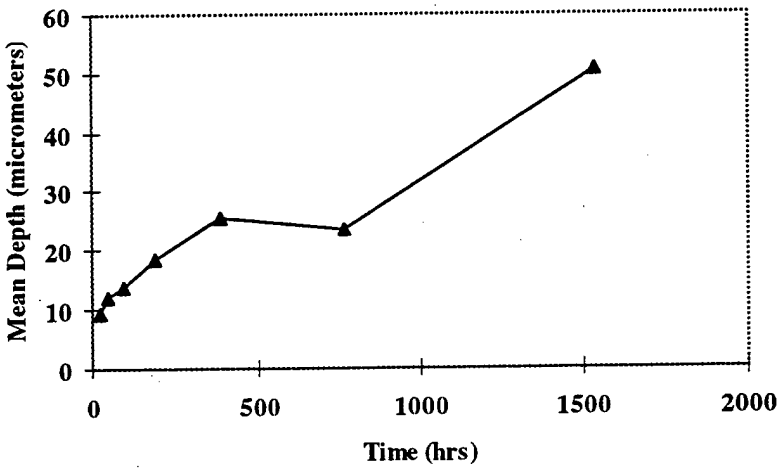


Figure 6

Pitting Factor (ASTM G46)

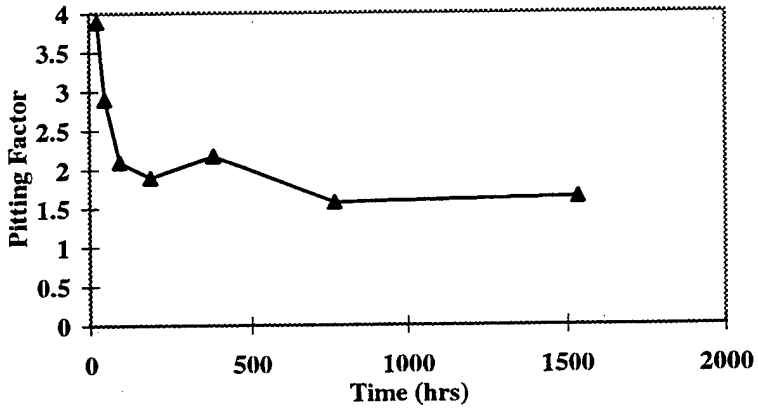


Figure 7

Weibull Characteristic Values ($y = 2.6x^{0.4}$, $R^2 = 0.99$)

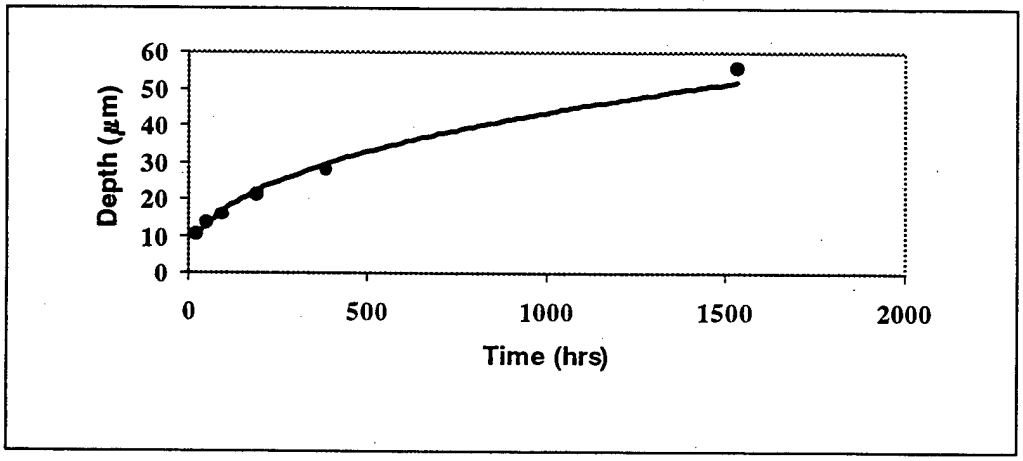
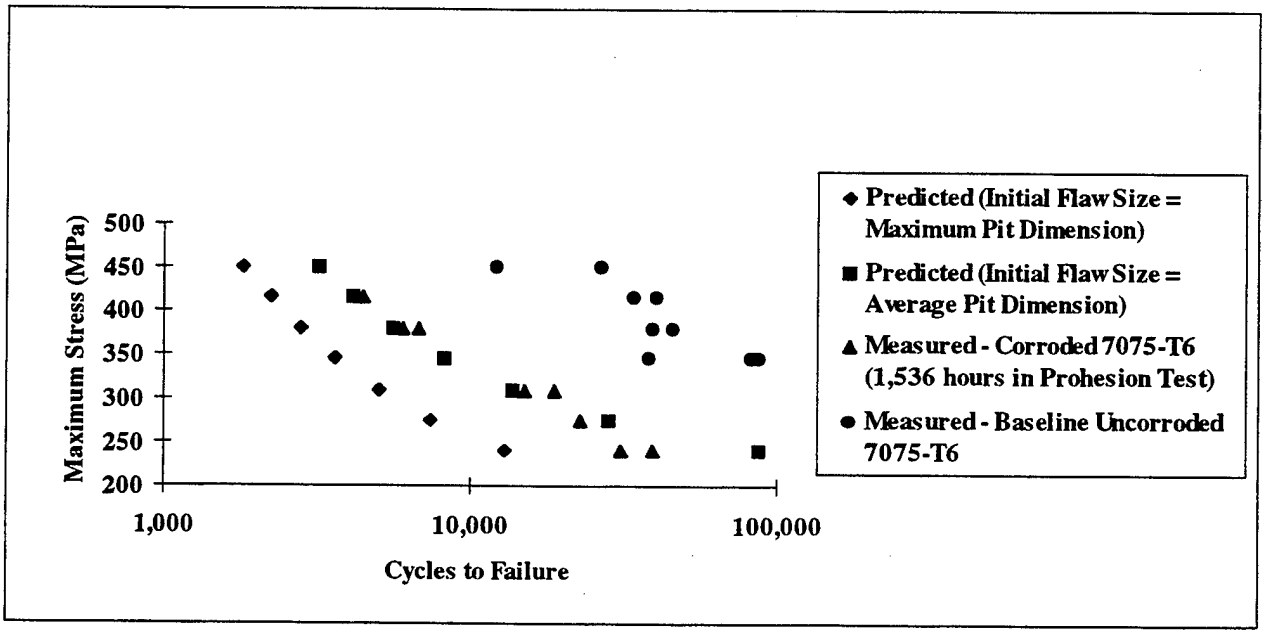


Figure 8

S-N Fatigue Data for 7075-T6, R = 0.02



Galvanic Corrosion of Tungsten Coupled with Several Metals/Alloys

F.C. Chang, J.H. Beatty, M. J. Kane, and J. Beck
U.S. Army Research Laboratory
AMSRL-WM-ME
Aberdeen Proving Ground, MD 21009

ABSTRACT

From an environmental perspective, tungsten is a more desirable material than depleted uranium(DU) for penetrator applications[1-4]. However, the ballistic performance attained by current tungsten alloys is inferior to DU. Recently, advanced tungsten-metal composites have been developed to improve their ballistic penetration, but the corrosion properties are unknown, and need to be determined. In this work, the galvanic corrosion behavior of tungsten coupled with several selected metals/alloys was investigated. Electrochemical potentiodynamic polarizations and galvanic couplings were employed. The testing was conducted in a 1 wt.% sodium sulfate solution. The selected metals/alloys were: pure tungsten, pure titanium, titanium 6Al-4V, hafnium, Invar, pure iron and CDA 260 brass. The galvanic corrosion of these couples are examined and discussed based on the results from electrochemical tests and visual observations.

INTRODUCTION

Depleted uranium(DU) and tungsten (W) based alloys are attractive candidate materials for kinetic energy penetrator applications because of their unique combination of mechanical properties and high density. Traditionally, DU penetrators have better ballistic properties than W penetrators, but the toxicity and radioactivity of DU creates environmental repercussions. Thus, efforts to develop W alloys to replace DU have been undertaken by the US Army and Department of Defense. Potential tungsten alloys have included W-Ni-Fe-Co, W-Ni-Co,W-Ni-Mn,W-Hf, W-Ti, and others[3].

These new tungsten alloys are being developed strictly for improved ballistic performance; their corrosion properties are of secondary importance. However, this study is looking to uncover potential galvanic corrosion issues in tandem with the alloy development. Tungsten alloys generally contain at least two discrete phases. In most alloys under consideration, relatively pure tungsten grains are encapsulated by a matrix consisting of of the other alloying elements[3], as shown in Figure 1 for W-Ni-Fe. Galvanic corrosion can occur between these two discrete phases. The work reported herein is a preliminary study of the galvanic corrosion behavior of tungsten-metal (W-M) couples immersed in test solutions. Both potentiodynamic scans and galvanic couple experiments were performed.

EXPERIMENTAL PROCEDURE

Samples for electrochemical testing were made from pure tungsten(W), and other seven other metallic materials selected for study, namely: brass (CDA 260), Hafnium (Hf), Invar (36Ni64Fe0.03C), Iron (Fe), Nickel (Ni), Titanium (Ti), and Titanium 6Al-4V(Ti-6-4). Their typical chemical compositions are listed in Table 1. Disk type specimens 0.318 cm thick and 1.588 cm in diameter were used in all of the tests. Immediately before initiating electrochemical tests, the specimens were polished with 600 grit silicon carbide paper, rinsed with distilled water, acetone degreased, and air dried. One square centimeter of each specimen was exposed to the test solution.

Tests were performed in a dilute sodium sulfate solution(1 wt.% Na_2SO_4) to simulate the humid industrial atmosphere. Potentiodynamic tests were conducted at room temperature in a cell manufactured by Princeton Applied Research, (PAR) Model K0235 containing about 325ml of test solution. A computer controlled PAR M273 potentiostat was used, with a sweep rate of 0.166 mV/s. Separate specimens were used for the anodic and cathodic portions of the curves. The solution was deaerated with argon gas. The open circuit corrosion potential was measured for a period of one hour before the scans commenced. Potentials were measured against the saturated calomel electrode(SCE).

The galvanic corrosion tests were conducted in a modified version of the PAR Model K0235 flat cell, as shown in Figure 2. Two PAR M273 potentiostats were utilized. A tungsten specimen is placed at one end of the cell, while the other specimen is clamped to the opposite end. The first potentiostat is set to keep the potential difference between the tungsten and the other sample at 0V (effectively a short circuit), and simultaneously measure the galvanic current (I_g)

generated. A second potentiostat is used to monitor the open circuit potential of the corroding couple (E_g) vs SCE. The galvanic couple cells were not deaerated, and galvanic currents were measured for a period of 3 days.

RESULTS AND DISCUSSION

In the galvanic tests, variations of the galvanic currents, Ig vs time, were recorded for the 72 hours of testing. I_g is useful as an indicator of the severity of galvanic corrosion. Additionally, potentiodynamic scans are often used to predict galvanic corrosion behavior using mixed potential theory. The following results will compare the predictions of mixed potential theory to the actual galvanic tests, and comment on the implications this will have on the corrosion resistance of tungsten alloys under development.

Figures 3a & 3b show the variation in galvanic current, I_g, as function of time. "Positive" currents in this case mean that the tungsten is behaving as the anode, while negative currents denote that tungsten is behaving as the cathode. These curves show that at the end of the 72 hour test, only iron and Invar behaved as anodes with respect to tungsten. Iron was more anodic than tungsten throughout the test, while Invar changed behavior from cathodic to anodic after a few hours of immersion. At the outset of the test Ni, Hf, Ti, & Ti-6-4 were anodic with respect to W in the W-Metal couples, but they all became more noble (cathodic) in less than 10 hours.

The results of the galvanic corrosion tests are summarized in Table 2. The couples are ranked in decreasing order of the magnitude of the galvanic current density.

When two metallic specimens are coupled together and immersed in an aqueous electrolyte, the well established mixed potential theory states that the corroding potential and corresponding galvanic current can be predicted form the potentiodynamic scans of each metal. Figure 4 shows a schematic illustrating this method. The mixed potential of the couple, E_m, and the galvanic current, I_m, can be represented by the intersection of the anodic polarization curve of the anode (the alloy/metal with the more active E_{corr}) and the cathodic polarization curve of the cathode (the alloy/metal with the more noble E_{corr}) as the two polarization curves are overlapped. Generally, I_m may be considered the corrosion rate of the anode in the couple.

Figures 5 a-g show the overlapped potentiodynamic scans of the couples under investigation and the corresponding values of E_m and I_m . Tables 3 and 4 summarize these

results, providing the open circuit potentials (E_{corr}) for each metal/alloy studied, as well as the E_m and I_m predicted from mixed potential theory. Comparing I_m to I_g shows that the mixed potential theory agrees reasonably well with the longer term galvanic couple data. The materials with large I_m's (Fe, CDA, Invar) show the largest I_g's. The Fe : W couple sustained the largest current density, at 1 x 10 -5 A/cm^2. The Invar : W couple shows a reversal of current that is not easily explained. The remaining materials (Ti, Ti-6-4, Ni, & Hf) have E_m's close to the E_{corr} of tungsten. This means that the tungsten, which is near its free corrosion potential, can behave either as an anode or a cathode as drifting of the corrosion potenital ocurrs. Long-term measurements of E_{corr} often show "drifting" from 10-30 mV, suggesting that changes in the anodic/cathodic relationship (current reversals) should be expected if the E_m is near E_{corr} of either material in the couple. Current reversals are seen for all of the couples except W-Fe and W-Brass. However, relatively small galvanic currents would be expected, and this is precisely what is observed.

It should be noted that there are certain limitations of the methods used in this preliminary study. For instance, the effect of grain boundaries, solid solubility, and intermetallic compound formation that may result in certain processes have been ignored. Also, other factors such as the ratio of anode/cathode surface area must be accounted for. However, because of the two discrete phases found in tungsten alloy composites (Figure 1), it is reasonable to assume that the galvanic effects measured in this study will agree well with the general corrosion behavior of the tungsten alloys under development.

CONCLUSIONS

Comparison of mixed potential theory and galvanic corrosion tests provided good agreement for the materials studied. Pure Ti, Ti-6Al-4V, Ni and Hf when coupled with tungsten showed small galvanic current densities ($< 1.0 \times 10^{-7}$A/cm^2) and maintained galvanic corrosion potentials near the E_{corr} of tungsten. Tungsten alloys utilizing these materials as the matrix material should show little or no galvanic corrosion. When tungsten was coupled to Fe, CDA Brass and Invar, significantly larger current densities were measured. This suggests that corrosion protection schemes will need to be developed for tungsten alloys under development using these materials in the matrix.

REFERENCES

1. M.Levy and F. Chang, Corrosion Behavior of High Density Tungsten Alloys, Proceedings of the Second International Conference on Environmental Degradation of Engineering Materials in Aggressive Environments, pp. 33-42. 1981.

2. F. Chang, M. Levy, and S.S. Lin, The Effect of Ion Implantation on the Corrosion Behavior of A High Density Sintered Tungsten Alloy, NACE Corrosion 85, Paper 71, 1985.

3. W.D. Cai, Y. Li, R.J. Dowding, F.A. Mohamed and E.J. Lavernia, A Review of Tungsten-Based Alloys As Kinetic Energy Penetrator Materials, Review in Particulate Materials, Vol 3, pp.71-131. 1995

4. M. Stern and A. Geary, J. Electrochem. Soc., **104**,56(1957).

Table I. Chemical compositions of metals and alloys selected for this study.

Material Studied	Nominal Composition
Pure W	99.99 W
Fe	99.99 Fe
Ni	99.7 Ni
Hf	95.3 Hf-3.5Zn-1.2Fe
Ti	99.9 Ti
Ti-6-4	90Ti-6Al-4V
Brass (CDA 260)	70Cu-30Zn

Table II Summary of galvanic corrosion tests.

(negative sign indicates the material was anodic with respect to tungsten)

Tungsten Coupled to:	Ig, Galvanic Current Density, A/cm^2
Iron	- 1 x 10-5
Brass	1 x 10-6
Invar	- 1 x 10-6
Nickel	1 x 10-7
Titanium	3 x 10-8
Ti-6Al-4V	3 x 10-8
Hafnium	0 x 10-8

Table III Mixed Potentials and Mixed Current Densities as determined from Polarization Curves.

Tungsten Coupled To:	Tungsten is More ? :	Em (V vs. SCE)	Im (A/cm^2)
Iron	Noble	-0.748	6.109 x 10-6
Nickel	Noble	-0.443	7.261 x 10-7
Hafnium	Noble	-0.431	2.158 x 10-7
Titanium 6-4	Noble	-0.431	2.094 x 10-7
Titanium	Noble	-0.431	1.315 x 10-7
Invar	Active	-0.403	(1.552 x 10-6)
Brass	Active	-0.383	(2.553 x 10-6)

Table IV Average Open Circuit Potentials measured after 1 hour of immersion .

Material	Ecorr (V vs. SCE)
CDA Brass	-195
Invar	-277
Tungsten	-431
Pure Titanium	-463
Pure Nickel	-522
Hafnium	-533
Ti-6Al-4V	-535
Pure Iron	-785

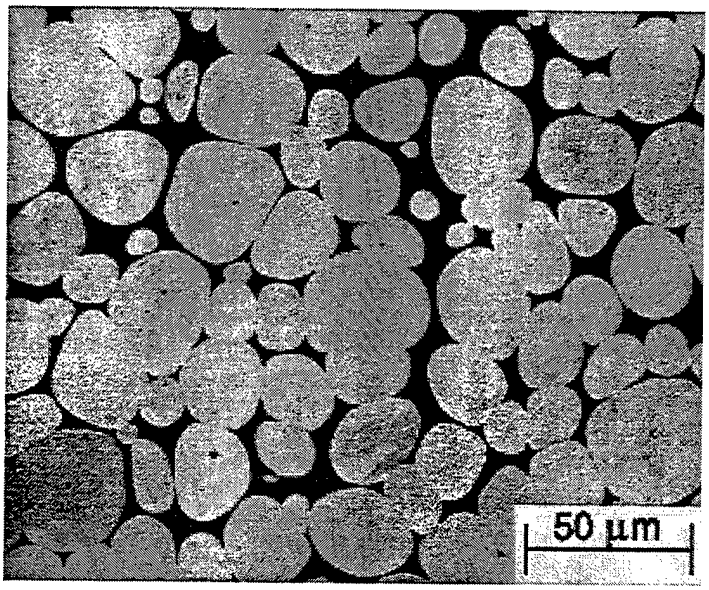


Figure 1. Typical microstructure of W-Ni-Fe alloys, taken from reference 3. The solubility of Fe and Ni in tungsten is extremely low, leading to almost pure tungsten grains surrounded by an Fe-Ni matrix. The alloy above is 95W-3.5Ni-1.5Fe.

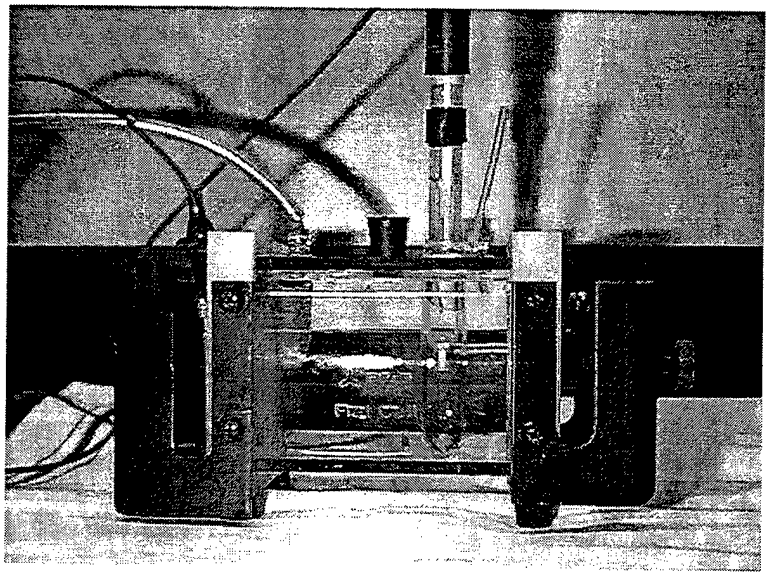
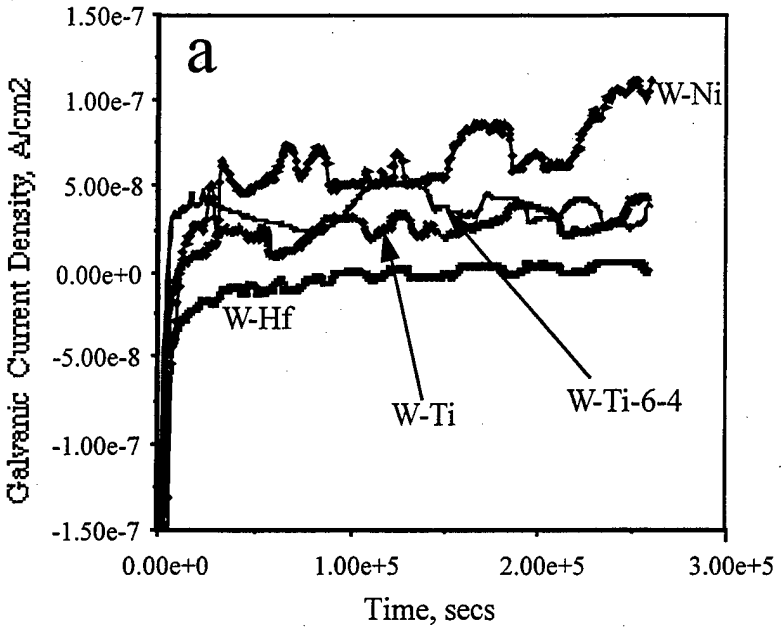


Figure 2. Experimental setup used for galvanic testing. Clamps at both ends secure each material of the couple being tested. The potentiostat is used to effectively short circuit each specimen and measure the galvanic current.



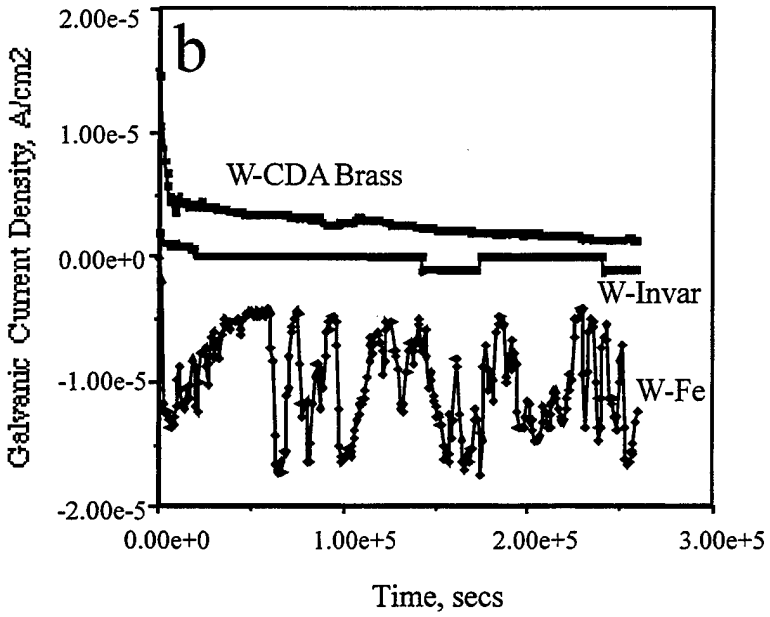


Figure 3. Galvanic corrosion current densities as a function of time. a) Tungsten coupled with Titanium, Ti-6Al-4V, Hafnium, and Nickel. b) Tungsten coupled with CDA Brass, Iron, and Invar.

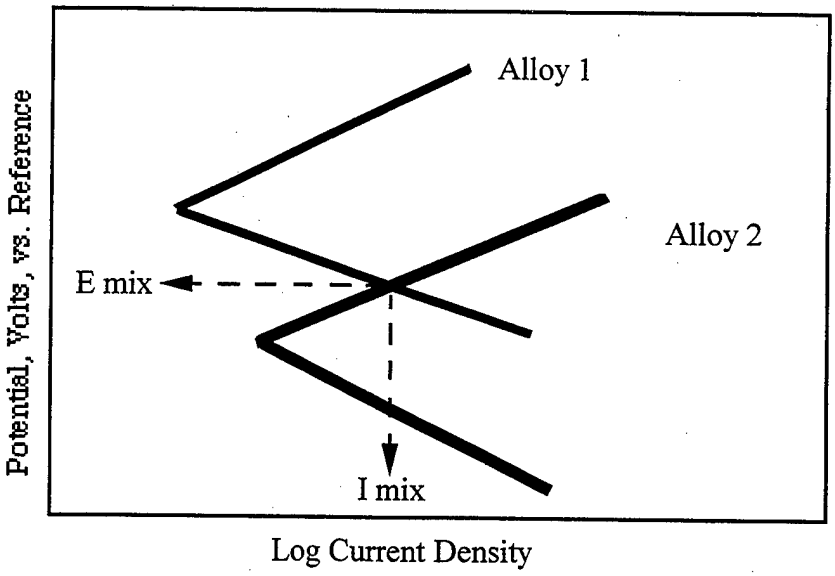


Figure 4. Schematic illustrating the mixed potential theory. The combined system must equilibrate to a common potential and common current density when the specimens are electrically connected. The common (mixed) potential is desginated E_m, and the current density obtained is I_m.

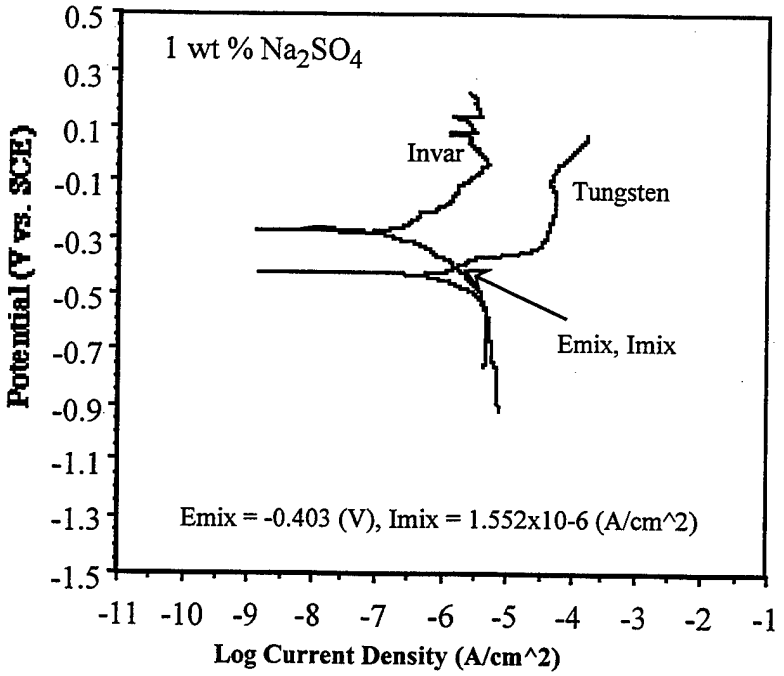


Figure 5a. Potentiodynamic scans and mixed potentials of Tungsten and Invar.

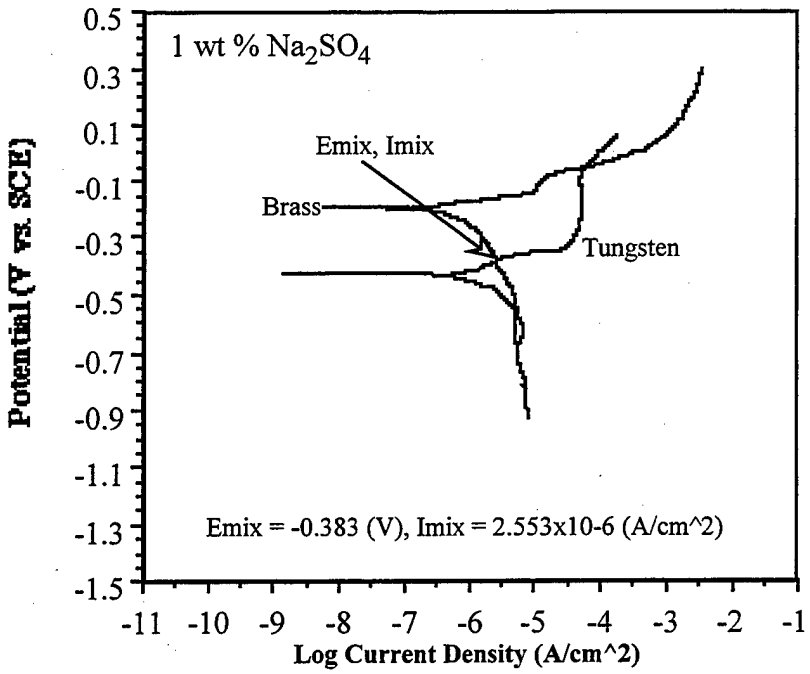


Figure 5b. Potentiodynamic scans and mixed potentials of Tungsten and Brass.

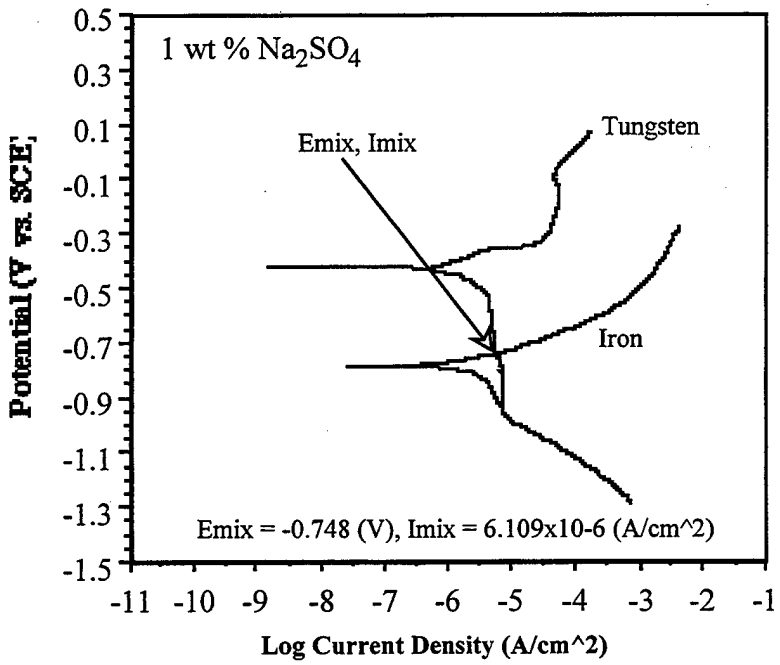


Figure 5c. Potentiodynamic scans and mixed potentials of Tungsten and Iron

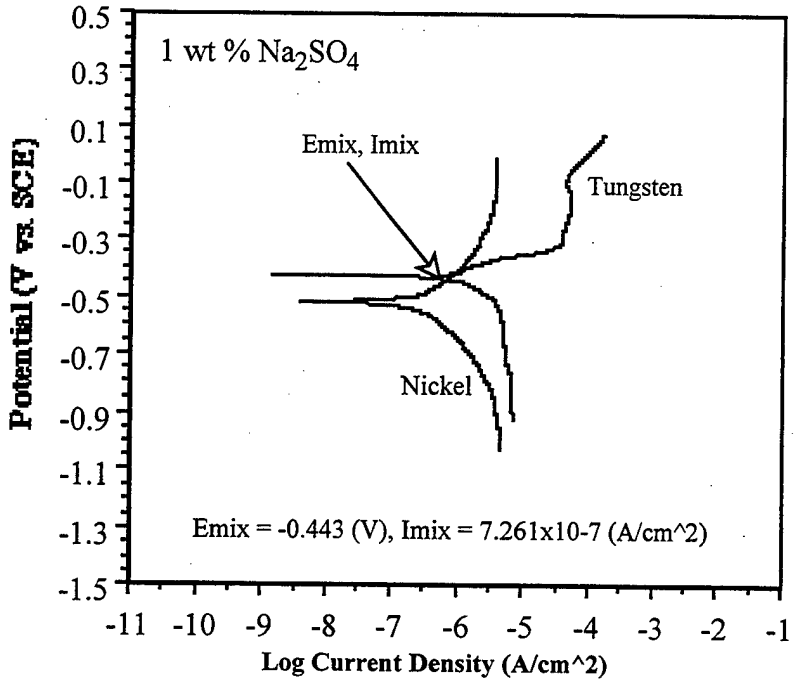


Figure 5d. Potentiodynamic scans and mixed potentials of Tungsten and Nickel.

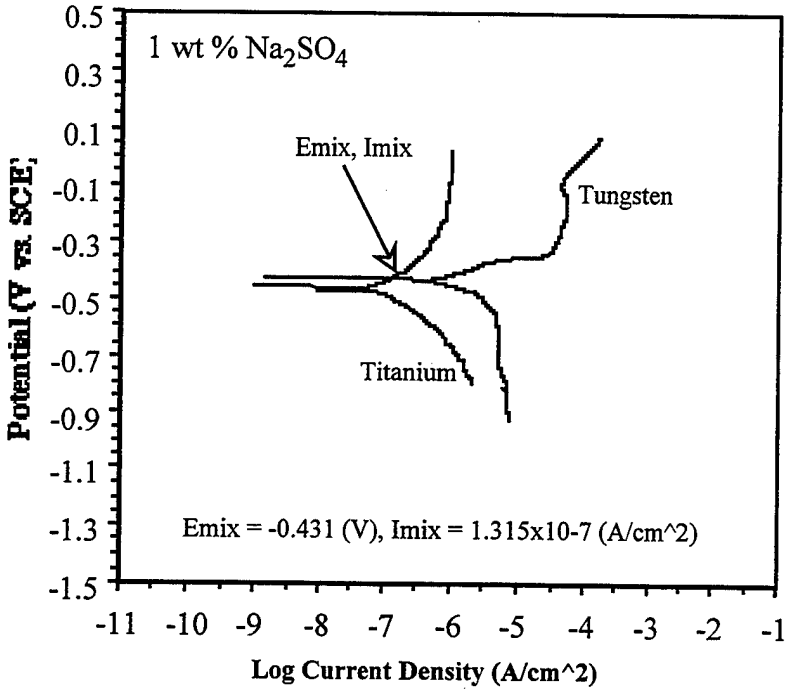


Figure 5e. Potentiodynamic scans and mixed potentials of Tungsten and Titanium.

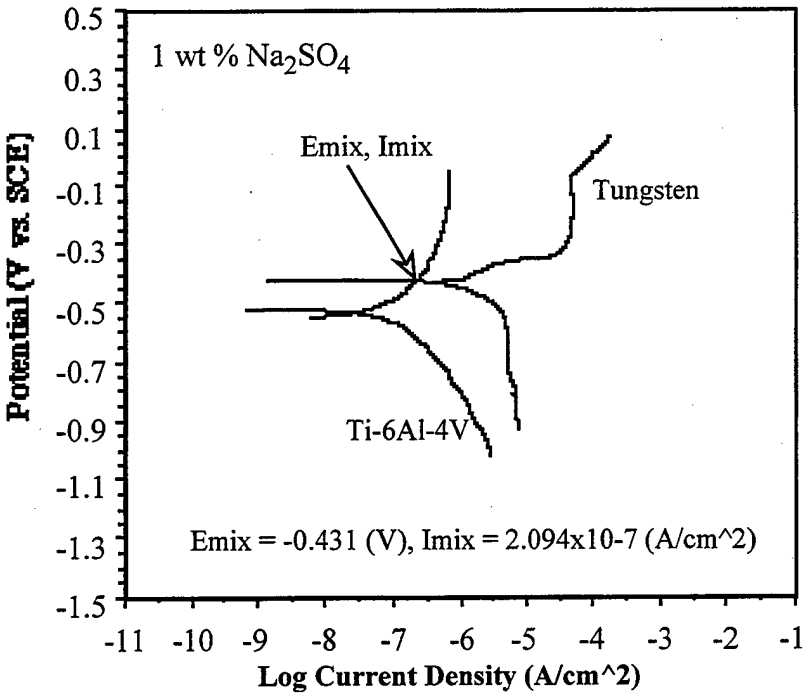


Figure 5f. Potentiodynamic scans and mixed potentials of Tungsten and Ti-6Al-4V.

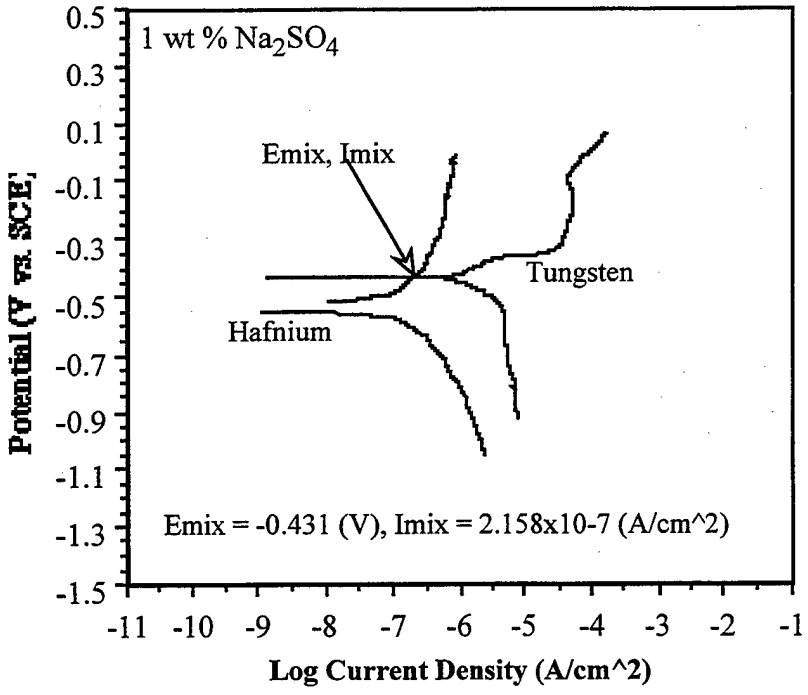


Figure 5g. Potentiodynamic scans and mixed potentials of Tungsten and Hafnium.

Effect of Marine Biofilms on Galvanic Corrosion

J. P. LaFontaine and S. C. Dexter
College of Marine Studies
University of Delaware
Lewes, DE 19958

ABSTRACT

Galvanic corrosion of copper, 1018 steel, 3003 aluminum and zinc coupled in turn to cathodes of stainless steel alloy N08367 was tested with and without natural marine biofilms on the cathode surface. Weight losses were significantly higher, and corrosion currents were up to two decades higher with a biofilm on the cathode surface for anodes of copper, steel and aluminum, but there was no difference for zinc. Results indicate that biofilms increase the rate of galvanic corrosion, but they will not increase consumption of sacrificial anodes with potentials equal to, or more active than zinc.

INTRODUCTION

Galvanic corrosion is one of the most common and damaging forms of corrosion. It occurs when two dissimilar metals or alloys are in electrical contact in an electrolyte, resulting in accelerated corrosion of the more electrochemically active of the two metals. Controlling galvanic corrosion is of great economic importance in many industries. In seawater galvanic corrosion is a serious problem due to high conductivity, which allows large currents to flow. On the other hand, cathodic protection uses sacrificial anodes and the principles of galvanic coupling to protect structures from corrosion. Galvanic corrosion becomes a complex process in natural waters which support the growth of microscopic organisms into biofilms. Biofilms have been defined by Characklis and Marshall as consisting of "cells immobilized at a substratum and frequently embedded in an organic polymer matrix of microbial origin[1]." The mature biofilm is structurally heterogeneous with large cell clusters and interstitial voids[2]. Adjacent to the large cell clusters can be areas where the biofilm is very thin or non-existent. Lewandowski and co-workers have presented evidence that this structure facilitates complex mass transport of nutrients and bacterial metabolites within the biofilm[2]. The chemistry of the water in such biofilms can be dramatically different from that of bulk waters[3-6]. The effect of biofilms and the chemistry they create on metals or alloys in a galvanic couple is the subject of this paper.

The presence of a biofilm on a metal surface can create chemical conditions that are vastly different from those of the ambient environment[3]. A microbial film can act as a diffusion barrier as well as a source or sink for chemical species that are important to corrosion processes[3]. Factors which vary little in the open ocean such as pH, dissolved oxygen, peroxide, and the

heavy metals Mn and Fe, can vary dramatically at the metal-biofilm interface[2, 6-8]. One consequence of chemical changes at the metal-biofilm interface is a shift of the open circuit potential (OCP) of passive metals in the noble direction, a phenomenon known as ennoblement. Ennoblement of passive metals due to biofilms is a well documented phenomenon[9-13] that occurs at all salinities[14] on a range of metals and alloys including stainless steels, titanium and platinum[15].

The effect of biofilms on the cathodic half reactions may have varied effects on the rate of galvanic corrosion according to mixed potential theory. Work summarized by Scotto and Mollica[15, 16] revealed that the kinetics of the oxygen reduction reaction are increased on passive alloys in the presence of a biofilm. It has been suggested by Mollica[15] and Dexter[17] that this shift in the cathodic kinetics may have varying effects on the corrosion of the anodic member of a galvanic couple. In the schematic Evans diagram shown in Figure 1, hypothetical cathodic polarization curves of bare and biofilmed stainless steel are superimposed upon anodic curves of copper and zinc. Points A and B are the respective intersections that represent the potentials and current densities for bare stainless steel-copper and biofilmed stainless steel-copper couples. Likewise, points C and D are the potential and current density intersection points for bare stainless steel-zinc and biofilmed stainless steel-zinc couples. In this schematic diagram, the corrosion current densities of both anodic materials, copper and zinc are increased in the presence of a biofilm on the stainless steel cathode. The increase is much greater however, for copper, as can be seen by the distance between points A and B. In couples with active potentials such as zinc, the increased reduction activity at cathodic surfaces may increase pH as a result of accelerated production of hydroxile ion[17]. Such an increase in pH may result in decreased ennoblement due to the thermodynamic effect of pH on the reversible potential of the oxygen electrode. In addition the effect of increased pH, perhaps to values of 10 or higher, may be sufficient to interfere with the metabolism of bacteria in the biofilm[18].

The purpose of the work reported in this paper was to determine: 1) the effect an increase in cathodic kinetics due to biofilms will have on the corrosion current in a series of galvanic couples with a range of couple potentials and 2) the implications of biofilm effects for control of galvanic corrosion in natural aqueous environments and cathodic protection using sacrificial anodes.

EXPERIMENTAL TECHNIQUES

In order to study the influence of biofilms on galvanic corrosion, the material used as the cathode member of the galvanic couple had to be passive in seawater, and it had to be resistant to initiation of localized corrosion during the initial biofilm forming immersion. For this purpose, stainless alloy NO8367 (AL-6XN) was selected, as it is widely used in commercial seawater applications. The nominal elemental composition of this alloy is shown in Table 1. Metals and alloys to be used as anodes were selected to represent both structural and anodic materials as well as a range of couple potentials. From the most noble to the most active, the anode metals and alloys selected were: copper, 1018 steel, 3003 aluminum and zinc. Their nominal elemental

compositions are also shown in Table 1. Copper and 3003 aluminum are used as structural materials, zinc is used as an anode material, and 1018 steel is used in both applications.

The cathode-to-anode (C/A) surface area ratio was set at 10:1 for all couples. The constant C/A ratio allowed for direct comparison of galvanic currents, and the 10:1 value insured that the generated galvanic current would be large enough to be measured. The NO8367 alloy was donated by Allegheny Ludlum Steel Corp., Brackenridge, PA. The stock alloy was cold rolled, annealed, pickled and shear cut into 35 cm square (12 by 12 inch) sheets of 0.2 cm thickness before shipment. Cathode coupons were then shear cut from these panels to dimensions of 10.12 by 15.2 cm (4 by 6 inches), degreased with acetone, rinsed with ethanol and finally deionized water. The alloy was used in the as received, cold rolled surface condition.

Nickel-chromium thermocouple wire was used as the electrical lead material for both cathodes and anodes. Two leads were spot welded to the top of each cathode coupon, and all junctions as well as the immersed portion of the leads were then coated with marine epoxy. Coating the area where the lead joined the coupon was necessary to avoid galvanic corrosion at the contact. It also allowed the entire coupon to be immersed, which avoided an air-water interface on the sample. Such an interface would possibly allow crevice corrosion to initiate, as well as surface area aberrations when the water level fluctuated in the tank.

Anode coupons of copper, 3003 aluminum, and 1018 steel were cut from 0.3 cm thick sheets using a band saw to rectangular dimensions of 7.2 cm by 2.5 cm. These coupons included an additional flag pole shaped stem to which the electrical lead was attached through a drilled hole, and by which the sample was suspended. Coupons were polished to 320 grit using silicon carbide metallurgical paper, and the entire stem with electrical lead contact area was coated with marine epoxy. Zinc samples were cut from mil. spec. zinc sacrificial anodes and milled to specification. Threaded holes were tapped into the top of the zinc samples for stainless steel screws to which electrical leads were attached, and the entire contact area was covered with marine epoxy. Special care was taken to make sure none of the stainless steel screw was exposed. All anode coupons were degreased with acetone, rinsed with ethanol, and deionized water, then dried in a dessicator prior to use.

Galvanic couples were immersed in seawater at the Shellfish Laboratory of the University of Delaware, located at Roosevelt inlet on Lower Delaware Bay. In this facility, once-through raw seawater from the inlet was continuously pumped directly into a settling tank to remove the larger particulates. It then flowed through a 250 micrometer mesh screen to prevent the larvae of macrofouling organisms from entering the immersion area, and into the tank in which the galvanic couples were exposed. The exposure tank had a capacity of 160 liters, and the water was nominally quiescent with an average flow velocity of approximately 0.1 cm/sec.

To observe the effect of the biofilm on galvanic corrosion, NO8367 cathodes were pre-immersed for 4 weeks and ennobled to approximately +320 mV SCE before coupling to the anodes. Couples in which the cathode was ennobled by biofilms will be referred to as "biofilmed

couples". Four biofilmed couples were made for each type of anode material by connecting the leads from the appropriate anodes and cathodes using an insulated copper wire with alligator clips. Both anodes and cathodes were immersed edge on into the flow of the water with a cathode-to-anode separation distance of 7.5 cm. This orientation exposed both sides of all samples to similar water flow. Three control couples without biofilms were also immersed for each anode material. The cathodes of these couples were changed daily to minimize biofilm formation and ennoblement. The procedure for changing the control cathodes was to immerse a clean cathode next to the one which was to be changed. The new cathode was immersed for at least an hour to allow for acclimation and equilibration with the seawater. Then the new, clean cathode was connected to the control anode and the old cathode was quickly disconnected. The momentary connection to two cathodes caused only a brief spike in the corrosion current.

Galvanic currents for each couple were measured daily for the first 4 weeks, then every other day for the rest of the immersion period. Currents were measured using a Thurston-Bell AM 1000 zero resistance ammeter. Due to the large number of couples, currents were not measured continuously. Currents were measured by attaching the leads of the ammeter to the cathode and anode of each couple, then removing the wire connection between the two couple members. After the reading, the connection was re-established before removing the ammeter leads, this procedure allowed the couple members to remain in electrical contact at all times. Statistical t-tests were performed to determine whether or not measured currents for the test couples with biofilms were significantly different from control using a P-value of 0.05. Open circuit and couple potentials were measured using a Beckman RMS 3060 digital multimeter with 22 megohm impedance. A total of 4 Fisher saturated calomel electrodes were used. Potential differences between electrodes were measured regularly, and only those which were within 10 mV of each other were used.

Dissolved oxygen, pH, salinity and temperature of the water were measured each day of the immersion tests. Dissolved oxygen measurements were done using the Winkler titration method. Water pH was measured to +/- 0.01 pH units using a hand held pH meter, which was calibrated immediately before each measurement using a series of buffers. Salinity was measured to +/- 0.1 psu using an optical salinometer, which needed no calibration but was tested for reliability each day by measuring freshwater.

Weight loss determinations were made on all anode coupons. Dessicator dried anodes were preweighed on a OHAUS model AP110S analytical electric balance before immersion, and before attachment of the electrical leads and epoxy. This scale had an accuracy of +/- 0.03 mg, and a precision of 0.02 mg. After the last current and potential measurements were made, electrical leads and epoxy were removed from the anodes and the corrosion products were removed as per NACE standards[19]. Copper anodes were cleaned in 20% HCl for 2-3 minutes at room temperature, followed by a light scrub. Steel anodes were cleaned in a boiling solution of 20% NaOH and 200 g/L for 5 minutes. Aluminum anodes were cleaned in 70 % HNO3 at room temperature followed by a light scrub. Zinc anodes were cleaned in saturated ammonium acetate at room temperature. All anodes were immediately dried in a desiccator for 48 hours, then

weighed on the electric balance. P-values were calculated to determine whether there were significant differences in weight loss between the test and control anodes for each couple type.

Corrosion behavior of galvanic couples was estimated through the use of potentio-dynamic polarization curves. A known area of the metal sample to be polarized was immersed in a standard one liter EG&G electrochemical cell. The set up included two platinum counter electrodes, and the reference electrode was a saturated calomel. Samples were polarized using a Princeton Applied Research Model 273A Potentiostat controlled by 352 PARC software. Scan rate for both anode and cathode curves was 0.1667 mV/second[20]. At least 5 samples of each material were polarized in the same untreated seawater as used for the immersion tests. An additional 5 clean, NO8367 coupons were used to predict the behavior of the control cathode. These latter coupons were polarized in sea water filtered through 0.2 micron mesh filter paper to minimize biofilm effects.

Biofilms were characterized using epifluorescence microscopy. Samples were rinsed in 0.2 μm filtered seawater, then immersed in 4% glutaraldehyde for 30 seconds. The DNA of the organisms in the biofilm was then stained with 0.1 mg/ml, 4,6-diamidino-2-phenyl-indole (DAPI)[21]. The population density of the bacteria in the biofilm was estimated by counting at 400 to 1000X using a Nikon epifluorescence microscope[22].

RESULTS AND DISCUSSION

Water temperature ranged from 29° C in late July to 16° C in November, while decreasing steadily throughout the immersion period. Dissolved oxygen concentration of the seawater ranged from 121 mmol/L in late July to 275 mmol/L in November. The pH of the seawater ranged from 6.9 to 7.8, and salinity from 18 to 32 psu. The NO8367 stainless steel coupons used as cathodes began with open circuit potentials between -210 and -190 mV SCE 1 hour after immersion. The potentials of all cathode coupons shifted in the electropositive direction to approximately +320 mV vs. SCE (as shown in Figure 2) prior to coupling with anode coupons.

Analysis by epifluorescence microscopy revealed these surfaces after immersion for 8 to 9 weeks to be covered with a heterogeneous biofilm, consisting of various protists and diatoms as well as bacteria. Areas of uniform bacterial distribution accounted for the large majority of the biofilm, and it was in these areas that bacterial counts were made. Coccoidal, rod and spirilla shaped bacteria were all identified in these areas. Other areas with large microbial colonies were also observed. Thus, population densities between 2.4×10^6 and 1.7×10^7 bacteria/cm^2 based on the uniformly distributed areas were probably underestimates. These biofilms are similar to those characterized by Zhang[23] and Chandrasekaran[6] formed on stainless steel and platinum coupons in seawater from the same source.

Of all the anodic materials used in this study, copper produced the greatest differences in corrosion currents between couples with biofilms on the cathode and those without biofilms (control). As shown in Figure 3, corrosion currents for all couples decreased steadily as corrosion

product films built up. During the first 10-12 days corrosion currents were highly variable as the couples equilibrated with the seawater. Average corrosion currents shown in Table 2 were calculated for the period from day 12 to day 60. They were 2 to 3 decades higher for copper couples with biofilms on the cathode than those for the corresponding control couples. Statistical t-tests were performed for data on days 12, 19, 27 and 60. These differences for the copper couples were all significant, with the P-values being 2.23×10^{-4}, 1.00×10^{-2}, 4.23×10^{-3}, and 3.00×10^{-3}, respectively. Weight losses on copper anodes coupled to biofilmed NO8367 were also significantly higher (P-value 6.55×10^{-3}) than those observed on control coupons (Table 2). Copper anodes coupled to biofilmed cathodes were visibly more corroded than those coupled to control cathodes. The corrosion products of the copper anodes in this study were layered, with a tightly adherent red layer at the metal surface. Over this was a black layer, and finally on top, a loose green layer. These corrosion products were not analysed, but they agree with descriptions of corrosion products in the literature. Polan[24] and Zuhmdahl[25] reported that the loose green layer on top was $CuCl_2.2H_2O$, the intermediate black layer was CuO, and the innermost red layer was Cu_2O.

After copper, structural steel is the next most noble material of the five used as anodes in this study. Significant differences in corrosion current developed between biofilmed and control couples after the first 10-12 days of immersion (Figure 4). P-values for corrosion currents on days 12, 19, 27, and 60 were 1.80×10^{-3}, 2.08×10^{-5}, 1.0×10^{-2}, and 3.90×10^{-4} respectively. Average corrosion currents for biofilmed couples ranged from 4.26 to 5.00 mA, compared to those of control couples, which ranged from 0.835 to 0.890 mA (Table 3). Corrosion potentials for biofilmed couples were on the average 30 mV more noble than those for control couples (Table 3). Weight losses on the 1018 steel coupons coupled to biofilmed cathodes were approximately 5 times higher than those found on 1018 steel coupons coupled to control cathodes (Table 3), and these differences were significant with $P = 1.26 \times 10^{-4}$. The difference was also confirmed by visual inspection of the test and control coupons.

The galvanic behavior of 3003 aluminum was similar in many ways to that of 1018 steel. The corrosion current for both biofilmed and control couples was most variable during the first 12 days of exposure (Figure 5). Average corrosion currents for biofilmed couples from day 12 on, ranged from 4.90 to 5.36 mA (Table 4), while control currents ranged from 1.04 to 1.23 mA. These differences were significant with P-values of 2.14×10^{-4}, 4.17×10^{-4} 5.27×10^{-5}, and 4.93×10^{-5} on days 12, 19, 27, and 60 respectively. The corrosion potentials for all couples were quite steady during the immersion study for both biofilm and control couples. Weight loss from 3003 aluminum coupled to biofilmed cathodes at 3.71 to 4.63 grams was significantly higher than control at 0.686 to 0.727 grams (Table 4) with a P-value of 4.17×10^{-5}.

Corrosion currents for all zinc couples, both biofilmed and control, were similar (Figure 6). Average corrosion currents for all zinc couples were within the range of 5.62 to 6.16 mA (Table 5), and those for biofilmed couples were not significantly different than control. The zinc coupon from biofilm couple 2 had to be replaced early in the immersion study. The electrical lead to the anode suffered water ingestion, which resulted in a dramatic increase in potential of

the couple. Weight loss values for all zinc coupons ranged from 6.21 to 6.85 grams, with the exception being the zinc coupon from biofilm couple 2 (3.94 grams) (Table 5). This zinc coupon was a replacement for the original, hence it was not exposed as long as coupons from the other couples. The P-value of 0.33 showed that there were no significant weight loss differences. There were also no visible differences in corrosion damage between samples from biofilmed and control couples.

The polarization curves measured[26, 27] for corroded anodes and biofilmed cathodes are shown in Figure 7. At potentials more noble than approximately -900 mV, the curves for all biofilmed NO8367 coupons were shifted to the right vs. control. This shift was most severe at potentials more noble than -250 mV. The increase in the limiting current on biofilmed coupons between -300 and -900 mV is significant, with P-values for the t-tests being below 3.0×10^{-5} at potentials of -400 and -700 mV SCE. The increase in current at these potentials as a result of the presence of a biofilm correlates well with the measured increases in galvanic currents and weight losses for the steel and aluminum anodes. However, that increase in limiting current is not likely due to an increase in oxygen transport to the metal surface. If anything, the biofilm would act as an additional physical barrier to oxygen diffusion. Dickinson and Lewandowski found numerous Mn rich deposits on stainless steel coupons ennobled by biofilms[28]. In abiotic experiments with MnO_2 on clean coupons they found almost identical electrochemical effects as found on naturally biofilmed coupons. Chandrasekaran also found elevated levels of Fe and Mn in biofilms from Lower Delaware Bay waters[6]. Thus, reduction of Mn as well as other heavy metals may be responsible for the increase in the limiting current. The increase in cathodic reduction kinetics due to the presence of a biofilm was found to diminish at potentials more active than approximately -900 mV vs. SCE. At these active potentials, pH at the metal-biofilm interface may increase resulting from increased production of OH^- from oxygen reduction as well as hydrogen evolution[29]. An increase in pH to above 9 at the metal-biofilm interface would inactivate most marine microorganisms[30].

The implications of biofilm effects for control of galvanic corrosion in natural aqueous environments or for cathodic protection by sacrificial anodes are dependent on the situation. Microbial films form on virtually all metal surfaces in natural waters. If the cathodic surface is well coated, however, biofilm effects on the cathodic properties of the metal will be negated. If the passive metal surface is not coated, the effect of a biofilm will be determined by the mixed potential of the couple. For couples with mixed potentials more noble than about -850 mV SCE, the data presented here indicate that corrosion of the anodic member of the couple will be increased due to the action of biofilms. The data also indicate that biofilms will increase the current necessary to protect stainless steel from pitting at a potential of -400 mV SCE, and that they will increase the consumption of the steel anodes often used for that purpose. For couples with anodes of zinc, or a more active material, however, our data indicate that the mixed potential should be active enough for there to be no increase in anode consumption. The practice of keeping surfaces clean is certainly reinforced by the results of this study. Allowing corrosion resistant alloy surfaces to foul may lead to an increased corrosion rate on an adjacent metal which is in galvanic contact.

SUMMARY OF CONCLUSIONS

Biofilms on passive alloys used as the cathodic member of galvanic couples in seawater increased the corrosion rate of the anode as compared to controls with clean cathodes. The effect, as measured by both corrosion current and weight loss, was largest on copper, which had the most noble couple potential, and it was still significant on steel and aluminum with intermediate couple potentials. In any case where biofilms on the cathodic member of a galvanic couple result in a systematic and significant increase in the reduction current at the mixed potential of the couple, an increase in consumption of the anode should be expected. Corrosion current and weight loss for biofilmed zinc couples were not significantly different than control. Thus, increased consumption of sacrificial anodes with potentials more active than zinc would not be expected due to biofilms.

ACKNOWLEDGMENTS

This work was supported by the Office of Naval Research under Contract Nos. N00014-94-1-0209 and N00014-95-1-0810.

REFERENCES

1. Characklis, W.G., Marshall, K.C., Biofilms, John Wiley & Sons Inc., 1990.
2. Lewandowski, Z., P. Stoodley and F. Roe, "Internal mass transport in heterogeneous biofilms," Corrosion/95, Paper No. 222, NACE International, Houston, TX.
3. Dexter, S.C., Biofouling, Vol 7, 1993, pp. 97-127.
4. Dexter, S.C. "Effect of biofilms on marine corrosion of passive alloys," In: Bioextraction and Biodeterioration of Metals, C.C. Gaylarde and H.A. Videla, eds., Cambridge Univ. Press, 1995, pp. 129-168.
5. Lewandowski, Z., F. Roe, T. Funk, and D. Chen, "Chemistry near microbially colonized metal surfaces," Proc. 2nd USA/Argentina Workshop on Biocorrosion and Biofouling, Buckman Laboratories International, Inc., Memphis, TN, 1993, pp. 52-61.
6. Chandrasekaran P., "Mechanism of Potential ennoblement on Passive Metals Due to Biofilms in Seawater," Doctoral Dissertation, University of Delaware, 1995.
7. Pope, D.H., T.P. Zintel, A.K. Kuruvilla and O.W. Siebert, "Organic acid corrosion of carbon steel," Corrosion/88, Paper No. 79, NACE International, Houston, TX.
8. Xu, K., S.C. Dexter and G.W. Luther, "Development of Voltammetric Microelectrodes for use in Corrosion Studies," Corrosion/97, Paper No. 300, NACE, International, Houston, TX.
9. Mollica A. and A. Trevis, "Correlation Entre La Formation de la Pellicule Primaire et la Mod. de la Cathodique sur des Aciers In oxydables Experinmentes en Eau de Mer aux Vitesses de 0,3 a 5,2 m/s," Proc 4th Intl. Cong. on Marine Cor. and Fouling, 1976, p. 351.
10. Scotto, V., R. DiCintio and G. Marcenaro, Corrosion Science, Vol. 25, No.3, 1985, p. 185.
11. Johnsen R. and E. Bardal, Corrosion, Vol 41, 1985, pp. 296-304.
12. Dexter S.C. and G.Y. Gao, Corrosion ,Vol 44, 1988, pp. 717-723.
13. Motoda, S., Y. Suzuki, T. Shinohara and S. Tsujikawa. Corrosion Sci., Vol. 31, 1990, p. 515.

14. Dexter, S.C. and H.J. Zhang, "Effect of biofilms on corrosion potential of stainless alloys in estuarine waters," Proc 11th Int. Cor. Congr, Florence Italy, 1990, pp. 4.333-4.340.
15. Mollica A., G. Ventura, E. Traverso and V. Scotto, "Cathodic Behavior of Nickel and Titanium in Natural Seawater," 7th Intl. Biodeterioration Symp., Cambridge, UK, 1987.
16. Scotto, V. "Electrochemical Studies on Biocorrosion of Stainless Steel in Seawater," EPRI Workshop on Microbial Induced Corrosion, G. Licina, ed., Electric Power Research Institute, Palo Alto, CA., 1989, pp. B.1-B.36.
17. Dexter, S. C., P. Chandrasekaran, H-J. Zhang and S. Wood, "Microbial Corrosion in Marine Environments: Effect of Micro-fouling Organisms on Corrosion of Passive Metals", Proc. 2nd USA/Argentina Workshop on Biocorrosion and Biofouling, Buckman Laboratories International, Inc., Memphis, TN, 1993, pp. 171-180.
18. Morel, F.M.M. and B. Palenik, "The aquatic chemistry of trace metals in biofilms," In: Structure and Function of Biofilms, W.G. Charaklis and P.A. Wilderer, eds., John-Wiley and Sons, 1989, pp. 289-300.
19. "Laboratory Corrosion Testing of Metals for the Process Industries," NACE Standard TM-01-69, NACE International, Houston, TX, 1976.
20. "Polarization Practice for Standard Reference Method for Making Potentiostatic and Potentiodynamic Anodic Polarization Measurements," ASTM Standard G 5, Amer. Soc. for Testing and Materials, Philadelphia, PA, 1982.
21. Fry, J.C., "Determination of Biomass," Methods in Aquatic Bacteriology, B. Austin, ed. John Wiley, 1988.
22. Kirchman, D., J. Sigda, R. Kapuscinski and R. Mitchell, Appl. and Env. Microbiol., Vol 44, 1982, pp. 376-382.
23. Zhang, H-J., "The Effect of Biofilms on Localized Corrosion of Stainless Alloys," Ph.D. Dissertation, University of Delaware, 1993.
24. Polan, N. W., Metals Handbook, 9th ed., 1987, Vol. 13, Corrosion, ASM, International, Metals Park, OH, p. 610.
25. Zuhmdahl, S.S., Chemistry. 2nd edition. D.C. Heath and Company, Lexington, MA, 1989.
26. Hack, H.P., "Galvanic Corrosion Prediction Using Long-Term Potentiostatic Polarization Curves," Corrosion/83, Paper No. 2, NACE International, Houston, TX.
27. Hack, H.P. and J.R. Scully. Corrosion, Vol. 42, No 2, 1986, p. 79.
28. Dickinson, W.H. and Z. Lewandowski, Biofouling, Vol.10, No. 1-3, 1996, pp. 79-94.
29. Dexter, S.C. and S.H. Lin, Corrosion, Vol. 48, No. 1, 1992, pp. 50-60.
30. Langworthy, T.A., "Microbial Life at Extreme pH Values," in: Microbial Life in Extreme Environments, E.J Kushner, ed., Academic Press, New York, 1978, p. 279.

Table 1. Nominal compositions (% by Weight) of metals and alloys used in this study.

Metal	Cr	Ni	Mo	Zn	Cu	Si	Mn	Fe	Al
NO8367	20.44	23.84	6.24		0.14	0.39	0.20	Bal	
Copper					99.90				
1018 steel	3.10		1.30			0.20	0.50	Bal	
3003 aluminum					0.20	0.6	1.5		Bal
zinc				99.9					

Table 2. Corrosion data, including standard deviations, for NO8367-copper couples immersed in Lower Delaware Bay Seawater. Average corrosion currents were taken from day 22 to day 60.

COUPLE	AVERAGE CORROSION CURRENT (mA)	AVERAGE CORROSION POTENTIAL (mV vs. SCE)	WEIGHT LOSS (grams)
Biofilm 1	**0.78 +/- 0.38**	**-135 +/- 39.6**	**6.39**
Biofilm 2	**0.57 +/- 0.40**	**-155 +/- 46.4**	**3.84**
Biofilm 3	**1.11 +/- 0.48**	**-11.1 +/- 83.4**	**5.75**
Biofilm 4	**0.95 +/- 0.40**	**-9.83 +/- 77.5**	**4.67**
Control 1	**0.0025 +/-0.0027**	**-145 +/-70.6**	**2.10**
Control 2	**0.0016 +/- 0.0017**	**-129 +/-88.8**	**1.93**
Control 3	**0.0020 +/-0.0013**	**-145 +/- 74.2**	**2.37**

Table 3. Corrosion data, including standard deviations, for both biofilmed and control NO8367 stainless steel-1018 steel couples immersed in Lower Delaware Bay Seawater. Average corrosion currents were taken from day 12 onward.

COUPLE	AVERAGE CORROSION CURRENT (mA)	AVERAGE CORROSION POTENTIAL (mV vs. SCE)	WEIGHT LOSS (grams)
Biofilm 1	4.26 +/- 0.92	-700 +/- 26.5	9.7
Biofilm 2	5.00 +/- 1.3	-699 +/- 33.9	10.8
Biofilm 3	4.54 +/- 1.1	-698 +/- 21.8	9.2
Control 1	0.875 +/- 0.44	-733 +/- 29.7	2.1
Control 2	0.835 +/- 0.38	-735 +/- 31.9	1.9
Control 3	0.890 +/- 0.35	-732 +/- 32.6	2.6

Table 4. Corrosion data, including standard deviation, for biofilmed and control NO8367 stainless steel-3003 aluminum couples immersed in Lower Delaware Bay Seawater. Average corrosion currents taken from day 12 onward.

COUPLE	AVERAGE CORROSION CURRENT (mA)	AVERAGE CORROSION POTENTIAL (mV vs. SCE)	WEIGHT LOSS (grams)
Biofilm 1	5.06 +/- 1.1	-732 +/-41.4	3.85
Biofilm 2	4.90 +/- 1.1	-727 +/- 32.1	3.71
Biofilm 3	4.95 +/- 1.3	-730 +/-36.4	3.87
Biofilm 4	5.36 +/- 1.1	-729 +/- 29.2	4.63
Control 1	1.04 +/- 0.51	-742 +/- 45.5	0.69
Control 2	1.17 +/- 0.41	-740 +/- 36.9	0.70
Control 3	1.23 +/- 0.54	-740 +/- 40.4	0.73

Table 5. Corrosion data, including standard deviations, for both biofilmed and control NO8367 stainless steel-zinc couples immersed in Lower Delaware Bay Seawater. Average corrosion current was taken from day 12 onward.

COUPLE	AVERAGE CORROSION CURRENT (mA)	AVERAGE CORROSION POTENTIAL (mV vs. SCE)	WEIGHT LOSS (grams)
Biofilm 1	5.62 +/- 1.44	-1.043 +/- 33.3	6.39
Biofilm 2	6.16 +/- 1.08	-1038 +/- 27.9	3.94
Biofilm 3	5.64 +/- 1.13	-1038 +/- 23.0	6.67
Biofilm 4	6.05 +/- 0.92	-1038 +/- 54.0	6.21
Control 1	6.75 +/- 1.72	-1017 +/- 42.7	6.44
Control 2	6.34 +/- 1.34	-1017 +/- 50.7	6.76
Control 3	6.50 +/- 1.15	-1013 +/- 54.8	6.85

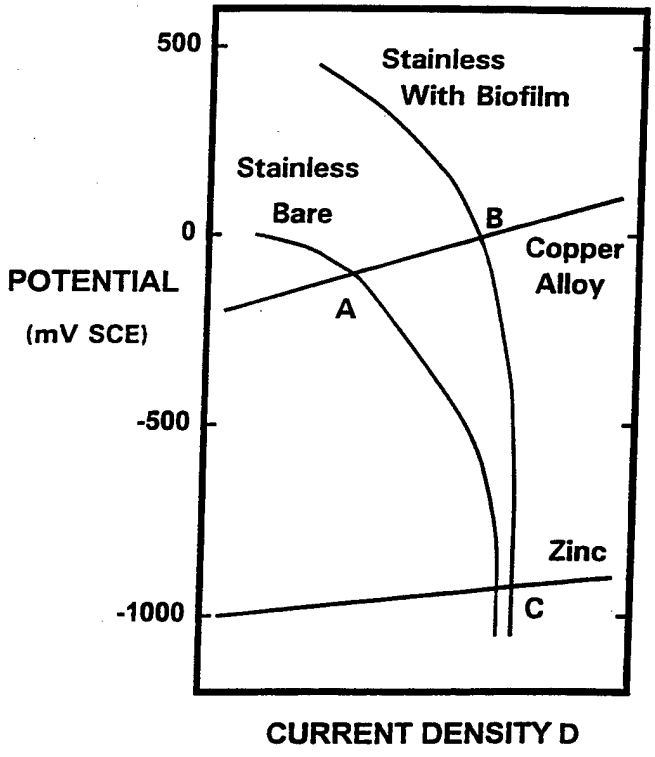


Figure 1. Schematic diagram of cathodic polarization curves for stainless steel with and without biofilms, along with anodic polarization curves for copper and zinc. The intersections at "A," "B" and "C" determine the galvanic corrosion rates.

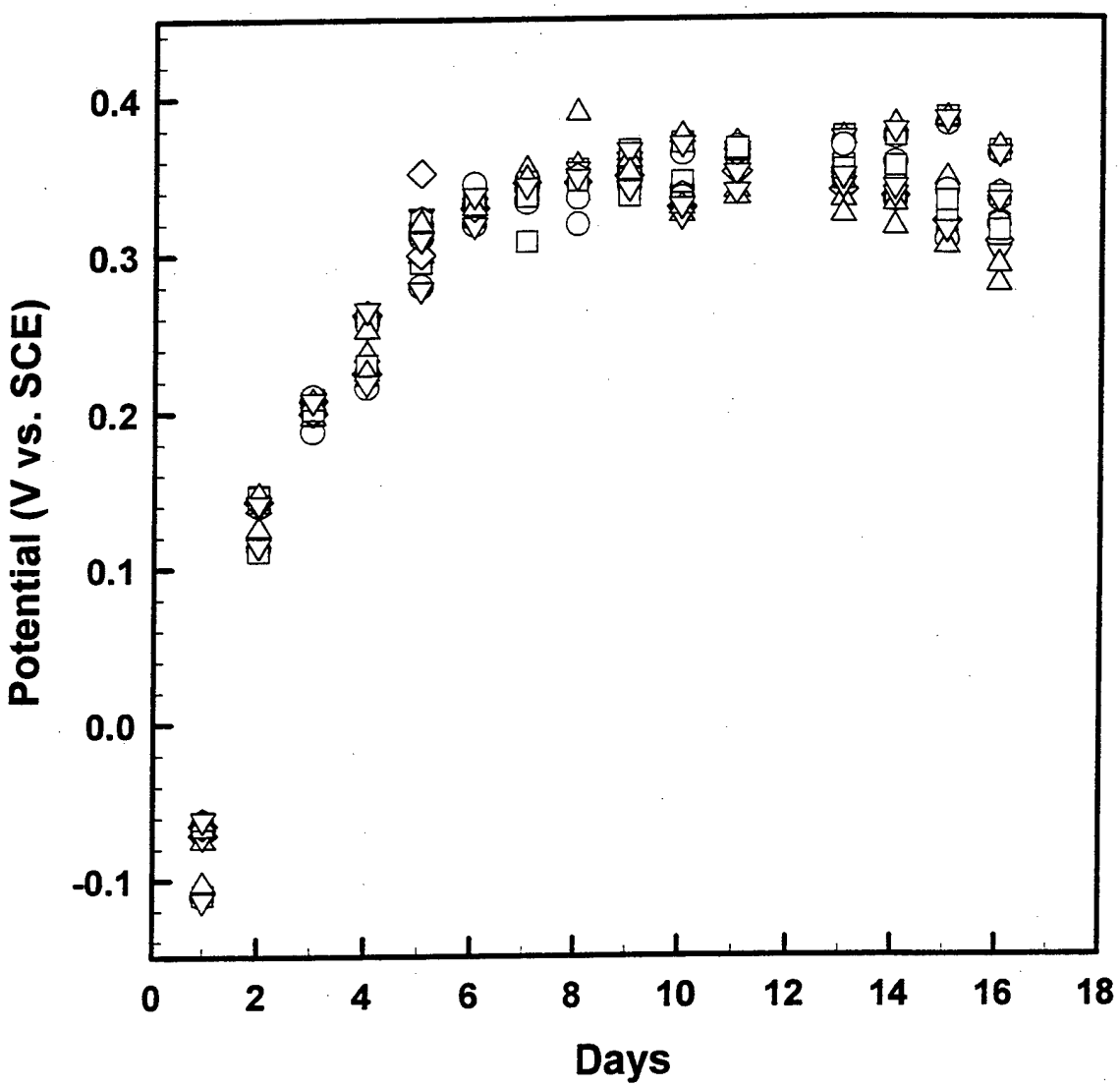


Figure 2. Ennoblement of the open circuit potential of alloy NO8367 cathode panels in Lower Delaware Bay seawater.

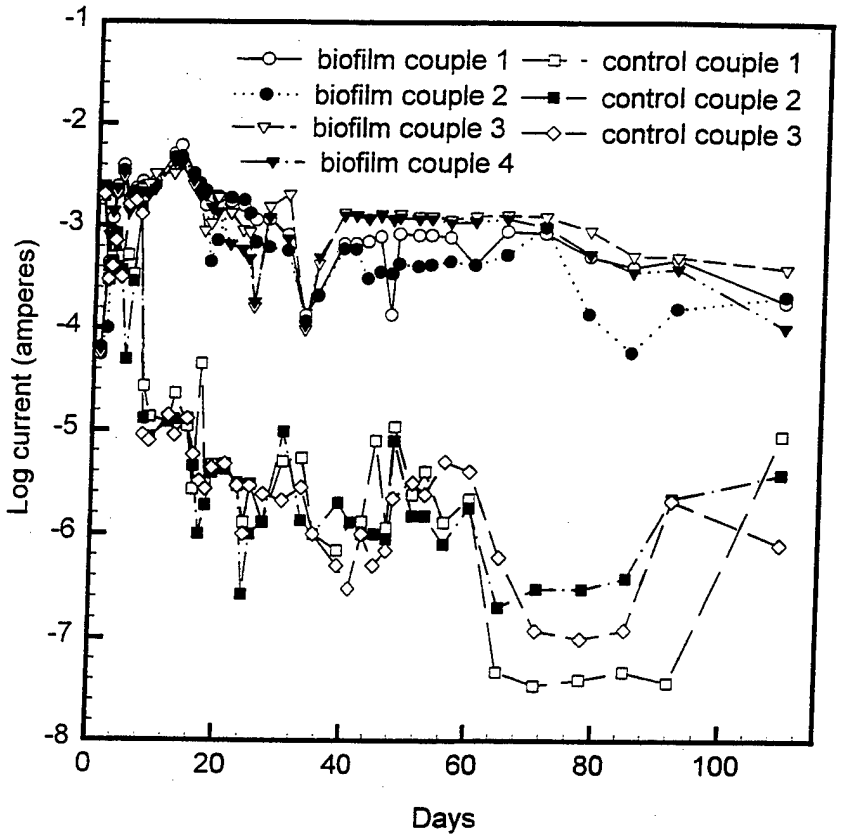


Figure 3. Corrosion currents for galvanic couples of alloy NO8367 vs. copper.

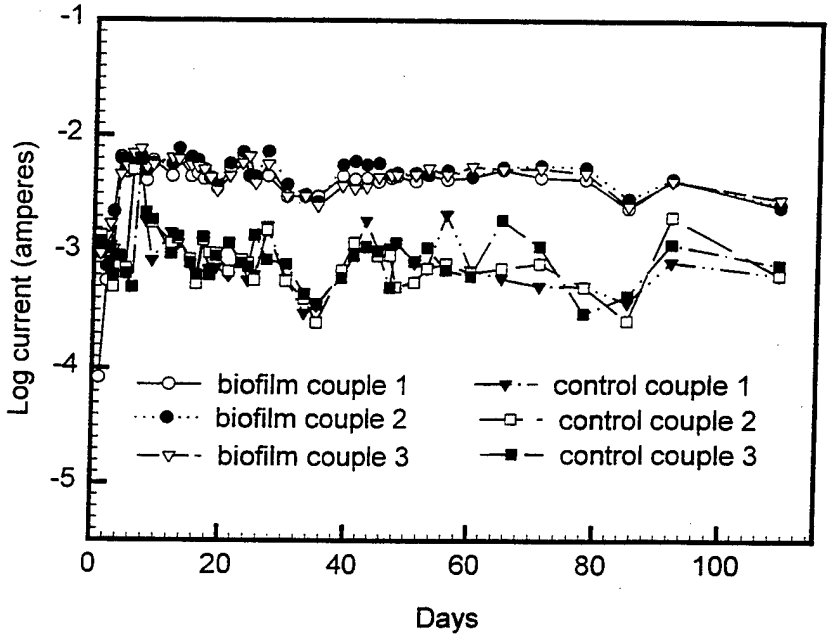


Figure 4. Corrosion currents for galvanic couples of alloy NO8367 vs. 1018 steel.

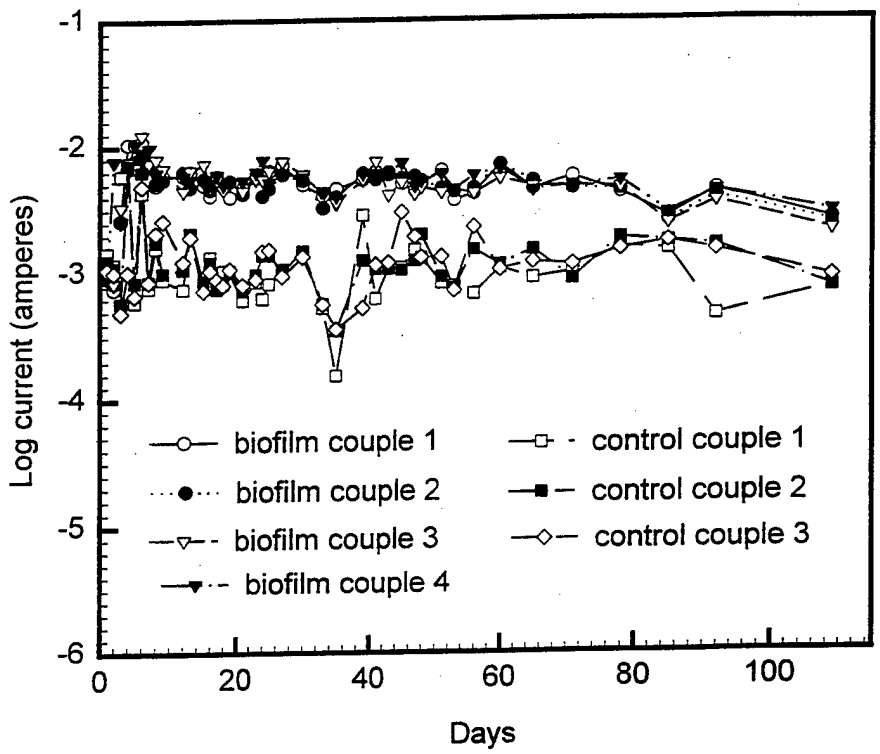


Figure 5. Corrosion currents for galvanic couples of alloy NO8367 vs. 3003 aluminum.

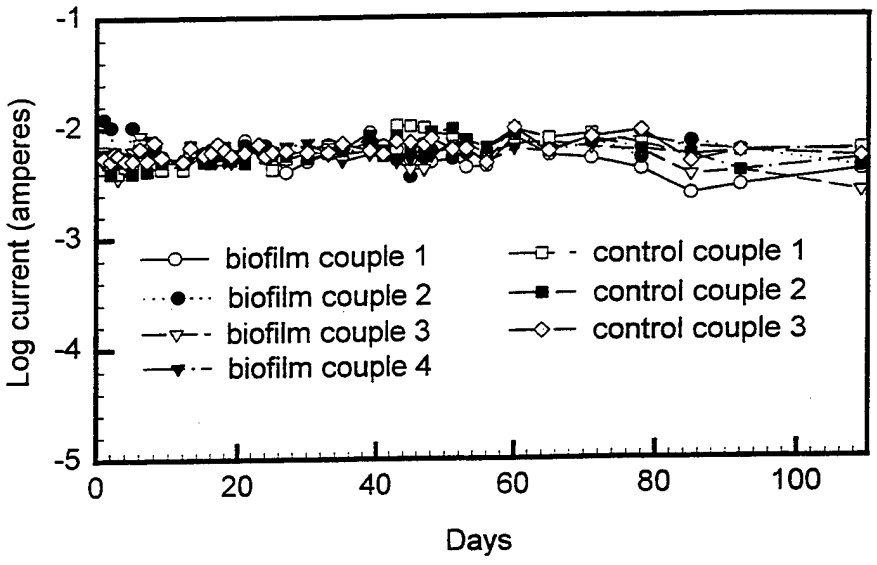


Figure 6. Corrosion currents for galvanic couples of alloy NO8367 vs. zinc.

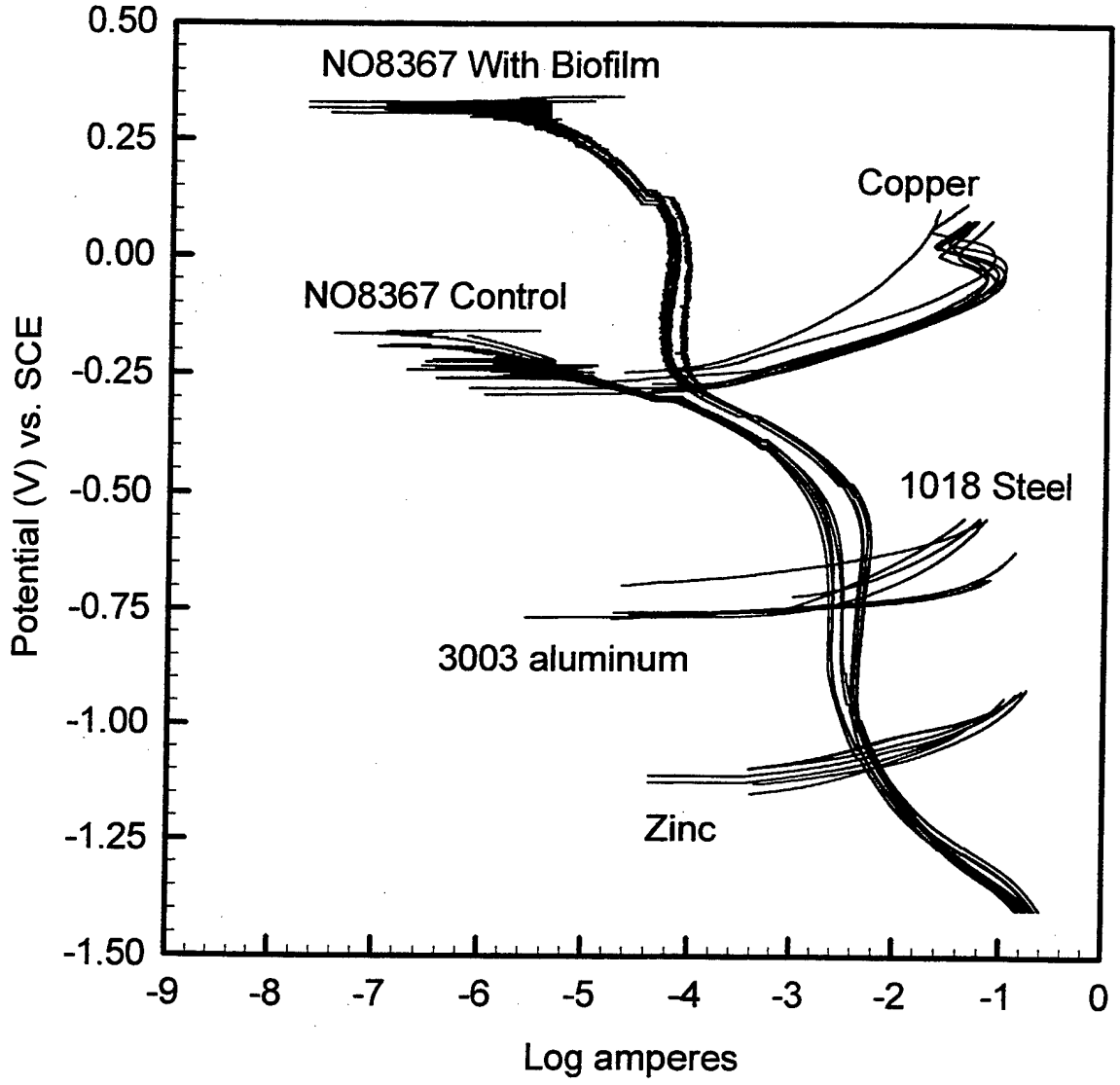


Figure 7. Cathodic polarization curves for alloy NO8367 stainless steel with and without (control) biofilms together with anodic polarization curves for copper, 1018 steel, 3003 aluminum and zinc in Lower Delaware Bay seawater. Anodic curves were taken from the corroded coupons at the end of the exposure period.

New Techniques for Galvanic Corrosion Prevention in Piping Systems

David A. Shifler
Carderock Division, Code 613
Naval Surface Warfare Center
9500 MacArthur Boulevard
West Bethesda, MD 20817-5700

Dennis Melton
LaQue Center for Corrosion Technology, Inc.
P. O. Box 656
Wrightsville Beach, NC 28480

Harvey P. Hack
Northrop Grumman Corporation
Oceanic Systems
P. O. Box 1488 - MS 9105
Annapolis, MD 21404

ABSTRACT

Mixtures of piping materials have been used in several piping systems during ship retrofitting . The use of dissimilar alloys may initiate galvanic corrosion of the more anodic member which could lead to piping failures. Several control methods have been applied which may introduce secondary corrosion and require periodic inspection and replacement. This study involved several newer galvanic corrosion control (cathodic protection, barrier coatings, bi-electrode) methods, which were used in mockup piping tests to monitor their effectiveness. These newer methods may provide alternative galvanic corrosion control techniques that may allow selective use of mixed piping systems with a minimization of shutdowns for removing, inspecting, and replacing system components.

INTRODUCTION

The coupling of dissimilar alloys in conducting, corrosive solutions such seawater can lead to accelerated corrosion of the more anodic alloy and protection of the more cathodic alloy. The extent of corrosion depends on factors such as the effective area ratio of the anodic and cathodic members of the galvanic couple, conductivity and flow characteristics of the solution, temperature, geometry, the difference in potential of the alloys, and the cathodic efficiency of the more noble metal or alloy [1, 2].

An earlier study for up to 2 years was conducted to determine the long-term effects of coupling a titanium alloy to several common marine machinery and structural alloys in quiescent

and flowing seawater [3]. Copper alloys when coupled to a titanium alloy in both quiescent and flowing unpolluted seawater showed increased corrosion by factors of 2 to 20 with the possible exception of CA719 (70-30 Cu-Ni with 2.5% Cr addition) which exhibited borderline behavior under flowing conditions. Nickel-based alloys 625 (UNS N06625) and C-276 (UNS N10276) experienced no measurable pitting, either uncoupled or coupled to a titanium alloy under flowing or quiescent conditions. Galvanic relationships between different alloys may be altered in sulfide-polluted seawater. Copper-nickel alloys exposed to flowing sulfide-polluted seawater experienced increased pitting and accelerated corrosion [4, 5].

Use of dissimilar pipe alloys for cooling system piping on ships has the potential to cause corrosion at each change-of-material interface. Current ship design includes an inspection/waster piece at the most corrosion prone area of each interface. These waster pieces are thicker than normal gauge piping, are inspected periodically, and replaced when excessive corrosion has occurred. This process is expensive and requires shutdown of critical ship systems. The use of the present waster pieces creates the possibility of corrosion induced wall thinning in sub-safe systems. Galvanic isolation and electrically isolated separator pieces may not always be viable control methods due to the complexity or available space of the systems.

Alternative galvanic control methods that would eliminate the need for inspection, improve safety, and control corrosion in piping systems are being investigated. Mitigation of galvanic corrosion would provide ship designers with more piping material options within piping systems. Several possible candidate methods for controlling galvanic corrosion are: (1) formation of calcareous deposits on the cathodic member of the couple (alloy 625 or titanium); (2) use of a dielectric or metallic spacer placed between the cathodic to the anodic members of the couple; (3) cathodic protection applied to the more anodic member of the galvanic couple; and (4) use of a bi-electrode device between the anodic and cathodic piping members of the dissimilar alloy interface..

Use of rapid polarization has been routinely used for offshore structures in connection with cathodic protection systems to form calcareous deposits which act as a natural coating and protect the steel substrate through lower cathodic currents. The application of an initially high current density to steel has resulted in formation of very protective calcareous deposits in natural seawater [6-12] that required lower maintenance long-term current densities than when lower initial current densities were applied. An optimum potential of -1.00 V(SCE) provided adequate protection. While hydrogen is generated at potentials less than -0.7 V(SCE), the calcareous deposits may protect against hydrogen adsorption by titanium and form a barrier to galvanic corrosion by reducing the cathodic efficiency and/or cathode area of galvanic couples.

The use of cathodic protection has been used extensively in controlling corrosion in many environments. Galvanic corrosion is controlled by driving the potential of the more active member of the galvanic couple electronegatively into its cathodic region; this lowers the corrosion rate of the active alloy as well as the more noble alloy. A new, unique design for controlling galvanic corrosion involves using a ring anode and a ring cathode in a spool piece located between dissimilar pipes. An external power supply is used to adjust current in the bi-electrode device (from the anode to the cathode) to cancel the electric field gradients caused by the galvanic

potential difference between the piping materials, thereby reducing or eliminating galvanic corrosion between the piping materials. The bi-electrode also can be used as a cathodic protection device, by making both ring electrodes anodic relative to the surrounding piping.

THEORY OF OPERATION OF THE BI-ELECTRODE

The bi-electrode concept was created during discussions between Dr. John Beavers and Dr. H. P. Hack about a paper presented at Corrosion/95 [13] and a patent has applied for.

When two dissimilar metal pipes are electrically connected in seawater, the potential difference between them causes a galvanic current to flow through their connection. To maintain charge neutrality, an equal ionic current must flow through the seawater path that separates them. The flow of current through the slightly resistive seawater creates an IR drop between the anodic pipe and the cathodic pipe, resulting in a potential gradient between them in seawater.

A bi-electrode device (BED) is a pair of ring electrodes which is inserted between the anodic and cathodic pipes, and electrically isolated from both. The bi-electrode generates an potential gradient which counters the ionic current from the galvanic couple. By proper adjustment of the bi-electrode current, the total potential gradient between the anodic and cathodic pipes can be made equal to the difference in their freely corroding potentials. The anodic pipe is exposed to the potential of the cathodic pipe plus the bi-electrode-induced potential gradient, the sum of which has been adjusted to be the same as the anodic pipe's free corrosion potential. The anodic pipe will therefore not have any driving force for galvanic corrosion, as the cathodic pipe has been "screened" from it by the bi-electrode potential gradient.

The advantages of a bi-electrode are that it does not require that the anodic and cathodic pipes be mechanically separated to remove the electrical connection, it does not require a physical separation between anodic and cathodic pipes apart from that introduced by the presence of the bi-electrode itself, it does not "throw" current into the anodic or cathodic pipes and so does not have a limited area that it can protect, and it requires no electrical connection to the anodic or cathodic pipes themselves. The disadvantages of the bi-electrode are that it must be physically placed between the anodic and the cathodic pipes, it requires an external power supply, and it will cause corrosion if hooked up backwards (like a cathodic protection system) or if operated at too high a current.

A major goal of this investigation was to test the feasibility and efficacy of the bi-electrode concept on a full scale piping system. The purpose of this study was to investigate the effectiveness of this and other newer countermeasures in controlling galvanic corrosion in piping systems, by determining the magnitude and distribution of galvanic corrosion of 70:30 copper-nickel piping when coupled to alloy 625 or titanium piping.

PROCEDURE

Mockup Loop Construction

A series of piping mockups was constructed to simulate the most probable geometry and environmental conditions that would be in the piping system of interest. Twelve piping mockups were designed with either alloy 625 or titanium coupled to 70:30 copper-nickel piping. These mockups were constructed and operated at the LaQue Center for Corrosion Technology, Wrightsville Beach, NC. The mockups were operated for a period of one year.

Ten-foot sections of nominal 2-in (5-cm) diameter pipes were procured of each material. 70:30 copper-nickel, type 1 seamless tubing was procured in accordance to MIL-T-16420K, grade 1, except that the wall thickness and inside diameter were required to be that of 2-in.(5 cm) diameter pipe. Alloy 625 welded tubing was procured to ASTM B705-82, class 2. Titanium piping was procured according to ASTM specifications. All nominal 2-in pipes were Schedule 40 thickness.

The main seawater supply to the mockup assembly was nominal 6-in. (15 cm) polyvinyl chloride (PVC) pipe. Service to the individual piping loops was accomplished by tapping the 6-in manifold PVC pipe with 4-in. (10 cm) tee connectors. Nominal 2-in.(5 cm) PVC globe valves were used, along with nominal 4-in. by 2-in. reducers, to regulate the seawater flow to each mockup. A rotameter was inserted in the discharge end of each mockup and examined daily to monitor seawater flow and maintain flow at 6 fps (2 m/s) during the test period. Seawater flow was once-through and was discharged for each mockup loop. Ambient seawater temperature flowing through the piping mockups at Wrightsville Beach ranged from 7 to 27 °C (see Table 1).

Twelve piping mockups were designed with either 10-foot (300 cm) sections of titanium or alloy 625 coupled to 10-foot lengths of 70:30 copper-nickel (Figures 1 and 2) The piping legs of six mockup loops were electrically isolated with a 0.25-in (0.6 cm) length of PVC 2-in diameter pipe. In the other six loops a PVC spacer about 10-in long was placed between the piping sections. A coal tar epoxy coat was applied to the first 6 inches (15 cm) of the pipe ends on the outside of each pipe section near the couple to minimize seawater exposure and mitigate any corrosion that would otherwise generate galvanic currents in a possible crevice area. A 2.5-in. (6.4 cm) diameter nylon-reinforced black rubber hose was placed over each of the pipe ends, and connected the piping sections and the PVC spacers. The sleeves were secured with care by two band clamps for each joint to minimize the formation of crevices and ensure leak free connections. PVC spacers 10-in. (25 cm) long were placed at the discharge to compensate for the difference of spacer length between the dissimilar alloy piping sections. Each piping condition with or without an applied galvanic corrosion countermeasure was tested in duplicate.

The bi-electrode device concept initially consisted of two platinized titanium rings embedded in a 10-in (25 cm) section of 2-in PVC pipe prevent local flow disruptions (Figure 3). The platinized ring electrodes were 4-in wide and spaced 2 in apart. Wires on the outside were connected to an external power source so that the device could act as either a cathodic protection device or as a bi-electrode capable of stopping the galvanic current flow. In cathodic protection

mode, a cathodic current of 20 mA was applied between both ring electrodes in parallel and the copper-nickel and alloy 625 pipe sections to examine the effects of cathodic protection applied to dissimilar metal piping couples. In bi-electrode mode, current was applied from the ring anode to the ring cathode of the bi-electrode of sufficient magnitude to reduce and eliminate the galvanic current between the alloy 625 and the 70-30 copper-nickel pipes. Two separate piping mockups used the bi-electrode in this way.

Calcareous deposits on two titanium pipes were formed in slowly flowing natural seawater (<1.0-fps) by connecting two 10-foot (300 cm) sections of titanium pipe to zinc anodes for a period of two weeks. Enamel paint was sprayed on the outside titanium surfaces to minimize current demand on the anodes and to prevent deposits from forming on the exterior. Two anodes were used, one on the upstream end and the other on the downstream end. The mixed potential of the titanium pipe/zinc anodes was -1.045 V(SCE).

Galvanic Current Measurements

Galvanic current measurements were made between the outer surface of the copper-nickel and the titanium or alloy 625 pipe section on all piping mockups. A zero-resistance ammeter (ZRA) was used for all current readings. Current measurements were made daily during the first week and weekly over the remainder of the 1-yr. exposure. The ZRA was connected only when the readings were actually taken. At other times the dissimilar outer pipe sections were in electrical contact by external wiring. To avoid current flow interruptions while connecting the ZRA, the ZRA was first connected in parallel to the regular wiring system, Then the normal wiring was disconnected while the current flow was measured by the ZRA. The regular wiring was reconnected before the ZRA wiring was disconnected after the measurement. The applied current of the bi-electrode was manually changed to maintain a galvanic current between Alloy 625 and 70:30 copper-nickel section below 5 $\mu A/cm^2$. During one two-week period, the galvanic currents in the bi-electrode mockups were monitored daily to evaluate the effectiveness of more frequent applied current corrections with the bi-electrode.

Potential Measurements

Potential measurements versus distance along the piping mockups were made several times during the 1-yr. exposure on all of the mockups. The measurements were made in 1-ft increments (30-cm) from the seawater inlet end through the first 9 or 10 feet, in one-inch increments in the regions coinciding with the PVC spacer or bi-electrode, and 1-ft increments in the copper-nickel section from the end of the PVC/bi-electrode to the discharge end. The potential measurements were made by a Luggin-Haber probe with a Ag/AgCl reference electrode. The probe was inserted in a mockup by opening a piping plug on the seawater inlet end and replacing it with the probe. This was accomplished without disturbing the flow of the other mockups by isolating the selected mockup by shutting off the inlet water of the selected mockup with the globe valve. After the mockup had stabilized, potentials were measured. Initially, potentials were measured by traversing the mockup length from inlet to outlet ends, but a second traverse was made to verify that the probe intrusion during the first traverse did not alter the

potential readings. The potential measurements on other mockups were not affected by the electric fields generated by mockups with cathodic protection or bi-electrodes.

After the conclusion of the 1-yr. exposure, the pipe mockups were disassembled and visually examined for the presence of corrosion product films and fouling. Physical measurements were made to map the distribution and depth of corrosion attack along the pipe interiors.

RESULTS

Mockup Current Measurements

The galvanic currents of the couples between titanium and 70:30 copper-nickel piping sections (loops 1 and 7) were initially below 100 μA, as shown in Figure 4. The currents gradually increased during the first month of exposure. After one month, a sharp rise in the galvanic currents occurred - peaking at over 6000 μA after 50 days exposure. Both loops displayed decreasing galvanic currents after 50 days and approached steady-state galvanic currents of 1800-2200 μA and 2500-4100 μA for loops 1 and 7 respectively. It appeared that there was some increase of the galvanic currents as seawater temperatures increased, which has been observed often in aerated natural seawater.

The galvanic currents measured between the titanium pipe sections with calcareous deposits and the 70:30 copper-nickel piping sections were relatively high (56-312 μA) during the first month, but quickly settled to 25 to 40 μA after 36 days exposure (Figure 5). The currents eventually decreased to 8-11 μA when the flowing natural seawater temperature was 7-10 °C. Later, as the water temperature increased, the galvanic currents gradually increased from 8 μA to 164 μA in loop 2 and from 11 μA to 96 μA in loop 8. The increasing currents may be due to some deposits flaking from the titanium surface, decreased calcareous deposit thickness due to increased solubility of the deposit in warmer seawater, or enhanced diffusion through the calcareous deposits. Calcareous deposits reduced the effective cathode area and the cathodic efficiency of the titanium section. When calcareous titanium was coupled to copper-nickel piping in seawater, galvanic currents decreased by a factor of 15 to 40 as compared to bare titanium/copper-nickel couples in this investigation.

The galvanic currents from the interaction between alloy 625 and 70:30 copper-nickel are presented in Figure 6. There was a general current increase from 100 μA after 1 hour exposure to over 1500 μA after 50 days for both loops 6 and 12. The behavior of loops 6 and 12 differed after 60 days. The measured galvanic currents from loop 6 quickly increased from 1800 μA on day 64 to 5700 μA after 72 days exposure and gradually decreased to a steady state current of 3700-3900 μA after 246 days. On the other hand, the measured galvanic currents of loop 12 gradually increased from 718 μA after 64 days exposure to 4800 μA after 162 days. Galvanic currents from loop 12 had not reached a steady state condition after 246 days, currents fluctuated between 3600 and 5600 μA.

The measured galvanic currents versus time from the alloy 625 and 70:30 copper-nickel couples which were separated by a 10-in PVC spacer (loops 5 and 11) are displayed in Figure 7. The currents increased gradually to 1000 μA during the first 35 days of exposure in the mockup testing loops. The currents rose abruptly to 4400-4800 μA in day 37 in both mockups and gradually decreased to 1900-2200 μA after exposures of 190 days. Currents slowly increased to 2800 and 3600 μA in loops 5 and 11 respectively as the seawater became warmer. The 10-in PVC spacer decreased the average galvanic currents by about 20 to 50 percent as compared to the alloy 625/Cu-Ni couples of loops 6 and 12 where the longer dielectric spacers were absent

Cathodic protection was applied to both the alloy 625 and 70:30 copper-nickel segments of mockups loops 3 and 9 using the bi-electrode as an impressed current anode between the piping segments. Application of 200 μA after 6 days reversed the natural galvanic currents in seawater from copper-nickel to alloy 625. However, this was short-lived, as the galvanic currents gradually increased with time for the 625/70:30 copper-nickel couple, as shown earlier. The galvanic currents eventually exceeded the impressed current supplied by the bi-electrode. During exposure day 12, the impressed cathodic protection current was increased to 20 mA. The galvanic currents on the cathodically protected galvanic couples are shown in Figure 8. The currents measured between the copper-nickel and alloy 625 piping sections slowly increased after increasing the protection current to 20 mA. During day 12 the galvanic currents were about 5700 μA and mostly increased with time for both mockup loops 3 and 9. The currents between alloy 625 and 70:30 were 15800 and 14600 μA in loops 3 and 9 respectively.

Current was applied from an external source to the bi-electrode device to impress a current field which opposed the natural galvanic ionic current distribution. The attempt was to keep the resultant galvanic current at or near zero by adjusting the current between the bi-electrodes. The current applied to the bi-electrodes is shown in Figure 9. The applied currents between the bi-electrodes increased with time. The initial applied currents required to provide zero resultant current were 7.5 mA and 9 mA for mockups 4 and 10 after 20 and 15 days respectively, but increased to a maximum of about 34 mA before beginning to revert to lower applied currents.

The resultant galvanic currents between the alloy 625 piping section and the 70:30 copper-nickel fluctuated as shown in Figure 10. Exposure of one week after the last manual current correction generally lead to relatively high resultant galvanic currents of 5-890 μA. Increasing the applied bi-electrode current returned the resultant galvanic current to within the test range goal of± 5 μA. Galvanic currents in Loop 4 was more variable than loop 10. Loop 10 exhibited stability during one 2 month period while loop 4 required daily alteration of the applied bi-electrode currents. After 210 days of exposure, the required applied currents for the bi-electrodes were 35 mA and 28.5 mA for loops 4 and 10 respectively. Increasing the frequency of current monitoring and modification of the applied bi-electrode currents from weekly to daily reduced the resultant galvanic current fluctuations. The resultant current changes during the daily monitoring were 0 to 51 μA. This more frequent manual control indicates the importance of automated control of the bi-electrode currents in maintaining low galvanic currents.

Mockup Potential Distribution Measurements

The potential distribution along the titanium/70:30 copper-nickel piping mockup vs. time is shown in Figure 11. The potential difference between the titanium and copper-nickel sections of loops 1 and 7 during the first 2 days exposure was less than 100 mV. The potential of the titanium leg at the inlet end was -133 to -143 mV(Ag/AgCl) while the potential of the copper-nickel leg was -190 to -213 mV. The potential profile of the mockup loops changed abruptly on exposure day 14. The potential of the titanium section during day 14 reached a maximum of +284 mV for both loops 1 and 7 respectively. Initially, about 6 ft (2-m) of the titanium pipe contributed to the galvanic couple while about 7 to 8 feet of copper-nickel pipe was affected by the galvanic interaction. At 51 days and later, the potential of the entire 10-ft (300 cm) length of titanium was influenced by the galvanic interaction while the length of copper-nickel pipe affected by the couple was 4 to 5 feet (120-150 cm). The maximum potential of the titanium leg generally decreased with time, likely due to organic films, slime, and deposits forming over the inner surface, since titanium is not inherently resistant to biofouling. The maximum titanium potential measured during the potential profile survey at 247 days was +82 mV. The potential of the copper-nickel piping at the interface with titanium was +95 mV during day 14. Most of the damage from the couple would be expected to occur in the first 18-24 inches (45-60 cm) of the copper-nickel piping as was observed earlier [12]. The potential at the Ti/Cu-Ni junction also declined with time - the potential from 51 to 157 days diminished from 44 to 11 mV. At 247 days the potential at the junction of the couple was -95 mV. During the period between 157 and 247 days, a potential trough of 20 to 30 mV was observed in the copper-nickel leg about 1-2 feet from the junction with titanium. The reason for this potential drop is unknown at this time. Lastly, the potential profile was dependent on flow velocity. The potential during day 157 was higher than measurements both before and afterwards due to a failure in the seawater supply pipe which had caused loss of flow for 4-10 hours before repair was completed.

The potential profile for calcareous deposit coated titanium coupled to 70:30 copper-nickel piping (loop 2) is illustrated in Figures 12. The potentials along both the entire coated titanium and copper-nickel segments are depressed as compared to bare titanium coupled to 70:30 Cu-Ni. The calcareous deposit acted to reduce the effective cathode surface area and/or reduced the cathodic efficiency by diminishing the current flow through the barrier coating from oxygen or hydrogen reduction reactions. Since the total current derived from the cathode (titanium pipe area) must equal the total anodic area represented by the copper-nickel surface, the resultant galvanic corrosion was lower on the copper-nickel from the calcareous coated titanium than from the bare titanium. The lower cathodic current reduced the current density at the copper-nickel surface substantially. The potential profiles also tended to be linear over the entire mockup length with the maximum potentials at the titanium inlet and the minimum at the copper-nickel outlet, suggesting that the calcareous deposits acted as a dielectric barrier to electron flow from the titanium surface. There appeared to be a gradual degradation of the calcareous barrier with time. This may have been due to some flaking of the deposit or because the deposit had thinned due to increased solubility as the water temperature increased. The potential at the calcareous deposit/copper-nickel junction of loop 2 increased from -309 mV after 1 hour exposure to -144 mV on day 119 to -99 mV after 233 days, although excursions to approximately 0 mV were measured at days 143 and 210. The junction potential of Loop 8 increased from -217 mV after 1

hour to between -147 and -191 mV during 1-233 days exposure (the lone exception being day 206 when the measured junction potential was -61 mV). The potential profile measurements would suggest that higher galvanic currents and galvanic corrosion of the copper-nickel pipe would be expected on mockup loop 2 than on loop 8. The current measurements of loops 2 and 8 confirm this observation.

The potential profile of an alloy 625/70:30 copper-nickel mockups (loops 6) is illustrated in Figure 13. Little polarization of the copper-nickel section by the alloy 625 was observed during the first 2 days of exposure. The potentials of the 625 legs were -110 to -200 mV while potentials of the copper-nickel piping sections stayed around -210 mV. The potentials of the alloy 625 in both were unstable in flowing seawater during the next 50 days, ranging from -150 to +260 mV. The potentials of alloy 625 in flowing seawater appear to have settled at day 100 and afterwards into a range of from +170 to +230 mV. The potential profile of the alloy 625/copper-nickel couple beginning in day 100 resembles an S-curve. The length of galvanic interaction along the 625 pipe was 6-7 feet (180-210 cm) while 5-7 (150-210) feet of copper-nickel piping was affected by the couple. The potential of the copper-nickel pipe leg tended to rise with time, although there was some fluctuations between -20 and -150 mV.

An approximately one-foot PVC spacer was placed between the alloy 625 and 70:30 copper-nickel pipe section of mockups 5 and 11. The potential profile of one of the mockups is shown in Figure 14. The one-foot PVC spacer did not alter the shape of the potential profile between of the alloy 625 and copper-nickel legs with exposure time as compared to the directly coupled (0.25" spacer) 625/70:30 Cu-Ni loops described earlier. The potential of the 625 segment coupled to copper-nickel using a one-foot spacer tended to be 20-60 mV lower than the 625 leg galvanically coupled to 70:30 but with only the minimal PVC spacer.

The potential profile of the coupled alloy 625/70:30 copper-nickel piping mockup under cathodic protection is presented in Figure 15. In this case, both of the electrodes of the bi-electrode device were used as impressed current anodes to apply current to the copper-nickel pipe. Initially, 200 μA were applied to the copper-nickel pipe which did not alter the potential profile from that observed in the other coupled alloy 625/70:30 mockups during the first days exposure in flowing seawater. Increasing the impressed current to 20 mA resulted in a deep potential trough between the alloy 625 and the copper-nickel piping sections. The potential minimum occurred at the bi-electrode device. Initially, 20 mA of impressed current dropped the minimum potential at the bi-electrode to -670 mV. The depth of the potential well decreased and the minimum potential increased with time with the fixed 20 mA impressed current. The minimum potentials after 210 days were -320 to -335 mV for the two piping mockups under cathodic protection (CP). CP affected both dissimilar alloy legs by depressing the potential below their free corrosion potentials. Initially, the alloy 625 inlet potential was -240 mV, but gradually increased to +170 to +200 mV after 120-210 days. The potential at the copper-nickel outlet also increased from -240 mV initially to -60 mV. At first, CP depressed the potential of the 625 segment over its entire 10-ft (300 cm) length, but after about 100 days exposure, only 6-7 (180-210 cm) feet were influenced by CP. CP consistently affected about 5 feet of the copper-nickel. The rise in the minimum potential with time at a fixed impressed current led to shorter lengths of the copper-nickel piping being adequately protected; after 210 days only about two feet of the copper-nickel pipe was at or below its free corrosion potential.

The potential profile caused by the bi-electrode on the galvanic couple between alloy 625 and 70:30 copper-nickel is illustrated in Figure 16. The galvanic current flow exited from the more anodic member of the couple (copper-nickel) and flowed upstream towards the cathodic 625 pipe. A current was applied to the bi-electrodes so that the bi-electrode-related current flowed downstream between the two ring electrodes and countered the natural galvanic current flow, resulting in a zero net galvanic current. As mentioned previously, manual adjusting of the applied current between the bi-electrodes was required to exactly counter the galvanic current. The potential of the respective alloy 625 and copper-nickel piping increased with time, which in turn, would tend to increase the galvanic currents. This required increased applied currents between the bi-electrodes. The potential drop across the bi-electrode was typically very sharp - a potential decrease of nearly 400 mV could occur over a span of 7-8 inches (18-20 cm). The applied bi-electrode current near the end of the exposure had to be decreased in order to maintain a zero net galvanic current flow. The cause for this can not be explained.

DISCUSSION

The total amount of galvanic corrosion of 70:30 copper-nickel pipe when connected with titanium or alloy 625 pipe of similar diameter under moderate seawater flow was lower than might be expected from looking at a galvanic series. In some non-critical areas, this couple may need no corrosion protection at all, or it may be sufficient to perform occasional inspection to monitor the degree of corrosion.

The titanium and alloy 625 pipes all had similar potentials and caused similar galvanic currents when in similar configurations. This is to be expected, as neither of these materials corrodes or has a thick protective film. Thus both should act as oxygen electrodes, yielding similar cathodic behavior. Similar long-term cathodic polarization behavior of these alloys in seawater has also been observed, which is consistent with similar galvanic currents [14].

The titanium and alloy 625 pipes all suffered ennoblement of several hundred millivolts at a time somewhere between 25 and 65 days, with the exception of the material with calcareous deposits. It therefore appears that the deposits prevented the ennoblement phenomenon, by a mechanism currently unknown. The galvanic current increased dramatically at roughly the same time as the ennoblement occurred, indicating a probable cause/effect relationship. Ennoblement of the cathode increases the potential difference between the anode and the cathode, which can increase galvanic current. The phenomenon of ennoblement is likely caused by microbial action which increases cathodic kinetics, which would shift the cathodic polarization curve to higher currents, also increasing galvanic current to the anode.

Calcareous deposits were highly effective in lowering galvanic currents to negligible levels. Galvanic currents increased later in the test, possibly due to thinning of the calcareous deposits or increasing due to seasonal changes in seawater temperature or dissolved oxygen.

The use of a 1-ft spacer between the anode and cathode pipes in the couples resulted in a 40-50% reduction in galvanic current. In a similar type test conducted earlier, a similar 1-ft spacer was not effective in reducing galvanic current, while a 3-ft spacer was required to get similar current reduction [13]. Longer spacers were shown in the previous study to have increased effectiveness in reducing galvanic corrosion due to the increased seawater IR drop introduced for longer spacers. The reason for the increased effectiveness of the spacer in this exposure test versus the previous one is unknown at this time.

Use of the bi-electrode as a pair of cathodic protection anodes was effective in shifting the potential of the copper-nickel enough to suppress the anodic corrosion reactions, and shifted the potentials of the cathodes enough to prevent them from causing galvanic corrosion. The cathodic protection usually shifted the potential far more than was required. Thus, more current was supplied than was needed to do the task of protection. Since the cathodic protection was set up under constant current control, the control of this system was simple and operation was safe and stable.

Use of the bi-electrode (BED) in its intended mode was very effective in shifting the potential of the copper-nickel enough to prevent galvanic corrosion, and the current required was small. When the bi-electrode was properly adjusted, the copper-nickel potential was flat across the entire pipe length, even near the cathode, indicating that the copper-nickel could not detect the presence of the cathodic material at all. The cathode pipe potential was also flat, indicating that it was supplying no current to the anodic pipe. The system, when adjusted correctly worked perfectly to stop galvanic corrosion with a minimum of current and no issues regarding "throwing power" as would arise if cathodic protection were used.

Control of the bi-electrode was difficult however. Daily manual adjustments were far more effective at keeping galvanic current low than weekly adjustments. In practice, this type of control is not possible, as the anode and cathode pipe would be shorted through common structure and pipe hangars, so galvanic current could not be measured. Another method of control must be sought. Just as hooking up a cathodic protection system backwards can accelerate corrosion, improper control of the bi-electrode can also accelerate corrosion. Thus, the issue of control must be resolved before this device can find use.

CONCLUSIONS

Titanium and alloy 625 behaved similarly in the galvanic couples with 70:30 copper-nickel piping. The ennoblement of both titanium and alloy 625 that occurred between 25 and 65 days resulted in a simultaneous increase in galvanic current. Calcareous deposits were highly effective in lowering galvanic currents to negligible levels. The use of a 1-ft spacer between the anode and cathode pipes in the couples resulted in a 30-50% reduction in galvanic current.

Use of the bi-electrode as a pair of cathodic protection anodes was effective in shifting the potential of the copper-nickel enough to prevent galvanic corrosion, and control of the cathodic

protection system was simple, however it usually supplied more current than was needed to do the task of protection.

Use of the bi-electrode in its intended mode was very effective in shifting the potential of the copper-nickel enough to prevent galvanic corrosion, and the current required was small. Control of the bi-electrode was difficult however. More frequent adjustments of the bi-electrode applied current reduced the galvanic current fluctuations Just as hooking up a cathodic protection system backwards can accelerate corrosion, improper control of the bi-electrode can also accelerate corrosion.

ACKNOWLEDGMENTS

This project was funded under the Surface Ship Materials Technology Program sponsored through Dr. John Sedriks of the Office of Naval Research (ONR). Work was conducted in the Corrosion Branch under the direction of Mr. Robert J. Ferrara. David East and Jim Chrzan of the LaQue Center for Corrosion Technology - under the direction of Mr. Dennis Melton - constructed the test loops and conducted the testing of the piping mockups.

REFERENCES

1 - J. W. Oldfield, "Electrochemical Theory of Galvanic Corrosion," *Galvanic Corrosion*, H. P. Hack, ed., ASTM, West Conshocken, PA, p. 5, 1988.

2 - R. Francis, "Galvanic Corrosion of High Alloy Stainless Steels in Sea Water," *British Corrosion Journal*, Vol. 29, p. 53, 1994.

3 - I.L. Caplan, H.P. Hack, "The Galvanic Effects of Titanium Coupled to Various Marine Alloys in Seawater", Report CDNSRDC-SME-80/54, NSWC, October 1980.

4 - J. P. Gudas, H. P. Hack, "Sulfide-Induced Corrosion of Copper-Nickel Alloys," Corrosion/77, paper 93, NACE International, Houston, TX.

5 - J. P. Gudas, *et al.*, "Accelerated Corrosion of Copper-Nickel Alloys in Polluted Water," Corrosion/76, paper 76, NACE International, Houston, TX.

6 - S. L. Wolfson, W. H. Hartt, *Corrosion*, Vol. 37, p. 70, 1981.

7 - W. H. Hartt, C. H. Culberson, S. W. Smith, *Corrosion*, Vol. 40, p. 609, 1984.

8 - S.-H. Lin, S. C. Dexter, *Corrosion*, Vol. 44, p. 615, 1988.

9 - J. E. Finnegan, K. P. Fischer, "Calcareous Deposits: Calcium and Magnesium Ion Concentrations," Corrosion/89, paper 581, NACE International, Houston, TX.

10 - K. P. Fischer, J. E. Finnegan, "Cathodic Protection Behavior of Steel in Sea Water and the Protection Properties of the Calcareous Deposits," Corrosion/89, paper 582, NACE International, Houston, TX.

11 - J. S. Luo, R. U. Lee, T. Y. Chen, W. H. Hartt, S. W. Smith, *Corrosion*, Vol. 47, p.189, 1991.

12 - K. E. Mantel, W. H. Hartt, T. Y. Chen, *Corrosion*, Vol. 48, p. 489, 1992.

13 - H. P. Hack, W. L. Wheatfall, "Evaluation of Galvanic and Stray Current Corrosion in 70/30 Copper-Nickel/Alloy 625 Piping Systems," Corrosion/95, paper 272, NACE International, Houston, TX.

14 - H. P. Hack, "Atlas of Polarization Curves for Naval Materials in Seawater," Report CARDIVNSWC-TR-61-94/44, NSWC, April 1995.

TABLE 1 Seawater Hydrology at Wrightsville Beach, NC				
DATE	Temperature	Dissolved Oxygen (mg/l)	pH	Salinity (g/l)
10/28/96	22.0	6.90	8.1	33.21
11/04	17.9	7.64	8.0	32.52
11/11	18.1	8.06	8.2	34.40
11/18	14.9	8.51	8.1	33.77
11/25	14.2	8.14	8.0	33.17
12/02	12.7	8.57	8.0	31.83
12/09	10.9	8.82	8.1	32.97
12/16	10.9	8.67	8.0	31.85
12/30	12.1	8.42	8.1	32.47
1/06/97	12.0	8.57	8.1	31.76
1/13	8.5	9.24	8.1	31.13
1/20	7.4	10.00	8.0	31.26
1/27	9.8	9.02	8.1	31.89
2/03	10.2	9.04	8.0	32.21
2/10	8.3	9.34	8.1	31.62
2/17	9.1	9.39	8.0	31.11
2/24	11.6	9.12	8.0	31.96
3/03	17.5	8.29	8.0	29.56
3/10	14.6	8.17	8.0	34.20
3/17	15.3	8.04	8.0	31.38
3/24	14.6	8.24	8.0	32.34
3/31	15.4	7.84	8.0	31.92
4/07	16.0	7.87	8.0	34.25
4/14	16.0	7.49	8.0	34.52
4/21	17.1	7.50	8.0	34.02
4/28	18.2	6.51	7.9	33.04
5/05	18.0	7.59	8.0	33.13
5/12	20.0	6.76	8.0	32.36
5/19	23.4	6.26	8.0	31.31
5/26	22.1	6.01	7.9	34.22
6/02	22.8	6.56	7.8	34.40
6/09	19.9	6.96	8.0	34.65
6/16	23.4	5.79	7.9	32.88
6/23	25.5	6.06	8.0	34.92
6/30	25.5	5.86	8.0	34.65
7/07	26.5	5.96	8.0	34.40
7/14	26.6	5.48	7.8	34.02
7/21	26.6	6.28	8.0	35.44
7/28	28.0	5.05	8.0	38.84

Figure 1
Schematic of Mockup Loops

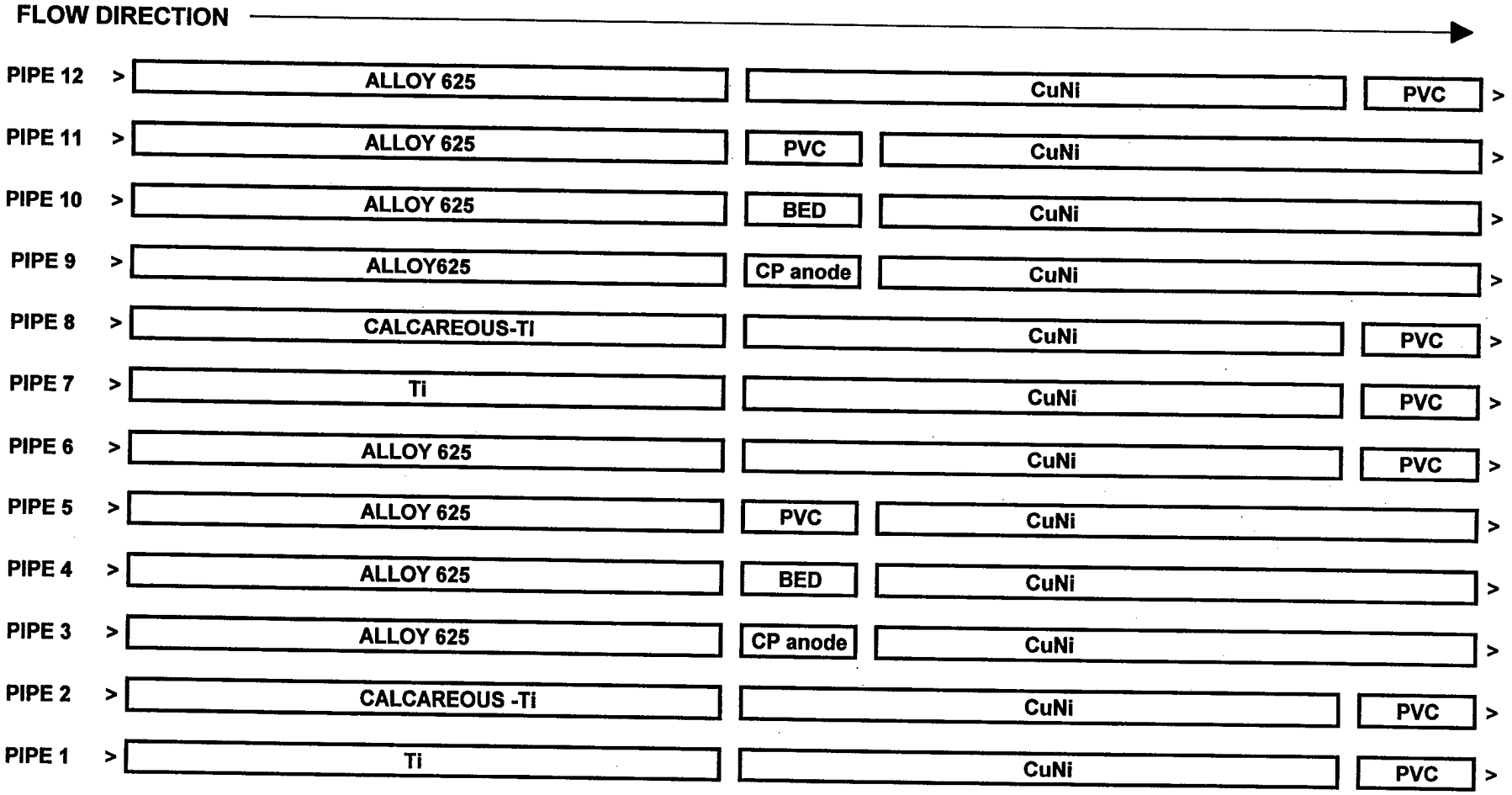
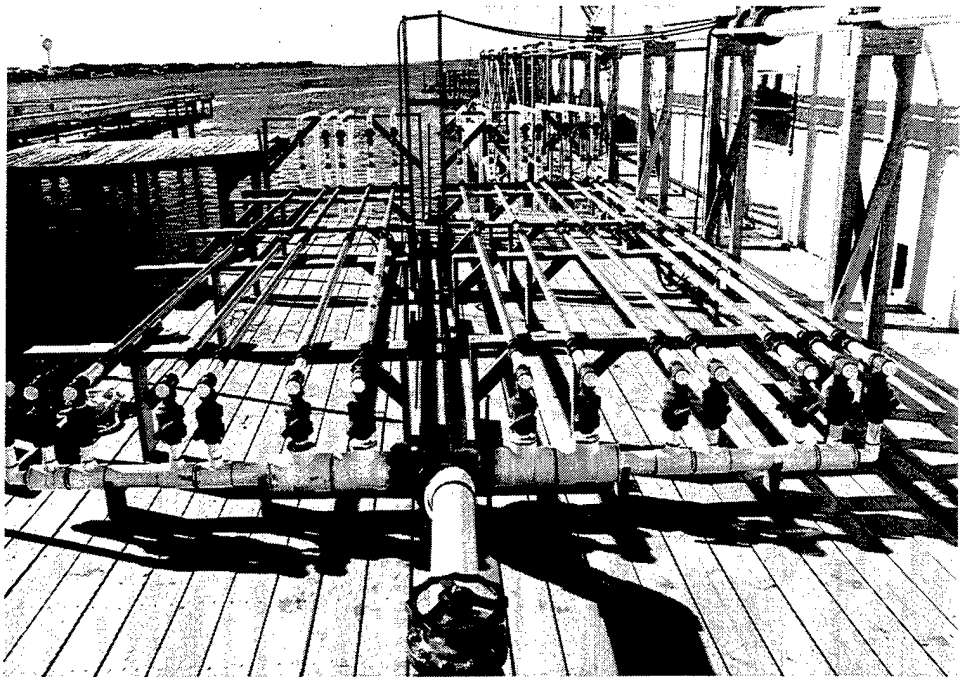


Figure 2 - Overall view of operating seawater piping mockups at LCCT



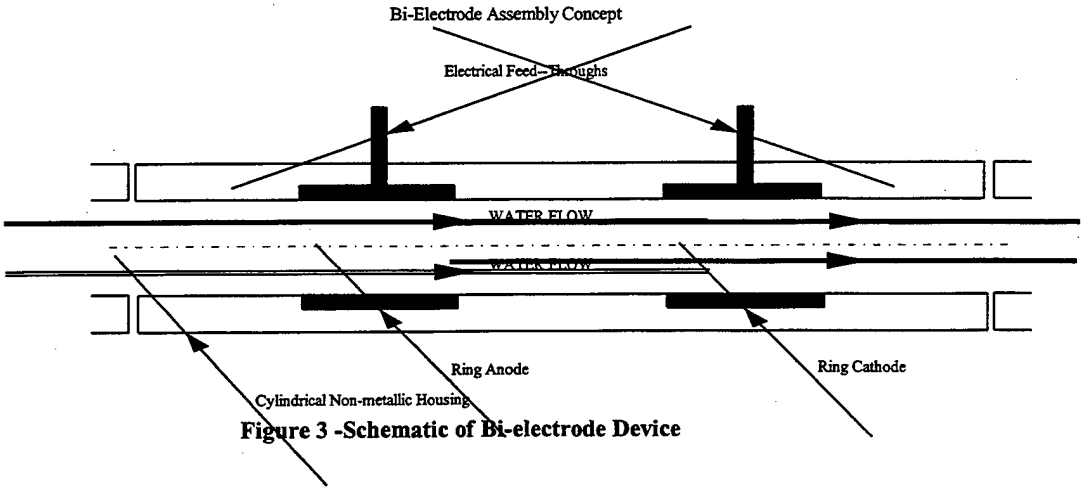


Figure 3 -Schematic of Bi-electrode Device

Figure 4
Titanium/70:30 Copper-Nickel Piping Couple
Galvanic Currents

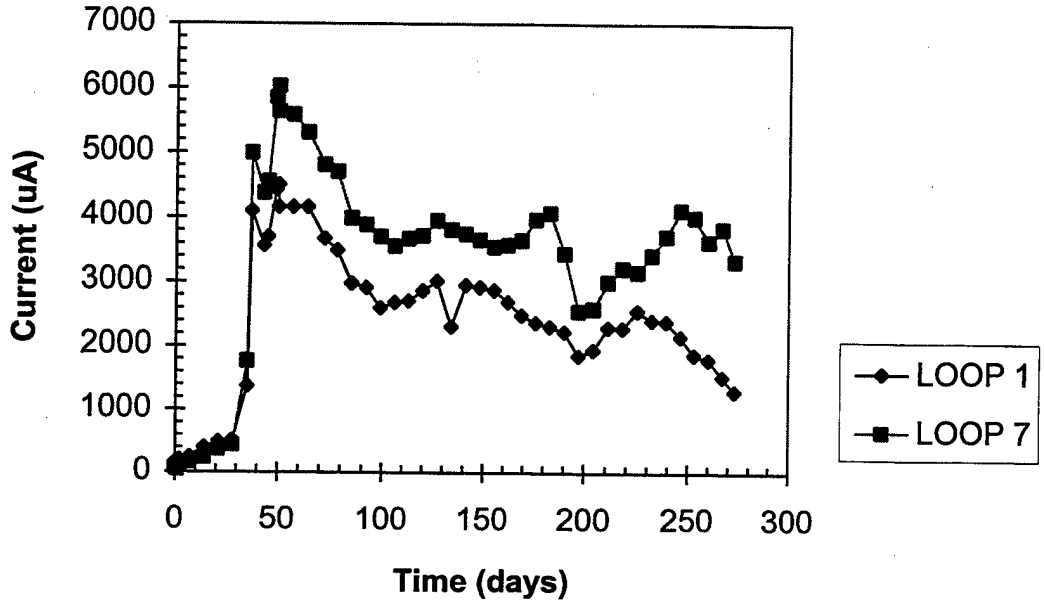


Figure 5
Calcareous Titanium/70:30 Copper-Nickel
Piping Couple Galvanic Currents

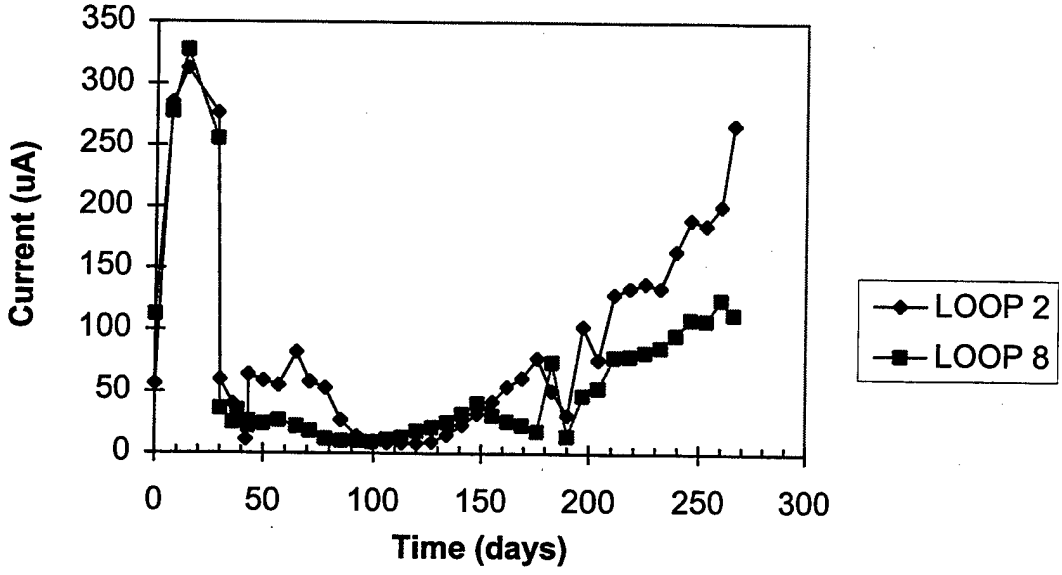


Figure 6
Alloy 625/70:30 Copper-Nickel Piping Couple
Galvanic Currents

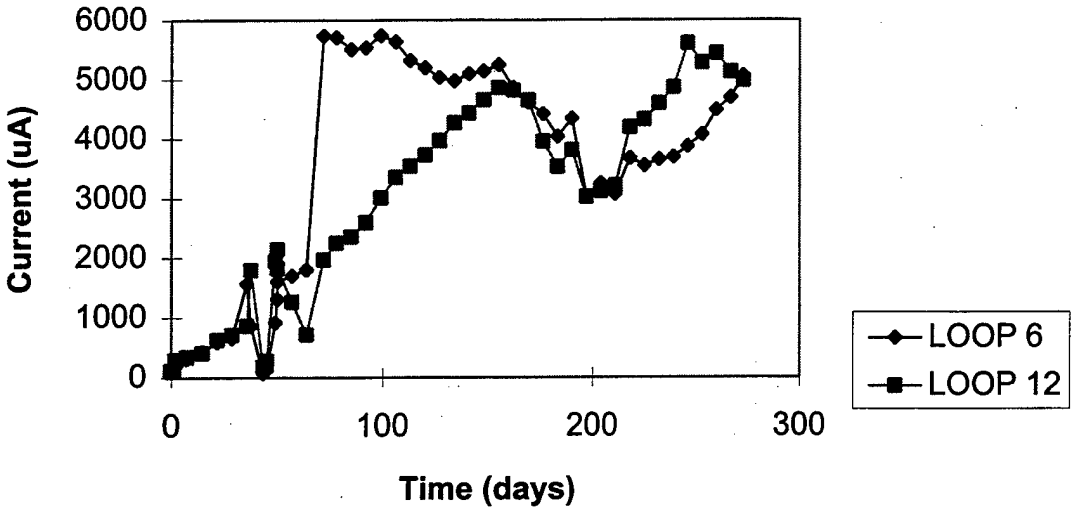


Figure 7
Alloy 625/70:30 Copper-Nickel Piping Couple with 1 Ft. PVC Spacer

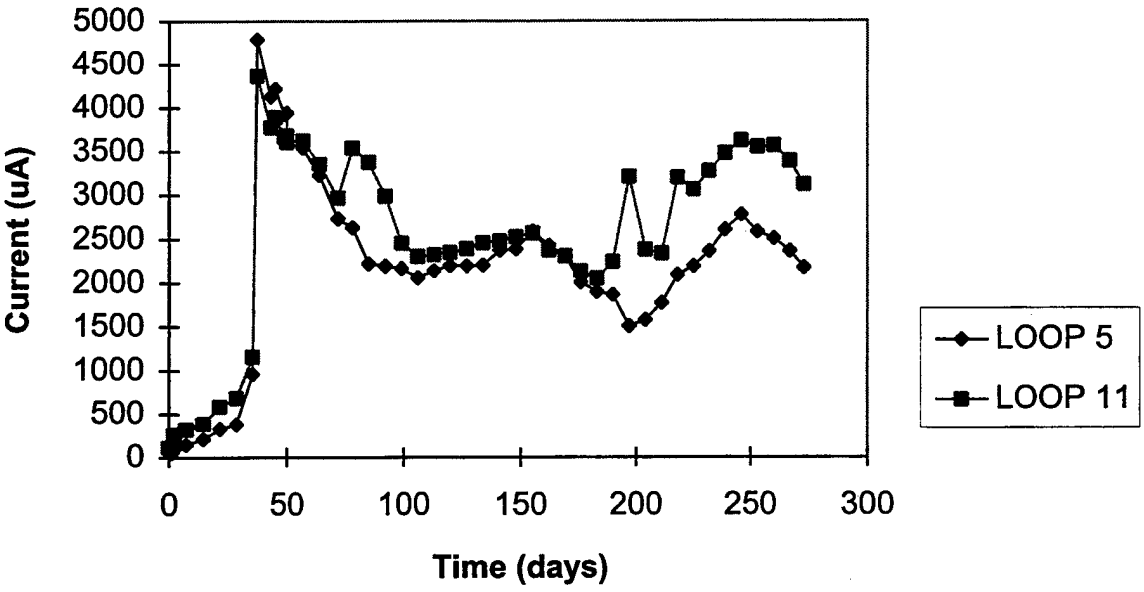


Figure 8
Alloy 625/70:30 Copper-Nickel
Piping Couple - CP Effects

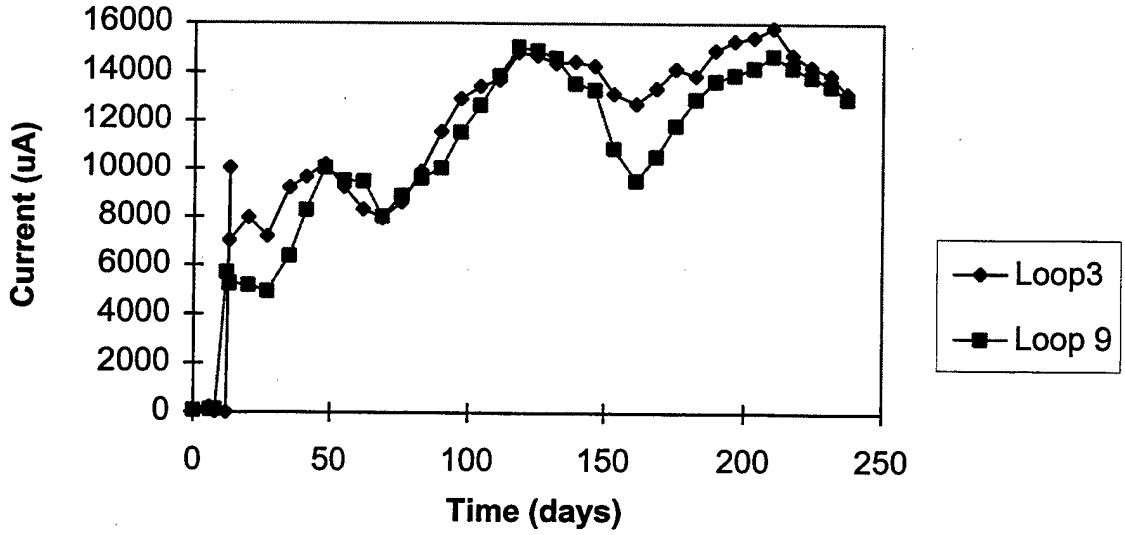


Figure 9
Applied Current to Bi-Electrode for Alloy 625/70:30 Copper-Nickel Piping Mockups

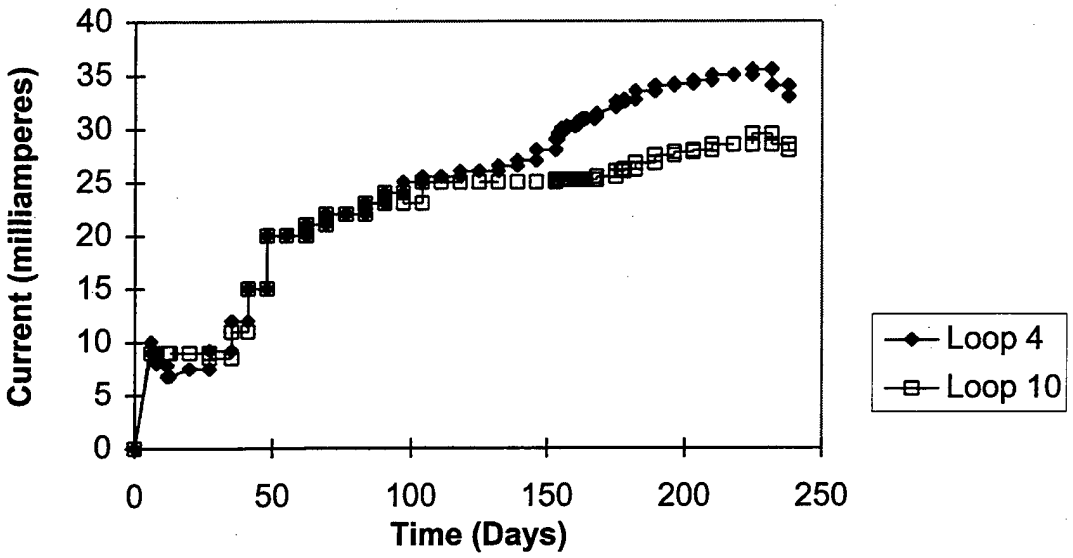


Figure 10
Galvanic Currents of Alloy 625/70:30 Copper-Nickel Piping Mockup Controlled by Bi-Electrode

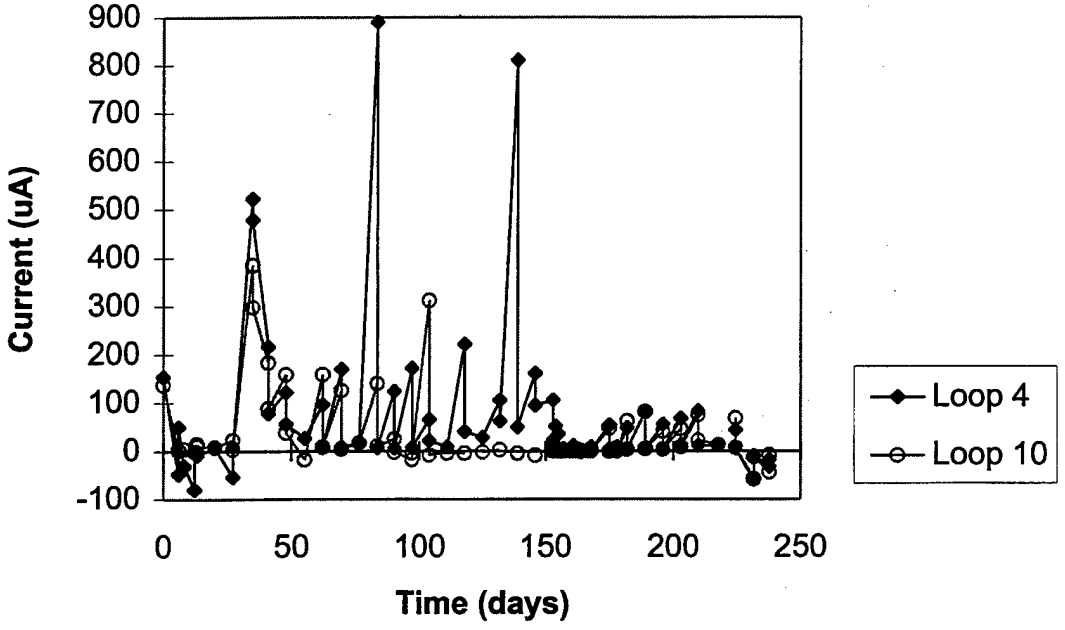


Figure 11
Titanium/Copper-Nickel Couple
Potential Profile - Loop 1

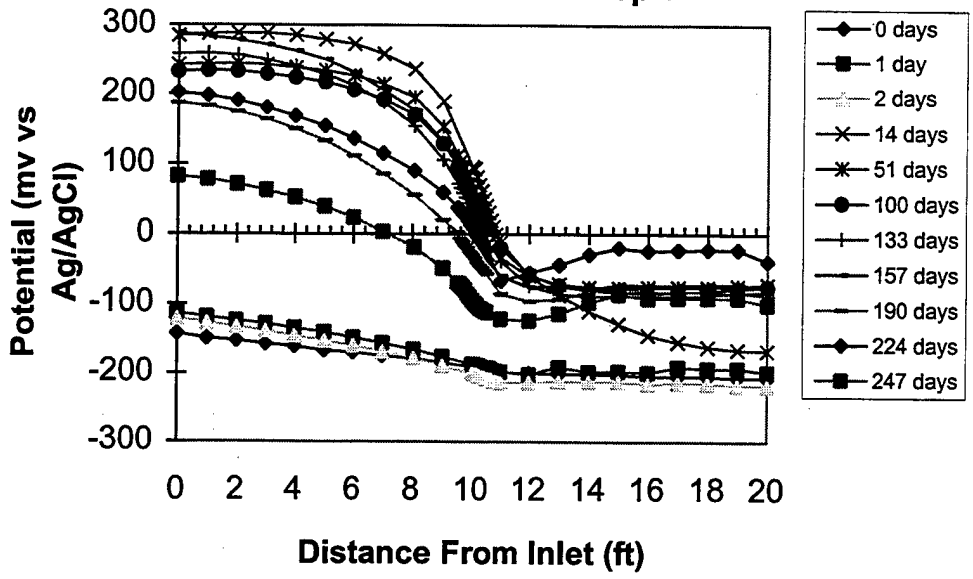


Figure 12
Calcareous Coated Titanium/70:30 Copper-Nickel Couple - Potential Profile

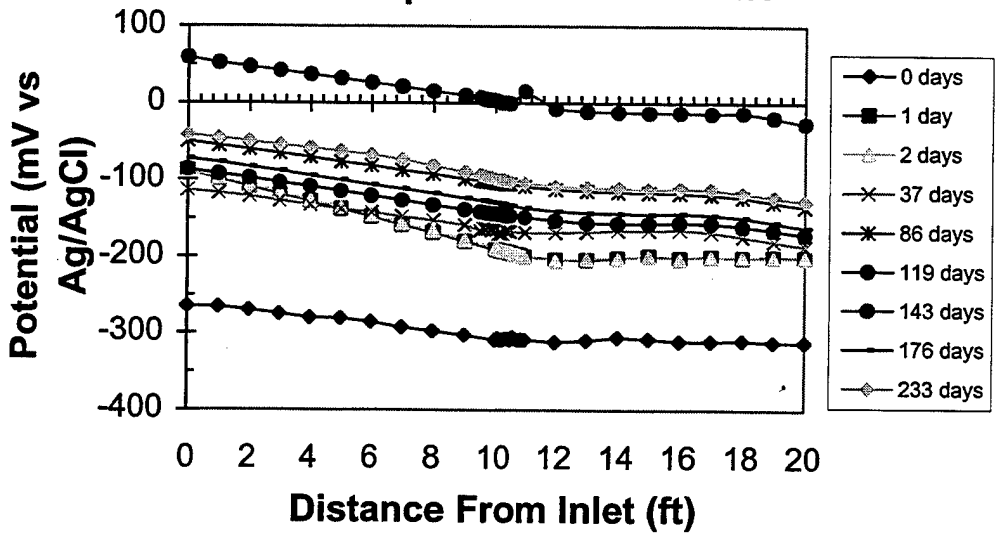


Figure 13
Coupled Alloy 625/70:30 Copper-Nickel Piping
Potential Profile - Loop 6

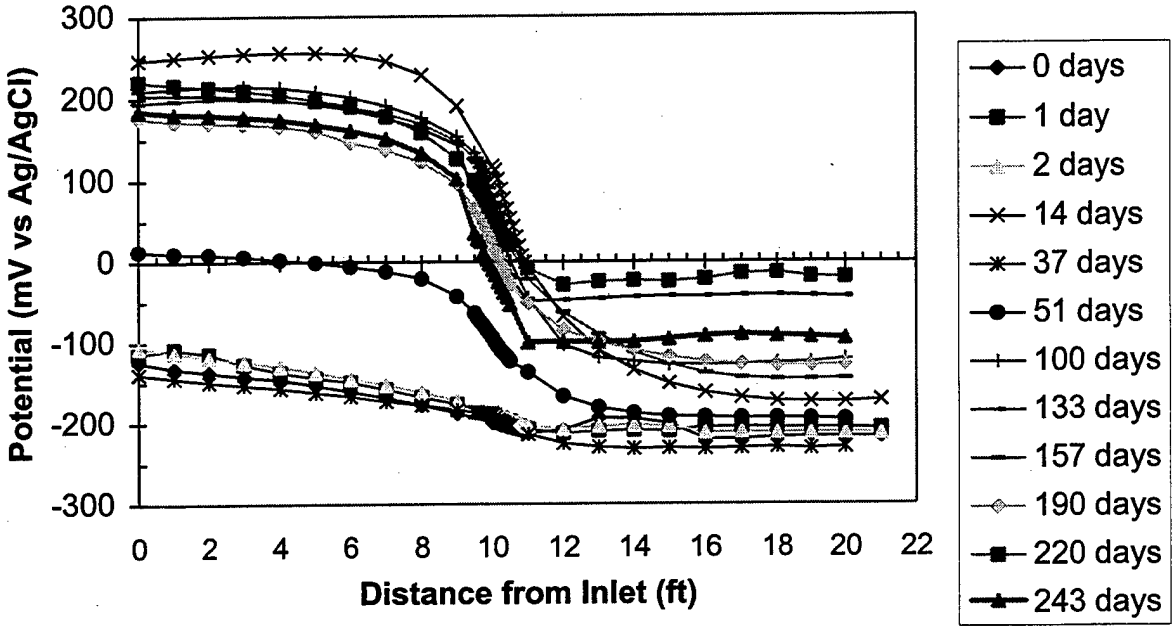


Figure 14
Potential Profile of Alloy 625/70:30 Copper-Nickel Piping with 1-Ft. PVC Spacer - Loop 5

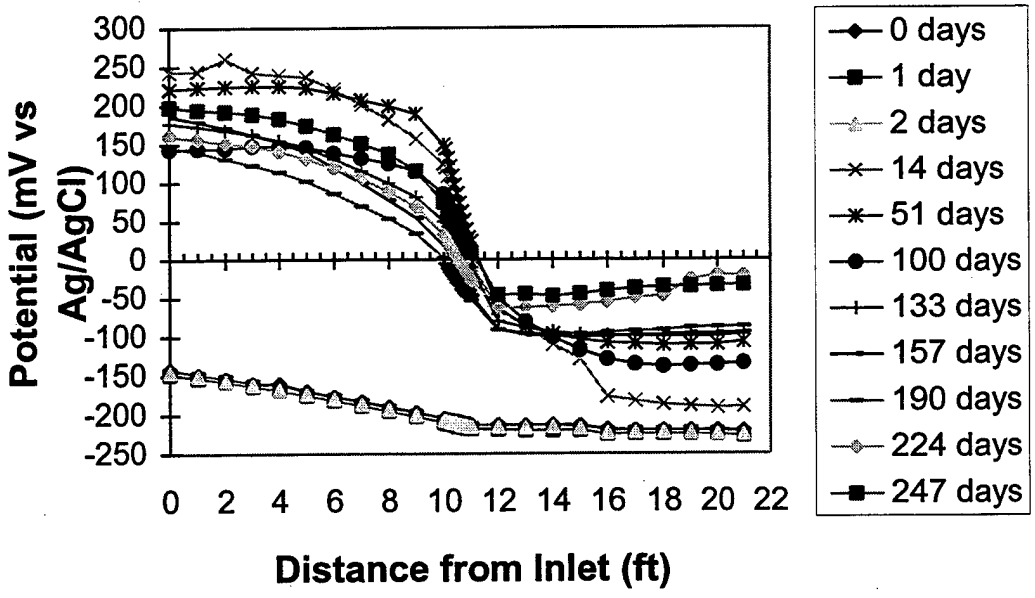


Figure 15
Potential Profile of Alloy 625/70:30 Copper-Nickel under Cathodic Protection - Loop 3

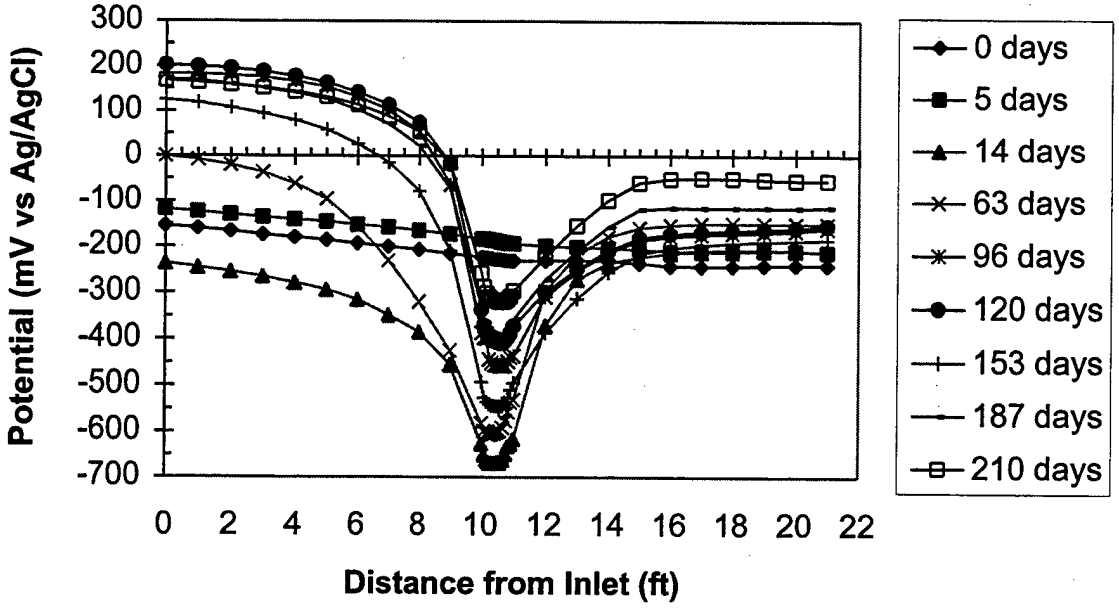
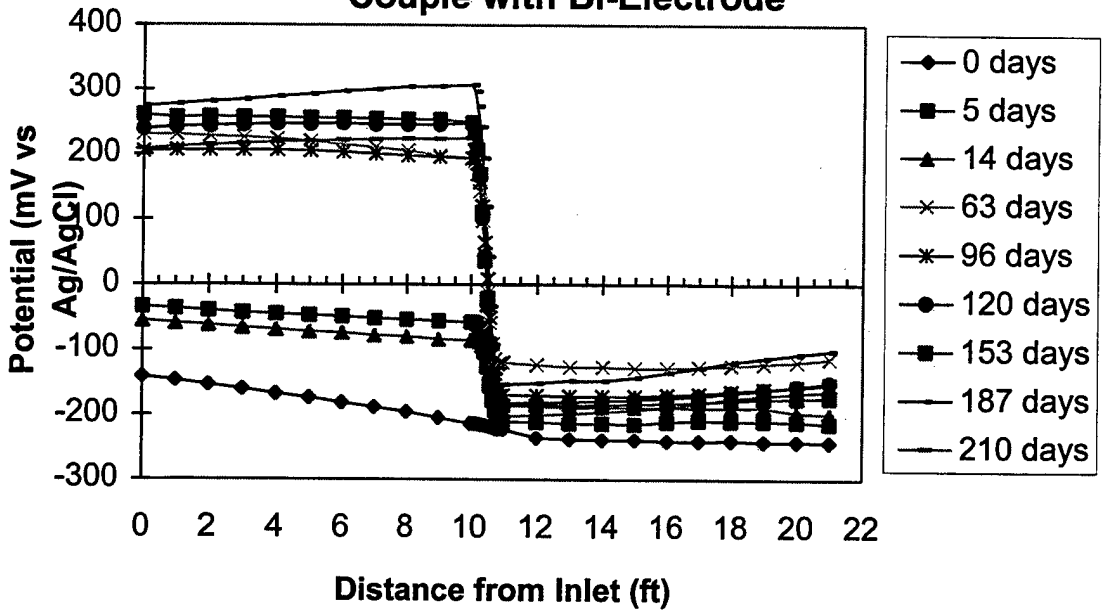


Figure 16
Potential Profile of Alloy 625/70:30 Copper-Nickel Couple with Bi-Electrode



Noble Metal Additions to Mitigate Hydrogen Embrittlement of Ultra High Strength Steels: Research In Progress.

Paul F. Buckley and John H. Beatty
Weapons and Materials Research Directorate
Army Research Lab
Aberdeen Proving Ground, MD 21005

Peter Searson
Materials Science and Engineering
Johns Hopkins University
3400 N. Charles St.
Baltimore MD 21218

ABSTRACT

A brief review of recent work performed to mitigate hydrogen embrittlement in high strength steels is presented. Hydrogen behavior in the presence of traps is used to interpret the effect of noble metal additions on hydrogen embrittlement resistance in ultra high strength steel. A method for examining these traps is described which will include the following experimental work : dynamic hydrogen permeation in palladium and iron, Forward Recoil Spectrometry, and Nuclear Reaction Analysis. Preliminary results and recommendations for future experimentation are presented.

INTRODUCTION

Hydrogen embrittlement has been identified as a problem in steels since 1873, when W.H. Johnson performed his initial work entitled "On Some Remarkable Changes Produced in Iron and Steel by the Action of Hydrogen in Acids." [1] More recently, the Army has encountered problems with high strength steels suffering from hydrogen assisted cracking. These include high strength steel armor components, helicopter control linkages and helicopter landing gear. Despite efforts to improve hydrogen resistance of high strength steels, it has remained the Achilles' Heel of these alloys.

Recently, Carpenter Technology introduced a new ultra high strength steel, Aermet^{tm} 100. Aermet^{tm} 100 can be heat treated to a Rockwell C hardness of 56 while maintaining a K_{IC} value of 100 ksi $\sqrt{in}$ or greater [2], and initially it was hoped that this alloy might alleviate hydrogen embrittlement problems. Steel alloys with hardnesses above Rockwell C 50 have consistently shown K_{IEAC} (K_I for environmentally assisted cracking (EAC)) values in the range of 10-12 ksi$\sqrt{in}$. Initially, open circuit K_{IEAC} values for Aermet^{tm} 100 were reported above 25ksi$\sqrt{in}$. However, subsequent testing[3] at more aggressive potentials (indicative of actual service with sacrificial coatings) showed K_{IEAC} values of only 10-12 ksi$\sqrt{in}$., as shown in Figure 1.

Obviously, there is a need to continue to develop stronger, tougher steels. No other class of material possesses the strength, toughness and affordability of ultra high strength steels. Never-the-less, the significant hydrogen embrittlement problem must be better addressed to realize the full potential of these steels. The ultimate goal of this research is to eventually eliminate the hydrogen susceptibility of high strength steels. This paper specifically discusses efforts to understand and utilize the effects of noble metals in reducing hydrogen embrittlement.

THEORY

Because of the catalytic nature of palladium and platinum, it might seem evident to any physical chemist that these elements would be helpful in reducing hydrogen embrittlement in ultra high strength steels. Numerous researchers have proposed these elements as possible treatments for hydrogen embrittlement. In previous work[4] Brown et al showed the benefit of implanting Pd or Pt into ESR 4340 steel. Notched tensile specimens showed an improvement of as much as 50% in their final failure load under hydrogen embrittlement conditions, as shown in Figure 2. Further work[5] by Buckley et al showed that this effect was limited to the surface region where the implanted species resided. Any crack extending beyond the implanted region lost the beneficial effect of the implanted species, causing the specimen to behave as an unimplanted specimen.

Additionally, Wilde et al have performed work demonstrating the benefit of adding palladium[6] to 4130 steel and PH 13-8 steel. They found that palladium or platinum

concentrations above 1% made the 4130 steel immune to sulfide stress cracking as shown in Figure 3. They concluded that the palladium segregated to inclusions or grain boundaries that were normally the initiation sites of hydrogen induced cracking. The palladium somehow mitigated the action of the hydrogen at these sites.

Scully et al investigated the beneficial effect of palladium in reducing hydrogen embrittlement in PH 13-8 steel[7] (Figure 4). They concluded that PdAl precipitates that resulted acted as beneficial hydrogen traps. Eberhart and others have shown with first principals calculations that Pd should increase the Fe-Fe bond resilience in the presence of hydrogen[8].

To effectively implement the various effects noted above, it is necessary to characterize the hydrogen transport and trapping in these alloys. This understanding should include the delineation of the bulk permeation constant for the hydrogen in these steels, the location of the hydrogen in the microstructure, the composition, location and structure of the hydrogen traps, and the trapping/detrapping constants for the exchange of hydrogen between the bulk alloy and the microstructural traps. Once these properties are known, it should be possible to manipulate these alloys and microstructures to promote "beneficial" hydrogen trapping while reducing the number of harmful traps, thereby maximizing their resistance to hydrogen assisted cracking phenomena.

Dynamic permeation is a technique that analyzes the flux through a membrane as a function of frequency. Cummings[9] has shown that the phase lag and amplitude ratio versus frequency of the input and output waves will reveal the trapping constants within the membrane. If one uses a square wave input, a broad range of frequencies can be studied simultaneously using Fourier theory.

The following is drawn directly from Cummings and Blackburn[9]. The one dimensional diffusion equation in the presence of trapping takes the form of equation 1, where z is the concentration of hydrogen in traps as shown in equation 2. For more detail, see Reference 9.

$$\frac{dc}{dt} + \frac{dz}{dt} = D\frac{\delta^2 c}{\delta x^2} \qquad [1]$$

$$\frac{dz}{dt} = k_a c - k_b z \qquad [2]$$

Equations 1 and 2 can be split into time dependent and steady state parts to produce the following equations.

$$\frac{dz}{dt} = k_a \mathbf{c} - k_b \mathbf{z}, \qquad k_a c_s = k_b z_s \qquad [3]$$

$$\frac{d\mathbf{c}}{dt} + \frac{d\mathbf{z}}{dt} = D\frac{\delta^2 \mathbf{c}}{\delta x^2}, \qquad D\frac{\delta^2 c_s}{\delta x^2} = 0 \qquad [4]$$

$$\mathbf{J} = -D\frac{\delta \mathbf{c}}{\delta x}, \qquad J_s = -\frac{D}{l}\left[c_s(0) - c_s(l)\right] \qquad [5]$$

The time dependent rate equation can be written according to equation 6.

$$\mathbf{z} = \left(\frac{d}{dt} + k_b\right)^{-1} k_a \mathbf{c} \qquad [6]$$

Conservation of mass produces equations 7 and 8.

$$\frac{dc}{dt} = -\frac{dJ}{dx} - \frac{dz}{dt} \qquad [7]$$

$$\left(\frac{d}{dt}+k_a+k_b\right)\frac{d\mathbf{c}}{dt}=D\left(\frac{d}{dt}+k_b\right)\frac{d^2\mathbf{c}}{dx^2} \qquad [8]$$

The solution for equation 8 describes the concentration modulations propagating through a membrane. It is of the form shown in equations 9 and 10, where **F** and **G** are determined by boundary conditions and **b** is a complex function of w, k_a, k_b and D.

$$\mathbf{c}(x)=\left\{\mathbf{F}\exp[\mathbf{b}(l-x)]+\mathbf{G}\exp[\mathbf{b}(x-l)]\exp(\mathbf{i}\omega t)\right\} \qquad [9]$$

$$\mathbf{J}(x)=D\mathbf{b}\left\{\mathbf{F}\exp[\mathbf{b}(l-x)]-\mathbf{G}\exp[\mathbf{b}(x-l)]\exp(\mathbf{i}\omega t)\right\} \qquad [10]$$

Substituting equation 9 into equation 8 provides the following condition on **b**.

$$D\mathbf{b}^2=\frac{k_a\omega^2+\mathbf{i}\omega\left(\omega^2+k_b{}^2+k_ak_b\right)}{\left(\omega^2+k_b{}^2\right)} \qquad [11]$$

If we take equations 9 and 10 and relate conditions at x=0 and x=l, we end up with the following relationship.

$$\begin{pmatrix}\mathbf{c}(0)\\ \mathbf{J}(0)\end{pmatrix}=\begin{pmatrix}\cosh(\mathbf{b}l) & \left(\frac{1}{D\mathbf{b}}\right)\sinh(\mathbf{b}l)\\ D\mathbf{b}\sinh(\mathbf{b}l) & \cosh(\mathbf{b}l)\end{pmatrix}\begin{pmatrix}\mathbf{c}(l)\\ \mathbf{J}(l)\end{pmatrix} \qquad [12]$$

If we keep the concentration at the output surface essentially at zero, then equation 12 reduces to a simplified expression shown in equation 13.

$$\mathbf{J}(0) = \cosh(\mathbf{b}l)\mathbf{J}(l) \qquad [13]$$

Therefore, Cummings[9] et al. have shown the relationship between the input and output flux is a complex hyperbolic cosine relationship. This relationship will display a characteristic phase lag and magnitude ratio as a function of frequency, diffusion constant, and trapping and detrapping constants. Figures 5 and 6 show a sample calculation for a material 0.1 mm thick with a diffusion constant of 3×10^{-7} cm^2/s. Dimensionless numbers A and B are used according to equation 14.

$$A = \frac{k_a l^2}{2D}, \qquad B = \frac{k_b l^2}{2D} \qquad [14]$$

These figures demonstrate that if we monitor the input and output fluxes using a square wave input we can obtain the resultant phase lag and magnitude ratios as a function of frequency. This information can be fit to our theoretical model and the trapping and detrapping constants can be obtained. Thus, we can quantify the effect of traps created by elements such as palladium. If we couple this technique with others that allow us to determine the nature and density of traps, we can then determine quantitatively the effect of noble metal additions to ultra high strength steels. Three techniques that will allow us to do this are Transmission Electron Microscopy (TEM), Forward Recoil Spectrometry (FReS) and Nuclear Reaction Analysis (NRA). TEM will be used to determine the chemical composition, location and structure of traps in the material. FRS and nuclear reaction analysis will allow us to determine the amount of hydrogen present as a function of depth. If we carefully manipulate the microstructure, and determine the trapping/detrapping parameters as a function of these changes, then we can determine the trapping due to a particular species. Subsequent TEM work will determine the trap composition and microstructure.

EXPERIMENTAL PROCEDURE

Dynamic permeation studies on palladium thin films have been completed. Samples of 99.95% pure palladium, 0.1 mm thick by 25 mm square were utilized. They were

annealed at 900°C for 3 hours and then etched in a 3:1 by volume mixture of HCl and HNO_3. A 2.5 cm^2 area was exposed on two sides to 0.1 N NaOH. The potential on the input side was modulated as a square wave at various characteristic frequencies ranging from 0.01 Hz to 0.001 Hz. The output flux (current) was measured at a potential of 0.3 V versus the saturated calomel electrode. The input and output signals were time marked in order to determine phase relationships. The resultant waves were then submitted to a fast Fourier transform to create a phase versus frequency profile and magnitude versus frequency profile. This information is compared to the theoretical models to determine the trapping activity in the material.

RESULTS AND DISCUSSION

Phase lag and magnitude ratio data for a sample subjected to a square wave input varying from 0.24 mA/cm^2 to 0.4 mA/cm^2 over a time period of 100 seconds are shown in Figures 7 and 8. The best fit to the data occurs for a diffusion constant of 3 x 10-7 cm^2/s and a trapping constant, A, of 100 and a detrapping constant, B, of 30. However, it is evident that a more extensive analysis needs to be performed to account for the jog in the experimental data phase lag, as well as the deviation from ideal trapping behavior seen in Figure 8.

Currently, our efforts are focused on resolving the difficulties outlined above. Additionally, we will examine the effect of surface kinetics and include them in the overall relationship previously derived by Cummings and Blackburn[9].

CONCLUSIONS

Noble metal additions show promise as a means to significantly reduce the susceptibility of ultra high strength steels to hydrogen embrittlement. Utilizing ion beam methods, dynamic permeation experiments, and transmission electron microscopy, we expect to describe the behavior of favorable traps. This description will include the trapping constants, the density and microstructure of the traps, and the concentrations of hydrogen as a function of the trap density.

REFERENCES:

1. W.H. Johnson, Proc. Roy. Soc., London, vol. 23, p 168-179, 1874-1875.

2. P.F. Buckley, J. Graves,. B. Placzankis and R. Brown, Proceedings of the 1992 Tri-Service Corrosion Conference, Plymouth, MA, 1992 .

3. P.F. Buckley, R. Brown, and J.H. Graves, E.U. Lee, C.E. Neu and J. Kozol. Proceedings of the 1993 Sagamore Army Materials Conference, Plymouth, MA, 1993.

4. Private correspondence and unpublished data 1989.

5. P. Buckley, B. Placzankis, L. Lowder, I.G. Brown and R. Brown, Surface Coatings and Technology , 49 , p 500-503, 1991.

6. B.E. Wilde, C.D. Kim, and J.C Turn Jr., Corrosion, Vol. 38, p 515-524, 1982.

7. J.R. Scully, J.A. Van Den Avyle, A.D. Cieslak, A.D. Romig Jr., Metallurgical Transactions, Vol. 22A, p 2429-244, 1991.

8. M. Eberhart, Under an ARL-MD contract, 1992.

9. D.L. Cummings and D.A. Blackburn, Metallurgical Transactions, Vol. 16A, p 1013-1024, 1985.

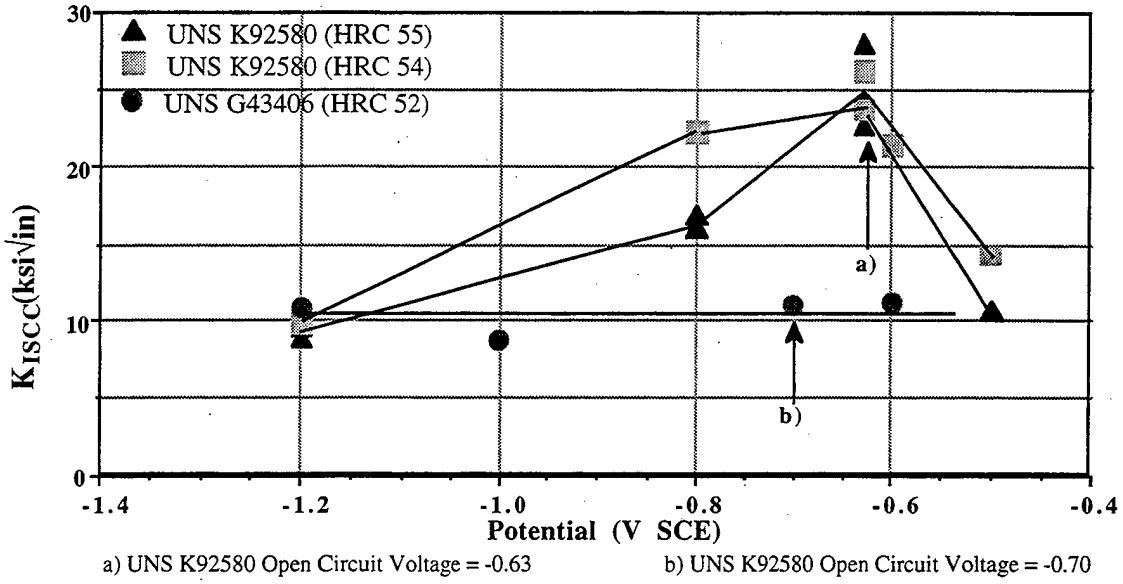


Figure 1. KIEAC as a function of potential for Aermet[tm] 100 (UNS K92580) and ESR 4340 (UNS G43406), from Reference 3.

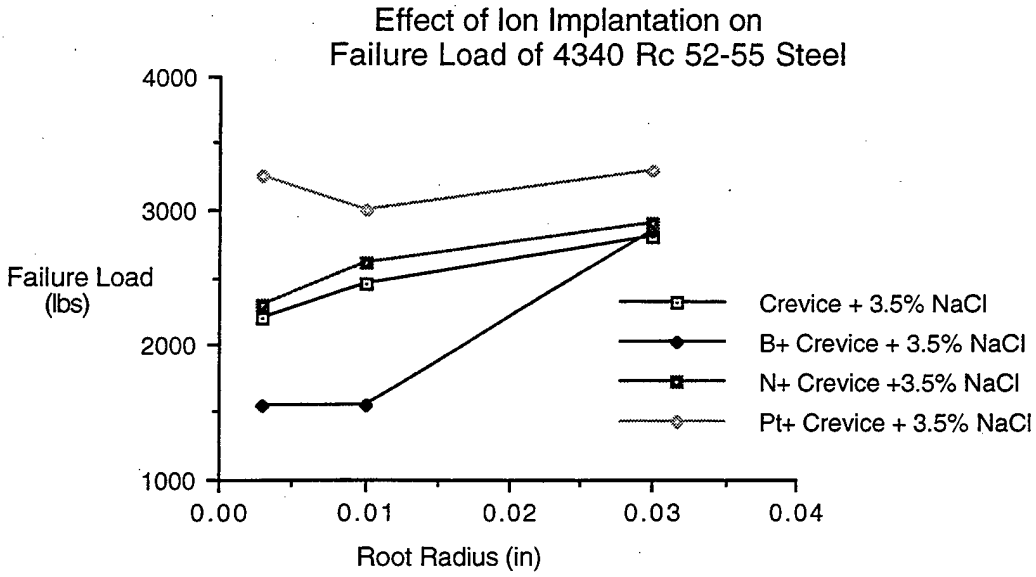


Figure 2. Failure load for notched tensile specimens under hydrogen embrittlement conditions, from Reference 4.

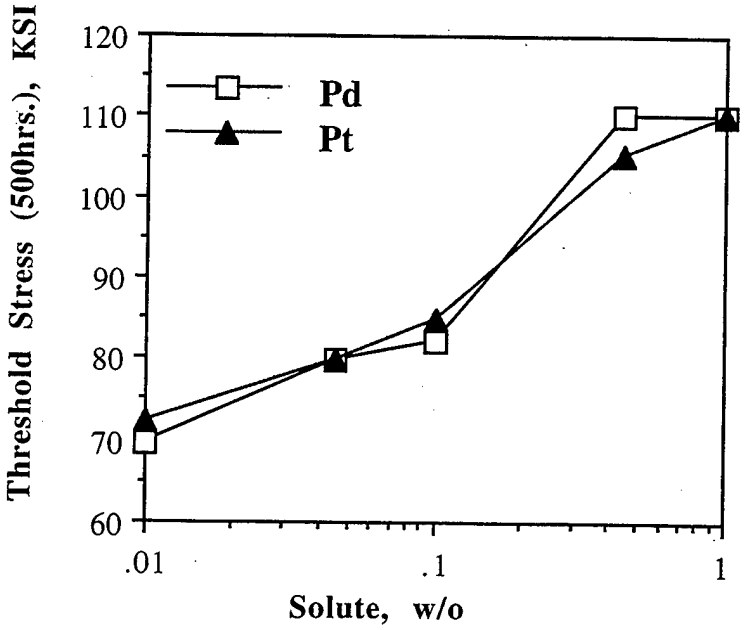


Figure 3. Effect of palladium additions for 4130 steel tested in NACE TM-01-77 sulfide stress cracking solution, from Reference 6.

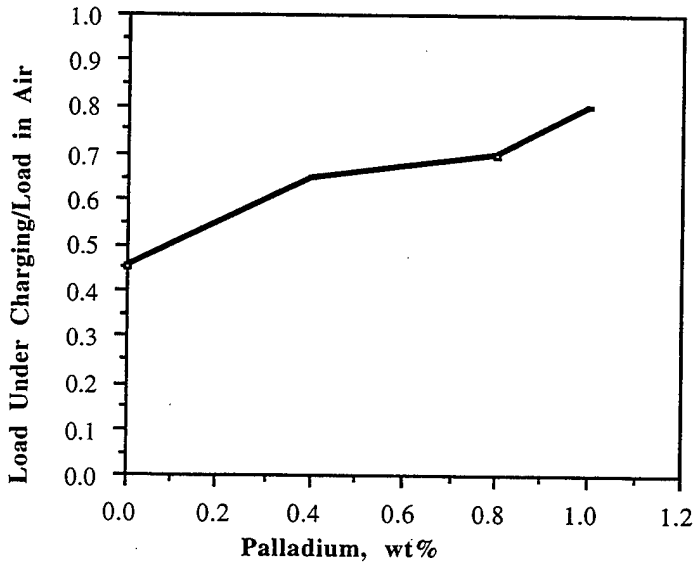


Figure 4. The effect of palladium additions to PH13-8 Steel. Notched tensile specimens were tested in 0.6 M NaCl under cathodic polarization of -25mA/cm^2 and a strain rate between 10^{-7} to 10^{-6} s^{-1}. From Reference 7.

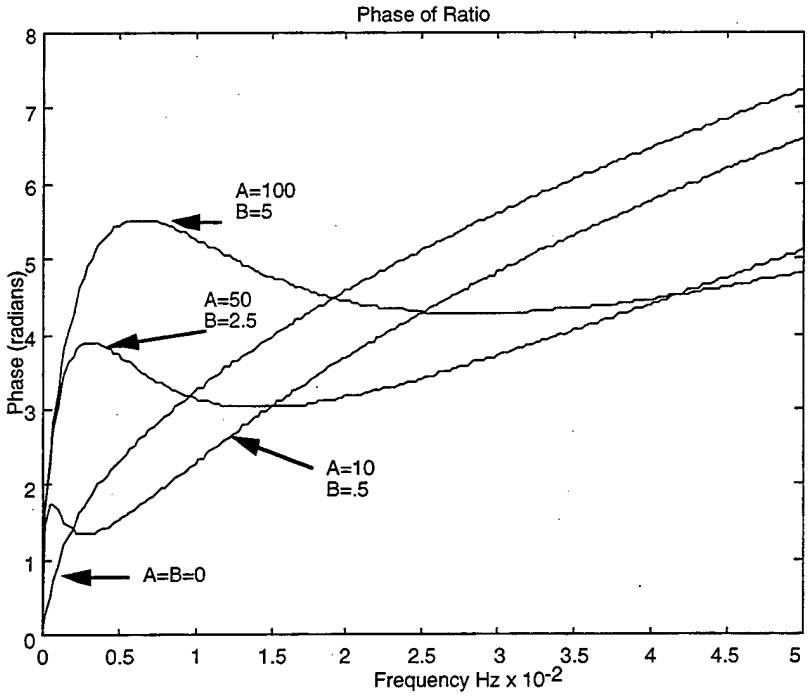


Figure 5. Calculated phase lag a function of frequency for a 0.1 mm sample with a diffusion constant of 3 x 10^{-7} cm^2/s.

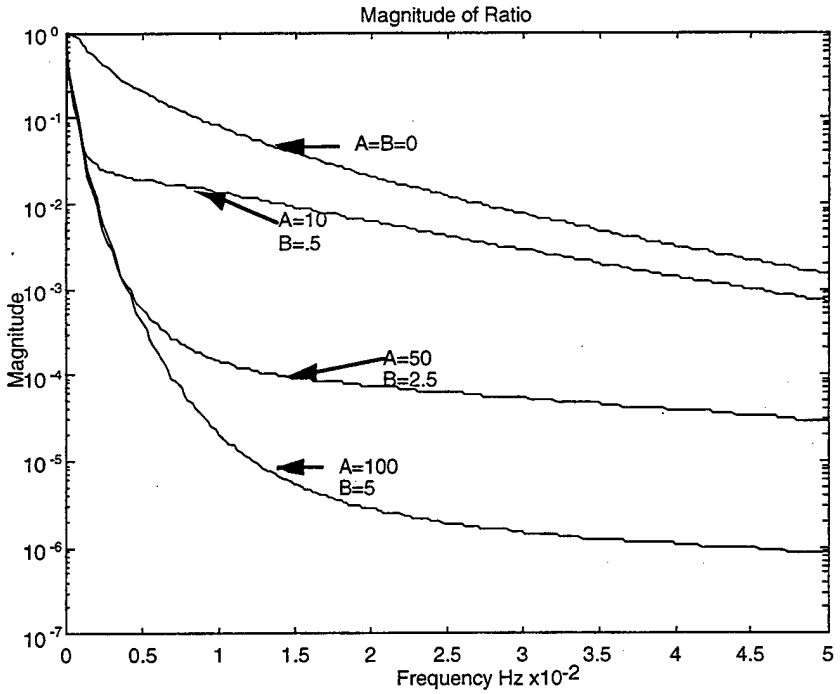


Figure 6. Calculated amplitude ratio as a function of frequency for a 0.1 mm sample with a diffusion constant of 3 x 10^{-7} cm^2/s.

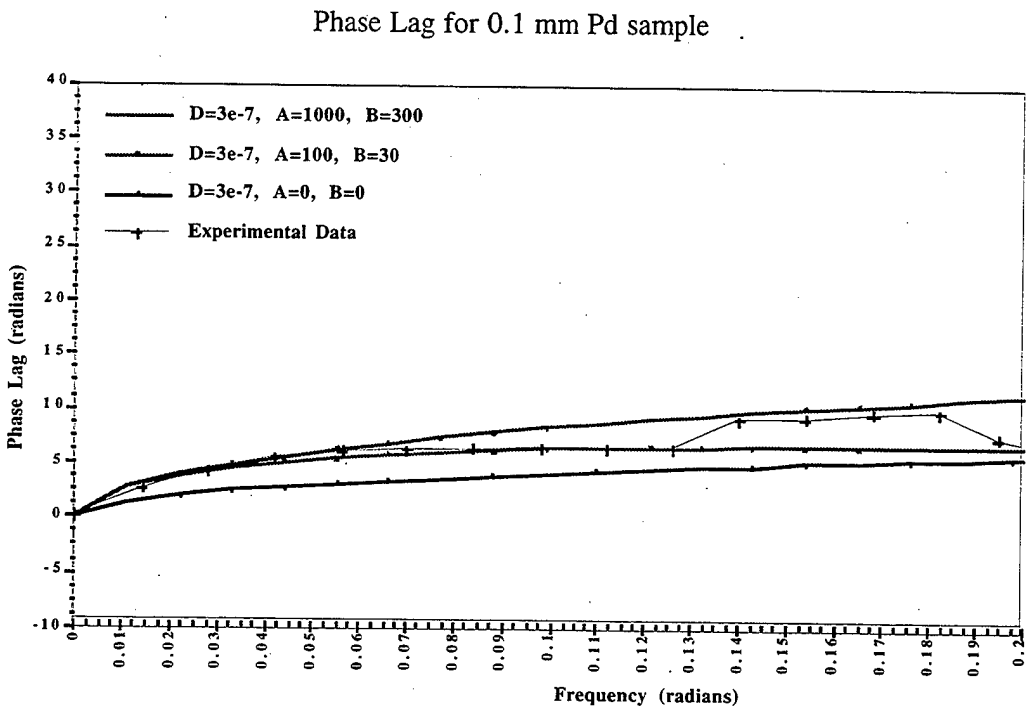


Figure 7. Experimental and calculated phase lag data for a sample subjected to a square wave input varying from 0.24 mA/cm^2 to 0.4 mA/cm^2 over a time period of 100 seconds.

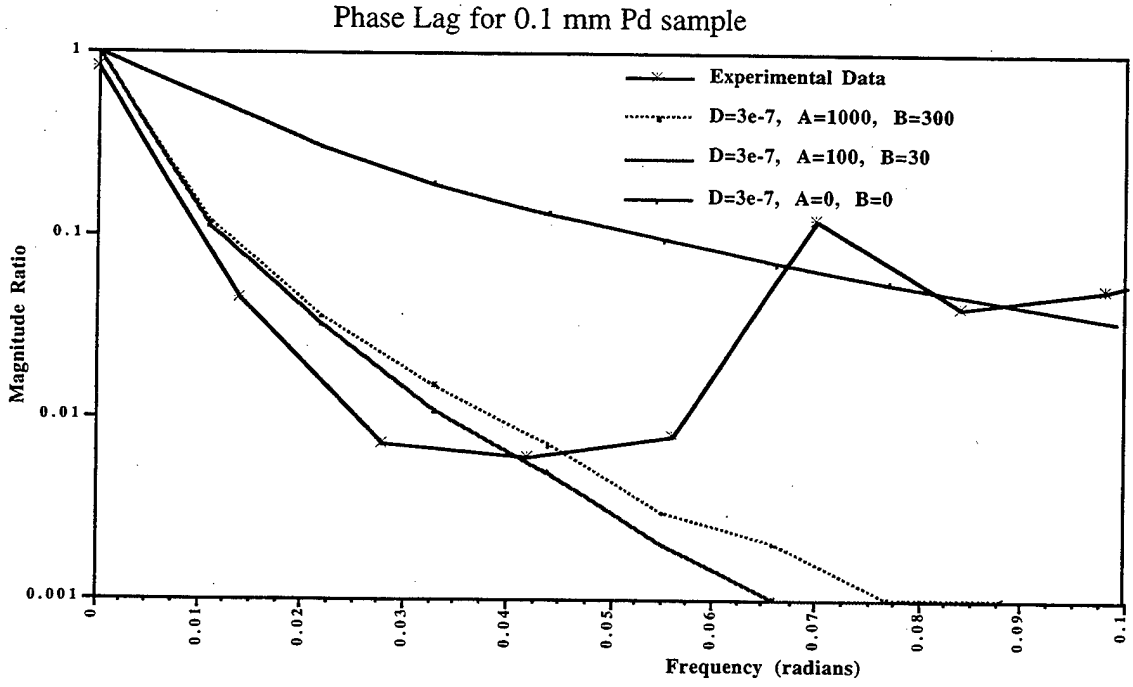


Figure 8. Experimental and calculated magnitude ratio data for a sample subjected to a square wave input varying from 0.24 mA/cm^2 to 0.4mA/cm^2 over a time period of 100 seconds.